ISSN 1806-7662

IWT 2009 International Workshop on Telecommunications

February 16th - 19th 2009 - São Paulo - Brazil

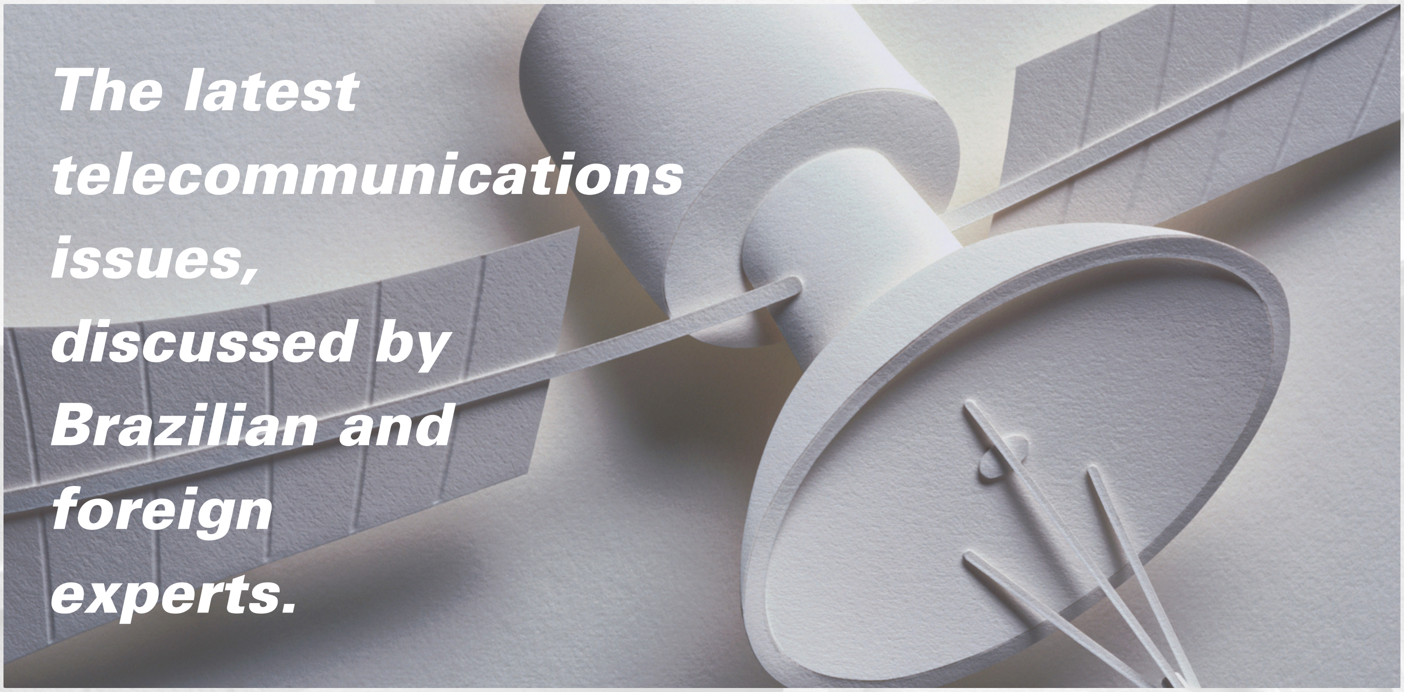

PROCEEDINGS

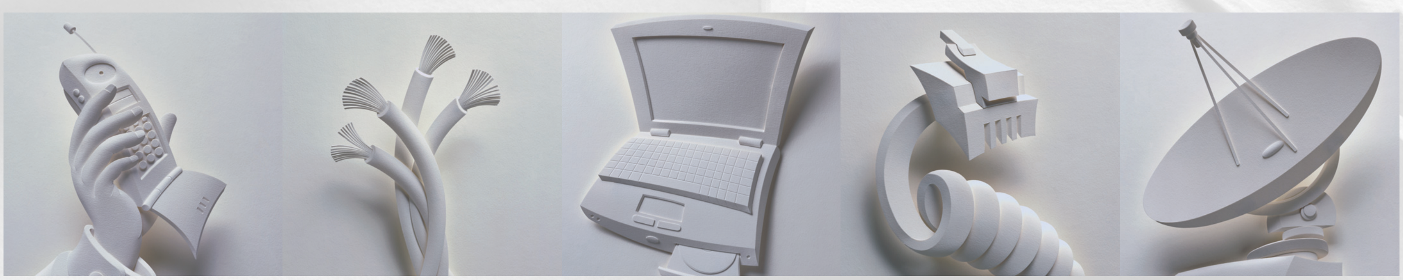

Realization

Inatel
Instituto Nacional de Telecomunicações

Technical Co-realization

UNICAMP

FEEC

Partner

ERICSSON
TAKING YOU FORWARD

IEEE
MG SECTION

Support

SBrT
Sociedade Brasileira de Telecomunicações

Sponsors

LINEAR

SENSE
Sensores e Instrumentos

ativa
SOLUÇÕES

IWT 2009 International Workshop on Telecommunications
February 16th - 19th 2009 - São Paulo - Brazil

IWT 2009
International Workshop on Telecommunications
São Paulo, SP, Brazil
February 16th-19th, 2009

PROCEEDINGS

Realization

Inatel
Instituto Nacional de Telecomunicações

Technical Co-realization

UNICAMP

FEEC

Partner

ERICSSON
TAKING YOU FORWARD

IEEE MG SECTION

Support

SBrT
Sociedade Brasileira de Telecomunicações

Sponsors

LINEAR

SENSE
Sensores e Instrumentos

ativa
SOLUÇÕES

LOCATION

Ericsson
Rua Maria Prestes Maia, 300
Vila Guilherme - São Paulo - SP, 02047000

I612 IWT 2009 – International Workshop on Telecommunications (2009: Santa Rita do Sapucaí)

Proceedings of the International Workshop on Telecommunications – IWT, 16-19 February 2009, Santa Rita do Sapucaí, Minas Gerais, Brasil. Published by Carlos Alberto Ynoguti. — Santa Rita do Sapucaí: INATEL, 2009.

256 p. il.
ISSN 1806-7662

1. Telecommunications - Workshop I. Título. II. Ynoguti, Carlos Alberto.

CDD - 621.38
CDU - 621.39

Message from the General Chair

On behalf of the Organizing and Technical Committees, it's our great pleasure to welcome you all to Ericsson in São Paulo. The International Workshop on Telecommunications (IWT2009) is the third issue of a very successful conference, and we hope it will serve as a forum for information and ideas exchange, an opportunity to expand our contacts and, why not, make some new friends.

In this opportunity, we would like to thank the Technical and Organizing Committees, the organizations that provided financial support, the secretariat, the participants, and everyone who made this conference possible.

We'd like to register our special thanks to Ericsson, that believed in our project and offered to be our partner in it.

On behalf of all the people who worked hard to prepare this conference, we welcome all the authors, participants, students and professionals that showed interest in participating and contributing to the development of such event.

Prof. Carlos Alberto Ynoguti
IWT2009 General Chair

ORGANIZING COMMITTEE

General Chair – Carlos Alberto Ynoguti – INATEL
Technical Program Chair – José Marcos Câmara Brito – INATEL
Technical Program Co-Chair – Dalton Soares Arantes – FEEC/UNICAMP
Technical Program Co-Chair – Ivanil S. Bonatti – FEEC/UNICAMP
Technical Program Co-Chair – Renato Baldini Filho – FEEC/UNICAMP
Proceedings Chair – Luciano Leonel Mendes – INATEL
Marketing Chair – Antônio Marcos Alberti – INATEL
Subscriptions Chair – Carlos Nazareth Motta Marins – INATEL
Local Arrangements Chair – Marcelo de Oliveira Marques – INATEL
Finance Chair – Carlos Augusto Rocha – INATEL

TECHNICAL PROGRAM COMMITTEE

Adão Silva - University of Aveiro - Portugal
Alfredo Goldman - University of Sao Paulo (USP) - Brazil
Anderson S. L. Gomes - Federal University of Pernambuco (UFPE) - Brazil
André L. Brandão - Communications Research Centre - Canada
Anilton Salles Garcia - Federal University of Espírito Santo (UFES) - Brazil
Antonio A. F. Loureiro - Federal University of Minas Gerais (UFMG) - Brazil
Antonio Marcos Alberti - Inatel - Brazil
Arismar Cerqueira Sodré Junior - University of Campinas (Unicamp) - Brazil
Bartolomeu Uchoa Filho - Federal University of Santa Catarina (UFSC) - Brazil
Carlos Alberto Ynoguti - Inatel - Brazil
Carlos Nazareth Motta Marins - Inatel - Brazil
Carlos Roberto dos Santos - Inatel - Brazil
César Kyn d'Ávila - CEDET - Brazil
Emily Rozenshine - Ben Gurion University - Israel
Geraldo Gil Ramundo Gomes - Inatel - Brazil
Gerson F. M. Lima - ProengTelecom - Brazil
Gustavo Corrêa Lima - Federal University of Santa Catarina - Brazil
Helen Karatza - Aristotle University of Thessaloniki - Greece
Ian F. Akyildiz - Georgia Institute of Technology - USA
Jaime Portugheis - University of Campinas (Unicamp) - Brazil
Joel J. P. C. Rodrigues - University of Beira Interior - Portugal
Jorge Moreira de Souza - Fitec - Brazil
José A. Apolinário Jr - Militar Institute of Engineering (IME) - Brazil
Luciano Leonel Mendes - Inatel - Brazil
Luis Fernando R. Molinaro - University of Brasília (UnB) - Brazil
Marcelo S. de Alencar - Federal University of Campina Grande (UFCG) - Brazil
Michel Daoud Yacoub - University of Campinas (Unicamp) - Brazil
Miguel Arjona Ramirez - University of Sao Paulo (USP) - Brazil
Mohammed Atiquzzaman - University of Oklahoma - USA
Moisés Vidal Ribeiro - Federal University of Juiz de Fora (UFJF) - Brazil
Nelson L. S. da Fonseca - University of Campinas (Unicamp) - Brazil
Omar C. Branquinho - Catholic University of Campinas (PUC) - Brazil
Otto Strobel - Esslingen University of Applied Sciences - Germany
Pascal Lorenz - University of Haute Alsace - France
Peter J. Chitamu - University of Witwatersrand - South Africa
Petre Dini - Cisco Systems - USA
Rainer Doster - University of Applied Sciences Esslingen - Germany
Rausley A. A. de Souza - Inatel - Brazil
Reginaldo Palazzo Jr. - University of Campinas (Unicamp) - Brazil
Sanwar Ali – Indiana University of Pennsylvania – USA
Shusaburo Motoyama - University of Campinas (Unicamp) - Brazil
Soong Boon Hee - Nanyang Technological University - Singapore
Yuzo Iano - University of Campinas (Unicamp) - Brazil

CONTENTS

Technical Session I - OPTICAL COMMUNICATIONS AND PHOTONIC

Technical Session II - NETWORKS I

Technical Session III - COMMUNICATIONS

Technical Session IV - ELECTROMAGNETISM, MICROWAVE AND SIGNAL PROCESSING

Technical Session V - NETWORKS II

Technical Session VI - DIGITAL COMMUNICATIONS

Technical Session VII - DIGITAL COMMUNICATIONS AND ANTENNAS

Technical Session IX - WIRELESS NETWORKS II

Technical Session IX - IMAGE, VOICE, SPEECH, VIDEO AND MOTION

Trends on Microwave Photonic Filters Based on Polarization Maintaining Fiber Delay Lines

Carla de Sousa Martins
Instituto Tecnológico de Aeronáutica - ITA
Pça. Mal. Eduardo Gomes, 50
S. J. dos Campos, SP - Brazil
carlasm@ita.br

Olympio Lucchini Coutinho
Instituto Tecnológico de Aeronáutica - ITA
Pça. Mal. Eduardo Gomes, 50
S. J. dos Campos, SP - Brazil
olympio@ita.br

José Edimar Barbosa Oliveira
Instituto Tecnológico de Aeronáutica - ITA
Pça. Mal. Eduardo Gomes, 50
S. J. dos Campos, SP - Brazil
edimar@ita.br

William dos Santos Fegadolli
Instituto Tecnológico de Aeronáutica - ITA
Pça. Mal. Eduardo Gomes, 50
S. J. dos Campos, SP - Brazil
fegadoli@ita.br

Vilson Rosa de Almeida
Instituto de Estudos Avançados - IEAv
Rod. dos Tamoios, km 5.5
S. J. dos Campos, SP - Brazil
vilson@ieav.cta.br

***Abstract*—Trends on research aiming microwave photonic filters (MPF) which comprises an electrooptic modulator and polarization-maintaining fiber (PMF) delay lines are addressed. MPF configuration in which light from a Mach-Zehnder modulator (MZM) feeds a PMF is modeled, bearing in mind that the time delay difference between the two orthogonal modes of the fiber gives rise to the filter unit time delay. A proof of principle MPF prototype having positive coefficients due to a single length of PMF was built and tested. Also investigated was the enhancement of its performance by adding an extra section of PMF, which enables a four tap MPF.**

***Index Terms*—Microwave filter, microwave photonics, microwave photonic filter, polarization-maintaining fiber (PMF).**

I. Introduction

Nowadays, optical processing of radio-frequency (RF) signals, especially microwave signals, has become a very attractive subject, because the use of photonic components to implement conventional electrical functions allows one to take advantage of photonics features such as high immunity to electromagnetic interference (EMI), wide bandwidth capability, low loss, light weight and parallelism [1]. While the optical processing of digital signals is well established, especially in the area of telecommunication, the optical processing of analog signals has been growing up mostly due to the advances made in fiber optics and electrooptic modulators design and fabrication. As a matter of fact, several research groups have demonstrated the application of optical signal processing in RF analog fiber optic link, namely radio-over-fiber applications, remote antenna control, phased array antennas, etc [2]-[5].

This publication addresses the issue of microwave filters on the context of optical processing of analog signals. To this aim, it emphasizes the MPF configurations having a MZM connected to a PMF based delay line. The required delay time can be achieved either with a single fiber section or by cascade connecting two or more properly oriented sections of PMF fiber, thus giving rise to two or more filter coefficients, respectively.

II. Theoretical Analysis

The schematic diagram of the proposed MPF is illustrated in Fig. 1.

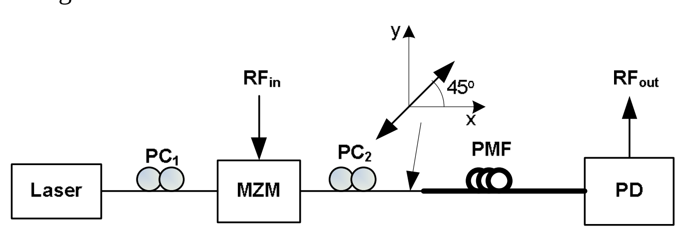

Fig.1. Schematic diagram of the MPF based on a MZM and a PMF delay line. MZM: Mach-Zehnder Modulator; PC: Polarization Controller; PMF: Polarization Maintaining Fiber; PD: Photodetector.

A linearly polarized CW laser source is sent to the MZM through a polarization controller PC1. Since the MZM is fed by a microwave signal, it yields a modulated light wave which is sent to the PMF. The wave polarization orientation at the entrance of the fiber is set to be at 45° with respect to the PMF fast axis (represented by x direction). Two guided orthogonal polarization modes with different group velocities are generated in the PMF, namely slow (s) and fast (f) modes, so a filter unit time delay is generated.

The optical field at the output of the MZM, can be mathematically expressed as

$$E(t)=\frac{E_0}{2}e^{j\omega_0 t}\left\{1+e^{-j\varphi}e^{jM\sin(\omega_m t)}\right\}, \tag{1}$$

where ω_m is the microwave angular frequency, M is the modulation index, φ is the initial phase difference between the two branches of the MZM and E_0 is the amplitude of the optical electric field generated by the laser source. In eq. (1) push-pull drive was ignored in order to simplify the manipulation of the equations. Applying the optical signal from the output of MZM to a PMF at a polarization angle of 45°, it can be divided in two orthogonal polarization modes, corresponding to the fast and slow axis of the PMF. Considering that $\hat{x}$ and $\hat{y}$ directions correspond to the fast and slow axes, respectively, we can write the input signal at PMF as

$$\begin{aligned}E_{in}^{(1)}(t)=\frac{E_0}{2\sqrt{2}}e^{j\omega_0 t}\Big\{&\left[1+e^{-j\varphi}e^{jM\sin(\omega_m t)}\right]\hat{x}\\ &+\left[1+e^{-j\varphi}e^{jM\sin(\omega_m t)}\right]\hat{y}\Big\}.\end{aligned} \tag{2}$$

Owing to the fiber birefringence, each orthogonal mode has a specific group delay, τ_s and τ_f. Thanks to this, after propagating through the PMF, a filter unit time delay is generated and is given by $T=\tau_s-\tau_f$, which corresponds to a free spectral range (FSR) of $1/T$. The optical field at the output of the PMF is

$$\begin{aligned}E_{out}^{(1)}(t)=&\frac{E_0}{2\sqrt{2}}e^{j\omega_0 t}\left[1+e^{-j\varphi}e^{jM\sin(\omega_m t)}\right]\hat{x}\\ &+\frac{E_0}{2\sqrt{2}}e^{j\omega_0(t+T)}\left\{1+e^{-j\varphi}e^{jM\sin[\omega_m(t+T)]}\right\}\hat{y}\Big\}.\end{aligned} \tag{3}$$

Considering a small modulation index ($M \ll 1$), we can further simplify eq. (3) as

$$\begin{aligned}E_{out}^{(1)}(t)=&\frac{E_0}{2\sqrt{2}}e^{j\omega_0 t}\left\{1+e^{-j\varphi}\left[1+jM\sin(\omega_m t)\right]\right\}\hat{x}\\ &+\frac{E_0}{2\sqrt{2}}e^{j\omega_0(t+T)}\left\{1+e^{-j\varphi}\left\{1+jM\sin\left[\omega_m(t+T)\right]\right\}\right\}\hat{y}.\end{aligned} \tag{4}$$

Since the polarizations of the two guided modes of the PMF are orthogonal, no interference would occur between them. So, the total photocurrent detected by the photodetector (PD) is the sum of each photocurrent generated by the two polarization modes and can be mathematically expressed as

$$I(t)=R\left|E_{out_x}^{(1)}(t)\right|^2+R\left|E_{out_y}^{(1)}(t)\right|^2, \tag{5}$$

where R is the responsivity of the PD. Neglecting dc and higher order harmonics, the recovered RF signal which is proportional to the photocurrent detected is then given by

$$E_{rf}(t)=\frac{RE_0^2}{4}M\sin\varphi\left\{\sin(\omega_m t)+\sin\left[\omega_m(t+T)\right]\right\}. \tag{6}$$

In order to evaluate the spectral contents of the photocurrent given in (6), one relays on the Fourier transform technique to obtain

$$\tilde{H}(\omega)=\frac{RE_0^2 M\sin\varphi}{2}\times\left[\delta(\omega-\omega_m)+e^{j\omega_m T}\delta(\omega-\omega_m)\right]. \tag{7}$$

It can be noted that eq. (7) corresponds to a two tap lowpass microwave filter, since the two coefficients are positive, provided that $\sin\varphi\neq 0$. The maximum amplitude of the recovered signal coincides with $\varphi=\pi/2$, which corresponds to the quadrature point of the MZM transfer function.

Now, let us consider a second length of PMF with its axis aligned at an angle of 45° relative to the axis of the first section of PMF. Then the two guided modes of the first section would be projected to the direction of the polarization axis of the second section and add coherently. Thus, the optical field at the input of the second section of PMF is

$$\begin{aligned}E_{in}^{(2)}(t)=&\frac{E_0}{4}e^{j\omega_0 t}\left\{1+e^{-j\varphi}\left[1+jM\sin(\omega_m t)\right]\right\}\hat{x}'\\ &+\frac{E_0}{4}e^{j\omega_0(t+T)}\left\{1+e^{-j\varphi}\left\{1+jM\sin\left[\omega_m(t+T)\right]\right\}\right\}\hat{x}'\\ &+\frac{E_0}{4}e^{j\omega_0 t}\left\{1+e^{-j\varphi}\left[1+jM\sin(\omega_m t)\right]\right\}\hat{y}'\\ &+\frac{E_0}{4}e^{j\omega_0(t+T)}\left\{1+e^{-j\varphi}\left\{1+jM\sin\left[\omega_m(t+T)\right]\right\}\right\}\hat{y}',\end{aligned} \tag{8}$$

where $\hat{x}'$ and $\hat{y}'$ corresponds to the fast and slow axis of the second section of PMF.

Considering that the second length of PMF provides a total delay difference between its guided modes that is twice the total time delay of the first section, we can write the optical field at the output of the second section of PMF as

$$\begin{aligned}E_{out}^{(2)}(t)=&\frac{E_0}{4}e^{j\omega_0 t}\left\{1+e^{-j\varphi}\left[1+jM\sin(\omega_m t)\right]\right.\\ &\left.+e^{j\omega_0 T}+e^{-j\varphi}e^{j\omega_0 T}\left\{1+jM\sin\left[\omega_m(t+T)\right]\right\}\right\}\hat{x}'\\ &+\frac{E_0}{4}e^{j\omega_0(t+2T)}\left\{1+e^{-j\varphi}\left\{1+jM\sin\left[\omega_m(t+2T)\right]\right\}\right.\\ &\left.+e^{j\omega_0 T}+e^{-j\varphi}e^{j\omega_0 T}\left\{1+jM\sin\left[\omega_m(t+3T)\right]\right\}\right\}\hat{y}',\end{aligned} \tag{9}$$

Recurring again to (5), taking into account the optical field at the output of the second section of PMF expressed in (9), and neglecting dc and higher order harmonics, the recovered RF signal would be given by

$$E_{rf}(t)=\frac{RE_0^2 M}{8}\times\begin{bmatrix}C_1\sin\omega_m t+C_2\sin\omega_m(t+T)\\ +C_3\sin\omega_m(t+2T)+C_4\sin\omega_m(t+3T)\end{bmatrix}, \tag{10}$$

where the coefficients obey the following relationship

$$\begin{cases} C_1 = C_3 = \sin\varphi + \sin\left(\varphi + \dfrac{2\pi c}{\lambda}T\right) + \sin\left(\dfrac{2\pi c}{\lambda}T\right) \\ C_2 = C_4 = \sin\varphi + \sin\left(\varphi - \dfrac{2\pi c}{\lambda}T\right) - \sin\left(\dfrac{2\pi c}{\lambda}T\right) \end{cases} \quad (11)$$

and λ is the free space wavelength of laser source and c is the velocity of light in vacuum.

The Fourier transform of (10) reveals a four tap microwave filter behavior, as stated below

$$\tilde{H}(\omega) = \frac{RE_0^2 M}{8} \times \begin{bmatrix} C_1\delta(\omega-\omega_m) \\ +C_2 e^{j\omega_m T}\delta(\omega-\omega_m) \\ +C_3 e^{j\omega_m 2T}\delta(\omega-\omega_m) \\ +C_4 e^{j\omega_m T}\delta(\omega-\omega_m) \end{bmatrix}. \quad (12)$$

A lowpass filter characteristic is achieved when C_1, C_2, C_3, $C_4 > 0$. Moreover, from (11) one observes that when $\varphi = \pi$ or $2\pi cT/\lambda = K\pi$ (K is an integer) the four coefficients have the same value; however under such conditions they are all null. For any other arbitrary φ, all coefficients are positive but different in magnitudes, producing an impulse response that is not symmetrical, and consequently distorted.

It can also be seen that when φ=0, equations (11) yield $C_1 = -C_2 = C_3 = -C_4 = 2\sin(2\pi cT/\lambda)$. This constraint leads to a bandpass filter characteristic, as a consequence of the negative coefficients, which will be maximized when $2\pi cT/\lambda = (2K+1)\pi/2$.

III. Experimental Results

The experimental setup used to make the measurements is shown in Fig. 2. We used a tunable diode laser at a wavelength of 1300 nm coupling light into a 10 Gb/s Mach-Zehnder intensity modulator with V_π = 6.6 V. The maximum optical power obtained from the laser source was 6.1 mW. The photodetector that was used in the experiment has a responsivity of 0.25 A/W. An additional RF amplifier with a gain of 33 dB and input impedance of 50 Ω was used in order to increase the level of the detected signal. Both PC_1 and PC_2 used were manual polarization controllers. In order to ensure the 45° polarization angle of light at the input of the PMF delay line, a polarizer should be placed before the PMF. But in this case, the output level of detected RF signal was not high enough to be considered. Thus, a two meter long polarizing fiber (PZ) Corning SP-1310, with an extinction ratio greater than 30 dB was used instead of polarizer in order to decrease optical losses. The PZ fiber was spliced with its axis aligned at an angle of 45° relative to the axis of the first PMF section. The PMF used was 3M-FS-HB-6621. The amplitude responses of the filter were obtained with Agilent 8714EF RF Network Analyzer.

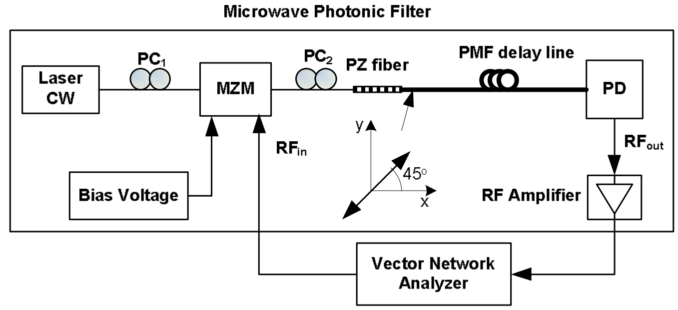

Fig.2. Experimental Setup for the MPF.

First we have considered a two tap MPF comprising a single PMF section with a length of 300 m that produces a differential group delay of 605 ps, which corresponds to a FSR of 1652.9 MHz. The measured amplitude frequency response for this filter is shown in Fig.3a whereas the theoretical normalized amplitude frequency response is shown in Fig.3b. It can be verified that the measured frequency response is in very good agreement with the predicted results.

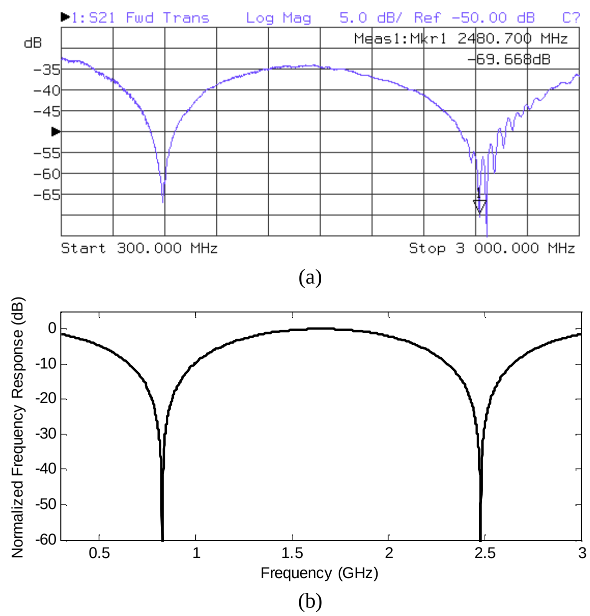

Fig.3. Measured (a) and theoretical (b) results for a two tap MPF.

A four tap MPF was also implemented by splicing a second section of PMF with a length of 150 m at an angle of 45° relative to axis of the first section, producing a differential group delay of 302.7 ps. The availability of PMF at laboratory has imposed the choice of this size of PMF as the second section. Unfortunately, this length of fiber has set the FSR of the four tap MPF at 3303.6 MHz, invisible to the RF network analyzer used. Results for this configuration are shown in Fig.4. A distorted lowpass filter characteristic was obtained by adjusting φ near π rad, as shown in Fig.4a. Note that is not possible to see the peak of the second resonance of the filter expected to be at around 3303.6 MHz.

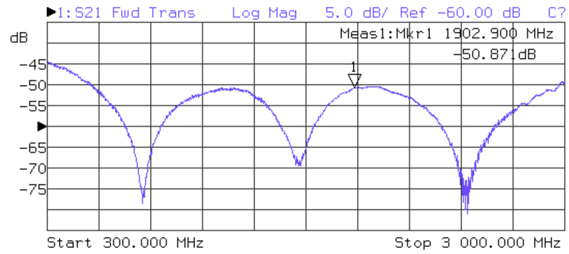

(a)

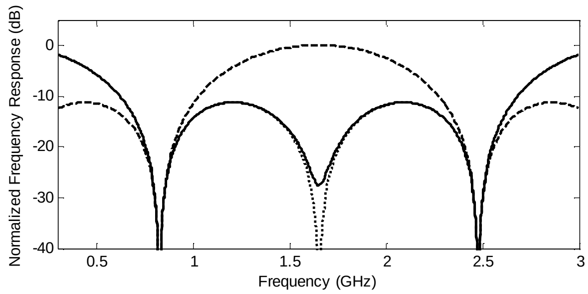

(b)

Fig.4. Measured (a) and theoretical (b) results for a four tap MPF. Solid line: distorted lowpass filter obtained when $\varphi \to \pi$ ($\varphi = 19\pi/20$); dashed line: bandpass filter response obtained with $\varphi = 0$; dotted line: ideal lowpass filter.

IV. Final Comments

As concluding remarks, we would like to point out that the subject of microwave photonic filters (MPF) which comprises an electrooptic modulator and polarization-maintaining fiber (PMF) delay lines was addressed. Special attention was given to MPF configuration in which Mach-Zehnder modulator (MZM) is cascade connected to sections of PMF. It was shown that measured results for a MPF with a single section of PMF were in very good agreement with theoretical predictions. Moreover, measurements and simulations carried out for a MPF having a two section PMF delay line have shown that its performance strongly depends on the optical wavelength.

The proposed MPF is not tunable, since the FSR of the filter is established by a fixed length of PMF. Also, the filter is not reconfigurable, because there is no flexibility in modifying filter coefficients, since in the two tap filter configuration the coefficients are always equal to each other, while in the four tap filter configuration the coefficients are dictated by the value of φ, and are not independent.

References

[1] R. A. Minasian, “Photonic signal processing of microwave signals”, *IEEE Transactions on Microwave Theory and Techniques*, vol.54, n^{o}.2, pp. 832-846, February 2006.

[2] J. Capmany, B. Ortega, D. Pastor and S. Sales, “A tutorial on microwave photonic filters”, *Journal of Lightwave Technology*, vol.24, n^{o}.1, pp. 201-229, January 2006.

[3] A.J. Seeds and K.J. Willians, “Microwave Photonics”, *Journal of Lightwave Technology*, vol. 24, no. 12, December 2006.

[4] K. Garenaux, T. Merlet, C. Fourdin, and J. Chazelas, “Recent Breakthroughs in Photonics for Radar Systems”, IEEE A&E Systems Magazine, pp. 3 – 8, February 2007.

[5] J. Yao, F. Zeng and Q. Wang “Photonic generation of ultrawideband signals”, *Journal of Lightwave Technology*, vol.25, n^{o}.11, pp. 3219-3235, November 2007.

Combined effect of dispersion, nonlinearities, and group velocity walk-off on the propagation of pulse trains in monomode optical fibers

Paula Brandão Harboe, David Santos Godoy
Department of Telecommunication Engineering, Federal Fluminense University (UFF)
Rua Passo do Pátria, 156, NIterói - RJ, CEP: 24210-240 Brazil
paula@telecom.uff.br

José Rodolfo Souza
[2]Department of Electronics and Telecommunications, Rio de Janeiro State University (UERJ)
Rua São Francisco Xavier, 525, Rio de Janeiro - RJ, CEP: 20550-900 Brazil
jrsouza@uerj.br

Abstract – **This paper investigates how the mechanisms of group-velocity dispersion (GVD), self-phase modulation (SPM), cross-phase modulation, and group-velocity walk-off impact the propagation of pulse trains along monomode optical fiber. The mathematical model is based on a set of of coupled nonlinear Schrödinger equations (NLSE), solved numerically with the Beam Propagation Method (BPM). The model allows for the evaluation of the alteration suffered by the waveform, and spectrum of pulses of different shapes, under different initial conditions of propagation. The numerical results obtained are in perfect accordance with others in the literature, and confirm the versatility, as well as the robustness of the model.**

Index Terms— **WDM Systems, Group-Velocity Dispersion (GVD), Fiber Nonlinearities (SPM, XPM), Pulse walk-off.**

I. Introduction

DWDM systems with high closely-spaced channel count allow for the utilization of the huge bandwidth offered by optical fibers, thus increasing the capacity of communication networks. However, the optical nonlinearities – self-phase modulation (SPM), cross-phase modulation (XPM), and four-wave mixing (FWM) – together with the group-velocity dispersion (GVD), cause channel interference that results in serious signal distortions, and degradation of the system performance.

The effect of SPM, XPM, and FWM originate at the nonlinear refraction, a phenomenon characterized by the dependence of the refraction index on the optical intensity. In SPM, a pulse modulates its own phase, inducing a frequency chirp. In the case of XPM, the same effect is observed, but now provoked by neighboring pulses. FWM occurs when the phase matching condition is satisfied, resulting in a beating of the channels, and generation of new optical frequencies.

The propagation of light waves in optical fibers is governed by the well-known Nonlinear Schrödinger Equation (NLSE), which in the majority of cases does not admit analytical solution. Therefore, one has to resort to numerical approximations, such as the Beam Propagation Method (BPM) [1].

The analysis and optimization of the performance of moderns WDM systems require the development of software tools that are robust, computationally efficient, and versatile, capable to simulate different practical situations at relatively low cost. The literature indicates, for example, that for a correct evaluation of FWM, the discretization step in BPM should be considerably smaller than that for the modeling of XPM [2].

An interesting, and computationally advantageous approach proposed by the authors consists in considering the effects of XPM, and SPM on the pulse propagation separately from the effects of FWM. Therefore, situations that promote the phase matching condition, inherently satisfied by XPM – and necessary for efficient FWM generation, must be identified, and avoided.

In previous [3], and recent [4] works, the authors investigated the penalty imposed by FWM in WDM systems based on G.652 (SMF – single-mode fiber), G.653 (DSF – dispersion-shifted fiber), and G.655 (NZDSF – non-zero dispersion-shifted fiber) compliant fibers, considering both uniform and non-uniform channel spacing. The results indicate that to reduce the deleterious effects of FWM, and maintain acceptable levels for the system signal-to-noise ratio, judicious choice should be made for one or more of the following: channel spacing, input power per channel, fiber type, positioning of the channels relative to the zero dispersion wavelength of the fiber, transmission rate, and link length.

The present paper investigates the impact of the mechanisms of GVD, SPM, XPM, and group velocity walk-off on the propagation of pulse trains in monomode optical fibers.

II. Discussion

The mathematical model is based on a set of couple NLSEs, solved numerically via BPM [1], [3], [4]. For a WDM system, the model allows for the evaluation of the modification imposed by the cited effects on the pulse envelope, and spectrum, considering different pulse shapes, as well as different initial propagation conditions. The practical situations chosen for the simulations serve to prove the versatility, and robustness of the model; the results obtained are in total accordance with others found in the literature. In this summary, two situations are illustrated: frequency shifting induced by XPM, and the generation of both bright, and dark pulses from a CW wave. In the case of SMF fibers, the pulse propagation is considered in the visible portion of the spectrum; in the case of DSF fibers, the pulse propagation is considered in the 1550 nm window.

In the first case, an analysis is made of the interaction between a Gaussian pulse of green light (530 nm, 100 mW), and a Gaussian pulse of orange light (630 nm, 100 W) propagating in an SMF (zero dispersion wavelength λ_0 = 1310 nm). For the low intensity green pulse, the XPM effect is heightened, while for the more intense orange pulse, the SPM effect is more significant. For pulse width T_0=10 ps, and short fiber lengths, the dispersion effects may be neglected; the pulse propagation is then affected by the combination of group velocity walk-off, SPM, and XPM. In this particular situation, the NLSE is amenable to analytical solution [1], which is then used to validate the results obtained numerically.

Figures 1 to 3 show, for three different situations: (a) the evolution of the green and orange pulse envelopes along the optical fiber, and (b) the green pulse spectrum at the end of the fiber. In Figure 1, the green, and orange pulses are launched simultaneously in the fiber, i.e. delay T_d = 0; in Figure 2, the orange pulse is launched with a delay T_d = 20 ps with respect to the green pulse; in Figure 3, the orange pulse delay with respect to the green pulse is T_d = 40 ps. In the simulations, the following parameters were used: $\gamma_1 P_2 L$ = 40, L = 4 m. The pulse envelopes remain unaltered, as the dispersive effects are neglected.

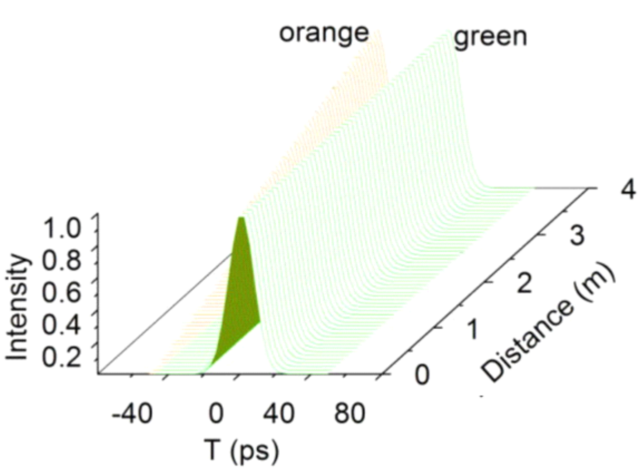

(a)

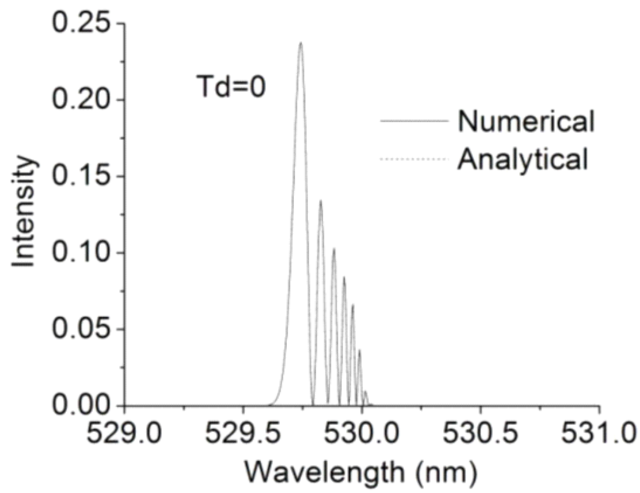

(b)

Figure 1: Evolution of the green and orange pulse envelopes along the optical fiber (T_d = 0), (b) spectrum of the green pulse at the end of the fiber.

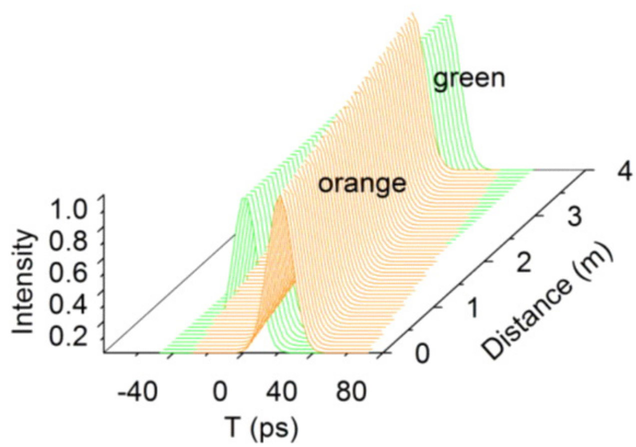

(a)

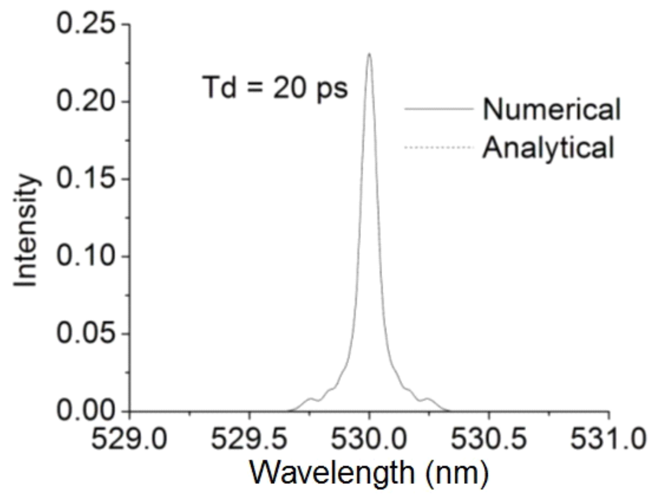

(b)

Figure 2: Evolution of the green and orange pulse envelopes along the optical fiber (T_d = 20 ps), (b) spectrum of the green pulse at the end of the fiber.

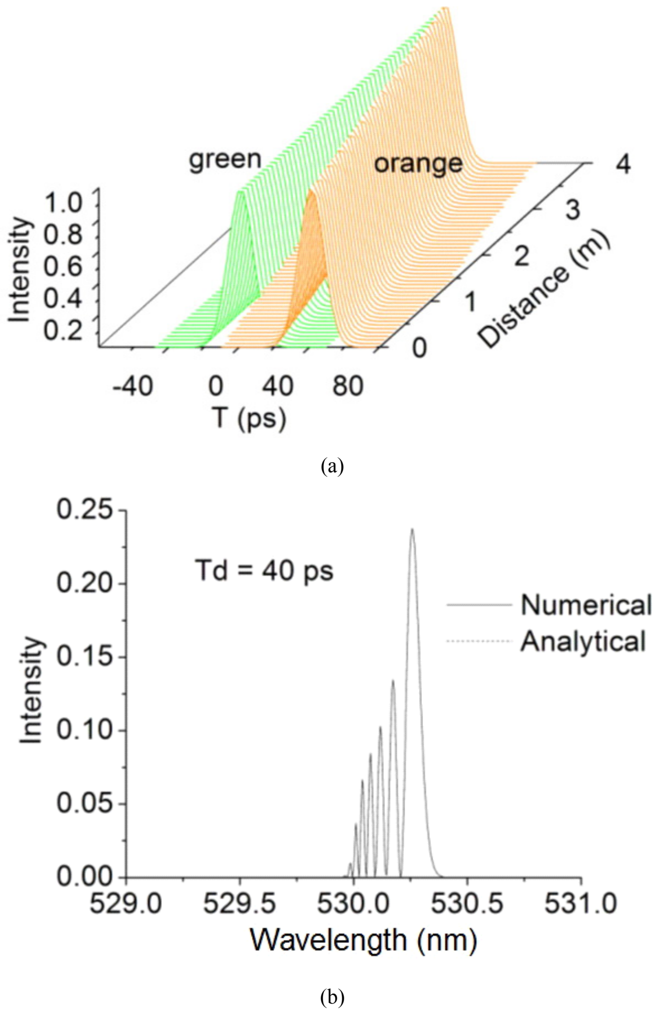

Figure 3: Evolution of the green and orange pulse envelopes along the optical fiber (T_d = 40 ps), (b) spectrum of the green pulse at the end of the fiber.

The way the spectrum of the green pulse is changed depends on the launching delay between the orange and green pulses. Keeping in mind that the orange pulse propagates faster than the green pulse, in the situation of Figure 1a, the green pulse interacts mostly with the trailing edge of the orange pulse during propagation; consequently, its spectrum widens, and suffers a shifting to the left. In the situation of Figure 2a, the orange pulse overtakes the green one at L/2, and the interactions with the leading and trailing edges of the green pulse practically cancel each other. Therefore, the spectrum of the green pulse suffers a symmetrical widening at the fiber output. In Figure 3a, the orange pulse only meets the green pulse at the end of the fiber; correspondingly, the green pulse interacts mostly with the leading edge of the orange pulse, and its spectrum widens, and is shifted to the right. The orange pulse is fundamentally affected by SPM, and the resulting frequency chirp (spectral widening) is almost symmetrical. In this situation, the spectrum of the orange pulse at the fiber output is similar to that of the green pulse, with T_d = 20 ps (Figure 2b).

In the second case considered, an analysis is made of the interaction between a CW signal of low intensity and two intense Gaussian pulses (1535 nm, T_{FWHM} = 8ps), along 5 km of DSF fiber (λ_0 = 1542 nm). The CW signal wavelength varies from 1538 to 1558 nm, so that its behavior in both the normal, and anomalous regimes can be observed. The parameters used in the simulations are the same as described in [5], whose results are used as comparison.

Figure 4 shows the evolution of the CW signal in the (a) normal (1540 nm), and (b) anomalous (1550 nm) dispersion regimes.

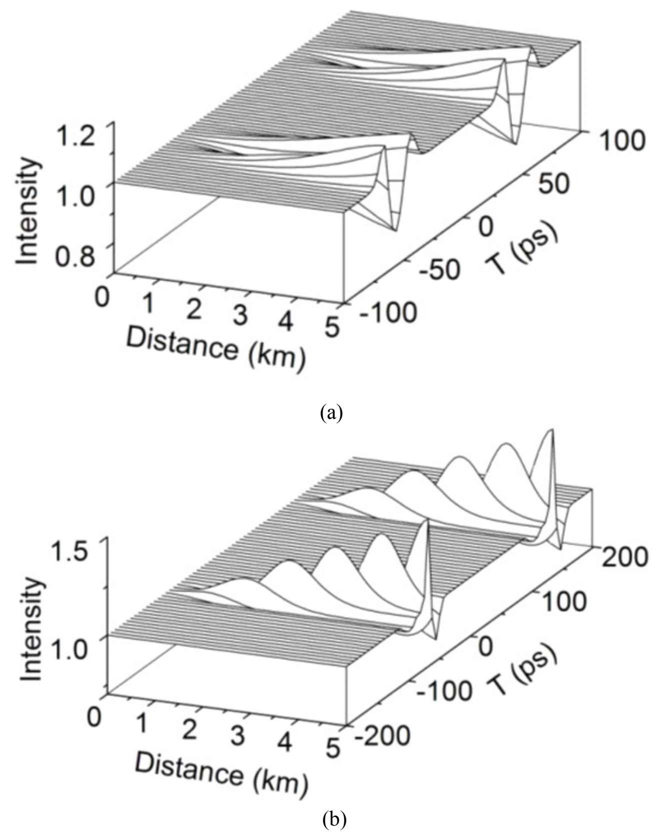

Figure 4: Evolution of the CW signal in the (a) normal (1540 nm), and (b) anomalous (1550 nm) dispersion regimes.

The phase of the low intensity CW signal is intensely modulated by the Gaussian pulses (XPM effect). The resulting grouping of frequencies coincides with that due do dispersion in the normal dispersion regime; an amplitude modulation ensues, offering a technique to generate a train of dark pulses. As seen in Figure 4a, a dark pulse is formed after about 1.5 km of fiber. On the other hand, in the anomalous dispersion regime, the frequency chirps induced by GVD, and XPM are opposite, and favors the formation of bright pulses.

III. Conclusion

The first case considered above shows that the chirp induced by XPM on the green pulse is affected by the group velocity walk-off, and depends critically on the initial delay between the pulses. The observed asymmetrical spectral widening is known as XPM induced frequency shifting, and finds applications in many areas of optical communications [1]. In the second case, the generation of dark, and bright pulses was observed in the normal, and anomalous dispersion regimes, respectively, and constitutes an important mechanism for the conversion of wavelength in optical networks [1].

IV. REFERENCES

[1] G.P.Agrawal. *Nonlinear Fiber Optics* (4th ed.), Academic Press, San Diego, USA, 2006.

[2] J. LEIBRICH, W. ROSENKRANZ. Efficient Numerical Simulation of Multichannel WDM Transmission Systems Limited by XPM, *IEEE Photonics Technology Letters*, v. 15, n. 3, p. 395-397, 2003.

[3] J. R. SOUZA, P. B. HARBOE. Assessment of Higher-Order Exponential Operators for the Simulation of High-Capacity Optical Communication Systems by the Split-Step Fourier Method, *Journal of Microwaves and Optoelectronics*, v. 3, n. 2, p. 9-22, 2003.

[4] P. B. HARBOE, E. SILVA, J. R. SOUZA. Simulador WDM para Análise das Penalidades Impostas por FWM em Fibras G.652, G.653 e G.655, Aceito para apresentação em MOMAG 2008: 13° SBMO – Simpósio Brasileiro de Microondas e Optoeletrônica e 8° CBMag – Congresso Brasileiro de Eletromagnetismo, Florianópolis – SC, 2008a.

[5] P. ÖHLÉN, B. OLSSON, D. J. BLUMENTHAL. Wavelength Dependence and Power Requirements of a Wavelength Converter Based on XPM in a Dispersion-Shifted Optical Fiber, *IEEE Photonics Technology Letters*, v. 12, n. 5, p. 522-524, 2000.

Experimental Development of a New Technique To Measure Atmospheric Turbulence in Horizontal Optical Links Throught Free Space

Vinicius Nunes Henrique Silva
Universidade Federal Fluminense
Phone: (21) 2629 – 5723
Niterói – RJ - Brazil
vinidelsilva@terra.com.br

Dr. Andrés Pablo Lopéz Barbero
Universidade Federal Fluminense
Phone: (21) 2629 – 5723
Niterói – RJ - Brazil
pablo@telecom.uff.br

Dr. Ricardo Marques Ribeiro
Universidade Federal Fluminense
Phone: (21) 2629 – 5723
Niterói – RJ - Brazil
rmr.rlk@terra.com.br

Abstract— **In this paper a new technique to measure the atmospheric turbulence in horizontal optical links is presented. The technique uses the direct measurement of the beam wander effect to determine the refractive index structure constant ( ) to evaluate the turbulence for a specific path. The mathematical theory and the experimental setup to demonstrate the new technique are described in this work.**

Index Terms— **Atmospheric Turbulence, Beam Wander, Refractive Index Structure Parameter, Free Space Optics.**

I. Introduction

Free Space Optics is a high bit rate technology that uses an optical wave carrier to transmit data through the atmosphere. High security, great mobility, low cost (when compared with confined optical communication systems) and free of electromagnetic interference are important features of FSO systems [1]. Because the worldwide demand for bandwidth and the last mile bottleneck, FSO has emerged as a viable point-to-point technology. However, FSO is subjected to atmospheric effects that can degrade the optical beam then reducing link viability. Beam obstruction, scattering, light absorption, atmospheric turbulence and weather conditions (rain, snow, fog) have to be mitigated to avoid excessive signal deterioration [2]. Weather changing has been observed around the world due to pollution increase and atmospheric turbulence levels ought to be measured. Methods to determine atmospheric turbulence in optical links was made using the correlation functions displacement of thin parallel beams and with a modulated interferometer to produce Doppler beats between a reference beam and one reflected plane mirror at a distance [3-4]**.** Commercial equipments to measure the atmospheric turbulence are already available [5]. This paper proposes and develops a new technique and a low cost related device to determine the atmospheric turbulence based on direct measurement of beam wander, tracking the optical beam at receiver plane.

The research objective is measurement of the refractive index structure constant (C_n^2) of the medium using the turbulence effect. The medium characterization is done by the measurement of the radial beam variance due to beam wander and then evaluate C_n^2 to consequently know the atmospheric turbulence level that a specific free space optics link.

II. Atmospheric turbulence

The heated surface of the earth may warms air pockets around it. Heating the air makes changes on the refractive index of the medium. This is because the refractive index of air is dependent upon its temperature. The heated air pockets increase in size and mix with cooler air up above leading to a heterogeneous and turbulent medium. The interaction of the laser beam with the turbulent medium leads to signal degradation and can be observed as random deviation of wave characteristics such as: power distribution, propagation direction and phase of the electrical field. This may cause three effects in reception: scintillation, beam wander and beam spread. Hence, it is commonly reported in the literature the use of the refractive index structure constant (C_n^2) to quantify atmospheric turbulence and the relation with the effects described elsewhere [6]. The beam wander is the randomly displacement of the instantaneous center of the beam ("hot spot") in the receiver plane, as shown in Figure 1. Thus, can be calculated using the weak fluctuation theory [7]. For a collimated Gaussian beam propagating through atmospheric turbulence, the rms displacement of the beam hot spot, σ_r, is defined [7-8] according to equation (1)

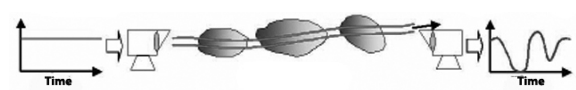

Figure 1 – The Beam Wander Effect

$$\langle\sigma_r^2\rangle = 2{,}42 C_n^2 W_0^{\frac{-1}{3}} L^3 \qquad (1)$$

where L is the link distance and W_0 the Gaussian width at the transmitter plane.

III. The proposed technique

An experimental set-up in laboratory was designed to validate the C_n^2 measurement of the proposed technique as shown in Figure 2. The technique consist to place three photo-detectors (D_i) in the receiver plane, where i = 1,2,3. Also, it ought to be known the relative position (x_i, y_i) of each photo-detector. The incident optical power (P_i) onto the effective area of each photo-detector should be measured. Hence, the calculation of the optical beam instantaneous center position (x_0, y_0) is carried out after the measurement of the light power in each photo-detector. Let's assume a transmitted and received Gaussian light beam pattern (see Figure 2 and Figure 3), which can be mathematically stated as:

$$P\ (x,y) = P_0\, e^{-\left(\frac{r}{W}\right)^2} \quad (2)$$

where r, W and P_0 means the radial distance to the center of the beam, the Gaussian beam-width and the power at center of the beam, respectively.

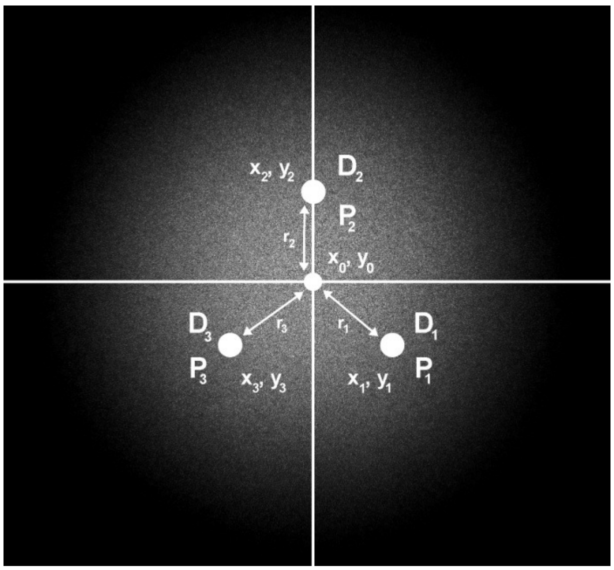

Figure 2 – Geometry of the receiver plane comprising its center and three photo-detectors with their coordinates. An image of a Gaussian-shaped optical beam is superimposed (see also Figure 4).

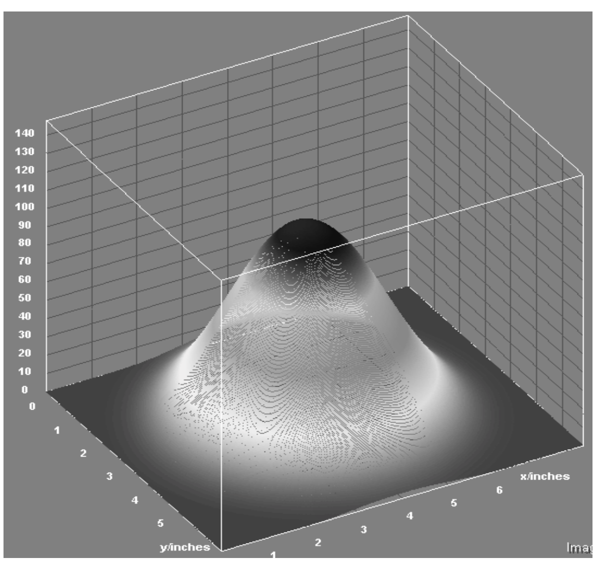

Figure 3 – The 3D pattern plot drawn from 2D contour plot of Figure 2 achieved by using ImageJ software.

After measuring the optical power P_i, the radial distances r_i of each photo-detector to the center of the beam (x_0,y_0), can be calculated from (2) as:

$$r_i^{\,2} = W(-ln\overline{P_i}) \quad (3)$$

where $\overline{P_i} = \frac{P_i}{P_0}$ is the normalized power.

The transformation equation from Cartesian to cylindrical coordinates is well known and is written as (4):

$$r_i = \sqrt{(x_i - x_0)^2 + (y_i - y_0)^2} \quad (4)$$

After substituting (3) in (4) the central position of the beam can be found solving the equation system:

$$\begin{cases} (x_0 - x_1)^2 + (y_0 - y_1)^2 - W(-ln\overline{P_1}) = 0 \\ (x_0 - x_2)^2 + (y_0 - y_2)^2 - W(-ln\overline{P_2}) = 0 \\ (x_0 - x_3)^2 + (y_0 - y_3)^2 - W(-ln\overline{P_3}) = 0 \end{cases} \quad (5)$$

IV. EXPERIMENTAL SETUP

The experimental set-up used in a Laboratory environment aiming to carry out measurements of the C_n^2 structure factor as shown in Figure 4.

A HiBi pigtailed laser diode (LD) emitting at 980nm is the light source. Because the output power distribution of the HiBi fiber isn't a circular Gaussian beam, it was spliced with a standard (STD) optical fiber with cut-off wavelength at 1300nm. The LD is powered by a Newport current source model 5030 and cooled by ILX Light Wave LDT-5525 temperature controller. A fiber modal filter (MF) is used to eliminate the high-order and the cladding modes and guarantee a circular Gaussian-shaped light that impinges onto the photo-detectors plane (Di). The light beam propagates through free-space up to reach the photo-detectors (Di). The distance between the light source (output of the standard optical fiber) and the photo-detectors plane is 21cm. An analog-to-digital converter (ADC) digitalizes the electrical signal generated from the incident optical power in each photo-detector and sends the data to a personal computer. The later can solves the equation system (5).

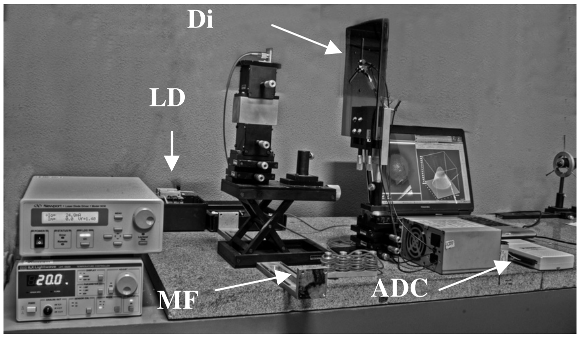

Figure 4 – The experimental Set Up – LD is the Laser Diode, MF is the Modal Filter, ADC is the Analogue-to-Digital converter and Detect is the photo detectors plane

V. RESULTS AND DISCUSSIONS

In order to simulate the beam shifts caused by the beam wander effect, the photo-detectors receiver plane was freely to move horizontally and vertically by means of an attached micrometric precision translation stage. In this experiment the receiver plane was shifted to draw a triangular picture with 5.0mm base and height. The achieved results can be seen in Figure 5. The dotted gray line means the movement done by the micrometric translation stage. The black line means the calculated coordinates after the measurements of the optical intensity and solving the equation system (5), as previously described.

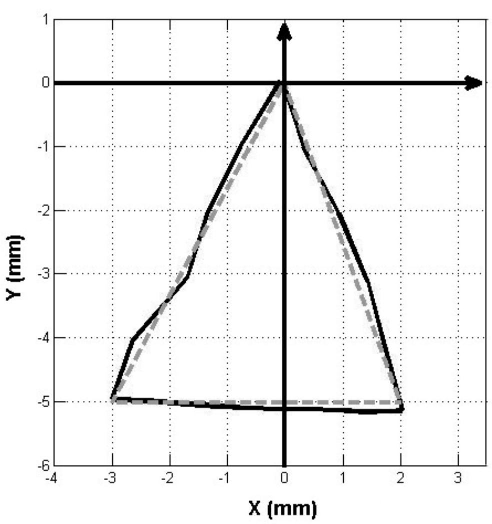

Figure 5 – Triangular patterns followed by the optical beam – the dotted gray line traces the applied movement and black line traces the coordinates as measured /calculated by the present device.

The largest distance between the gray line and black line is the error measurement for the worst case. The error is computed 0.2mm. It is straightly related to the experimental signal to noise ratio. The experimental results are in quite agreement with "theoretical" values acquired directly from the micrometer translation stage. Hence, the proposed technique is able to measure the atmospheric turbulence using Equation 1 that permits to calculate de refractive index structure constant, through the tracking of the beam in the receiver.

VI. CONCLUSION AND FUTURE SUGGESTIONS

It was presented that the technique is capable to measure the atmospheric turbulence tracking the optical beam at receiver plane. Moreover, the device can be integrated to a FSO system to measure the local turbulence or/and to track the optical signal. The aim is to check the installation viability and to monitor the signal quality along the time, mapping the atmospheric turbulence profile in that region thus forecasting future undesired random effects. Furthermore, the technique allows a mechanical device to be attached on the transmitter in order to mitigate the consequences of the turbulence improving the FSO performance. It has been seen that our technique, concerning the optical tracking of the beam, can be used to monitor vibrations and displacements in structures in general. [9].

ACKNOWLEDGEMENT

A.P.L. Barbero would like to thanks the Brazilian funding agencies CNPQ (grant number 482657/2007-3) and CAPES, and also the Brazilian Ministry of Defense and RNP, for the financial support to this work. V.N.H. Silva would like to thanks CAPES and the Brazilian Ministry of Defense (through the Pro-Defesa Projetc) for the financial supporting of his Master Scholarship.

REFERENCES

[1] L. S. Fredrik, *Design and Analysis of All-optical Free-space communication Link*. Linkopings Universitet, 2002
[2] C. P. Colvero, M. C. R. Cordeiro and J. P. von der Weid, "FSO Systems: Rain, Drizzle, Fog and Haze Attenuation at Different Optical Windows Propagation". *International Microwave & Optoelectronics Conference*, 2007.
[3] C. Anna, O. Kevin, "Measuring the inner scale of atmospheric turbulence by correlation of lateral displacement of thin parallel laser beams". *Waves in Random Media 3 (85-92)*, UK, 1993.
[4] I. Goldstein, P. A. Miles and A. Chabot, "Heterodyne Measurements of Light Propagation through Atmospheric Turbulence". *IEEE Proceedings*, vol. 53, no. 9, p. 1172, 1965
[5] OSI – Optical Scientific, Inc. [online]. Available at Internet via WWW. URL: http://www.opticalscientific.com/LOA-005%20Features.htm. (Last visit: 24/11/2008).
[6] C. Carlos, *Understanding the atmospheric turbulence structure parameter,* C_n^2. Universidade of Puerto Rico, 2006.
[7] L. C. Andrews, R. L. Philips, *Laser Beam Propagation through Random Media.* Spie Press, 2005.
[8] W. Heinz, G. Baksheesh, *Free Space Optics: Enabling Optical Connectivity in Today's Networks*. Sams, 2001.
[9] Sitek Eletroc Optics. [online]. Available at Internet via WWW. URL: http://www.sitek.se/. (Last visit: 24/11/2008).

Packet Latency Reduction in Optical Networks by Triggering SOA-Based Switches with Pre-Step Pulses

Raniere N. de Carvalho and Atílio E. Reggiani
CPqD Telecom and IT Solutions
Postal Code: 13086-902
Campinas - SP - Brazil
ranierec@cpqd.com.br

Evandro Conforti and Aldário C. Bordonalli
Faculty of Electrical and Computer Engineering
Unicamp Postal Code: 13083-970
Campinas - SP - Brazil
ranierec@cpqd.com.br

***Abstract* — Packet latency was investigated as an SOA-based switch was triggered by different-shape current pulses. Pre-step pulses in comparison to ordinary pulses reduced switching time and kept high bit contrast, leading to shorter network latency. Results are presented in ideal environments, simulated and real, with rates of transmission in the order of 10 Gb / s.**

***Index Terms* — Semiconductor optical amplifier, optical switching, optical packets.**

I. Introduction

Fiber-to-the-premises (FTTP) has been expected for 20 years as the ultimate solution for the last mile capacity bottleneck in between the metro networks and the customer premises of businesses and residential users. Optical access networks have the potential of providing symmetric high bandwidth capacity, which is necessary for applications such as online gaming, peer-to-peer and e-learning services. Also, optical-domain signal processing has become increasingly necessary in optical packet networks since it allows the growth of data stream with shorter latency [1-3].

In particular, the optical switching is a fundamental technology for future optical network systems and the SOA has the potential to be employed as a microwave current controlled electro-optical switch due to its small size and fast response. The reduction of the switching speed is important to improve the rerouting time of space switches in wavelength-division-multiplexed WDM networks, but the biggest problem of this networks based on all-optical packet switch are the lost of information after the processing and switching of data packets [3-4].

In this sense, packet latency was studied as an SOA-based switch was set off by different-shape current pulses. The switch was formed by an ordinary and commercially-available SOA that allowed (ON) or blocked (OFF) the light traveling through an optical path. The off state was obtained by keeping the SOA bias current below threshold level.

This paper show the quality of data after all process, using this technique based on a microwave circuit capable of generating a fast pre-impulse signal to be added at the beginning of the step signal that normally is used to switch the SOA.

II. Optoelectronics Prject and Experiment

The design of assembly and the steps followed for the analysis of the technique of ultra-fast switching were based on the study of networks of optical switching package (optical packet switching - OPS), as stated earlier. From the analysis in Fig. 1, has been a reference for how to implement the experimental assembly of the project and then evaluate the results.

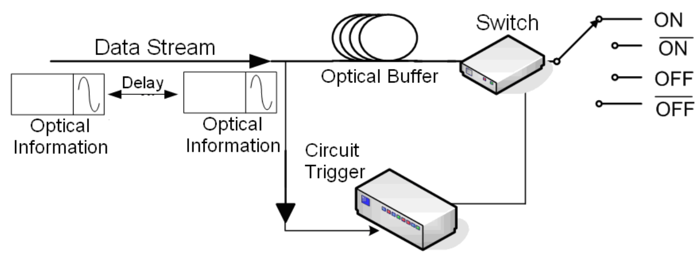

Fig. 1. Optical packets networks with switching.

The packets of information to reach a directional coupler, which sampled a portion of the traffic and sends a driving circuit of the key. This circuit interprets the header of the package and then decide whether or not the activation of the key, the positions, for example, turned on (ON) or off (OFF), respectively. An optical delay line (buffer) properly designed slows the package section of the same key in achieving the precise moment at which it is-selected. Especially in the case of keys based on people, would pass the information below (ON) with a degree of amplification, or would be lost in the key (OFF) by absorption in the semiconductor material. To that end, it is with the monitor-polarization of SOA through pulses of electric current, which put the amplifier operating above (ON) or below your threshold (OFF).

The Fig. 2 shows the experimental diagram used for the analysis of the switching package in SOAs. In this case, the combination of a source of generation of data to a optical modulate produces the packets of information in an optical channel. These packets travel by a line of fiber before it reaches the SOA. Both the entrance of the optical modulator to the quantity of SOA were placed controls of polarization, not shown in Fig. 2. To simplify the experimental apparatus, the functions of sampling and the driving circuit of the key were engaged in indirect way. In other words, despised is the electronic processing of the header of the packet to trigger the switch, which has been done from a timing (clock) between the construction of information in optical data generator and driving the switching device for a circuit of the jet stream.

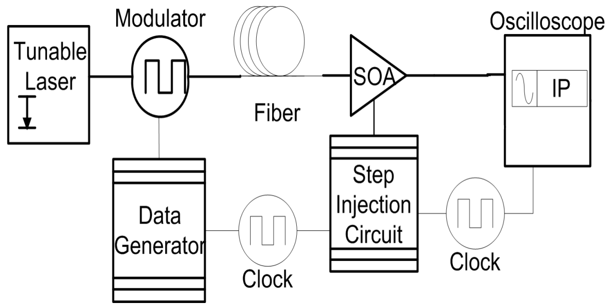

Fig. 2. Switching process experiment.

The optical channel in 1550 nm was generated by a tunable laser (Santec TSL-210V) and modulated on a scale of the microwave signal comes from a data generator (Agilent 81141A), which simulated the IP type packets at rates of 10 Gb/s, a known sequence. As mentioned above, this event had a parallel circuit with the synchronism of the current injection of SOA, determining the moment of trigger (amplification) and no (attenuation) of the key, after being considered the arrival of packets to the SOA, delays in row fiber and cables, microwaves and the responses of equipment. After the acquisition of sync, considered to be the time for switching of the moment as SOA and the key drive could contribute to the deterioration of information during the passage of the packages. This analysis was made ob-aging is the output signal of SOA in an oscilloscope with optical input (HP 81134A), also synchronized with data generator.

The operation of the key depends on the level and range of injection carriers during the passage of each packets, assuming that the synchronism between the trigger and the key generator of traffic has been carefully adjusted. For there is no distortion of information above acceptable levels, particularly in the key state of trigger, the interval injection of carriers should always be greater than the range of duration of the package. Under these circunstances, the difference between these different intervals depends on the speed at which the SOA can be switching. The timing of switching the provisions Device depends directly of the supply of carriers, that is, as is the injection of carriers, and how the device responds to this injection, in other words, how your gain varies. Therefore, in the case of trigger the switch requires that the level of injection of carries is sufficient to ensure that the gain level on reaching desired compatible when the photon signal started to focus inside the cavity of SOA., avoiding the deterioration of the first bits of information from the packets. In the case of turn-off switch, you must stop the injection of carriers or to decline to the point of the device operating slightly below or above the threshold. However, with the optical power amplified within the SOA, the consumption of carriers is strong and the time of switching stays faster.

Thus, to reduce the time for switching the SOA, especially in the key drive, it is polarized near the threshold and injection of carriers is made in the form of electric pulses with fast time to climb, like that shown in Fig. 3 (a) . The oscillations observed in the wrist are the result of neglect on the line connecting the drive circuit of the SOA. Another option to drive the key is to use a technique of pre-injection of current (pre-impulse-step injected current - PSICO) on the device [5], where a pulse of short duration is overridden by a simple pulse of current, as shown in Fig. 3 (b). This technique, developed by the group, promotes a very rapid increase in the number of carriers in the cavity of the SOA, which compensates for the initial delay of the response of the device in relation to what is achieved with a simple wrist. This is the first time that the technique is tested at systemic.

III. Results

Using the experimental assembly at Fig. 2 and the sequence described in the previous section, the switching packet was run for two different conditions. In one, used to be simple pulses of electric current, as shown in Fig. 3 (a). In the sequence, such as pulses PISIC Fig. 3 (b) were employed in driving the switch. The Fig. 4 shows the results in both situations. The turn-on or turn-off is considered the switch from the beginning of the increase or decrease the amplitude of the signals shown in Fig. 4, respectively, until the stabilization of same in an average. Besides the analysis of the actual time of switching, it should be emphasized that the findings concerning the deterioration of the bits inside the packages were essential-focused initially on the first bit and the last bit, because they are the closest to the edges of the package during the on/off of the optical switch. In the case of single pulses, the Fig. 4 (a) shows that the time to trigger the switch was approximately 2 ns, while the time of shutdown was 1.5 ns. Moreover, with the trigger-up of key route PISIC, the Fig. 4 (b) shows a substantial reduction in time of switching to around 180 to 200 ps in the on/off of the switch. Furthermore, in both cases, note that the integrity of the bits of information first and last were considered and kept during the measures, to reduce errors in reception.

The Fig. 4 (b) shows the exact moment in which there is a drive of the device in relation to the passage of the package of bits, emphasizing efficiency in the use of the key with a technique of ultra-fast function of trigger, compared to the show Fig. 4 (a).

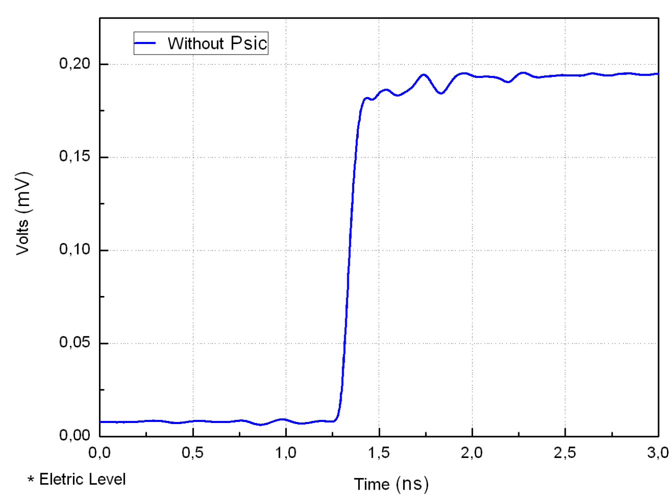

(a)

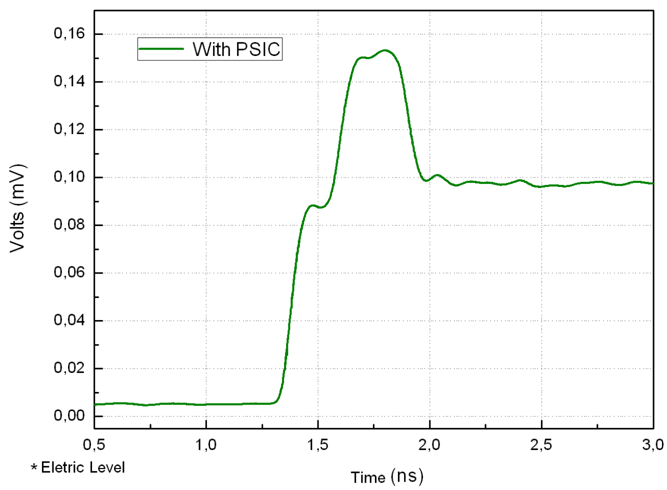

(b)

Fig. 3. Current injection with (a) simple step and (b) PISIC technique.

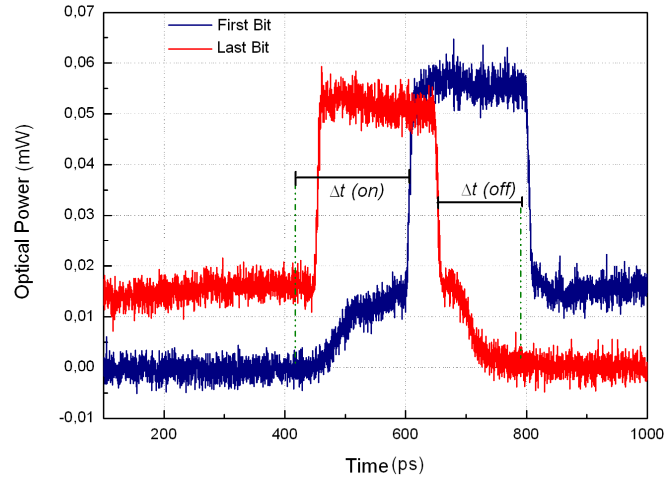

(

b)

Fig. 4. SOA optical answer with (a) simple step and (b) PISIC technique.

Thus, in a situation where the whole process of traffic on the network and routing of information to the destination chosen are considered, either to a condition where the key works to block the information (single path, such as analysis) or to a situation where it operates with another SOA in parallel (double track), the switching with PSIC results in a considerable improvement in the time of switching. Thus, through the data, it is interesting to make an associantion between the use of this technique in networks with optical and packet switching to a decrease in latency in the traffic of the packages.

For example, consider the case of OPS networks with variables packets sizes and time of arrival of packages modeled by a Poisson distribution. In addition, assume the use of the Internet protocol, datagram with the minimum size of 20 bytes and a maximum of 65,535 (64 kbytes), where the maximum size of datagram that any node requires to be able to handle the information is 576 bytes [6] - [7]. Based on these aspects, setting up traffic adopted in this analysis is that a network of 10 Gb/s packets with sizes of 100 bytes, for effects to simplify the calculates and better understanding.

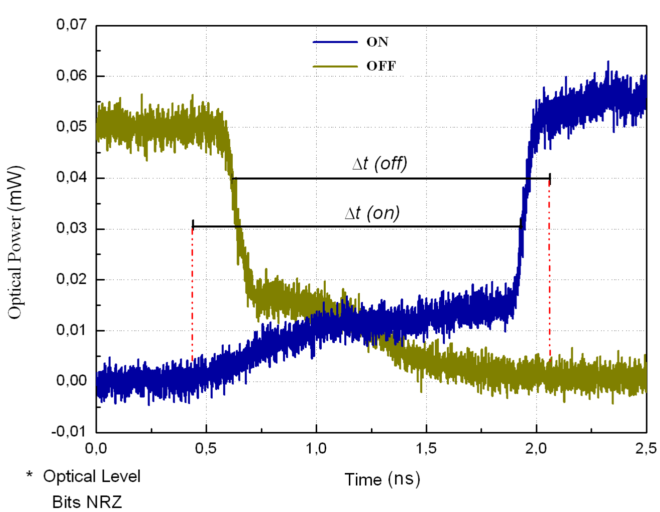

(a)

So, taking as basis the fact that the keys to commercial use SOAs takes, on average, about 4.5 ns to perform the process on/off switch, the results from the experiment presented here show that it is possible increase the traffic capacity in the system where about 400 bits per each process of switching that occurs on average in the network or the node in question, or even to reduce the latency to achieve a better performance in the time of his career information. For the purpose of understanding, Fig. 5 shows the detailed analysis prior to a network with traffic ranging from 10 to 10^{10} packages in a given time and they will suffer switching. Please note that the numbers of switching on the network are random, to facilitate viewing. In addition, the number of cases of switching on the network is directly related to the number of packet traffic on the network that will suffer routing or some other type of processing that requires its direct route through the technique of switching, especially using the SOA.

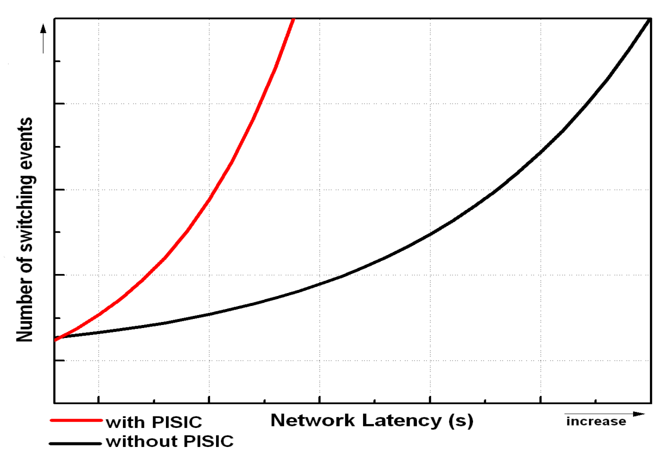

Fig. 5. Relative number of switching events with and without PSIC as a function of the network packet latency.

For composition of Fig.5, initially used software developed by the research group, Z-SOA, which simulates the operation of the optical amplifier as the key. Despite the difficulties in obtaining the real and intrinsic parameters of the semiconductor optical amplifier used in the experiment, there was a good correlation between the results obtained in the laboratory and those provided by Z-SOA. In the sequence, the data for simulation of Z-SOA were used to feed the second software, Network Simulator [8], which provided the figures that resulted in the chart.

Finally, the experimental procedure of switching the packets was also played in a real external network of optical packets (Kyatera network), set in single mode fiber optics. Thus, effects of dispersion and attenuation were incorporated to bits over distances of 20 and 40 km in length. The Fig 6 (a) illustrates the experimental apparatus used in the assembly and in detail in Fig 6 (b), the connection box, which allows the output to the external network.

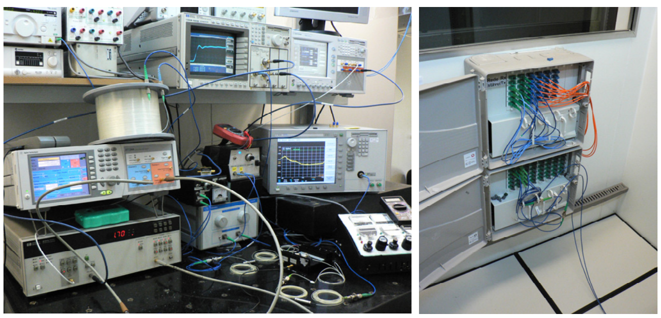

(a) (b)

Fig. 6. Ilustration of the experimental apparatus (a) and (b) the box to connect external network

IV. Final Coments

In this work, proved to be an experimental analysis of the use of a technique of ultra-fast optical switching and the implications of using this in the compromise and traffic information in a optical packets networks. The technique used was authorized based on pre-injection of current in the semiconductor optical amplifier, where a pulse of short duration is overlaid with a single pulse of current. The results of this technique were compared with conventional techniques of switching SOAs, which are known and used commercially. There was a reduction considers the considerable number of times of switching to about 180 ps with the technique PISIC, suggesting that a possible to reduce bottlenecks of optical networks judged in the comparator process. Consequently, the congestion we have seen in optical networks may be reduced due to lower processing time of information, generating a smaller latency in the network.

Furthermore, with improvements in times of switching, you can, for example, increasing the number of packet traffic on mesh networks and provide a partial reduction in the time between the packets. Thus, it ensures better efficiency in the use of bandwidth at any time of traffic [9] - [10].

Referências

[1] D. J. Blumenthal, B.-E. Olsson, G. Rossi, T. E. Dimmick, L. Rau, M. Masanovic, O. Lavrova, R. Doshi, O. Jerphagnon, J. E. Bowers, V. Kaman, L. A. Coldren e J. Barton, "All-optical label swapping networks and technologies," *OSA/IEEE J. Lightwave Technol.*, vol. 18, no. 12, pp. 2058-2075, 2000.

[2] E. Kehayas, J. Seoane, Y. Liu, J. M. Martinez, J. Herrera, P. V. Holm-Nielsen, S. Zhang, R. McDougall, G. Maxwell, F. Ramos, J. Marti, H. J. S. Dorren, P. Jeppesen e H. Avramopoulos, "All-optical network subsystems using integrated SOA-based optical gates and flip-flops for label-swapped networks," *IEEE Photon. Technol. Lett.*, vol. 18, no. 16, pp. 1750-1752, 2006.

[3] H. J. S. Dorren, M. T. Hill, Y. Liu, N. Calabretta, A. Srivatsa, F. M. Huijskens, H. de Waardt e G. D. Khoe, "Optical packet-switching and buffering by using all-optical signal processing methods," *OSA/IEEE J. Lightwave Technol.*, vol. 21, no. 1, pp. 2-12, 2003.

[4] I. M. White, M. S. Rogge, Y.-L. Hsueh, K. Shrikande e L. G. Kazovsky, "Experimental demonstration of the HORNET survivable bi-directional architecture," em *Proc. Optical Fiber Communication Conference*, vol. 70, pp. 346-349, 2002.

[5] C. M. Gallep e E. Conforti, "Reduction of semiconductor optical amplifier switching times by pre-impulse-step injected current technique", *IEEE Photon. Technol. Lett.*, vol. 14, no.7, pp. 902-904, 2002.

[6] I. Chlamtac, V. Elek, A. Fumagalli e C. Szabo, "Scalable WDM access network based on photonic slot routing," *IEEE/ACM Trans. Networking*, vol. 7, pp. 1-9, 1999.

[7] H. Zang, J. P. Jue e B. Mukherjee, "Capacity allocation and contention resolution in a photonic slot routing all-optical WDM mesh network," *OSA/IEEE J. Lightwave Technol.*, vol. 18, pp. 1728-1741, 2000.

[8] V. Elek, A. Fumagalli e G.Wedzinga, "Photonic slot routing: a cost effective approach to designing all-optical access and metro networks," *IEEE Commun. Mag.*, vol. 39, pp. 164-172, 2001.

[9] S. Akiba, "The future of optical communications", em *Proc. IEEE/LEOS Annual Meeting,* PLE3, pg. 7-8, 2002.

[10] B. Meagher *et al.*, "Design and implementation of ultra-low latency optical label switching for packet-switched WDM networks," *OSA/IEEE J. Lightwave Technol.*, vol. 18, no. 12, pp. 1978-87, 2000.

Ultrashort Pulse Transmission from Bragg Fabry-Perot Filter

José Luiz Sousa Lima
Laboratório de Telecomunicações e
Ciência e Engenharia de Materiais - LOCEM
Campus do Pici - Bloco 930
60455-760 Fortaleza - CE - Brasil
lima@fisica.ufc.br

Rogério Nunes Nogueira
Instituto de Telecomunicações
Campus Universitário de Santiago
3810-193 Aveiro - Portugal
rnogueira@av.it.pt

António Teixeira
Instituto de Telecomunicações
Campus Universitário de Santiago
3810-193 Aveiro - Portugal
teixeira@ua.pt

Paulo Sérgio de Brito André
Instituto de Telecomunicações
Campus Universitário de Santiago
3810-193 Aveiro - Portugal
pandre@av.it.pt

João Lemos Pinto
Universidade de Aveiro
Campus Universitário de Santiago
3810-193 Aveiro - Portugal
jlp@fis.ua.pt

***Abstract*— We report ultrashort optical pulse propagation in a Bragg Fabry-Perot filter formed by two uniform gratings. We examine the sequence of output pulses in order to determine the ideal reflectivities of the gratings such as the output pulses experience the peak power maximum. We assume a symmetric transform-limited 2-ps Gaussian pulse as the ultrashort input pulse to the filter. The results indicate that the reflectivities of the gratings must be equal in order to maximize the peak power of the transmitted pulses. We also consider the case of two input pulses with 10 ps time shift are incident on the input of the filter.**

***Index Terms*— Fiber Bragg grating, Fabry-Perot filter, pulse propagation.**

I. INTRODUCTION

There is a continuous growth of interest in passive fiber optic components for fiber communication systems, fiber sensors and optical instrument testing. The developments in techniques for writing fiber Bragg gratings (FBGs) [1]-[5] have resulted in an increased interest in the numerous applications and possibilities for grating-based devices. One of the basic passive device is the Bragg Fabry-Perot (BFP) filter [6], [7]. This optical device is formed by two spatially separated FBGs written in high photosensitive fiber which play the role of mirrors. Like FBGs, BFP have various advantages such as low cost, low insertion loss, flexibility of spectrum, electromagnetic interference immunity. This component has been a successful device for demonstrating a range of optical processing functions including dispersion slope compensator [8], measuring of thermal expansion coefficient [9], optical sensors [10], [11], optical clock recovery [12] and naturally optical filters [6], [13]-[15]. For applications to wavelength-division-multiplexed (WDM) optical communication systems, the free spectral range (FSR) of the BFP should correspond to the typical channel spacing of 100 GHz or 50 GHz thus requiring lengths of 1-2 mm between the FBGs.

The BFP has the same basic physical concept as a Fabry-Perot cavity. The BFP spectrum is a convolution of a Bragg grating reflection spectrum and a Fabry-Perot transmission spectrum. The characteristics of the BFP depend on several parameters: such as the reflectivity, bandwidth of the two gratings and the cavity length. The reflectivity determines the coupling strength between the two gratings, the group delay, dispersion and dispersion slope curve; the separation distance of the two gratings determines the free spectral range (FSR, defined by the separation between the group delay peaks) over the usable bandwidth of the device. The length, strength of the grating and the separation distance can be varied to control the dispersion/dispersion slope, bandwidth and free spectral range of the device.

Typically, grating-based devices and applications involve optical pulses or other types of wave propagation. However, there is a lack of study concerning pulse propagation through a BFP filter. Then, the propagation of ultrashort optical pulses has been investigated. In this paper, we report numerical studies of the ultrashort pulses propagation through a BFP filter. The device length is relatively short and written in photosensitive fiber, which is very easily fabricate and make

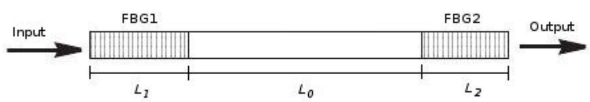

Fig. 1. Schematic diagram of the BFP filter formed by arrangement of two uniform FBGs (FBG1 and FBG2). L_1 and L_2 are the physical lengths of FBGs and L_0 is the distance between them.

our design more economically interesting. We focus mainly on the reflectivities of the gratings. The aim is determine the best reflectivities such as the output pulses experience peak power maximum.

II. Theory

A BFP filter formed by two uniform FBGs that act as partial mirrors and defines between them a Fabry-Perot cavity is shown in Fig.1. In continuous wave regime, this configuration results in interference between the two gratings and interference phenomenon takes place in both reflection and transmission. The interference generates multiple peaks in spectrum of the reflection, transmission, group delay, and the dispersion of the reflection and transmission. Although the group delay and dispersion of uniform grating are very small, in the configuration of the Fabry-Perot cavity, the light is trapped inside the cavity for many trips and experiences enhanced delay and dispersion [8]. In ultrashort pulse regime, the pulse also will be trapped inside the cavity for some trips and a sequence of output pulses will emerge from output of the filter.

To describe optical pulse propagation through a BFP filter, at first we consider a one-dimensional grating structure with a refractive index given by

$$n(z) = \bar{n} + n_1(z)\, cos\left[\frac{2\pi}{\Lambda}z\right] \tag{1}$$

where $\bar{n}$ is the average refractive index change of the fiber mode, $n_1(z)$ is the amplitude of periodic index change, and Λ is the Bragg period. At low intensities, the electric field inside the grating satisfies the coupled mode equations [16]

$$+i\frac{\partial A_+}{\partial z} + i\frac{1}{\upsilon_g}\frac{\partial A_+}{\partial t} + \delta A_+ + \kappa A_- = 0 \tag{2}$$

$$-i\frac{\partial A_-}{\partial z} + i\frac{1}{\upsilon_g}\frac{\partial A_-}{\partial t} + \delta A_- + \kappa^* A_+ = 0 \tag{3}$$

where z and t are space and time coordinates. $A_+ \equiv A_+(z,t)$ and $A_- \equiv A_-(z,t)$ are the complex field amplitudes for the forward and backward propagating modes, both of which are assumed to be slowly varying in space and time, $\upsilon_g = c/n_g$, n_g is the group index and c is the speed of light in vacuum. The detuning parameter δ is defined as

$$\delta = k - k_B \tag{4}$$

where $k = \bar{n}\omega_0/c$ is the propagation constant, ω_0 is the carrier frequency at which the pulse spectrum is initially centered, and $k_B = \pi/\Lambda$ is the Bragg wave number, where Λ is the Bragg period. The last parameter κ is the linear coupling coefficient defined as

$$\kappa(z) = \frac{\pi n_1(z)}{\lambda_B} \tag{5}$$

where $\lambda_B = 2\bar{n}\Lambda$ is the Bragg wavelength.

Now, considering a short fiber cavity, pulse evolution inside is governed by equation [18]

$$\frac{\partial A}{\partial z} + \frac{1}{\upsilon_g}\frac{\partial A}{\partial t} + \frac{\alpha}{2}A = 0 \tag{6}$$

where α is the fiber loss. Note that for conventional optical fiber $n_g \approx n_{eff}$, where n_{eff} is the effective index (the difference between n_g and n_{eff} is $\sim 1\%$ for fused silica at 1.5 μm), thus in eqs. (2), (3) and (6) were used the same υ_g. This set of equations depict the whole system.

III. Numerical Procedure

In the geometry of Fig 1, L_1 and L_2 are the physical lengths of two uniform FBGs and L_0 is the cavity length (distance between the FBGs). However, the effective length of the cavity will be $L_c = L_0 + L_{eff1} + L_{eff2}$, where L_{eff1} and L_{eff2} are the effective lengths of the gratings. For a single grating, the effective lengths L_{eff} is given by [19]

$$L_{eff} = L\frac{\sqrt{R}}{2\ atanh(\sqrt{R})} \tag{7}$$

where L is the grating physical length and R is the power reflection coefficient which can be defined as the ratio between the power of the reflected and incident pulses at the beginning of the grating

$$R = \frac{P_r}{P_i} = \left|\frac{A_-(0,t)}{A_+(0,t)}\right|^2 \tag{8}$$

where $P_i = |A_+(0,t)|^2$ is the input power and P_r is the reflected power. By the same way, the transmission coefficient T_n of the BFP filter for the *n*th output pulse can be evaluated as the ratio of the transmitted pulse power at the output and the incident pulse power at the input

$$T_n = \frac{P_t}{P_i} = \left|\frac{A_+(L_T,t)}{A_+(0,t)}\right|^2 = (1-R_1)(1-R_2)R_1^{n-1}R_2^{n-1} \tag{9}$$

where P_t is the transmitted power, $L_T = L_0 + L_1 + L_2$ is the total length of the device, R_1 and R_2 are the reflectivities of the FBG1 and FBG2 respectively. The Eq. (9) is valid for a single incident pulse whose the physical length is shorter than the device length.

The Eqs. (2) and (3) are solved numerically using the Euler's method [20] and the Eq. (6) is also solved numerically but using the split-step Fourier method.

The BFP filter considered has $L_1 = L_2 = 0.4\ mm$, $\bar{n} = 1.46$ and $\lambda_B = 1550\ nm$. The cavity length was set at $L_0 = 0.7\ mm$ what leads to a total length of the device $L_T = 1.5\ mm$. The input pulses chosen have Gaussian profile with pulsewidth of 2.0 ps at 1550 nm.

IV. Results and Discussion

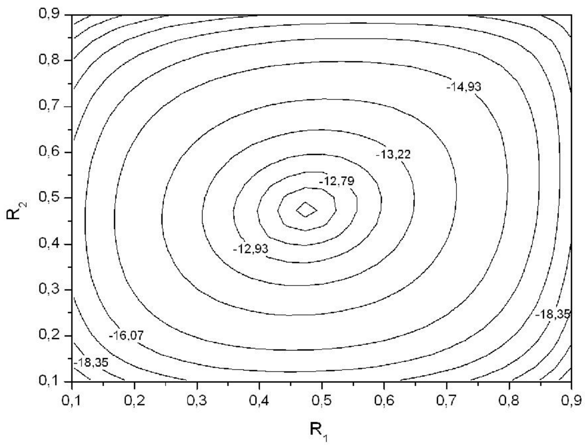

(a)

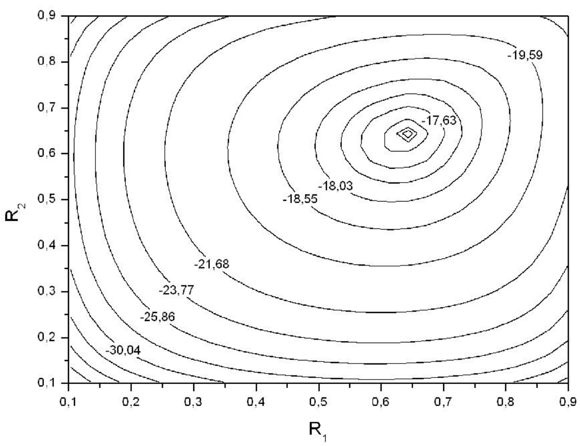

(b)

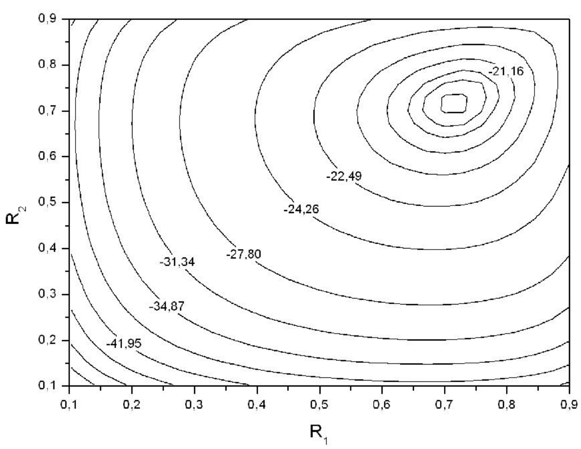

(c)

Fig. 2. Contour plots showing the transmission (in dB unit) as a function of $R_{1,2}$ for the (a) 2nd, (b) 3rd and (c) 4th output pulses.

At first, we will consider that a single pulse is incident on the left end of the BFP filter (see Fig.1) located at $z = 0$. Once a fraction of the pulse penetrate the cavity, it will be trapped due to the gratings and it will perform some round trips. As a result, the BFP filter will pump out a sequence of pulses until the whole energy vanishes. The output pulse stream will have a bit rate of $B = v_g/2L_{eff}$.

We have analysed every output pulse emerging from output and evaluated the transmission (Eq.(9)) in dB unit. We want to know what are the best reflectivities $R_{1,2}$ such as the output pulses provide the transmission maximum. Then, $R_{1,2}$ have been varied and it was evaluated the transmission for every output pulse. To obtain $R_{1,2}$ varying from 0.10 to 0.90, the parameter κ was adjusted suitably (see Eq. (5)).

Fig. 2 shows the contour plots of the transmission as a function of R_1 and R_2 when the second, third and fourth output pulses are monitored. From Fig. 2(a) one can notice that the ideal reflectivity such as the second output pulse experience peak power maximum is about $R_{1,2} = 0.47$. However, for the third output pulse which is shown in Fig. 2(b), the best value is $R_{1,2} = 0.62$ and, from Fig. 2(c) for the fourth transmitted pulse, the best value is $R_{1,2} = 0.70$.

These results denote that the BFP filter must be formed with two identical uniform FBGs in order to obtain peak power maximum of the output pulses. On the other hand, it is not possible to obtain a single value for R_1 and R_2 such as all of output pulses can experience peak power maximum.

The accurate values for $R_{1,2}$ can be obtained analytically from Eq. (9). Making $R_{1,2} = R$, the Eq. (9) reduces to

$$T_n = (1 - R)^2 R^{2(n-1)}. \quad (10)$$

Now, taking the derivative of Eq. (10) and setting it to zero, R is found to satisfy

$$nR^2 - (2n - 1)R + n - 1 = 0. \quad (11)$$

This equation can be easily solved to get $R = 1$ or

$$R = \frac{n-1}{n}. \quad (12)$$

Thus, using Eq. (12), the accurate values are 0.50, 0.66 and 0.75 to maximize the second, third and fourth output pulse respectively. In table I one has the sequence of the output pulses (up to 10th) and the values for R_1 and R_2 that provide the respective output pulse to emerge with peak power maximum.

TABLE I
Ideal reflectivity for transmission maximum ($R_{1,2}$)

Sequence of output pulses	Numerical Simulation	Analytical from Eq. (12)
2nd	0.47	0.50
3rd	0.62	0.66
4th	0.70	0.75
5th	0.75	0.80
6th	0.78	0.83
7th	0.81	0.86
8th	0.83	0.87
9th	0.84	0.89
10th	0.86	0.90

To increase the number of output pulses, we have to increase the reflectivity of the gratings. Thus, the input pulse will

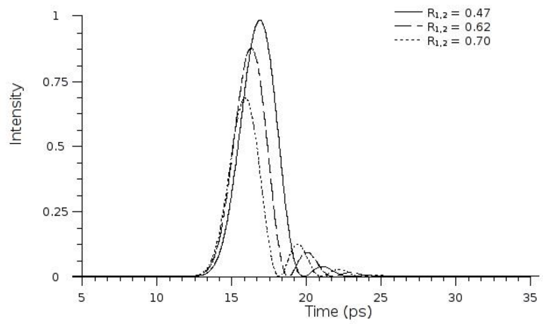

(a)

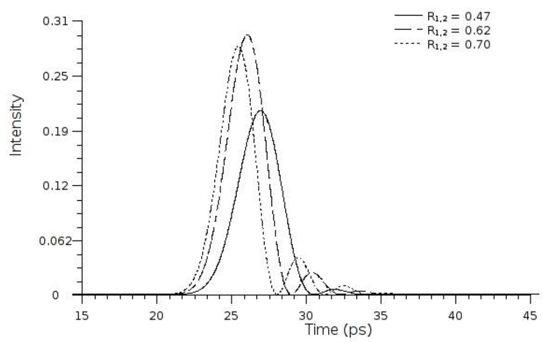

(b)

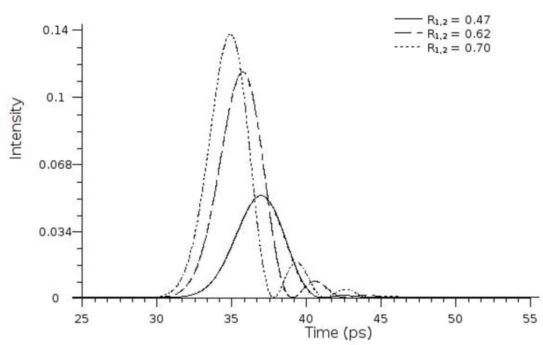

(c)

Fig. 3. Pulse shape of the (a) 2nd, (b) 3rd and (c) 4th output pulse for three different values of $R_{1,2}$ (0.47, 0.62 and 0.70).

perform a larger number of round trips before its power vanishes. However, increasing the reflectivities of the gratings, a lower fraction of the input power will penetrate into the cavity. Thus, it will be necessary to increase the input power when R_1 and R_2 are strong.

Fig. 3 shows the transmitted pulse shape for the second, third and fourth output pulses considering three different values of R_1 and R_2. In Fig. 3(a), one can notice that the second output pulse presents the most peak power maximum for $R_{1,2}$ = 0.47. In the same way, for the third output pulse in Fig. 3(b), $R_{1,2}$ must be 0.62 and for the fourth output pulse in Fig. 3(c) this value must be 0.70.

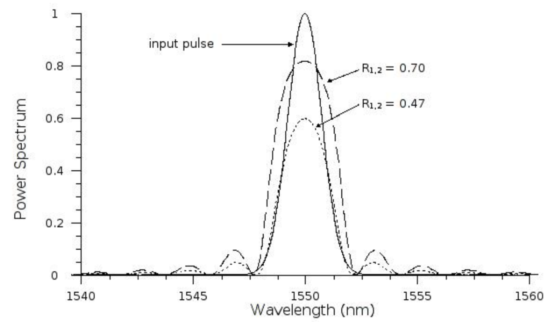

Fig. 4. Spectral responses of two different uniform gratings and the spectrum of the input pulse.

We can also notice that the output pulses have time duration greater than the input pulse. This is due to the interaction with the gratings inside the cavity. When the pulse is reflected, it will have a time duration equal to the round trip propagation time through the grating [17]. Since the pulse inside the cavity undergoes several reflections, for instance, the pulse is reflected four times before the third output pulse to be transmitted, the output pulses get more and more dispersion. The delay time observed in Fig. 3 caused by the device varies because of the effective length of the cavity depends on the reflectivities of the gratings (see Eq. (7)).

We also can see that when the reflectiveties of the gratings increase, there is the appearance of output subpulses. This behaviour is related with spectral responses of the gratings and the spectral bandwidth of the input pulse. If the input pulse has a bandwidth narrower than the gratings, the subpulses arise due to the sidelobes of the grating spectrum [16], [21] when the pulses are reflected inside the cavity by the gratings. Fig. 4 shows the spectral responses of two uniform gratings with reflectivity of $R_{1,2} = 0.47$ and $R_{1,2} = 0.70$, and the spectrum of the input pulse. In the case of $R_{1,2} = 0.70$, subpulses will be arisen because of the granting bandwidth is broader than the pulse bandwidth. On the other hand, when $R_{1,2} = 0.47$, the granting and the pulse bandwidth are almost equal, then the subpulses will have very low intensity. Thus, increasing reflectivities of the gratings, the subpulses will increase as well.

Now, consider the case of two Gaussian input pulses with time delay of 10 ps between them are incident on the input of BFP filter. The reflectivities of the gratings was set $R_{1,2} = 0.47$. A Fig.5 shows the transmitted power for second, third and fourth output pulses as a function of phase difference $\Delta\varphi$ between the two input pulses. We can see that depending on the phase difference between the two input pulses, the output power for every transmitted pulse will change. For the second output pulse, the minimum output power is around -12 dB when $\Delta\varphi = 0$ and the output power maximum is around -5.5 dB when $\Delta\varphi = \pi$. In fact, the output power maximum will occur when $\Delta\varphi = m\pi$, where m is odd integer. This

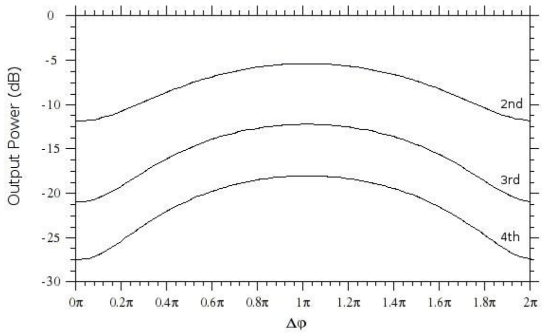

Fig. 5. Output power for 2nd, 3rd and 4th output pulses as a function of phase difference between the input pulses.

behaviour is related with the interference between the mode fields of the two input pulses inside the cavity. When the first input pulse propagates over one round trip, it experiences a phase shift of βL_{eff}, where β is the propagation constant. If the phase of the second input pulse is identical, it will occur constructive interference and the transmission will be a maximum.

V. Conclusion

We have presented ultrashort optical pulse transmission in a BFP filter formed by two uniform FBGs. The input pulses considered have Gaussian profile with time duration of 2 ps at 1550 nm. Examining the sequence of output pulses, it has been shown that the reflectivities of the gratings must be equal to obtain peak power maximum of the output pulses. However, it is not possible to obtain a single value for R_1 and R_2 such as all of output pulses experience peak power maximum.

The amount of pulses in the output pulse stream depend on the reflectivities of the gratings. They have to have high reflectivities in order to get more pulses in the output pulse stream. But, increasing the reflectivities of the gratings, it will also increase the output subpulses.

It was also observed that when two input pulses are incident on the input of the BFP filter, the peak power of the output pulses will depend on the phase difference of the input pulses. In our case, the output pulses will present peak power maximum when the phase difference of the input pulse is $m\pi$. In general, always the phase difference $\Delta\varphi = \beta L_{eff}$ lead to peak power maximum for every output pulse.

References

[1] C. Yang e Y. Lai, *Apodized fibre Bragg gratings fabricated with uniform phase mask using low cost apparatus*, Electron. Lett., vol. 36, no. 7, pp. 655-657, 2000.
[2] R. Kashyap, *Assessment of tuning the wavelength of chirped and unchirped fibre Bragg grating with single phase-mask*, Electron. Lett., vol. 34, no. 21, pp. 2025-2027, 1998.
[3] K. C. Byron e H. N. Rourke, *Fabrication of chirped fibre gratings by novel stretch and write technique*, Electron. Lett., vol. 31, no. 1, pp. 60-61, 1995.
[4] K. O. Hill, B. Malo, F. Bilodeau, D. C. Johnson, and J. Albert, *Bragg gratings fabricated in monomode photosensitive optical fiber by UV exposure through a phasemask*, Appl. Phys. Lett., vol. 62, no. 10, pp. 1045-1047, 1993.
[5] G. Meltz, W. W. Morey, and W. H. Glenn, *Formation of Bragg gratings in optical fibers by a transverse holographic method*, Opt. Lett., vol. 14, no. 15, pp. 823-825, 1989.
[6] S. Legoubin, M. Douay, P. Bernage, and P. Niay, *Free Spectral range variations of grating-based Fabry-Perot filters photowritten in optical fibers*, J. Opt. Soc. Am. A, vol. 12, pp. 1687-1694, 1995.
[7] R. Kashyap. *Fiber Bragg Gratings*, Academic Press, chapter 6, 243, 1999.
[8] X. Yang, C. Zhao, J. Hong Ng, J. Zhang, X. Dong, K. Hian Ng, X. Guo, X. Zhou, C. Lu, *Simultaneous dispersion slope compensation for WDM channels using a Fabry-Perot Etalon formed by double FBGs*, Opt. Commun., vol. 231, pp. 227-231, 2004.
[9] P. L. Swart, A. A. Chtcherbakov, and A. J. van Wyk. *Multiplexed fibre Bragg grating Fabry-Perot interferometers for measuring the coefficients of thermal expansion of anisotropic solids*, Meas. Sci. Technol. vol. 17, pp. 1146-1151, 2006.
[10] J.H. Chow, I.C.M. Littler, G. de Vine, D.E. McClelland, and M.B Gray, *Phase-sensitive interrogation of fiber Bragg grating resonators for sensing applications*, J. Lightwave Technol., vol. 23, pp. 1881-1889, 2005.
[11] X. Wan, and H. F. Taylor, *Intrinsic fiber Fabry-Perot temperature sensor with fiber Bragg grating mirrors*, Opt. Lett., vol. 27, pp. 1388-1390, 2002.
[12] V. Roncin, Q.-T. LE, J. Poette, S. Lobo, L. Bramerie, J.-C. Simon, D. Chevallier, C. L. Rouzic, L. Lablonde, and B. Cadier, *Passive All-optical Clock Recovery demonstration at 42.66 Gbit/s with Bragg-gratings based Fabry-Perot Filter*, ECOC 2007, Berlin (Germany), Tu04.5.4.
[13] R. Slavík, S. Doucet, and S. LaRochelle, *High-performance all-fiber Fabry-Perot filters with superimposed chirped Bragg gratings*, J. Lightwave Technol., vol. 21, No. 4, 1059-1065, 2003.
[14] S. Doucet, R. Slavík, and S. Larochelle, *High-finesse large band Fabry-Pérot fiber filter with superimposed chirped Bragg gratings*, Electron. Lett., vol. 38, pp. 402-403, 2002.
[15] G. E. Town, K. Sugden, J. A. R. Williams, I. Bennion, and S. B. Poole, *Wide-band Fabry-Pérot-like filters in optical fiber*, IEEE Photon. Technol. Lett, vol. 7, pp. 78-80, 1995.
[16] L. R. Chen, J. E. Sipe, S. D. Benjamin, H. Jung, and P. W. E. Smith, *Dynamics of ultrashort pulse propagation through fiber gratings*, Opt. Express, vol. 1, pp. 242-249, 1997.
[17] L. R. Chen, S. D. Benjamin, and P. W. E. Smith, J. E. Sipe *Ultrashort pulse reflection from fiber gratings: A numerical investigation*, J. Lightwave Technol., vol. 15, No. 8, 1503-1512, 1997.Opt.
[18] G. Agrawal, *Nonlinear fiber optics*, Academic Press, 2001.
[19] Y. O. Barmenkov, D. Zalvidea, S. Torres-Peiró, J. L. Cruz, and M. V. Andrés, *Effective length of short Fabry-Perot cavity formed by uniform fiber Bragg gratings*, vol. 14, No. 14, pp. 6394-6399, 2006.
[20] J. H. Mathews, and K. D. Fink, *Numerical methods using Matlab*, 4th Ed., Upper Saddle River, Prentice-Hall, New Jersey, 2004.
[21] L. R. Chen, S. D. Benjamin, P. W. E. Smith, and J. E. Sipe, *Ultrashort pulse reflection from fiber gratings: A numerical investigation*, J. Lightwave Technol., vol. 15, No. 8, pp. 1503-1512.

Modeling and Analysis of Multicast and Unicast IPTV Traffic

Toni Janevski
University "Sv. Kiril i Metodij",
Faculty of Electrical Engineering and Information Technologies,
Karpos 2 bb, 1000 Skopje, Republic of Macedonia
tonij@feit.ukim.edu.mk

Zoran Vanevski
University "Sv. Kiril i Metodij",
Faculty of Electrical Engineering and Information Technologies,
Karpos 2 bb, 1000 Skopje, Republic of Macedonia
zoran.vanevski@telekom.mk

Abstract—**This paper addresses important area related to bandwidth efficient IPTV distribution, modelling instant channel changing traffic on popular channels. We calculate the correlation coefficients and self-similarity degree by using Hurst parameter. The analyses are performed for different traffic types, such as multicast and unicast, as well as for total. Our experimental studies have shown that total network traffic from popular channels is self-similar, and can be modeled with unicast instant channel changing traffic models.**

Index Terms— **ICC, IPTV, multicast, unicast, traces, traffic.**

I. Introduction

Today IPTV is seen as one of the killer services, due to transition from analogue to digital television on one side, and having IP as common networking technology for all telecommunication services in near future, as well as having huge market for television services. Main challenges are transport of new real time sensitive traffic in their IP networks in order to keep the leading position as Internet services providers. Pre-request of using new services is creation of new statistical models of IPTV traffic. Currently, IPTV providers provide mainly two types of traffic: 1) multicast for delivering video channels and 2) unicast dedicated for channel changing, video on demand and other applications [1]. Here, we capture traffic traces from a live network and then examine the self-similarity of IPTV traffic with so-called Hurst parameter and autocorrelation function in different approach than traditional IP traffic models [2].

II. Instant Channel Change

A. How it works?

Instant Channel Change (ICC) is using a buffering technique on channel changing servers. This method creates multiple unicast streams that are sent to the customer along with the broadcast multicast and it gets buffered for the amount of time that equals the anticipated multicast establishment time. So, when the user requests a channel swap it immediately switches to the buffered content as it proceeds with new multicast request.

Channel changing servers maintain sliding windows of live TV service streams for some period of time. The exact time depends on the bit rate of the stream, the structure of the key "I" frames, and the delay characteristics of the stream, but a reasonable guess is around 10 seconds for standard definition. Channel changing servers supply unicast television service to customers (this data is transmitted in RTP using UDP). If a server fails while it is attached to a client, the client switches to another channel change server carrying the same service, and if this server is again not reachable the subscriber will receive multicast stream directly with around 1 sec interruption.

Overhead has direct influence on two points in the network, limited bandwidth at customer premises and utilizing of backbone links. First point is during worst case scenario when the customer has two STBs and change channels in same time so overhead directly depends from maximum bandwidth at customer device. Second point is unicast traffic generated during channel changing should be transported through IP backbone links. The capacity of a Digital Subscriber Line ("DSL") channel is limited. Engineering a network to support channel change as described above requires several Mbps of reserved bandwidth. Such a configuration will either reduce the DSL serving area, reduce the number of video streams that can be delivered, and/or compromise other services during channel changing periods.

If IPTV provider using DSL technology then it will set very low overhead, than time and distributed unicast traffic is very high so it will utilize backbone links. IPTV providers should made calculations and measurements on access network and first input for calculating overhead should be DSL bandwidth. Reasonable value for overhead is 20 %, with 3,2 Mbps bitrate and burst time is around 10 seconds for standard definition stream, as we can see on Fig. 1, there are measured bursts with different parameters.

B. Locating of channel changing servers

The number and location of Channel changing servers depend on number of expected subscribers and capacity of links. As the number of subscriber grows the number of stream will increase and will consume more bandwidth in the core network. It prevents the user from getting a real time broadcast experience. In the beginning Channel changing servers will be placed at a Central location near IPTV servers, lately they will be placed in Remote locations and also in other sites with IP network Points of Presence (PoPs) if there is a need. Dimensioning of the demand for bandwidth in this paper is based on the prediction that ICC generates 30% more traffic than multicast stream due to ICC overhead.

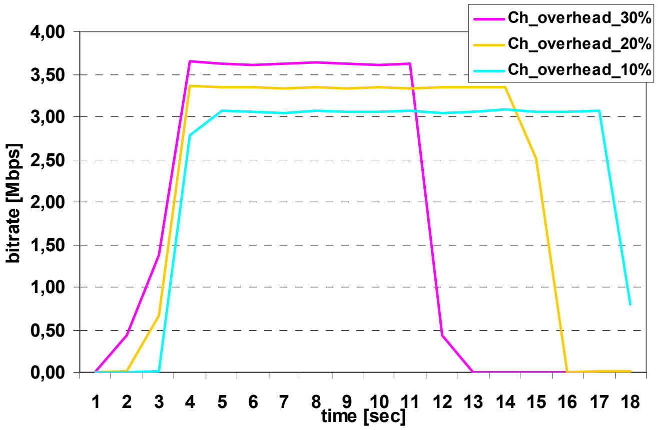

Fig 1. Measured unicast bursts for different value of overhead

III. Mathematical Background

A. Model of single user

IPTV users in this paper will be defined with a two state model. First state is an active state *A(t)* which occurs with probability *P(A(t)),* and with two possible rates R_{UC} during channel changing and R_{MC} is defined as a multicast rate while the user is watching channel. Second state is when users is non active *N(t)* - STB is turn off, and it happens with probability P(*N(t))=1-P(A(t))*. If the user has changed channel during a measurement period at least once, then it is in state *U (t)*, otherwise it is in *M (t)* state. The probability distribution of the rate viewer demands at time *t* then is given by:

$$R_i(t) = \begin{cases} R_{MC} & \text{with probability} \quad P(A(t))P(M(t)) \\ R_{UC} & \text{with probability} \quad P(A(t))P(U(t)) \\ 0 & \text{with probability} \quad P(N(t)) \end{cases} \quad (1)$$

where R_{UC} is peak rate while ON, and R_{MC} is average rate.

B. Burstiness and self-similarity

Bursty traffic is more difficult to handle in a queuing system than traffic generated from non-bursty sources which produce a more continuous workload. Transmission burstiness is often measured by the following expression:

$$b = 1 - \frac{\overline{R}}{R_{MAX}} \quad \text{clearly } 0< b< 1; \quad (2)$$

For b equal to zero, the source is not bursty, for b approaching 1 we have a bulk arrival process.

Our statistical analysis of IPTV traffic traces will be presented with autocorrelation function [3]. We obtain correlation coefficients from the traffic trace in the following manner: for a given measurement with N samples, with samples $y_1, y_2, \ldots, y_N$, at time moments $x_1, x_2, \ldots x_N$, the lag k correlation coefficient is defined as:

$$r_k = \frac{\sum_{i=1}^{N-k}\left(Y_i - \overline{Y}\right)\left(Y_{i+k} - \overline{Y}\right)}{\sum_{i=1}^{N}\left(Y_i - \overline{Y}\right)^2} \quad (3)$$

The degree of self-similarity can be defined using the so-called Hurst parameter *H*, which expresses the speed of decay of the autocorrelation function. If $H \to 0.5$ the time series is short range dependent, for $H \to 1$ the process becomes more and more self-similar. The slope can be estimated using linear regression, leading to the Hurst parameter, which is determined by function (4):

$$H = 1 - \frac{\beta}{2} \quad (4)$$

In the following discussion, long tailed distributions will be used to describe packet sizes and inter-arrival times. By a definition, a distribution is said to be long- or heavy-tailed if its complementary cumulative distribution function (CCDF), regardless of its shape for small values of the random variable, has the following asymptotic behavior:

$$P(T \geq t) \sim t^{-\alpha} \quad \text{for } t \to \infty, \text{ and } 0<\alpha<2 \quad (5)$$

The Pareto CDF is a power curve that can be easily fit to observed data. It will be used to describe packet sizes later. Its CDF is given by:

$$F(t) = \begin{cases} 1 - \left(\frac{t}{k}\right)^{-\alpha-1} & if \ \ t > k \\ 0 & otherwise \end{cases} \quad (6)$$

The probability for $t<k$ is zero; k is the minimum value which can occur in a sample set. The probability density function (pdf):

$$f(t) = \begin{cases} \alpha k \left(\frac{t}{k}\right)^{-\alpha-1} & if \quad t > k \\ 0 & otherwise \end{cases} \quad (7)$$

Parameter α dependence and can be calculated from Hurst parameter with this function (8):

$$\alpha = 3 - 2H \quad (8)$$

IV. Statistical Analysis

Single user model definitely depends from customer behaviours for channel changing and watching. This model like we said in previous section will be presented as Markovian model with all probabilities, and should be generated from IPTV providers measurements like on the Fig. 1. The arrows between three states are probabilities of transition from one to another state. Three states are defined as probability of changing channel *P(U(t))* probability of channel watching *P(M(t))* and probability when STB is off or in “stand by” mode *P(N(t))*.

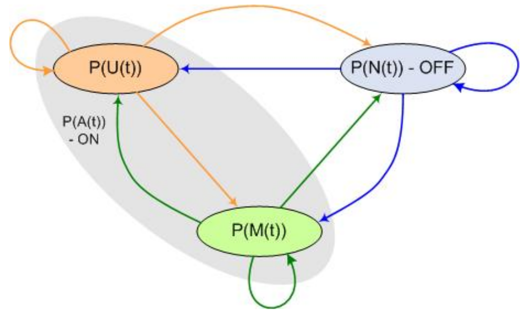

Fig 2. Markovian model for average customer behaviour

The model given in Fig.2 is derived from the real-traffic measurements shown as captured IPTV traffic generated from single IPTV user (Fig. 3). In Fig.3 channel changing marked with red color is unicast traffic and others are aggregate traffic and traffic per channel (channel 1, 2 and 3, respectively). Autocorrelation functions shown as correlation coefficients for single user case (from Fig. 3) are given in Fig. 4. This kind of model (Fig. 2) can be used in future planning of new channel changing servers and utilizing network links. Also we can use to dedicate separate server for particular group of subscribers.

If we look into the popularity of channels reports [4], top 10-20% of channels account for nearly 80% of the viewer share, indicating that channel popularity follows the Pareto Principal (or 80-20 rule). We also observe that the distribution during all day for top popular channels is constantly (static). This demand of bandwidth is covered by multicast distribution. Measured unicast traffic for changing of popular channels is around 80% of all ICC unicast traffic.

We made also and 100 seconds traces, scanning live IPTV traffic on edge router network interface towards clients' side. Measurements and analyses are made per traffic type, multicast from all popular channels and unicast from all instant popular channels changing as well as the aggregate traffic (Fig.5).

Autocorrelation functions of all mentioned traffic types are shown on Fig. 6. The autocorrelation of unicast and aggregate traffic decays hyperbolically rather than exponentially fast. This shows that are self-similar processes while Multicast traffic is not.

Using the calculated Hurst parameters for IPTV traces, given in Table 1, one can conclude that Hurst parameter for unicast and aggregate traffic are higher than the one for the multicast. The Hurst value for unicast IPTV is 0.75, which shows that this traffic has middle-level of self-similarity. Additionally, we can conclude that IPTV traffic model can be approximated with unicast traffic model, which heavily depends upon users' behaviour.

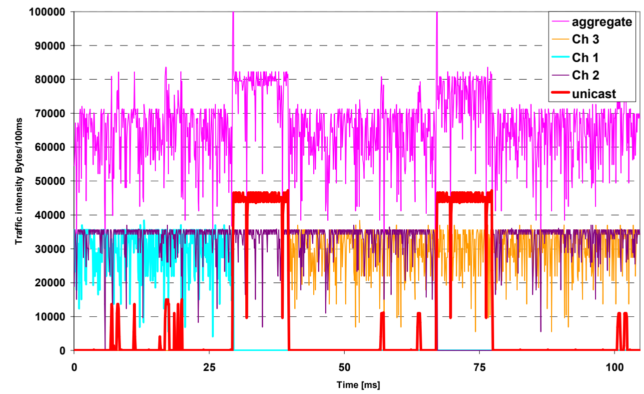

Fig. 3. Single user IPTV traffic traces

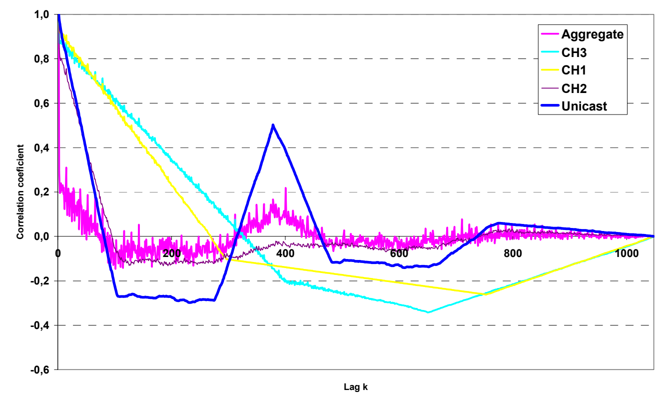

Fig. 4. Autocorrelation Function for Single user IPTV traffic

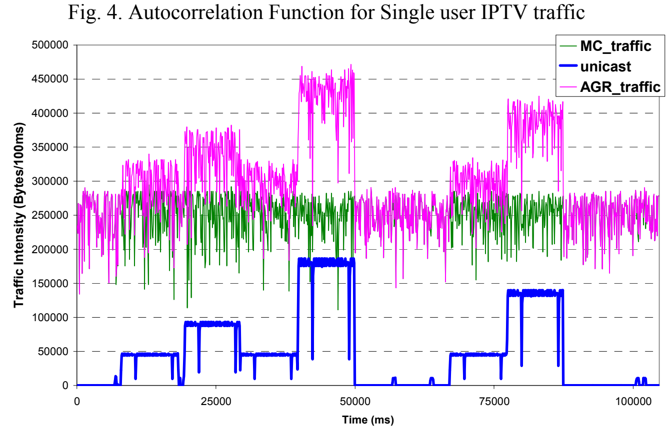

Fig. 5. IPTV traffic traces

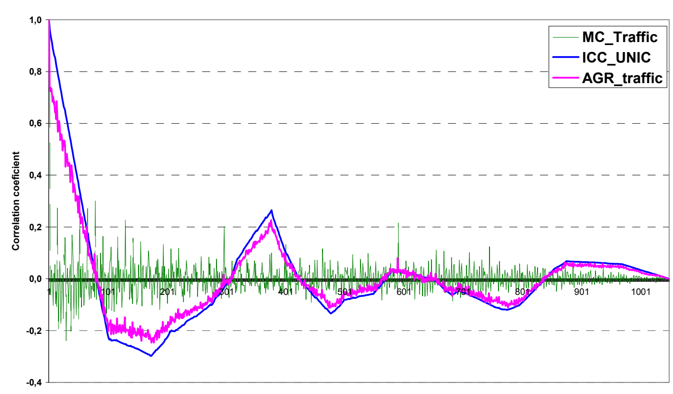

Fig. 6. Autocorrelation Function for Multicast, Unicast and Aggregate traffic

TABLE I
HURST PARAMETER, β, α and b - burstyness

Traffic	H	β	α	b
Aggregate	0.7133	0.5734	1.5734	0.3620
Multicast	0.5882	0.8236	1.8236	0.1550
Unicast	0.7565	0.4870	1.4870	0.7223

Pareto is very convenient because it posses long-tailed autocorrelation function and slow-decay variance, properties characteristic for asymptotically second-order self-similar processes, as Internet traffic is. On the other side, this distribution is described with the least parameters from all known distributions with self-similar properties. Therefore, we are using Pareto distribution to model aggregated IPTV traffic as well as unicast traffic traces.

Further, our aim is to fit the first two moments of the measured Internet traffic traces with the Pareto distribution. In other words, we need to obtain the optimal parameters of the Pareto distribution that best models the measured traffic. Considering the analysis of traffic traces the parameter α from Pareto distribution is obtained from its relation with the Hurst parameter and results in table 1 for α.

Aggregate IPTV traffic depends with a high percentage from unicast channel changing traffic, hence we are proposing the following for practical IPTV system implementations:

1. IP multicast distribution in the backbone should use static trees, where popular channels are delivered to all end users. Only the tree branch for all others channels, from IPTV Platform to customers dynamically to change.

2. Information about which are popular channels should be delivered to STB. During the channel surfing of popular channels STB should not use unicast bursts from channel changing servers, but Adjacent Multicast Join approach.

V. CONCLUSION

We performed statistical analysis of the captured IPTV traffic from a real testbed network, which should be commercially launched in near future. We analyzed the traffic per type, i.e. multicast, unicast, as well as aggregate traffic.

First main conclusion in this paper is that the unicast IPTV traffic has middle-level self-similarity, i.e. Hurst parameter is around 0.75, while the classical multicast distribution has lower level of self-similarity, with Hurst below 0.6. Second is that models of aggregate IPTV traffic can be approximated with models for ICC unicast traffic (e.g. Pareto). Such models can be used for simulation or analytical analyses of IPTV services, which is of paramount importance for analysis and design of channel changing servers as well as dimensioning and engineering of IP backbone links.

REFERENCES

[1] Microsoft Corporation, *Microsoft TV: IPTV Edition*, http://www.microsoft.com/tv/

[2] Will E. Leland, Walter Willinger, Murad S. Taqqu, and Daniel V.Wilson, *On the self-similar nature of ethernet traffic (extended version)*, pp. 1–15, IEEE/ACM Transactions on Networking, September 1993.

[3] Toni Janevski, *Traffic Analysis and Design of Wireless IP Networks*, Artech House Inc., 2003.

[4] Meeyoung Cha, Pablo Rodriguez , Sue Moon, *On Next-Generation Telco-Managed P2P TV Architectures*, IPTPS'08, Florida, February 2008.

QVoip – A tool to evaluate the quality of VoIP calls using E-model

Fabio Pessoa Nunes
School of Electrical and Computer Engineering
State University of Campinas - UNICAMP
P.O. Box 6101 - 13083-852
Campinas - SP - Brazil
fpnunes@decom.fee.unicamp.br

Fabio Sakuray
Computer Science Department
State University of Londrina - UEL
P.O. Box 6001 - 86051-990
Londrina - PR - Brazil
sakuray@uel.br

Leonardo de Souza Mendes
School of Electrical and Computer Engineering
State University of Campinas - UNICAMP
P.O. Box 6101 - 13083-852
Campinas - SP - Brazil
lmendes@decom.fee.unicamp.br

Mario Lemes Proença Jr.
Computer Science Department
State University of Londrina - UEL
P.O. Box 6001 - 86051-990
Londrina - PR - Brazil
proenca@uel.br

***Abstract*—The VoIP systems are very sensitive to some parameters that can change according to the utilization of the network where they pass. The tool QVoip is capable of making VoIP calls and measuring voice quality. This measurement is made with the utilization of E-model using factors from the VoIP application and variables from the network to evaluate quality. With this tool it is possible to analyze the factors that degrade the voice and help designers to evaluate if a network is good for VoIP.**

***Index Terms*—E-model, QoS, VoIP.**

I. INTRODUCTION

Communication is one of the main factors of the evolution of humanity. Nowadays everyone can exchange information in an easy way using many means of communication. Telephony was invented many years ago and many people around the world still use it throughout the day to communicate. The Internet also became a great way to correspond with others since the users stay connected all day to the network, accessing information from everywhere in just a few seconds.

With the advance of the technology, now we can use telephony through the Internet. This new way to make calls is know as VoIP (Voice over Internet Protocol). The principal advantage of VoIP is the cost reduction in phone calls, once the calls use the Internet and have a low cost. Other advantages of the Voice over Internet Protocol is a range of functionality that it brings, like the possibility of have a phone number from a specific city being in any part of the world, voicemail and follow me.

Unfortunately, make calls through Internet can sometimes have some problems. Unlike traditional telephony, VoIP doesn't have dedicated channels for the voice traffic. On VoIP, the voice is transported as data packets through the network and can have the same problems as normal data packets. These packets can be lost in any part of the network or have some extra delay due to some network problem. Voice packets of the VoIP are time sensitive and any of these problems can affect the final quality of a call, many times becoming impossible to use this kind of telephony.

This work presents a tool to evaluate the voice quality of VoIP that a user is experiencing during a call. With this tool, the user will be capable to evaluate if a network is appropriate for VoIP calls and if the VoIP provider is offering a good service. In section II we present related works that evaluate voice quality in VoIP calls. Section III presents the model used to make the quality evaluation, the E-model [1], and the Qvoip tool. The results of the tool can be found in section IV. And the final comments are presented in section V.

II. RELATED WORKS

The quality evaluation works are separeted in two groups: subjetive evaluation and objective evaluation. In the subjetive group some users evaluate the sound given a grade and the mean of all grades is the quality of the system. One of most used subjetive method is the MOS (Mean Opinion Score) [2], largely used to evaluate codecs and VoIP equipments. In the objective method, the transmission equipment and its characterists, giving quality grades to the system. The main objectives methods are the PSQM (Perceptual Speech Quality Measure) [3], PESQ (Perceptual Evaluation of Speech Quality) [4] and E-model.

Bross et. al. [5] presents a comparison between the Public Switched Telephone Network and Internet Telephony. The authors analyzed the voice quality in many scenarios and using different codecs, showing that the codec is fundamental to guarantee the VoIP quality. In the paper, the tests used the E-model to do the evaluation and was proved that the QoS of today's VoIP solutions is satisfactory for end-user and that

VoIP is a potential substitute for the PSTN.

At paper [6], the authors present a vital element to provite quality in VoIP calls, the Call Admission Control (CAC). The CAC manage the calls of the system to garantee quality, so the system only accepts new calls if it is not overload. Without the CAC the systems would always accept new calls, and can damage all current calls.

Most of the quality measure papers present evaluations based on tools that were planned to be used with english language. However, each language has different behavior in VoIP quality. In [7], the authors evaluated VoIP quality in different languages, english and chinese, using PESQ evaluation method. Based on the realized tests, they proposed to add a variable in E-model calculation to consider the user language. The tests were done using G.729 and G.711 codecs.

Shin et. al. [8] presents an evaluation of VoIP in a real wireless network and compared it with simulators results. This comparison shown that some variables were standardized in past works, but it does not give the real state of a network, presenting a wrong network capacity.

The objective of this work is to evaluate VoIP calls using E-model in different networks and situations, demonstrating the worst factors and situations to use the Voice over IP.

III. The E-model and the Qvoip tool

To evaluate the behavior of VoIP calls in a network, this work presents the Qvoip tool to analyze the sound quality received by the users during a call. The Qvoip is an application capable of making calls through a data network while at the same time capturing data from the network to measure the quality of the VoIP. This tool will analyze in real time if a network is appropriate to make VoIP calls and validate if the VoIP quality matches what was sold by the telephony company. To elaborate this tool, all the necessary calculations were incorporated to the Linphone software [9], which is an open-source software capable of making VoIP calls.

Based on some works [10,11], the E-model was chosen as the most appropriate recommendation to make this evaluation, once the measurement can be done in real-time by the Voice over IP application. This method makes some calculations using factors that affect the VoIP quality and presents a grade, named R factor, which is a value from 0 to 100, with 100 representing the best quality and 0 representing the worst quality. The ITU-T G.107 recommendation [1] shows that the E-model follows the equation (1) bellow:

$$R = R0 - IS - Id - Ief + A \qquad (1)$$

In the equation, *RO* represents the signal-to-noise ratio, including circuit and room noise. *IS* represents a combination of all impairments which occur more or less simultaneously with the voice signal. The *Id* represents the impairments caused by the end-to-end delay. *Ief* represents impairments caused by characteristics of the equipment, like codec. And *A* represents an advantage factor used to compensate the known faults of the system.

The ITU-T G.107 recommendation presents some mathematical expressions and default values to determine the signal-to-noise ratio. Then, Lustosa [11] determined by default that the *R0* is 92.77. The author also determined that the *IS* also can have a default value, which will be 1.41. Finally, the value for *A* was defined as 0, a value recommended to VoIP applications.

So, Lustosa et. al. [12] presents a reduced E-model equation, showed in equation (2):

$$R = 93.36 - Id(Ta) - Ie(codec, loss) \qquad (2)$$

The variable *Id(Ta)* is related to end-to-end delay at the network, in other words, the time taken for the voice of a user to be heard by the other user. The *Ie(codec,loss)* is a function that depends on the codec used and packet loss ratio.

According with Lustosa [11], *Id(Ta)* can be found by the equation (3) bellow:

If ($Ta \leq 177.3$):

$$Id(Ta) = 0.024 * Ta$$

If ($Ta > 177.3$):

$$Id(Ta) = 0{,}134 * Ta - 18{,}103 \qquad (3)$$

According to Lustosa [11], *Id(Ta)* in (3) can be found by the equation (4) bellow:

$$Ta = Tcodec + Tnetwork + Tbuffer \qquad (4)$$

Tcodec represents the delay added by the codec used and can be found at *ITU-T G.114* recommendation [13]. The *Tnetwork* is the delay (expressed in *ms*) of the voice packets to reach the destination. And the *Tbuffer* is the delay (expressed in *ms*) added by the dejitter buffer.

The *Ie(codec,loss)* variable in equation (2) can be calculated using the equation (5), also described by Lustosa [11].

$$Ie(codec, loss) = Ie + ((95 - Ie) * PPL / (PPL + BPL)) \qquad (5)$$

Ie represents the loss factor related to the equipment used by the VoIP and this value can be obtained in recommendation ITU-T G.103 Appendix I [14]. The PPL indicates the percentage of packet loss in the period of the quality measurement and this packet loss should be evaluated at the dejitter buffer. Finally, the BPL is the quality factor of each codec related to loss packets, values that can be found for some codecs in [14,15].

Some of the variables presented by the E-model are related to choices made by the VoIP application during the use. The codec influences some variables of this evaluation method, so is important to find out the most appropriate codec for a specific network. The dejitter buffer, also related to application, adds delay in the network packets. Many times this buffer has the same size, but some works show the advantages of using a buffer which can vary during the use. The objective of this work is to analyze the network factors which degrade the voice quality, so we determined the use of G.711 codec and a dejitter buffer of 30 ms.

Two of the main variables of the E-model are directly related to the network, so informations of the network state are necessary to obtain these values. One of these variables is the *Tnetwork*, which is the delay of the packets in the network. There isn't an exact way to obtain this value from the network once it's difficult to keep two hosts with synchronized clocks. Therefore, in this work we followed Schulzrinne et. al. [16] work, which gives a good approximation of this value. Voice applications in data networks need to exchange information between the users to know what the status of the call is. To have this control, the application sends RTCP packets during the call, so it can be used to measure the packets' delay in the network. At constant intervals of time the application sends a Sender Report (SR) RTCP packet which has the timestamp of the moment that the packet was sent by the application. When the packet reaches the destination, it is processed by the host and a response is sent back in a Receiver Report (RR) RTCP packet with the SR timestamp and the time it took for the host to process the SR and send the response. After the RR reaches the first host, the application calculates the actual timestamp and subtracts the timestamp and the processing time of the SR, both in the RR packet. In this way, the time it took for a packet to pass over the network and go back to the host can be found, the RTT (Round Trip Time). By dividing the RTT in half, it is possible to obtain an approximate value of the time it takes for a packet to pass over the network, finding a good approach of the time it takes a packet to reach the other host in the network. The packet loss (PPL) is another fundamental variable in this model. Not only the packets which don`t reach the destination can be considered lost packets. Many times some packets reach the destination with a high delay, missing the right time to be played, so these packets are considered lost too. Carvalho et. al. [7] said that the packet loss rate only can be measured in application level, once the application does the final processing of the voice packets and will know if a packet doesn't reach the destination. The packet loss verification is made by verifying the sequence number of each packet to check if it is missing any packet in the sequence at the moment of the processing to play the audio. The right location to make this verification is the dejitter buffer, because this buffer adds a little delay in the reproduction to give a chance for delayed packets to reach the destination in time to be played.

Despite the constant variation of these variables, some range of values are considered acceptable for VoIP calls. According to ITU-T G.114 recommendation [13], the end-to-end delay in one way shouldn't be higher than 150 ms to maintain high quality calls and delays higher than 400 ms are unacceptable for most of the networks. Related to the packet loss, each codec accepts a range of lost and the *BPL* variable indicates if the codec has a good treatment to packet loss. The G.711 is considered one of the best quality codecs and has low influence of packet loss.

The ITU-T related in [17] some range of R factor values and user satisfaction. This comparison can be found in table 1 bellow:

TABLE I
DEFINITION OF CATEGORIES OF SPEECH TRANSMISSION QUALITY

Range of E-model Rating R	Speech transmition quality category	User satisfaction
$90 < R \leq 100$	Best	Very satisfied
$80 < R \leq 90$	High	Satisfied
$70 < R \leq 80$	Medium	Some users dissatisfied
$60 < R \leq 70$	Low	Many users dissatisfied
$50 < R \leq 60$	Poor	Nearly all users dissatisfied

Choosing the Linphone application and analyzing the E-model, we could incorporate the evaluation model to the VoIP application making some modifications to collect the necessary data from the network. The basic scenario used in this work and the variables from E-model are represented in figure 1. The figure demonstrates that almost all variables from the E-model are related to the VoIP software, like *BPL*, *IE* and codec delay. The packet loss is related to the network, but is measured in the application. Finally, the delay in the network is calculated with the RTT, obtained by the RTCP packets.

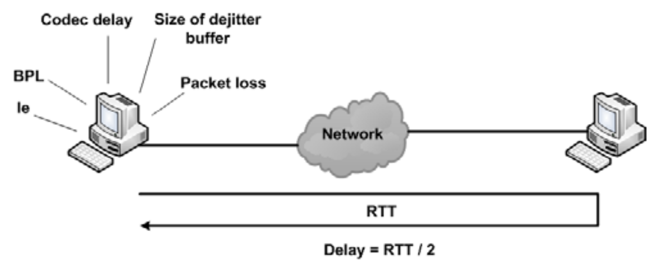

Fig. 1. VoIP scenery and the E-model variables

IV. RESULTS

To evaluate the proposed tool, the application was tested in two real scenarios. For 24 hours, the QVoip tool was used to make 5 minutes calls every 15 minutes. In these calls both end users used the tool to evaluate the speech quality of the calls using the variables of the E-model equation.

Figure 2 shows the result of the R factor evaluated by the QVoip tool during a call in one of the tested scenarios.

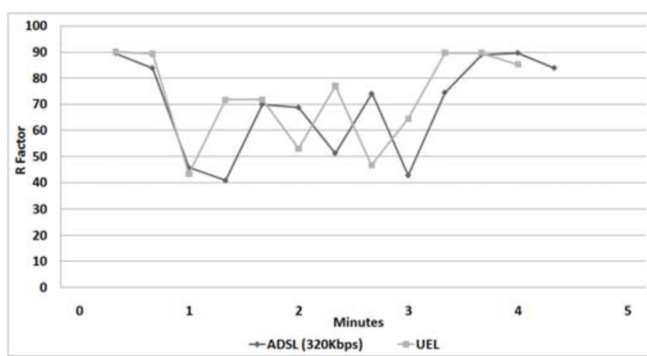

Fig. 2. Quality measure in a VoIP call.

The graph shows how the quality varies in a 5 minutes call. Any of these grades presents the quality of a VoIP call that the user would be listening to at that moment. Since the quality is measured every time the application calculates the delay, if one of the RTCP packets is lost in the network, the model will not be able to generate a grade at that moment. Each call using

QVoip can be represented by a grade in R factor that is calculated with the arithmetic mean of all grades of that call.

In both test scenarios, the source equipment of the call was in the State University of Londrina (UEL). The Internet link of the university is shared by almost 5000 computers in the same network. So, at some periods there is a high use of the link resulting in moments that the user couldn`t obtain a good quality in the VoIP. During work days in the university, the use of the Internet link is high from 08:00 am until approximately 10:00 pm and low during the rest of the time. This utilization of the Internet link in UEL is represented in figure 3.

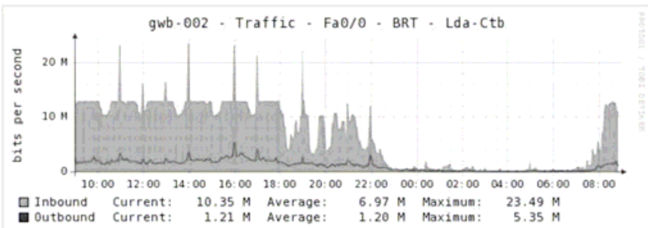

Fig. 3. Use of the Internet link at UEL.

In one of the test scenarios, the calls were made between UEL and a 320 Kbps ADSL connection in the same city. During the test period, as demonstrated in figure 3, it is possible to prove that in periods of high utilization of the Internet the VoIP quality varies and in some moments the VoIP is not good for the user make calls. As was presented in figure 3, the use of the Internet grows after 08:00 am, same time that it is possible to observe that the voice quality begins to vary, as show in figure 4. This voice quality variation happens during the whole day until 10:00 pm, after that the use of the Internet link has a low utilization.

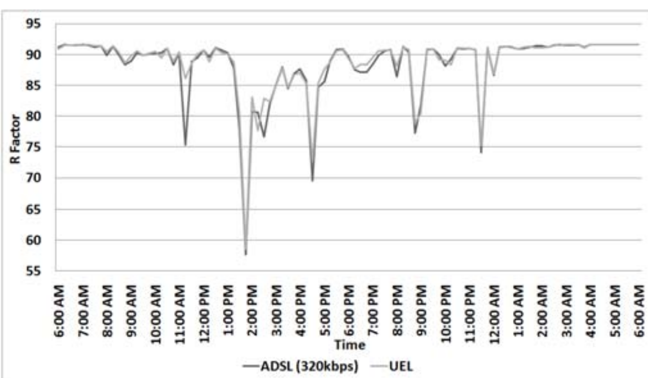

Fig. 4. VoIP quality between UEL and ADSL.

Figure 5 shows the graph of the mean delay between UEL and ADSL during the whole day. It was observed that throughout the whole period of low utilization of the Internet the delay does not have a high variation. However, during the period of high utilization it is possible to observe high delays at some points. Comparing this graph with figure 4, we can check that at moments of low quality the application had the highest delays. This comparison shows that the delay has a high influence in voice quality. During the worst quality period of the day, 01:45 pm, the application detected a high delay in the network, 370.31 ms for the ADSL user and 371.44 ms for the UEL user.

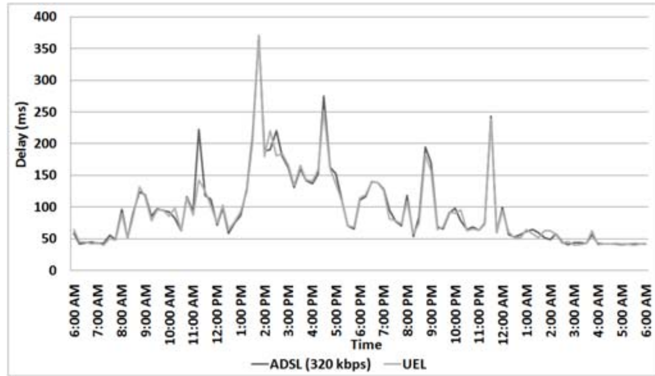

Fig. 5. Mean delay between UEL and ADSL.

The percentage of packet loss that the VoIP calls had in this same scenario is presented in figure 6. We can notice also a higher packet loss in the period of high Internet utilization; however it is not possible to observe a closer relation of quality and packet loss, because in some moments of high losses the quality remained at a good level. Another factor presented in this picture is the higher packet loss in the ADSL. This fact is a result of the low speed of the ADSL, however the quality graph shows that the quality is almost the same for both users.

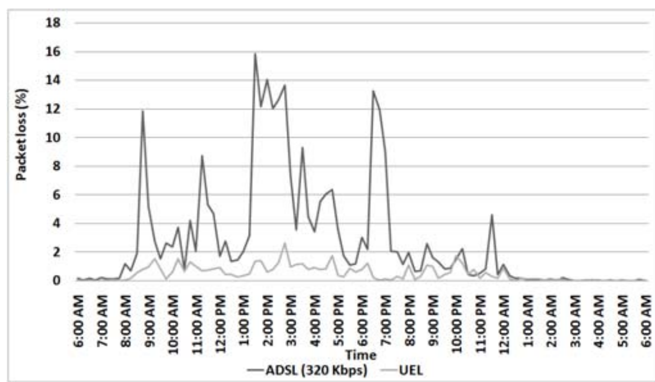

Fig. 6. Mean packet loss between UEL and ADSL.

The second scenario was between State University of Campinas (UNICAMP) and UEL, following the same parameters as the last tests. Figura 7 shows how the calls were at these tests. For these tests we still can observe that the quality is worst during times of high utilization of the Internet, however the quality is more uniform than in the other tests.

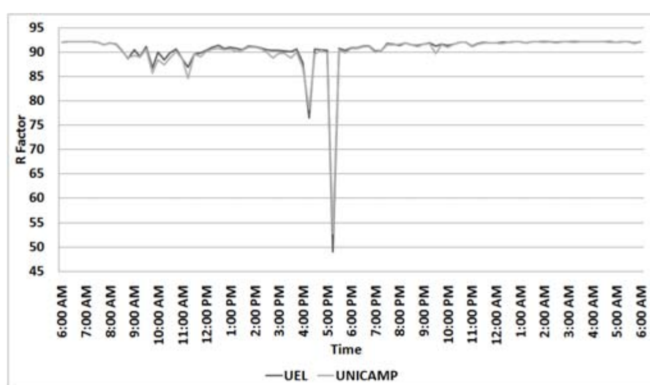

Fig. 7. VoIP quality between UEL and UNICAMP.

During almost all the test period between UNICAMP and UEL the grades were higher than 85, representing a good voice quality. The high bandwidth in both places brings better results in VoIP quality, differently from the ADSL scenery where we have a lower bandwidth.

Despite the better quality, these calls also had moments of bad quality, probably because there occurred some high load in the network in the measured moment. We can observe at 05:15pm a R factor of 52.82 at UNICAMP and 49.11 at UEL, revealing that it would be impossible to have a good VoIP conversation between these places. Figure 8 shows the delay in the network during the whole day between UEL and UNICAMP. The graph indicates a higher delay in packets at moments of high Internet utilization in both universities and a low delay from 00:00 am until 08:00 pm, moments when the links have low utilization.

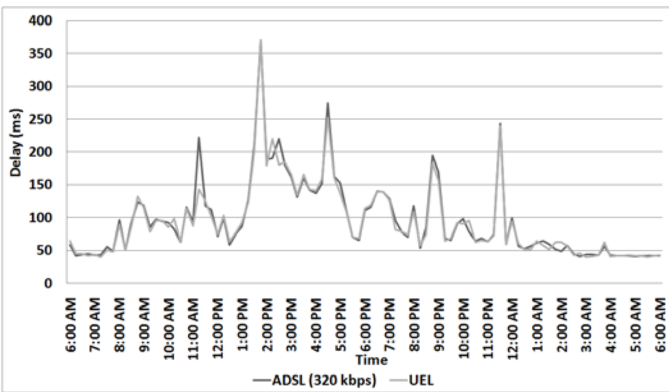

Fig. 8. Mean delay between UEL and UNICAMP.

At the moment of the worst quality call of the day, demonstrated by the R factor, at 05:15 pm, the tool also captured a high delay in the network during the day, 401.98 ms at UNICAMP and 423.82 ms at UEL. The figure shows that the VoIP quality call is directly related to network delay, so the VoIP will have bad quality in networks with delay. According to figure 9, which represents the packet loss in all the test periods, more packets are lost in periods of high network utilization. However, in some moments there is a high packet loss rate, but the quality is still good. This behavior is a result of the codec used, which has a good packet loss acceptation. Using low quality codecs would result in low quality with the increase of packet loss.

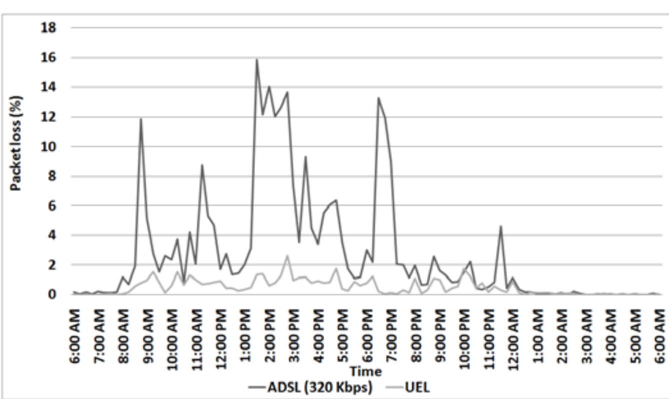

Fig. 9. Mean packet loss between UEL and UNICAMP.

V. Final Comments

This work showed that the E-model is an effective way to evaluate the VoIP calls. It gives a technical review of VoIP quality, giving users and providers a way to have detailed results about the quality. We also proved that the increase of the data traffic in the network is inversely proportional to voice quality, because the higher traffic changes the variables important to quality, like delay and packet loss. This kind of work is important because it shows that VoIP can be largely used when we have good networks.

In future works we should vary others variables from E-model, like codec and dejitter buffer. Doing this, we will analyze the effects of these variables in calls using IP protocol and find ways to always have good VoIP calls.

Acknowledgment

The authors would like to thank FINEP for the financial support for the project of Monitoring VoIP System – QvoIP.

References

[1] ITU-T G.107, *The E-model, a computational model for use in transmission planning*, 2004.
[2] ITU-T P.800, *Methods for subjective determination of transmission quality*, 2006.
[3] ITU-T P.861, *Objective quality measurement of telephone-band (300-3400 hz) speech codecs*, 1996.
[4] ITU-T P.862, *Perceptual evaluation of speech quality (PESQ): An objective method for end-to-end speech quality assessment of narrow-band telephone networks and speech codecs*, 2001.
[5] J.F.M. Bross, C. Meinel, C., *Can VoIP Live up to the QoS Standards of Traditional Wireline Telephony?*, Fourth Advanced International Conference on Telecommunications, vol. 1, pp. 126-132. June 2008.
[6] A M.A.Hoque, F.Afroz, *Call admission control: QoS issue for VoIP*, 3rd International Conference on Communication Systems Software and Middleware and Workshops, vol. 1, pp. 757-761. January 2008
[7] J.Ren, H.Zhang, Y.Zhu, C. Gao, *Assessment of effects of different language in VOIP*, Conference on Audio, Language and Image Processing, pp 1614-1628. July 2008.
[8] S.Shin, H.Schulzrinne, *Experimental Measurement of the Capacity for VoIP Traffic in IEEE 802.11 WLANs*, 26th IEEE International Conference on Computer Communications, vol. 1, pp. 2018-2026. May 2007.
[9] "*Linphone, an open-source sip video-phone for linux and windows available at http://www.linphone.org.*"
[10] F. David, *Ferramentas de monitoração ativa e passive para avaliação da qualidade de redes VoIP*, Master thesis, UFRJ, Rio de Janeiro, 2003.
[11] L. C. G. Lustosa, *Arquitetura de monitoração de qualidade de chamadas telefônicas IP*, Master thesis, UFRJ, Rio de Janeiro, 2005.
[12] L. C. G. Lustosa, L. S. G. Carvalho, P. H. de A. Rodrigues, E. de S. Mota, *Utilização do modelo e para avaliação da qualidade da fala em sistemas de comunicação baseados em Voz sobre IP*, XXII Simpósio Brasileiro de Redes de Computadores (SBRC 2004), May, 2004.
[13] ITU-T G.114, *One-way transmission time*, 2003.
[14] ITU-T G.113 Appendix I, *Provisional planning values for the equipment impairment factor Ie,* 2007.
[15] ITU-TSG12, *Estimates of Ie and BPL parameters for a range of codec types*, 2003.
[16] H. Schulzrinne, S. Casner, R. Frederick , V. Jacobson, *Rtp: A transport protocol for real-time applications*, 2003.
[17] ITU-T G.109, *Definition of categories of speech transmission quality*, 1999.

VoIP quality improvement with a rate-determination algorithm

Demóstenes Zegarra Rodríguez
Electronic Systems Engineering Department
Escola Politécnica, University of São Paulo
demostenes@lps.usp.br

Miguel Arjona Ramírez
Electronic Systems Engineering Department
Escola Politécnica, University of São Paulo
miguel@lps.usp.br

***Abstract*— This article proposes a rate-determination algorithm (RDA) for the G.726 speech coder recommended for use in packetized speech systems. It determines the bit rate based on the MOS value at the destination end point obtained by Recommendation P.563 for improvement of speech quality and bandwidth efficiency in a communication scenario with time-varying network load. Quality ranges from the highest MOS value of 3.980 at a 40 kbit/s rate to the lowest one of 3.185 at a 16 kbit/s rate. Rate switching combinations provide intermediate quality. When the RDA detects a lower MOS value at the communication node, it switches to a lower rate that brings about a reduction in network load.**

***Index Terms*— RDA, variable bit rate, G.726, bandwidth, QoS, VoIP, MOS**

I. Introduction

With the increasing availability of Voice over IP equipments the bandwidth is becoming a big concern in telecomunication designs, as much in cabled or wireless networks as in cellular communications. One way to solve these bandwidth issues is to move away from a traditional fixed-bit rate (FBR) codec scheme toward variable bit rate (VBR).

Variable bit rate (VBR) designates the bitrate used in audio or video encoding. As opposed to constant bitrate (CBR) streams, VBR streams vary the output data rate for each time segment in general. Several strategies have been proposed to adjust bitrates and studies [1] and [2] about the limitations associated with rate selection strategies attempt to integrate perceptual notions in VBR coders. In algorithms [1] and [2], speech frames are phonetically classified (e.g., as voiced, unvoiced, or onsets) according to pitch periodicity and spectral flatness measures. Indeed, shaping the quantization error according to the masking properties of the human ear is a common practice in several speech coding standards. VBR speech codecs offer improved coding efficiency, which is particularly important for multiple access systems and packet-switched networks.

Central to VBR coders is the rate-determination algorithm (RDA).

The existing RDAs have the following characteristics:

- they employ psychoacoustically-blind statistical metrics to estimate a suitable encoding bitrate;
- they have little flexibility to differentiate weak fricatives from background noise;
- they suffer from misclassification of background noise and speech, particularly, in the presence of high acoustic noise levels.

Consequently, the VBR codecs either fail to synthesize both the acoustical noise and active speech with reasonable perceptual quality or result in higher average bit rates.

Essentially, articles [1], [2], [3] and [4] are based on the signal by means of voice activity detection (VAD) and throughput measurements. This means that the RDA algorithms determine the codec rate following the characteristics of the input signal.

The main contribution of this work is an RDA that selects a codec rate according to speech quality in the network based on estimated MOS value. This work not only proposes an RDA, but it further describes a mechanism for transmitting the MOS estimate at the terminal across the network to another terminal

The whole setup in Fig. 1 was developed with open source software and consists of a network emulator, an MOS back transmitter and an ITU-T speech coder.

An MOS value ranges from 1 for an unacceptable call to 5 for an excellent call.

II. Theoretical Revision

The following describes two objective methods for estimating quality of the signal transmitted through a network and a

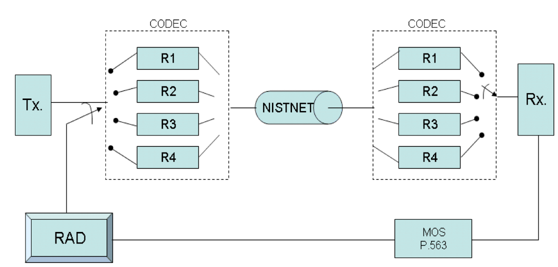

Fig. 1. A general architecture for an RDA

This work was supported by Coordenação de Aperfeiçoamento de Pessoal de Nível Superior (CAPES) with a scholarship and Fundação de Amparo à Pesquisa do Estado de São Paulo (FAPESP) under Grants no. 2007/08288-2 and 2004/13206-7.

brief description of P.800, an RDA, the G.726 codec and the RDA notification system that is responsible for notifying the rates to be changed.

A. The rate-determination algorithm

The rate-determination algorithm (RDA) [9], [10], [11] and [12] is a mechanism that depends on some external factors to be able to switch the current rate to another one.

For the proposed RDA, the control factor is the quality of the signal at the receiver side.

B. On Recommendation P.862

ITU-T P.862 Recommendation [13] for Perceptual Evaluation of Speech Quality (PESQ) is a tool for the estimation of speech quality using two input signals: the original signal and the degraded signal.

PESQ is an objective measurement tool that predicts the results of subjective listening tests on telephone systems. PESQ uses a perceptual model to compare the original, unprocessed signal with the degraded signal from the network or network element. The resulting quality score is converted to an estimated *Mean Opinion Score* (MOS) that should actually be measured using panel tests according to ITU-T P.800. The PESQ scores are averaged over a large database of subjective tests.

The ITU-T selection process that resulted in the standardization of PESQ involved a wide range of conditions, with demanding correlation requirements set to ensure that it has good performance in assessing conventional fixed and mobile networks and packet-based transmission systems.

PESQ takes into account coding distortions, errors, packet loss, delay and variable delay, and filtering in analogue network components.

This powerful test tool can be deployed in many different areas of a business, on any speech carrier technology:

- In the research laboratory; providing rapid feedback on promising areas of signal processing development, validation of design implementation, ranking alternative design solutions, providing a higher degree of confidence before submission to subjective testing;
- In network equipment evaluation; comparing different vendor offerings and determining their impact on network performance;
- In network installation and rollout of new technologies; ensuring that the desired speech quality is being delivered as the network complexity and loading increases;
- In troubleshooting network and customer problems; determining the scale of the problem, the effectiveness of the solution.

C. On Recommendation P.563

The model for the P.563 Recommendation [14] is a non-intrusive one based on signals at a node and taking measurements at the listening side, without requiring any reference signal.

The P.563 Recommendation is based on the same fundamental principles of human hearing used in intrusive methods such as PSQM, the PAMS and PESQ.

For the estimation of distortions and parameter extraction an analysis of the vocal tract is performed, the signal and noise statistics are analyzed by segment of speech, and the signal interruptions and periods of silence are detected.

D. On Recommendation P.800

The ITU-T P.800 [21] describes several methods and procedures for conducting subjective evaluations of transmission quality. The most commonly used method is Absolute Category Rating (ACR) test which gives the Mean Opinion Score (MOS). Degradation Category Rating (DCR) is also used in some occasions, which gives Degradation Mean Opinion Score (DMOS).

This work only describes the Absolute Category Rating (ACR).

1) Absolute Category Rating (ACR): For Absolute Category Rating (ACR) listening test, subjects (untrained listeners) are asked to rate the overall quality of a speech utterance being tested without being able to listen to the original reference. The rating of quality is based on an opinion scale as shown in Table I The average of opinion scores of the subjects gives the Mean Opinion Score (MOS).

TABLE I
OPINION SCALE FOR ACR TEST

Category	Speech Quality
5	Excellent
4	Good
3	Fair
2	Poor
1	Bad

E. On the G.726 speech coder

The original adaptive differential PCM (ADPCM) algorithm standardized by the ITU in 1984 included only the 32 kbit/s bit rate, and met the goal of coding speech at half of the bit rate necessary for G.711 [5] while maintaining the same speech quality. This version, known as the Red Book ADPCM, was found to have a flaw in transmitting voice-band data signals modulated using Frequency Shift Keying (FSK), and was replaced by another version published in 1988 [6]. At the same time, 24 and 40 kbit/s extensions were also approved for the algorithm and published in Rec. G.723 [7]. In 1990, the two Blue Book recommendations were merged into G.726 [8] with the addition of the 16 kbit/s bit rate. The G.726 algorithm encodes the input 8 bit, A or u-law, PCM samples into 2-5 bit ADPCM samples. The ADPCM algorithm exploits the predictability of the speech signals. It uses an adaptive predictor to predict the present signal sample based on the past expanded input log-PCM samples. The difference between the predicted and actual sample is quantized by an adaptive quantizer using the number of bits allowed by the current bit rate. The quantizer bits are sent to the decoder where they are packed to recover the level codes that point to the quantizer levels. The difference signal is added to the adaptive predictor output at the decoder.

F. RDA notification system

We propose a notification system for the RDA rates based on the MOS estimated at the receiving network node.

According to the change in MOS index it sends notifications every 20 milliseconds. This transmission period was selected because it has been used in [16] and [17], via socket (a port between the implementation process and the transport end-to-end protocol).

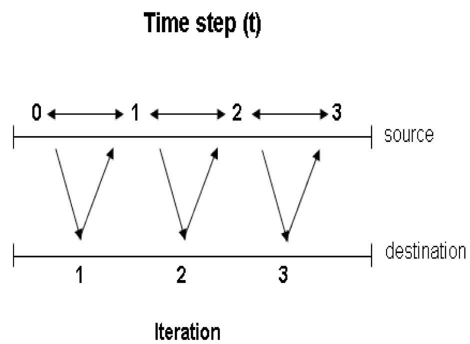

Fig. 2. Message exchange between source and destination

Fig. 2 shows the UDP (User Datagram Protocol) communication exchanged between source and destination.

The operating principles are based on [18] and further explained below.

At the receiving node the signal quality is estimated using ITU-T P.563 recommendation. This MOS estimate is stored in a variable X and then it is sent to the source point by a UDP communication, where it is input to the RDA which selects among the four rates of 16, 24, 32 or 40 kbit/s for the communication between source and destination.

This algorithm was implemented in C and is based on ITU G.191 [19] Recommendation.

III. Simulation Scenario

The experimental setup is shown in Fig. 1, where the encoded input signal is transmitted to the receiving end point through the network. The communication between the source and destination terminal computers is mediated by the Nistnet software, which has been selected to be the network emulator. It is a general purpose freeware that is widely accepted by the network research community. It injects a traffic source which may be a stream generated from a data file or an interactive audio stream originating at a microphone. For further detail the reader is referred to [15].

The network emulator can modify the transmission parameters: PDT, PDV, BW, THRU and PLR. It is also possible to define the route to be followed by the packets.

Since the objective of this work is to evaluate the behavior of the RDA in different network scenarios and at different levels of signal quality at the destination node, the encoder and decoder are isolated in order to facilitate the tests and the network is supposed to be ideal because the loop for the retransmission of the MOS estimated is not taken into account. This avoids possible extraneous impairments to the operation of the RDA. It was done by the simulation of the estimated MOS input to the RDA so that the bit rate switches in accordance with them.

The rate switching scheme is represented in Fig.3. The RDA Input is a list of different MOS values that represent different speech quality levels at the end point in order to switch the bit rate. Additionally, these values are read at each time t. In order to evaluate the RDA performance, it was performed some tests each one with a different time t obtaining scenarios with different number of switching rate during the transmission of the same speech signal which is T seconds long.

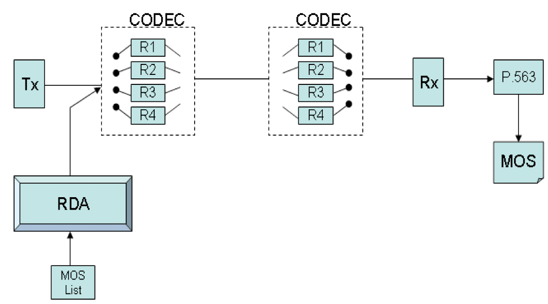

Fig. 3. Simulation Testbed

IV. Results and Discussion

The MOS is initially estimated at fixed bitrates and compared with the MOS estimated for variable bitrate combinations.

In the simulation tests the performance of the RDA was evaluated based on the P.563 tool.

Tests were conducted for quality range based on Table I and the following rate switching rules:

- $MOS \geq$ 3.7 then $rate = 40$ kbps;
- $MOS \leq$ 3.4 or $MOS \geq$ 3.2 then $rate = 32$ kbps;
- $MOS \leq$ 3.2 or $MOS \geq$ 3.0 then $rate = 32$ kbps;
- $MOS \leq$ 3.0 then $rate = 16$ kbps.

In all cases, the simulation has been performed 20 times in order to ensure the validity of the results. The standard deviations (SDs) are reported in Tables II, III and IV.

Table II shows the values obtained for each fixed-bitrate. It is remarked that all the signals are eight-second long.

Table III shows the MOS estimated for each test scenario conducted using the RDA that controls the rate of G.726 encoder among the bit rates of 16, 24, 32, 40 kbit/s.

The values displayed in Table III were obtained as the averages over 6 different audio files repeated 20 times each.

TABLE II

MOS ESTIMATES FOR FIXED-BITRATES.

RATE (KBPS)	AVERAGE MOS	SD
40	3.980	0.0098
32	3.906	0.0045
24	3.723	0.0029
16	3.185	0.0036

TABLE III

MOS ESTIMATES FOR DOUBLE-BITRATES.

RATE (KBPS) RATE 1 - RATE 2	MOS	SD
40 - 32	3.973	0.0022
40 - 24	3.948	0.0024
40 - 16	3.926	0.0029
32 - 24	3.822	0.0022
32 - 16	3.809	0.0027
24 - 24	3.723	0.0012
24 - 16	3.497	0.0031

These audio files are each eight-second long at a 16 bit sample resolution and an 8 kHz sampling rate.

Table IV shows the estimates obtained of MOS index for triple-bit rates.

TABLE IV

MOS ESTIMATES FOR TRIPLE-BITRATES.

RATE (KBPS) RATE 1 - RATE 2 - RATE 3	MOS	SD
40 - 32 - 24	3.909	0.0032
40 - 32 - 16	3.362	0.0029
40 - 24 - 16	3.315	0.0037
32 - 24 - 16	3.299	0.0034

The results in Tables II, III and IV are consistent because they show that when the RDA switches to a lower rate the MOS estimate decreases too.

Additionally, in an overloaded network the RDA meets the goal by switching to a lower rate to ensure a good communication between source and destination points.

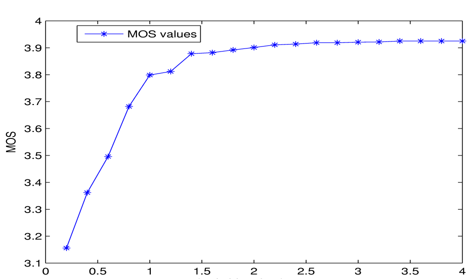

Fig. 4. MOS values for different switch time

The MOS estimates obtained by switching to different coding rates are shown in Fig. 3. For this case the double bit-rate of 40 and 32 kbit/s was used. It can be observed that a decrease in switching period entails a decrease in quality as well. In other words, when the number of rate switchings increase, the quality of the signal decreases. This trend in the results agree with [20].

V. CONCLUSION

This work shows that using an RDA based on the quality of the signal at the reception point there is an improvement in the use of the transmission channel and hence on the quality of the transmission of the signal.

The results look reliable since the higher rate corresponds to the highest quality. It is further concluded that when the number of rate switchings increase for a given speech signal, the resulting quality tends to decrease.

The bandwidth can be better used to avoid a network overload.

It is also observed that the setup can be perfectly reproduced by other researches because it consists of free tools and their interconnection makes for an easy implementation.

The continuation of this work is expected to highlight that variable rate switching results in an increase in MOS estimates and improved VoIP quality.

Experiments with network noises are planned to measure the sensitivity of the RDA additional tests will be performed more tests for evaluating how much each one of the network parameters (PDT, PDV, BW, THRU and PLR) affect the RDA performance.

REFERENCES

[1] Paksoy, E.; Gersho, A.,*Multimode and variable-rate coding of speech*, in Speech Coding and Synthesis, Eds. W. B. Kleijn and K. K. Paliwal, Elsevier, 1995.

[2] Gersho, A.; Paksoy, E.,*Variable rate speech coding for cellular networks*, in Speech and Audio Coding for Wireless and Network Applications, Eds. B. Atal, V. Cuperman, Kluwer Academic Publishers, 1993.

[3] Paulus, J. W.,*Variable bitrate wideband speech coding using perceptual motivated thresholds*, IEEE Workshop on Speech Coding for Telecommunications, pp 35-36, 1995.

[4] Hermansky, H.,*Perceptual linear predictive (PLP) analysis of speech*, J. Acoust. Soc. Amer., pp 1738-1752, 1990.

[5] ITU-T Rec. G.711, *General Aspects of Digital Transmission Systems Terminal Equipments - Pulse Code Modulation (PCM) of Voice Frequencies*, 1972. http://www.itu.int/rec/T-REC-G.711/en.

[6] CCITT R. G.721, *32kbits/s adaptative differential pulse code modulation (ADPCM)*, IXth Plenary Assembly, Melbourne, 14-25 Nov. 1988, Blue Book.

[7] ITU-T Rec. G.723.1, *General Aspects of Digital Transmission Systems - Dual Rate Speech Coder for Multimedia Communications Transmitting at 5.3 and 6.3 kbit/s*, May. 2006. http://www.itu.int/rec/T-REC-G.723.1/en.

[8] ITU-T Rec. G.726, *General Aspects of Digital Transmission Systems, Terminal Equipment - 40, 32, 24,16 kbit/s Adaptive Differential Pulse Code Modulation (ADPCM)*, 1990. http://www.itu.int/rec/T-REC-G.726/en.

[9] S. El-Ramly, A. Tawfik, *A Rate-Determination Algorithm for Variable-Rate Speech Coder*, IEEE Workshop on Speech Coding for Telecommunications, pp 697-701, 2004.

[10] Atti, V. Spanias, A., *Rate determination based on perceptual loudness*, IEEE International Symposium on Circuits and Systems, Vol 2. , May 2005.

[11] Sheung. C. N., *Rate determination algorithms in IS-95 forward traffic channels*, Vehicular Technology Conference, 1998. VTC 98. 48th IEEE, Vol 13, Sept. 2005.

[12] Tammi, M. Jelinek, M. Ruoppila, V.T., *Signal Modification Method for Variable Bit Rate Wide-band Speech Coding*, IEEE Transactions on Speech and Audio Processing, Vol 13, no. 5, pp 799-810, Sep. 2005.

[13] P.862, *Perceptual evaluation of speech quality (PESQ): An objective method for end-to-end speech quality assessment of narrow-band telephone networks and speech codecs*, 2005. http://www.itu.int/rec/T-REC-P.862/en.

[14] P.563, *The ITU-T Standard for Single-Ended Speech Quality Assessment*, 2005. http://www.itu.int/rec/T-REC-P.563/en.

[15] Rodriguez D. Z., Ramirez M. A., *Determinação do comportamento de codificadores em diferentes condições de rede em um cenário experimental*, XXVI Simpósio brasileiro de Telecomunicações, 2008.

[16] Kambiz, H.,*Rate adaptative speech coding for Universal Multimedia Access*, IEEE Signal Processing Magazine, 2003.

[17] Usman, M.,*Performance analysis for Adaptative source rate control algorithm for VoIP*, Proceedings of the American Control Conference, 2003.

[18] Cerello, P.,*The FINUDA Data Acquisition System as Event Monitor*, IEEE Transations on Nuclear Science, Vol. 4, 1998.

[19] G.191, *Software tools for speech and audio coding standardization*, 2005. http://www.itu.int/rec/T-REC-G.191-200509-I/en.

[20] Hoene C., Karl H., *Perceptual Quality Model Intended for Adaptive VoIP Applications*, International Journal of Communication Systems, 2005.

[21] P.800, *Methods for Subjective Determination of Transmission Quality*, ITU Recommendation P.800, August 1996.

QoS Analysis of Packet Scheduling Algorithms for HSDPA Mobile Networks

Kire Jakimoski
University "Sv. Kiril i Metodij",
Faculty of Electrical Engineering and Information Technologies,
Karpos 2 bb, 1000 Skopje, Republic of Macedonia
kire_jakimoski@yahoo.com

Toni Janevski
University "Sv. Kiril i Metodij",
Faculty of Electrical Engineering and Information Technologies,
Karpos 2 bb, 1000 Skopje, Republic of Macedonia
tonij@feit.ukim.edu.mk

***Abstract* –This paper analyzes and compares packet scheduling algorithms for HSDPA that are most likely used in different network scenarios. We provide results given in average throughput, average delay and fairness of the users for each of the schedulers, changing the number of the users, radius of the cell and propagation environment. The results have showed that the number of the users, radius of the cell and propagation environment in a given coverage area are very important factors when choosing which packet scheduler to use. The obtained results provide important information in the process of satisfying the desired quality of service for the mobile users, and for the vendors who will have to take into account factors that are investigated in this paper when choosing the packet scheduling algorithm.**

***Index Terms* — FCDS, HSDPA, max C/I, RR, Scheduling.**

I. Introduction

UMTS added a new feature in 3GPP Release 5, High Speed Downlink Packet Access (HSDPA) in order to enhance the bit rates as well as the spectral efficiency. HSDPA [1-3] helps to maintain UMTS as a very competitive technology to provide high bit rates in mobile communications. To achieve the requirements of shorter delay and high throughput, three key techniques are added in HSDPA: Adaptive Modulation and Coding (AMC), Hybrid Automatic Repeat Request (ARQ) and fast Packet Scheduling. All of them can be regarded as link adaption technologies, which represent the further improvement of WCDMA in the fields of variable spread-spectrum and power control.

One of the most important features of HSDPA is fast packet scheduling. Packet scheduling algorithms are not standardized by the 3GPP [4]; consequently, these algorithms are vendor specific. They are an active research topic in the scientific community and many research papers implementing different scheduling algorithms have been published [5-7]. Nevertheless, HSDPA is likely to implement one of the traditional packet scheduler algorithms. These traditional algorithms are round robin, maximum C/I, proportional fair, minimum bit rate scheduling, minimum bit rate scheduling with proportional fairness and maximum delay scheduling. Nonetheless, the algorithm will aim to achieve a compromise between throughput, coverage and user fairness.

Packet scheduling algorithms will have to take into account several factors, such as for example free cell/network resources (codes and power), traffic class, UE category and capability, channel conditions, or buffered data in Node B [7]. This fact is used as a motivation in this paper to investigate the influence of the number of the users, cell radius and propagation environment on the packet scheduling algorithms performances. These factors are not enough researched in the existing literature, when talking about the performance of the packet schedulers.

Provided results in the paper are for three packet scheduling algorithms that are most popular (round robin, max C/I and FCDS), changing the number of the users, cell radius and propagation environment. The results are given in average throughput and average delay. We provide analysis of throughput, fairness and packet delay for different scheduling schemes for HSDPA by using simulated scenarios in one cell. The main goal is to research the importance of the number of the users, cell radius and propagation environment when choosing which scheduler to use and to provide results that will help in the design process of HSDPA mobile networks, aiming to get better throughput and fairness for the users.

The paper is organized as follows. Section II describes the fast packet scheduling algorithms which are used in the simulations; section III describes simulation conditions, scenario schemes and traffic model. Simulation results are presented in section IV. Finally, Section V concludes the paper.

II. Packet Scheduling Algorithms

In this paper we used the three most popular packet scheduling algorithms: round robin, max C/I and FCDS.

Round Robin scheduler (RR): Users in round robin algorithm are served in a round robin (i.e. cyclic order) manner. The scheduler selects the user that has not been served for the longest time [8-9]. The difference and variations of channel conditions for each user is not concerned. Although this algorithm doesn't make any use if the instantaneous channel quality of the users and hence may suffer from low throughput, it is fair in the sense that each user gets the same amount of resources in terms of time slots.

Maximum C/I Scheduler (Max C/I): Probably the most straightforward and aggressive advanced packet scheduler is the maximum-throughput or maximum C/I packet scheduler, which always schedules the user with the best instantaneous channel quality. The main drawbacks of this scheduler are mainly its inherent unfairness and coverage limitations. This scheduler essentially ranks all the users according to their instantaneous carrier-to-interference (C/I) ratios. This scheduler is optimal in obtaining the maximum network throughput. In this case, the UE in favorable positions will have the highest throughput, but system services may unavailable to the users in unfavorable positions. Max C/I is a kind of channel-dependent scheduler since the variations of radio channel condition is used for scheduling.

Fair Channel-Dependent Scheduler (FCDS): It is a more practical scheduler which has a strategy that incorporates the RR method and the Max C/I method, i.e. it uses variations of the radio channel conditions to improve system capacity while implementing a degree of fairness. Thus it can be concerned as a trade-off between the two extreme scheduling methods.

III. Simulation parameters

Performance evaluation of the RR, the Max C/I and FCDS was based on a discrete event simulations using Network Simulator 2 (NS2), version ns-2.30. However, NS2 by itself does not support UMTS and HSDPA. Therefore an extension to NS2 was used in the evaluation process called EURANE (Enhanced UMTS Radio Access Network Extension for NS2). Eurane patch for ns-2.30 Eurane-1.12 was used for evaluating the above-mentioned scheduling algorithms. The simulated environment consisted of one cell where Node B is located in the middle of that cell (Figure 1).

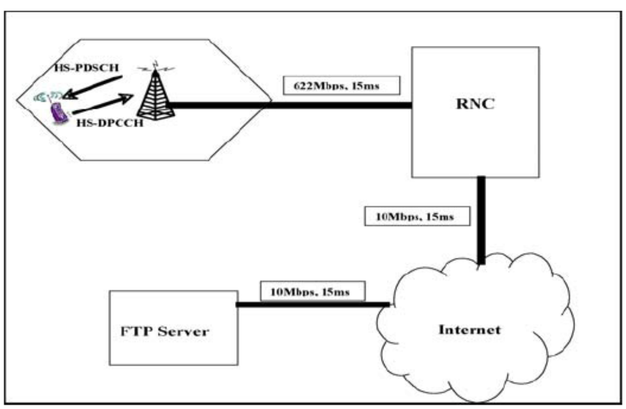

Fig.1. The simulated environment

The user is connected to Node B on the downlink by HS-PDSCH channel that is shared among all users and by HS-DPCCH on the uplink, which is dedicated for each user. Node B is connected to RNC by a duplex link of 622 Mbps bandwidth and 15 ms delay. RNC is connected to the Internet by a duplex link of 10 Mbps bandwidth and 15 ms delay. There is also an FTP server that is connected to the Internet by a duplex link of 10 Mbps and 35 ms delay. Two propagation environments have been used in these simulations which are recommended by the International Telecommunication Union: Pedestrian A and Vehicle A environments (Table 1).

TABLE I
Pedestrian A and Veciluar A propagation environment charachteristics

BS Transmission power (dBm)	38
Base station antenna gain (in dBi)	17
Linit (distance loss at 1 km)	1.374000e+002
Iintra (intra cell interference)	30
Iinter (inter cell interference)	-70
HARQ cycle period	6
Time delay (TTI) in CQI	3
Minimum CQI value	0
Maximum CQI value	30

Table 2 gives the created simulation scenarios for this paper, i.e. changing the number of users and distance from the Node B for the two propagation environments. For the simulated scenario with 20 users on 500 metres distance from the Node B, two users are located on every 50 meters distance from the Node B.

TABLE II
Simulation scenarios

Propagation environment	Number of users	Distance from the Node B (meters)
Pedestrian A	10	500
Pedestrian A	10	1000
Pedestrian A	20	500
Pedestrian A	20	1000
Vehicular A	10	500
Vehicular A	10	1000
Vehicular A	20	500
Vehicular A	10	1000

As a traffic source FTP traffic generator is used within TCP agent. All cell users cause traffic simultaneously. All users are Category 5 users (we use 5 parallel codes per HS-DSCH) with achievable maximum data rate of 3.6 Mbps. All users are uniformly distributed in the cell. First one is distanced 50m from Node B, second one - 100m, third - 150m and so on depending on the distance in the simulation whether is 500m or 1000m. In Pedestrian A environment users move with a speed of 3 km/h on their we can say orbits in respect to Node B, and in Vehicular B environment users move with a speed of 120 km/h. To current simulations trace files were generated using Matlab pre-processing/generation of input trace files for the EURANE simulator of ns-2 tool. In EURANE, the input power trace files are pre-computed from Matlab scripts, to generate the Channel Quality Indicator, a pre-requisite parameter *P_out* is calculated with the following equation:

$$P\_out = PTx - 10 * \lg(10^{\frac{I_{intra}}{10}} + 10^{\frac{I_{inter} + Ploss}{10}}) \qquad (1)$$

In the Equation 1, *PTx* is total transmit power of base station, *Iintra* is the intra-cell interference and *Iinter* is the inter-cell interference. The last parameter *Ploss* is the total path loss which depends on the user's configuration, containing the fast fading, slow (i.e. shadow) fading, distance loss and base station antenna gain. All parameters in this equation are logarithmic. Thus *P_out* can be regarded as instantaneous estimated signal to noise ratio, SNR, of the channel, and further be mapped to an appropriate CQI. The

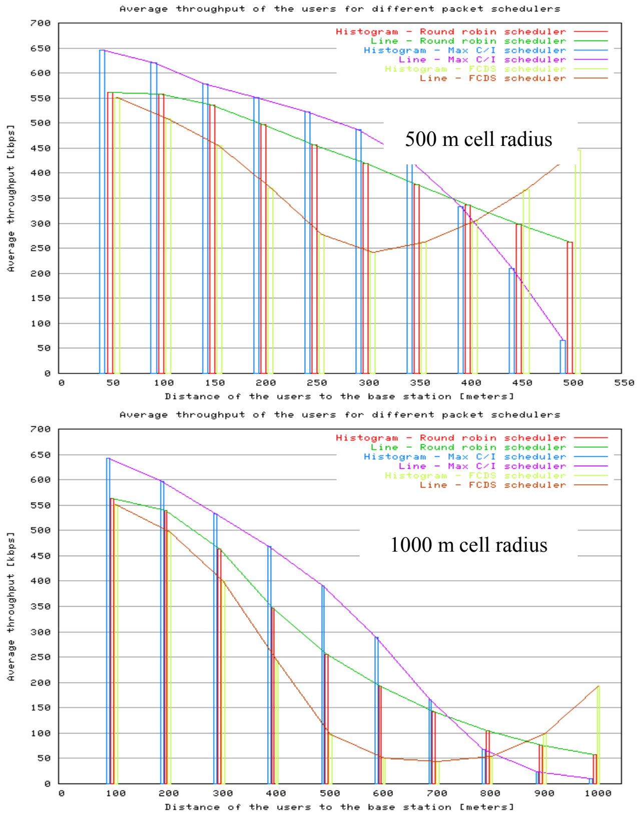

a. Pedestrian A propagation environment

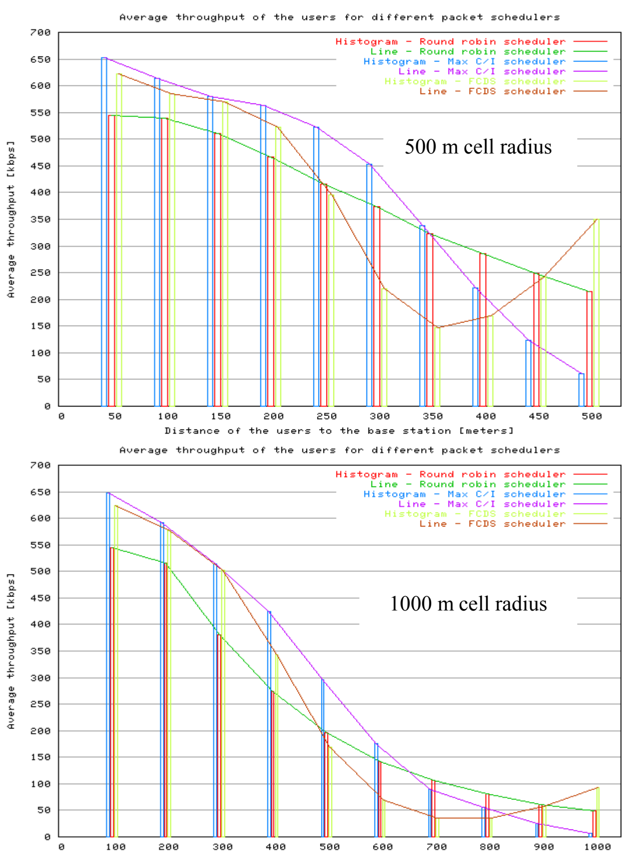

b. Vehicular A propagation environment

Fig.2. Average throughput for 10 users for different cell radius and propagation environment

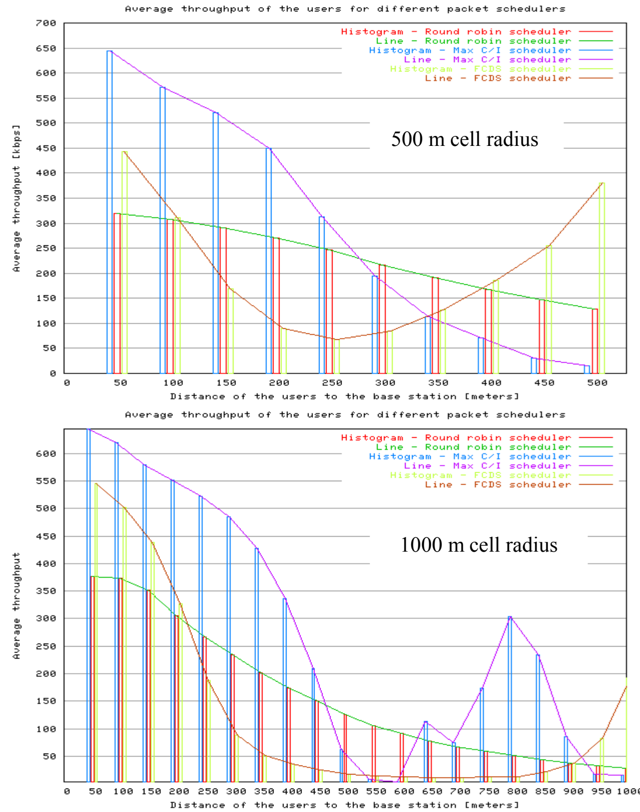

a. Pedestrian A propagation environment

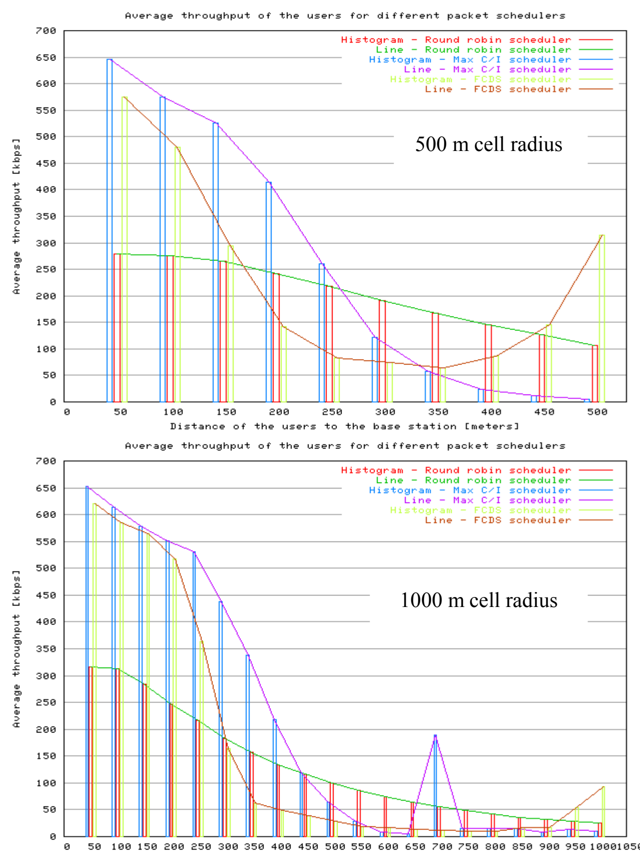

b. Vehicular A propagation environment

Fig.3. Average throughput for 20 users for different cell radius and propagation environment

limitation of this formula is, however, that the base station (Node B) is supposed to operate HS-DSCH only. Hence the available transmit power is a constant (set to 38 dBm in EURANE Matlab scripts), as it is written in Table 1.

Awk was used to process and prepare statistics and plots has been made with gnuplot under Linux.

IV. Simulation results

A. The impact of the number of the users, cell radius and propagation environment on the average throughput for the three packet scheduling algorithms

In Fig.2 and Fig.3 are presented results for average throughput changing the number of the users from 10 to 20, cell radius from 500 meters to 1000 meters and propagation environment from Pedestrian A to Vehicular A in order to obtain the best solution for the users. They depict the main results obtained from our simulation series for average throughput. Our main goal here was to analyze the behavior of the average throughput when using 10 and 20 users in the cell for the three well known packet schedulers. If we compare Fig. 2 and Fig. 3, we can notice different results for the average throughput for each of the packet schedulers.

If we compare the results for average throughput for 10 and 20 users in Fig.2 and Fig.3, we can see that the values of average throughput are dropping as the number of the users is increasing at all three schedulers. The average throughput for max C/I and FCDS scheduler is almost the same for the first user that is closest to the Node B for 10 and 20 users, but the difference is obvious with the other users. When there are 20 users in the cell, the average throughput drops faster with max C/I and FCDS scheduler, compared with a cell with 10 users. This is because when the number of the users is increasing, the users that are closer to the Node B have better channel qualities and automatically have better chance to use the system services. We can conclude that max C/I and FCDS scheduler is better option for lower number of users in the cell. Round robin scheduler has also lower results in average throughput when we increase the number of the users. But here the values are drastically different at the first user that is closest to the Node B when we change the number of the users, and then the values for average throughput drops slower when we increase the number of the users. These differences are more obvious when the radius of the cell has lower values.

We can conclude that max C/I scheduler is the best solution for the scenarios with low number of users, when we want to get the best values of throughput. When the number of users gets higher, max C/I is good solution only for the users that are closer to the Node B and round robin scheduler for the users that are more distant from the Node B. From the Fig.3 we can see that max C/I scheduler although the number of the users is high is the best solution even for the users that are more distanced from the Node B for the case of 20 users with 1000 meters cell radius in Pedestrian A propagation environment. Only in this case round robin scheduler is not the best solution for the users that more distant from the Node B, when the number of the users is higher.

FCDS scheduler, when increasing the number of the users in Fig.2 and Fig.3 is closer to the max C/I scheduler with the average throughput values. FCDS scheduler is also closer with the average throughput values to the max C/I scheduler when we use Vehicular A propagation environment compared with Pedestrian A propagation environment. This happens because in the simulations the parameter “alpha” which defines the amount of weighting used in the FCDS algorithm was set to 0.9. A value of 0.0 would equate to the Round Robin case, while a value of 1.0 would equate to the Maximum C/I case. The value of 0.9 is closer to the value of 1.0 0 the max C/I case. That’s why when the number of the users and the velocity of the users gets higher in the simulations, the FCDS scheduler is closer with the average throughput to the max C/I scheduler.

Cell radius has lower impact on deciding which packet scheduler to use in order to obtain better throughput for the users. Max C/I scheduler has better average throughput for the users when the cell radius is increased. That is not the case with round robin and FCDS scheduler which have worse values of average throughput when the cell radius is increased from 500 meters to 100 meters.

Propagation environment has the lowest impact on the average throughput at the all three packet schedulers. When we compare the Pedestrian A propagation environment with Vehicular A in Fig.2 and Fig.3, the curves of the schedulers are closer to each other with the values of average throughput. The max C/I and round robin scheduler have lower values of average throughput for the users when the Pedestrian A environment is substituted with the Vehicular A environment. That is not the case with the FCDS scheduler which has higher average throughput for the users that are closer to the Node B, when Pedestrian A environment is substituted with Vehicular A environment. However, the overall cell throughput for all three packet scheduling algorithms in Vehicular A environment is much less than Pedestrian A environment because the path loss and multi-path fading effects are higher in Vehicle environment since the mobile speed is higher.

B. The impact of the number of the users, cell radius and propagation environment on the average delay for the three packet scheduling algorithms

The results shown in Fig.4 and Fig.5 represent the values of average delay having the same simulation scenarios as in Fig.2 and Fig.3. The first obvious result is that average delay gets worse as the number of the users gets higher for the all three packet schedulers. Max C/I scheduler has the best values for average delay for 80% of the users when their number is 10, the cell radius is 500 meters and the propagation environment is Pedestrian A. At the last two users the average delay for max C/I scheduler has the worst values of all three schedulers in this case. When the number of the users is 20, the max C/I scheduler is the best solution when we are talking about average delay for 60% of the users, with a cell radius of 500 meters and Pedestrian A propagation environment. The other 40% of the users that are more distanced from the Node B have the worst values of average delay between the all three

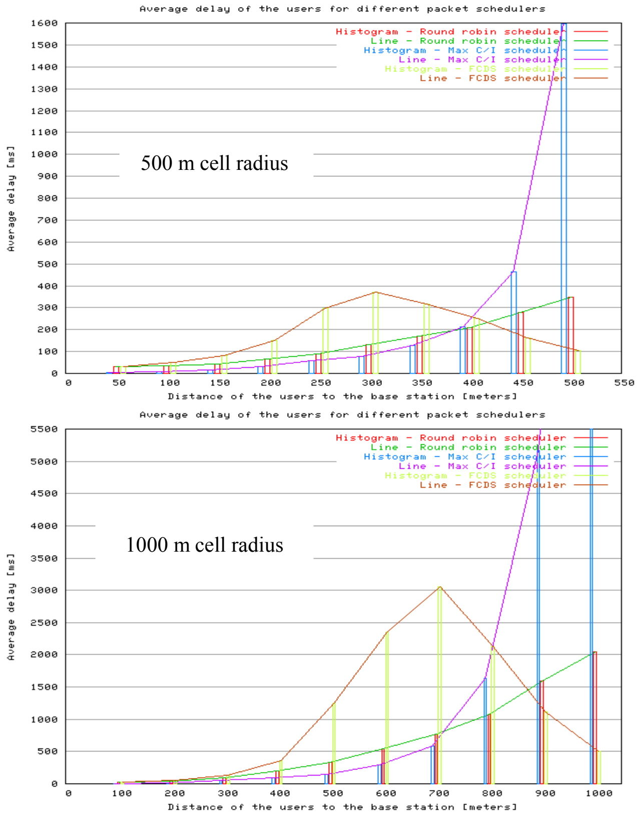

a. Pedestrian A propagation environment

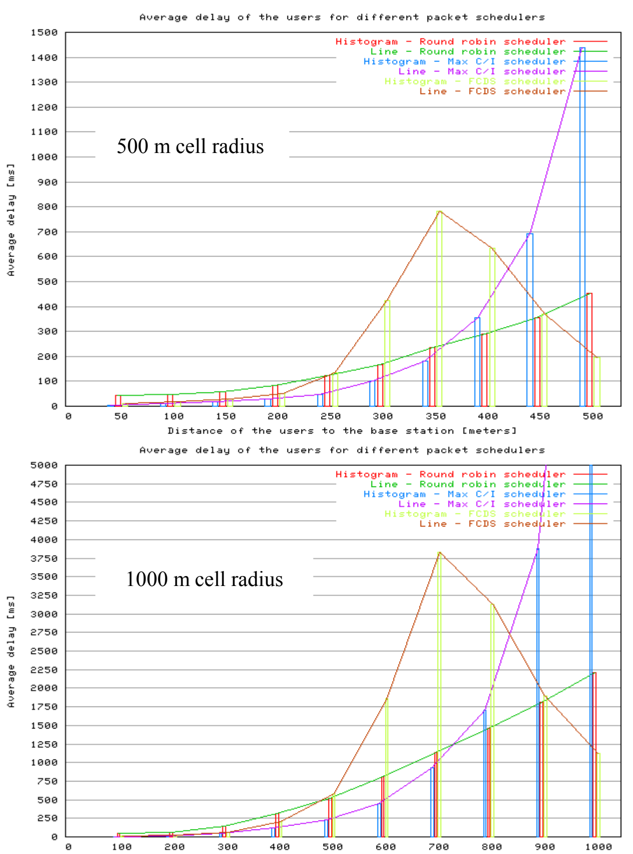

b. Vehicular A propagation environment

Fig.4. Average delay for 10 users for different cell radius and propagation environment

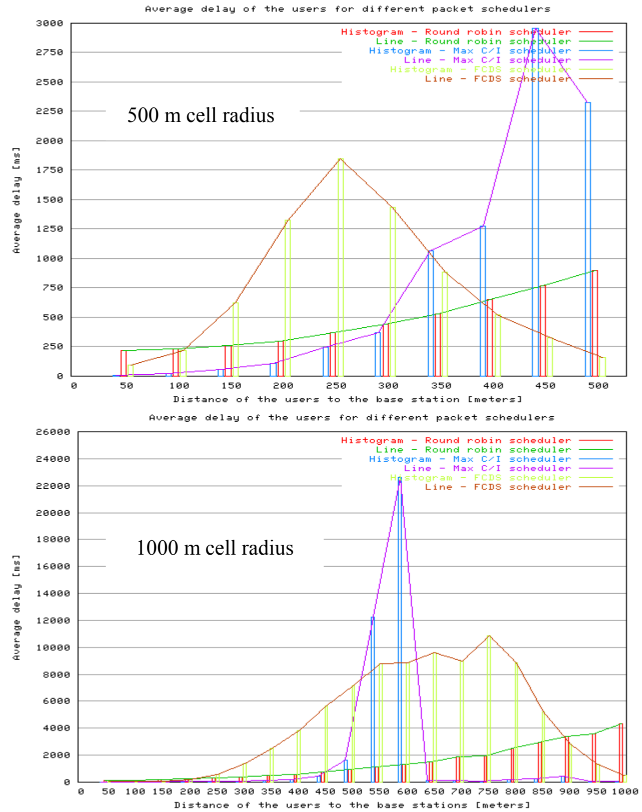

a. Pedestrian A propagation environment

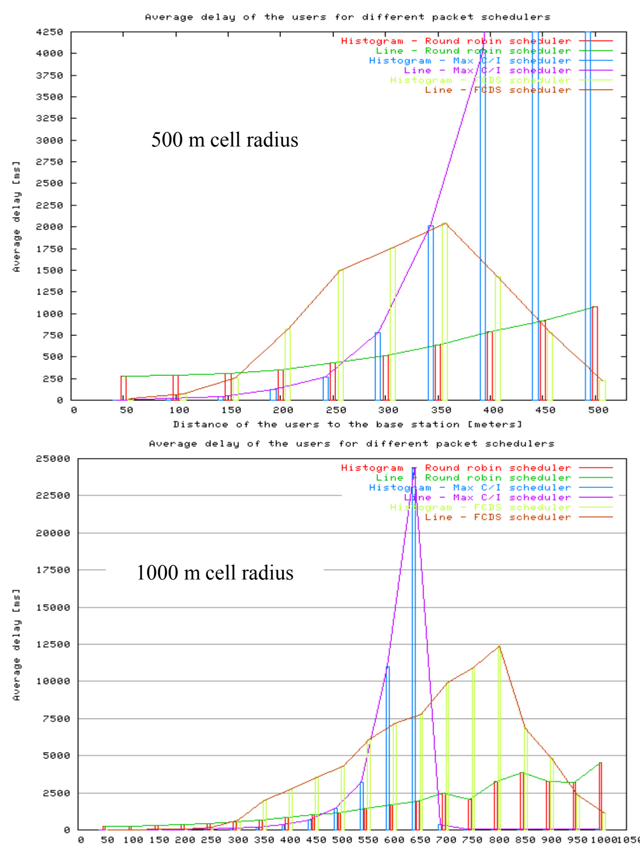

b. Vehicular A propagation environment

Fig.5. Average delay for 20 users for different cell radius and propagation environment

schedulers. We can conclude that max C/I scheduler is better solution when the number of the users is lower for majority of the users in the cell, but when the number of the users is increasing max C/I is the best solution only for the users that are closer to the Node B. But if we observe the graphs in Fig. 4 and Fig. 5 that represent the average delay values for 20 users on 1000 meters cell radius, we can point out that max C/I scheduler in this case has the worst values of all schedulers just for three users in the middle of the cell. That is 15% of the users and the other 85% of the users have the best results when talking about average delay with the max C/I scheduler.

For the majority of the users when their number is increased the best solution for getting lower values for average delay is round robin scheduler, as we can see in Fig.4 and Fig.5, no matter if the radius cell is 500 meters or 1000 meters, or if the propagation environment is Pedestrian A or Vehicular A. The FCDS scheduler is the best solution for average delay in the all simulated scenarios in Fig.4 and Fig.5 just for the last two users most distanced from the Node B. So, we can say that choosing FCDS scheduler in these scenarios for average delay is the worst decision for the users.

As user number augmenting, the scheduler mechanism causes more users waiting or queuing on the transmission link, so the delay of individual user will increase. Comparing Fig.4 and Fig.5 we can find that RR scheduler behave much better than the other two schedulers in delay results.

V. Conclusion

In this paper we have analyzed the impact of the number of the users, cell radius and propagation environment on the average throughput and delay at the three most popular packet scheduling algorithms, i.e. RR, max C/I and FCDS. Simulation results showed that various scenarios regarding the number of the users, cell radius and propagation environment in one cell cause changes in the behavior of the packet schedulers performances in average throughput and delay. Because of this fact, when choosing which packet scheduler to use, we must take into account the number of the users in the cell, cell radius and propagation environment in the coverage area in order to have better throughput and fairness of the users.

The results showed that round robin scheduler is the best when fairness is a matter of question no matter how man users we have in the cell. But, if we want effective use of the system sources, max C/I is the best choice to get better throughput, but not for all of the users. We concluded also that max C/I scheduler is better option when the number of the users is lower in the cell. When the number of the users is higher, max C/I scheduler has the best average throughput for the closer users to the Node B, and FCDS scheduler for the further users from the Node B for Pedestrian A propagation environment and round robin scheduler for the further users from the Node B for Vehicular A propagation environment.

From the obtained results we can also conclude that the number of the users is the most important factor when choosing the adequate packet scheduler, but as we explained the cell radius and propagation environment are also important factors when deciding the packet scheduler.

Having different results for throughput and delay with the all three schedulers, we can say that we must negotiate between the throughput, delay and fairness of the users in order to obtain the optimal quality of service for the users. When talking about fairness our results showed that no matter how many users are active or how great is the cell radius or which propagation environment is used, round robin scheduler is the best solution for all users. But when we are interested in better throughput for the users in the cell and lower delay, we must use max C/I scheduler. But in this case the further users from the Node B, especially if the number of the users is higher suffer from low throughput. That is why we can use here FCDS or round robin scheduler depending of the cell radius and propagation environment.

The results in this paper can be very useful for the network operators when deciding which scheduler to use in different real scenarios in mobile HSDPA networks.

References

[1] H. Holma and A. Toskala, “HSDPA/HSUPA for UMTS”, John Wiley & Sons, Ltd, Jun.2006.

[2] E. Dahlman, S. Parkvall, J. Sköld and P. Beming, “3G evolution: HSPA and LTE for Mobile Broadband”, First edition 2007.

[3] H. Holma and A. Toskala, “WCDMA for UMTS – HSPA Evolution and LTE”, Fourth Edition, John Wiley & Sons, Ltd, 2007.

[4] Jose Luis Pradas Adan, “Effect of Multiple Simultaneous HSDPA Users on HSDPA End-User Performance for Non-Real Time Services in One Cell System”, Helsinki University of Technology, Department of Electrical and Communications Engineering, Espoo, 7 August 2006.

[5] B. Al-Manthari, “Performance of Packet Scheduling Algorithms in High Speed Downlink Packet Access”, Telecommunication Research Lab School of Computing, Queen’s University, Winter 2005.

[6] R. Gluchowski, Dr A. Bak, “Packet Scheduling Algorithms in HSDPA”, Warsaw University of Technology, Information Technology & Electronics Department, Institute of Telecommunications, 30.05.2007. [7] P. José, A Gutiérrez, “Packet Scheduling and Quality of Service in HSDPA”, Department of Communication Tecnology, Institute of Electronic Systems, Aalborg University, Ph. D. Thesis, October 2003.

[8] Z. Haichuan, W. Jianqiu, “Implementation and Simulation of HSDPA Functionality with ns-2”, Linköping, March 21, 2005.

[9] H.vand den Berg, R. Litjens, J. Laverman, “HSDPA Flow Level Performance: The Impact of Key System and Traffic Aspects”, COST 290 Management Committee Meeting, Colmar, Feb. 3-4, 2005.

Quality of Service in a PLC Network

Ulysses R. C. Vitor, Eduardo M. L. D'Amorim,
Lucas G. Gueiros, Rafael M. C. Britto,
Marcos T. de Melo, Mauro R. Santos,
Antônio J. Belfort, and Hermano A. Cabral
Departamento de Eletrônica e Sistemas
Universidade Federal de Pernambuco
Av. Acadêmico Hélio Ramos, S/N, 50.740-530
Recife - PE - Brazil
marcos@ufpe.br

Maurício Lobo
Unidade de Engenharia de Telecomunicações
Companhia Energética de Pernambuco - CELPE
Av. João de Barros, 111, Sl. 303, 50050-902
Recife - PE - Brazil

***Abstract*— Power Line Communication (PLC) is a technology that enables data communication over power lines. This paper presents an evaluation, from the point of view of quality of service, of the first PLC deployment in the state of Pernambuco using the power grid of the local electric company, CELPE. The pilot case is a public school with an aging and poorly maintained electrical infrastructure. The paper investigates the suitability of this PLC network for providing real-time applications like audioconferences and videocalls by measuring the following quality of service parameters: packet error rate, throughput, delay, and jitter.**

***Index Terms*— PLC, quality of service, jitter, multipath.**

I. Introduction

Broadband Power Line Communication[1][2], also called BPL - Broadband over Power Lines, enables communications, service sharing, information sharing, and Internet access over power lines, an ubiquitous electric medium found in almost all homes and buildings.

Electric power lines, however, were not designed for data communications, and hence it is a medium which adds a large amount of attenuation and noise to the information signal[3]. Furthermore, in some cases, much of the power lines are also underground, where they are more susceptible to humidity and other aggressive agents. To overcome all these impairments, PLC makes use of a large frequency bandwidth (up to tens of megahertz) and several flexible communication techniques, like OFDM (Orthogonal Frequency-Domain Modulation) and adaptive bit loading.

Many examples of successful deployment can be found throughout the world. In Brazil, there have been pilot PLC projects in several cities, among which it can be cited the cities of Belo Horizonte (MG), Barreirinhas (MA), Vitória (ES) and Porto Alegre (RS). Presently, Barreirinhas is in its second phase and Porto Alegre has 2.5 km of network installed in Restinga, one of the poorest suburbs of the city. Recently, thanks to a partnership between the Federal University of Pernambuco - UFPE - and the Electric Power Company of Pernambuco - CELPE, Recife (PE) also has a pilot project using this technology, where two test PLC networks were built, one in laboratory and another in a state school, the latter being the largest.

From the viewpoint of the end user, quality of service is an important measure in data networks of its capacity of guaranteeing user satisfaction[4]. To the best of the knowledge of the authors, however, there has not been yet a scientific paper concerning measures of the quality of service for PLC networks. The goal of this work, then, is to show that, the aforementioned problems notwithstanding, it is possible to use the power line infrastructure, even in a harsh environment typically found in old buildings in cities like Recife, to carry data, voice and video at high rates with good quality of service.

This paper is organized as follows. Section II gives a brief introduction to the PLC technology, highlighting its main characteristics and impairments. It is followed by Section III, which describes the parameters of interest that, for the purposes of this paper, are used to measure quality of service. Next, Section IV describes the pilot network deployed at the state school. Section V presents the results obtained from the experiments, and lastly the conclusions are presented in Section VI.

II. Power Line Communications

Power Line Communications, or PLC for short, is a technology for transmitting information over electric wires at rates in a wide range that goes from a few hundreds of kilobits per second to several tens of megabits per second. There are two main appeals for PLC, both deriving from its use of the power line infrastructure as a communication medium. The first is the fact that power lines can be found in almost any building but the most remote ones, which provides an excellent coverage area for the service at a small cost for deploying it. The second related reason is that many electric equipments already need an electric cable to operate, which, with PLC, can also play the role of the communication medium, easing the installation and maintenance of the system as a whole.

The power line infrastructure, however, was designed for the transmission of low-frequency electric power, and has several disadvantages for the transmission of high-frequency, communication-bearing signals. An electrical network has a topology with a typically large number of branches deriving from a main cable, none of which is impedance-matched to it. This can be exacerbated by an aging infrastructure, where one can easily find multiple points of corrosion, leaky insulation and faulty electrical installations. Furthermore, those branches have different, potentially time-variant loads on it which, likewise, are not matched to the transmission line. All these impedance mismatches give rise to reflections of the transmission signal which arrive at the reception end with amplitude and phase different from those of the original signal. Hence, even though electric wires are a guided transmission medium, they have somewhat similar multipath characteristics as a wireless, non-guided one. This causes the particularly severe impairment of frequency-selective attenuation, where some frequencies are more attenuated than others, with deep nulls in the corresponding transfer function.

Another class of impairment found in PLC is noise, which can be divided into the following types[5]:

IMPULSIVE NOISE: Noise which may occur at random times or periodically, but which has short duration and a high Power Spectral Density (PSD). It can be subdivided into periodic and aperiodic impulsive noise, with the former including noise occurring synchronously with the mains frequency (60Hz in Brazil) and asynchronously.

NARROBAND NOISE: Modulated sinusoidal signals generated by various radio-emitting sources and received by the unshielded electric wires.

BACKGROUND NOISE: Noise with a relatively low PSD, caused by a summation of many low power noise sources.

Lastly, another constraint in PLC is caused by the fact that unshielded electrical wires act as a radiating antenna, and thus can cause interference in other nearby equipments. To avoid this interference, it is necessary to place an upper limit on the transmitting power, which, in consequence, constrains the maximum rate at which information can be transmitted, according to Shannon's theorem.

To overcome all these limitations, OFDM is usually employed in PLC[6]. OFDM is a multi-carrier modulation, i.e., it divides the available bandwidth into many non-overlapping sub-carriers with a smaller bandwidth. It then partitions the information bits to be transmitted and impinges them into those sub-carriers, each transmitted at a low rate to satisfy the constraint on the sub-carrier bandwidth. However, even though each sub-carrier data rate is low, their overall aggregate rate, which is the data rate for the OFDM system, is proportional to the original available bandwidth, and can be quite high. Moreover, one can balance the distribution of the data bits to match the signal-to-noise ratio (SNR) of each sub-carrier (a procedure called bit-loading) allocating more bits to those sub-carriers with a higher SNR and therefore optimizing the use of the channel. This characteristic of OFDM is quite valuable for channels with a transfer function varying in frequency, where some frequencies are more attenuated than others, as in PLC.

Beside this adaptive behavior, there is another advantage to the fact that the sub-carriers are independent. Since the noise affecting PLC, including impulsive noise, is inherently narrowband, only a few sub-carriers are affected by them, which limits the errors the noise can produce. For these reasons, OFDM is one of the most used modulations in PLC.

III. PARAMETERS OF INTEREST

Although the definition of quality of service can vary significantly depending on the field of work, for the purposes of this paper it will mean four parameters, namely, throughput, delay, jitter, and packet error rate, defined as follows:

THROUGHPUT: The data rate, at the TCP (Transmission Control Protocol) level, achieved by the system from one point to another, measured in bits per second.

DELAY: Also called *latency*, it is the average time a packet of data takes to travel from one system to another over the network.

JITTER: The mean absolute deviation of the difference in the delay between packets in a flow of data from one system to another. This is the definition used by the Internet Engineering Task Force RFC 1889[7]. Also named *Packet Delay Variation.*

PACKET ERROR RATE: The expected fraction of transmitted packets that are received in error. For the purposes of this paper, this also includes missing packets which were transmitted but never made through to the end user.

The above definitions can be made more precise using a mathematical notation. Let t_{d_i} and t_{a_i} be the departure and arrival time, respectively, for packet i, for $i = 1, 2, \ldots, n$, and let b_i be its size in bytes. Define the inter-arrival time d_i for packet i as the difference between the sending and arrival times, $d_i = t_{a_i} - t_{d_i}$. The throughput T can be defined then as

$$T = \frac{\sum_{i=1}^{n} b_i}{t_{a_n} - t_{d_1}},$$

while the delay D can be expressed as the average of the inter-arrival times,

$$D = \frac{1}{n}\sum_{i=1}^{n} d_i.$$

To find an expression for the jitter J, let Δ_i be the difference between the inter-arrival times for packets $i+1$ and i, i.e.,

$$\Delta_i = d_{i+1} - d_i, \quad i = 1, \ldots n-1.$$

Then, J, by the definition above, is

$$J = \frac{1}{n-1}\sum_{i=1}^{n-1} |\Delta_i - \overline{\Delta}|,$$

where $\overline{\Delta}$ is the average inter-arrival time, i.e.,

$$\overline{\Delta} = \frac{1}{n-1}\sum_{i=1}^{n-1} \Delta_i.$$

It should be noted that this is not the only possible definition for jitter. Another definition is, for example, as the standard deviation σ of the inter-arrival times d_i. In this paper, however, the first definition will be used.

Each of these parameters has a range of admissible values for a given application. For the present work, the main applications are audioconferences and videocalls using the software Skype, which have some stringent real-time requirements. For the delay parameter D, for example, the acceptable range is up to 250 ms to avoid it being noticeable to the user[8]. Jitter is even more problematic, as too much jitter may make jitter compensation mechanisms ineffective, causing defects on the audio or video arriving at the end user. Jitter values up to 75 ms are considered to be of good quality, and up to 125 ms of medium quality. For the packet error rate parameter, packet loss of up to 1% is considered acceptable as many voice encoders can handle these values[9]. Finally, based on the audio and video codecs used by Skype, the throughput requirement for audioconferences is 10 kbps and for videocalls, 30 kbps.

IV. Test Setup

The PLC network at the state school, depicted in Figure 1, is built on an aging underground three phase electrical infrastructure and makes use of equipments called *master*, *repeater*, and *modems* (CPE). These equipments were manufactured based on Mitsubishi technology and operate as layer 2 network equipments. The master equipment and the repeaters work in a similar way as an Ethernet switch, with the basic difference of using electrical wires as the transmission medium.

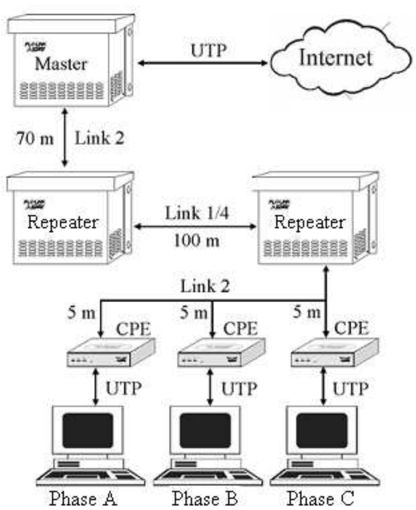

Fig. 1. The Deployed PLC Network at the State School

As shown in Figure 1, the entry point of the PLC network is the master equipment, which is physically located at the utility pole with the transformer closest to the school. It has a standard IEEE802.3 Ethernet port and so it can make the bridge between the external (Ethernet) network and the PLC side, injecting the PLC signal into the power network.

The signal propagates over the wires and reaches the first repeater, located at the entrance of the school. This repeater has two goals. The first, as with any repeater, is to regenerate the signal to increase its range, allowing it to reach the end user with as few errors as possible. The second goal is to bypass the power meter, which could otherwise introduce a large unwanted attenuation to the PLC signal. At the user end, the modems receive the signal directly from the electrical outlet and deliver it to the corresponding computer through an UTP (unshielded twisted pair) cable.

Inside the school, the power lines are underground, ill-maintained and under the high temperature and high humidity conditions commonly found in many regions in Brazil, which made it necessary to use another repeater near the computers. This repeater injects the signal in only one of the three phases, but, through mutual induction, the signal is passed to the power lines of the other phases, allowing a computer plugged in any phase to receive the signal.

To realize the measures of the quality of service parameters, four experiments were performed. In the first, raw TCP packets were sent from one computer in the PLC network to another connected after the master equipment, slowly increasing the data rate until the channel was saturated. The second experiment was similar to the first, but it used raw UDP (User Datagram Protocol) packets which were sent at several fixed rates. The third experiment consisted in four users, one outside the PLC network and the others each at its own computer inside the network, making an audioconference among them. The outside user played a standard audio and the three users in the PLC network captured the incoming and outgoing packets for later analysis. In the fourth experiment, similar to the third, two users at different computers in the PLC network performed a videocall instead.

The analysis for the last two experiments was done based on the correlation between the outgoing packets on the transmitting computer and the incoming packets on the receiving one. This correlation allowed the identification of the departure and arrival times for each IP (Internet Protocol) packet in a datastream. The UDP/IP fields of packet length and UDP checksum were used in the correlation. For each source packet, the values for these two fields were used to search among the destination packets, choosing the one with the same values. Any ambiguity was resolved by choosing the destination packet closest in time to the source packet in question.

If both computer's clock were perfectly synchronized, the above information would be enough to compute the parameters described in Section III. This, unfortunately, is rarely the case. To overcome the problem of clock synchronization, the minimum inter-arrival time (computed as indicated in the previous section) in a given datastream was subtracted from all inter-arrival times in the datastream, effectively making them relative times. Independent measures of the round-trip time for ping packets indicate that the minimum inter-arrival time (excluding clock synchronization) should be between 5 to 10 ms. This should be borne in mind when reading the delay results in the next section.

V. Results

The results obtained are as follows. Packet error rate (which includes packet losses) was measured for the third and fourth experiments, where overall more than 450000 packets were transmitted. These packets were divided between the three phases, with phase C receiving about 40% less packets than the other two. The actual values are given in Table I.

TABLE I
PACKET ERROR RATE RESULTS

Phase	Number of Packet Errors	Number of Packets	Packet Error Probability
A	40	170143	$2.35 \cdot 10^{-4}$
B	3	187049	$1.6 \cdot 10^{-5}$
C	5	108420	$4.6 \cdot 10^{-5}$

From these values it can be seen that, even for the worst case, i.e., phase A, packet error rate is not a problem for the applications considered in this paper.

Regarding the throughput, the values for a series of ten runs for each of the three phases, measured when there was no other activity in the network, are shown in Table II. The results show that PLC should be able to accommodate a fairly large amount of simultaneous audio and videocall, as well as file transfers of moderate to large sizes.

TABLE II
THROUGHPUT VALUES

Phase	Throughput (Mbits/s)
A	3.89
B	4.36
C	3.06

Jitter was measured both in the second experiment, where raw UDP packets were sent from one computer in the network to another, and for the audio and videocall experiments. All tests were done on an idle network. In the first case, the application *iperf* was used with three fixed data rates (300, 600 and 1000 kbits/s), and the jitter for the three runs in all three phases were recorded. *Iperf* uses the RFC 1889 definition for jitter as given in Section III. The average jitter for the three runs is shown in Table III.

TABLE III
JITTER VALUES

Phase	300kbits/s	600kbits/s	1000kbits/s
A	9.42 ms	12.01 ms	11.02 ms
B	9.50 ms	12.99 ms	11.81 ms
C	10.05 ms	13.10 ms	11.13 ms

For the audioconference, the jitter was measured at the receiver on all three phases. The delays were also computed. The results for the audioconference are shown in Table IV. As can be seen, even taking into account the fact that the delay times are relative, as described in the previous section, the results are well within the constraints specified in Section III.

For videocalls, the results were similar to the results for audioconference, and are within the acceptable limits. Table V lists the jitter and delay results.

TABLE IV
AUDIOCONFERENCE RESULTS

Phase	Delay (ms)	Jitter (ms)
A	17.8	13.92
B	26.17	14.21
C	19.86	13.48

TABLE V
VIDEOCALL RESULTS

Phase	Delay (ms)	Jitter (ms)
A⇒C	19.97	13.86
C⇒A	16.83	10.05
B⇒C	36.76	17.54
C⇒B	35.75	17.53
B⇒A	28.97	14.84
A⇒B	27.46	14.50

VI. CONCLUSIONS

These results all satisfy the quality of service parameters mentioned above in Section III and hence indicate that a PLC network should be able to accommodate audioconferences and videocalls with good quality of service, even in harsh conditions as those found in old buildings. Since the power electric infrastructure is one of the most important infrastructure with the greatest social penetration, this paper shows it can provide these and other services that require broadband communication to a wide public without the need for cabling deployment, an important advantage for a country like Brazil.

VII. ACKNOWLEDGEMENTS

The authors would like to thank CELPE for its funding for the project “Sistema de Comunicação Piloto Usando PLC Banda Larga na Área de Distribuição da CELPE”, which provided the necessary support for the realization of this work.

REFERENCES

[1] Halid Hrasnica, Abdelfatteh Haidine and Ralf Lehnert, “Broadband Powerline Communication,” Dresden University of Technology, Germany, John Wiley & Sons Ltd.
[2] H. Meng, S. Chen, Y. L. Guan, C. L. Law, P. L. So, E. Gunawan, and T. T. Lie, “Modeling of Transfer Characteristics for the Broadband Power Line Communication Channel,” IEEE Transactions on Power Delivery, Vol. 19, No. 3, July 2004.
[3] E. Biglieri, ”Coding and modulation for a horrible channel,” IEEE Communications Magazine, vol. 41, No. 5, pp. 92–98, 2003.
[4] B. Furht, “Multimedia Systems: an Overview,” IEEE Multimedia, Vol. 1, No. 1, pp. 47–59, 1994.
[5] M. Zimmerman and K. Dostert, “Analysis and Modeling of Impulsive Noise in Broadband Powerline Communications,” IEEE Transactions on Electromagnetic Compatibility, vol. 44, No. 1, February 2002
[6] Y. H. Ma, and E. Gunawan, “Performance Analysis of OFDM Systems for Broadband Power Line Communications Under Impulsive Noise and Multipath Effects,” IEEE Transactions on Power Delivery, Vol. 20, No. 2, April 2005.
[7] RFC 1889, “RTP: A Transport Protocol for Real-Time Applications ”, January 1996.
[8] ITU-T Recommendation G.114, “One-way Transmission Time,” May 2000.
[9] P. Goyal, A. Greenberg, C. Kalmanek, W. Marshall, P. Mishra, and D. Nortz, “Integration of Call Signaling and Resource Management for IP Telephony,” IEEE Network, Vol. 13, No. 3, pp. 24–32, 1999.

A Fuzzy Approach to Provide QoS in IEEE 802.16 Networks

Max Mauro de Oliveira Silva
Universidade Federal
do Espírito Santo - UFES
Campus de Goiabeiras - 29060-900
Vitória - ES - Brazil
maxm.silva@gmail.com

Anilton Salles Garcia
Universidade Federal
do Espírito Santo - UFES
Campus de Goiabeiras - 29060-900
Vitória - ES - Brazil
anilton@inf.ufes.br

Edson de Paula Ferreira
Universidade Federal
do Espírito Santo - UFES
Campus de Goiabeiras - 29060-900
Vitória - ES - Brazil
edinho@ele.ufes.br

***Abstract*— The IEEE 802.16 standard aims to define a metropolitan wireless broadband access network technology. It introduces several advantages, including the support for QoS at the MAC layer. To ensure the fulfillment of the QoS requirements to the applications, must be defined an algorithm to efficiently distribute resources. Whereas the dynamic and unpredictable nature of the converging network, this work proposes a new approach to distribute bandwidth in the 802.16 network downlink channel. As an alternative to traditional analytical solutions, the presented approach is based on fuzzy logic. As advantage, fuzzy approach provides greater flexibility and generality to the solutions due to it low specificity and by allowing the inclusion of ad hoc decisions.**

***Index Terms*— IEEE 802.16, QoS, resource allocation, multimedia applications, fuzzy logic.**

I. Introduction

The IEEE 802.16 standard aims to define a metropolitan wireless broadband access network technology. It introduces several advantages, including the QoS support at the MAC layer. Nevertheless, in many aspects, the document concerns only about what "to do", but do not specifies "how to do". Thus, features such as admission control, traffic policing and packet scheduling are left as the responsibility of implementers. Among all features, the packet scheduling can be considered the one that most influences the system performance. An efficient scheduling algorithm is essential to ensure that the QoS requirements are fulfilled.

Although the standard IEEE 802.16 provides facilities to support QoS, it is important to emphasize that, in this context of convergence technology, the traffic on the network is increasingly unpredictable and dynamic. This is consequence of the service sophistication. In this context, generally, the quality of service assurance mechanisms does not have exact information and in time about the controlled communication system. These factors contribute to make the analytical modeling, tool widely adopted in solutions in this area, a very complex task.

In scenarios like this, complex and full of inaccuracy, the fuzzy modeling can be considered a more attractive alternative than the conventional approaches. As advantage, fuzzy approach provides greater flexibility and generality to the solutions due to it low specificity and by allowing the inclusion of ad hoc decisions. Overall, the fuzzy logic allows the use of human causal knowledge allied to the approximate reasoning, it being a means of reproducing the ability of a human operator in decision making [3], [7], [11].

The general objective of this paper is to contribute to the QoS architecture in WiMAX networks. Whereas the dynamic and unpredictable nature of the converging network, this work proposes a new approach to distribute the bandwidth in the IEEE 802.16 network downlink channel. As far as the author is aware, this is the first work that proposes a fuzzy approach to deal with this subject. As expected result, the proposed scheme must be able to distribute available resources among different service classes in a fair manner, adapting to the dynamics of the network and taking into account the different QoS requirements. This work has as significant contribution the study of fuzzy approach to deal with QoS in WiMAX networks as an alternative to traditional analytical solutions.

The remaining of this paper is organized as follows: Section II shortly describes IEEE 802.16 standard, especially QoS-related aspects; Section III describes the strategy based on fuzzy logic to support different kinds of service, including multimedia services; Section IV presents the numerical results obtained in a simulation model to WiMAX networks; finally, Section V brings the main conclusions of the paper.

II. The IEEE 802.16 Standard

The architecture of an 802.16 network is composed by two basic elements: SS (Subscriber Station) and BS (Base Station). The BSs are arranged in a cellular topology, as in mobile telephony. The standard considers the PMP (Point-to-Multipoint) mode operation and TDD (Time Division Duplexing) duplexing technique. In the TDD mode, the channel is segmented in the time with fixed-size frames. Each frame is divided into two sub-frames: one for the DL direction and another for UL direction. The BS dynamically controls the duration of these sub-frames in accordance with the demand for bandwidth in each direction. Specifically, the DL is broadcast channel and is used by BS to transmit control information and data addressed to some SS in its coverage. The BS maps the traffic in segments of time to send it into a TDM signal (Time Division Multiplexing) [4].

The IEEE 802.16 standard provides mechanisms to support QoS in both directions of communication. For this, the MAC layer is connection-oriented in the sense that all communication is established through a negotiated connection between each SS and the BS. Each connection receives a 16 bits identifier named CID (Connection ID), it being this the main QoS mechanism defined by the standard. The CID can be considered as an identifier even for connectionless traffic like IP, since it agregates itself information about the destination and the flow context [1].

All PDU (Protocol Data Unit) is mapped into objects named by standard as service flow. This object can be interpreted as a transport service of MAC layer, which provides unidirectional transport of packets in both DL and UL channels. Each flow has a unique identification, the SFID (Service Flow ID), which is associated with the corresponding CID. In addition, the 802.16 MAC specifies four different service classes, which define QoS levels: Unsolicited Grant Service (UGS) - specifies the CBR (Constant Bit Rate) traffic, such as VoIP without silence suppression; real time Polling Service (rtPS) - suitable to real time data flow with variable packet size, such as MPEG video and interactive games; non real time Polling Service (nrtPS) - represents applications that are not in real time but need a higher service level than the "best effort", as FTP (File Transfer Protocol); Best Effort (BE) - uses the remaining bandwidth, some examples are HTTP and Telnet protocols. The service flow is classified into one of these classes.

The MAC layer is also responsible for resource distribution, task originally held in upper layers. The bandwidth allocation is made on demand and it follows the priority attached to the service flow. Specifically, the DL channel scheduling is made according to instant demand perceived in the queues that receives packets from the core network. While the SS does not know in advance the traffic demand generated by remote application, it can not require DL bandwidth sending messages to the BS. Therefore, only the BS can determine how the DL resources are distributed among the SSs.

III. Fuzzy Strategy

Noting the class of service descriptions in IEEE 802.16 standard, it is possible to classify them into two major groups: UGS and rtPS services represent real-time applications and nrtPS and BE the non real-time applications. The first group of applications is delay sensitive but is tolerant to packet loss, unlike the second, which is tolerant to delays but packet loss sensitive. The QoS mechanisms must to fulfill these and others requirements. Nevertheless, to achieve success, the control should be end to end; that is, must be applied at each node along the route between the end hosts.

The scope of this work is restricted to the DL channel between the BS and the SSs covered in a IEEE 802.16 cell. Based on the services characteristics previously presented, the goal is to contribute to the role of WiMAX node in the task of end to end QoS control. To that end, the proposal aims to mitigate the delay in the UGS and rtPS queues and packet loss in the nrtPS and BE queues. The strategy adopts fuzzy logic to dynamically decide the best configuration for the bandwidth distribution, taking account the total resource available, the priority among the classes and the state of queues. The Figure 1 illustrates the schematic model of this proposal.

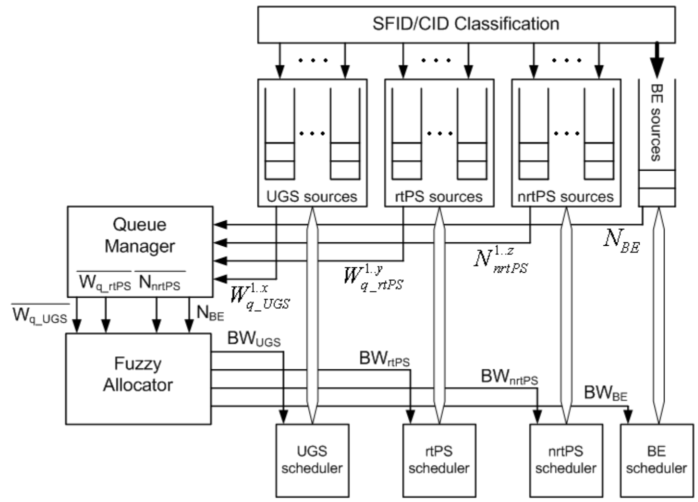

Fig. 1. Strategy to distribute resources among the class services.

This strategy was implemented as part of the QoS architecture developed on [1]. In this same work, also was developed to the NS-2 (Network Simulator 2) a simulation model with the main functionalities of WiMAX networks. For this reason, the strategy in this paper was implemented aiming its integration with the simulation model. Thus, it is possible to validate the strategy and evaluating it performance with respect to the fulfillment of QoS restrictions associated with each service class. Each of the modules is summarized below.

A. Packets Classification

The packets that cross the BS MAC layer are mapped to the corresponding queue as stated by the adopted classification parameters. This work uses the IP destination together with the service class. When the packet is inserted into the queue, it is marked with a timestamp value to permit the computation of monitored parameters.

The queue design at BS is composed by M UGS priority queues, M rtPS priority queues, M nrtPS priority queues and a BE FIFO queue. M is the number of SSs served by the BS, which means that, for each SS, there is a priority queue for each service class different of BE. The queues capacity is finite and adjusted according to the proposed simulation scenario. Finally, the queues are separated in groups: UGS sources, rtPS sources, nrtPS sources, BE sources.

B. Queue Management

To achieve the established goals, the average waiting time of UGS and rtPS queues and the occupancy of nrtPS and BE queues are monitored by the module *Queue Manager*. These measures are represented respectively by the variables

$W^i_{q\_UGS}$, $W^i_{q\_rtPS}$, N^i_{nrtPS}, N_{BE} where i indicates the *i-th* queue on each service class. The measurement is carried out in a multiple of TDD frame number, and its duration is specified to adapt to the network dynamics.

The queue delay of each packet is computed when it is sent. The current time (moment of packet transmission) minus the timestamp mark (moment of packet arrival) is the queue delay value. The queue delay of each packet is accumulated during the measurement interval. The average delay during the interval is the value of delay accumulated divided by the number of packets sent. Moreover, a counter is associated to each queue to compute its occupancy. At last, is computed the average of associated measures to each group of queues. Thus, four new parameters are obtained:

- $\overline{W_{q\_UGS}}$:average among UGS queue delays;
- $\overline{W_{q\_rtPS}}$: average among rtPS queue delays;
- $\overline{N_{nrtPS}}$: average among nrtPS queue occupancies;
- N_{BE} : BE queue occupancy.

The module adopts a hysteresis mechanism for network monitoring. Such mechanism is based on the configuration of two thresholds (upper, lower) for each parameter described before. These thresholds are used as a criterion to determine whether some event occurred on the network and it requires the bandwidth redistribution. There are four possible events: under-allocation, over-allocation, inactive class and active class. The under-allocation event occurs when some of the calculated parameter exceeds the corresponding threshold. The over-allocation event occurs when one or more parameters is between its upper and lower thresholds while at least another one is below of it threshold. In the end, when consecutives measures of the same parameter change from non-zero to zero means that, at least in this frame, there are not packets on the corresponding queues waiting to be transmitted. In this case, the class is inactive. Otherwise, when a parameter associated to a class changes from zero to non-zero in consecutive measures, the class is active and needs resource. The Figures 2 and 3 reflect in algorithms the presented ideas.

If it was identified any of the previous events in the network, the Fuzzy Allocator module is driven to reallocate the bandwidth among service classes. This mechanism and the measure interval avoid the Fuzzy Allocator module be executed every frame. This reduces the computational load. Thus, if the traffic profile in the network does not change over the time, only the circular scheduling on queue level is executed.

C. Fuzzy Allocation

The Fuzzy Allocator module is a kind of expert system whose input and output spaces are composed, each one, by four linguistic variables: $\overline{W_{q\_UGS}}$, $\overline{W_{q\_rtPS}}$, $\overline{N_{nrtPS}}$, N_{BE} to the input space and BW_{UGS}, BW_{rtPS}, BW_{nrtPS}, BW_{BE} to the output space. The input variables, described in the previous section, are presented to the module when it is executed. The output variables are the decision object of the resource distribution strategy. They represent the fraction of the total bandwidth available reserved for each service class.

```
ALGORITHM queueMonitor
    double higherUGS = h1;          bool UGSto0;
    double upperUGS = u1;           bool UGSfrom0;
    double higherRTPS = h2;         bool rtPSto0;
    double upperRTPS = u2;          bool rtPSfrom0;
    double higherNRTPS = h3;        bool nrtPSto0;
    double upperNRTPS = u3;         bool nrtPSfrom0;
    double higherBE = h4;           bool BEto0;
    double upperBE = u4;            bool BEfrom0;
    bool event = false;
    //Under allocation event
    if ((W_q_UGS > h1) or (W_q_rtPS > h2) or (N_nrtPS > h3) or (N_BE > h4))
        return (event = true);
    //Over allocation event
    if ((W_q_UGS < u1) xor (W_q_rtPS < u2) xor (N_nrtPS < u3) xor (N_BE < u4))
        return (event = true);
    //Inactive class event
    if ((UGSto0) or (rtPSto0) or (nrtPSto0) or (BEto0))
        return (event = true);
    //Active class event
    if ((UGSfrom0) or (rtPSfrom0) or (nrtPSfrom0) or (BEfrom0))
        return (event = true);
    return event;
```

Fig. 2. Algorithm responsible for determining the occurrence of an event.

```
ALGORITMO Allocation
    unsigned measureInterval = mi;
    bool event = false;
    //frameCount indica o número atual de quadros transmitidos.
    if ( (frameCount mod mi) == 0) {
        computeDelay;
        computeOccupancy;
        event = queueMonitor (W_q_UGS, W_q_rtPS, N_nrtPS, N_BE);
        if (event == true)
            fuzzyAllocator (W_q_UGS, W_q_rtPS, N_nrtPS, N_BE);
    }
```

Fig. 3. Algorithm responsible for puting in action the fuzzy allocator in case of any event detected.

The fuzzy partition of each mentioned variables and its membership functions settings are designed to suit the characteristics of the network where the system will be deployed. This work adopts triangular and trapezoidal functions whose advantages are the simple and efficient implementation, usually without loss to the quality of results that justify the use of more complex functions [2], [6]. The set of linguistic terms to the variables is formed by the values "low", "medium" and "high". This is the minimum number of words needed to model the problem and it leads to a minimum number of rules for the decision. It followed the usual strategy of fuzzy modeling, in other words, starting with the simplest structure. More elaborate models, with higher number of terms and more complex functions, may be employed if is necessary to refine the control over the system.

It is important to emphasize that the settings for each input variable, reflected in their respective membership functions, aim to translate the particular characteristics of applications that it represents. Furthermore, the guidelines to set the output variable is exclusively the priority among the classes.

The criterion used to model the membership functions related to the $\overline{W_{q\_UGS}}$ and $\overline{W_{q\_rtPS}}$ variables was based on the delay restrictions presented in [5] and the ITU-T G.114 [9] recommendation. Both works define similar ranges of delay to characterize service levels. Nevertheless, the values in the documents refer to the total delay, in other words, the sum of all categories of delay along the path between the end hosts. So, this work adopts fractions of these intervals to qualify only the delay in BS queues. As the fuzzy partitions, these intervals are parameterized and adjusted according to the definition of service levels admitted to the network. The Figure 4 indicates the membership functions associated to the corresponding linguistic terms.

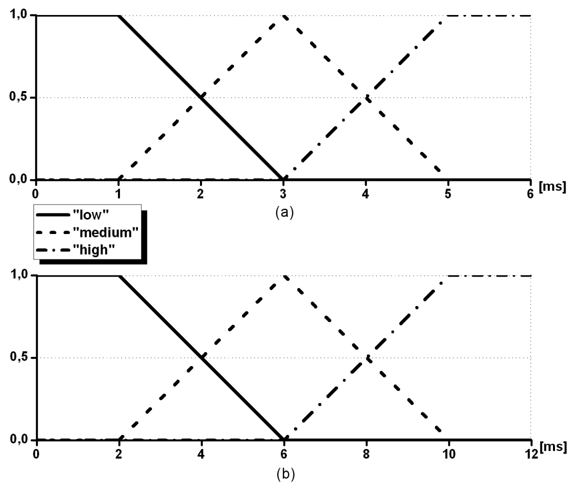

Fig. 4. Fuzzy partitions to the input variables: (a) $\overline{W_{q\_UGS}}$, (b) $\overline{W_{q\_rtPS}}$

The Figure 5 shows the membership functions of $\overline{N_{nrtPS}}$ and N_{BE} linguistic variables. To these shapes was used the RED (Random Early Detection) algorithm [5], [10] as guideline. However, in this solution the RED intervals indicate the level of resources that is necessary to avoid packet loss.

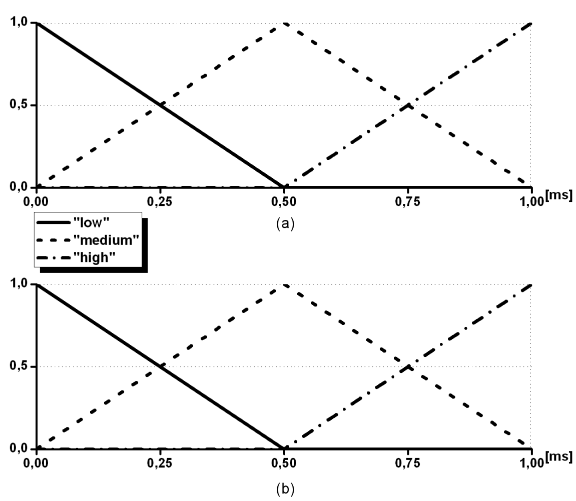

Fig. 5. Fuzzy partitions to the input variables: (a) $\overline{N_{nrtPS}}$, (b) N_{BE}

The Figure 6 presents the membership functions of output variables BW_{UGS}, BW_{rtPS}, BW_{nrtPS} e BW_{BE}. It is worth mentioning that may be established other criterion to set the membership functions, from both the input as the output space. The configuration must be such that the fuzzy system reproduces the expert knowledge on the particular environment where the system will operate.

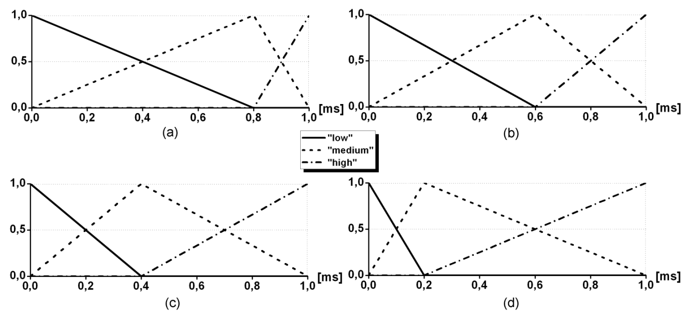

Fig. 6. Fuzzy partitons to the output variables (a) BW_{UGS}, (b) BW_{rtPS}, (c) BW_{nrtPS}, (d) BW_{BE}.

To map all possible state combinations, the rule base has 81 entries. In principle, the base construction was empirical. For each input, an expert evaluates what should be the output. In other words, for each combination of input variable is evaluated which should be the instance ("low", "medium", "high") to each output variable in order to suit the demand as better as possible. Next, with the simulation environment, the base has been adjusted gradually, evaluating the parameter measures and the traffic applied. When the expert noted that the resources allocated to each class could be better distributed, the rules triggered on this specific allocation were revised.

After the defuzzification stage, the sum of the resource percentages allocated to each class is not necessarily equal to 1. Moreover, even when is verified an inactive class event, bandwidth is allocated to this class. This happen because the adopted defuzzification process and others tested to this work never reaches the extremes of decision, that is, it never permits the values 0.0 % or 100.0 % of allocation. The explanation for the COG (Center of Gravity), method used in this study, is quite intuitive, since the center of gravity of a flat compact surface, as are the fuzzy sets obtained after the inference process, will never be in one of its bounds. Thus, the scalar value calculated, abscissa of the center of gravity, does not reach neither 0 nor 1.

To solve these issues, the fuzzy expert system was complemented with a pos-processing block. In this block, the values of allocation are normalized so that the sum of resources is exactly 100.0 % of available bandwidth. Additionally, the resources allocated to inactive class are redistributed equally among the active class.

D. Schedulers

Resources allocated to each class are shared among it queues. In principle there is no priority among the queues within the same class and the resources are distributed in a circular manner, specifically RR (Round Robin) discipline. To avoid starvation, the scheduling at the next TDD frame starts from the last queue served at the last frame. This is important especially in a scenario of statistics QoS (situation in which the demand may exceed the level of resources in some moment of operation).

IV. Numerical Results

Several scenarios were developed in order to validate the strategy and evaluate its performance with respect the QoS requirements compliance. Two of these scenarios are presented below. In both, the measurement interval fixed to the Queue Manager module is 10 MAC frames. In these tests there were not packets losses. The thresholds values set for the input variables are listed in Table I.

TABLE I
Thresholds values fixed to the histeresis mechanism.

Threshold	Value
upper_UGS	3.00 ms
lower_UGS	1.00 ms
upper_rtPS	6.00 ms
lower_rtPS	3.00 ms
upper_nrtPS	40.0 %
lower_nrtPS	20.0 %
upper_BE	60.0 %
lower_BE	30.0 %

A. Scenario 1

The objective of the first scenario is to allow a better understanding of how the membership functions configuration determines the interpretation of the subjective term “priority”. Thus, it is possible to realize the behavior of the bandwidth allocation when two or more classes need resources during the simulation. Applications classified as UGS and BE are applied, classes with opposite priorities on IEEE 802.16 standard. Each application generates traffic with a load proportional to the bandwidth available. Three simulations are carried out, each one with 60 seconds: the first one, the priority of BE is greater than that of UGS, the second one, the priorities are equal and the third one, the priority of UGS is greater than that of BE. For each simulation, it is configured a set of output membership functions, as presented on section III-C. Each set function reproduces a priority order among the classes. The same base rule is used on the three simulations. Moreover, in this scenario, the hysteresis mechanism operates observing only the under-allocation event. The Figure 7 illustrate the network defined and the Table II summarizes the traffic parameters.

TABLE II
Traffic parameters to the first scenario.

Class	Application	SS	Start-Finish (s)	Load
UGS	VoIP	SS_2	$5-30$	10.0 %
UGS	VoIP	SS_2	$5-30$	20.0 %
BE	Telnet	SS_4	$20-40$	60.0 %

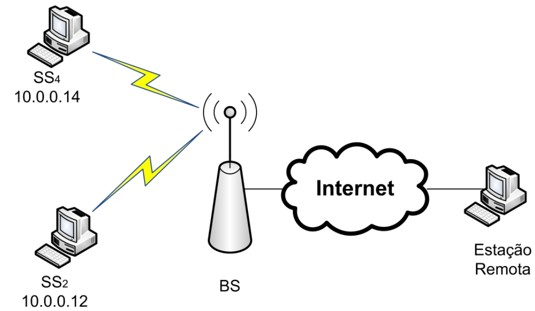

Fig. 7. Network to the first scenario.

From the figures below, it is possible to observe that the configuration of the priority order directly influences the values of weights assigned, hence the values of the monitored parameters. Specifically, the delay reaches 3 ms due to the threshold configured to the hysteresis mechanism, as can be seen in Figure 8. From this point, the Fuzzy Allocator module is executed, as Figure 9 shows. Observing simultaneously the Figure 8 and 9, it is possible to realize that the delay on UGS queues fall to 0 ms after the bandwidth redistribution. The simulation in which UGS has higher priority (dark blue line), the rate at which the delay decays is more accentuated, agreeing with the larger allocation (85.0 % of the DL bandwidth). As the priority UGS decreases, also decreases the amount of allocated resources (blue line indicates 76.0 % and light blue line 67.0 %), and consequently the rate at which the delay falls.

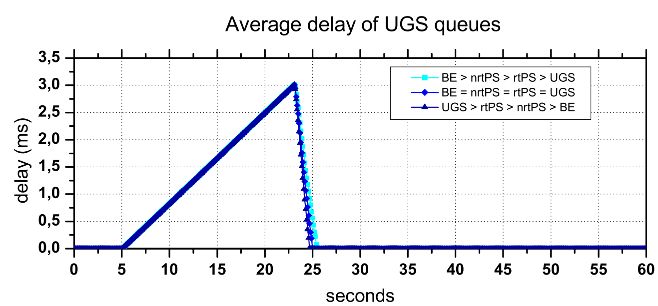

Fig. 8. Average waiting time of UGS queues.

For the BE class, the correlation between weight and monitored parameter is still more explicit. The Figure 10 points that the occupancy level of BE queue reaches the upper threshold on different instants, depending on the configuration of priority term. This occurs because the Fuzzy Allocator was executed when the UGS parameter reaches its upper threshold, as explained earlier. From this instant, the simulations pass with different allocations values. At time 23.2 s, moment of this first resource redistribution, the Figure 10 presents a breakpoint. From this point, the velocity at which the occupation of BE queue occurs depend on the amount of resources reserved to this class. According to the Figure 11, when BE has highest

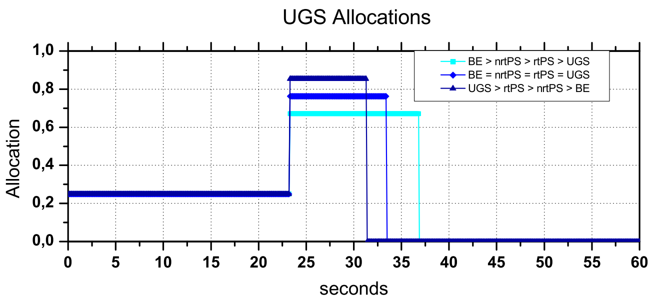

Fig. 9. Proportion of resurces reserved to UGS class.

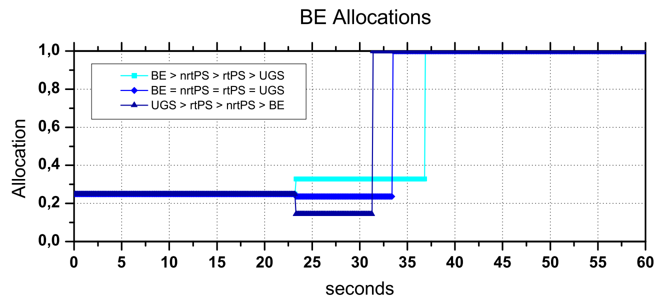

Fig. 11. Proportion of resurces reserved to the BE class.

priority, light blue line, more resources are available for this class, so the occupancy level of the queue grows more slowly, reaching the upper limit (0.6) of the hysteresis mechanism later. The same thought can be extended to the others two simulations.

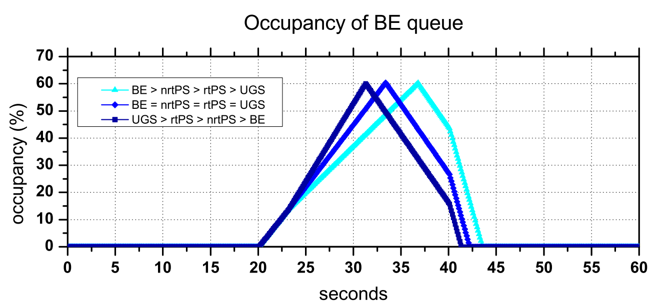

Fig. 10. Occupancy on BE queue.

The Figure 11 also indicates that the second fuzzy system execution on each simulation occur at 31.3 s, 33.4 s and 36.8 s; points on dark blue line, blue line and light blue line, respectively. Its important to point out that the UGS traffic stop at 30.0 s, so when the allocator is set in action again, all bandwidth is assigned only to the BE class, as can be seen on Figure 11. For this reason, the Figure 10 shows that the rate at which the occupation falls is the same for all three simulations. Another point must be observed: from instant 40.0 s, the occupation falls in greater speed, evidenced by the breakpoint on lines of Figure 10. This occurs because the traffic BE ended exactly at this moment.

The previous discussion permits to conclude that the proposed fuzzy system reserves more resources to the class with higher priority, as expected. It is important to note that the priority level assigned to each class can be configured not only on the base rule but also on the membership functions. The fuzzy term "priority" can be interpreted in endless ways, and that subjectivity may be reproduced in the memberships functions of output space, for example. In summary, the adjustment can be made as the distinguishing characteristic of the environment to which the system was planned.

B. *Scenario 2*

This second scenario simulates applications of all IEEE 802.16 classes. Each class demands 20.0 % of the bandwidth during all the simulation time. In different intervals the UGS and BE classes demand another 20.0 % of the bandwidth, adding up a demand of 40.0 % for each of this two classes during the specific interval. These service classes represent applications with different QoS requirements and with different priorities. Hence, the objective of this scenario is to verify the fuzzy strategy performance on serving different applications with pretty distinct characteristics in case of peaks of demand. In this context, the necessary resources must be allocated to the classes at its higher demand moment, always taking account the priority, the total resources available and state of queues. The Figure 12 illustrates the network defined and the Table II summarizes the traffic parameters.

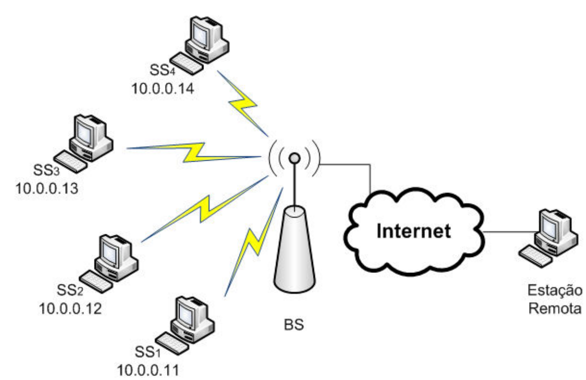

Fig. 12. Network to the second scenario.

As soon as the simulation begins, the Figure 17 indicates that occur the first executions of Fuzzy Allocator. The occupancy measurement of nrtPS queues changes from different of zero to zero, and right away change to different of zero again. The result of this last allocation is as follows: UGS, 39.2 %; rtPS, 29.4 %; nrtPS, 20.3%; BE, 11.1 %. This weights remains for several seconds, as can be seen in the Figure 17.

At the 8.3 s of simulation, the last configuration changes cited. With a accentuate difference between demand and resources, 40.0 % e 11.1 % respectively, the BE queue oc-

TABLE III
TRAFFIC PARAMETERS TO THE SECOND SCENARIO.

Class	Application	SS	Start-Finish (s)	Load
UGS	VoIP	SS_1	$0 - 60$	20.0 %
UGS	VoIP	SS_3	$30 - 50$	10.0 %
UGS	VoIP	SS_4	$30 - 50$	10.0 %
rtS	MPEG Streaming Audio	SS_1	$0 - 60$	8.0 %
rtS	MPEG Streaming Audio	SS_2	$0 - 60$	12.0 %
nrtPS	File Transfer	SS_3	$0 - 60$	15.0 %
nrtPS	File Transfer	SS_4	$0 - 60$	5.0 %
BE	HTTP	SS_1	$0 - 60$	15.0 %
BE	Telnet	SS_2	$0 - 60$	5.0 %
BE	HTTP	SS_3	$0 - 20$	12.0 %
BE	HTTP	SS_4	$0 - 20$	8.0 %

cupancy grows quickly, as Figure 16 presents. For this reason, consecutive allocations increase the amount of resources to BE as the occupancy grows. These allocations mitigate the occupancy rate in BE queue, but are still insufficient. After 20.0 s, finish the BE flows to SS_3 e SS_4 and the demand of this class comes back to 20.0 %. Thus, the occupancy begins to fall and, proportionally, also fall the resources reserved to BE. At the end of this series of allocation, exactly at 27.4 s of simulation, the fixed configuration is: UGS, 29.0 %; rtPS, 21.8 %; nrtPS, 20.1 %; BE, 29.1 %.

The sum of 29.0 % of resources is sufficient to cover the initial demand of 20.0 % of the UGS class. Therefore, the delay average remains 0 ms until the moment when new sources add another 20.0 % of demand (30.0 s of simulation). When the delay reaches the threshold set for the class (1 ms), as can be verified on Figure 13, consecutives redistributions increase the resources to the UGS class, illustrated on Figure 17. Comparing the Figures 13 and 17, can be noted that as the amount of resources increase, the delay growth decreases. When the UGS traffic stop, the average delay falls to zero.

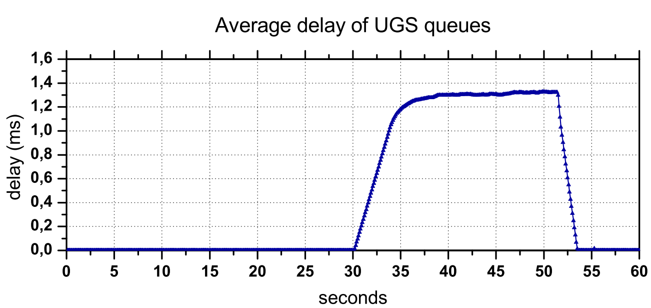

Fig. 13. Average waiting time of UGS queues.

The rtPS demands remains constant throughout the simulation, 20.0 % of available bandwidth. During almost all the time, the amount of allocated resources exceeds demand and that is why the average delay in rtPS queues remains within a range between 0 and 0.13 ms, according to Figure 14. The exception is the interval between 39.0 s and 51.5 s, a period in which the sum of resources is slightly below the demand, according to Figure 17. In this case, the rtPS delay begins to grow, reaching a peak of 0.74 ms. It is worth mentioning that the fuzzy system aimed to reserve to rtPS class a fair bandwidth for its demand, fact shown in Figure 17. The times in which it does not occur coincides with the highest allocation for UGS, class with the highest priority. Similar reasoning can be applied to the nrtPs class. However, due to the nrtPS priority is smaller than rtPS, it gives up more resources.

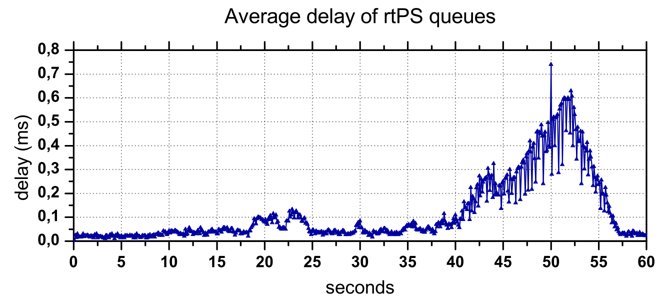

Fig. 14. Average waiting time of rtPS queues.

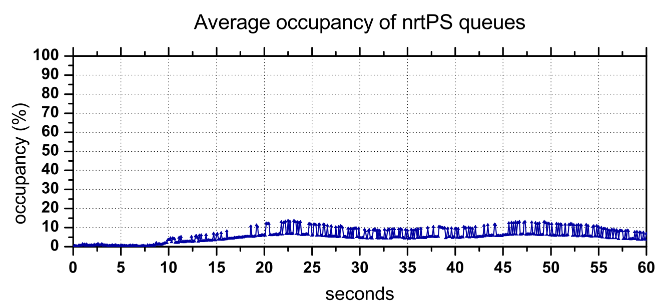

Fig. 15. Average occupancy of nrtPS queues.

Since BE has the lowest priority, it is always penalized when the other classes require resources. For this reason, as can be seen in Figure 16, the occupancy in BE queue grows until the 20.0 s, instant at which the BE flow returns to 20.0 % of the bandwidth. Nevertheless, in spite of the growth of occupancy, the allocations ensure that this growth is not even higher. Also, even with lower priority, BE receives most of the resources between 8.3-27.4 s, as indicated in Figure 17. After the end of BE traffic to SS_3 and SS_4 the occupancy falls to a certain level, which remains constant until the end of the simulation. The reason is that in later allocations, the resources for BE back to 20.0 %, value equal to the demand.

The previous graphic analysis proves that the strategy was successful to support different services with dynamic demand. The system can identify the traffic profiles and dynamically allocate the resources, following the priorities weighted by the demand among the classes and the available resources.

V. CONCLUSIONS

This work presented a new approach to deal with bandwidth scheduling in IEEE 802.16 DL channel. The proposal was

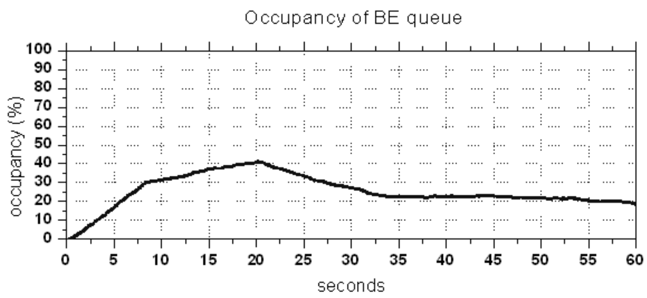

Fig. 16. Occupancy of BE queue.

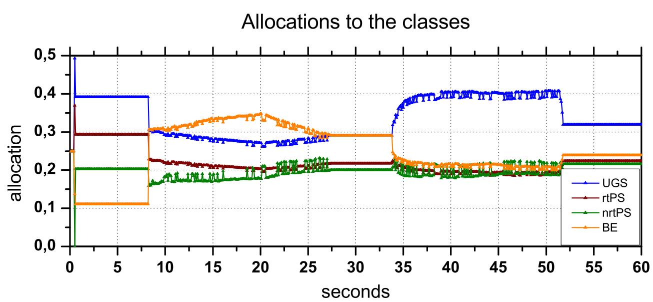

Fig. 17. Proportion of resurces reserved to the classes on scenario 2.

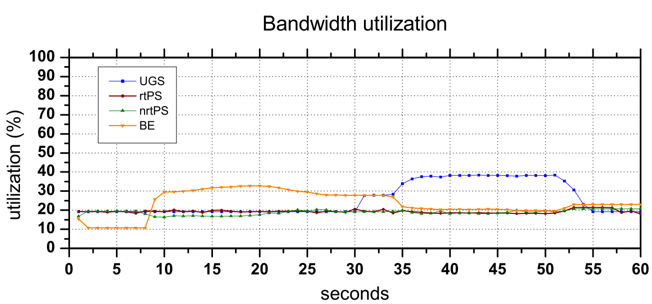

Fig. 18. Bandwidth utilization during the simulation.

based on fuzzy logic. The strategy was implemented and validated in an environment with the main WiMAX network functionalities.

Given the presented scenarios, it is feasible to conclude that the Fuzzy Allocator module follows the established priorities and it can be configured to reproduce the characteristics of each service with regard to it QoS requirements. Moreover, it is possible to realize how the adjustment of the memberships functions influences in the interpretation of parameters values and consequently in the inference process.

These results prove the potential use of fuzzy logic in solutions to QoS assurance mechanism. The fuzzy approach stood out mainly by allowing more general and flexible solutions, since the tool allows configuring the system to fit the environment. As shown, setting a fuzzy system is simpler than build an analytical model, taking account that, generally, when the system conditions change, the analytical model needs to be almost entirely rebuilt.

The fuzzy term "priority" can be interpreted in endless ways, and that subjectivity may be reproduced in the memberships functions of output space, for example. In summary, the adjustment can be made according to the specificities of the environment to which the system was planned.

References

[1] R. Q. Malini, *Uma Arquitetura de QoS e Modelo de Simulação para o Padrão IEEE 802.16d como Suporte a Serviços Multimídia Distribuídos.*. Programa de Pós-Graduação em Informática, Universidade Federal do Espírito Santo,Vitória, ES, 2007.

[2] R. A. Resende, *Qualidade de serviço em rede IP utilizando logica fuzzy.*. Faculdade de Engenharia Elétrica e de Computação, Universidade Estadual de Campinas,Campinas, SP, 2006.

[3] L. A. Zadeh, Fuzzy Sets. *Information and Control*, 8. ed. [S.1.:s.n.], 1965, pp 338-353.

[4] ANDREWS, J. G.; GHOSH, A.; MUHAMED, R., Broadband wireless access with WiMax/802.16: current performance benchmarks and future potential. *IEEE Communications Magazine*, IEEE Press, vol. 43, no. 2, pp 129-136, February 2005.

[5] LEE, K. O.; HAHM, J. H.; KIM, Y. S., QoS Application Method in Portable Internet. *Proceedings of Asia-Pacific Conference on Communications*, IEEE Press, pp 237-239, October 2005.

[6] P. Siripongwutikorn; S. Banerjee; D. Tipper, Adaptive bandwidth control for efficient aggregate QoS provisioning. *SIGCOMM Comput. Commun. Rev.*, ACM, New York, NY, USA, vol. 32, no. 3, pp 19–19, 2002.

[7] C.C. Lee, Fuzzy Logic in control systems: Fuzzy logic controller. II. *Systems, Man and Cybernetics, IEEE Transactions on*, IEEE Press, vol. 20, no. 2, pp 419-435, April 1990.

[8] *IEEE Std. 802.16, IEEE Standard for Local and Metropolitan Area Network Part 16: Air Interface for Fixed Broadband Wireless Access System*, October, 2004.

[9] ITU-T Recommendation G.114, *One way transmission time.*. International Telecommunication Union, Geneva, May 2003.

[10] A. S. Tanenbaum, *Redes de Computadores*, Tradução da 4ª ed., Editora Campus, Rio de Janeiro, RJ, October 2004.

[11] C. T. Lin; C. S. G. Lee, *Neural fuzzy systems: a neuro-fuzzy synergism to intelligent systems*, Prentice-Hall PTR, Upper Saddle River, NJ, 1996.

Galileo BOC(1,1) Signal Acquisition and Tracking

Elvis Alves de Oliveira
Instituto Tecnológico de Aeronáutica - ITA
CEP 12.228-900
São José dos Campos - SP - Brasil
+55 12 3947-6903
elvis@ita.br

Fernando Walter
Instituto Tecnológico de Aeronáutica - ITA
CEP 12.228-900
São José dos Campos - SP - Brasil
+55 12 3947-5962
fw2@ita.br

Abstract— **Galileo is the forthcoming European navigation satellite system. Focuses on software implementation defined radio receivers for Galileo E1-B BOC(1,1) signal is presented. The aim is to acquire and track the BOC(1,1) signal, using PRN codes transmitted by the first Galileo satellite GIOVE-A (Galileo In-Orbit Validation Element). In a MatLab® simulator two GUI (Graphical User Interface) for generation, acquisition and tracking of the BOC(1,1) signal was developed, allowing modifications of the relative parameters in the generation of Signal-In-Space (SIS), acquisition, and tracking.**

Index Terms— **Acquisition, Galileo System, Global Navigation Satellite Systems (GNSS), Software Define Radio (SDR), Tracking.**

I. INTRODUCTION

The GNSS are today sources of many applications such as vehicle tracking, personal navigation, aircraft navigation, road and rail management, precision agriculture, only to mention some few examples. The European navigation system Galileo appears on this scenario to improve the performance of the navigation information presenting new solutions for global navigation. This improvement is mainly due the use of modulation techniques such as BOC (Binary Offset Carrier), and PRN codes, at least four times larger than GPS codes [1 and 2].

To understanding the Galileo E1-B BOC(1,1) signal processing a software receiver was developed (SWR). Signal characteristics and simulations carried out for different signal-to-noise density ratios (C/No) are presented. A Graphical User Interface was developed which allows evaluating the receiver performance when changes are made in the signal transmitted parameters (such as: Code delay, Doppler, and signal-to-noise density ratio).

II. GALILEO SYSTEM

Galileo is the forthcoming European navigation satellite system. The Galileo operational phase is envisaged starting from 2013 with a total of 30 Medium-Earth Orbit (MEO) satellites in three approximately circular orbits, called Walker 27/3/1 constellation, where three of them are spares. The orbits will have, approximately, 56º inclination and 14h 22m of period.

Galileo envisages the provision of a large variety of services [2 and 3]. The Galileo Satellite-Only Services (GSOS) are systems nucleus. The GSOS will provide services that have been grouped around the following five types: 1) Open Service (OS); 2) Commercial Service (CS); 3) Safety of Life (SoL); 4) Support to Search and Rescue (SAR); and 5) Public Regulated service (PR).

The satellites will broadcast a total of eleven signals. One of them will be applied in SAR service, broadcasting in 1,544 MHz to 1,545 MHz. The main primary Galileo navigation signals parameters are reported in Table I [4].

TABLE I
PRIMARY GALILEO NAVIGATION SIGNALS PARAMETERS.

Signal	Chip Rate (Mcps)	Description	Symbol Rate (sps)	Service
E5a-I	10.23	Open access code	25	OS/SoL
E5a-Q			N/A	OS/SoL
E5b-I	10.23	Open access code	125	OS/SoL/CS
E5b-Q	10.23		N/A	OS/SoL/CS
E6-A	5.115	Restricted access code	100	PRS
E6-B		Controlled access code	1000	CS
E6-C			N/A	CS
L1-E1-A	2.5575	Restricted access code	100	PRS
L1-E1-B	1.023	Open access	250	OS/SoL/CS
L1-E1-C			N/A	OS/SoL/CS
L6 downlink	N/A	N/A	N/A	SAR

N/A: Not Available

All Galileo satellites will share de same frequencies by Code Division Multiple Access (CDMA) technique and use a pseudorandom codes (PRN) generated by tiered codes. Every PRN sequence is formed by two codes (primary and secondary) [5, 6 and 7].

III. SIGNAL-IN-SPACE

A. *Signal-In-Space Galileo E1*

The Galileo E1 signal-in-space is transmitted on the frequency f_{E1} = 1,575.42 MHz. Two signals are present in this frequency: 1) Restricted access signal (E1P): channel E1-A, Equation 1; and 2) Open access signal (E1F): channels E1-B e E1-C, Equations 2 and 3. All E1 channel are multiplexed taking a power sharing of 50% for E1P and 50% for E1F. This technique, called Coherent Adaptive Subcarrier Modulation (CASM), Equation 4, ensures that the signal transmitted has a constant power envelope.

$$e_{E1-P}(t) = d_{E1-P}(t).c_{E1-P}(t).s_{BOCc(15,2.5)}(t) \qquad (1)$$

$$e_{E1-B}(t) = d_{E1-B}(t).c_{E1-B}(t).s_{BOC(1,1)}(t) \qquad (2)$$

$$e_{E1-C}(t) = c_{E1-C}(t).s_{BOC(1,1)}(t) \qquad (3)$$

$$\begin{aligned} s_{E1}(t) &= \frac{\sqrt{2}}{3}\left[e_{E1-B}(t) - e_{E1-C}(t)\right] + \\ &j\frac{1}{3}\left[2.e_{E1-P}(t) + e_{E1,\mathrm{int}}(t)\right] \end{aligned} \qquad (4)$$

Where: d_{E1-P}, d_{E1-B} are the navigation data; c_{E1-P}, c_{E1-B}, c_{E1-C} are the PRN codes; $s_{BOCc(15,2.5)}$, $s_{BOC(1,1)}$ represents the BOC modulations; and $e_{E1,int}(t)$ is the intermodulation product. The intermodulation product ensures a constant power envelope.

$$e_{E1,\mathrm{int}}(t) = e_{E1-P}(t).e_{E1-B}(t).e_{E1-C}(t) \qquad (5)$$

B. BOC Modulation

Taking in mind reduction of the mutual interference between signals modulated over the same carrier frequency, the Binary Offset Carrier (BOC) modulation will be implemented in Galileo E1-B signal. The BOC modulation introduces a frequency shift on spectrum due to the subcarrier. In addition, BOC modulation improves the acquisition and tracking performance resulting in a narrower autocorrelation function (ACF) with the presence of side peaks, as shown in figure 1, in accordance to [2, 6 and 7].

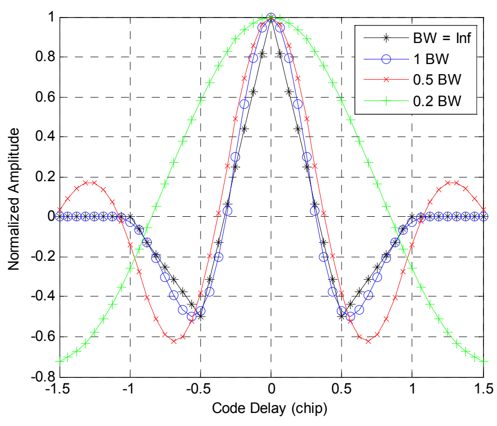

Fig. 1. ACF for BOC(1,1) signal with normalized bandlimit (BW = 24.552 MHz) [6]. The function b = inf represents the theoretical ACF. Other functions: **1 *BW***, **0.5 *BW*** and **0.2 *BW***.

The BOC modulation is usually described as BOC(n, m) where n is the subcarrier frequency multiples of 1.023 MHz and m is the chip rate multiples of 1.023 Mcps. The BOC signal is described by Equation 6.

$$s(t) = \sqrt{P}\sum_{i=-\infty}^{+\infty}\left\{c_i d_i r\left(t - i\frac{T_R}{m}\right) sign\left[\sin\left(2\pi\frac{n}{T_R}t\right)\right]\right\} \qquad (6)$$

Where $T_R = f_R^{-1}$ = 977.52 ns is the reference time, P is the power signal, c_i is the sequence of the code chips, d_i are the data and *r(.)* is a rectangular pulse shape of unitary amplitude and duration of T_R/m. When the argument of the function *sign(.)* is odd the BOC modulation is denoted by BOC_{sin}. Otherwise, if is even the BOC modulation is denoted by BOC_{cos}. For both sine and cosine functions, the frequency is $f_{SC} = n/T_R$.

IV. GALILEO RECEIVER

A. GNSS Receiver Overview

After the Front-End stage, the processing functions are executed in a channelized structure. The channel is divided in five main functions. Figure 2 gives an overview of one GNSS receiver channel [8].

The two main structures of receiver are: 1) Acquisition: gives rough estimates of PRN code delay and carrier frequency deviation; 2) Tracking: gives fine estimates from obtained acquisition parameters and keep locked a local signal with the received signal using a PLL (Phase Locked Loop) or FLL (Frequency Locked Loop) and DLL (Delay Locked Loop).

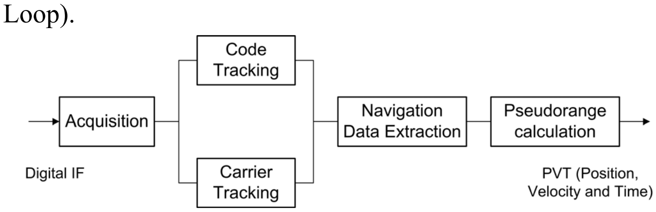

Fig. 2. GNSS receiver channel. The acquisition gives rough estimates of signal parameters (code delay and carrier frequency deviation). These parameters are refined by the tracking stage (Code and Frequency tracking).

B. Acquisition

Before allocating a channel to a specific satellite (PRN), the receiver must know which satellites are visible. The determination of the visible satellites may be done in two ways: 1) Cold Start: the receiver does not have any previous information of visible satellites, therefore being necessary the search for all possible satellites (up to 50 PRN codes for Galileo); and 2) Hot/Warm Start: information of visible satellites, code delay and frequency deviation are previously available on receiver. Using a Hot/Warm start, the determination of the first fix (Time To the First Fix – TTFF) is reduced drastically [7].

In acquisition process the receiver generates a local signal for each channel (frequency and PRN code generators). The received signal is crosscorrelated with a local signal generated at different code phases and frequency bins. This process is made for different frequencies and PRN code delays until these deviations are estimated. Due to BOC modulation is necessary a local subcarrier generation. The Figure 3 shows the block diagram of the parallel code phase search algorithm.

C. Tracking

After acquisition, the received signal is processed in the next stage called tracking. The main purpose of tracking is refining the coarse values of code phase and frequency deviation. Since the frequency and code delay signal changes over time due to the variation of the dynamics between user and satellite [8, 9].

IGNSS [11] analyzes three methods of Galileo E1 signal tracking: 1) BOC-BOC (E-L) Costas Loop; 2) BOC-PRN (Direct Prompt) Costas Loop; and 3) BOC-PRN (E+L) Costas Loop. The BOC-BOC (E-L) Costas Loop architecture represents a good solution in lower signal-to-noise density ratios. BOC-BOC (E-L) Costas Loop architecture is presented in Figure 4.

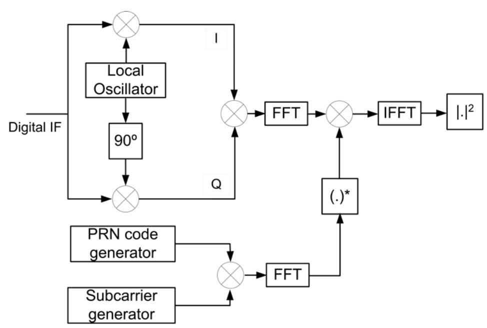

Fig. 3. Parallel acquisition in time domain using FFT.

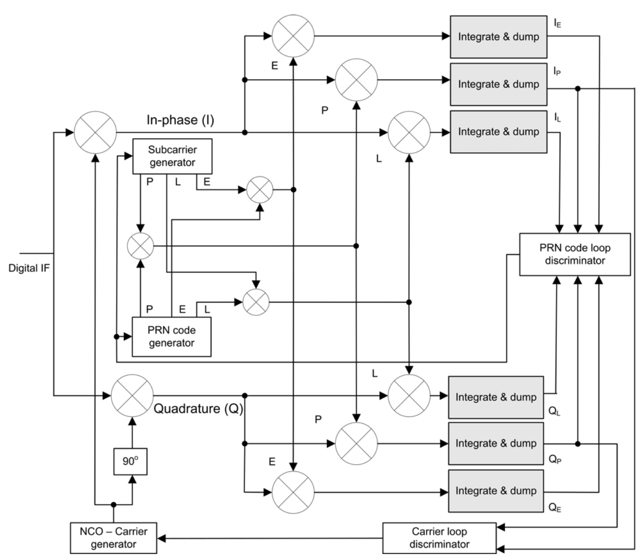

Fig. 4. BOC-BOC (E-L) Costas Loop architecture.

V. PROCESSING RESULTS

To simulate the SIS, acquisition and tracking stages a Graphical User Interfaces (GUI) in MatLab® had been implemented (Appendix – Figure A).

Figures 5 and 6 presents BOC(1,1) signal and its spectrum, respectively, for different signal-to-noise density ratios.

The figure 7 presents the simulated Galileo E1-B signal after the Front-End. An AWGN channel model was used in these simulations.

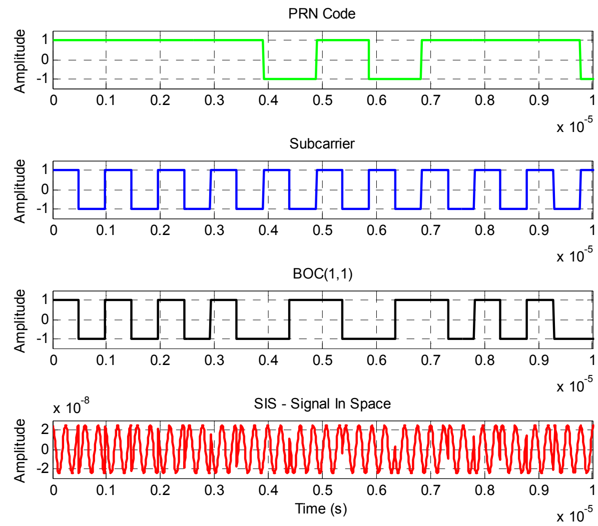

Fig. 5. PRN # 1; Subcarrier; BOC(1,1); and dataless SIS.

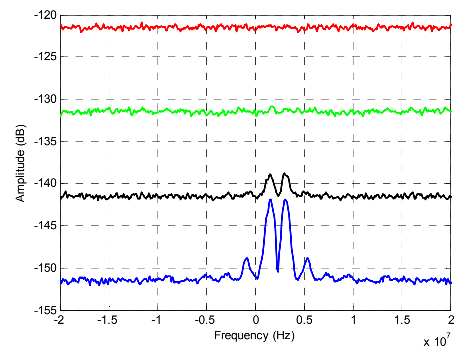

Fig. 6. Galileo BOC(1,1) PSD @ f_{IF} = 2.25 MHz and f_S = 10 MHz. (Top to Bottom): **C/No** = 25 dB-Hz; **C/No** = 35 dB-Hz; **C/No** = 45 dB-Hz; **C/No** = 55 dB-Hz.

The acquisition stage of a GNSS receiver has to search in a two-dimensional search space (code delay and Doppler shift) for each satellite of the constellation. The search space represents all possible code and frequency deviations for the received signal.

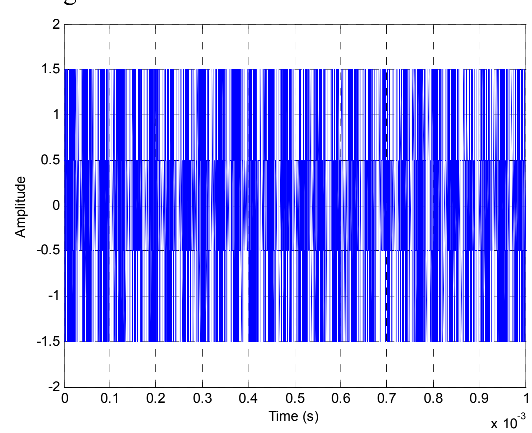

Fig. 7. Galileo E1-B signal: BW = 4,4 MHz; f_{IF} = 2.25 MHz and f_S = 10 MHz; C/No = 47 dB-Hz and 2 bits (Signal and Magnitude).

Figure 8 shows the acquisition results for Galileo PRN # 1.

The parallel plan to the Frequency/Magnitude plan (Figure 8) that passes for the correlation maximum (carrier profile) and the parallel plan to the Code/Magnitude plan that passes for the correlation maximum (code profile) is presented in figure 9.

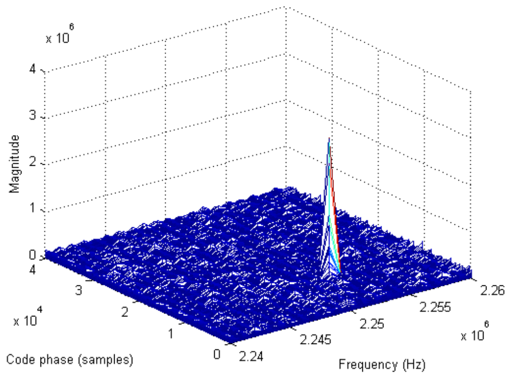

Fig. 8. Acquisition results: PRN # 1; C/No = 47 dB-Hz; P = -157 dBw; f_{IF} = 2.25 MHz; $f_{Doppler}$ = 2 kHz; and $d_{Código}$ = 10,000 samples.

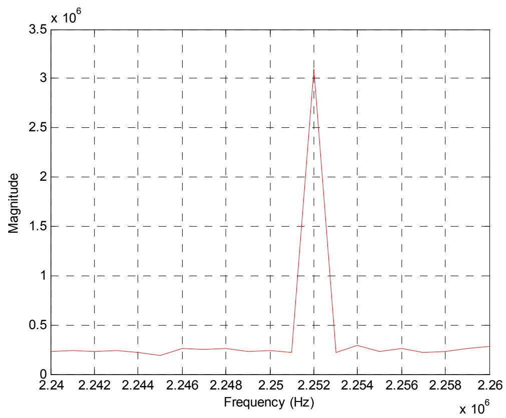

(a)

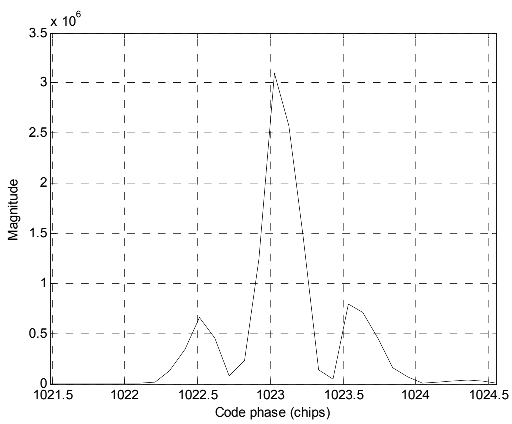

(b)

Fig. 9. Correlation profile: a) frequency and b) code. C/No = 47 dB-Hz.

As the signal-to-noise density ratio falls the correlation peak is reduced in relation to the noise peaks. Figure 10 shows the acquisition for the same parameters of figure 8, but with a signal-to-noise density ratio equal to 35 dB-Hz. The profiles in carrier frequency and code are presented in figure 11.

Due to the probability of false acquisition caused by false correlation peaks as result of low signal-to-noise density ratios, a criterion of confirmation is necessary.

The confirmation of the detected satellite uses binary algorithms of decision to analyze the presence or absence of the signal. The majority of GNSS receivers use the Tong or M on N algorithm for detection validation [11 and 12]. For both, Tong and M on N algorithms, a definition of a decision threshold is necessary, that will be compared with the correlation peak. In case the result of the correlation is greater than the threshold, the satellite is confirmed. The threshold is calculated from the definition of the probability density function (PDF) of detection and false alarm [12]. Table II shows results of the acquisition for different signal-to-noise density ratios.

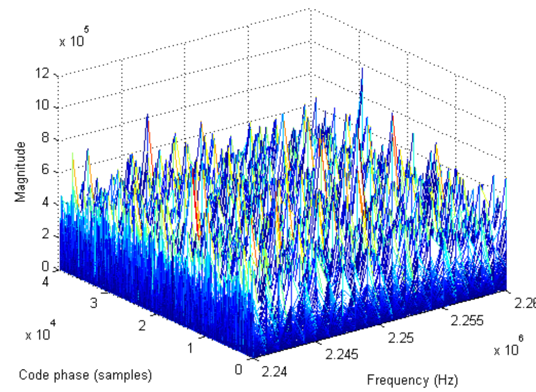

Fig. 10. Acquisition results for C/No = 35 dB-Hz.

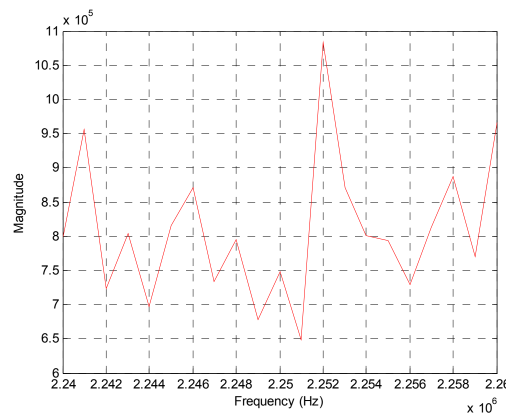

(a)

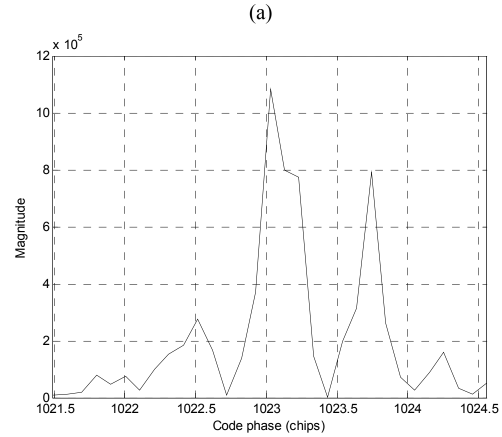

(b)

Fig. 11. Correlation profile: a) frequency; and b) code. C/No = 35 dB-Hz.

After the acquisition stage, the signal and the estimated parameters are processed on tracking loops. The PLL and DLL settings parameters are shown in table III.

Simulations were done taking in account signal-to-noise density ratios starting from 55 dB-Hz to 25 dB-Hz. A signal with 3 seconds of length (750 PRN code periods) and a specific bit sequence feed the tracking stage.

TABLE II
ACQUISITION RESULTS.

C/No (dB-Hz)	Doppler (Hz)	Code Delay (samples)	Processing Time (s)
55	2,000	10,001	4,1111
50	2,000	10,001	3.9313
45	2,000	10,001	3.8647
40	2,000	10,001	3.8729
35	5.000	17,109	3.9433
30	-1.000	25,072	3.8411
25	7.000	3,755	3.8749

Aquisition: PRN # 1; P = - 157 dBw, f_{FI} = 2.25 MHz; f_s = 10 MHz, $f_{doppler}$ = 2 kHz; $d_{código}$ = 10,000 samples (1,023 chips) and 21 frequency bins.

TABLE III
TRACKING PARAMETERS.

Parameter	PLL (Costas Loop)	DLL
Noise Bandwidth	25 Hz	10 Hz
Gain Loop	5	0.4
Integration Time	4 ms	
E-L distance	0.125 chip	
Damping ratio	0.707	

The tracking results are showed in Figure 12.

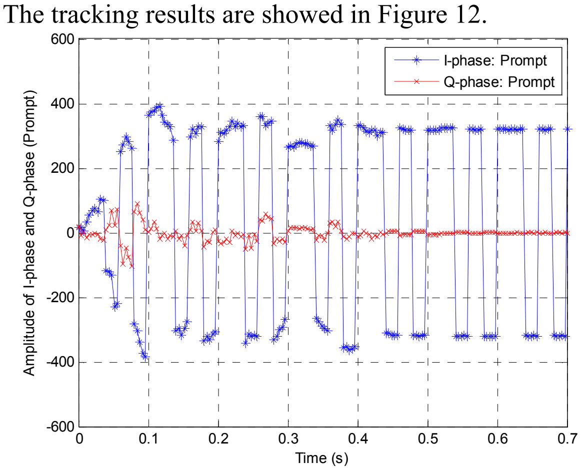

Fig. 12. Tracking results for both I and Q channels.

The behavior of the carrier and code frequency are shown in figure 13 and 14, respectively.

VI. CONCLUSIONS

An acquisition method must be used to determine the visible satellites and coarse values of carrier frequency and code phase of the satellite signals. The stage after signal acquisition is the signal tracking that will make a fine tunning of Doppler frequency and PRN code delay. In this way the navigation messages are recovered and finally the user PVT (Position, Velocity, and Time) is determined.

The narrowed ACF allows the receiver to operate in low signal-to-noise density ratios, typically found in indoor environments or with low satellite visibility. Comparing figures 8 to 11, and table II, the BOC signal simulated presented immunity to signal-to-noise density ratios above 35 dB-Hz. For lower relations, the estimated values diverge.

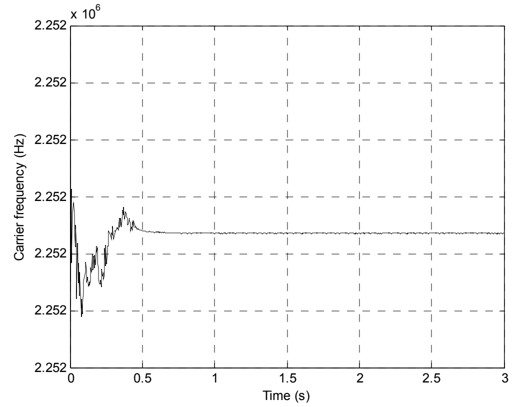

Fig. 13. Carrier frequency results in tracking process.

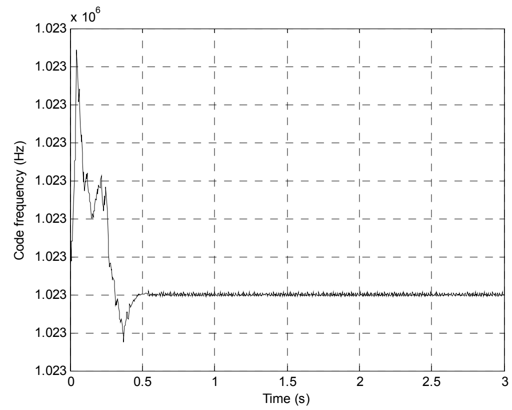

Fig. 14. Code frequency results in tracking process.

In a lower signal-to-noise density ratio is convenient the division of search space in a larger number of frequencies bins. Simulation in this scenario showed that this strategy results in a process more adequate to a low signal-to-noise density ratio signal, but is penalized by the increase of processing time.

The tracking stage of Galileo E1-B signal using BOC-BOC (E-L) Costas Loop architecture keep the local generated signal aligned with a received signal. The code delay error stays between ± 0.07 chip (figure 15 and 16), while the carrier frequency error below 7 Hz (figure 17 and 18). Despite these errors, the bit sequency is recovery (figure 12).

The error between local frequency/code signal and received signal is related to DLL and PLL circuits' parameters, such as early and late distance chip, noise bandwidth, integration time, DLL and PLL loop gain, and others. A study on possible discriminators for Galileo E1-B signal can be found in [2, 7, 10 and 11].

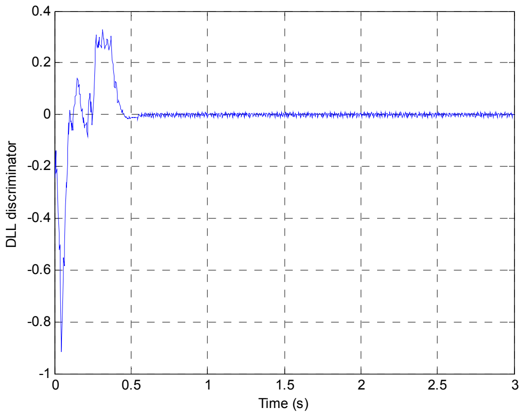

Fig. 15. DLL discriminator output.

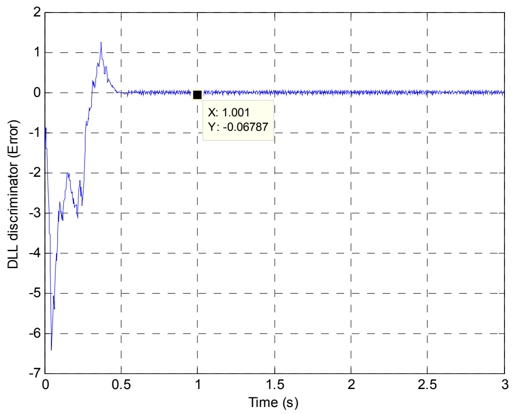

Fig. 16. Code frequency error.

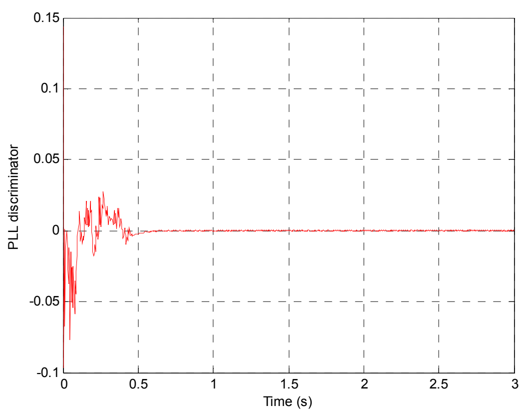

Fig. 17. PLL discriminator output.

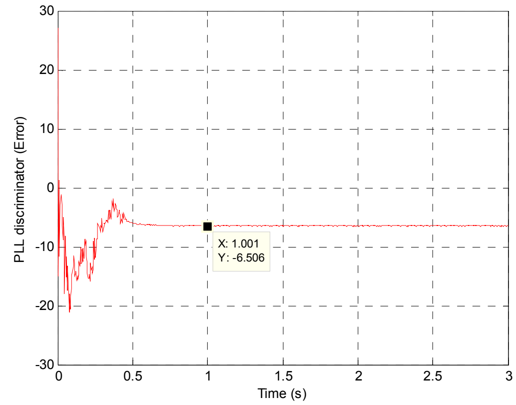

Fig. 18. Carrier frequency error.

References

[1] Mulassano, Paolo, 2007. *Introduction to Global Navigation Satellite Systems*, Politecnico de Torino.

[2] Fantino, M., *Study of Architectures and Algorithms for Software Galileo Receivers*, Tesi di Dottorato, Politecnico di Torino

[3] Prasad, R. e Ruggieri, M., 2005. *Applied Satellite Navigation Using GPS, Galileo, and Augmentation Systems*, Mobile Communications Series, Artech House.

[4] *GIOVE-A Navigation Signal In Space*, Interface Control Document, 2007. Galileo Project Office.

[5] *Directions For The Galileo Evolution, Session 9*, Munich Satellite Navigation Summit 2008.

[6] Galileo Open Service – *Signal In Space, Interface Control Document OS SIS ICD*. European Space Agency e Galileo Joint Undertaking

[7] Mulassano, Paolo, 2007. *GPS and Galileo Receivers*, Istituto Superiore Mario Boella.

[8] Borre, K. et al., 2007. *A Software-Defined GPS and Galileo Receiver* – A single-frequency Approach, Birkhäuser Boston.

[9] Kovár, Pavel et al., 2005. *Galileo Receiver Core Technologies*. Journal of Global Positioning Systems, Vol. 4, No. 1-2: 176-183.

[10] IGNSS. *Galileo GIOVE-A Acquisition and Tracking Analysis with a New Unambiguous Discriminator*, International Global Navigation Satellite Systems Society, IGNSS Symposium, 2007.

[11] Krumvieda, K. et al. *A Complete IF Software GPS Receiver: A Tutorial about the Details*. US Air Force, Air Force Research Laboratory, Wright-Patterson AFB.

[12] Carvalho, F. A., 2007. *Receptor GPS em Software em Tempo Real Empregando o Processador de Sinais Digitais TMS 320C6711,* Dissertação de Mestrado em Engenharia de Telecomunicações, ITA.

Appendix

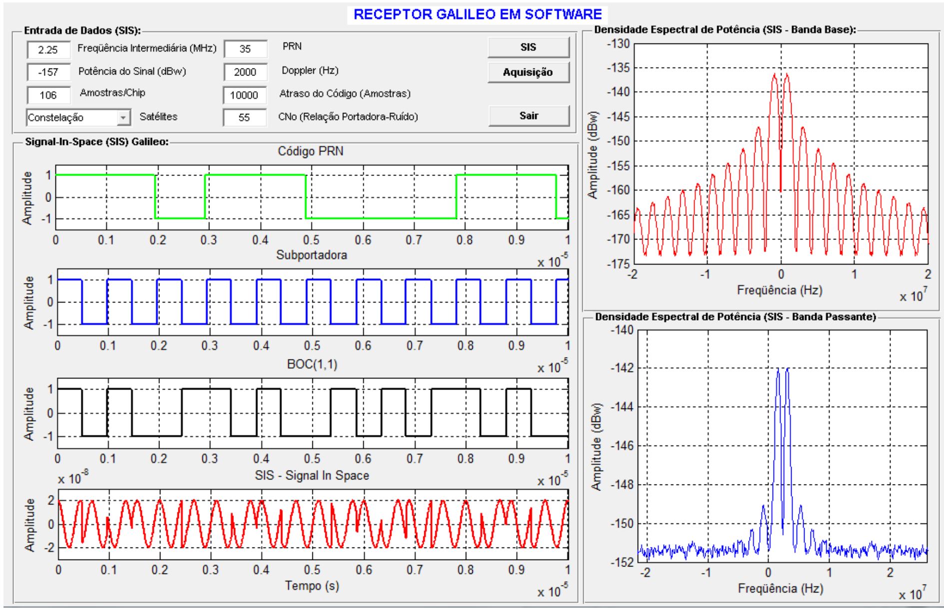

(a)

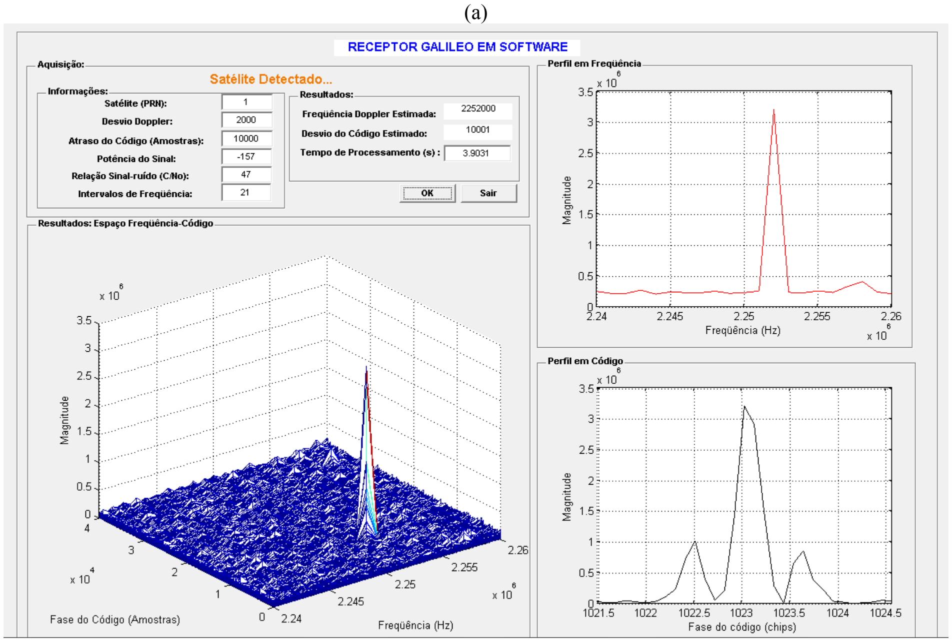

(b)

Figure A. (a) Software defined Galileo receiver user interface: SIS Generation using PRN codes transmited by GIOVE-A (Left). Power spectral density in baseband and passband. (b) Acquisition and tracking for BOC(1,1) using PRN # 1 and C/No = 47 dB-Hz.

Channel Estimation of Powerline Communication Systems

Renata Bráz Falcão da Costa
Center for Telecommunication Studies
Pontifícia Universidade Católica do Rio de Janeiro
Rio de Janeiro - RJ - Brazil
rbfcosta@gmail.com

Marco Antonio Grivet Mattoso Maia
Center for Telecommunication Studies
Pontifícia Universidade Católica do Rio de Janeiro
Rio de Janeiro - RJ - Brazil
mgrivet@cetuc.puc-rio.br

***Abstract*— This document describes a novel method for estimating PLC channels based on the Expectation/Maximization (ME) Method in the frequency domain. Although mathematically cumbersome, this approach can be implemented in simple and fast computer program. Its performance is run against classical methods like Zero Forcing (ZF) and Minimal Mean Square Error (MMSE) in OFDM systems. The results obtained revealed that this method has a very similar performance even when only a small fraction of OFDM pilot symbols are used.**

***Index Terms*— EM, OFDM, Power Line Communications.**

I. Introduction

The use of powerline systems for communication purposes is receiving an enormous attention during the last decade mainly because of the huge demand for telecommunication services [1],[2],[3],[4]. The great advantages of such systems are the needless of new wires, the low cost of the devices and the easy of the installation. Nevertheless, this area is still full of yet-to-solve problems. One of them is the system's performance under heavy noise environment, a situation revealed as common in several every day scenarios. This article tries to tackle this problem from a different viewpoint. Although we acknowledge that noise can be dealt with in several ways, we believe that if the communication channel is properly estimated and the communication system fully uses this information, this will act as the first and relevant step towards noise's mitigation. Therefore this paper presents a method for the estimation of powerline channels on the frequency domain, where the EM (Expectation Maximization) algorithm has a major hole. The results obtained for several channels under several levels of noise do suggest that this technique requires further attention and therefore it is worth investigating.

II. The Problem of Channel Estimation

An adequate channel model for the powerline environment is supposed to deal with two predominant impairments, namely, the multipath behavior and conductor losses. One mathematical model fairly used in this kind of environments is due to Zimmermann [5], [11], where the channel's transfer function is given by:

$$H\left(f,\underline{\theta}\right)=\sum_{k=1}^{K}\mu_k.\exp\left\{-\left[\alpha.\sqrt{f}+\beta.f+j\left(\gamma.f+\delta_k\right)\right].d_k\right\} \tag{1}$$

Vector $\underline{\theta}$ describes all the model's parameters and it is composed by: i) α, β and γ are parameters of general nature and they are related to the physical and electrical characteristics of the electric network that are assumed to be known and ii) $\underline{\psi}_k=\{\mu_k,\delta_k,d_k\}$ characterize each propagation multipath that need to be estimated. Hence, assuming that we have a channel with K multipaths, we need to estimate $3.K$ parameters. The observed channel's transfer function under a noise environment can be generalized as follows:

$$H_{obs}\left(f\right)=\left[\sum_{k=1}^{K}H_k\left(f,\underline{\psi}_k\right)\right]+N\left(f\right)f\in\left[-B,B\right] \tag{2}$$

In this equation $H_k(.)$ is the transfer function associated to the k-th multipath, $N(f)$ is the Fourier transform of the noise and B is the bandwidth of interest. The noise $n(t)$ in the time domain is assumed to be a zero mean wide-sense stochastic process and consequently in the frequency domain the noise $N(f)$ is also a zero mean wide-sense stationary stochastic process but with a particular autocorrelation function. The main idea of the method here described is to express the observed transfer function as a member of an infinite dimensional vector space generated by the eigenfunctions $\{\phi_i(f), i=1,2,...\}$ of the above mentioned autocorrelation function. If we truncate such an expansion up to level L, then equation 2 can be approximated by the following equivalent L-dimensional vector equation:

$$\underline{y}=\sum_{k=1}^{K}\underline{w}_k\left(\underline{\psi}_k\right)+\underline{n} \tag{3}$$

If we rewrite vector noise n as a sum of $(K+1)$ independent and identically distributed vector noises whose overall effects are identical to those generated by the original noise, equation 3 can be conveniently rewritten as:

$$\begin{aligned}\underline{x}\left(\underline{\theta}\right)&=\underline{w}\left(\underline{\theta}\right)+\underline{\eta}\\ \underline{y}&=H.\underline{x}\left(\underline{\theta}\right)+\underline{v}\end{aligned} \tag{4}$$

where:

$$\underline{x}(\underline{\theta}) = \begin{bmatrix} \underline{x}_1(\underline{\psi}_1) \\ \underline{x}_2(\underline{\psi}_2) \\ \vdots \\ \underline{x}_K(\underline{\psi}_K) \end{bmatrix} = \begin{bmatrix} \underline{w}_1(\underline{\psi}_1) \\ \underline{w}_2(\underline{\psi}_2) \\ \vdots \\ \underline{w}_K(\underline{\psi}_K) \end{bmatrix} + \begin{bmatrix} \underline{n}_1 \\ \underline{n}_2 \\ \vdots \\ \underline{n}_K \end{bmatrix} \tag{5}$$

$$\underline{x}(\underline{\theta}) = \underline{w}(\underline{\theta}) + \underline{\eta} \tag{6}$$

From the above equations we can easily identify that they are the basic equations of the so-called EM (Expectation/Maximization) algorithm [20], a well-known method on the realm of the optimization theory. It is possible to show, after several and long straightforward but cumbersome manipulations (see details in [18]) that the equation to be maximized on such algorithm can be written as:

$$\begin{array}{l} \min\limits_{\underline{\theta}'} z = \sum\limits_{k=1}^{K} \Pi_k^*(\underline{\theta}, \underline{\theta}') \\ \text{where :} \\ \Pi_k^*(\underline{\theta}, \underline{\theta}') = \\ = \int_{-B}^{B} \left\{ |W_k(f, \underline{\theta})|^2 - 2.\mathrm{Re}\left\{ \Delta_k^*(f, \underline{\theta}').W_k(f, \underline{\theta}) \right\} \right\} .df \\ \Delta_k(f, \underline{\theta}') = W_k(f, \underline{\theta}') + \frac{1}{K+1}.\varepsilon(f, \underline{\theta}') \\ \varepsilon(f, \underline{\theta}') = Y(f) - \hat{Y}(f, \underline{\theta}') \\ \hat{Y}(f, \underline{\theta}) = \sum\limits_{k=1}^{K} W_k(f, \underline{\theta}) \end{array} \tag{7}$$

At this point we can identify the first nice feature of this algorithm, namely, the fact that the underlying optimization problem involving $3.K$ parameters can be partitioned in a sequence of K optimization problems on 3 parameters, in a round-robin type scheme. Needless to say that convergence issues on optimization problems are best solved when its dimension is low and the capability to deal with 3-dimensional problems is immensely improved when compared with those of $3.K$ dimensions.

A second point which is also very important is the fact that due the nature of the chosen model described by [5], each one of the 3-dimensional optimization problems cited above can be analytically solved for variables μ_k, δ_k thus reducing to a 1-dimensional problem involving only variable d_k, that can be trivially solved (see details in [18]). Hence the general algorithm developed here consists of a round-robin scheme of solving K 1-dimensional optimization problems where the decision variable lives in a finite support. It is also important to say that this form does not preclude the algorithm to find local instead of global solution but since each 1D optimization problem finds a global solution, the chances of having an overall global solution is much higher.

III. Results Related to Channel Estimation

For the test purposes, a computer program was developed capable of determining the transfer function of an electrical circuit characterized by the diagram presented in Figure 1 that represents a PLC network having N residential branches.

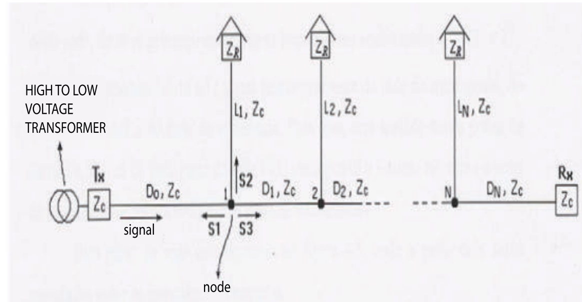

Fig. 1. PLC network's model of N residential branches

The parameter values used on the simulation of the above model are: $L = 7m$, $D = 10m$, $Z_C = 394\Omega$, $Z_R = 8\Omega$, $f_{min} = 0,3$ MHz, $f_{max} = 60$ MHz, $\alpha = 2.3 \times 10^{-3}$, $\beta = 6.37 \times 10^{-4}$ and $\gamma = 3.33 \times 10^{-2}$. The real and estimated channels are below presented in the frequency domain. From there it can be seen a fairly nice adjustment in some frequency bands, as for instance, from 3.5 MHz to 8.5 MHz. This band is 6 MHz wide and therefore can for instance support TV transmission, internet and any other high band service. Although not shown here due to lack of space, this procedure was applied to several channels of different order (several other PLC channels and those reported by [19]), and in all of them the behavior was similarly good.

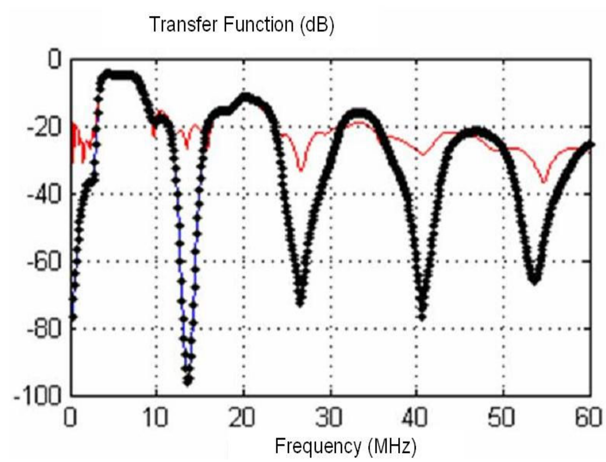

Fig. 2. Measured and Estimated Transfer Functions

IV. Transmission and Reception

The OFDM modulation [8], [9], [10], [11], [13], [15], [16] is receiving considerable attention on PLC scenarios. It consists of the parallel data transmission on several sub-carriers, each one of them transmitting a fraction of the total bit rate. The main advantage of this scheme is that since each sub-carrier has a small bandwidth, fading can be considered flat in each one of these data channels.

This kind of system is receiving considerable attention from the telecommunications community and it is currently being employed on systems such as Digital TV Broadcast, among others.

One interesting application is the possibility of distributing Digital TV over residential electrical power lines, thus saving large quantity of cables. By no means, this article has the goal to clear this matter to its highest point, but on contrary, we would like to shed some light into this application and bring this issue to the discussion of the scientific community. The rest of this section is devoted to present results of OFDM BER's performance when the Zero Padding (ZP) scheme is used in conjunction to BPSK modulation. We have measured the performance of this channel estimation method against the situations where two classical equalizers, namely, Zero Forcing (ZF) and Minimal Mean Square Error (MMSE) are deployed. The graphs below show the obtained results when the percentage of symbols per frame used for channel's estimation (pilot symbols) are respectively 100%, 80%, 60% and 40%. There:

- the blue curve is the BER when the channel is ideal
- the red curve is the BER when the channel is fully known
- the black curve is the BER when channel is unknown and ZF equalizer is used with 100% of pilot symbols.
- the green curve is the BER when channel is unknown and MMSE equalizer is used with 100% of pilot symbols.
- The purple curve is the BER when channel is unknown and the method here discussed is employed.

The blue and red curves respectively represent the performance upper and lower bounds and they are used in this work as references.

It can be easily noticed that in all cases, the performance of the channel estimation algorithm here presented is very similar to those obtained when ZF and MMSE equalizers are employed, even when the pilot symbols is as low as 40% of the total and under Eb/N0 values as low as 5 dB.

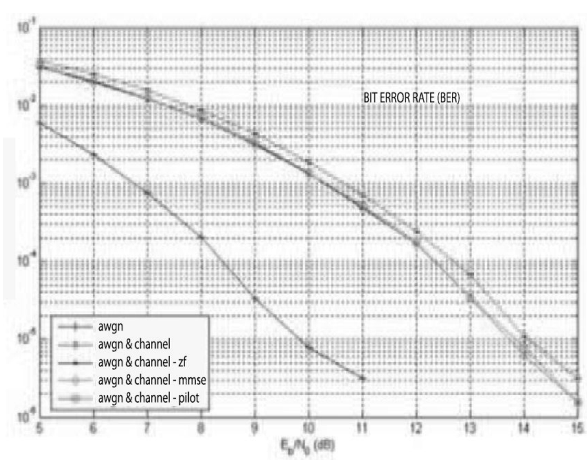

Fig. 3. Performance for the ZF-OFDM with 100 % of pilot symbols

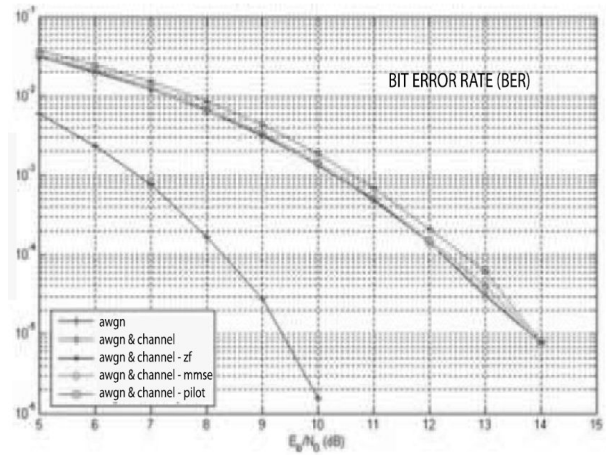

Fig. 4. Performance for the ZF-OFDM with 80 % of pilot symbols

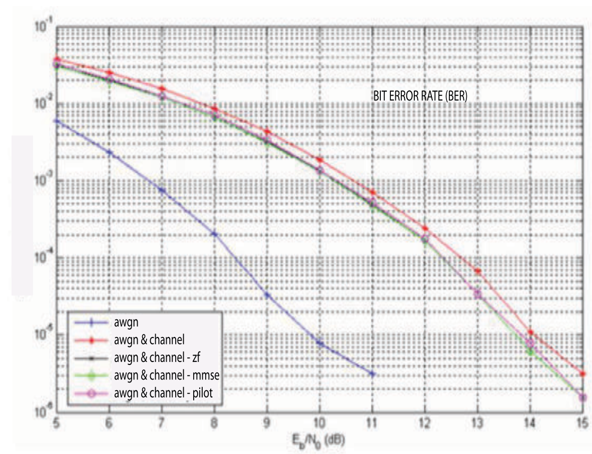

Fig. 5. Performance for the ZF-OFDM with 60 % of pilot symbols

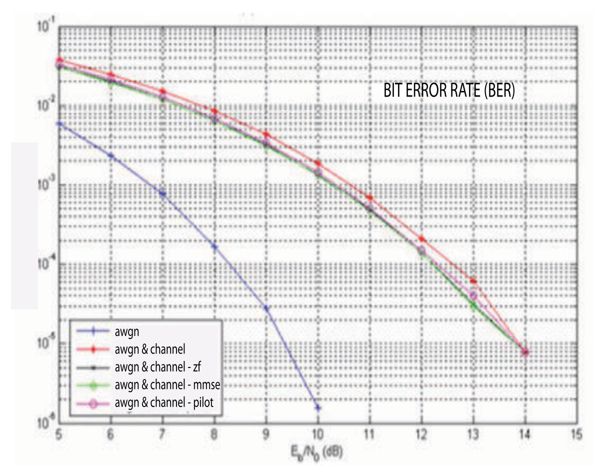

Fig. 6. Performance for the ZF-OFDM with 40 % of pilot symbols

V. Conclusions

PLC is a technology by which the electric power distribution network is used as the physical medium for the transport of telecommunication signals. Nevertheless, these networks were not originally conceived for this purpose and consequently this can only be achieved if the PLC transmission medium is properly characterized. The parametric model here discussed for the estimation of PLC channels considers the two most predominant features, namely, the multipath effects and the conductor's losses.

Central to this method is the application of the EM algorithm in the frequency domain. By means of this technique and further developments made, it was possible to transform de original 3.K dimensional optimization problem into a round-robin or carrousel procedure in which K optimization problems in one variable are required to be solved. The resulting procedure has shown to be fast and computationally efficient, requiring few seconds to produce the mentioned results.

This method was compared with two other estimation methods where ZF and MMSE equalizers are employed and the results shown a comparable performance even when only 40 % of pilot symbols are used for estimation.

Finally it is relevant to mention the static nature of the assumed channels that at a first glance seems inadequate for the PLC case. The mentioned speed of the proposed algorithm allows to contemplate the possibility of a real time system in which the algorithm is periodically executed in order to cope with such a variability.

REFERENCES

[1] E. Biglieri, *Coding and Modulation for a Horrible Channel*, vol.41, no. 4, pp. 92-98, May 2003.

[2] F.J. Cañete, J.A. Cortés, L. Díes and J. T. Entrambasaguas, *Modeling and Evaluation of the Indoor Power Line Transmission Medium*, IEEE Communication Magazine, vol.41, no. 4, pp. 41-47, April 2003.

[3] Konate, M. Machmoum and J. F. Diouris, *Multipath Model for Power Line Communication Channel in the Frequency Range of 1MHZ - 30MHz*, EUROCOM 2007.

[4] H. Meng, S. Chen, *Modeling of the Transfer Characteristics for the Broadband Power Line Communication Channel*, IEEE Transactions on Power Delivery, vol. 19, no. 3, pp. 529-551, July 2004.

[5] M. Zimmermann, K .Dostert, L. Díes and J. T. Entrambasaguas, *A Multi-Path Model for the Power Line Channel*, IEEE Transactions on communications, vol.50, no. 4, pp. 553-559, April 2002.

[6] C. Ioannis Papaleonidopoulos, G. Constantinos Karagiannopoulos, J. Nickolas Theodorou, L. Díes and J. T. Entrambasaguas, *Statistical Analysis and Simulation of Indoor Single-phase Low Voltage Power-Line Communication Channels on the basis of Multi path Propagation*, IEEE Transactions on Power Delivery, vol. 49, no. 1, pp 89-99, February 2003.

[7] A. D. Oliveira and H. F. Silva, *Powerline Communication Using Orthogonal Frequency Division Multiplexing with a Gray Code Variation*, Electronic Systems Lab (LabSel) Engineering College Federal University of Juiz de Fora (UFJF), 2003.

[8] F. Tlili, F. Rouissi and A. Ghazel, *Precoded OFDM for Powerline Broadband Communication*, IEEE Transactions on Power Delivery, vol. 49, no. 1, pp 89-99, February 2003.

[9] E. Tooraj, R. Frank Kschischang and P. Glenn Gulak, *In-building power lines as high-speed communication channels: channel characterization and a test channel ensemble*, International Journal of Communication Systems 2003, pp 381-400, May 2003.

[10] Prassad, R., Van Nee R., *OFDM for wireless multimedia communication*, Artech House, 2000.

[11] M. Zimmermann and K. Dostert, *An Analysis of the Broadband Noise Scenario in Power Line Networks*, Proc. 4th. Int'l. Symp. Power Line Commun. and Its apps., Limerick, Ireland, pp. 131-138, 2003.

[12] Y. Zhang, C. Shijie, J. Nguimbis and L. Xiong, *Analysis and Simulation of Low-voltage Powerline Channel using Orthogonal Frequency Division Multiplexing*, Journal of Electrical and Eletronics Engineering, vol.3, no.1, pp. 827-833, Istanbul University, 2003.

[13] Vasegui, S.V., *Signal Processing and Digital Noise Reduction*, Wiley-Teubner, 1996.

[14] Rodrigo Pereira David, *Channel Estimation Techniques Using Pilot Symbols in OFDM Systems*, M.Sc. Dissertation, PUC-Rio, April 2007.

[15] Aureo Serrano, *Channel Equalization and Estimation in OFDM Systems*, M.Sc. Dissertation, PUC-Rio, July 2005.

[16] Rodrigo Silva Mello, *Modeling the PLC Channel*, M.Sc. Dissertation, PUC-Rio, March 2005.

[17] D. Anastasiadou and T. Antonakopoulos, *Multipath Characterization of Indoor Power-Line Networks*, IEEE Trans. on Power Delivery, vol.20, no.1, January 2005.

[18] Renata B.F. da Costa, *Channel Estimation in Comunication Systems over Power Lines*, D.Sc. Dissertation, PUC-Rio, September 2007.

[19] Proakis, J.G. , *Digital Communications*, 3rd. Edition - McGraw Hill International Editions - 1995.

[20] Ljung, L , *System Identification : Theory For the User*, Prentice Hall Information and System Sciences Series - 1987.

Accurate Time Transfer on a Wireleless Telecomunication Link

Carlos Nazareth Motta Marins
National Institute of Telecommunications – Inatel
Campinas State University - Unicamp
P.O. Box 05 - 37540-000
Santa Rita do Sapucaí - MG - Brazil
carlosn@inatel.br

Pierre Kaufmann
National Institute of Telecommunications – Inatel
Mackenzie Prebysterian University – CRAAM
Campinas State University - Unicamp
São Paulo – SP - Brazil
kaufmann@craam.mackenzie.br

Antônio Alves Ferreira Júnior
National Institute of Telecommunications – Inatel
P.O. Box 05 - 37540-000
Santa Rita do Sapucaí - MG - Brazil
antonioa@inatel.br

Marcelo Carneiro de Paiva
National Institute of Telecommunications – Inatel
P.O. Box 05 - 37540-000
Santa Rita do Sapucaí - MG - Brazil
mcpaiva@inatel.br

Rafael Mendes Vilela*
National Institute of Telecommunications – Inatel
P.O. Box 05 - 37540-000
Santa Rita do Sapucaí - MG - Brazil
rafael-mendes@inatel.br

Adonias Costa da Silveira
National Institute of Telecommunications – Inatel
P.O. Box 05 - 37540-000
Santa Rita do Sapucaí - MG - Brazil
adonias@inatel.br

***Abstract*—This paper presents the implementation of a radio link that operates with a time counting system. This new system makes possible the precision time transference for remote time synchronization and precision distance measurement. The system uses digital electronic solutions that offer precision and stability for various applications in navigation, target localization and tracking, digital telecommunications, command of time-controlled actuators such as wireless sensor networks.**

***Index Terms*—Clocks, remote synchronization, distance measurement, time dissemination.**

I. Introduction

Precise time dissemination and remote slave clock synchronization is a key requirement for navigation, target localization and tracking, digital telecommunications, command of time-controlled actuators such as wireless sensor networks [1]. High time transfer accuracy is also required in new applications, as for the new concept for remote geo-positioning, currently being developed in Brazil here referred as Geolocal [2-6]. It uses time dissemination by wireless telecommunication links requiring accuracy of tens of nanoseconds (in order to obtain position linear accuracies less than 10 meters). The present study addresses to the problem of high precision time transfer stability in a single wireless telecommunication link. An innovative clock reading concept was developed derived from the time-to-digital-converter (TDC) principle [7,8]. We propose obtaining of ns accuracy with clock reading based on counts at low frequencies, allowing its construction at reduced costs.

II. Precision clock using TDC technique

The time transference and distance measurement through a radio link demand good performance of the system in two main parameters. The first parameter is the time count with the use of high precision clocks obtained with small counting steps. The second parameter is the phase stability of the communication link that influence the time measurement.

Figure 1 illustrates the main blocks of the clock system that was implemented with a STRATIX II FPGA (Field Programmable Gate Array) tool from ALTERA [9]. An OCXO (oven controlled crystal oscillator) frequency signal is fed into an enhanced PLL (phase lock loop) that raises the frequency to be compared to a VCO (voltage controlled oscillator).

Each one of the N VCO outputs submitted to software-driven logic element to produce the desired delay. Every delayed element is fed into independent and identical counters. The registers freeze the counters results for every time coded sequence (TCS). A given time clock is then obtained just by mathematical operations on the registered values.

The clock time obtained by other systems based on TDC principle is derived from one encoder or converter that process all delayed outputs. This process may bring time interpolation non-linearity problems [7]. The newly conceived clock system is based on time-to-digital converter (TDC) principle to generate, transfer and compare time coded sequences (TCS) with nanoseconds accuracy, using a wireless telecommunication link. The TCS are transmitted to a remote

* Presently at Freescale Semicondutores do Brasil, Campinas, SP, Brazil.

transponder that distributes them to receiving stations where the clock readings are processed [8].

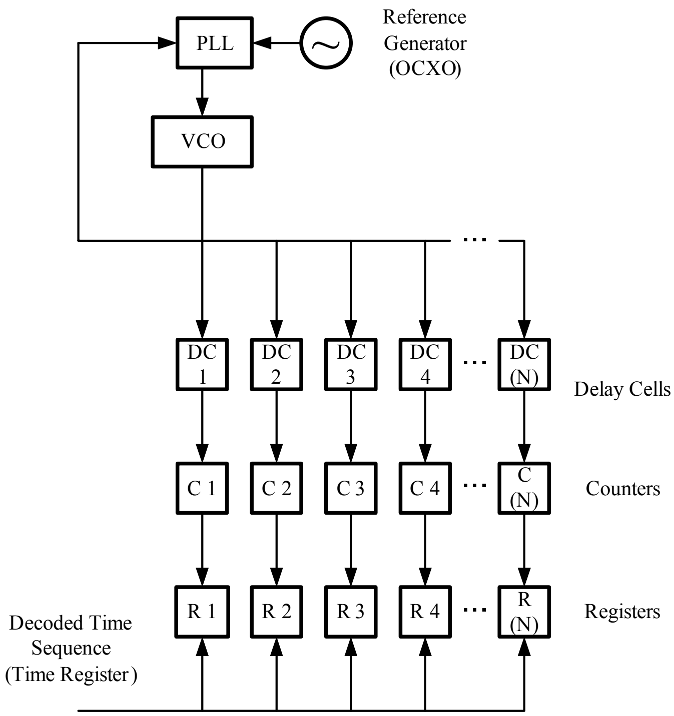

Fig. 1. Clock block diagram showing he OCXO standard oscillator, the frequency synthesizer made of voltage controlled oscillator (VCO) phase locked loop (PLL), followed by the phase shifters, counters and registers.

Figure 2 shows the phase shifted waveforms needed for accurate time determinations [8].

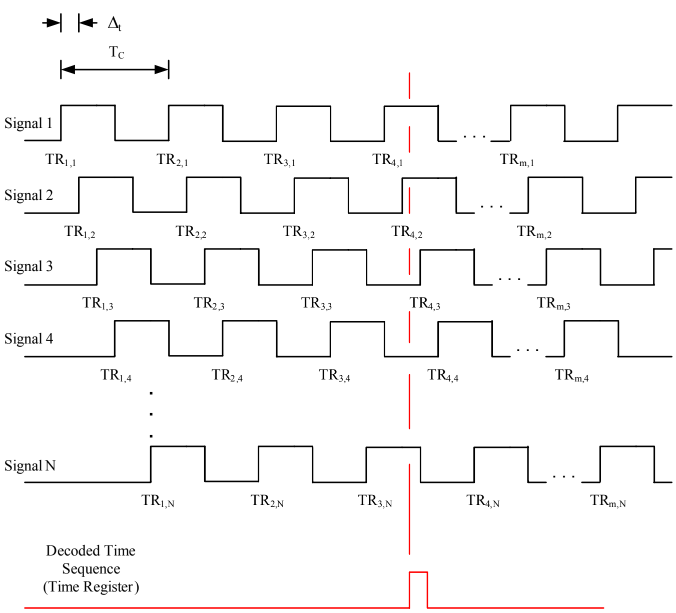

Fig. 2. The clock reading concept, showing a set of the offset waveforms, and one time marker response to the TCS [8].

It is possible to measure the time difference Δ_t between successive waveform rise transitions, which correspond to the minimum measurable time interval, or the clock reading accuracy. The phase shift between waveforms progresses linearly, such as:

$$\begin{aligned} D_{1-2} &= \Delta_t \\ D_{1-3} &= 2 \cdot \Delta_t \\ &\vdots \\ D_{1-N} &= (N-1) \cdot \Delta_t \end{aligned} \quad (1)$$

where $D_{1\text{-}2}$ is the phase shift between waveforms 1 and 2, $D_{1\text{-}3}$ between waveforms 1 and 3 and so on, until $D_{1\text{-}N}$ for the last waveform. As the counters' registers change as a function of the waveform rise transition fed in, these transitions are represented in Figure 2 by $TR_{m,N}$ where m is the transition number and N the respective counter number. The relationship between the number of counters and the phase shift between waveform rise time transitions is as follows:

$$\Delta_t = \left(\frac{T_C}{N}\right) = \left(\frac{1}{N \cdot F_C}\right) \quad (2)$$

where F_C is the FPGA operating frequency, related to the number of counters needed to obtain a given accuracy.

In Figure 2, the decoded time sequence (time register) triggers the clock reading. In this example the time register in on waveform transition 4 for the first counter, which means a time reading equal to $4\ T_C$.

The reading accuracy is improved taking a Δ_t increment for each counter for which the time register remains at the same waveform transition as the first counter. In this example, the accurate reading becomes $4\ T_C + \Delta_t$. We can express the time measured by the general equation:

$$Time = \left(TR_{m,1} \cdot T_C\right) + \sum_{i=2}^{N}\left(B_i \cdot \Delta_t\right) \quad (3)$$

where m is the transition number, index i is the counter number (varying from 2 to N). Factor B =1 when i is the same as counter number 1, and B=0 when i is different from counter number 1.

III. Wireless Telecommunication Link

A simple short-range wireless telecommunication link was assembled to demonstrate the system. The repeated TCS are received back and compared to the reference clock. Figure 3 illustrate the complete experimental setup. We describe the clock, the telecommunication setup, and the electrical and electronic sources of delays.

The first complete time coded sequence transfer link was successfully installed, tested and operated, using low cost radios and electronic units. They were operated without any special temperature control on any unit, showing a quite robust performance in face of ambient environmental conditions.

The TCS signal propagation by the radio electronics sections undergoes degeneration by jitter produced by the frequency conversion stages. The time domain jitter measurement can be made through an oscilloscope as presented in figure 4 and 5.

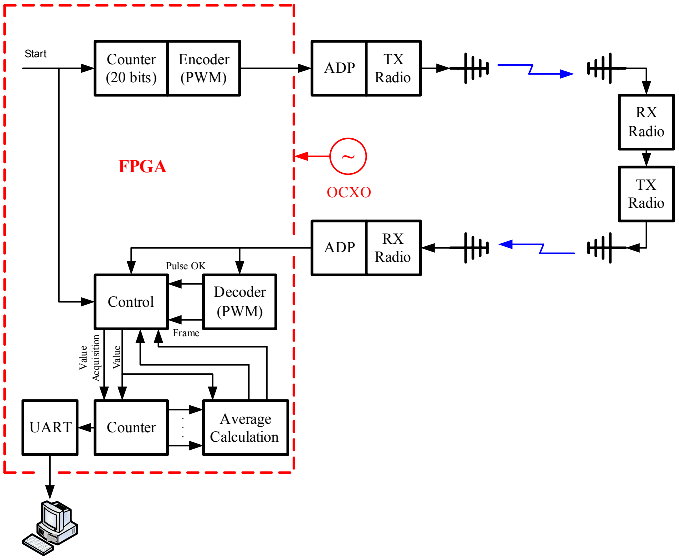

Fig. 3. Block diagram showing the complete time transfer system, from time generation (upper branch), transfer, reception and clock reading analysis (lower branch) [8].

The TCS signal propagation by the radio electronics sections undergoes degeneration by jitter produced by the frequency conversion stages. The time domain jitter measurement can be made through an oscilloscope as presented in figure 4 and 5. To analyze the jitter features we used the same TDC tool developed for time count. Figure 5 presents the jitter distribution that exhibited a symmetrical Gaussian distribution with 31 ns r.m.s. To overcome this effect, 100 TCS were averaged, defining a single mean TCS every 0.629 seconds. The final accurate clock reading is obtained at UART (universal asynchronous receiver transmitter) interface providing the total time delay that includes the propagation times (ranging) and the delays produced by the electronic units.

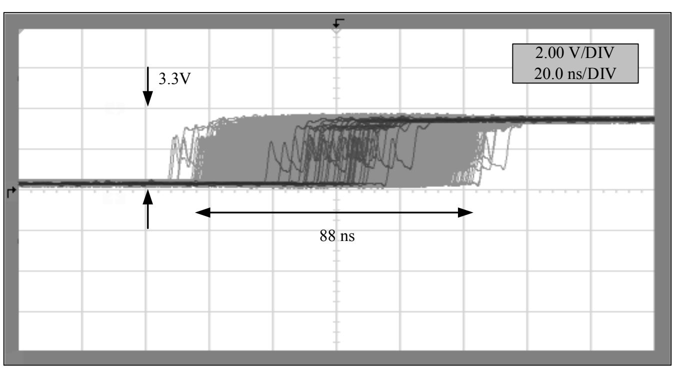

Fig. 4. The jitter due to instrumental random phase variations on the incoming signal before being averaged [8].

Comparison of mean TCS taken every 0.629 s exhibited 36 nanoseconds time stability along time interval scales of hours (see Figure 6). The Geolocal system was designed to work with uncertainties up to 52 ns to guarantee maximum errors of 10 (m) in the navigation process. With the results it is possible to conclude that this radio link takes care of the basic requirements of the Geolocal system.

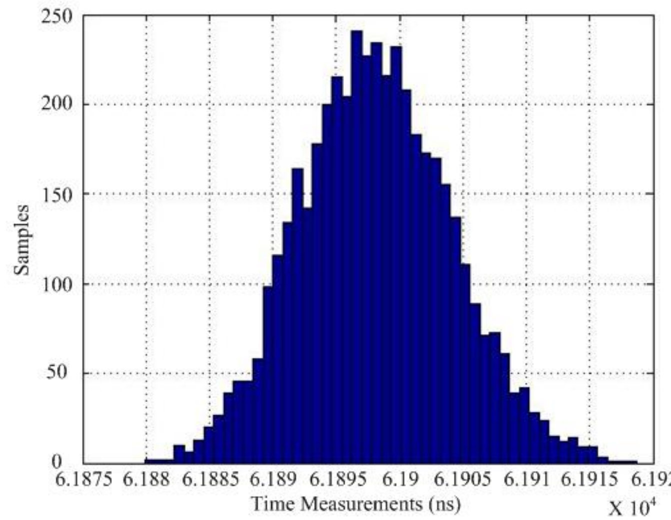

Fig. 5. The jitter distribution.

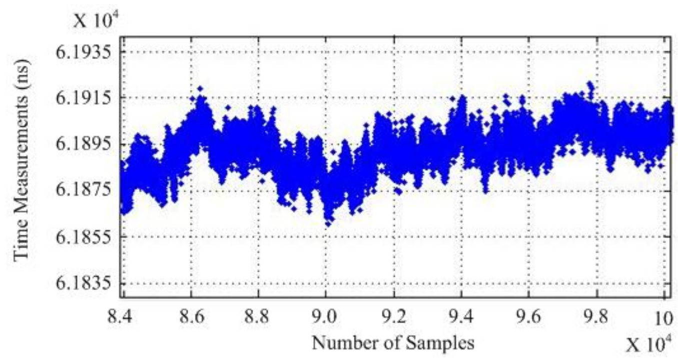

Fig. 6. The final clock reading obtained at the UART (universal asynchronous receiver transmitter) interface providing the total time delay that includes the propagation times (ranging) and the delays produced by the electronic units. The readings are (in units of 10^{-5} s) are accurate to one nanosecond.

IV. Time Measurements Results with the Radio Link

The system performance for time transference and distance measurements can be described using the Allan variance [10], also known as two samples variance, defined as :

$$\sigma_y^2(\tau) = \frac{1}{2}\left\langle \left(\bar{y}_{k+1} - \bar{y}_k\right)^2 \right\rangle \quad (4)$$

where the expression inside brackets denotes the average over a large number of samples, and k=1,2,3,…The differences are used to calculate the Allan variance is shown by the following equation:

$$\bar{y}_{k+1} - \bar{y}_k = \frac{1}{\tau}\left[x(t_k + 2\tau) - 2x(t_k + \tau) + x(t_k)\right] \quad (5)$$

where x(t) is proportional to the instantaneous phase, but has dimension of time, and is also sometimes termed phase-time.

For the measurement period shown Figure 6 containing 16,000 samples, for data taken every 0.629 seconds, we obtained AVAR = 5.742 10^{-17}. The Allan deviation is defined as the square root of the Allan variance, i.e. 7.6 10^{-9} at τ =1second, or 1.5 10^{-11} at τ =1000 seconds [8].

V. Conclusion

This performance satisfies the accuracy required by the Geolocal system [2-6]. Its principle is based on three ground-based references sites, with well determined geodesic positions, carrying synchronized clocks, a transmitter in one base emitting time coded marks, and one repeater in the sky. Base 1 acts as a reference in the time dissemination, transmitting to all other stations the clock time information. To accomplish this, the signal transmitted by base 1 is retransmitted by the repeater in the sky to all stations, including base 1.

The clocks at the stations allow the comparison of the time at the origin, from base 1. With a single coded clock transmission it is possible to determine the distances from the stations to the repeater, and its position coordinates in the sky.

When the repeater is moving, (e.g. in an airplane or a satellite), its navigation is immediately accomplished. The target coordinates are determined from several measurements, in succession with a moving repeater, or simultaneously if multiple repeaters are present at different locations in the sky.

The implementation of a fully operational Geolocal system brings the possibility to allow real-time independent determinations, to compare and provide support to other systems (i.e., GPS and similarly conceived systems GLONASS, GALILEO, COMPASS).

The system is applicable over regional areas which extensions depends on the altitude of the repeater with respect to the bases and targets. It might cover tens to hundred km for repeater in low altitude flying balloons or aircrafts, to thousands km for repeater in satellite. It has potential to become particularly robust with respect to severe transmission conditions imposed by space weather disturbances which are known to affect other systems.

References

[1] J. Levine, “Introduction to time and frequency metrology”, *Rev. Sci. Instrum.* **70**, 2567, 1999.

[2] P. Kaufmann and A. Costa da Silveira, “Geolocal: new space telecommunication concept for remote positioning and navigation” Proc. of the IWT/2004 – International Workshop on Telecommunications, Santa Rita do Sapucaí, MG, Brazil, August 23-27, 2004, pp. 69-72, 2004.

[3] P. L. Kaufmann *et al.,* "Non recursive algorithm for remote geolocation using ranging measurements", *Math. Problems in Engineering*, v. 2006, pp. 1-9, Article ID79389, DOI:10.1155/MPE/2006/79389,2006. http://www.hindawi.com/GetArticle.aspx?doi=10.1155/MPE/2006/79389.

[4] C. N. M. Marins *et al.*, “Digital Telecommunication Ranging Network for New Geopositioning Demonstration”, *Proc. MOMAG 2006, 12th. SBMO Brazilian Society of Microwaves and Optoelectronics and 7th. Brazilian Electromagnetic Meeting*, Belo Horizonte, MG, Brazil, 8-10 August, 2006.

[5] “Sistema e Processo de Posicionamento Geográfico e Navegação”, Brazil Patent PI 9101270, granted 30.09.1997, Filed 25.03.1991, and Brazil Addition Certificate CI 9101270, Filed 17.05.2002

[6] “Geographic and space positioning system and process”, Brazil Patent PI 03003968-4, Filed 08.10.2003, and International Patent Cooperation Treaty PCT/BR2004/000190, Filed 04.10.2004.

[7] D.I. Porat, “Review of sub-nanosecond time-interval measurements”, *IEEE Trans. on Nucl.Sci.* **NS-20**, 36-51, 1976.

[8] C. N. M. Marins et al., "Precision clock and time transfer in a wireless telecomunication link", submitted, 2008.

[9] Altera Corporation, PLLs & Clock Networks, Tratix II Device Handbook, v. 1, San Jose, CA, 2007.

[10] D.W Allan, “Statistics of atomic frequency standard”, *Proc. IEEE* **54**, 221-231,1966.

A Study of Handover for Mobile TV Broadcasting Networks using SFN in the ISDTV System

Késia Cristiane dos Santos
Federal University of Campina Grande - UFCG
Institute of Advanced Studies in Communications - Iecom
Campina Grande - PB - Brazil
kesia_santos@yahoo.com.br

Marcelo Sampaio de Alencar
Federal University of Campina Grande - UFCG
Institute of Advanced Studies in Communications - Iecom
Campina Grande - PB - Brazil
malencar@dee.ufcg.edu.br

***Abstract*— This paper presents a study of handover in mobile broadcast networks, showing the main challenges related to this process. Single Frequency Network (SFN) are used to provide efficient coverage for digital TV broadcast systems. Some handover algorithms used, in broadcast networks, are discussed. The method of RSSI measurement is investigated for use in the International System for Digital Television (ISDTV) standard. The synchronization in the seamless transmission among cells is analyzed. Simulation results are obtained considering the minimum field intensity criterion.**

***Index Terms*— ISDTV, seamless handover, mobile broadcast system, power consumption.**

I. INTRODUCTION

The Brazilian digital television system standard, called International System for Digital Television (ISDTV), is prepared to transmit video, audio and data for terrestrial, portable and mobile devices. The multimedia transmission for mobile or portable devices requires more attention from both, broadcast and telecommunications operators [1]. The ISDTV standard defines a continuous mobile reception of television programs or services that one offered to the users in the coverage area [2]. The main concerns relative to mobile devices are: battery power consumption, screen size and mobility, with an acceptable quality of service in the system coverage area.

Studies show that the use of a Single Frequency Network (SFN) in broadcast systems is capable of improving the coverage, and reducing the transmitters power [3], [4], [5], [6]. However, regarding mobile devices, it is necessary to maintain the continuity of the transmission while the mobile device moves inside the coverage area, according to the scenario illustrated in Figure 1.

The handover occurs when the receiver switches from a frequency to another one, or from a cell to another. Soft handover means that radio links are added and removed in such a way that the device always keeps at least one radio link to a base station [7]. Thus, when a user moves from a broadcaster cell to another, the mobile terminal tries to synchronize with the new cell frequency, without interruption. Handover occurs between two different SFN areas, which are part of the same Multiple Frequency Network (MFN), or between two different networks. Thus, in this context, cell refers to a subsystem consisting of one or more transmitters sending identical content in the same frequency (SFN).

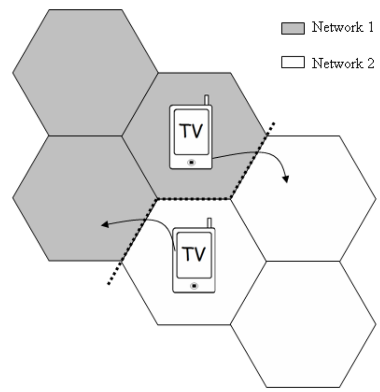

Fig. 1. Illustration of a handover situation between SFNs.

Handover is one of the main issues in performance analysis of mobile terminals. The main challenge for mobile TV broadcasting networks is the transmission continuity, while the TV receiver moves in critical conditions of reception. This is a challenging issue also for other broadcasting systems [7], [8], [9].

A. *Challenges of Handover Process in Broadcast Systems*

The handover process study points out some problems due to poor signal coverage, as it may cause the ping-pong effect, which is the result of the variation of the received field strength when the mobile is at the cell edge or in electromagnetic shadowed areas. This effect makes the receiver start a repeated handover process between cells, in order to synchronize it with the frequency of the strongest signal [7].

This effect also increases the mobile battery power consumption that is a critical issue in mobile devices, and causes a reduction in the received signal quality. The planning of a broadcasting network significantly affects the handover [10], and a correct planning can decrease the frequent need for handover.

In a broadcasting network, the information sent from transmitter to the receiver passively, and the receiver can not send information to the base station as in the mobile telephony networks, thus the receiver is responsible for the handover process.

II. Synchronization

In an SFN all the delayed copies of the signal arriving at the receiver from different transmitters can be combined or the strongest signal is selected. In order to attack the interference the Coded Orthogonal Frequency Division Multiplexing (COFDM) is used. The signal with time interval T, is composed of a useful symbol part with time interval T_u and a guard interval T_g.

If the delay spread of a signal is smaller than the guard interval T_g, no intersymbol interference (ISI) occurs and the signal contributes totally to the wanted signal. When signals arrive with time interval larger than T, then are treated as interfering signals. This phenomenon is called self-interference. The COFDM block interval is $T_t = T_u + T_g$. In an SFN the received signal is the sum of all the arriving signals inside T_t. The signal in the RF range is given by [2]

$$s_{(t)} = \sum_{n=0}^{\infty} \sum_{k=0}^{K-1} a_n^k \; e^{j2\pi f_k t} \; g_k \left(t - nT_u\right), \tag{1}$$

in which g_k represents the waveform for the transmitted pulse, n is the number of symbol, a_n^k is the information symbol on sub-carrier k, K represents the total number of carriers (mode 1: 1405, mode 2: 2809, mode 3: 5617), T_u is the duration of the useful portion OFDM symbol.

In fixed reception the received signal is the sum of all multipath signals

$$r_{(t)} = \sum_{i=1}^{N} \delta_i \; s\left(t - \tau_i\right), \tag{2}$$

in which N is the number of transmitters in the SFN, τ_i is the propagation delay from transmitter i to the receiver, $\delta\left(i\right)$ is statistically independent fading of the each i path.

In mobile reception the strongest signal is selected, the receiver measures the signal strength in all the cells in the Network Information Table (NIT). After the detection of the strongest signal the receiver tries to synchronize with this new transmitter.

Synchronization is important because the mobile terminal needs to receive synchronized signals when entering a new cell with a different frequency. The process of synchronization with the new cell must happen in order to avoid interruptions of service to end users.

In the transport layer of ISDTV, there are two levels of multiplexing. In first level, the information elementary streams of audio, video, and data associated with programs are transformed in packetized elementary streams. Data associated with programs include captions and additional information to monitor the content of programming. The second level includes data unrelated to the content of television, called datacasting. In this level multiplexed information on the structure of the signal, and the network or infrastructure of the broadcasting system [11].

In the ISDTV system the services of the mobile devices (called one-seg receiver) and fixed terrestrial (called full-seg receiver) are multiplexed in the same transport stream and then transmitted. The receiver uses the cell identification (cell_id) in the NIT to identify the transmitter.

In the ISDTV system the transmission is continuous by broadcasting, thus soft handover is not possible without two front-end solutions in which the receiver can receive two signals simultaneously. This enables the receiver to use one front-end for synchronizing to the signal of the consumed services and the other for handover.

III. Analysis of Algorithms for Handover

The handover process in wireless networks involves the base station and mobile terminal. However, in broadcasting networks the handover process, a transmitter can not get any information from receiver measurements. Thus, for the broadcast network handover is unidirectional. The handover process is started and completed by the mobile device.

The handover for broadcast TV is called passive handover, because the transmitter is not involved in the process [12]. The handover consists of three stages: handover measurement, handover decision-making, and handover execution [8].

During the measurement stage, data are obtained from the Received Signal Strength Indicator (RSSI) or SNR (Signal-to-Noise Ratio), and are necessary for the handover decision-making process. In the decision stage, the receiver evaluates the need for handover, according to pre-defined criteria, using data obtained during the measurement stage. The last stage is the handover execution, which is accomplished by the mobile terminal synchronization device.

The algorithms seek the exact moment to start the handover process, in order to reduce the amount of repeated handover and battery power consumption. Many algorithms have been proposed for digital television broadcasting systems, and some of those are described in the following.

In 2004, J. Väre [13] published the first article about soft handover in digital television broadcast systems DVB-H. The paper presents a simple scheme based on measurements of RSSI in adjacent cells and executes the handover to the cell which has the strongest RSSI value.

The RSSI value can vary due to multipath and Doppler effects, and does not provide an average indication of field strength measurement. Thus, the receiver may start a handover unnecessarily, causing the ping-pong effect.

In 2004 X. D. Yang [7] proposed another scheme of soft handover based on post-processing of the SNR. The main idea was to calculate the cumulative distribution functions (CDFs) for all the SNR values. Since it depends not only of the current SNR value, but on its history, it is possible to eliminate the occurrence of frequent handover caused by the instantaneous RSSI value.

Handover aided by the UMTS (Universal Mobile Telecommunication System) network is utilized in broadcast network. The UMTS base station in the handover position area informs the terminal broadcast the handover moment [8], [14]. The disadvantage of this algorithm is the dependence of the broadcasting network regarding mobile telephony.

The handover algorithm based in hysteresis, i.e, the handover occurs when the signal field strength from new transmitter exceeds that of current by a hysteresis level. However, for this algorithm the mobile can make an unnecessary handover when the signal from two transmitters is strong [15].

IV. Ray Tracing Method

Ray-optical propagation models are very often used for the prediction of the field strength in indoor and urban scenarios, they are accurate because consider wave-guiding effects in street canyons (urban) or corridors (indoor) and they include diffraction at corners [16].

the ray tracing method is based on ray optical techniques, in which different rays emitted by the transmitting antenna are subject to reflection, scattering and diffraction at walls and edges of buildings and similar obstacles. The computation is performed with help of the Universal Theory of Diffraction (UTD).

In the ray tracing method algorithm, all the rays which can transfer energy from the transmitter location to the receiver location are computed until a maximum number of successive reflections/diffractions occur (also known as order of prediction).

The disadvantages of the ray tracing refer at the computation time and cost of the database. However, the Intelligent Ray Tracing method (IRT) accelerate the computation time [17], [18]. As the database of the considered buildings remains the same and only the position of the transmitter changes, the overwhelming part of the different rays remains unchanged, only the rays between the transmitting antenna and primary obstacles or receiving points in line-of-sight are changing if different transmitter locations are compared [19]. This is the basis for a Data Base Pre-processing using by IRT. This method was used to obtain the field strength data from the analyzed area.

V. Proposal for Handover from in the ISDTV System

During initialization, the receiver scans the signals within the frequency range of the current region/country (e.g. VHF and UHF). Information regarding each network of interest is stored in the Network Information Table (NIT) containing the cell identification (cell_id), the operation frequency of each one, and their coordinates. Then, the measurement stage follows. During this stage, the candidate signal is selected, e. g. one that presents the the strongest RSSI. This requires the receiver to update the INT after each handover. The receiver locates neighboring cells by comparing their locations (x_i, y_i).

In the process of measurement may occur an effect called "fake signal", this effect is characterized by the existence of a signal that has a similar frequency and cell_id as another one stored in the NIT, but is actually from another network [13]. Figure 2 illustrates a "fake signal".

This situation can be avoided by comparison of the cell_id stored in NIT with the cell_id of the candidate signal. Another way to avoid the "fake signal" is the correct planning of the network, which will not allow two adjacent networks to have identical frequency and cell_id pairs, see Figure 3.

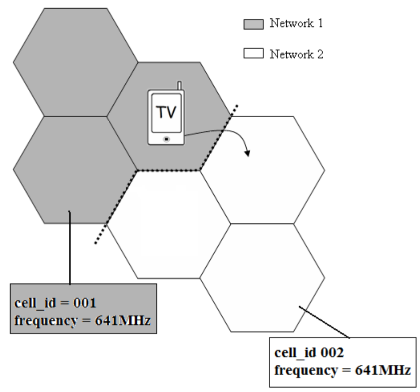

Fig. 2. Fake signal during handover.

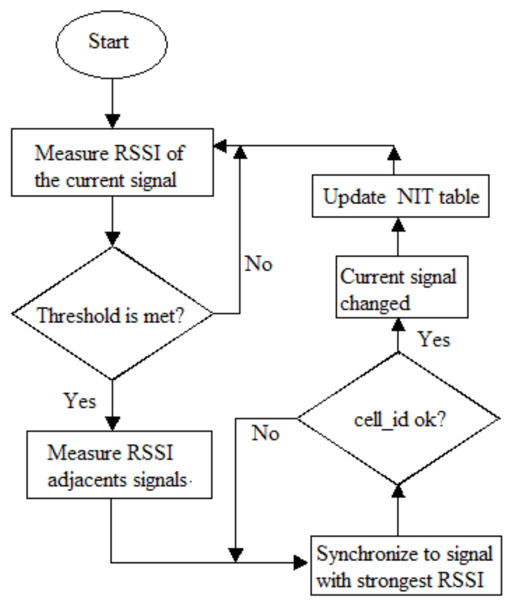

Fig. 3. Handover measurement and decision.

Consider a receiver moving in a trajectory between two transmitters T_{x1} and T_{x2}, during the trajectory the mobile terminal accomplishes measurements of RSSI from the current signal, at each time step $k = 1, 2, 3, \cdots, n$. Thus, measurements unnecessary are avoided, and as well as battery power consumption.

VI. Simulation and Analysis

Two transmitter stations were positioned in different places in towers with height of 100 m and power transmission of 2.5 kW. A receiver moving in a straight line between two transmitters stations (T_{x1} and T_{x2}) is simulated, and the signal behavior of the two stations is presented in the Figure 4.

Observing the curves it can be verified that the receiver has only one region of indecision, which represents the border

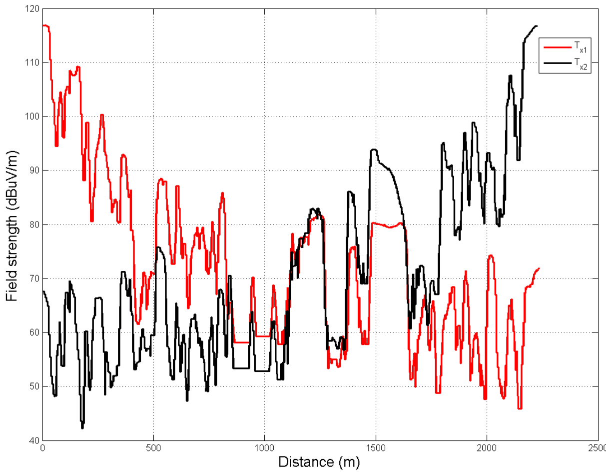

Fig. 4. Field Strength between T_{x1} and T_{x2}.

between the two cells, to execute handovers between the two transmission stations.

VII. Final Comments

When the broadcasting network is divided into SFN cells, to form an MFN, it is important to analyze the most adequate handover algorithm, in view of the challenges associated with this process.

In the synchronization of received signal the cell identification in the NIT is used to identify the transmitter, besides of the two front-end solutions in receiver which allows continuous reception.

The algorithm uses RSSI measurements and handover decision in defined time intervals, avoiding battery consumption with unnecessary measurements.

References

[1] C. Shchiglik, S. J. Barnes, and E. Scornavacca, *Mobile entertainment services: a study of consumer perceptions towards games delivered via the wireless application protocol*, Int. J. Serv. Stand., vol. 1, 2004.

[2] *ABNT NBR 1504 Digital terrestrial television – Receivers*, 2007.

[3] D. G. Barquero, A. Bria, *Scalability of DVB-H Deployment on Existing Wireless Infrastructure*, 16th IEEE International Symposium on Personal, Indoor and Mobile Radio Communications, 2005.

[4] D. G. Barquero, A. Bria, *Feasibility of DVB-H Deployment on Existing Wireless Infrastructure*, International Workshop on Convergent Technologies (IWCT), 2005.

[5] W. Joseph. D. Plets, L. Martens, E. Deventer, H. Gauderis, K. Van Bruwaene, *DVB-H Broadcast Network Design for Indoor Reception of DVB-H in Flanders*, 57th Annual IEEE Broadcast Symposium, Washington, DC, USA, 2007.

[6] K. C. Santos, E. F. Silva, M. S. Alencar, *Statistical Analysis of Digital Television Planning for the ISDTV System*, 58th Annual IEEE Broadcast Symposium, October 2008, Virginia, USA.

[7] X. D. Yang et al., *Seamless Soft Handover in DVB-H Networks*, Proc. Softcom, pp. 27 – 30, 2004.

[8] X. D. Yang et al., *An Investigation and a Proposal for Handover Decision-making in DVB-H*, 14th IST Mobile & Wireless Commun. Summit, Dresden, Germany, June, 2005.

[9] A. L. Gonzaléz, J. M. Bundio, G. F. Ubiergo, *Synchronization architecture for DVB-H seamless handover*, IEEE International Symposium on Broadband Multimedia Systems and Broadcasting, April, 2008.

[10] X. D. Yang et al., *Survey of Handover Algorithms in DVB-H*, IEEE Communications Surveys, 4th Quarter 2006, vol. 8, no. 4.

[11] M. S. Alencar, *Digital Television*, Érica Publisher Ltd, São Paulo, 2007.

[12] H. Hu, Y. Zhang, J. Luo, *Distributed Antennas Systems: open architecture for future wireless communications*, Auerbach, Publications, 2007.

[13] J. Väre, M. Puputti, *Soft-handover in Terrestrial Broadcast Networks*, IEEE International Conference on Mobile Data Management (MDM), 2004.

[14] X.D. Yang, Y.H. Song, T.J. Owens, J. Cosmas, T. Itagaki, *Intersystem Soft Handover for Converged DVB-H and UMTS Network*, IEEE Journal on Selected Areas in Communications, 2005.

[15] R. Vijayan and J. M. Holtzman, *A model for analyzing handoff algorithms*, IEEE Trans. Veh. Technol., vol. 42, no. 3, 1993.

[16] R. Hoppe, P. Wertz, G. Wolfle, and F. M. Landstorfer, *Wideband Propagation Modelling for Indoor Environments and for Radio Transmission into Buildings*, The 11th IEEE International Symposium on Personal, Indoor and Mobile Radio Communications, PIMRC, 2000.

[17] G. Wolfile, B. E. Gschwendtner, F.M. Landstorfer, *Intelligent ray tracing - A new approach for the field strength prediction in microcells*, 47th Vehicular Technology Conference (VTC) 1997, USA, pp. 790-794, May, 1997.

[18] R. Hoppe, G. Wolfle, F. M. Landstorfer, *Fast 3D Ray Tracing for the Planning of Microcells by Intelligent Preprocessing of the Database*, 7th COST 259 MCM-Meeting in Thessaloniki, Greece, January, 1999.

[19] A., Aschrafi, P., Wertz, M., Layh, P. M., Landstorfer, G., Wolfle, R., Wahl, *Impact of Building Database Accuracy on Predictions with Wave Propagation Models in Urban Scenarios*, IEEE 63rd Vehicular Technology Conference, 2006. VTC 2006-Spring, May, 2006.

RF Optical Link for Remote Station Applications

Euclides Chaves Pimenta Júnior
Aeronautics Institute of Technology - ITA
São José dos Campos - SP - Brazil
euclides@ita.br
12-3947-6873

Gefeson Mendes Pacheco
Aeronautics Institute of Technology - ITA
São José dos Campos - SP - Brazil
gpacheco@ita.br
12-3947-6819

***Abstract*—The well known benefits presented by optical systems are attractive for a variety of applications, especially when it comes to high frequency signals. Limitations such as high loss and electromagnetic interference (EMI) in coaxial cables are severely reduced when optical fibers are employed. Based on this scenery, this paper presents a brief theory of analog optical links focusing on remote station applications and the primary results of an optical link designed for a set of remote antennas stations.**

***Index Terms*—Antenna remoting, intensity modulation, optical fiber, radio frequency.**

I. Introduction

In the past years, radio frequency (RF) optical links are being subject of research in many laboratories throughout the world. The interest on this area has been mainly driven by the necessity to overcome limitations in conventional waveguides, such as coaxial cables, principally when it comes to high frequency signals, where attenuation increase as a frequency function [1]. Optical fiber offers many advantages over coaxial cable for the transmission of RF signals in many applications, such as cable television (CATV) signal distribution networks, phased-array and antenna remoting, as well as cell phone networks and radar [2,3]. These benefits are due to the well known characteristics of optical fiber, which shows significantly less attenuation, higher bandwidth and immunity to electromagnetic interference (EMI). In addition to that, optical fibers enable considerable size and weight savings when compared to conventional waveguides.

Optical links are suitable for specific systems that need to transmit or distribute their analog signals without going through digital conversion. This can be explained by limitations in the conversion process, where analog information cannot be reproduced accurately by digital bits at high bandwidths. [4].

In such systems, coaxial cables impose that all wideband elements on it be located physically at the same local to reduce de impact of RF losses, that can reach values of 15 dB/km at 40 GHz. The low loss of fiber optics means that, for distances out to several hundred meters the performance of a system employing RF photonics is nearly independent of the distance between the various components [2].

Despite of all the striking characteristics of optical systems, there is a large difference among analog and digital transmission requirements. While high … are the prime requirements for the latter, linearity and signal to noise ratio, SNR, are the key features for transmission of analog signals. Such differences lead to different approaches and equipments.

RF optical links are characterized by the same parameters used conventionally to measure conventional RF systems, such as power gain, noise figure and dynamic range. Two causes of signal degradation are electro-optic source nonlinearity and noise, which mostly arises from optic-electro conversion [4].

At present, there is a program research in course at the Photonics Laboratory of the Aeronautics Institute of Technology (ITA) to develop and characterize different experimental setups of such links aiming remote processing for receiver setups. One of the main motivations of this work is that besides it is a well known system in some countries, up to the authors' knowledge, RF optical links techniques for that purpose, are not diffused at national research institutes. In this work we propose a setup of a RF optical link directed for transmitting and receiving systems operating at microwave frequencies sited away from the control/processing station, presenting the primary experimental results of the proposed setup.

The perspective use of the system under consideration is for a radar station, the Itapetinga Radio Observatory (ROI) and the Brazilian Decimetric Array (BDA), which is a set of 38 antennas coordinated by the National Space Research Institute (INPE).

This work will enable to determine suitable parameters for a prospective radar station and antenna ensemble according to the desired results.

II. Theoretical Presentation

On a RF optical link, optical carriers are modulated by microwave signals. Once modulation is reached, these optical carriers propagate over an optical fiber. After transmission and distribution, the modulated optical carriers are detected and demodulated by a photodetector, in order to recover the original signal. At this process, the photodetector produces a current that is directly proportional to the light intensity, which in turn is proportional to the optical power [5]. On the entire process, the modulation signals are subjected to attenuation, dispersion and possible changes in polarization.

There are two common ways to achieve intensity modulation of the electro-optical source: direct and external modulation. The first one is basically the applying of modulation signal directly to the optical source, which results in an optical intensity which varies accordingly to the RF signal. This mechanism is limited by high frequencies due to frequency chirping [4].

An alternative for that is external modulation, where a continuous optical carrier is applied to an external intensity modulator.

We have chosen to adopt external modulation in this work due to better performances over directly configuration, especially when it comes to higher frequencies. A general block diagram of a generic RF optical link is shown in Fig. 1.

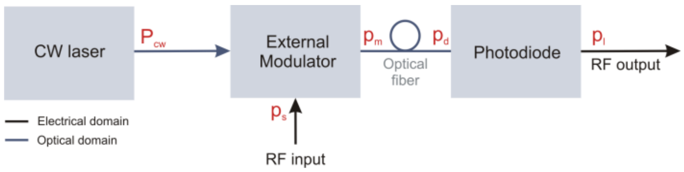

Fig. 1. Block diagram of an intrinsic externally modulated link

Initially, optical amplifiers are excluded from the link definition to emphasize and visualize the impact on signals caused by the link components. On Fig. 1, the variable P_{CW} is the continuous wave power, p_s, p_m and p_l indicate the resulting power from the modulation source, modulator device and photodetector, respectively. The amount of power that reaches the detector device is denoted by p_d.

At present, a commonly used external modulator in analog optical links is the Mach-Zehnder interferometric (MZI) modulator with lithium niobato substrate [3]. In such modulators, an optical waveguide is fashioned close to the top surface of the material. This waveguide is made to split into two waveguides that run in parallel for a given length and then recombine into one waveguide. In the middle section, the two parallel optical waveguides traverse a region in which an applied electric field changes light phase light in one waveguide relative to the other, affecting the interferometric recombination of these two guided waves. The electric field, and, therefore the modulator's optical output, is modulated by the small-signal RF modulation voltage across a set of electrodes on the surface of the substrate [5].

A parameter that is used to specify the performance of an external modulator is called V_π, that is the voltage necessary to shift the optical phase in one arm of the waveguide by π radians relative to the other. This is a critical parameter since the DC bias voltage applied on the modulator to produce an electric field is a function of V_π, consequently, the modulated optical intensity has a strongly dependence on this bias voltage.

In analog links employing external MZ modulators, the sinusoidal transfer function usually dictates the linearity of the link. Electrooptic intensity modulators have inherently nonlinear transfer functions [5] which may limit the dynamic range of the link through the appearance of harmonic and intermodulation distortion. These parameters are important to evaluate the performance of RF optical links, as well as gain, noise figure and dynamic range, that are the commonly figures of merit used do characterize conventional RF links.

A common solution to minimize the nonlinear effects of modulators is to set the bias voltage to half the value of V_π, that is known as quadrature point, which is the region that the transfer function of the modulator behaves close to a linear function [1].

Biasing the modulator at quadrature yields the highest slope point and the highest link gain or lowest loss. In addition, operation at quadrature yields an odd transfer function, thus minimizing the second-order-distortion output.

Usually, linearity is characterized in terms of spur-free dynamic range, SFDR, which can be defined as the maximum signal to noise ratio when the intermodulation distortion signals rise to the noise level. Intermodulation distortions arise from the mixing of signals in different frequencies. Such distortion can be quantified by the two-tone test, which consists of applying two frequency offset signals, ω_1 and ω_2, on the modulator with same amplitude. The intermodulation products can be seen on a spectrum analyzer.

For single-octave applications where the signal bandwidth is narrow, the dominant intermodulation distortions products at $2\omega_1$-ω_2, $2\omega_2$-ω_1 cannot be filtered easily, whereas the even order distortions, such as $2\omega_2$, $2\omega_1$, can be filtered out by using a filter. Conversely, for multioctave applications, the second order distortions are dominant and cannot be ignored. Since the fundamental signal and the intermodulation distortion can be bias dependent, the corresponding multioctave and single-octave SFDR can vary with the bias point. The SFDR of the modulator can be calculated from the derivatives of the transfer function [3].

A high linearity, in particular, requires a low third-order intermodulation distortion light source with a low relative intensity noise as the key component for such systems to achieve adequate signal quality.

Assuming that the MZ modulator is biased at the quadrature point and that the modulator's RF input and output load impedances are matched, the intrinsic gain of the link can be obtained by

$$g_t = T_{MD}{}^2\, g_m g_d \tag{1}$$

where T_{MD} indicates the transmission coefficient between the modulation device and the detector, taking in account attenuation and connectors losses; g_m indicates the modulation stage gain and g_d refers to the detection stage gain.

An analysis of the individual stage gain allows an adjustment of the components according to the desired result. Therefore, their expressions are

$$g_m = \left(\frac{\pi T_{FF}\, P_{CW}}{2\mathrm{V}_\pi}\right)^2 \frac{R_S}{(0{,}5\mathrm{j}\omega\mathrm{C}_{\mathrm{MZ}} R_S + 1)^2} \tag{2}$$

and

$$g_d = \frac{R_L r_d{}^2}{[1 + (j\omega C_D)(R_D + R_L)]^2} \tag{3}$$

where T_{FF} is the fraction of the total laser power in the modulator input that is coupled into the modulator output fiber when the modulator is biased for maximum transmission, P_{CW} is the continuous wave laser power, R_S is the output source impedance, r_d is the responsivity of the photodetector, R_D and C_D are the impedance and capacitance of the photodiode, respectively, and R_L is the load impedance.

A further relevant parameter is the noise figure of the link, which defines the degradation of signal-to-noise ratio. Noise figure is a critical parameter in sensing systems that employs RF optical links because it is the parameter that dictates the system's sensitivity to received signals.

In general, exists three noise sources that affect optical links: thermal, shot and relative intensity noise (RIN) [5, 6]. The noise figure of a link is defined by

$$NF = 10 \log\left(\frac{p_{on}}{kT\, \Delta f\; g_t}\right) \qquad (4)$$

where p_{on} is the link output noise power, k is the Boltzmann's constant, T is the temperature in Kelvin and Δf is the resolution bandwidth of the photodetector. As can be seen, noise figure is a parameter that depends on the link's gain, so the choice of the components involves several design trade-offs.

Noise figure of externally modulated links is often dominated by shot noise originated by the photodiode [1].

As long as the harmonic output is smaller than the noise, the signal to noise determines the system performance. When the fundamental is large enough to generate distortion terms that rise above the noise floor, such terms can be often degrade system performance. For that reason, distortion effects are included, they set a maximum level limit of the fundamental. The signal level that generates distortion terms equal to the noise floor is the maximum signal for which the link output is free from distortion. Hence this is the spur-free, or intermodulation free, dynamic range. The bandwidth dependence of the SFDR depends on the order of the distortion, because of different signal power dependencies of the fundamental and distortion terms [7].

For an analysis of harmonic distortion, the output current delivered to the load can be split into harmonics portions. So, the fundamental and third order harmonics at the link output are given by

$$i_{fund}\,(t) = -\cos(\omega t)\left\{\left[1+\left(\frac{\Gamma_m}{4}\right)^2\right] T_{FF}\Gamma_m \sin\left(\frac{\pi V_{DC}}{V_\pi}\right)\right\} \quad (5)$$

and

$$i_{3rd}\,(t) = -\cos(3\omega t)\left[\frac{T_{FF}}{48}\Gamma_m{}^3 \sin\left(\frac{\pi V_{DC}}{V_\pi}\right)\right] \qquad (6)$$

where Γ_m is the modulation efficiency and it is given by

$$\Gamma_m = \frac{\pi v_m}{V_\pi} \qquad (7)$$

Expressions (5) and (6) are plotted in Fig. 2 as a function of input and output RF power, which varies accordingly to the RF modulation voltage, v_m.

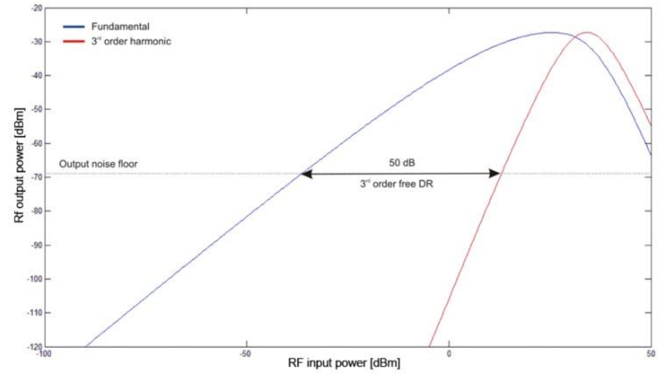

Fig. 2. Demonstration of the dynamic range of an intrinsic link with parameters values of the experimental setup presented on section III

As can be seen in the above picture, link's dynamic range related to harmonic distortion is around 50 dB.

III. Experimental Setup

The schematic block diagram of the experimental setup under consideration is depicted in Fig. 3. It consists of a 1546 nm DFB laser with maximum rated output power of 20 mW, a 20 GHz Mach-Zehnder modulator with V_π = 7.8 V, connected to the receiving stage by five meters of single mode optical fiber. The photodetector is a InGaAs photodetector with output impedance of 50 Ω and responsivity of 1 A/W at operation wavelength.

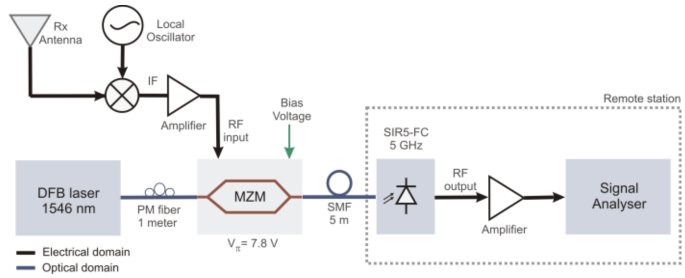

Fig. 3. Schematic of the experimental link setup employing a MZI modulator

One frequency mixer with range of 10 to 2000 MHz was employed to down convert the RF signal from antenna to an intermediate frequency, IF. As antenna and local oscillator, LO, two analog signal generators with maximum output power of +13 dBm were used.

Finally, two signal amplifiers of 25 dB gain with frequency range of 0.2 to 2 GHz with noise figure of 1.8 dB were employed at the link. One at the modulator RF input and the other to the photodetector output.

An illustrative picture of the experimental mount is showed in Fig. 4.

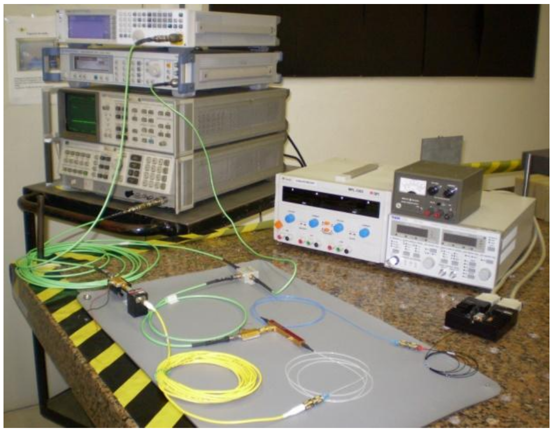

Fig. 4. Picture of the experimental mount

IV. RESULTS AND DISCUSSION

After some analysis, the frequencies of the RF and LO were set as 2 GHz and 800 MHz, respectively, resulting on an IF of 1.2 GHz, that is a value of our interest. Usually, IF frequency is lower than LO frequency. The set of frequencies values used in this work was determined by the available mixer and its characteristics. Despite that constraint IF frequency was according initial remote station aims.

Setting the output power of the RF signal and LO to -13 dBm and +10 dBm, respectively, and optical power average of 16 mW, a gain of 11 dB was reached. Fig. 5 shows the frequency spectrum when applying a RF power of – 5 dBm.

An attenuator of 10 dB was connected to the analyzer spectrum input to prevent occasionally damage from DC signal.

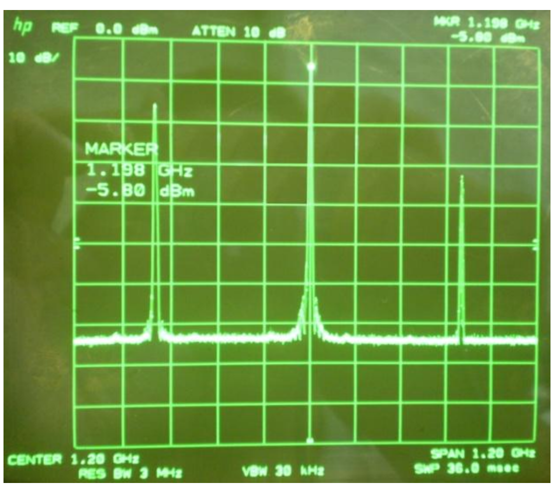

Fig. 5. Signal spectrum at link output

The central component on Fig. 5 is the fundamental signal, while the left and right ones, are the LO at 800 MHz and a resulting component of the frequency mixer at 1.6 GHz. So, the system has a bandwidth of 800 MHz, with SNR of 61 dB, and noise figure of 43 dB. A linear response of the system was observed varying the RF input signal from -66 dBm up to -8 dBm.

V. CONCLUSION

It was presented in this work a brief theoretical approach of RF optical links and a proposal of a setup directed to remoting applications, as well as the primary experimental results. Such results showed good perspectives for the use of the system, especially on applications limited by conventional lossy cable and waveguides.

Although reasonable values of figures of merit were reached, the proposed system can be improved by using suitable components, such as mixers and amplifiers, which were restrictive on our mount, where the frequency range was limited by those components. Besides that, higher gain can be reached using higher optical power and intensity modulator with a lower V_{π}.

Even though a length of five meters of optical fiber was used, it is widely known [8, 9, 10] that longest lengths will not decrease the signal significantly.

The presented results show that the remote station application is a real and feasible solution for distributed receiver technologies.

REFERENCES

[1] COX, C. H., “Analog Optical Links: Theory and Practice”. Cambridge University Press, 2004.
[2] AL-RAWESHIDY, H., KOMAKI, S. P., “Radio over fiber technologies for mobile communications networks”. Artech House, 2002.
[3] CHANG, W. S. C., “RF Photonic Technology in Optical Fiber Links”. 1 ed. Cambridge University Press, 2002.
[4] IEZEKIEL, S., “Measurement of Microwave Behavior in Optical Links”. IEEE Microwave Magazine, pp. 100-120, June, 2008.
[5] YARIV, A., YEH, P., “Optical Waves in Crystals”. 2 ed. New York: Wiley-Interscience, 1984.
[6] LATHI, B. P., “Modern Digital and Analog Communication Systems”, Oxford University Press, Ed. 2, NY, USA, 1995.
[7] WILLIAMSON, R. C., ESMAN, R. D., “RF Photonics”. Journal of Lightwave Technology, vol. 26, no. 9, May, 2008.
[8] SEEDS, A. J., WILLIAMS, K. J., “Microwave Photonics”. Journal of Lightwave Technology, vol. 24, no. 12, December, 2006.
[9] COUTINHO, O. L., ALMEIDA, V. R., MARTINS, C. S., OLIVEIRA, J. E. B., “Aplicação de Enlace a Fibra Óptica em Transmissão de Sinais Radar”. MOMAG 2008, pp. 719-724, Brazil, September, 2008.
[10] HARTMANN, P., QIAN, X., WONFOR, A., PENTY, R. V., WHITE, I. H., “1-20 GHz Directly Modulated Radio over MMF Link”. International Topical Meeting on Microwave Photonics (MWP 2005), South Korea, October, 2005.

Design of Frequency Selective Surfaces with Koch Fractal Elements

Rossana Moreno Santa Cruz
Federal University of Rio Grande do Norte – UFRN
P.O. Box 59072-970
Natal – RN - Brazil
mscrossana@gmail.com

Paulo Henrique da Fonseca Silva
Federal Center of Technological Education of Paraíba – CEFET-PB
P.O. Box 58015-430
João Pessoa – PB - Brazil
henrique@cefetpb.edu.br

Paulo Fernandes da Silva
Federal Center of Technological Education of Paraíba
P.O. Box 58015-430
João Pessoa – PB
pfs1224@yahoo.com.br

Albanisa Felipe dos Santos
Federal Center of Technological Education of Paraíba
P.O. Box 58015-430
João Pessoa – PB
albanisa@oi.com.br

Adaildo Gomes D'Assunção
Federal University of Rio Grande do Norte
P.O. Box 59072-970
Natal – RN
adaildo@ct.ufrn.br

***Abstract*—This work investigates the use of fractal geometries for the design of Frequency Selective Surfaces (FSSs). The objective is to design fractal FSSs that are able to resonate at more than one frequency, which is difficult to obtain with Euclidean arrays. The property of auto-similarity, presented in most fractal geometries, is used for the design of multiband FSSs. The FSS periodic arrays are composed of rectangular patch elements. The design of these structures is accomplished through the use of C*omputer Aided Design* (CAD) tools, such as the commercial softwares Ansoft Designer^{TM}, MATLAB and Corel Draw. The computational simulated results are compared with the measured ones, obtained through the fabrication of some prototypes, in order to validate the investigation proposed. The measurements are performed with the aid of a vetorial network analyzer.**

***Index Terms*—Fractal geometry, frequency selective surfaces, measurement, numerical analysis.**

I. Introduction

Frequency Selective Surfaces (FSSs) [1–4] present each time more applications and greater importance for the modern telecommunication systems, also those operating in high frequencies (millimeter waves and microwaves) [5]. The researches on the FSSs have been carried through for the manufacture of devices that protect indoor environments against interferences and people against excessive levels of radioelectric exposition. Currently, for example, the use of FSSs for the manufacture of microwave's doors [6], antennas [1], [4] and radomes [7] is already common. The FSSs are bidimensional structures, composed by periodic arrays of metallic elements that are printed on one or more dielectric substrates [1]. When the FSS is exposed to the incident electromagnetic radiation, the array of metallic elements resounds in one given band of frequencies, according to the geometry and the periodicity of its conducting elements, as well as of the properties of the dielectric substrate [6-15].

Since frequency selective surfaces are devices which rely on the constructive and destructive phases transmitted from a periodic arrangement of elements to provide spatial filtering or focusing effects, these devices can increase the usability of antenna systems, such as in the design of a dual-band reflector system. Therefore, fractal geometries can be incorporated into these surfaces to provide spatial filtering over several frequency bands [16].

A frequency-selective surface has a signature that, in general, is dependent on the frequency of the incident wave, the incident angle, and the incident polarization. Several iterations of the fractal can be used to design an FSS that has a multiband frequency response that correlates to the scales of the geometry that is present in the structure. The Sierpinski Sieve fractal, utilized previously as a multiband monopole [17], has been used to design a multiband FSS [18], which has also been utilized as a radome [19]. However, this particular structure is sensitive to only one polarization. Various pre-fractal FSS configurations have also been designed that can be dual-polarized due to the symmetry in the geometry [20], [21]. The fractal property of having multiple scales of similar geometry presented in the final structure has also been incorporated with dipoles [22].

In this work, we investigate the use of fractal geometry for the design of FSSs. The objective is to control the resonant frequency and bandwidth of the structure without modifying its original dimensions. Instead of that, the goal is to make the indentation of the rectangular elements using the Koch curve fractal geometry. The design of the fractal FSSs is accomplished using the CAD tools already mentioned. Simulated and measured results are obtained for comparison in order to validate the study proposed.

II. The Fractal Geometry

The property of auto-similarity, common to the fractal figures, is also used in the design of fractal FSSs. The fractals are geometric forms with complex standards that are repeated infinitely, even if they are limited to a finite region. A fractal filter can be created using fractal figures since the inherent qualities of these geometries allow the construction of this device with original performance and a size reduction of about 50% to 75%, in relation to the traditional types [23].

Currently, the fractals are applied in several areas of science and technology, since biology until engineering. For example, the union between the electromagnetism and the fractal geometry originated the area called of fractal electrodynamics. In this area, the characteristic properties of fractal geometry reveal useful for the construction of filters, frequency selective surfaces and antennas, making possible practical solutions for a variety of applications in the ISM band.

Euclidean geometry deals with geometric objects with regular forms, as the point, the curves and the surfaces that are characterized in terms of their topological dimensions: 1, 2 and 3, respectively. However, there are many irregular forms found in the nature that are not related to the Euclidean geometry, such as: surfaces of clouds and mountains, coastal lines, roots and branches of trees, nerves and vessels of the human body [24]. The fractal term was introduced in 1975 for the mathematician Benoit Mandelbrot [25], refering to the objects constructed recursively where one aspect of the object is infinite and the other is finite. For definition, a fractal is a set for which the dimension of Hausdorff-Besicovitch strict exceeds the topological dimension. Therefore, the fractal objects possess superior dimensionality to the Euclidean ones, occupying more efficiently an area or finite volume. The fractal dimension, the auto-similarity, the fulfilling of space and the iterative construction are common properties of the fractals [26].

The fractal periodic arrays of FSSs proposed in this work were constructed from the conventional array of rectangular patch elements illustrated in Fig. 1(a). The periodicity of the elements is given by $t_x = W_c$, in the x axis and $t_y = L_c$, in the y axis, where W is the width and L is the length of the rectangular patch; W_c is the width and L_c is the length of the cell element. For the synthesis of the FSSs, a coarse empirical model was used. The dimensions of each rectangular patch element are given as a function of the effective scaled wavelength λ, as we can see in Fig. 1(b). In this case, we consider the low-cost FR-4 fiberglass substrate with dielectric constant ε_r = 4.4, thickness h = 1.5 mm and dielectric loss tangent tan δ = 0.02. The effective wavelength was calculated by $\lambda = \lambda_0 [(1+\varepsilon_r)/2]^{0.5}$, where λ_0 is the free space wavelength.

Using this procedure, and considering for a resonant frequency of 10 GHz, the dimensions of the rectangular patch elements were obtained: W = 9.2428 mm, L = 18.4856 mm, t_x = 12.3238 mm and t_y = 24.6475 mm. From this rectangular patch element, refered as generator or level zero fractal, the new FSSs proposed in this work were designed based on the Koch curve fractal elements.

The original Koch fractal geometry appeared in 1904, after one publication of the mathematician Niels Fabian Helge von Koch, and it is characterized for constituting curves without tangents [23]. Fig. 2 shows an iterative construction of these fractal curves. A Koch curve can be characterized by two parameters: the number of iterations (or levels) and the iteration factor.

In particular, from a rectangular patch element we consider a rectangular construction of Koch curve with two fractal iterations and a variable iteration factor (a). The geometry of the proposed FSS Koch fractal elements is shown in Fig. 3. As we can observe, in a given iteration, a rectangular Koch transformation is applied to each linear side of the previous patch element. A picture of the behavior presented by the proposed FSSs with Koch fractal elements was verified as a function of the number of iteration.

III. Results and discussion

For all the results presented in this section, a normally incident plane wave was considered to be impinging on the surface and the resulting transmission profile was calculated. It was also considered the TE polarization that refers to the case in which the electric field is perpendicular to the long dimension of the patch.

In Fig. 4 we present the simulated results for FSS transmission coefficient obtained with the Ansoft Designer™ software considering until two iterations. We can observe a reduction of resonant frequency as the iteration number is increased. At level zero, there is a fort rejection band at the resonant frequency f_{r1} = 10.99 GHz. Introducing the first level of iteration, we can observe the reduction of the cutoff frequency and the appearance of a second rejection band. Finally, at level two we can verify a greater reduction at the resonance and bandwidth of the two rejection bands for structures using the same iteration factors of level one.

The results shown in Fig. 4, for a = 3.5, prove that the introduction of fractal geometries is responsible for the reduction at the cutoff frequency and the rejection bands of a given FSS and it can also be applied to the case of multiband structures. Tab. 1 shows the numerical results for other values of the iteration factor (a) comparing the three levels of iteration investigated.

We strongly consider the influence of the iteration factor at the control of the resonant frequency. For example, the set of level one Koch fractal elements, considering for the range of $3.05 \le a \le 10.0$, is shown in Fig. 5.

The respective transmission coefficients for each designed FSS with level one Koch fractal elements were simulated with the Ansoft Designer™ software. The obtained results are presented in Fig. 6. We can verify the variation of the resonant frequency as a function of iteration factor, making possible to control the response of the structure only varying the iteration factor used for the Koch fractal geometry.

Four FSS prototypes had been constructed for the validation of simulation results, which were compared to the measurements for the power transmitted through the structures. Each of the arrays consists of a plate with 20 cm of height for 15 cm of width. Fig. 7 shows the photographs of the fabricated FSS prototypes.

The equipment and instruments used in the measurement procedure were two horn antennas (one for transmission and other for reception), two waveguides, a network analyzer (N5230A, Agilent Technologies) that operates from 6.0 GHz up to 13.5 GHz, beyond handles and connectors. A fixed distance of 9 cm, equivalent to two wavelengths of the cutoff frequency of the waveguides (6.8 GHz), was adopted between the horn antennas.

After setting all the instruments to the network analyzer, a measurement was performed, in order to obtain the level of the power transmitted and received by the antennas, without any FSS structure between them. This reference level was used to adjust the return loss graphically displayed at the network analyzer screen, when the FSS structures are placed, one by one, between the horn antennas. The measured data were interpolated with the aid of the MATLAB 7 software for the generation of the curves presented in Fig. 8, which correspond to the measurements for three fabricated level 1 prototypes. The measured results agree very well with the simulated ones, obtained with the Ansoft Designer^{TM} software.

A suitable difference between measured and simulated results can be observed and it can be explained if we consider the losses due to the instruments (handles, connectors, waveguides) and the objects which were present at the laboratory where the measurements were accomplished (desks, tables, boards etc.). A more accurate measurement procedure would be able with the aid of an anechoic chamber.

The measurements of the level 2 prototypes were accomplished but are not included in this work because the resonant frequencies (about 5 GHz up to 6 GHz) observed are out of the range of measurements of the horn antennas utilized. The multiband behavior was observed but also not included in the results, because the second resonant frequencies of the FSSs analyzed, which were simulated with the Ansoft Designer^{TM} software, are between 15 GHz and 18 GHz, therefore out of the range of measurement of the network analyzer used.

IV. Conclusion

This work considered the problem of computing the scattering parameters of a periodic array consisting of a fractal FSS, composed by rectangular patch elements. These structures were printed on a single layer of the low cost FR-4 fiberglass dielectric substrate. The analysis was performed with the aid of the Ansoft Designer^{TM} commercial software for simulations and some of the FSS structures designed were fabricated and experimentally analyzed. The measured results validated the simulated ones, as well as the investigation proposed.

Finally, the proposed FSSs with Koch fractal elements permit us to control the resonant characteristics and to tune a desired operation frequency. In relation to the conventional rectangular patch elements and considering the same resonant frequencies, this type of fractal FSS element can also be used to reduce the dimensions of the cells and consequently the overall size of FSS.

References

[1] T. K. Wu, *Frequency Selective Surface and Grid Array*. John Wiley & Sons, Inc. New York, 1995.

[2] J. C. Vardaxoglou, *Frequency Selectiv Surfaces: Analysis and Design.* Wiley & Sons, Inc. New York, 1997.

[3] C. K. Lee, *Modeling and design of frequency selective surfaces for reflector antennas.* Ph.D. dissertation, Kent University, 1987.

[4] R. C. H. Mittra, Chan and T. Cwik, "Techniques for analyzing frequency selective surfaces – a review". *Proc. IEEE*, Vol. 76, No. 12, 1593-1615, 1988.

[5] G. R. Medeiros, *Análise de Superfícies Seletivas de Freqüências para Aplicações em Ondas Milimétricas*, MSc. Dissertation, UFRN, Natal – RN, Brazil, 2001.

[6] A. Qing, C. K. Lee, "An Improved Model for Full Wave Analysis of Multilayered Frequency Selective Surface with Gridded Square Element". *Progress In Electromagnetics Research, PIER 30*, 285-303, 2001.

[7] G. H. Schennum, "Frequency-Selective Surfaces for Multiple Frequency Antennas". *Microwave J.* **16** (5), 55-57 (1973).

[8] S. W. Lee, "Scattering by dielectric-loaded screen". *IEEE Trans. Antennas Propagat.*, Vol. AP-19, No. 5, 656-665, 1971.

[9] C. K. Lee and R. J. Langley, "Equivalent circuit models for frequency selective surfaces at oblique angle of incidence". *IEE Proc. Microwaves, Antennas, Propagat.*, Vol. 132, No. 6, 395-398, 1985.

[10] T. A. Cwik and R. Mittra, "Scattering from a periodic array of free-standing arbitrarily shaped perfectly conducting or resistive patches". *IEEE Trans. Antennas Propagat.*, Vol. AP-35, No. 11, 1226-1234, 1987.

[11] T. Cwik and R. Mittra, "The cascade connection of planar periodic surfaces and lossy dielectric layers to form an arbitrary periodic screen". *IEEE Trans. Antennas Propagat.*, Vol. AP-35, No. 12, 1397-1405, 1987.

[12] C. H. Chan and R. Mittra, "On the analysis of frequency selective surfaces using subdomain basis functions". *IEEE Trans. Antennas Propagat.*, Vol. AP-38, No. 1, 40-50, 1990.

[13] A. Styllanou, P. Debono and J. C. Vardaxoglou, "Iterative computation of current and field distributions in multilayer frequency selective surfaces". *IEE Proc. Microwaves, Antennas, Propagat.*, Vol. 139, No. 6, 535-541, 1992.

[14] A. Karlsson et al, *Frequency Selective Surfaces with Sthocastic Deviations*, Department of Electroscience Electromagnetic Theory, Lund Institute of Technology, Sweden, 2003.

[15] J. A. Reed and D. M. Byrne, "Frequency-Selective Surfaces with Multiple Apertures within a Periodic Cell". *J. Optical Society of America.* A/Vol. 15, nº 3. March, 1998.

[16] J. P. Gianvittorio and R. S. Yahya, "Fractal antennas: a novel antenna miniaturization technique and applications". *IEEE Trans. Antennas and Propagation Magazine*, Vol. 5, N1, February, 2002.

[17] C. J. Puente, R. Romeu, R. Pous, X. Garcia and F. Benitez, "Fractal multiband antenna base don the Sierpinski gasket". *Electronics Letters*, vol. 32, no. 1. 4th January 1996.

[18] J. Romeu and Y. Rahmat-Samii, "Dual band FSS with fractal elements". *Electronics Letters*, vol. 35, no. 9. pgs. 702-3. 29th April 1999.

[19] V. K. Varadan, K. J. Vinoy, K. A. Jose and V. V. Varadan, "Conformal Fractal Antennas and FSS for Low RCS Applications". *Proceedings of the SPIE – The International Society for Optical Engineering*, vol. 3990, pgs. 138-45. March, 2000.

[20] D. H. Werner and D. Lee, "Design of dual-polarized multiband frequency selective surfaces using fractal elements". *Electronics Letters*, vol. 36, no. 6. pgs. 487-8. 16th March 2000.

[21] J. P. Gianvittorio, Y. Rahmat-Samii and J. Romeu, "Fractal FSS: Various Self-Similar Geometries Used for Dual-Band and Dual-Polarized FSS". *Proceedings of the IEEE Antennas and Propagation Society International Symposium*, vol. 3. pgs. 640-3. 2001.

[22] P. P. Sarkar, D. Sarkar, S. Das, S. Sarkar and S. K. Chowdhury, "Experimental Investigation of the Frequency-Selective Property of an Array of Dual-Tuned Printed Dipoles". *Microwave and Optical Technology Letters*, vol. 31. no. 3. pgs. 189-90. 5th November 2001.

[23] S. Reed, L. Desclos, C. Terret and S. Toutain, "Patch Antenna Size Reduction by Means of Inductive Slots", *Microwave and Optical Technology Letters*, Vol. 29, N2, April, 2001.

[24] L. F. Costa and A. G. C. Bianchi, "A outra dimensão da dimensão fractal", *Ciência Hoje Magazine*, Vol. 31, No. 183. pp. 40-47. June, 2002.

[25] B. Mandelbrot, *Objectos Fractais: forma, acaso e dimensão*. Gradiva Publicações, Lisboa, 1991.

[26] K. Falconer, *Fractal geometry: mathematical foundations and application*. 2 ed. Wiley & Sons, Ltd., p. 337. London, 2003.

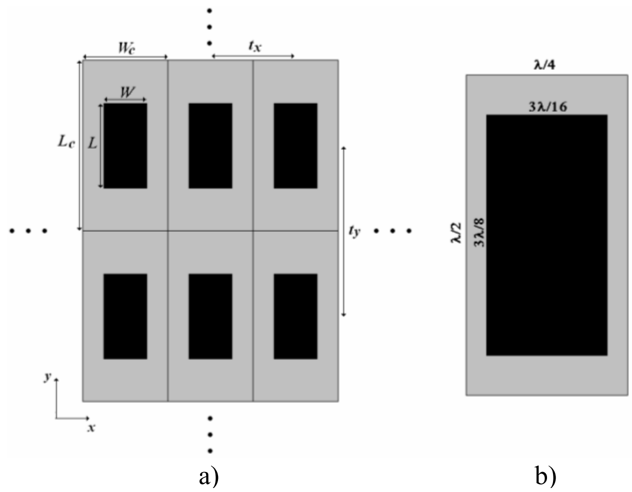

Fig. 1. (a) FSS with rectangular patch elements, (b) designed patch element dimensions.

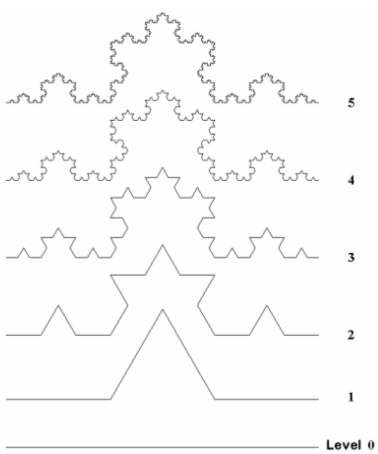

Fig. 2. Iterative construction of Koch fractal curves.

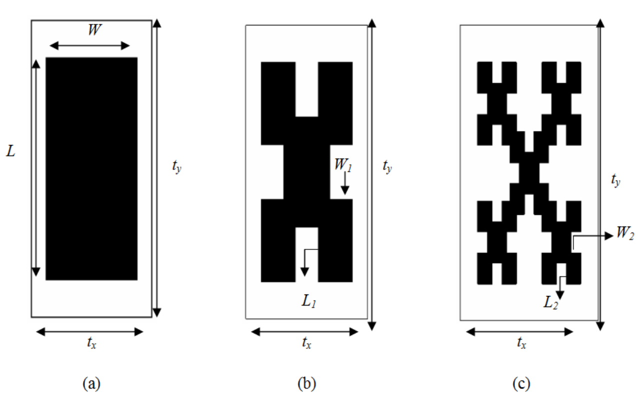

Fig. 3. Geometry of the FSS Koch fractal elements for $a = 3.5$, $t_x = 12.3238$ mm and $t_y = 24.6475$ mm: (a) level zero: $W = 9.2428$ mm; $L = 18.4856$; (b) level one: $W_1 = W/\mathrm{a} = 2.6408$ mm; $L_1 = L/\mathrm{a} = 5.2816$ mm; (c) level two: $W_2 = (W - W_1)/2a = 0.9431$ mm; $L_2 = (L - L_1)/2a = 1.8863$ mm.

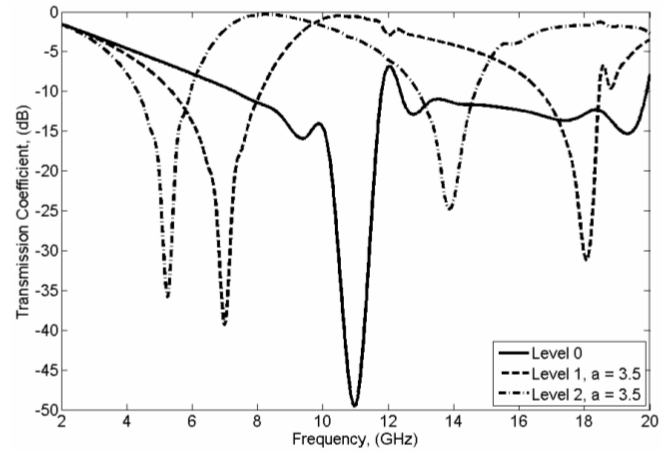

Fig. 4. Simulated results of the transmission coefficient for the prototypes illustrated in Fig. 3.

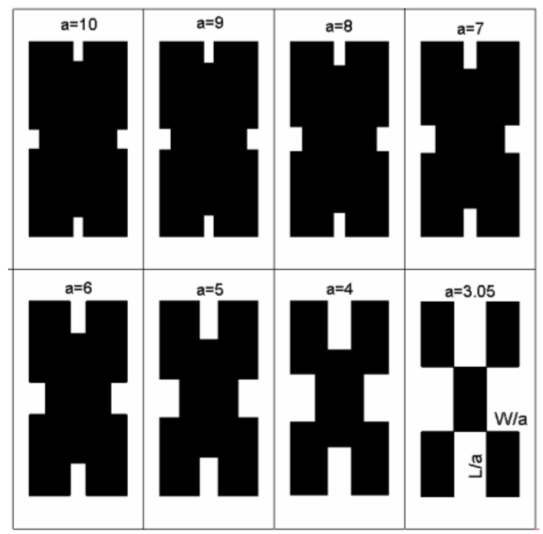

Fig. 5. Rectangular patch elements with different iteration factors.

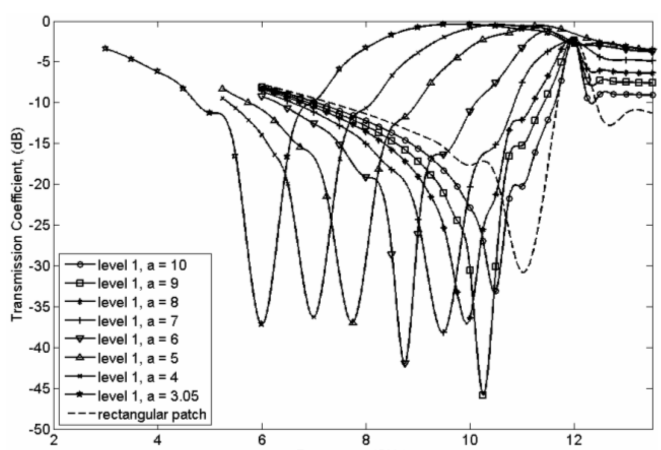

Fig. 6. Simulated results of the transmission coefficients of the fractal FSSs as a function of the frequency and the iteration factor.

TABLE I
VALUES OF THE SIMULATED RESONANT FREQUENCIES AND BANDWIDTHS, IN FUNCTION OF THE ITERATION FACTOR, FOR THE THREE LEVELS OF FRACTAL ELEMENTS.

Koch Fractal FSSs Level 0		
Iteration Factor (a)	f_{r1}(GHz)	BW (GHz)
0	10.99	4.500
Koch Fractal FSSs Level 1		
Iteration Factor (a)	f_{r1}(GHz)	BW (GHz)
3.05	6.01	2.190
3.5	6.99	2.740
4	7.73	3.190
4.5	8.25	3.550
5	8.75	3.820
7	9.93	4.450
9	10.46	4.570
Koch Fractal FSSs Level 2		
Iteration Factor (a)	f_{r1}(GHz)	BW (GHz)
3.05	4.75	1.410
3.5	5.24	1.630
4	5.51	1.780
4.5	5.76	1.900
5	6.00	2.000
7	6.71	2.330
9	7.18	2.550

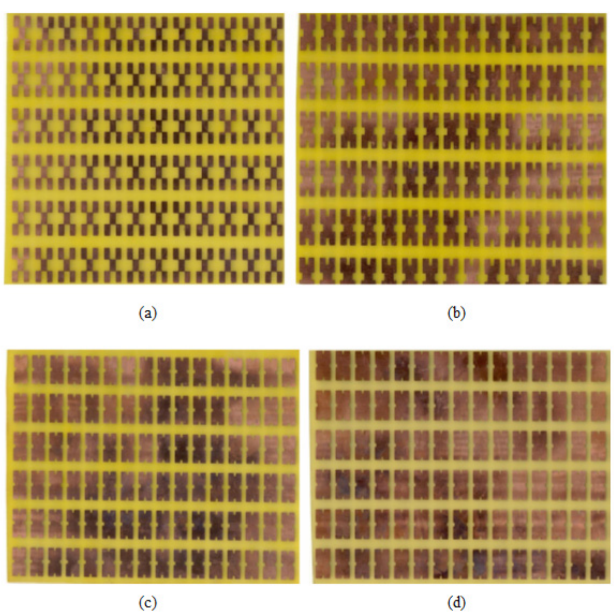

Fig. 7. Photographs of the fabricated fractal FSS prototypes with level one Koch fractal elements and different values of iteration factor: (a) a = 3.05; (b) a = 5; (c) a = 7; (d) a = 9.

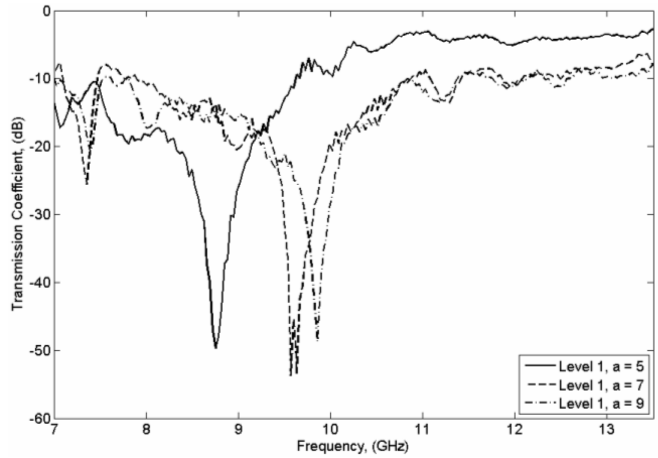

Fig. 8. Measured transmission coefficient (S_{21}) in dB of the fabricated FSSs prototypes with the level one Koch fractal elements and different values of iteration factor.

Analysis of Dielectric-loaded Cylindrical Cavity Using Nonuniform One Dimensional Finite Element Method

Salime Fazlali
Islamic Azad University of Qazvin, Qazvin, Iran
Salime_fazlali@yahoo.com

Mahmoud Mohammad-Taheri
Islamic Azad University of Qazvin, Qazvin, Iran
mtaheri@ut.ac.ir

Abstract--**In this paper we introduce a general, simple and powerful numerical method for the analysis and design of a dielectric-loaded cylindrical cavity. The method can be used for any number of dielectric resonators placed axisymmetrically in a metallic cylindrical cavity. The proposed method is a one dimensional nonuniform finite element method combined with H-vector variational formulation which is used to calculate the resonant frequencies and field amplitudes of all modes of dielectric-loaded cylindrical cavity. The results can be used in the design of microwave compact filters and multiplexers. The basis function is a first degree finite element function. In this method, the radial direction of the cavity is divided into number of elements and radial variations of the magnetic field components are expressed in term of first degree finite element polynomials in each element while axial variations of the field components are approximated by trigonometric functions. Due to concentration of the field inside the high dielectric constant material, we used more nodes with smaller element inside the dielectric to increase the accuracy of the method. Comparing the numerical results with those obtained with other well-known methods and measured data shows excellent agreement**

I. Introduction

Weight and volume are two critical factors in the design and construction of satellite transponder where the components should be kept as light as possible in order to reduce launching cost and increase satellite life. Due to use of many low losses metallic cavities for the realization of multiplexers and demultiplexers in the satellite transponder, reducing weight and volume of these filters are the main requirement in the design and construction of the transponder. As the size of each filter is inversely proportional to the $\sqrt{\varepsilon_r}$ which ε_r is relative dielectric constant of material filling the filter, the use of high dielectric constant resonators is growing. However for the filter using dielectric resonators, the analytical formula is not available and to find filter parameters, one should implement numerical methods. These material filling the filter, the use of high dielectric constant resonators is
growing. However for the material filling the filter, the use of high dielectric constant resonators is growing. For the filter using dielectric resonators, the analytical formula is not available and to find filter parameters, one should implement numerical methods. These methods are used to calculate field amplitude and resonant frequency of dielectric loaded cylindrical cavity(center frequency of the filter). Although for $TE_{01\delta}$ mode in dielectric loaded cylindrical cavity, the approximation methods such as magnetic wall [1] and dielectric waveguide [2] are widely used but the accuracy of these methods is not good enough for filter design.

II. Numerical Method

In this paper a simple, general and flexible method is introduced which can be used for the analysis of dielectric loaded cylindrical cavity. The work presented in this paper has originated from a need for a flexible but powerful method of determining all modes in cylindrical cavities loaded axisymmetrically with several dielectrics (Fig. 1).
Nonuniform one dimensional finite element method As we mentioned before, wave equation in a dielectric loaded cavity cannot be solved by analytical methods and to calculate the resonant frequencies and the amplitude of field components, the numerical methods has been implemented. Among these methods, the mode matching technique [3-5] becomes complicated when there are many dielectrics inside the metallic cavity and two dimensional finite element method [6] is not efficient when the dielectric extends all the way to the end plate of the metallic cavity, since in this case, field variation in the axial direction is sinusoidal and using finite element function in this direction is not necessary. However the method introduced in this paper has no any disadvantages associated with the mentioned numerical methods and can be easily used to analysis metallic cavity with any number of dielectric and any configuration.
To use this method, the structure in the radial direction of the cavity is divided into elements consisting of two nodes. A first degree polynomial with the value of 1 at n*th* node and zero at others (Fig. 2) is then associated with $N_n(r)$. Due to the concentration of field inside the dielectric, the element size inside it is smaller than that of taken outside the dielectric. In the other word, most of the nodes are taken inside the dielectric to more precisely approximate the field distribution inside it. Considering the above fact, the magnetic field basis functions are expressed as follows:

$$
\begin{aligned}
H_z &= \begin{bmatrix} \cos m\theta \\ \sin m\theta \end{bmatrix} \sum_{n=1}^{N} A_n N_n(r) \sum_{p=1}^{P} D_p \sin \frac{p\pi}{L} z \\
H_r &= \begin{bmatrix} \cos m\theta \\ \sin m\theta \end{bmatrix} \sum_{n=1}^{N} B_n N_n(r) \sum_{p=0}^{P-1} E_p \cos \frac{p\pi}{L} z \\
H_\theta &= \begin{bmatrix} \sin m\theta \\ \cos m\theta \end{bmatrix} \sum_{n=1}^{N} C_n N_n(r) \sum_{p=0}^{P-1} F_p \cos \frac{p\pi}{L} z
\end{aligned} \tag{1}
$$

Where L is cavity length and A_n, B_n and C_n are amplitude of finite element basis functions. N is the number of nodes taken in the radial direction and P is number of sinusoidal term in axial direction. If we take M node out of N node inside the dielectric resonator, the nonuniform finite element basis function outside the dielectric region ($k \geq M$) can be expressed as follows:

$$
\begin{aligned}
N_k &= -\frac{N-M}{b-a} r + \frac{N-M}{b-a} a + k - M + 1 \\
N_{k+1} &= \frac{N-M}{b-a} r - \frac{N-M}{b-a} a + k - M
\end{aligned} \tag{a-2}
$$

The basis function inside the dielectric ($k \leq M$) can also be expressed as follows:

$$
\begin{aligned}
N_k &= -\frac{M-1}{a} r + k \\
N_{k+1} &= \frac{M-1}{a} r - k - 1
\end{aligned} \tag{b-2}
$$

In the above equations, *a* and *b* are dielectric and metallic cavity radius respectively. In the uniform finite element method [7], the number of node inside dielectric, M, is obtained by the following equation:

$$M = (N-1)\frac{a}{b} + 1 \tag{3}$$

It means that if dielectric radius is small compared with cavity radius ($\frac{a}{b}$ is small), only few node will be located inside the dielectric. For example for *N*=101 and $\frac{a}{b} = 0.1$, then M=11, which means only 11 nodes out of 101 nodes are located inside the dielectric which considerably reduce the accuracy of the calculation. In addition we have to choose N such that M becomes integer in (3) and this is other limitation of using uniform finite element method. These disadvantages are eliminated in nonuniform finite element method in which M can be any arbitrary number.

Equations (1) can be simplified to the following equations:

$$
\begin{aligned}
H_z &= \begin{bmatrix} \cos m\theta \\ \sin m\theta \end{bmatrix} \sum_{n=1}^{N} \sum_{p=1}^{P} A_{np} N_n(r) \sin \frac{p\pi}{L} z \\
H_r &= \begin{bmatrix} \cos m\theta \\ \sin m\theta \end{bmatrix} \sum_{n=1}^{N} \sum_{p=0}^{P-1} B_{np} N_n(r) \cos \frac{p\pi}{L} z \\
H_\theta &= \begin{bmatrix} \sin m\theta \\ \cos m\theta \end{bmatrix} \sum_{n=1}^{N} \sum_{p=0}^{P-1} C_{np} N_n(r) \cos \frac{p\pi}{L} z
\end{aligned} \tag{4}
$$

Where $A_{np} = A_n D_p$, $B_{np} = B_n E_p$ and $C_{np} = C_n F_p$. Substituting (4) in the following H-vector variational formulation:

$$\omega_0^2 = \frac{\int_v (\overline{\nabla} \times \overline{H}) \varepsilon^{-1} (\overline{\nabla} \times \overline{H})^* dv + s \int_v \left| \overline{\nabla} . \overline{H} \right|^2 dv}{\int_v \mu \overline{H} . \overline{H}^* dv} \tag{5}$$

and minimizing the expression with respect to the field amplitudes by the following equations:

$$
\begin{aligned}
&\frac{\partial \omega_0^2}{\partial A_{np}} = 0 \qquad n = 0,1,2,...N \quad P = 1,2,...P \\
&\frac{\partial \omega_0^2}{\partial B_{np}} = 0 \qquad n = 0,1,2,....N \quad P = 0,1,...P-1 \\
&\frac{\partial \omega_0^2}{\partial C_{np}} = 0 \qquad n = 0,1,2,....N \quad P = 0,1,...P-1
\end{aligned} \tag{6}
$$

where integrals are performed over volume of the cavity, one can arrive to the following matrix equation:

$$\overline{A}\overline{x} = \lambda \overline{B}\overline{x} \tag{7}$$

Where $\lambda = \varepsilon_0 \mu_0 \omega_0^2$ is eigenvalue and $\overline{x}$ is eigenvector which is a vector containing field amplitudes $A_{np}\,(n = 1,..N, p = 1,..P')$, $B_{np}\,(n = 1,..N, p = 0,..P')$ a nd $C_{np}\,(n = 1,..N, p = 0,...P')$ where $P' = P - 1$.

This vector is a $3NP \times 1$ vector. $\overline{A}$ and $\overline{B}$ are $3NP \times 3NP$ square matrixes which due to the nature of finite element basis function are very sparse. The number of nonzero elements for matrix $\overline{A}$ is $9P^2(3N-1)$ and that of matrix $\overline{B}$ is $3P^2(3N-1)$. In other word for N=100, only 3% and 1% of matrix elements for $\overline{A}$ and $\overline{B}$ are respectively nonzero. This property considerably reduces computer time and memory. It should be mentioned that parameter s in (4) is used to eliminate the spurious modes which is inherent property of finite element method. Solving equation (6) one can calculate resonant frequencies, f_0 and field amplitudes of all mode for the dielectric loaded cylindrical cavity of Fig.1.

III. NUMERICAL RESULTS

Finite element methods gives upper limit to the resonant frequency of the cavity and by increasing the number of node, the result converge to the actual resonant frequency. Fig.3 shows the variation of the resonant frequency of TM_{030} versus M, the number of nodes taken inside dielectric.

As we can see, the resonant frequency converges to its actual value as M increases. To show the accuracy of the method we also calculated the resonant frequency of dielectric loaded cavity shown in Fig. 1 with $b = 1cm$, $\varepsilon_r = 37, h = L = 3cm$ and depicted in Fig. 4. For this figure all supporting dielectrics have dielectric constant equal to 1($\varepsilon_{r1} = \varepsilon_{r2} = \varepsilon_{r3} = \varepsilon_{r4} = \varepsilon_{r5} = 1$). In this figure variations of the resonant frequencies of first three modes versus filling factor (dielectric to cavity radius ratio) are depicted. The resonant frequencies corresponding to $\frac{a}{b} = 0$ and $\frac{a}{b} = 1$ refer to the resonant frequencies of empty and fully loaded cavity with dielectric resonator respectively which analytical solution for these frequencies exist. As it is clear from the figure, the resonant frequencies decrease by increasing the filling factor (for $\frac{a}{b} = 1$, the resonant frequency decreases by factor of $\sqrt{\varepsilon_r}$ with respect to empty cavity). Comparison is also made for Fig.1 with $\varepsilon_r = 36.2,\ l_1 = l_2$ and other references which are shown in table I ($\varepsilon_{r1} = \varepsilon_{r2} = \varepsilon_{r3} = \varepsilon_{r4} = \varepsilon_{r5} = 1$). As can be seen, the results obtained by the present method are in excellent agreement with both other references and measurement. Table II shows the comparison between the resonant frequencies of different modes calculated by presented method and those in other references for cylindrical cavity loaded with dielectric ring. As it is evidence, the results are in excellent agreement with other methods.

IV. CONCLUSION

In this paper a simple but general and flexible numerical method was presented for the calculation of all parameters of dielectric loaded cylindrical cavity. The method used one dimensional nonuniform finite element method which is capable of designing various dielectric loaded cavity microwave filters for systems in which weight and volume should be kept as low as possible. The accuracy of the method was verified by comparing the results with those obtained with well known numerical method and also measured data.

REFERENCE

[1] S.B Cohn, “Microwave band pass filter containing high-Q dielectric resonators”, IEEE, Trans. Microwave Theory Tech., vol. MTT-16, pp.218-227, 1968.

[2] Y. Kobayashi, “Mic application of dielectric resonator”, papers of technical group on microwaves, I.E.C. E. Japan. MW71-74, 1971.

[3] K. A. Zaki and A. Atia, “Modes in dielectric-loaded waveguide and resonators”, IEEE, Trans. Microwave Theory Tech., Vol. MTT-31, pp.1039-1044, 1983.

[4] S. Vigneron and P. Guillopn, “Mode matching method for determination of resonant frequency of a dielectric resonator placed in a metallic box”, Proc. Inst., Elec. Eng., pt. H., vol. 34, no.2, pp.152-155, 1987.

[5] Y. Kobayashi and M. Miura, “Optimum design for shielded dielectric rod and ring resonator for obtaining best mode separation”, IEEE MTT-S Int., Microwave Symp. Dig., pp. 184-186, 1984.

[6] J. B. Davies, F. A. Fernandez, and G. Y. Philippou, “Finite element analysis of all modes in a cavities with circular symmetry”, IEEE, Trans. Microwave Theory Tech., Vol. MTT-32, pp.922-928, 1984.

[7] M. Mohammad-Taheri and D. Mirshekar-Syahkal, “Accurate determination of modes in dielectric loaded cylindrical cavities using a one-dimensional finite element method”, IEEE, Trans. Microwave Theory Tech., Vol. MTT-37, pp.1536-1541, 1989.

[8] T. Itoh and R. Rudokas, “New method for computing the resonant frequencies of dielectric resonators”, IEEE, Trans. Microwave Theory Tech., Vol. MTT-25, pp.52-54, 1977.

[9] M. Jaworski and M. W. Pospieszalski, “An accurate solution of the cylindrical dielectric resonator problem”, IEEE, Trans. Microwave Theory Tech., Vol. MTT-27, pp.639-643, 1979.

[10] M. W. Pospieszalski, “Cylindrical dielectric resonators and their applications in TEM line microwave circuits”, IEEE, Trans. Microwave Theory Tech., Vol. MTT-27, pp.233-238, 1979.

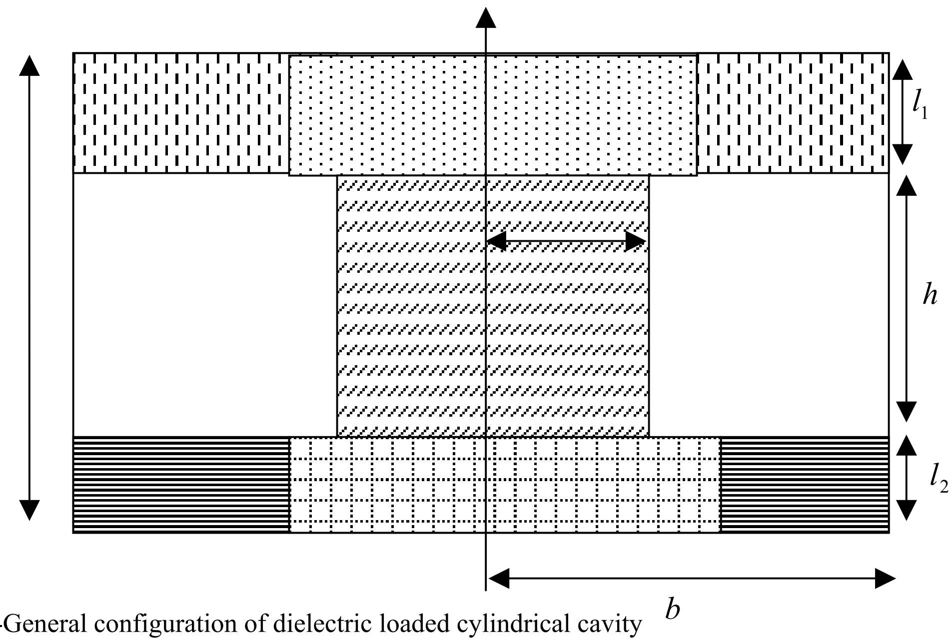

Fig. 1-General configuration of dielectric loaded cylindrical cavity

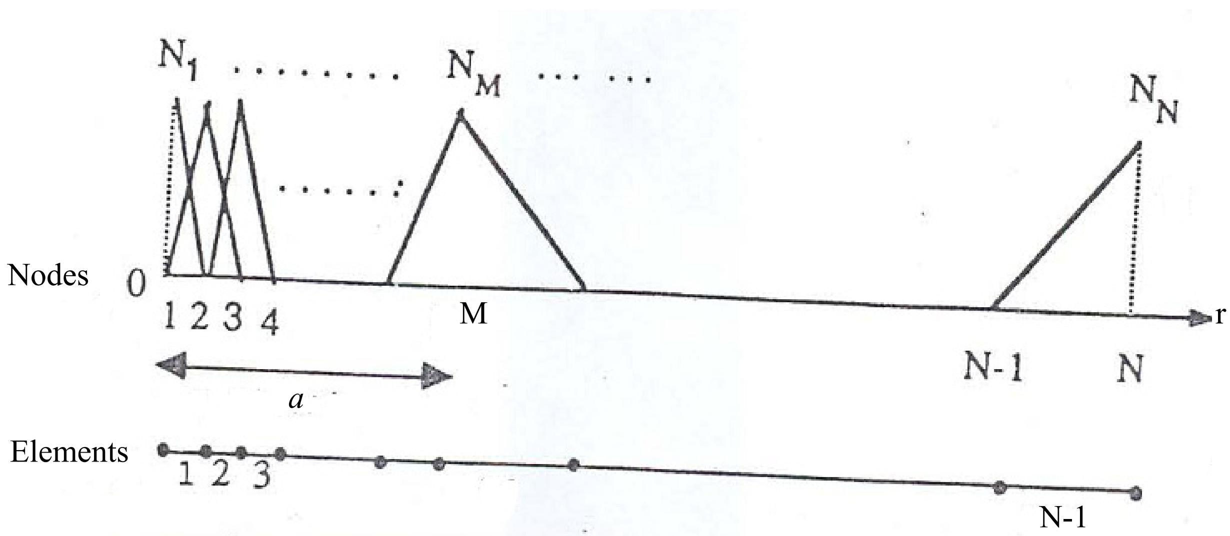

Fig.2-Discritizing radial direction of cavity into elements and defining finite element function

Table I
COMPARSION OF RESONANAT FREQUENCIES (GHz) CALCULATED BY THE PRESENT METHOD AND THOSE GIVEN IN [7-10] FOR TE_{01} MODE (CONVENTIONALLY KNOWN AS $TE_{01\delta}$) OF SEVERAL PARALLEL PLATE RESONATOR LOADED WITH SHORT CYLINDRICAL DIELECTRIC.

D(mm)	H(mm)	l_1/h	Ref[7] (GHz)	Ref[8] (GHz)	Ref[9] (GHz)	P.M (GHz)	Ref[10] (GHz) Measured
4.06	5.15	0.568	10.53	10.86	10.5	10.51	10.48
6.03	4.16	0.82	7.95	8.31	7.94	8.01	7.94
5.98	2.95	1.36	8.64	9.16	8.61	8.62	8.64
6.02	2.14	2.07	9.36	10.08	9.33	9.38	9.4
7.99	2.14	7.87	7.87	8.38	7.76	7.75	7.79

PM=Present Method

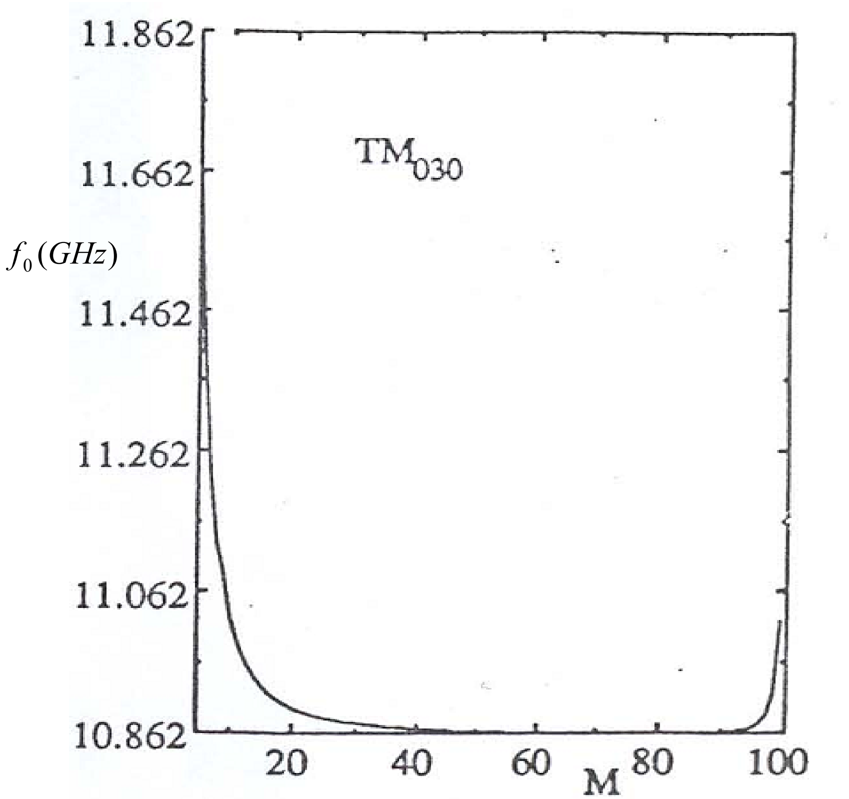

Fig 3. Variation of the resonant frequency of TM_{030} versus M, the number of the node taken inside dielectric

Table II
COMPARSION OF RESONANT FREQUENCY (GHz) CALCULATED BY PRESENT TECHNIQUE AND THOSE GIVEN IN [7] AND [11] FOR A CYLINDRICAL CAVITY LOADED WITH A DIELECTRIC RING.
$(\varepsilon_r = 37.5,\ h = 4.124mm,\ L = 6.124mm \quad d = 3.044mm,\ D = 9.051mm, b = 7.22mm,\ l_1 = l_2)$

Mode	Ref[7] (GHz)	Ref[11] (GHz)	P.M (GHz)
TE_{01}	6.64	6.64 ($TE_{01\delta}$)	6.63
TE_{02}	10.49	10.50 ($TE_{01\delta+1}$)	10.49
TM_{01}	8.42	8.38 ($TM_{01\delta}$)	8.36
HE_{11}	8.86	8.79($HE_{11\delta}$)	8.80
HE_{12}	9.84	9.78 ($EH_{11\delta}$)	9.82

D and d are outer and inner diameter of dielectric ring respectively. (PM=Present Method)

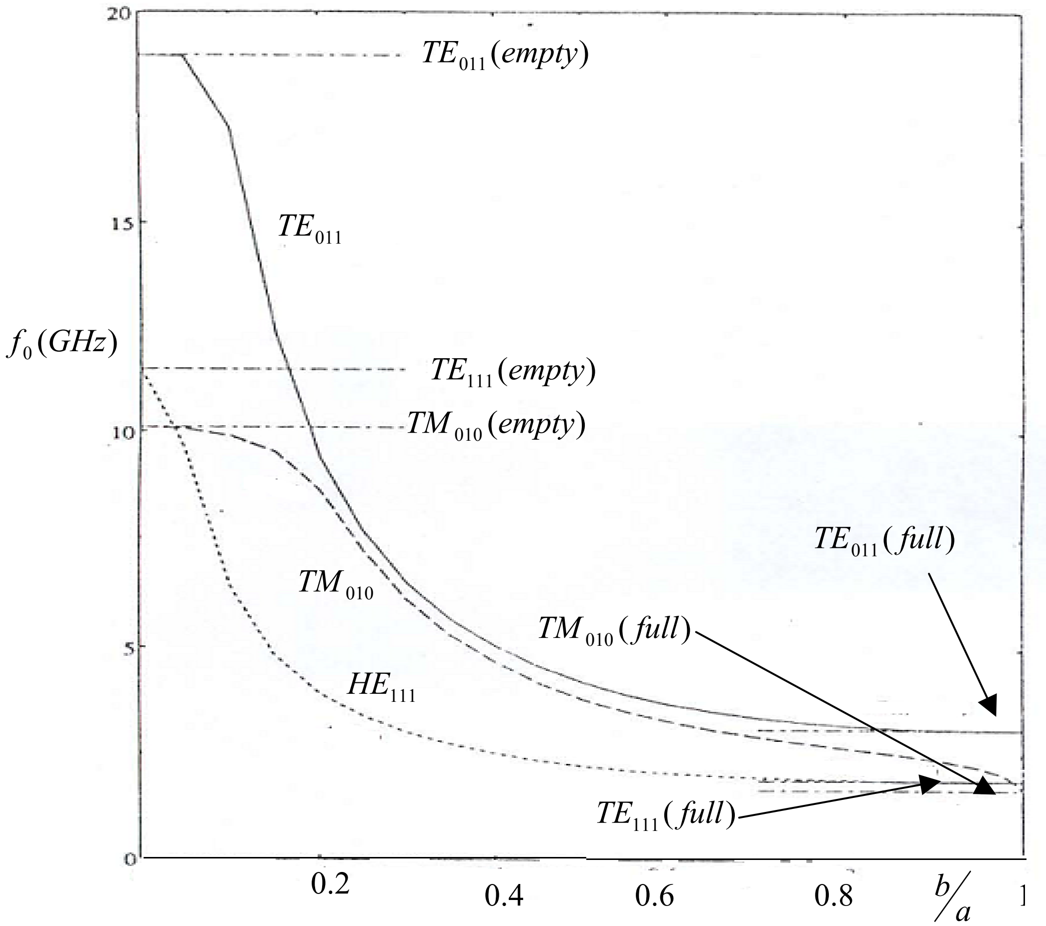

Fig.4. Variations of the resonant frequencies of TE_{011}, HE_{111} and TM_{010} versus filling factor

An adaptive RLE encoder to compress electrocardiograms

Cristiano Marcos Agulhari
Telematics Department
FEEC / P.O.Box 6101
University of Campinas - UNICAMP
13083-970, Campinas, SP, Brazil
agulhari@dt.fee.unicamp.br

Ivanil Sebastião Bonatti
Telematics Department
FEEC / P.O.Box 6101
University of Campinas - UNICAMP
13083-970, Campinas, SP, Brazil
ivanil@dt.fee.unicamp.br

Pedro Luis Dias Peres
Telematics Department
FEEC / P.O.Box 6101
University of Campinas - UNICAMP
13083-970, Campinas, SP, Brazil
peres@dt.fee.unicamp.br

***Abstract*— A compression method, based on the choice of a wavelet that matches the electrocardiogram to be compressed, is proposed in this paper. The scaling filter that minimizes the distortion of the compressed signal is used on the determination of the wavelet, being retained only the most significant coefficients of projection of the signal on the wavelet subspaces. The threshold for the selection of the most significant coefficients is obtained to satisfy a pre-specified distortion measure. The significant coefficients and the bitmaps of location in each wavelet subspace are encoded by applying a modified version of the Run Length Encoding technique using codewords whose lengths are adapted for each subspace. Several tests with electrocardiograms from the MIT-BIH database illustrate the efficiency of the method.**

***Index Terms*— Data compression, electrocardiogram signals, ECG, run length encoding, wavelet.**

I. Introduction

Multichannel electrocardiogram (ECG) signals provide the cardiologists with essential informations to diagnose heart diseases in a patient. In an ambulatory monitoring system, the volume of ECG data is necessarily large, as a long period of time is required in order to gather enough information about the patient [1]. With the crescent usage of the telemedicine [2], [3], [4], ECG data can be obtained remotely and transmitted to the proper destination. Therefore, an efficient scheme of data compression for the ECGs is a key component both for communication systems and for data storage. The compression methods can be divided into two categories: the lossless compression, in which the recovered signal must be identical to the original signal [5] and the lossy compression, in which the recovered signal may present a certain distortion when compared to the original signal [1], [6], [7].

Lossy compression schemes used in ECGs fall into one of two categories: direct and transform schemes. Among the transform schemes, the wavelet transform has been shown promising because of their properties of good location in the time and frequency domains. A good analysis and comparison among several compression methods is presented in [8].

Lossless compression methods can be used associated to the lossy ones since the encoding of the original data with as lesser number of bits as possible is essential to the good performance of the system. In the case of transform methods, the coefficients of representation of the signal in the transform domain that are not significant can be discarded, and the retained coefficients can be encoded and stored using lossless compression techniques like the Run Length Encoding (RLE) technique [9], which consists of identifying sequences of repeated symbols and representing such sequences by the number of occurrences of these symbols, instead of storing the entire sequence.

In [10] it is presented a good example of the association between lossless and lossy compression methods. The algorithm presented consists of first preprocessing the signal by applying it to a lowpass filter and a bandstop filter, in order to attenuate high frequency and baseline noises. The wavelet decomposition procedure is applied on the preprocessed signal using a fixed wavelet and the resultant coefficients are passed through a linear prediction filter. The errors of prediction are thresholded in a way that only the greatest absolute values are retained (lossy compression). The retained errors are then encoded with the bitmap that informs the positions of the retained error values. The encoding is performed using a modified Run Length Encoding (lossless compression).

The well-known compression algorithm called Set Partitioning in Hierarchical Trees (SPIHT), developed by Lu & Pearlman [1], presents good results and is used in a great number of recent papers to compare the performance of the recently proposed compression methods. The SPIHT algorithm is based on the wavelet transform and its main charateristic is on the encoding of the significant coefficients. The principles of this encoding are partial ordering of the transform coefficients by magnitude with a set partitioning sorting algorithm, which guarantees that the most significant coefficients are encoded first; ordered bit plane output, which guarantees that the output string can be truncated at any time without compromising the validity of the compreesion; and exploitation of self-similarity across different layers, which allows the encoding of the position of several non-significant coefficients using only a few bits.

The method proposed by Benzid *et al.* [6] is also based on the wavelet transform. The coefficients of representation of the ECG on the subspaces are obtained from the wavelet decomposition procedure using a fixed wavelet function. A great number of coefficients is so small that no significant modification is made in the shape of the signal when it is reconstructed by setting these coefficients to zero. Therefore, the retention of the coefficients that present an absolute value greater than a threshold results in a compression with a distortion controlled by the value of the threshold. the retained wavelet coefficients are quantized and encoded, along with the bitmap that informs the position of the retained coefficients, using the Two-Role Encoder method.

An improved version of the method presented in [6] is proposed in this paper. The wavelet is adapted to each ECG in order to minimize the distortion of the recovered signal, instead of using the same wavelet for every ECG. The significant wavelet coefficients are retained, quantized and encoded using a specific number of bits for each decomposition subspace associated to the chosen wavelet. The final string contains sequentially the encoded coefficients when the related coefficient is significant and the run length encoding of the zeros of the bitmap when a sequence of insignificant coefficients occurs.

The paper is organized as follows. Section II details the proposed method. The choice of the wavelet is explained in the Section III. Section IV presents the algorithms used for the retention, quantization and encoding of the wavelet coefficients. An example that shows some results of the application of the proposed method in an ECG is presented in the Section V. A series of experiments to compare the proposed method with the one presented in [6] and with the SPIHT is presented in the Section VI. The final considerations and the conclusion are presented in the Section VII.

II. Proposed Compression Method

The objective of the compression methods based on transforms, in the compression context, is to concentrate the energy of the signal into a small amount of transformed coefficients. Consequently, it is possible to discard the coefficients that are lower than a given threshold without affecting considerably the distortion of the reconstructed signal.

The proposed ECG compression method briefly consists of:

- *Pre-processing* of the ECG in order to attain a resulting signal with a zero mean, since in the ECG signals the important part is not the signal level but the time variation of the ECG waveform [11];
- *Choice of the wavelet* that results on the best ECG compression;
- *Selection of the significant wavelet coefficients* by retaining the coefficients with absolute values greater than a threshold. The threshold is determined by a bisection algorithm presented in the Section IV;
- *Quantization of the significant coefficients* using a specific number of bits for each subspace considered, as explained in the Section IV;
- *Encoding of the position of the significant coefficients*, defined by a bitmap constructed as the following: if the coefficient is significant then there is a correspondent 1 in the sequence, otherwise a 0 is used. The sequence is encoded along with the quantized values of the coefficients retained by the application of the method described in the Section IV.

The steps of the ECG decompression method consist of:

- *Decoding* the bitmap and the sequence of values of the retained coefficients;
- *Reconstruction of the ECG samples* by the wavelet reconstruction procedure. The values of the insignificant coefficients are equal to zero.

The Compression Ratio (CR) is defined by

$$CR = \frac{s}{c+h} \tag{1}$$

being s the total number of bits of the samples of the orignal ECG, c the total number of bits used to encode the final string (compressed signal) and h the length of the header containing the parameters necessary to reconstruct the signal.

The distortion of the reconstructed signal is measured by the Percent Root-mean-square Distortion (PRD) given by

$$\text{PRD} = \left(\sum_k (\nu_k - \hat{\nu}_k)^2\right)^{1/2} \left(\sum_k \nu_k^2\right)^{-1/2} \tag{2}$$

being ν_k the original signal without the mean value and $\hat{\nu}_k$ the reconstructed signal.

The compression ratio CR and the distortion measure PRD depends on the number of significant coefficients, on the wavelet, on the number of quantization levels and on the techniques used to encode the coefficients and the bitmap of location of the significant coefficients.

III. Choice of the Wavelet

A nonzero real function $\varphi(x)$ that can be expressed in terms of a weighted sum of shifted $\varphi(2x)$ as

$$\varphi(x) = \sum_k \ell_k \sqrt{2}\varphi(2x-k), \qquad k \in \mathbb{Z}, \quad x,\ \ell_k \in \mathbb{R} \tag{3}$$

is a scaling function, being ℓ_n the scaling filter [12]. The wavelet function is defined from the scaling function as

$$\psi(x) = \sum_k h_k \sqrt{2}\varphi(2x-k), \tag{4}$$

where h_n is the wavelet filter. The filter h_n can be obtained from the filter ℓ_n as

$$h_n = (-1)^n \ell_{m-n-1}, \tag{5}$$

where m is the order (number of coefficients) of the scaling and wavelet filters.

The fast-forward (decomposition procedure) and inverse (reconstruction procedure) wavelet transforms are implemented as tree-structured, perfect-reconstruction filter banks. The input signal is filtered by the analysis filter pair to generate low-pass and high-pass signals, which are then downsampled by a factor of two. This analysis filter pair is then applied to the downsampled low-pass signal recursively to generate layered wavelet coefficients, as shown in Equations (6) and (7), being $a_k[n]$ the coefficients of projection in the scaling subspace on the level k, $b_k[n]$ the coefficients of projection in the wavelet subspace on the level k, $*$ the convolution operator and $\{.\}_{\downarrow 2}$ the downsample operator.

$$a_{k-1}[n] = \{\ell_{-n} * a_k[n]\}_{\downarrow 2} \tag{6}$$

$$b_{k-1}[n] = \{h_{-n} * a_k[n]\}_{\downarrow 2}. \tag{7}$$

The decomposition procedure starts by considering that the coefficients of decomposition of the signal ν_n in the highest level $a_\eta[n]$ are equal to the samples of the signal, which means

$$a_\eta[n] = \nu_n. \tag{8}$$

To recover the original signal, i.e., for the discrete inverse transform, the lowest-frequency wavelet coefficients are upsampled by a factor of two (zeros are inserted between successive samples), filtered by the low-pass and high-pass synthesis filter and added together to produce the low-pass signal for the next layer, as shown in Equation (9), being $\{.\}_{\uparrow 2}$ the upsample operator.

$$a_k[n] = \ell_n * \{a_{k-1}[n]\}_{\uparrow 2} + h_n * \{b_{k-1}[n]\}_{\uparrow 2} \tag{9}$$

The number M_k of coefficients of $a_k[n]$ and $b_k[n]$, $k = \{0, \ldots, \eta - 1\}$ is given by

$$M_{k-1} = \left\lfloor \frac{M_k + m - 1}{2} \right\rfloor \tag{10}$$

with $M_\eta = N$, being N the number of samples of the original signal.

This process is repeated for all the subspaces until the original size of the signal is reached to complete the inverse transform. The selection of the different analysis-synthesis filter pairs, which correspond to the different wavelet bases, is very important for obtaining effective data compression, thus the choice of a wavelet basis that results on the better compression for a given signal is reduced to the problem of determining the proper scaling filter ℓ_n.

In order to determine the proper scaling filter, a set of constraints must be satisfied. Since there exists $m/2 + 1$ constraints applied to the scaling filter with m coefficients, there are γ degrees of freedom on the choice of ℓ_n, being γ given by

$$\gamma = \frac{m}{2} - 1. \tag{11}$$

Using the method described in [13], it is possible to express the scaling filter ℓ_n using a set of parameters θ in a way that the constraints applied to the scaling filter are embedded in the parametrization and the search for a satisfatory scaling filter becomes a search on the domain of the parameters.

The wavelet function that results on the better compression of an ECG is obtained by the resolution of the following optimization problem

$$\min_{\theta \in [0,\pi]^\gamma} \mathrm{PRD}(\theta) \tag{12}$$

The measure of distortion $\mathrm{PRD}(\theta)$ depends on the parameters θ since the shape of the reconstructed signal $\hat{\nu}$ is variant with the set of parameters θ used. In order to ease the notation, the measure of distortion will be denoted simply as PRD. Let $f_k[n]$ an orthonormal basis for the signal ν_n and c_k the coefficients of representation of the signal on the basis. The PRD in Equation (2) can be rewritten as

$$\left(\sum_r \left(\sum_k c_k f_k[r] - \sum_{k \in \mathcal{K}} c_k f_k[r] \right)^2 \left(\sum_r \nu_r^2 \right)^{-1} \right)^{1/2}, \tag{13}$$

being $\mathcal{K}$ the set of indexes of the retained coefficients whose reconstruction yields the signal $\hat{\nu}$. Since the functions $f_r[n]$ are orthonormal, Equation (13) becomes

$$\mathrm{PRD} = \left(1 - \sum_k \hat{\nu}_k^2 (\sum_k \nu_k^2)^{-1} \right)^{1/2}. \tag{14}$$

The PRD resulting from the compression using the wavelet and scaling functions resultant from the parametrization θ can be computed using the Equation (14) since the basis in this case is orthonormal. The PRD can also be directly calculated from the wavelet decomposition coefficients by the application of the Parseval Theorem, since

$$\mathcal{E} = \sum_k \nu_k^2 = \sum_k |c_k|^2 \quad , \quad \hat{\mathcal{E}} = \sum_k \hat{\nu}_k^2 = \sum_{k \in \mathcal{K}} |c_k|^2 \tag{15}$$

being $\mathcal{E}$ the energy of the original signal, $\hat{\mathcal{E}}$ the energy of the recovered signal from the wavelet subspaces and c_k the coefficients of projection, resulting in

$$\mathrm{PRD} = \left(1 - \sum_{k \in \mathcal{K}} |c_k|^2 (\sum_k |c_k|^2)^{-1} \right)^{1/2}. \tag{16}$$

The vector c_k is arranged in the following way:

$$c[n] = a_0[n], \quad 1 \le n \le M_0,$$
$$c\left[n + 1 + \sum_{r=0}^{k} M_r \right] = b_k[n], \quad 1 \le n \le M_k. \tag{17}$$

Since the PRD function is a non-convex function with several local minima, the optimization problem is solved using a sequential quadratic programming implemented by the function FMINCON in the Optimization Toolbox of Matlab [14]. It is necessary to provide the FMINCON function with an estimated starting point. In the implementation of the proposed method the parameters of four scaling functions are used as starting points: the parameters of the Haar scaling function, the parameters that generate the Daubechies scaling function with size m corresponding to the γ used and two random sets of parameters. The function FMINCON is executed for each starting point and the set of parameters that generates the lower PRD is stored.

The computation of the value of PRD in the optimization problem described by Equation (12) is described in the following steps:

1) Determine a retention ratio σ which will be constant for all the procedure;
2) Find, for a set of parameters θ, the coefficients of the scaling and wavelet filters;
3) Compute the resolution η by
$$\eta = \left\lfloor \log_2 \left(\frac{2(\rho - 1)}{m - 1} \right) \right\rfloor, \tag{18}$$
being ρ the number of samples of a beat pulse of the ECG. The value of η is an integer value calculated in order to produce a value of ρ approximately equal to κ (number of samples of the discrete version of the scaling function) given by
$$\kappa = (m - 1)2^{\eta - 1} + 1; \tag{19}$$
4) Decompose the ECG signal in η subspaces as described in Equations (6) and (7), compose the vector c_n as specified in Equation (17) and retain approximately K/σ coefficients, being K the total number of coefficients of decomposition obtained. The coefficients that are not significant are substituted by zero;
5) Compute the quadratic distortion PRD by using Equation (16).

In order to analyze locally the distortion of the compressed signal, the function of measure named Moving Average PRD (MAPRD) is proposed. The MAPRD$[n]$ measures the distortion between the samples n and $n + w$, being w the length of the window defined by the user, and is given by
$$\text{MAPRD}[n] = \left(1 - \sum_{k=n}^{n+w} \hat{\nu}_k^2 (\sum_{k=n}^{n+w} \nu_k^2)^{-1} \right)^{1/2}. \tag{20}$$

IV. Retention, Quantization and Encoding

After the choice of the wavelet filter that results on the better compression and the obtention of the coefficients from the decomposition procedure using the chosen wavelet filter, it is necessary to define a threshold to limit the coefficients in a way that only the coefficients whose values are greater than the threshold are retained, being the distortion of the signal reconstructed from the retained coefficientes compatible with the user-defined PRD (UPRD) within a certain tolerance ϵ. The Algorithm 1, based on the bisection algorithm presented in [6], shows the algorithm used to determine the threshold value.

Algorithm 1 $[T] = \text{Bisection}(c, \epsilon, UPRD)$
$PRD \leftarrow 100$; $T_{min} \leftarrow 0$; $T_{max} \leftarrow \max_n |c_n|$
while $|PRD - UPRD|/UPRD > \epsilon$ **do**
$T \leftarrow (T_{min} + T_{max})/2$
$\mathcal{K} \leftarrow \{\arg_k |c_k| \geq T\}$
$PRD \leftarrow (1 - \sum_{k \in \mathcal{K}} |c_k|^2 (\sum_k |c_k|^2)^{-1})^{1/2}$
if $PRD < UPRD$ **then** $T_{min} \leftarrow T$ **else** $T_{max} \leftarrow T$
end while

The retained wavelet coefficients are quantized using the quantization method proposed in this paper, which consists of defining a number of quantization bits different for each subspace considered. The amplitude of the coefficients usually changes significatively depending on the subspace, so a lesser number of bits is needed to quantize the coefficients with lower amplitudes, whose usually occur in the higher resolution subspaces, to yield approximately the same quantization error.

In the proposed quantization, the number q_n of bits used to quantize the n-th subspace is equal to the minimum number of bits that causes a distortion on the recovered signal lower than the UPRD within a tolerance ϵ_q. The distortion caused by the quantization of one subspace is calculated by reconstructing the signal using the quantized coefficients of the subspace analyzed along with the retained non-quantized coefficients from the remaining subspaces. This procedure is repeated for all the subspaces.

The quantized coefficients must be stored with the bitmap that informs the position of the retained coefficients. In the bitmap, if a coefficient is retained then the respective bit is changed to 1, otherwise it is kept as a 0. In this paper a new method to encode both the quantized coefficients and the bitmap is proposed and consists of the following steps:

1) For each subspace, do the following procedure:
   a) If there exists more ones than zeros in the bitmap, return a bit 1 and invert the values of the bitmap in the current subspace. Otherwise, return a bit 0;
   b) Construct a vector v that contains the lengths of the sequences of consecutive zeros. The number of bits used to encode each sequence in the current subspace is given by
   $$q_z = \lfloor \log_2(\text{mean} + \text{std}) \rfloor, \tag{21}$$
   being "mean" and "std" the mean and the standard deviation of the vector v, respectively. The sequence of zeros that appears after the last significant coefficient (considering all the coefficients of all the subspaces) is not considered in the calculation of q_z;
   c) Insert in the output string the value q_z using a fixed number of bits (usually three bits);
   d) Analyze the sequence of bits related to the current subspace: if a bit 1 occurs, insert in the output string a bit 1 and the quantized value of the wavelet coefficient related to this position; if a bit 0 occurs, insert in the output string a bit

0 and the length of the sequence of consecutive zeros, using q_z bits, that starts with this bit 0.

The algorithm continues until the last significant coefficient is inserted into the string, since the sequence of zeros that occurs after the last significant coefficient does not need to be encoded and stored. It is necessary to store not only the output string but also the header that contains the information needed to reconstruct the signal. The header is composed by the following informations:

- The values of the parameters θ, each parameter stored using 11 bits;
- The number of bits of quantization q_n used in each subspace, encoded using 4 bits;
- The absolute value of the smaller coefficient and the quantization step considered in each subspace, both stored with 11 bits.

V. Example

In this section the results of the application of the proposed compression method are presented and analyzed for the ECG from the MIT-BIH database of signals of arrythmia [15] correspondent to 2 minutes (43202 samples) of the signal identified as 117. The considered signal presents 100 beat pulses and approximately 433 samples per beat, being decomposed in $\eta = 6$ subspaces. The specified distortion is $UPRD = 4\%$, the tolerance of retention is $\epsilon = 1\%$ and the tolerance of quantization is $\epsilon_q = 10\%$. Figure 1 shows part of the original and recovered signals that contains the window with worst MAPRD, which is also presented in the figure. The window length used is $w = 433$, equal to the approximate number of samples per beat. Note that even in the window where the distortion is greater the recovered signal presents a low distortion when compared to the original signal.

Table I shows the results obtained from the application of the proposed method on the signal 117. Note that the percentage of the retained coefficients and of the retained energy decrease as the resolution of the subspaces increase, implying on the increasing of the frequency of occurrence of zeros in the bitmap. Such increasing can also be observed by the analysis of the number of bits used to represent the lengths of the sequences of zeros in the subspaces. Note that the bits are inverted in the first three subspaces, therefore the number of zeros in these subspaces is very small and this number increases as the other subspaces are analyzed. The increasing on the number of bits used to represent the sequences of zeros is a direct consequence of the increasing of the mean length of the sequences of zeros and, consequently, of the increasing of the frequency of occurence of these zeros. At last, the number of bits of quantization of the retained coefficients presents a little deviation for the first five subspaces and decreases considerably in the last two subspaces, which means that the amplitude of the coefficients of the last two subspaces is lower and such coefficients can be represented by a fewer bits. The decreasing of the amplitude of the coefficients on the last two subspaces can also be observed by the analysis of the values of the mean the of the standard deviation of the retained coefficients and by the analysis of the percentage of the retained energy. Such feature is not considered in the method presented in [6], in which the number of bits of quantization is constant for all the coefficients considered.

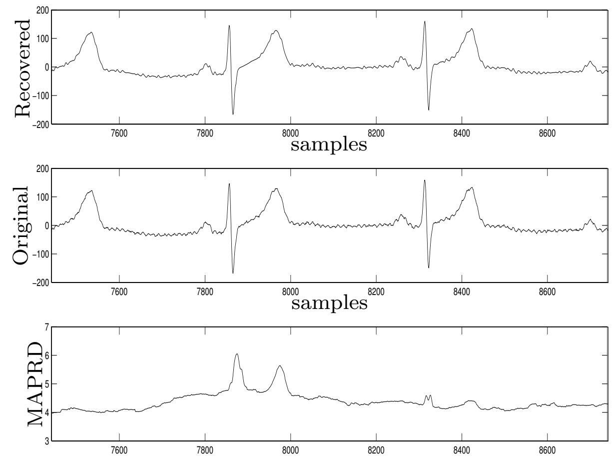

Fig. 1. Part of the recovered (top) and original (middle) signal of the electrocardiogram number 117 of the MIT-BIH database. The part shown contains the window of worst MAPRD, which is presented in the bottom. The worst value of MAPRD occurs for the window starting at the sample 7875.

VI. Numerical Experiments

In this section, the proposed method is compared with the Two-Role Encoder (TRE) [6] and the SPIHT [1]. Eleven different arrythmia ECG signals (43202 samples each) from the MIT-BIH database [15] are used in the experiments, being these eleven signals the ones used in the experiments performed by [6]. In the proposed method it is used the tolerances $\epsilon = 1\%$ and $\epsilon_q = 10\%$ as used in [6], the signals are decomposed into $\eta = 6$ wavelet subspaces and the number of coefficients of the scaling and wavelet filters is $m = 10$, implying in $\gamma = 4$ parameters. The SPIHT algorihtm is implemented by segmenting the signal into segments of 1024 samples and applying the SPIHT compression into each segment, the wavelet used is the biorthogonal bior4.4 wavelet whose scaling and wavelet analysis filters present lengths $m = 9$ and $m = 7$, respectively, and the signal is decomposed into $\eta = 6$ wavelet subspaces. In the TRE algorithm the wavelet bior4.4 is used, the signal is decomposed into $\eta = 6$ wavelet subspaces and the values of tolerance used are $\epsilon = 1\%$ and $\epsilon_q = 10\%$. The user-defined PRD is UPRD = 4% for all cases.

The values of the compression ratio obtained using the proposed and the TRE methods are presented in the Figure 2 and the Figure 3 shows the values of the compression ration obtained using the proposed and the SPIHT methods. In these figures each point represents the CR resultant from the application of both methods in one ECG and each point

TABLE I
RESULTS OF THE PROPOSED METHOD: SIGNAL 117 MIT-BIH.

Subspace	a_0	b_0	b_1	b_2	b_3	b_4	b_5
Number of coefficients	683	683	1358	2708	5408	10807	21605
Percentage of the retained coefficients	97,80	92,24	70,77	43,35	50,94	4,26	0,001
Percentage of the retained energy	99,99	99,99	99,96	99,89	99,00	66,57	0,75
Mean of the absolute value of the retained coefficients	213,77	83,17	54,49	25,28	10,12	0,55	0,001
Standard deviation of the absolute value of the retained coefficients	181,24	86,37	75,82	68,79	24,38	2,81	0,12
Bits of quantization	8	6	7	8	7	2	1
Mean of the sequences of zeros in the bitmaps	41,75	13,12	6,81	3,57	1,94	8,95	9,27
Standard deviation of the sequences of zeros in the bitmaps	45,64	11,55	3,74	3,21	1,50	24,98	28,19
RLE bits in the bitmaps	6	4	3	2	1	5	5
Inversion of the bits in the bitmaps	Yes	Yes	Yes	No	Yes	No	No
Percentage of retained coefficients	15,38						
Compression Ratio (CR)	7,92						
Distortion (PRD)	4,07 %						

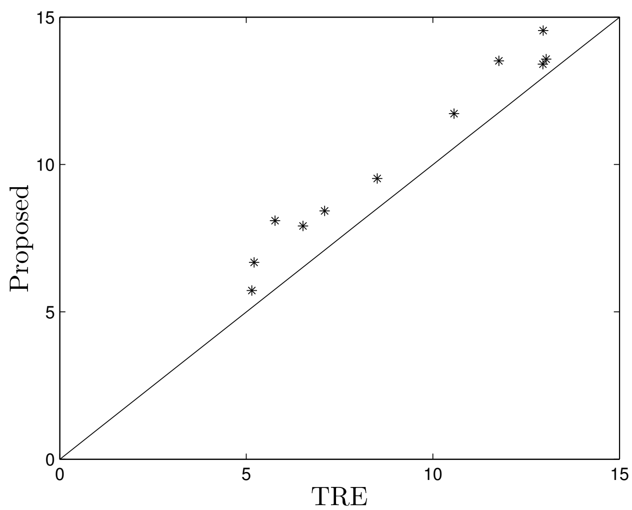

Fig. 2. Compression ratios from the proposed method and from [6] for eleven electrocardiogram arrythmia signals.

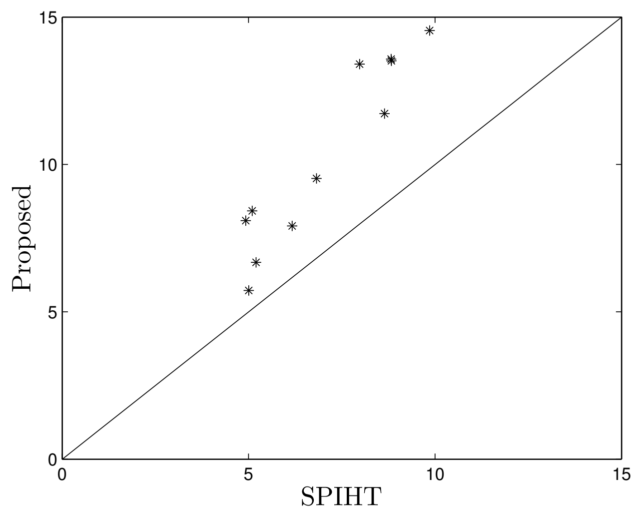

Fig. 3. Compression ratios from the proposed method and from [1] for eleven electrocardiogram arrythmia signals.

above the line means that the proposed method yielded a better result, which is the case for all the signals considered.

VII. Conclusion

An electrocardiogram compression method, composed by three main steps, has been proposed in this paper: i) adaptive choice of the wavelet that better fits to the signal; ii) selection of significant coefficients that satisfies a pre-established distortion measure; and iii) Run Length Encoding method adapted for each wavelet subspace. Numerical experiments were conducted in order to compare the proposed method with the Two-Role Encoder [6] and with the classical SPIHT [1]. The experiments have shown that the method proposed in this paper presents a superior performance when compared to the other two methods for all the signals analyzed.

References

[1] D. Y. K. Z. Lu and W. A. Pearlman, “Wavelet Compression of ECG Signals by the Set Partitioning in Hierarchical Trees Algorithm,” *IEEE Transactions on Biomedical Engineering*, vol. 47, no. 7, pp. 849–856, July 2000.

[2] Y. Choi, J. Krause, H. Seo, K. Capitan, and K. Chung, “Telemedicine in the USA: standardization through information management and technical applications,” *Communications Magazine, IEEE*, vol. 44, no. 4, pp. 41–48, April 2006.

[3] B. Gonçalves, J. G. P. Filho, R. V. Andreão, and G. Guizzardi, “ECG Data Provisioning for Telehomecare Monitoring,” *23rd*

ACM Symposium on Applied Computing - ACM SAC 2008, Fortaleza, Brazil, pp. 1374–1379, 2008.

[4] R. Komiya, "A proposal for telemedicine reference model for future standardization," *Enterprise networking and Computing in Healthcare Industry, 2005. HEALTHCOM 2005. Proceedings of 7th International Workshop on*, pp. 224–228, 23-25 June 2005.

[5] J. A. Storer, *Data compression: methods and theory.* New York, NY, USA: Computer Science Press, Inc., 1988.

[6] R. Benzid, F. Marir, and N.-E. Boughechal, "Electrocardiogram compression method based on the adaptive wavelet coefficients quantization combined to a modified two-role encoder," *IEEE Signal Processing Letters*, vol. 14, no. 6, pp. 373–376, June 2007.

[7] R. M. R. Silveira, C. M. Agulhari, I. S. Bonatti, and P. L. D. Peres, "Compressing electrocardiogram signals using parameterized wavelets," *23rd ACM Symposium on Applied Computing - ACM SAC 2008, Fortaleza, Brazil*, pp. 1348–1352, 2008.

[8] S. M. S. Jalaleddine, C. G. Hutchens, R. D. Strattan, and W. A. Coberly, "ECG data compression techniques - A unified approach," *IEEE Transactions on Biomedical Engineering*, vol. 37, pp. 329 – 343, April 1990.

[9] S. Golomb, "Run-length encoding," *IEEE Transactions on Information Theory*, vol. IT-12, pp. 399 – 401, 1966.

[10] A. Al-Shrouf, M. Abo-Zahhad, and S. M. Ahmed, "A novel compression algorithm for electrocardiogram signals based on the linear prediction of the wavelet coefficients," *Digital Signal Processing*, vol. 13, pp. 604–622, 2003.

[11] A. Alshamali and A. S. Al-Fahoum, "Comments on "An efficient coding algorithm for the compression of ECG signals using the wavelet transform"," *IEEE Transactions on Biomedical Engineering*, vol. 50, no. 8, pp. 1034 – 1037, Aug. 2003.

[12] I. Daubechies, *Ten Lectures on Wavelets*, 8th ed. Society for Industrial amd Applied Mathematics, 1992.

[13] R. M. R. Silveira, C. M. Agulhari, I. S. Bonatti, and P. L. D. Peres, "Compressão de sinais de eletrocardiogramas com *wavelets* determinadas por otimização genética," *Simpósio Brasileiro de Telecomunicações - SBrT 2007, Recife, Brasil*, 2007.

[14] J. R. Buck, M. M. Daniel, and A. C. Singer, *Computer Explorations in Signals and Systems Using MATLAB®*, 2nd ed., ser. Signal Processing. Prentice Hall, 2002.

[15] A. L. Goldberger, L. A. N. Amaral, L. Glass, J. M. Hausdorff, P. C. Ivanov, R. G. Mark, J. E. Mietus, G. B. Moody, C.-K. Peng, and H. E. Stanley, "PhysioBank, PhysioToolkit, and PhysioNet: Components of a new research resource for complex physiologic signals," *Circulation*, vol. 101, no. 23, pp. 215–220, June 2000.

Performance Evaluation of Fundamental Frequency Estimation Algorithms

Tiago Fernandes Tavares
Department of Communications
School of Electrical and
Computer Engineering
State University of Campinas
Unicamp - Campinas - SP - Brazil
tavares@decom.fee.unicamp.br

Jayme Garcia Arnal Barbedo
Department of Communications
School of Electrical and
Computer Engineering
State University of Campinas
Unicamp - Campinas - SP - Brazil
jgab@decom.fee.unicamp.br

Amauri Lopes
Department of Communications
School of Electrical and
Computer Engineering
State University of Campinas
Unicamp - Campinas - SP - Brazil
amauri@decom.fee.unicamp.br

***Abstract*— A method for evaluation of the performance of fundamental frequency estimation algorithms is proposed. The method determines the minimum signal-to-noise ratio (SNR) necessary for given frequency estimation algorithm to work properly and also provides the accuracy of the estimates. Therefore, the proposed method allows one to determine if a given frequency estimation algorithm is adequated for a specific application, taking into account the available SNR and the precision requirements.**

***Index Terms*— digital signal processing, fundamental frequency, performance evaluation.**

I. Introduction

Fundamental frequency (F0) is the inverse of the fundamental period, which is defined as the shortest shift in time that makes a signal invariant [1]. F0 is closely related to the psychoacoustic phenomenon of pitch, which is the property of sounds that allow them to be ranked in a scale that goes from bass to treble [2]. Pitch allows, for example, distinction between musical notes or between some prosodic speech intonations like exclamation (“Hello!”) and interrogation (“Hello?”). Non-audio applications may also benefit from F0 detection. For example, it may be used as a part of a control system for heavy machinery whose movement is kept at a certain rate.

F0 detection is, today, a well known problem. Many algorithms are capable of detecting the F0 of a signal, each adapting to different conditions regarding precision, stability and noise robustness. Most algorithms model periodic signals as a sum of N sinusoidal waves, called *partials*, each presenting its own amplitude A_n, phase ϕ_n and frequency nF0:

$$S(t) = \sum_{n=1}^{N} A_n \cos(nF0t + \phi_n). \quad (1)$$

It is noticeable that different applications often demand F0 detection to be performed on signals presenting different signal-to-noise ratios (SNR) or to provide different precision levels. For example, it is usually accepted that music transcription requires F0 detection with a relative deviation lesser than 2.98%, which is equivalent to half the frequency difference between two consecutive notes, while automatic instrument tuners require a much more accurate estimate.

The choice of the correct F0 estimation algorithm for each application has motivated comparative studies. Santamaria [3] compared F0 estimation methods aiming applications on machine control, like vibration analysis on hydroelectric turbogenerators. The tested algorithms were executed over synthesized harmonic signals (as the model in Expression 1) containing white noise. Manfredi [4] analyzed algorithms for pitch estimation on pathological voices. Evaluation was performed in both synthesized and real signals, and some modifications in the studied methods were proposed in order to improve performance for voice analysis applications. DeCheveigné [5] proposed a comparative study of F0 estimators in the context of speech analysis. Tested algorithms were executed over a speech database, and a comparison between a reference and the estimation determined the relative error. Later, each estimation is classified as gross error (over 20%) or fine error (under 20%).

The results provided by previous work are bounded to specific requirements and may not be used for different applications. Also, such results are unable to show what are the condition under which a certain algorithm fails.

This article presents a method that performs objective evaluation of the effects of noise in F0 detection algorithms assuming that requirements regarding, for example, signal models and observation time, have been met. For example, a signal containing a unpitched sound will certainly lead to errors, and, therefore, should not be used. This means that all tested algorithms should work for the signals provided. The presented method allows not only the classification of results as “right” and “wrong”, but also makes evident the precision and the noise resilience of tested algorithms for frequencies in a suitable range. This means that applications with different requirements may benefit from the same results, as it will be shown.

II. Proposed method

The evaluation method is based on a scrutinization on both frequency and noise parameters, aiming the analysis of the effect of additive noise on the accuracy of F0 detection algorithms. It begins multiplying a noise-free signal $S(t)$ with known F0 and length T by a descending ramp, granting full amplitude on the beginning and null amplitude at the end. Then, a noise (white or colored) signal $\Phi(t)$ with known power is multiplied by an ascending ramp, granting null amplitude at the beginning and full amplitude at the end. Next, both signals are summed. This generates a test signal $\hat{S}(t)$:

$$\hat{S}(t) = S(t)(1 - \frac{t}{T}) + \Phi(t)\frac{t}{T}. \quad (2)$$

It may be observed that, when $t \to 0$, Expression 2 is very close to the noise-free signal $S(t)$. This is especially true for large T. Then, the SNR gradually decreases and, when $t \to T$, the test signal is very close to $\Phi(t)$.

The F0 detection algorithm analyzes $\hat{S}(T)$ over time (in a framewise basis, if necessary). It is expected that, at some point, the algorithm will fail due to the low SNR presented by $\hat{S}(t)$. By failure, we mean that the detected F0 will deviate from the expected F0 value (which may be either a manual input or the F0 detected by the tested algorithm on the clean signal $S(t)$) by more than a pre-defined tolerance P_{max}, which is left as a parameter, since requirements for different applications may vary. The SNR at the failure point is defined as the noise resilience of the algorithm at the expected F0, or $N(f)$. The process is repeated for many F0 values, defining as many $N(f)$ values as needed. Also, the average error $E(f)$ (for SNR above the estimated noise resilience) is calculated.

Together, $N(f)$ and $E(f)$ provide information about how precise is the estimate provided by the tested algorithm, and under which conditions this estimate may be considered correct.

III. Validation tests and results

Aiming both validation and to provide an example on how to analyze results, the method is used to evaluate the performance of three algorithms commonly found in audio applications. The first one is the classic autocorrelation (ACC) algorithm [6], which is known for its speed and reliability. The second one is the Yin method [1], which is based on an improved analysis of the square difference between the input signal and a shifted version of itself. Last, a recent method (FDA, [7]) based on heuristic analysis of the frequency domain version of the signal is also tested. These three methods are briefly explained below. White, Gaussian noise signal, equivalent to the “hiss“ noise produced by most audio equipments, was used in the process as the noise signal $\Phi(t)$. The error tolerance was 5.9%, keeping consistency with a semitone (one key of a piano) error.

A. Autocorrelation (Acc)

Autocorrelation is the base for many F_0 estimation methods, as may be noticed in [6], and it is well known for its speed and reliability.

The autocorrelation function of a given signal $X[n]$ with length N is calculated by Expression 3.

$$R_{xx}[k] = \sum_{n=1}^{N} x[n]x[n-k]. \quad (3)$$

The autocorrelation function $R_{xx}[k]$ is a measure of the likelihood of the signal $x[n]$ and the signal $x[n-k]$. Therefore, $R_{xx}[T_0]$, where T_0 is a fundamental period of $x[n]$, is a local maxima.

Heuristic search may be performed to retrieve the index k_m of a local maxima of $R_{xx}[k]$ that corresponds to a fundamental period of $x[n]$. In addition, in order to reduce time quantization error, $R_{xx}[k_m]$ is interpolated together with its immediate neighbors to a parabola. The x-coordinate of the maxima of the interpolated parabola is assumed as the fundamental period of $x[n]$.

B. The Yin method (Yin)

The Yin method [1], presented in 2002 aiming speech analysis, is based on the same time-shifting principle of the autocorrelation. However, instead of calculating the likelihood between $x[n]$ and $x[n-k]$, it calculates the quadratic difference funcion using Expression 4.

$$D[k] = \sum_{n=1}^{N} (x[n] - x[n-k])^2. \quad (4)$$

Next, the difference function normalized by the cumulative mean is calculated using Expression 5.

$$D'[k] = \begin{cases} 1 & \text{if } k = 0 \\ \frac{D[k]}{\frac{1}{k}\sum_{i=1}^{k} D[i]} & \text{if } k > 0 \end{cases}. \quad (5)$$

The algorithm searches, then, for the first local minima of $D'[k]$ below a threshold, which, in this work, was set to 0.05. This local minima is then used in parabolic interpolation, together with its immediate neighbors, in order to minimize time quantization errors. The x-coordinate of the minima of the interpolated parabola is assumed as the fundamental period of $x[n]$.

C. Frequency domain analysis (Fda)

The Discrete Fourier Transform of a harmonic signal as described by Expression 1 presents magnitude peaks corresponding to the frequencies of its partials. This motivated an inference process [7] that begins with the estimation of a list of peaks, containing amplitudes and frequencies. In this work, the frequency of a peak was estimated with the derivative method studied in [8].

The F0 estimation begins with the assumption that the peak with the greatest amplitude is part of the harmonic series. Thus, if such a peak corresponds to the frequency F_x, the candidates for fundamental frequencies are F_x, $\frac{F_x}{2}$, $\frac{F_x}{3}$ and so on. Each candidate generates a harmonic series candidate H_k and the amplitude of its n-th harmonic is referred as $H_{n,k}$.

After that, the remaining peaks are sorted by descending amplitude. Each peak is assigned to the candidate harmonic series in the most proper position, observing that a peak may only be assigned to an open position if its frequency does not deviate from the expected frequency by over 5.95%, which corresponds to the interval of one semitone. This means that $H_{n,k}$ will be zero in some positions if no peak fits this condition.

Then, it is necessary to calculate which harmonic series candidate is the best estimate. Each harmonic series has its salience calculated by the sum of the amplitude of its k partials, weighted by the function described in Expression 6. The weighting function (Expression 7) attenuates the amplitudes of higher partials according to the psycho-acoustic model of Expression 8.

$$E(n) = \sum_{k=1}^{K} H_{k,n} W(k). \tag{6}$$

$$W(i) = \left\{ \begin{array}{rl} 1 & \text{if } i \leq 4 \\ z(i) - z(i-1) & \text{if } i > 4 \end{array} \right. . \tag{7}$$

$$z(n) = log_{2^{1/3}} \left\{ n \sqrt{\frac{n+1}{n}} \right\}. \tag{8}$$

The F0 corresponding to the harmonic series with the greatest salience is chosen as the best estimate.

Results provided by the method show that the evaluated algorithms present different behavior regarding noise resilience and average error. Figure 1 shows the results obtained from the application of the method on synthesized sinusoidal signals of different frequencies ($S(t) = sin(2\pi f t)$). Figures 1(a) and 1(b) show the results using as reference the synthesized sinusoid frequency. Figures 1(c) and 1(d) show the results using as reference the clean signal estimate of each algorithm.

Figure 1 shows that although the FDA method provides the most accurate F0 estimate (less than 0.1% average error), it is also the less resilient to noise, providing unreliable results when the SNR is less than 25dB, considering most of the frequency range. The ACC algorithm shows opposite behavior: a good noise resilience implies in a large average error.

Figures 1(c) and 1(d) are especially important when dealing with accoustic signals. It is usually not possible to generate an acoustic recording that presents an accurate, pre-defined F0. Also, it is a reasonable assumption that the F0 detected by an algorithm in a clean signal is the best possible estimate that the algorithm may obtain. Therefore, failure on the F0 detection must be calculated using as base the F0 detected on the clean signal $S(t)$.

By similar observations, the presented method allows to determine the lowest levels for the SNR below which the results provided by a given estimation algorithm may not be trusted for an specific application. The results in Figure 1 show that an automatic music transcription device, which aims to obtain a list of notes that compose a musical piece, should operate on a signal presenting SNR greater than 20dB if operating with the Yin algorithm, or greater than 30dB if operating with the FDA algorithm. The method also allows to conclude that, if a high SNR is obtained, the FDA algorithm provides more accurate results.

Although these results are based in requirements of automatic music transcriptors, they may be extrapolated for other common applications. For example, an automatic instrument tuner, which is a device that shows a musician the tuning deviation of string instruments, should be designed to provide a high-accuracy F0 estimation. Above results indicate that the FDA algorithm is the most adequate for such application, provided that an adequate SNR is available. However, for speech analysis, where a higher error is acceptable, the Yin method may also provide accurate results, as shown in [5], while keeping a greater resilience to noise, as shown if Figure 1.

IV. Conclusion

A method for evaluating frequency estimation algorithms was presented. The method aims to determine the minimum SNR levels that allow proper functionality of frequency estimation algorithms. The definition of proper functionality is open to the user, as it may vary for different applications. The presented method assumes that requirements regarding signal models and observation time, have been met.

References

[1] Cheveigné, A. and Kawahara, H., "YIN, a fundamental frequency estimator for speech and music," *J. Accoust. Soc. Am.*, vol. 111, no. 4, pp. 1917–1930, Apr. 2002.

[2] Harry F. Olson, *Music, Physics and Engineering*, 2nd ed. Dover Publications Inc.

[3] Santamaria, I., Pantaleon, C., and Ibanez, J., "A comparative study of high-accuracy frequency estimation methods," *Mechanical Systems and Signal Processing*, vol. 14, no. 5, pp. 819–834, 2000.

[4] C. Manfredi, M. DAnielloa, P. Bruscaglionib, and A. Ismaellib, "A comparative analysis of fundamental frequency estimation methods with application to pathological voices," *Medical Engineering and Physics*, vol. 22, no. 2, pp. 135–147, 3 2000.

[5] de Cheveigné, A. and Kawahara, H., "Comparative evaluation of f0 estimation algorithms," in *Proceedings of Eurospeech 2001*, 2001.

[6] Trevilatto, N., Barbedo, J. G. A., and Lopes, A., "Transcrição Automática de Sinais de Áudio Monofônico (in portuguese)," in *Anais do 10 Simpósio Brasileiro de Computação Musical*, vol. 1, 2005, pp. 291–294.

[7] Mitre, A., Queiroz, M., and Faria, R. R. A., "Accurate and Efficient Fundamental Frequency Determination from Precise Partial Estimates," in *Proceedings of the 4th AES Brazil Conference*, May 2006, pp. 113–118.

[8] Keiler, F. and Marchand, S., "Survey on Extraction of Sinusoids in Stationary Sounds," in *Proc. DAFx-02 Digital Audio Effects Conference*, Hamburg, Sep. 2002, pp. 51–58.

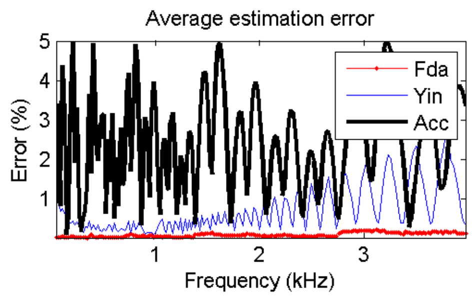

(a) Average deviation from ground-truth

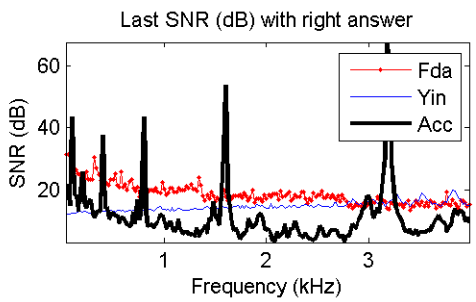

(b) Noise resilience with ground-truth reference

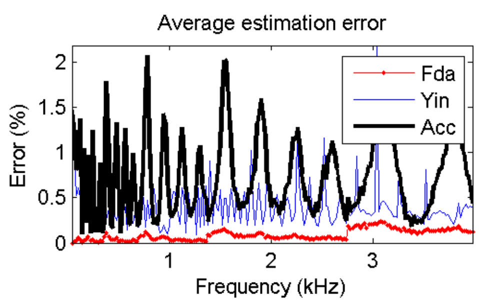

(c) Average deviation from clean signal estimate

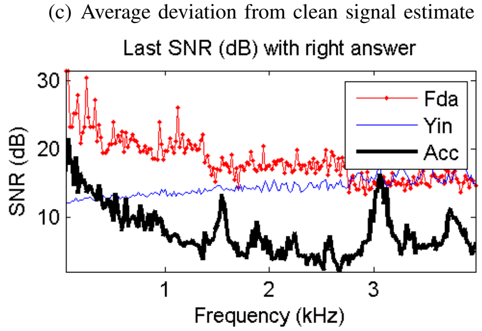

(d) Noise resilience with clean signal estimate reference

Fig. 1. Average deviation and noise resilience obtained from executing the evaluation method using a ground-truth reference and a clean signal estimate reference.

A Novel Design of Robust Video Steganographic System

Waleed Farag
Department of Computer Science at Indiana University of Pennsylvania
Indiana, PA 15705 - USA
farag@iup.edu

Abstract—**In the communication era that we are currently living in, ensuring the security of transmitted data is virtually a requirement for a broad spectrum of applications. Cryptography, an effective solution to such a requirement, tries to hide the contents of messages using various encryption techniques. On the other hand, steganography, a technique attempting to conceal the fact that a communication exists, is rapidly attracting the attention of the research community. In this paper, the design of a robust and secure steganographic system that uses MPEG video as cover media is presented. The paper starts by introducing the problem followed by a brief survey of the literature. The proposed design for a video steganographic system is presented along with various issues and design trade-offs. A discussion of the multi-hierarchical algorithm developed to hide the secret information into the steganographic cover and to enhance system robustness is followed. In addition, the hybridization technique adopted in order to improve the security of the overall design is expounded. Finally, the paper concludes by introducing preliminary results in particular those related to the average bandwidth of the employed covert channel.**

Index Terms—**Communication security, Data hiding, MPEG video, and Video steganography.**

I. Introduction

The widespread use of digital data, a result of the ever-increasing popularity of the Internet and the World Wide Web, necessitates the urgent development of new techniques for securing data communications and even hiding the fact that a communication is being conducted. Some of the driving forces are the need to protect copyright of digital media authors and the search for new techniques to secure information and maintain privacy. As a result of these needs, the area of information hiding has started gaining the interest of many researchers. Generally, information hiding techniques [6] can be divided into two types:

- *Steganography*: An art that studies different ways of making communication invisible by hiding information in innocuous messages using a covert channel. These messages are called covers and can be of any type such as text, images, etc.
- Digital Watermarking: This area studies ways to embed digital watermarks in digital media data to protect copyrights of media owners.

The word steganography means covered writing, a process in which a covert channel is used to send information to a specific recipient. Covert channels can be defined as communication paths that were neither designed nor intended to transfer information. This kind of communications usually requires hiding the message meta-content that is the identity of the sender and receiver. At this point, it is useful to point out the basic difference between steganography and cryptography, two techniques with the objective of conducting secure communications. Cryptography [4] was one of the first introduced solutions to tackle the communication security problem by attempting to conceal the content of messages using various encryption algorithms. Although cryptography was a successful solution, recent issues have called for the advent of other techniques that can be used either alone or in conjunction with a cryptosystem. Steganography is a promising candidate to such a requirement. While cryptography is about protecting the content of messages, steganography is about concealing their very existence.

On the other hand, digital watermarking techniques embed a digital code in the underlying media. This code should be robustly and imperceptibly embedded in the host data to be protected. This process is not meant to prevent illegal copying of the media but it helps in taking other affirmative actions against violators.

A framework for secret data communication in a steganographic system is given in Fig. 1, where two persons (traditionally Alice and Bob from Cryptography) want to communicate securely. Alice randomly selects a cover object (c) and embeds the secret message (m) into that cover using a secret key (k) forming what is known by the stego-object (s). The stego-object is transmitted to Bob over a communication channel susceptible to eavesdropping. Eavesdroppers can be of three types (passive: who just listen to the transmission, active: who can modify the transmitted message, and malicious: who can forge messages and send them to Bob). Upon the reception of the stego-object, Bob will use the secret key to extract the message (m) from that object. This model assumes that both Alice and Bob have access to a key generation facility.

The security of the invisible communication system diagrammed in Fig. 1 lies mainly in the inability to distinguish covers from stego-objects. Thus, good covers should contain sufficient redundant data to be replaced by secret information so noisy data are good candidates as well as Multimedia data. Theoretically, a stego system can be perfectly secure provided that the embedding process does not alter the probability distribution of the cover. Another very desirable characteristic of stego-systems is robustness, a term describing the degree by which a system can withstand cover alterations. In general, there is a trade-off between security and robustness. Robustness can be achieved by either foreseeing possible cover modifications and making the embedding process immune to such changes or reversing the modifications that have been applied to the cover.

The remainder of this paper is organized as follows. In section 2, a survey of some currently proposed techniques by various researchers is presented. Section 3 introduces our digital video steganographic system architecture along with the proposed algorithms for performing the embedding process. In section 4, we provide some preliminary results. Finally, section 5 draws the conclusions and emphasizes the importance of balancing security and robustness in newly proposed steganographic systems.

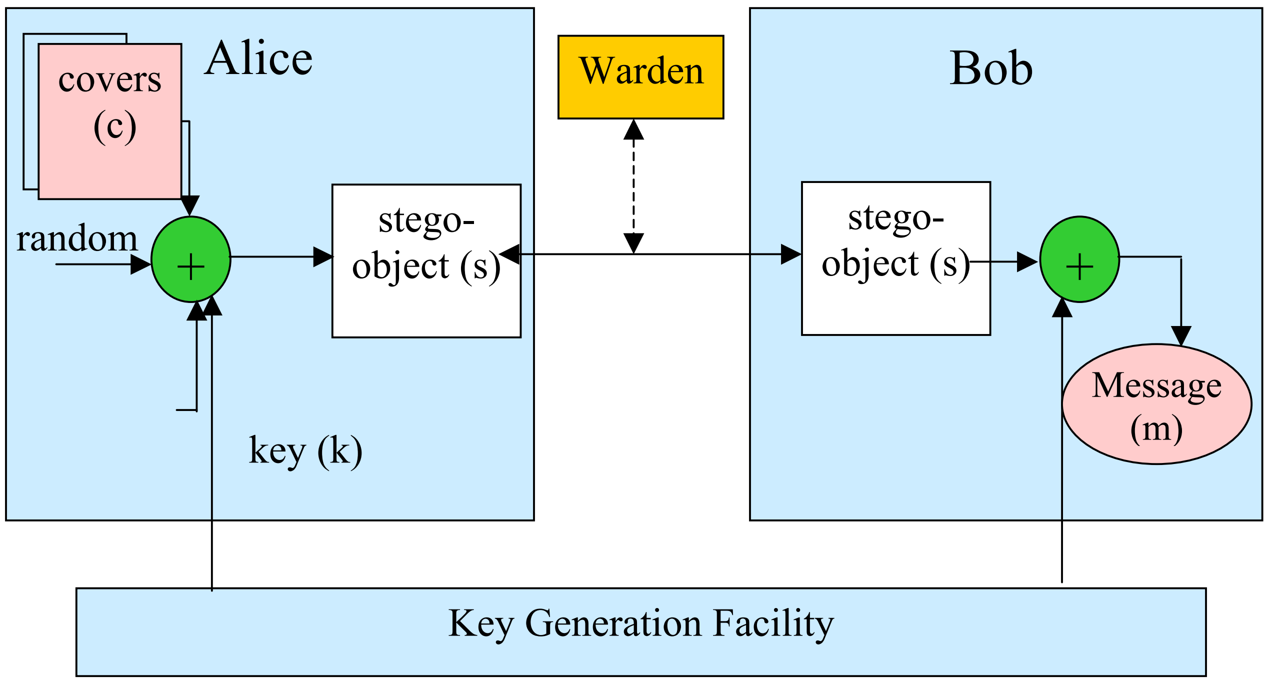

Fig. 1. A Framework for secret data communication.

II. Background Review

Steganography is a promising candidate to requirements imposed by many applications in various domains [7], such as unobtrusive communications, securely linking confidential data to patients in the health care industry, and copyright protection. Consequently, a number of researchers conducted productive research in steganography and used different media such as text, images, audio data, etc.

One of the simplest methods to send secret message is called Least Significant Bit (LSB) insertion [6], a process in which the LSB of each cover element is replaced by a single bit of the secret message. These techniques are commonly used and are easy to apply in image and audio. But, LSB significantly changes the statistical properties of covers therefore these systems can be easily broken by analyzing covers statistical properties.

In order to improve the robustness of stego systems, most of the current techniques operate in some sort of transform domain. The reason is that transform domain methods hide data in significant parts of the source object thus making them more robust to attacks such as cropping and format conversion than LSB approach. One example of image steganography [1] where the vector quantization technique is used in source coding the data to be embedded then channel coding and discrete Wavelet transform are both used to hide the obtained indices into the source image.

Other methods use the concept of spread spectrum coding where the secret message is spread over various parts of the cover media in a way that resist modifications. So, even if part of the embedded message could be removed, enough information should be encoded in other bands to enable message recovery at the recipient. An example of such techniques is presented in [12]. Some steganographic systems encode information by changing several statistical characteristics of the cover and use hypothesis testing in the extraction process [7].

A number of other systems adopt distortion techniques where the original cover is distorted according to the bits of the secret message. At the receiver side, the embedded message is restored by measuring the difference between the received message and the original cover. Therefore, one disadvantage of these methods is the assumption that the original cover is known at the receiver side. In [8], a text-based stego system that uses the distance between consecutive lines of text and consecutive words to transmit secret information is proposed. A similar technique can be applied to images where encoding zero is achieved by leaving the pixel unchanged and one is encoding by adding a random value to the pixel's color. Another class of techniques hides information by changing the covers statistical profile in a way that it matches the profile of any normal text. Other representative research efforts that use images and audio as the cover media can be found in [5, 10-11].

From this brief survey, one can see that most of the current systems utilize text, images, or audio as cover objects due to the fact that it is relatively easy to embed secret messages into these covers. Video data, another cover candidate, have unique characteristics that distinguish them from other multimedia covers. In this paper we introduce a new stego system that adopts these kinds of covers. The proposed system also employs other techniques to improve both security and robustness, resistance against cover modifications.

III. The Proposed System

In this section, a brief overview of our prototype digital video steganographic system is presented. The system has been design with the major goal in mind to develop a secure and robust system for sending/receiving secret messages using MPEG video streams as cover objects. MPEG is the current international standard [9] for representing digital video data and this is one of the reasons behind selecting it. MPEG is actually a family of state-of-the-art standards that includes MPEG-7 and MPEG-21 [2] as the most recent ones. A brief explanation of the basic structure of an MPEG video stream follows as it pertains to the overall understanding of the proposed embedding and extraction algorithms. The MPEG standard uses three different types of frames:

- I frames: Intracoded frames that can be decoded without reference to any other frames.
- P frames: Forward predicted frames that are encoded using previous I or P frames.
- B frames: Bi-directionally encoded frames that are predicted from forward and/or backward I and/or P frames.

Fig. 2 shows a sequence of MPEG frames in the display order (that is different from the coding order) indicating the relation between these three types of frames. MPEG uses the YCbCr color space so that all RGB values are first converted to their corresponding luminance and chrominance components, then each frame is divided into blocks of 8X8 pixels. Six blocks (4 Y, 1 Cb, and 1 Cr) forms what is called a Macroblock which is the basic unit in MPEG encoding. Fig. 3 illustrates how 6 blocks form a single Macroblock and how the pixel values of that Macroblock can be reconstructed using the Y, Cb, and Cr values. The MPEG standard achieves compression by exploiting two properties of video streams; spatial redundancy by using the DCT transform and time redundancy by using motion compensation techniques.

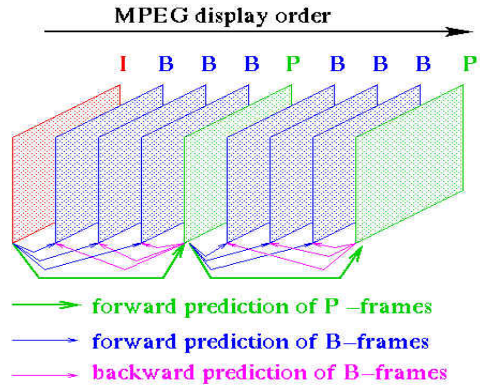

Fig. 2. A sequence of MPEG video frames with prediction relationships.

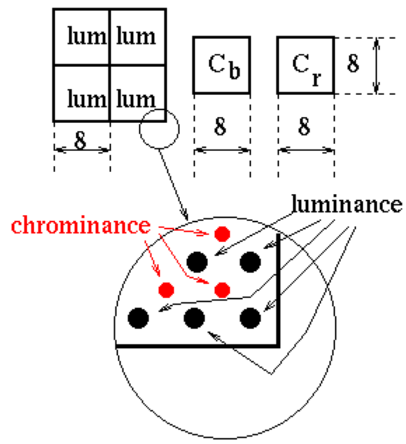

Fig. 3. Components of one Macroblock and relationships between Y, Cb, and Cr components.

Our goal is to insert secret messages into these streams. We can assume, without loss of generality, that all secret messages are sequences of bits. The proposed algorithms improve the system's robustness by applying the cover modification process in the transform domain and at the same time improve the system's security by adopting a multilevel hierarchical protocol to hide the information.

The proposed cover modification technique can be briefly described as follows:

- Encrypt the secret message using the private key of the adopted symmetric encryption algorithm
- For each block in a chosen frame calculate the Discrete Cosine Transform (DCT) for that block
- Apply the quantization table to the DCT coefficients
- Calculate the average of the quantized coefficients and compare it with a certain threshold (α, a system parameter)
    - if average > α and the encrypted secret message bit is one, do nothing
    - if average < α and the encrypted message bit is one, equally add values to coefficients to make the average > α
    - if average < α and the encrypted message bit is zero, do nothing

  - if average > α and the encrypted message bit is zero, subtract values from coefficients to make the average < α
- Apply Huffman or Arithmetic encoding to compress the block

In addition, a multilayer hierarchical protocol for hiding secret messages into MPEG video steams is devised. The advantage of this proposal is twofold, its novelty on one hand and the security it adds to the systems by varying the level in which secret information is hidden on the other hand. This protocol uses two layers:

- The first one controls the selection of the frame to be used in the embedding process. A number of alternatives being investigated are:
  - I, P or B frames
  - The selected key frames or a subset/superset
  - Any combinations of the above (for instance the first I, P& B frames in a group)

- A mathematical function that determines the selection of frame indices

The second layer is the choice of the block to be used (of course, it has to be part of an already chosen frame). Available options are:
  - All blocks
  - All blocks except those that will produce considerable image distortion
  - A mathematical function that determines the selection of block indices

Two pieces of secret information need be known to communication parties. The first part identifies the frame/block selection strategy while the second one is the threshold chosen for the average value of the quantized DCT coefficients (α).

The proposed system can be designated as a hybrid stego/crypto system. The secret key of the stego system and the private key of the integrated symmetric cryptographic algorithm are transmitted to all interested parties using public key cryptography. All other secret information is transmitted after being encoded using the symmetric encryption algorithm. This integration of two cryptographic systems with a stego system enables the proposed system to be considerably more secure and efficient. The added security is achieved by encrypting all information passing through the covert channel. Meanwhile, the efficiency is significantly improved as a result of using a symmetric cryptographic algorithm to encrypt all secret messages before sending them except while exchanging the private keys of both the stego and the symmetric crypto systems in the very beginning. Thus, the processes of encryption/decryption will be very efficient while solving the traditional key distribution problem of all symmetric cryptosystems.

IV. Preliminary Results

A trial to estimate the average bandwidth of the secret communication channel we are proposing as a result of using our steganographic system is introduced in this section. We consider an example MPEG video clip from [3]. To analyze that clip, we utilize a video analysis tool and list all the information pertaining to this clip in TABLE I. Part of this analysis is to select a number of key frames to represent each shot. The basic reason for selecting these key frames is to summarize the large amount of information in each video shot. The underlying theory behind this summarization process is the inherit similarity between successive frames in a video stream. These key frames can play a significant role in our embedding system. Fig. 4 lists the three selected key frames for the first shot of the considered example clip.

TABLE I
DIFFERENT CHARACTERISTICS OF THE SELECTED VIDEO CLIP.

Size	1 MB
Frame Size (in pixels)	352X240
Number of Frames	178
Frame Rate (f/s)	29.97
Number of Shots	3
Shot 1: number of frames / key frames	52 / 3
Shot 2: number of frames / key frames	53 / 2
Shot 3: number of frames / key Frames	73 / 1

To come up with an average estimate of the bandwidth of the secret channel, we assume that the frame selection algorithm will select even frames (i.e half of the frames in the clip) and about 50% of the maximum number of blocks will be considered in the embedding process. The last clip has 178 frames 89 of them will be used by the system. 50% of 1320 blocks in each chosen frame will be selected which is equal to 660 blocks. So, an average estimate of the total number of bits that can be hidden in that very short clip is 660*89 = 58740 bit. The previous figure is about 7 KB of hidden data, a number that is considered a fairly large amount of hidden information in such a small video clip. That number can be further improved if the message to be embedded is compressed first. Besides, compression can slightly improve the security of the proposed system by adding randomization to the secret data to be embedded.

V. Conclusions

In this paper, we presented a brief introduction to digital stego systems and surveyed a number of related information hiding techniques starting with the simplest ones that use LSB insertion to those that use transform domain and spread spectrum encodings. After that, our current digital video steganographic system is introduced. The architecture of the system is described along with the proposed algorithms to perform the embedding process. The robustness of the system is improved by working in the transform domain while the security property is achieved by adopting a new multilevel hierarchical protocol for hiding secret data. Our system is currently in the development phase; we are evaluating various options and design decisions and have started the implementation phase. Our system can be categorized under secret key steganography. One of the inherit advantages of our system is that video streams contain sufficient redundant data that can be replaced by a considerably large amount of secret information without compromising the system's security. By introducing such a secret communications paradigm, we attempt to balance the trade-off between security and robustness. At the same time, the proposed system tries also to exploit the advantages of both steganographic and cryptographic techniques to further improve efficiency and security.

Fig. 4. The three selected key frames for the first shot of the example clip.

REFERENCES

[1] N Abdulaziz and K. Pang, "Coding techniques for data hiding in images," Proceedings of the IEEE Sixth International Symposium on Signal Processing and its Applications, pp. 170-173, 2001.

[2] S-F. Chang, T. Sikora, and A. Puri, "Overview of the MPEG-7 Standard," IEEE Transactions Circuits and Systems for Video Technology, vol. 11, no. 6, pp.688-695, 2001.

[3] Waleed Farag and Hussein Abdel-Wahab, "A New Paradigm for Analysis of MPEG Compressed Videos," Journal of Network and Computer Applications, vol. 25, no. 2, pp. 109-127, 2002.

[4] N. Ferguson and B. Schneier, *Practical Cryptography*, John Wiley and Sons, 2003.

[5] K. Gopalan, "Audio Steganography by cepstrum modification," Proceedings of the IEEE ICASSP '05, pp. 18-23, 2005.

[6] N. Johnson, Z. Duric, and S. Jajodia, Information Hiding: Steganography and Watermarking-Attacks and Countermeasures, Kluwer Academic Publishers, 2001.

[7] S. Katzenbeisser and F. Petitcolas, Information Hiding: Techniques for Steganography and Digital Watermarking, Artech House Publishers, Boston, 2000.

[8] S. Low, N. Maxemchuk, and A. Lapone, "Document Identification of Copyright Protection Using Centroid Detection," IEEE Trans. on Comm., vol 46, no. 3, pp. 372-383. 1998.

[9] J. Mitchell, W. Pennebaker, C. Fogg, and D. LeGall, MPEG Video: Compression Standard, Chapman and Hall, 1997.

[10] M. Shirali-Shahreza, and S. Shirali-Shahreza, "Collage Steganography," Proceedings of the IEEE/ACIS International Conference on Computer and Information Science, pp. 316-321, 2006.

[11] S. Torres-Maya, M. Nakano-Miyatake, and H. Perez-Meana, "An Image Steganography Systems Based on BPCS and IWT," Proceedings of the IEEE International Conference on Electronics, Communications and Computer, Mexico, pp. 51-56, 2006.

[12] J. Vila-forcén, O. Koval, S. Voloshynovskiy, and T. Pun, "Asymmetric spread spectrum data-hiding for laplacian host data," Proceedings of the IEEE International Conference on Image Processing, ICIP, pp. 42-45, 2005.

Influence of background traffic on delay-centric path selection algorithm for multihomed SCTP

Igor Gavriloff
Universidade Federal do Paraná - UFPR
Curitiba - PR - Brazil
igor@wisehelp.com.br

Eduardo Parente Ribeiro
Universidade Federal do Paraná - UFPR
Curitiba - PR - Brazil
edu@eletrica.ufpr.br

***Abstract*— Latency is a very important parameter for real-time multimedia applications like voice and video communication which are very sensitive to delay. This work analyzes the influence of a stochastic background traffic with different intensities on the path selection strategy based on end-to-end delay. E-Model was used to obtain an estimation of subjective quality in terms of MOS to analyze how the algorithm performs.**

***Index Terms*— background traffic, multihomed, path selection, SCTP.**

I. Introduction

Multihomed sites are becoming increasingly common to end users with the broader availability and cheaper Internet connectivity available nowadays. This not only adds fault tolerance but also allows a performance increase when properly choosing the best interface for a given data flow. The usual handling of multihomed sites is done with exterior routing protocols like BGP (Border Gateway Protocol) but has the pitfall that they don't scale well. In practice, this restrict their use to very large clients that have their own address range. The SCTP (Stream Control Transmission Protocol) is a relatively new transport layer protocol that has intrinsic multihoming functionality. Multiple paths can be used during the same session to provide resilience and to improve performance.

This work analyzes a path selection strategy based on the smaller end-to-end delay[1][2]. The path delay estimation is given by the internal protocol's SRTT (Smoothed Round Trip Time) on the active path and by the heartbeat (HB) mechanism on the idle one. This approach seeks to improve overall latency which is a very important parameter for real-time multimedia applications that are very sensitive to delay like voice and video communication. All the performed tests were done using the network simulator NS-2. A voice codec payload is used as reference data but any delay sensitive multimedia traffic is expected to get a similar benefit. In order to evaluate this algorithm, performance is assessed by a metric that reflects the perceived subjective audio quality at the receiver taking in consideration both the delay and packet loss. The metric value is given by the MOS rating from the E-model. It was previously shown[3] that this algorithm can provide a performance gain.

The influence of stochastic background traffic with different intensities is considered in this work. Parameters related to the traffic on the available paths that results in varying queue occupancy and delay such as minimum, mean, maximum and amplitude variations are presented in this study in order to relate those variables to the figure of quality.

II. Related work

There are several strategies on how to chose a path in a multihomed configuration aiming to provide a better service. The idea to select a path with smallest delay is not new and has been proposed by some works[4][5]. With the advent of the SCTP as a transport protocol this strategy became more attractive due to the protocol's native multihoming functionality. The strategy to constantly monitor path round trip time and switch to another path with smaller delay has been successfully demonstrated for SCTP[1][2]. Most of the works targets wireless or mixed fixed-wireless environments where the path select decision is done regarding signal strength, battery level and packets measurements to control handovers[6][7].

A preliminary investigation in a typical multihomed residential scenario indicated that significant performance gains can be obtained for web, voice and video applications[8] using the smallest delay path selection strategy. Another work has proposed a similar path selection metric but using an estimated MOS instead of raw packet delays[9]. A simple scenario with CBR traffic representing VoIP calls was simulated on NS-2 to demonstrate that the estimates have a good agreement with the MOS experienced by a VoIP node added to the network.

In the present work a quantitative evaluation of delay-centric performance gain is pursued. The investigated environment seeks to mimic a situation that might be found in ISP's core networks by using a Poison process for packet interarrival times[10]. Although it is still a matter of evaluation and discussion the approach with Markovian model has the advantage of having queue mean delay mathematically well characterized by link occupancy. Controlling the network congestion in the bottleneck links creates the paths delays to which the algorithm must react.

III. SCTP overview

SCTP protocol was originally conceived to be a telephony signaling transport. It has a number of functions that are critical for that kind of application. It is a session-oriented protocol, having a similar (thought a bit more robust) handshake initialization as TCP's. A established relationship of two

SCTP endpoints is named association. Multiple independent data streams can be transmitted inside one association. The byte boundaries from sender to receiver are preserved, making it message-oriented other than byte-oriented like TCP. It allows unordered message receipt thus eliminating head-of-line blocking, what is ideal for transactional applications protocols.

SCTP's main feature explored in this work is its multihoming functionality. Each SCTP endpoint can have more than one IP address. This way each association can have more than one destination. The normal use of this functionality is to provide resiliency where only one of the destinations is used at a time. Whenever a flow failure is detected in the active destination due to excessive packet transmit errors, another destination is selected. Inactive paths are continuously monitored by periodicals packets called Heartbeats (HBs) to be sure that they are still operational.

One last feature explored in this work is the unreliable packet transmission, where lost packets are not retransmitted. That feature fits just well for realtime applications where a packet information has a limited lifetime significance. A packet retransmission would likely exceed the original packet lifetime. Other functionalities such Concurrent Multipath Transfer (CMT) were proposed for SCTP but they are not explored in this work.

IV. Methodology

A. Topology

The network topology built in NS-2, shown in figure 1, presents two paths. Each path has 2 intermediate routers that represents an ISP's core routers. Those paths do not share any common node. Two SCTP agents (one transmitter and one receiver) carry out a single transmission over these two independent paths using the protocol's multihoming capabilities.

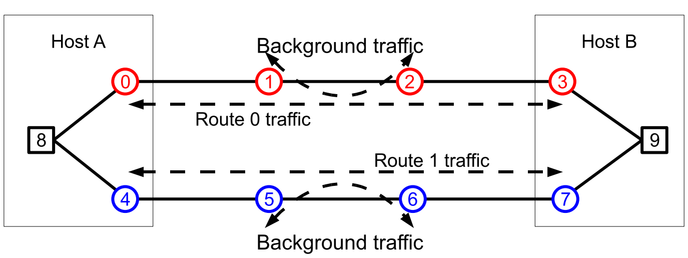

Fig. 1. Network topology with respective traffic indications

B. Background traffic

The background traffic is meant to simulate a generic traffic situation. Therefore a random traffic generator with a well known behavior was selected. The generator follows a Markov process, thus it is possible to use the average queue size from the M/D/1 model equation (1) to estimate the average queue delay in respect of the traffic bandwidth utilization factor (ρ). This traffic model was chosen due its well known behavior. The generator was implemented using the NS-2 Exponential On-Off traffic generator with only one packet during the burst period and with a exponentially random idle period [11].

$$\bar{q} = \frac{\rho}{1-\rho} - \frac{\rho^2}{2(1-\rho)} \tag{1}$$

Five NS-2 traffic generators constitutes the background traffic generator itself. The aggregation of Markovian traffics results in another Markovian traffic therefore this aggregation still presents the same characteristics of a single generator. Simulated background traffic was previously validated and the measured averaged delay error was always smaller than 10% on the range from 30 to 200 milliseconds.

C. Scenario dynamics

Only one path is used at any given time to transmit the data. The paths displays variable averaged delays induced by a controlled background traffic that may have alternating periods of heavier/lighter load. This imposed modulation was used to represent traffic variations along a session. During cycles of 20 seconds the background traffic keeps steady at a high rate and then during another period with the same time interval at a low rate. The generators are in phase opposition to each other (figure 2).

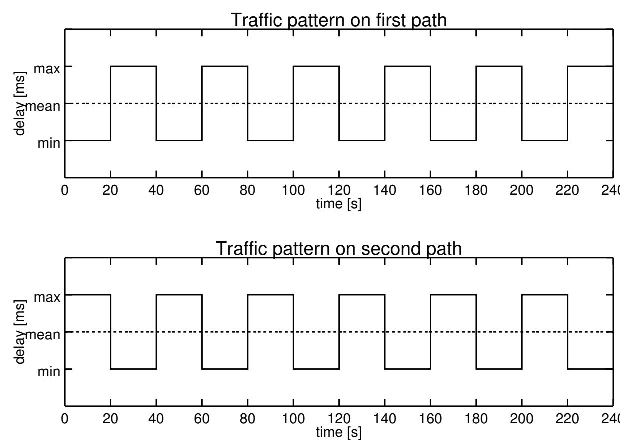

Fig. 2. Background traffic generators patterns

The mean and the amplitudes variations used for the simulations are listed in table I. This delay oscillation is to cause the decision algorithm to react by choosing a new route whenever a route with a smaller delay than the current one is detected. An important configuration where both path have the same mean delay and hence no modulation was also studied.

D. Multimedia traffic

A voice codec is used as payload of the SCTP stream. In order to simulate the G.711 codec, frames of 160 bytes at a rate of 64Kbps are transmitted by the SCTP agent. A generic CBR traffic generator from NS-2 is used to create the stream's payload. The data rate found in the simulation is greater than 64Kbps due to the SCTP and IP protocols overhead. Transmission occurs thru only one of the available routes at any given time.

TABLE I
MEAN AND AMPLITUDE MODULATION OF AVERAGE-DELAY VALUES

Mean average delay [ms]	Pattern amplitude variation [ms]
30	0 10 20
50	0 10 20 30 40
70	0 10 20 30 40 50 60
100	0 10 20 30 40 50 60 70 80 90
120	0 10 30 50 80
150	0 10 30 50 80 100 120
170	0 10 30 50 80 100 120
200	0 10 30 50 100 150
250	0 40 60 80 10 100 120 140 160 180 200 220
300	0 10 40 60 80 100 120 140 160 180 200 220 240 260 280
350	0 50 100 150 200 250 300
400	0 100 200 300 350
500	0 100 200 300 400
600	0 100 200 300 400 500
700	0 100 200 300 400 500 600
800	0 100 200 300 400 500 600 700
1000	0 100 200 300 400 500 600 700 800 900

E. Algorithm actuation

SCTP's Selective Acknowledgment (SACK) and Heartbeat packets updates the active and inactive paths delays estimates, respectively. The SCTP's default heartbeat interval is 30 seconds, but in this work this value was reduced to one second. Smoothed Round Trip Time (SRTT) calculated internally by SCTP is used to make the path selection decision. The decision occurs upon a SRTT update.

In order to obtain these data in a TCL script, a new C++ class that inherits the original SCTP class in NS-2 was developed. The main purpose of this class is its ability to pass the delay update information (SRTT) to a callback specified by the user in the TCL script. The route changes are accomplished by setting the SCTP agent's primary destination. No modification to the protocol was made.

Another parameter to the algorithm, called hysteresis, makes the switch occurs only when the routes delay difference is greater than the specified value. Previous study showed that different hysteresis values affected basically the number of route changes[3], therefore a value of 10ms was used in all scenarios studied in this work.

F. Evaluation

In order to evaluate the algorithm's behavior, the MOS rating metric from the E-model (2) is used. All parameters in this equation are constants except for Id which represents the impairment due to delay. To calculate its value the effective multimedia stream mean delay is used. The delay taken in consideration is only from the data packets (this excludes the heartbeats) independently of which route they were transmitted.

$$R = Ro - Is - Id - Ie + A \tag{2}$$

The MOS rating (3) is a non-linear mapping of the E-model transmission rating factor R:

$$MOS = \begin{cases} 1 & R < 0 \\ 1 + 0.035R + R(R-60)(100-R)7\text{e-}6 & 0 \le R \le 100 \\ 4.5 & R > 100 \end{cases} \tag{3}$$

An analysis of the path selection algorithm gain improvement can be obtained by comparing a given scenario using the selection algorithm with the same scenario but without the algorithm.

Every scenario is simulated 10 times using the default seed but with different pseudo sub-streams. Special care should be taken into account when selecting NS-2 seeds[11]. The results from 10 simulations provided a standard deviation of 0,7 in the MOS ratings for a fixed path and a standard deviation of 0,008 when the selection algorithm was active.

V. RESULTS

The background traffic generator has a bursty behavior in which during relatively long periods there are almost no packets and then eventually a large amount of packets are generated during a short period. The system when observed for large amounts of time will present in average a delay with a value close to the one that was specified. This averaged characteristic tends to disappear when the time observation window is narrowed up to a scale where the delay spikes and valleys can be observed.

The delay value analyzed by the path selection algorithm is not the instantaneous delay value but a smoothed average value given by the SRTT variable calculated by the SCTP agent. Depending on how many and how high are the spikes inside a time window covered by the SRTT average, one of the routes can be presented by the path selection algorithm as the best route even if it is equivalent or inferior.

A. Burstness

In order to analyze the influence of this variable delay in short periods of time the two paths were configured to have the same mean delay with no variations along a 200 seconds session. This translates to a zero amplitude modulation in the methodology explained before.

Table II lists the results for some delays created by the background traffic generator. There are two kind of delays listed in this table: the specified value to the traffic generator and the effective delay that the multimedia stream experienced. The columns are arranged in two groups: one that has the results for a situation where the path selection algorithm is not used and another group where it is used. This second group has an additional column that shows the average number of route changes occurred in that situation. It is not a integer because it is an average of the number of route changes of all the scenario's seed sub-streams.

When the algorithm is not in use, the resulting effective delay is slightly higher than the delay specified into the background traffic generator. But when two routes are available and the path selection algorithm is used to switch the transmission to the path with smallest delay, the effective delay is smaller

TABLE II

RESULTS FOR SAME BACKGROUND TRAFFIC ON BOTH PATHS (NO MODULATION).

Specified	Single route		Multiple routes		
delay [ms]	Effective delay [ms]	MOS	Effective delay [ms]	MOS	Route changes (avg.)
30	34.378	4.3625	25.133	4.3670	25.3
50	56.183	4.3514	33.047	4.3631	28.5
70	77.737	4.3258	38.440	4.3605	29.5
100	120.609	4.1976	43.423	4.3581	29.2
150	176.840	4.0898	49.664	4.3551	29.8
200	207.353	4.0216	54.047	4.3530	30.6

than the delay from each route's average delay. This confirms that the algorithm can benefit from the adjacent route's periods of smaller delays.

There are two interesting remarks about these results. The first one is that although both paths have exactly the same mean delay it is observed that the switching path strategy provided a performance gain. It helped to keep the MOS elevated (close to 4.3) even for a high mean path delay of 200 milliseconds that degraded a fixed path transmission MOS to 4.0. The second remark is the number of route changes which did not alter very much among the different average delays specified in the traffic generators.

B. Background traffic dynamics influence

Some situations like a route change in the core network or a even due a sudden overload can severely modify the network latency. Investigation about the algorithm's capability of changes adaptation can be achieved by making these delay changes occur frequently. That is the traffic generator alternating modulation goal. Four parameters from this pattern are used as metric in this analysis: the minimum, maximum, mean and amplitude value of path mean delay for the alternating periods. In order to evaluate the algorithm's performance gain, tests are repeated with the algorithm disabled making only one effective path available.

In figure 3 the MOS rating results for different average delays values are grouped in respect of algorithm's usage. Only two values are shown for the sake of simplification/clarity. The MOS ratings are plotted against the background traffic generator pattern's minimum average-delay. In all situations the MOS rating decreases whenever the minimum average delay increases. Two factors contribute to the curves' slope: the algorithm usage and mean average delay. For low mean average delays the algorithm's improvement is not that big but it makes difference for higher mean average delay cases. When multi-path is active the MOS rating is still inside a range of a good perception even for situations where the delay is not favorable.

The good performance of the algorithm is also seen in figure 4 where MOS is plotted as a function of mean average delay. All the amplitudes for a given mean average delay are plotted together. The amplitudes values used grows from zero up to

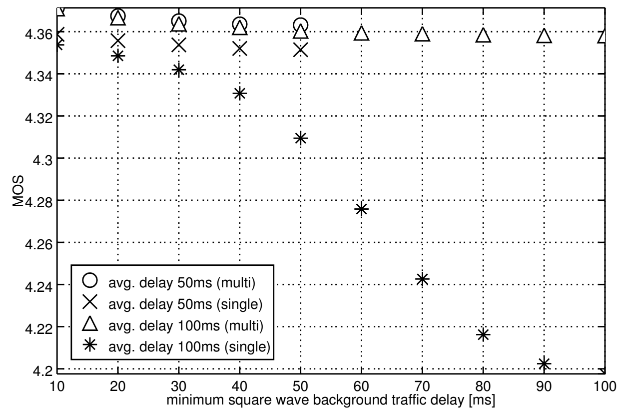

Fig. 3. MOS versus minimum average-delay of background traffic grouped by mean value for single and multi-path

almost the mean value. For fixed path it can be observed that MOS degrades for higher mean average-delay values as expected. Multi-path algorithm was able to maintain an elevated MOS regardless of mean average-delay value. This is in accordance to algorithm behavior that is able to switch path when SRTT detects an increase in route latency. As a remark, the used background traffic generator produced smaller delays than expected for high occupancy scenarios (highest percent error was 50% at an average delay of 1 second). A precise quantitative examination for average-delays greater than 200 milliseconds is affected. Nonetheless this distortion on the x-axis does not prevent the above qualitative analysis.

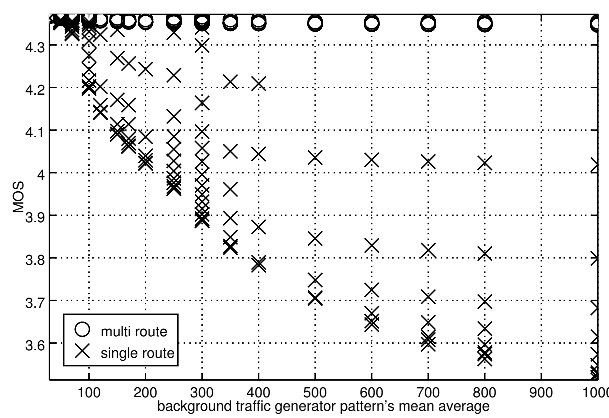

Fig. 4. MOS versus mean average-delay of background traffic for several amplitude modulations

Observing MOS rating versus maximum value of background traffic generator pattern (figure 5) results in the opposite behavior from what is in the minimum value (figure 3). Fixed route exhibits higher MOS for increasing maximum value. This is due to the alternating nature of background traffic generator. When maximum value increase minimum value decreases accordingly.

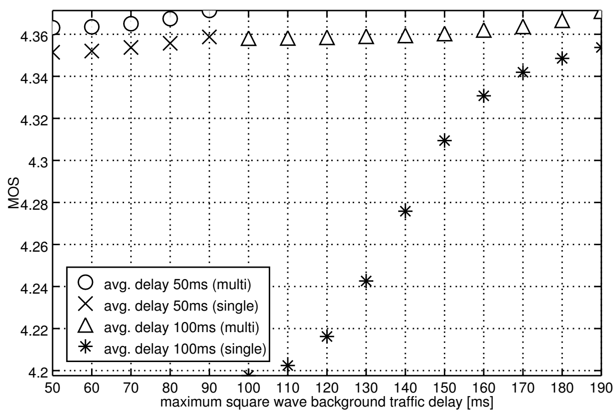

Fig. 5. MOS versus the maximum value of background traffic average-delay grouped by the mean average-delay value for single and multi-path

A similar plot is seen when the horizontal axis represent the modulation amplitude (figure 6). In this plot the difference is only on a zeroed offset where the points starts being plotted.

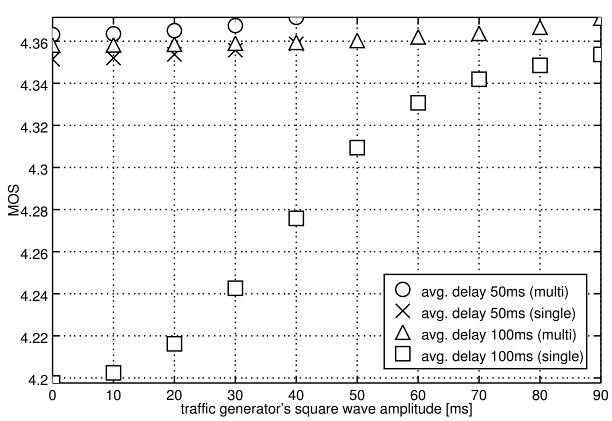

Fig. 6. MOS versus amplitude of modulated background traffic grouped by mean average-delay for single and multi-path

VI. Conclusion

A quantitative evaluation of the SCTP delay-centric path selection algorithm actuating in scenarios with varying averaged-delays simulating a network core was carried out. The perceived measured quality was studied as a function of parameters regulating background traffic on both paths such as minimum, mean and maximum averaged delay values for every mid-term cycle. The stochastic traffic considered was based on Poison model and had the occupancy changed in each cycle causing high and low averaged delays on each path alternately. This work established a relation between the perceived quality and the studied traffic parameters in terms of the mean opinion score (MOS) estimated by the ITU's E-Model.

The path selection strategy shown itself to be very responsive to fast delay changes. It was able to react to the background traffic variations switching path appropriately to maintain transmission with low latency and elevated MOS. Even when both paths exhibited the same large average-delay the algorithm was able switch paths and keep MOS rating at an elevated range providing a good performance gain over a fixed path conventional transmission.

References

[1] A. Kelly, G. Muntean, P. Perry, and J. Murphy, "Delay-centric handover in sctp over wlan," *Transactions on Automatic Control and Computer Science*, vol. 49, no. 63, pp. 211–216, 2004.

[2] J. Noonan, P. Perry, S. Murphy, and J. Murphy, "Simulations of multimedia traffic over sctp modified for delay-centric handover," *World Wireless Congress*, 2004.

[3] I. Gavriloff and E. P. Ribeiro, "Seleção de caminho baseada em atraso para sistemas multi-abrigados usando SCTP," *XXVI Simpósio Brasileiro de Telecomunicações - SBrT'08*, 2008.

[4] N. Yamai, K. Okayama, H. Shimamoto, and T. Okamoto, "A dynamic traffic sharing with minimal administration on multi-homed networks," *Proc. IEEE Int. Conf. Commun. (ICC2001)*, vol. 5, pp. 1506–1510, june 2001.

[5] A. Akella, B. Maggs, S. Seshan, A. Shaikh, and R. Sitaraman, "A measurement-based analysis of multihoming," *COMPUTER COMMUNICATION REVIEW*, vol. 33, no. 4, pp. 353–364, 2003.

[6] L. Ma, F. Yu, V. C. M. Leung, and T. S. Randhawa, "A new method to support umts/wlan vertical handover using sctp," *IEEE WIRELESS COMMUNICATIONS*, vol. 11, no. 4, pp. 44–51, 2004.

[7] S. J. Koh, M. J. Chang, and M. Lee, "msctp for soft handover in transport layer," *IEEE COMMUNICATIONS LETTERS*, vol. 8, no. 3, pp. 189–191, 2004.

[8] A. Habib and J. Chuang, "Improving application qos with residential multihoming," *Computer Networks*, vol. 51, pp. 3323–3337, 2007.

[9] J. Fitzpatrick, S. Murphy, and J. Murphy, "Sctp based handover mechanism for voip over ieee 802.11b wireless lan with heterogeneous transmission rates," *IEEE International Conference on Communications - ICC'06.*, pp. 1–6, 2006.

[10] T. Karagiannis, M. Molle, M. Faloutsos, and A. Broido, "A nonstationary poisson view of internet traffic," *INFOCOM 2004. Twenty-third AnnualJoint Conference of the IEEE Computer and Communications Societies*, vol. 3, pp. 1558–1569 vol.3, March 2004.

[11] B. Hechenleitner and K. Entacher, "On shortcomings of the NS-2 random number generator," in *Communication Networks and Distributed Systems Modeling and Simulation (CNDS 2002.* International, 2002.

Performance Evaluation of Adaptive Routing and Survivability in Dynamic Grooming WDM Networks

Paulo Ribeiro Lins Júnior
Department of Electrical Engineering
UFCG/Iecom
Campina Grande - PB - Brazil
paulo.ribeiro.lins.jr@gmail.com

Edmar Candeia Gurjão
Department of Electrical Engineering
UFCG/Iecom
Campina Grande - PB - Brazil
ecandeia@dee.ufcg.edu.br

Marcelo Sampaio de Alencar
Department of Electrical Engineering
UFCG/Iecom
Campina Grande - PB - Brazil
malencar@iecom.org.br

***Abstract*— This paper considers a dynamic grooming WDM networks that have implemented a protection scheme of the type 1+1 or 1:1. With this scenario, it is evaluated the performance of the adaptive routing as tool for obtaining of a smaller blocking probability and a better load distribution in the network. The results obtained shown that the use of adaptive routing improve the performance of the network, considering the blocking probability and load distribution as evaluation metrics, for all cost functions, with prominence for the two cost functions. But, the results shown too a strong relationship between the performance of a function cost and the topology of the studied network.**

***Index Terms*— adaptive routing, survivability, traffic grooming**

I. Introduction

Users in wavelength-routed networks are connected by lightpaths, that consists in a path composed by physical links between the source and destination nodes with a particular wavelength, that are routed and switched by intermediary nodes through OADMs (Optical Add-Drop Multiplexers) and OXCs (Optical Cross-connect) [1].

For a better characterization, beyond a route and a wavelength, it is necessary that a lightpath has also attributes of quality of service (QoS). These attributes are agreed between providers and client networks (IP, SDH/SONET and/or ATM networks) from the establishment of a Service Level Agreement (SLA). The SLA can guarantee acceptable levels for certain parameters that act directly on the QoS [2]. One way to ensure acceptable levels of QoS is by use of Traffic Engineering, that to search decrease congestion and maximize the traffic flow.

Traffic engineering refers to the optimization of operational networks. The idea is to use existing resources most effectively, which is complementary to dimensioning, where one adds resources to meet the requirements for serving customers properly. On one hand, there is a network which has a limited capacity, on the other hand the customers who offer traffic to the network and have to be served sufficiently [3]. Both capacity and traffic demands vary on the long range, operators build new infrastructure and the customer demands new services.

For WDM networks, there are several mechanisms of Traffic Engineering, each include: coordination of the Traffic Engineering functions between client networks and optical network, survivability, protection and restoration functions of traffic in the event of failure, traffic grooming, load balancing by using adaptive routing protocols, routing based on physical layer restrictions.

In this work, three of these mechanisms are considered: adaptive routing for load balancing in the network, traffic grooming and survivability schemes.

The dynamic route and wavelength assignment (RWA) algorithm selects a lightpath based on state information of the network. Each router periodically broadcasts its neighboring link information to all other routers. This information is used to construct the network topology with the associated link cost functions.

When a lightpath is required, the router uses its routing table to determine the entire path from source to destination. It then attempts to assign a wavelength along this path by propagating a wavelength request to all the routers along the path. If wavelength conversion is available in the network, then a lightpath can be established using different wavelengths on different links.

If this request fails, a different wavelength is chosen the search in routing table is performed and this processed is repeated until the least available wavelength. If this fails, then the request is blocked, i.e. the lightpath can not be set up.

The traffic grooming algorithm used in this work is based on the Direct-link algorithm [3], whose tries to optimize the wavelength utilization. The proposed algorithm searches a lightpath established with bandwidth sufficient for the requisition. If no active lightpath has sufficient bandwidth, then a new channel is established. This algorithm is presented as a modification of the First-Fit heuristic for wavelength assignment [5].

Survivable network architectures are based either on protection or on dynamic restoration. In protection, spare capacity is reserved during call setup. In dynamic restoration, the spare capacity available within the network is utilized for restoring services affected by a failure.

This work investigates those traffic engineering strategies in a dynamic WDM optical networks. For the adaptive routing, five cost functions which are used for routing table update, associated to the Dijkstra algorithm and the first-fit wavelength assignment heuristic. These functions were presented in [4] and are based on the number wavelengths (used and total) in the link. The traffic grooming algorithm considers the wavelength sub-channel bandwidth allocated on demand. One survivability schemes presented in [6] is considered in this study.

The remaining of the paper is organized as follow. Section II presents a summary of the principal survivability schemes, with prominence for the technique considered in the study. Section III are presented a review of adaptive routing and traffic grooming, with details of the proposed solution. Section IV presents the simulation environment and the performance analysis from results. Section V presents the results and discussion over the simulations. Section VI conclude the paper.

II. Survivability in WDM Networks

In WDM technology a single fiber carries various channels, so it is important to study the survivability and reliability of a fiber in order to maintain high bandwidth traffic.

We assume that the network is survivable or protected against any single link failure at the optical layer. Such protection is provided by using a path-based protection scheme, more specifically, at the time of establishing a primary path (working), a link-disjoint backup (protection) path is also established. The results in this paper are valid for both 1+1 and 1:1 based protection as long as one assume that no backup path bandwidth sharing occurs. For the wavelength-continuous-networks one considers two different cases for protection:

- Type I: The primary path and the backup lightpaths need to be assigned the same wavelength. This sort of wavelength assignment may be necessary when the source and destination of a lightpath have agreed in advance on the emitting and sinking wavelengths and/or routes according to some policy constraints. This constraint could also be necessary when there are not enough tunable transmitters and/or receivers at the source and destination nodes, or at any other node in the network.
- Type II: The primary path and the backup lightpaths can be assigned different wavelengths. This sort of wavelength assignment assumes that there are no constraints as described in Type I path protection. For the wavelength-convertible-networks, with complete conversion at every node, any available wavelength on any link along the route can be assigned to the primary and backup lightpaths by definition. Again it is implicitly assumed that there are no constraints on RWA as in Type I protection scheme described above.

The second type of protection has been chosen, in which the secondary route is disjoint of the primary route, as it have or not the same wavelength.

That approach brings with itself a problem. Whenever a connection is established, two ligthpaths (two paths and two wavelengths) are busy. That causes a larger block probability in the network, once the largest amount of resources being used at the same time in the network.

The paper presents the use of adaptive routing with traffic grooming as a possibility to improve the use of the resources of the net and to reduce the blockade probability in agreement with the work [4].

III. Adaptive Routing and Traffic Grooming

Adaptive routing approaches increase the likelihood of establishing a connection by taking into account network state information. For the case in which global information is available, routing decisions may be made with full information as to which wavelengths are available on each link. In order to find an optimal route, a cost may be assigned to each link, and a least-cost routing algorithm may be executed.

Each node in the network must maintain complete network state information [1]. Each node may then find a route for a connection request in a distributed manner. When the network state changes, all of the nodes must be informed. Therefore, the establishment or finalization of a connection in the network may result in the broadcast of update messages to all nodes in the network.

The minimum granularity of a connection in a wavelength-routed network is the capacity of a wavelength. However, the requirement of end-users such as Internet service providers, universities and industries are still much lower than that of the wavelength capacity. The bandwidth requirement is projected to increase in the future; but, even doubling the current bandwidth would be more than sufficient to handle the projected demand for the near future [1].

The merging of traffic from different source-destination pairs is called traffic grooming. Nodes that can groom traffic are capable of multiplexing or demultiplexing lower rate traffic onto a wavelength and switching them from one lightpath to another. The grooming of traffic can be either static or dynamic. In static traffic grooming, the source-destination pairs for which requirements are to be combined are predetermined. In dynamic traffic grooming, connection requests from different source-destination pairs are combined depending on the existing lightpaths at the time of the request.

In this paper, we have considered five cost functions which are used for routing table update. These functions are based in link state information will also include WDM specific status such as number of available wavelengths and total wavelengths.

To description the cost functions, we denote, for the link between i and j nodes, $(i,j) \in E$:

- λ_{ij}^{U} – number of used wavelength on the link when link state information was gathered;
- λ_{ij}^{T} – number of total wavelengths on the link;
- C_{ij} – path cost between the nodes i and j.

The initial condition of problem is the initial cost of all links, $C_{ij}^{0} = 1, \forall (i,j) \in E$. The setup of a connection increase the cost value and the liberation of a connection decrease this cost. This situation occur up to maximum cost value $C_{ij} = \infty$. This value represent the occupation of all wavelength on the link. Therefore, if a connection was established in a route, the cost of links of this route will be major for the next requisition, avoiding the occupation of these links. The result of this operation is a uniform distribution of the load in the network.

The cost functions C_{ij} studied are:

Based in the number of links (NE) – In this case, the cost is

$$C_{ij} = 0, \forall (i,j) \in E. \tag{1}$$

This is the more basic case, which routing is not adaptive. It will be used for comparison with the others functions.

Based in the link capacity 1 (CE1) – This function sum one to cost value when a connection is established and decrease one to cost value when a connection is finished in the lightpath. Therefore, the cost function is

$$C_{ij} = \begin{cases} C_{ij}^{-1} + 1, & \text{if a new connection is established,} \\ C_{ij}^{-1} - 1, & \text{if an active connection is finished.} \end{cases} \tag{2}$$

Based in the link capacity 2 (CE2) – This function, based in the work of [**?**], is

$$C_{ij} = \begin{cases} \dfrac{\lambda_{ij}^{T}}{\lambda_{ij}^{T} - \lambda_{ij}^{U}} & \text{if } \lambda_{ij}^{U} < \lambda_{ij}^{T}, \\ \infty & \text{if } \lambda_{ij}^{U} = \lambda_{ij}^{T}. \end{cases} \tag{3}$$

In this function, when the number of used wavelengths (λ_{ij}^{U}) increase, the cost value increase exponentially. This characteristic indicate a preference for the selection of links with minor number of used wavelengths.

Based in the link capacity 3 (CE3) – This function, based in the work of [**?**], is

$$C_{ij} = \begin{cases} 1 - \log\left[\left(1 - \dfrac{\lambda_{ij}^{U}}{\lambda_{ij}^{T}}\right)^{\lambda_{ij}^{U}}\right] & \text{if } \lambda_{ij}^{U} < \lambda_{ij}^{T}, \\ \infty & \text{if } \lambda_{ij}^{U} = \lambda_{ij}^{T}. \end{cases} \tag{4}$$

This function use the probability of a link is not in use. In accordance with [**?**], the probability that all wavelengths are occupied in the future is given by

$$p = \left(1 - \frac{\lambda_{ij}^{U}}{\lambda_{ij}^{T}}\right). \tag{5}$$

Therefore, when a path is composed of multiple links, the p value is maximized for all links that constitute this particular path. Due to the additive nature of Dijkstra's algorithm, he uses a logarithmic function to compute the cost.

Based in the link capacity 4 (CE4) – That is the function proposed in this paper as alternative to others functions presented. The cost is altered as follow

$$C_{ij} = 1 + \lambda_{ij}^{U} \cdot \exp\left(\frac{\lambda_{ij}^{U}}{\lambda_{ij}^{T}}\right). \tag{6}$$

The use of exponential function as cost function have the same motivation of CE3: avoid the additive nature of Dijkstra's algorithm.

The traffic grooming algorithm used in this work is based on the Direct-link algorithm [3] that goal is optimize the wavelength utilization. The algorithm proposed search a lightpath established with bandwidth sufficient for the requisition. If none lightpath active has sufficient bandwidth, then a new channel is established.

IV. Simulation and Analysis

We designed and developed in C++ language a simulator to implement routing and wavelength assignment in all-optical networks. It has as input parameters the number of nodes in the network, weight link, number of wavelengths per fiber and number of connection requests. Some of the calls may be blocked because of the unavailability of free wavelength on links along the route from the source to the destination. All these parameters can be initialized before running the simulations to obtain results for a given selection of parameters.

In the experiments, we consider three mesh topology, show in the Figures 1, 2 and 3.

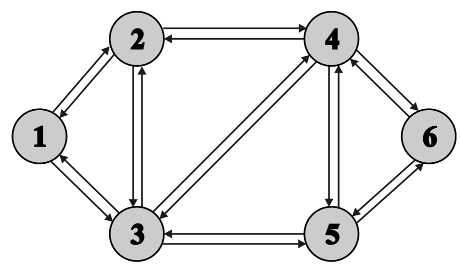

Fig. 1. Mesh topology with six nodes.

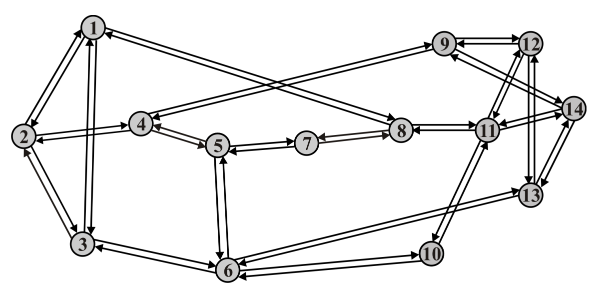

Fig. 2. NSF network topology.

It is performed 50.000 requests to each load value. The load has its values ranging from 400 erlangs to 700 erlangs. Each connection has a duration or holding time which is exponentially distributed and the arrive time which a Poisson distribution. Each wavelength support 10 Gbits/s and your minimal granularity is 1 Gbit/s. All simulations are performed five times and a source-destination pair of each request is randomly determined to consider uniformly distributed traffic in the network.

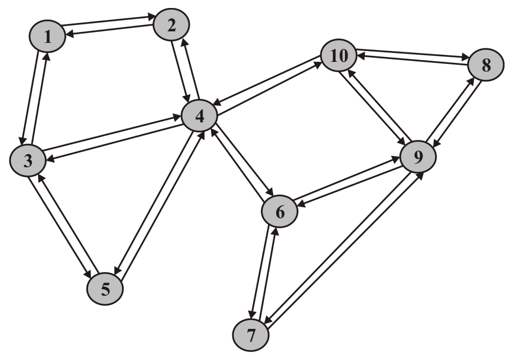

Fig. 3. Ring tree topology.

The output of the simulator is the blocking probability and link average utilization for the specified parameters along with the detailed information of connections. The blocking probability is expressed as the fraction of the rejected connection requests due to wavelength unavailability divided by the total number of connection requests at the simulation run. The link utilization is expressed as the ratio between the number of connections established in a link and the total number of connection established in the network. In this study, the link utilization is calculated to 410 erlangs, for a better preview. The results of link utilization are shown in a graph of the percentage of connections established for each link in the network. This links are indexed according to the Tables I, II and III.

TABLE I
INDEXES OF LINKS IN THE SIX NODES TOPOLOGY.

Index	Link	Index	Link	Index	Link
1	1 – 2	7	3 – 2	13	4 – 6
2	1 – 3	8	3 – 4	14	5 – 3
3	2 – 1	9	3 – 5	15	5 – 4
4	2 – 3	10	4 – 2	16	5 – 6
5	2 – 4	11	4 – 3	17	6 – 4
6	3 – 1	12	4 – 5	18	6 – 5

TABLE II
INDEXES OF LINKS IN THE NSF NETWORK TOPOLOGY.

Index	Link	Index	Link	Index	Link
1	1 – 2	15	5 – 7	29	10 – 11
2	1 – 3	16	6 – 3	30	11 – 8
3	1 – 8	17	6 – 5	31	11 – 10
4	2 – 1	18	6 – 10	32	11 – 12
5	2 – 3	19	6 – 13	33	11 – 14
6	2 – 4	20	7 – 5	34	12 – 9
7	3 – 1	21	7 – 8	35	12 – 11
8	3 – 2	22	8 – 1	36	12 – 13
9	3 – 6	23	8 – 7	37	13 – 6
10	4 – 2	24	8 – 11	38	13 – 12
11	4 – 5	25	9 – 4	39	13 – 14
12	4 – 9	26	9 – 12	40	14 – 9
13	5 – 4	27	9 – 14	41	14 – 11
14	5 – 6	28	10 – 6	42	14 – 13

TABLE III
INDEXES OF LINKS IN THE RING TREE TOPOLOGY.

Index	Link	Index	Link	Index	Link	Index	Link
1	1 – 2	8	4 – 2	15	6 – 4	22	9 – 6
2	1 – 3	9	4 – 3	16	6 – 7	23	9 – 7
3	2 – 1	10	4 – 5	17	6 – 9	24	9 – 8
4	2 – 4	11	4 – 6	18	7 – 6	25	9 – 10
5	3 – 1	12	4 – 10	19	7 – 9	26	10 –4
6	3 – 4	13	5 – 3	20	8 – 9	27	10 – 8
7	3 – 5	14	5 – 4	21	8 – 10	28	10 – 9

V. RESULTS AND DISCUSSION

In the simulation, we were considered as study scenarios WDM optical networks with traffic grooming capacity, where an 1:1 or 1+1 protection schemes exists. Then the acting of that network was verified in terms of blocking probability and usage considering non-adaptive routing, represented by the NE function and adaptive routing, represented by the other cost functions. The simulation results are presented in the Figures 4 to 9.

For the six nodes and ring tree networks, the results obtained without adaptive routing are worse. In the six nodes network, the CE3 and CE4 present a better performance if compared the others cost functions. Already in the ring tree, CE1 and CE4 presents a better performance in the load range analyzed.

It is interesting to notice that, until a certain load value, all functions have the practically same performance, for the rings tree topology. Only when the load is larger than 580 erlangs is that the two cited functions if they highlight and the others have your deteriorated performance.

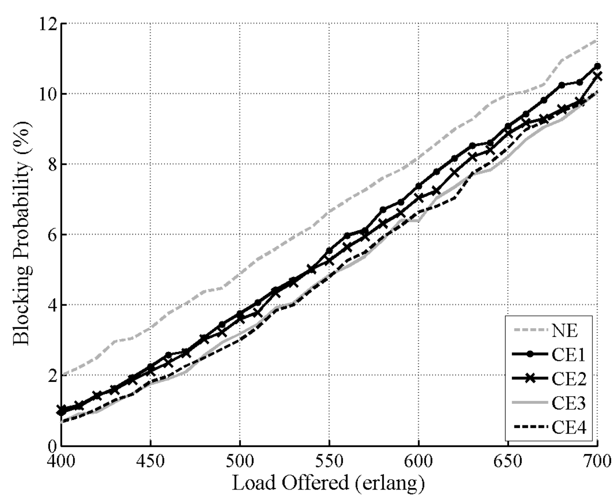

Fig. 4. Blocking probability versus load offered to the six node network.

For the NSF network, only CE3 and CE2 have a better performance than the NE function. This result could be related with the great amount of connections in the network, that can take the CE1 function to a worse performance than all the other functions.

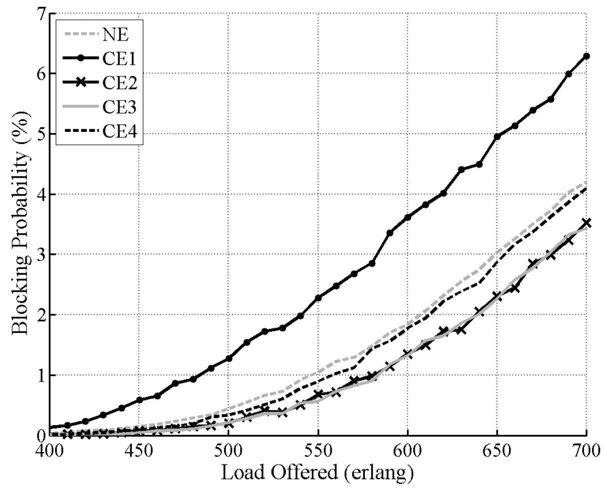

Fig. 5. Blocking probability versus load offered to the NSF network.

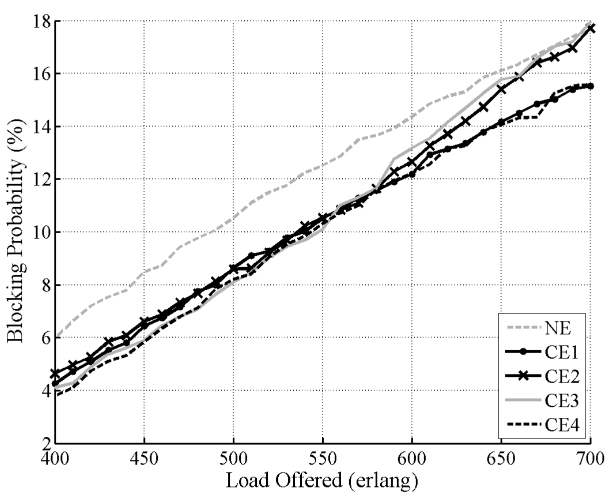

Fig. 6. Blocking probability versus load offered to the ring tree network.

For the links usage the results show that the load distribution in a network considering non-adaptive routing is worse than in a network with adaptive routing, as shown in the Figures 7 and 9 for the six nodes and rings tree topologies, respectively. This result is expected, because the alone traffic grooming does not alter the link costs, not taking that network has has a more uniform load distribution. Like this, the performance with adaptive routing tends to distribute uniformly the load in the links.

However, a same performance is not observed in the result presented for the NSF network. In that topology, the use of adaptive routing doesn't guarantee a better load distribution, as shown in the Figure 8, in the which the performance of the CE1 function is worse than of NE function. Again, that result can be justified being taken into account the size of the network.

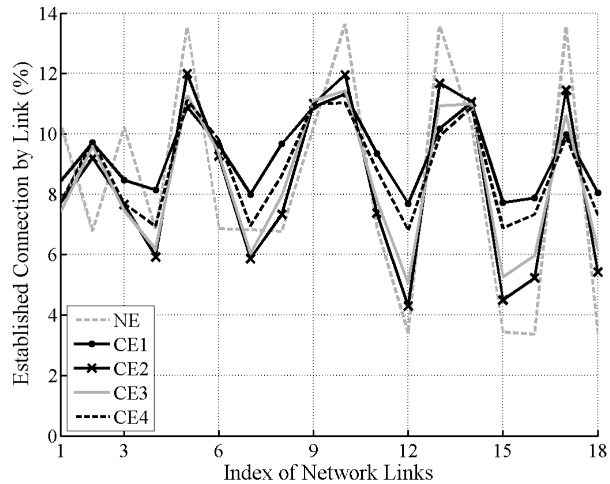

Fig. 7. Percentage of established connections for each link to the six node network.

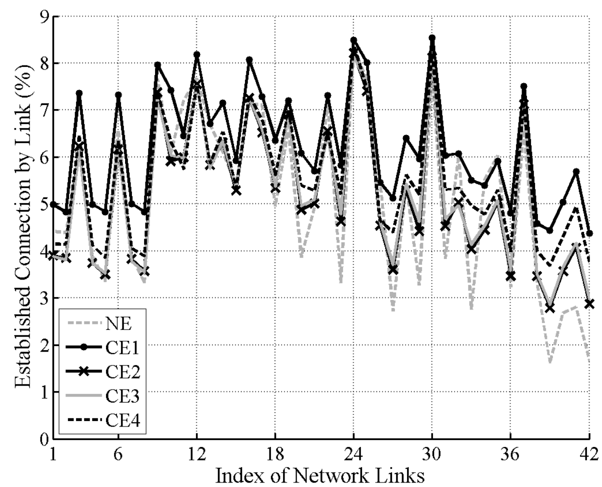

Fig. 8. Percentage of established connections for each link to the NSF network.

VI. Conclusions

In this work we were analyzed three traffic engineering strategies: adaptive routing, traffic grooming and survivability. For the adaptive routing, five cost functions for the costs in the graph of the network are studied, of which one is proposed and the others were obtained from the literature, associated to the Dijkstra algorithm and the first-fit wavelength assignment heuristic. The traffic grooming algorithm considers the wavelength sub-channel bandwidth allocated on demand.

The goal of that work was to evaluate the performance of adaptive routing algorithms, considering the five cost functions, in a dynamic WDM network with traffic grooming capacity, where it exists implemented an protection scheme of the type 1+1 or 1:1.

The results obtained shown that the use of adaptive routing

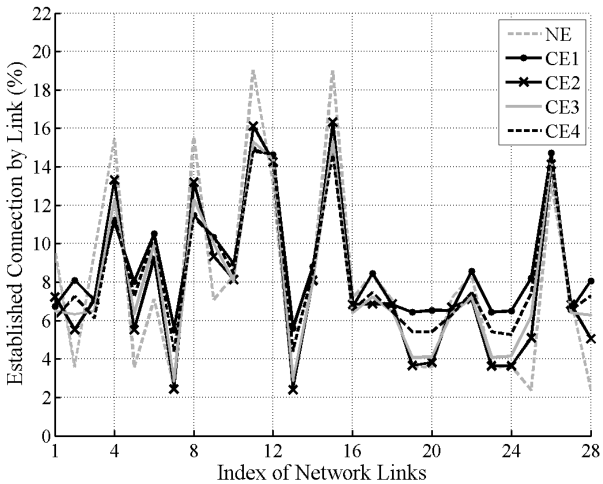

Fig. 9. Percentage of established connections for each link to the ring tree network.

improve the performance of the network, considering the blocking probability and load distribution as evaluation metrics, for all cost functions, with prominence for the functions CE3 and CE4. But, the results shown too a strong relationship between the performance of a function cost and the topology of the studied network. That is outstanding for the results obtained for the NSF network.

Based on the results obtained, one could say that selecting the approach of routing to be used to make a balance between the performance presented with regard to the blocking probability and the load distribution in the network, aiming thus better benefit for the network use. For a better resources use, considering the use of survivability schemes, the traffic grooming appears as a tool that, when coupled with adaptive routing, generates both decreased blocking probability and a more uniform distribution of available resources on the network.

REFERENCES

[1] R. Ramaswami and K.N. Sivarajan, *Optical Networks: a Practical Perspective*, Morgan Kauffmann Publishers, 1998.

[2] I. E. Fonseca. “Uma Abordagem para Aprovisionamento e Diferenciação de QoS Óptico na Presença de FWM em Redes Ópticas Transparentes”, Tese de doutorado, Universidade Estadual de Campinas, Campinas, SP, novembro 2005.

[3] E. Salvadori, “Traffic Engineering in Dynamic Optical Networks”. PhD Thesis. University of Trento, Trento - Italy, February 2005.

[4] P. Ribeiro, “Roteamento Adaptativo com Agregação de Tráfego em Redes Ópticas Dinâmicas”. Master Dissertation. UFCG. Campina Grande - PB, Brazil, June 2008.

[5] H. Zang, J.P. Jue e B. Mukherjee, “A Review of Routing and Wavelength Assignment Approaches for Wavelength-Routed Optical WDM Networks”, *Optical Networks Magazine*, vol. 1, pp. 47-60, January 2000.

[6] A. K. Somani, *Survivability and Traffic Grooming in WDM Optical Network*, Cambridge Press, 2006.

[7] J. Zhang and B. Mukherjee. “A Review of Fault Management in WDM Mesh Networks: Basic Concepts and Research Challenges”. IEEE Network, 2004.

An Approach for Evaluating the Buffer Queueing Behavior of Multifractal Network Traffic Flows.

Jeferson Wilian de Godoy Stênico
School of Electrical and
Computer Engineering
State University of Campinas - UNICAMP
PO Box 6101-13.083-970, Campinas, SP, Brazil
jstenico@decom.fee.unicamp.br

Flávio Henrique Teles Vieira
Federal University of Goiás - UFG
School of Electrical and Computer Engineering
Av. Universitária, n. 1488, Qd. 86, Bloco A 3ºpiso,
74605-010, Setor Leste Universitário
Goiânia - Goiás
flavio@eeec.ufg.br

Lee Luan Ling
School of Electrical and
Computer Engineering
State University of Campinas - UNICAMP
PO Box 6101-13.083-970, Campinas, SP, Brazil
lee@decom.fee.unicamp.br

Abstract - In this paper, we propose an analytical expression for calculating the byte loss probability for multifractal traffic arrivals at a single server queue. Initially, we address the theory concerning the multifractal processes, especially the Hölder exponents of the multifractal traffic traces. Next, we focus on the second order statistics for the multifractal processes. More specifically, we assume that an exponential model is adequate for representing the variance versus time scale aggregation. Finally, we evaluate the performance of the proposed approach by estimating the theorectical byte loss probability against the results obtained by simulations with real traffic traces and that through a method based only on monofractal characteristics.

Keywords: Loss Probability, Multifractal Processes, Network Traffic.

I. INTRODUCTION

The research about network traffic has shown an evident relationship with the fractals theory since the publication of the research work by Leland, Taqqu, Willinger and Wilson [8]. Leland et al verified experimentally that traffic traces collected in the Ethernet network of Belcore Marristow Research and Engineering Center showed fractals properties such as self-similarity and long-range dependence. After this, some later studies found the presence of fractals properties also in traffic generated by transmission of video on variable rate [2,7], high speed network [12], world-wide web [3], and others. It was noted that such fractal properties, with emphasis on the long-range dependence, strongly influence the network performance [9], but cannot be properly shaped by Markovian stochastic processes. It was found that the long-range dependence is an important feature of traffic with important implications in several areas such as queueing theory and network design. The heavy tail distribution of the size or duration of the sessions or connections which result from traffic aggregation is the cause of observed self-similar characteristics [3],[11].

Different mathematical models have been proposed with the objective of representing network traffic with self similar properties. Among them, the model capable of incorporating self-similar characteristics observed in traffic, is the fractional Brownian approach.

However, it has been observed that, while in time scales of the order of hundred milliseconds and more, the traffic behavior was well represented by self-similar models, whereas, in smaller time-scales, self-similar models cannot effectively match real traffic characteristics. This finding has led the search for more comprehensive traffic models, in order to obtain a more faithful description of the network traffic.

Investigations involving WAN TCP/IP traffic [6],[13], found that different properties of the observed traffic in small time-scales could be adequately described by using the multifractal analysis. These properties, observed in small time-scales are due to the action of protocols prevailing in the considered networks, and the end-to-end existing congestion control mechanisms of the Internet, which determine the behaviors of the information flow between different layers in the hierarchy of TCP/IP protocols [5].

Self-similar processes present only a global scaling behavior, corresponding to monofractal scaling properties. Multifractal processes, on the other hand, can be viewed as a generalization of monofractal processes, allowing their regularity and scaling laws to vary in time, and therefore, providing a better description for irregular procedures.

This paper is organized as follows: in Sections II, we define monofractal and multifractal processes, and present some multifractal traffic properties under network traffic processes. In Section III, we investigate the second-order moments of traffic traces with long-range dependence. In Section IV we present the method proposed by Duffield and O'Connell, for estimating lower bounds of loss probability in connections [4]. In Section V we present our proposal for the estimation of the loss probability in connections based on queueing theory. In Section VI we show the results of the experimental investigations and validation of the proposed approach. Finally in Section VII we present our conclusions.

II. CHARACTERIZATION OF MONOFRACTAL AND MULTIFRACTAL PROCESSES

A. *Monofractal and Multifractal Processes*

Multifractal processes are characterized by their moments which has non linear variation in terms of time-scales. Furthermore, Multifractal processes have their local regularity parameter α presenting a varying value with t.

A process z(t) is called monofractal, when the following relationship is hold:

$$Z(ct) \overset{d}{=} c^H Z(t) \tag{1}$$

where $0 < H < 1$, (known as Hurst parameter), c a constant scaling factor and the symbol $\overset{d}{=}$ representing equality in distribution. The multifractal theory generalizes the definition stated in (1) by providing a more general multi-scales relation as:

$$Z(ct) \overset{d}{=} M(c) Z(t) \tag{2}$$

with Z(t) and M(c) are mutually independent and the scaling factor M(c) is a random variable whose distribution does not depend on t. Clearly that Z(t) is a Monofractal process, whenever $M(c) = c^H$. Frequently (2) is written as:

$$Z(ct) \overset{d}{=} c^{H(c)} Z(t) \tag{3}$$

in terms of a general index H(c) = log M(c). In contrast to Monofractal processes, now the index H(c) is a function of c. Therefore, multifractal processes allow varying behaviors in scales.

Multifractal processes also present non – isolated singularities. In fact, their singular behaviors can be observed almost everywhere. In order to characterize their peculiar structures, it is necessary to precisely quantify the regularity of the multifractal process at each time instance. For this end, the pointwise Hölder exponent is one of the measures most widely used to quantify the pointwise regularity of a signal.

Definition 1 (Pointwise Hölder exponent): Let α be a real number and C be a constant, both strictly positive, and $x_0 \in R$.

The function *f*: R→ R is $C^{\alpha}(x_0)$ if we can find a polynomial P_n, of degree n < α such as:

$$\left| f(x) - P_n(x - x_0) \right| < C \left| x - x_0 \right|^a \tag{4}$$

The pointwise Hölder exponent h of the function f at x_0 is defined as:

$$h = Sup\left\{ a > 0 \mid f \in C^{\alpha}(x_0) \right\} \tag{5}$$

Notice that such a polynomial P_n can be found even the expansion Taylor series of *f* around x_0 does not exist.

B. *The Holder Exponent and Network Traffic*

As presented in Definition 1, the Hölder exponent of a time process at a particular point time instant t_0 is related to the regularity level of the signal at that point. In the context of network traffic traces, the exponent measures the degree of local variations of the traffic processes. More precisely, here we show how the traffic traces vary in terms of number of bytes or packages, on a range $[t_0; t_0 + \Delta t]$ of size Δt in t_0.

The Hölder exponent α can be interpreted as a real number which locally controls the multi-scale behavior of a process. The networks traffic is said having local multi-scale behavior with Hölder exponent $\alpha(t_0)$ at time t_0, if the traffic process rate behaves according to $(\Delta t)^{\alpha(t_0)}$ when $\Delta t \to 0$.

In terms of traffic behavior, when $\alpha(t_0)$ has smaller value near to zero, the traffic burst intensity becomes larger. On the other hand, when $\alpha(t_0)$ approaches to one, low intensity of traffic rate variation is generally observed.

For illustration propose, figure 1 shows in gray levels, the magnitudes of the Hölder exponent of traffic trace DIAL 3. This traffic trace is given by the number of packages at 1 millisecond time scale collected from FDDI(fiber Distributed Data Interface) ring at AT&T research laboratories,[5]. Notice that the smaller the Hölder exponent, the more intense traffic burstiness and the darker gray level will become. In contrast, a clearer gray level is used to indicate regions with low bursts occurrence, or higher Hölder exponent magnitudes.

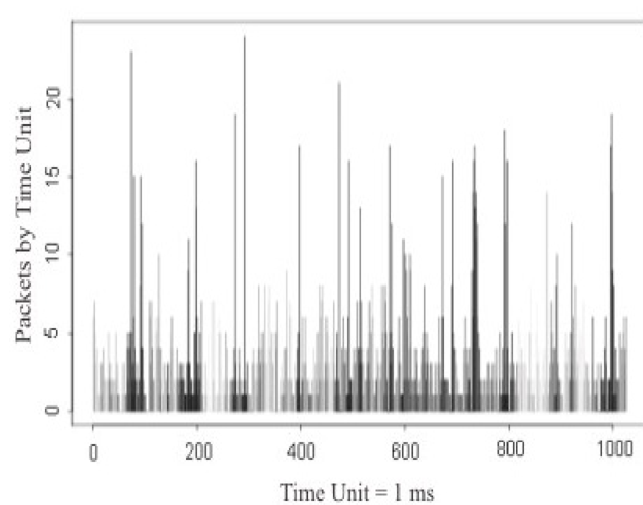

Fig. 1. – Local Regularity of Dial 3 traffic trace represented in different gray levels:: (Dark) small Hölder Exponents; (Clear) large Hölder Exponents.

III. SECOND-ORDER MOMENT OF MULTIFRACTAL PROCESSES

Stochastic processes with multi-scale behavior depend strongly on the first and second moments. The first and second order moment of a multi-scale (multifractal) process are given respectively by [13]

$$\mu = \lambda T \tag{6}$$

$$\sigma^2 \sim \tau^{2\alpha(T)} \tag{7}$$

where μ and σ^2 are mean and variance respectively of process, λ is the average traffic rate , α(T) is Hölder Exponent and T is time scale.

The estimation of Hölder exponent α(T) at time scale T of a process can be simplified by assuming that it has a normal distribution N($\tilde{\alpha}$,$\tilde{\sigma}^2$) with mean $\tilde{\alpha}$ and variance $\tilde{\sigma}^2$, respectively. Therefore, under this assumption, Equation (8) relates the variance of the distribution of the process to the scale time T.

$$\sigma^2 \sim \int_{-\infty}^{\infty} \frac{1}{\sqrt{2\pi}\,\tilde{\sigma}} \exp[-\frac{(\alpha-\tilde{\alpha})}{2\tilde{\sigma}^2}] T^{2\alpha}\, d\alpha \tag{8}$$

Let z = $T^{2\alpha}$, then α = ln(z) / (2ln(T)) and *dα/dz* = *dz* / (2ln(T)z) then the equations (8) can be rewritten from the change of variable as:

$$\sigma^2 \sim \int_{0}^{\infty} z \frac{1}{\sqrt{2\pi}(2\ln(T)\tilde{\sigma})z} \exp[-\frac{(\ln(z)-(2\ln(T)\tilde{\alpha})^2}{2(2\ln(T)\tilde{\sigma})^2}]dz \tag{9}$$

The right hand side of eq. (9) show that σ^2 has simply log-normal distribution with parameters 2ln(T) $\tilde{\alpha}$ and (2ln(T) $\tilde{\sigma}$)^2. For the log-normal given by (9) the following equations for the mean μ and variance σ^2 of multifractal process are valid:

$$\mu = \exp(\varpi + \theta^2/2) \tag{10}$$

$$\sigma^2 = \exp(2\varpi + \theta^2)[\exp(\theta^2)+1] \tag{11}$$

Therefore

$$\varpi = \ln\mu - \frac{1}{2}\ln(\frac{\sigma^2}{\mu^2}+1) \tag{12}$$

$$\theta = \sqrt{\ln(\frac{\sigma^2}{\mu^2}+1)} \tag{13}$$

In this work, instead of a normal distribution, an exponential function *f(x) = a exp(bx)* is used to describe the behavior of the variance σ^2 under time scale T. This modification is justified by traffic trace analysis as illustrated in Figure 2.

Figure 2 shows the variance in functions of time scale T. For Internet multifractal traffic trace, dec_pkt_3. The lower modeling error is obtained for the exponential function modeling in comparison to the normal distribution based approach. More precisely, the root mean square error of exponential modeling is equal to 0.002928.

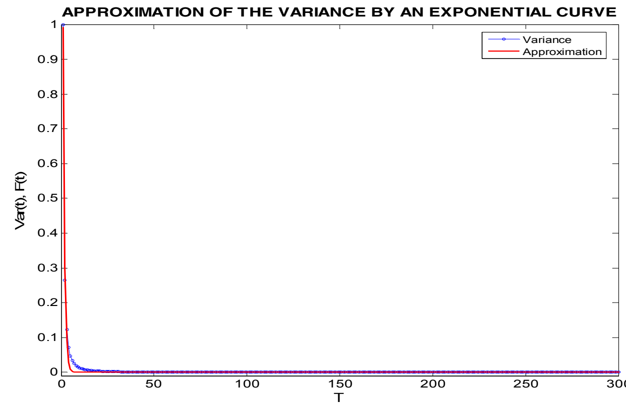

Fig. 2. Time in function of Variance and Exponential Function

Using the exponential function *f(x) = a exp(bx)* to represent the distribution of variance σ^2 and replacing (6) in (12)and (13) we have:

$$\varpi = \ln[\frac{\lambda T}{(c/\lambda^2)a\exp(bx)+1)}] \tag{14}$$

$$\theta = \sqrt{(c/\lambda^2)a\exp(bx)+1)} \tag{15}$$

where c is a constant.

IV. LOSS PROBABILITY ESTIMATIONS FOR LRD PROCESSES

Several issues of traffic engineering, such as estimation of buffer size estimation and traffic flow control, are intimately related to the queueing behaviour at routers. The of long-range dependence (LRD) characteristic of traffic can cause significant impacts on the behaviour of traffic queue [10].

Norros [10], and Duffield and O´Connell [4] proposed some lower bounds for loss probability P(Q>b) at queue under self-similar processes input. However, in many situations, these lower bounds underestimate the real loss probability since. The lower limit for P(Q>b) decay asymptotically in accordance with a Weibull function for large buffer. Consequently the probability function of buffer occupation has a much 'heavier' tail than one predicted by the exponential distribution under traditional buffer overflow models of short range dependence. The probability distribution of buffer occupation or the loss probability of a given process with global scale measure H ∈ (0.5,1) can be estimate by [4]:

$$\lim_{b\to\infty} b^{-2(1-H)} \ln P(Q>b) = -a^{-2(1-H)}(a+C)^2/2 \tag{16}$$

where a=C/H –C.

V. A NEW APPROACH FOR LOSS PROBABILITY ESTIMATION WITH MULTIFRACTAL INPUT PROCESSES

Let X(t) be a multifractal process with log-normal distribution as follows

$$f_{X(t)}(x) = \frac{1}{x\theta\sqrt{2\pi}} e^{\frac{-(\ln(x)-w)^2}{2\theta^2}} \tag{17}$$

The distribution parameters ω and θ can be determined by the knowledge of mean μ and variance σ^2 of the process X(t) as follows.

We assume that there is a stable single queue with buffer having enough capacity to accommodate eventual transient burst and the following balance equation can be established:

$$Q(t_0) + V(t - t_0) = Q(t) + O(t - t_0) \tag{18}$$

where Q(t) is the queue length at time t, $V(t-t_o)=W(t)-W(t_o)$ is the cumulative traffic load in the period $[t,t_0]$, and

$$O(t) = C(t - I(t)) \tag{19}$$

In (19) C is the constant service rate and I(t) denotes the total number of server idle at time t. Therefore Q(t) can be written as:

$$Q(t) = \max(V(t) - O(t), 0) \tag{20}$$

Let Y(t) = V(t) – Ct and Δ(t) = C.I(t). equation (20) can be expressed as :

$$Q(t) = \max(Y(t) + \Delta(t), 0) \tag{21}$$

Applying the law of total probability, the loss probability in queue cam be calculated as:

$$\begin{aligned} P_{loss}(t) &= P(Q(t) > q) = P(Y(t) + \Delta(t) > q, Y(t) > q) + \\ &P(Y(t) + \Delta(t) > q, Y(t) \le q) \\ &= P(Y(t) > q) + P(Y(t) \le q < Y(t) + \Delta(t)) \end{aligned} \tag{22}$$

The first term P(Y(t) > q) is called the absolute loss probability (P_{abs}) and the second term P(Y(t) ≤ q ≤ Y(t) + Λ(t)) the opportunistic loss probability (P_{opp}). Assuming Q(t) stationary, and let $\rho = 1 - \eta = 1 - \lambda/C$ using the result derived by Benes [1] the second term (P_{opp}) can be written as:

$$P_{opp}(t) = P(Y(t) \le q < Y(t) + \Delta(t)) = \rho \int_0^t f_{v(u)}(v)|_{v=Cu+q}\, du \tag{23}$$

Also the absolute loss probability (P_{abs}) can be written as an integral:

$$P_{abs}(t) = P(Y(t) > q) = P(V(t) > Ct + q) = \int_{Ct+q}^{\infty} f_{V(t)}(v)dv \tag{24}$$

Thus, the fully characterized queuing behavior of eventually any traffic type in term of information loss is given by:

$$P_{loss}(t) = \int_{Ct+q}^{\infty} f_{V(t)}(v)dv + \rho \int_0^t f_{V(u)}(v)|_{v=Cu+q}\, du \tag{25}$$

the first term on the right side of eq.(25) further detailed expressed

$$P_{abs}(t) = \int_{Ct+q}^{\infty} f_{V(t)}(v)dv = \frac{1}{2} - \frac{1}{2} erf[\frac{\ln(Ct+q) - \varpi(t)}{\sqrt{2}\theta(t)}] \tag{26}$$

Thus, the loss probability under stationary state is

$$P_{steady} = \lim_{t\to\infty} P_{loss}(t) = \rho \sup_{t>0}\{\rho \int_0^t f_{V(u)}(v)|_{v=Cu+q}\, du\} \tag{27}$$

$$P_{steady} = (1 - \frac{\lambda}{C}) \int_0^{\infty} \frac{1}{x\theta\sqrt{2\pi}} e^{\frac{-(\ln(x)-w)^2}{2\theta^2}} |_{x=Cu+q}\, du \tag{28}$$

Note that for multifractais traffic series the variables ϖ and θ can be calculated using equations (14) and (15), respectively. Using relations given by the equations (14) and (15) into (28), we get a new expression for the loss probability:

$$P_{steady} = (1 - \frac{\lambda}{C}) \int_0^{\infty} \frac{\exp\left[\frac{-[\ln((Cx+q)\sqrt{(c/\lambda^2)a\exp(bx)+1}) - \ln(\lambda x)]^2}{2\ln((c/\lambda^2)a\exp(bx)+1)}\right]}{\sqrt{2\pi\ln((c/\lambda^2)a\exp(bx)+1)}(Cx+q)} dx \tag{29}$$

VI. EXPERIMENTAL INVESTIGATION AND RESULTS

Simulation investigations were carried out involving some real network traffic traces to validate the proposed loss probability estimation approach (dec_pkt_3, lbl_pkt_5 and dec_pkt_1). Previous papers state that the traffic traces used in this work presents multifractal characteristics [13]. This fact is revealed through an analysis involving different time scale of aggregation. The following configuration for the simulation of a single-server queue was considered:

TABLE I CONFIGURATION

Traffic Trace	Server Capacity (Bytes/s)	Buffer Size (Bytes)
dec_pkt_3	25×10^4	3×10^4
lbl_pkt_5	5.7×10^4	3×10^5
dec_pkt_1	26.7×10^5	3×10^5

Table II compares the loss probability estimates (in bytes) for these traffic traces in a single server queue scheme, obtained through the following methods: by simulations, applying the Duffield's method [4] and the proposed one.

TABLE II LOSS PROBABILITY

Traffic Trace	Simulation	Duffield	Proposed
dec_pkt_3	1.538×10^{-9}	7.063×10^{-23}	8.804×10^{-9}
lbl_pkt_5	5.2059×10^{-9}	1.6805×10^{-36}	9.5024×10^{-9}
dec_pkt_1	1.7703×10^{-9}	8.0962×10^{-15}	1.0776×10^{-9}

Notice that the proposed approach considerably outperforms the method proposed by Duffield. Mostly important, the proposed method that provides loss probability estimates that clearly match to those obtained is the simulations.

Figure 3 to 5 compares how loss probability estimates from vary with size buffer. Again, the performance measures of the proposed approach are much closer to that observed in the simulations than the values obtained by applying the monofractal approach (Duffield)[4].

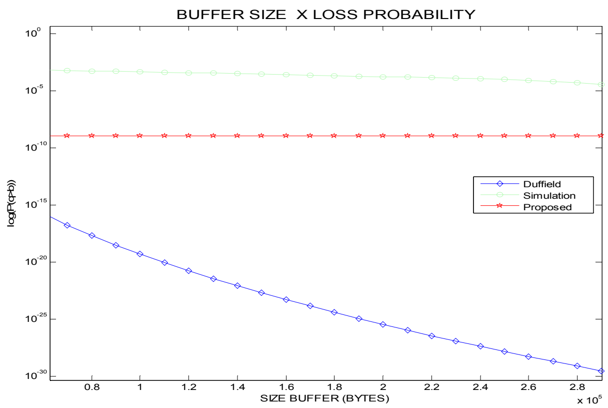

Fig. 3. Loss Probability versus Size of Buffer for the traffic trace dec_pkt_3

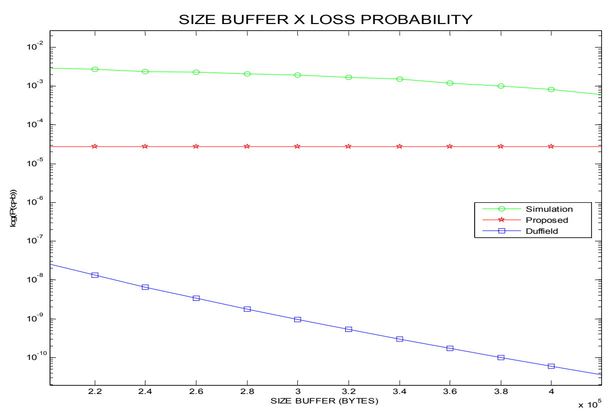

Fig. 4. Loss Probability versus Size of Buffer for the traffic trace lbl_pkt_5

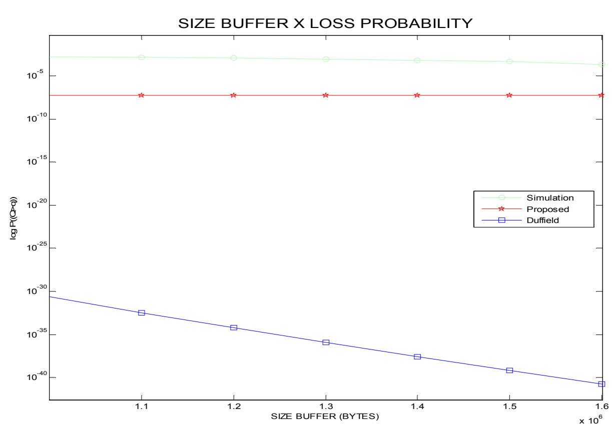

Fig. 5. Loss Probability versus Size of Buffer for the traffic trace dec_pkt_1

Figure 6 to 8 we show how, loss probability changes in terms of different serve capacities. Once again the proposed approach provides more accurate estimation and outperforms the method proposed in.[4]

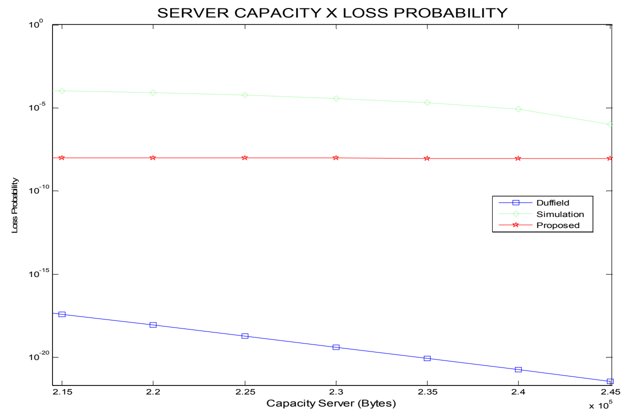

Fig. 6. Loss Probability versus Capacity Server for the traffic trace dec_pkt_3

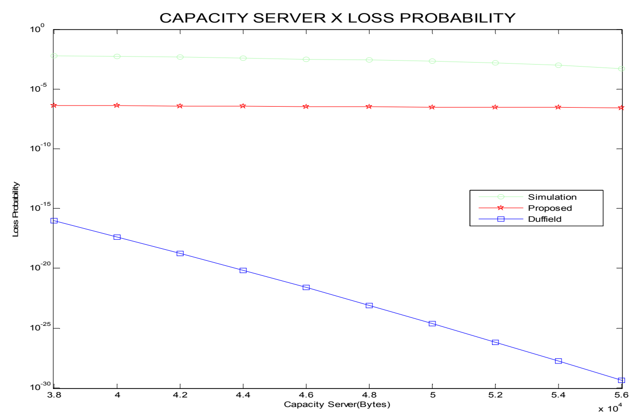

Fig. 7. Loss Probability versus Capacity Server for the traffic trace lbl_pkt_5

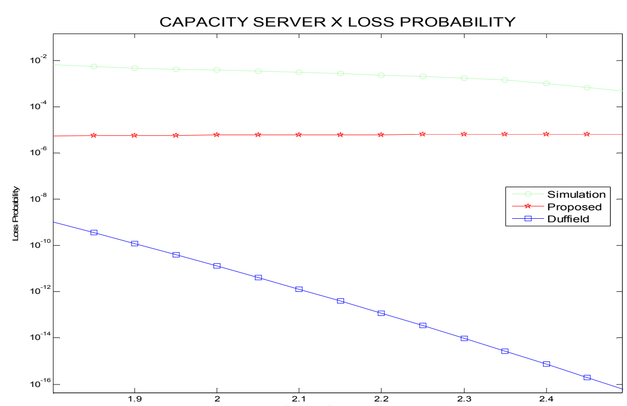

Fig. 8. Loss Probability versus Capacity Server for the traffic trace dec_pkt_1

VII. CONCLUSIONS

Traffic models based on the fractal theory are capable of capturing important features of network traffic and therefore enhancing our understanding and allowing us to study the effects of the parameters of the model in the network performance.

In this paper we present a new approach for calculating the loss probability for network traffic traces that have multifractal characteristics. To do this, first we show that an exponential function can be used to model the variance of traffic which is time dependent scale aggregation. Using the queueing theory and some multifractal properties (for example, log-normal distributions) we are able to derive an expression to estimate the loss probability of the data in connections.

The experimental results demonstrate the efficiency of the proposed method which provides more accurate estimations than the monofractal method.

REFERENCES

[1] Benes V.(1963) General Stochastic Processes in the Theory of Queues Reading, MA: Addison Wesley.

[2] Beran, J. et al.(1995) Long range dependence in VBR video traffic. IEEE Transactions on Communications, v.43, p.1566-1579.

[3] Crovella, M. E.; Bestavros,(1996) A. Self-similarity in world wide web traffic - evidence and possible causes. Proceedings of ACM Sigmetrics, p.160-169.

[4] Duffield,N.G.e O'Connell,N.(1993). Large deviations and overflow probabilities for the generalsingles-server queue, with applications,"Dublin Institute dor Advanced Studies-applied Probability Group, Tech.1 Rep.Disas-STP-93-30.

[5] Feldmann, A.; Gilbert, A.; Willinger, W. and Kurtz, T. G (1998). The changing nature of network traffic: Scaling phenomena. ACM Computer Communication Review, v.28, p.5-29.

[6] Feldmann, A.; Gilbert, A.; Willinger, W (1998). Data networks as cascades: Explaining the multifractal nature of Internet WAN traffic, Proceedings of ACM Sigcomm, p.42-55.

[7] Garret M. W.; Willinger, W.(1994) Analysis, modeling and generation of self-similar VBR vide traffic. Proceedings of ACM Sigcomm, p.269-280.

[8] Leland, W. E. et al. On the self similar nature of Ethernet Traffic (extended version). IEEE/ACM Transactions on Networking, v.2, n.1, p.1-15.

[9] Norros,I(1994). A storage model with self-similar input, queueing Systems,v.16,pp.387-396.

[10] Norros,(1995) I. On the use of fractional Brownian motion in the theory of connectionless networks. IEEE Journal on Selected Areas in Communications, v.13, n.6, p.953-962.

[11] Park, K.; Willinger, W. (2000) (Eds.) Self-similar network traffic and performance evaluation. New York: Wiley.

[12] Paxson, V.; Floyd S.,(1995) Wide area traffic: The failure of poisson modeling. IEEE/ACM Transactions on Networking, v.3, n.3, p.226-244.

[13] Riedi, R. H. et al.(1999) A Multifractal Wavelet Model with Application to Network Traffic. IEEE Transactions on Information Theory, v.45, p.992-1018.

A network traffic monitor based on Python, Plone and RRDTool

Antonio João Ferreira Francisco
ANSP/Núcleo de Apoio à Rede Acadêmica (NARA)
R.Dr.Ovidio Pires de Campos, 215 - 2nd. floor - 05403-010
São Paulo - SP - Brazil
antonio@ansp.br

Marcio Antonio Costa
ANSP/Núcleo de Apoio à Rede Acadêmica (NARA)
R.Dr.Ovidio Pires de Campos, 215 - 2nd. floor - 05403-010
São Paulo - SP - Brazil
marcio@ansp.br

Paulo Cesar Costa dos Santos
ANSP/Núcleo de Apoio à Rede Acadêmica (NARA)
R.Dr.Ovidio Pires de Campos, 215 - 2nd. floor - 05403-010
São Paulo - SP - Brazil
pccs@dim.fm.usp.br (FAPESP fellowship)

Jorge Futoshi Yamamoto
ANSP/Núcleo de Apoio à Rede Acadêmica (NARA)
R.Dr.Ovidio Pires de Campos, 215 - 2nd. floor - 05403-010
São Paulo - SP - Brazil
yamamoto@ansp.br (ANSP is a project sponsored by FAPESP)

Abstract— **This paper presents a system to check ANSP network traffic developed for Zope/Plone platform. The data from network equipments is acquired through SNMP protocol using standard MIBs. The collected data is processed by scripts written in Python language that feed a RRD database and the results are graphed by the RRDTool program.**

I. INTRODUCTION

ANSP (an Academic Network at Sao Paulo) is an WAN installed in São Paulo State, Brazil, sponsored by Fapesp (Fundação de Amparo à Pesquisa do Estado de São Paulo) since 1989. The main universities and research centers are connected among them by ANSP. It is also responsible for provide them Internet Commodity and Internet2.

A tool named monitor is available for ANSP participants to check their network traffic in bits. It is customized from Round Robin Database Tool (RRDTool), developed by T. Oetiker [4].

About five year ago ANSP team decided to migrate ANSP site from standard Apache Server to Zope server but any changes were made in monitor tool. Zope is an open source framework application server written in Python language and maintained by Zope Foundation.

Created in 2001, Plone is a content management system built on Zope framework. ANSP site adopted it three years ago and our team began to study an way to developed a new monitor tool in Zope/Plone environment.

II. OBJECTIVE

The aim of this paper is to present the development of a time statistical network tool in a object-oriented environment. There are many software with the same functionality but ANSP monitor intends to be an option to whom adopted Plone/Zope server.

III. MATERIAL AND METHODS

A. Description

The principal tools utilized in ANSP monitor are described below.

1) Zope and ZEO: The Zope application server is a transactional object system written in Python [3] with a oriented-object database, named ZODB (Zope Object DataBase), where an in-memory cache of objects can be interacted with in many ways [7]. ZODB manages a single file in a hard disk identified typically as `data.fs`. Two or more Zope servers can not share the same file: this forbids to adopt multiprocessor systems.

Zope Enterprise Objects (ZEO) was created to take advantage of multiprocessor systems [6]. With ZEO, many Zopes instances distributed on many processors are connected to a Zope Storage Server (ZSS). When one Zope changes an object, the changes are sent to the ZSS, which sends a message to the other Zopes. The other Zopes then remove the object from their cache. If the object is needed on a subsequent request, the Zopes fetch the object from the ZSS.

A balance web access system can be coupled to the ZEO. The ANSP monitor application takes advantage of both systems: one user access the service, the balance system takes the less occupied Zope instance and ZEO gives the required data. ANSP adopted a balance web access solution from Foundry Networks.

2) Plone: Plone[2] is Content Management System (CMS) built upon Zope that allows easy website management for non technical people, like adding and editing pages or news. It also creates navigation links based on the content, controls users permissions and index the content. For those reasons ANSP team decided to migrate ANSP site to Plone.

However, the legacy ANSP monitor application did not integrate with Plone, so a new application was developed, mapping network entities, like routers and interfaces, to Plone content types.

B. ANSP monitor modules

Two modules compose ANSP monitor. The first one collects traffic information from network hardware and saves the data.

The second one is dealing with recording general information about links, like IP addresses and interfaces, and it generates traffic graphics. The intersection point between them is a relational database, where all information is stored.

- Collector module: this module consists of one Python script, that runs at a periodic time (usually five minutes), started by the cron system in a UNIX server with at least read rights access to all network equipments. Data collection uses SNMP[5] protocol, through PySNMP library. Once the data is available, it is stored in a RRDTool database, through PyRRD library. The five minutes interval is adopted for some reasons. First, a larger interval would make the results very inaccurate because SNMP returns the average traffic between two moments. Second, a smaller one would increase CPU usage from both the collecting machine and the network device, what could cause interference in the network. For example, suppose an interval of thirty minutes is used, and a link had a traffic that usually ranges from 10 Mb/s to 12 Mb/s. If, during thirty seconds, the link has its traffic increased to 100 Mb/s, and in the rest of the time it is 10 Mb/s, the graphic will not show the high traffic, because the average traffic will be 11.5 Mb/s. But, if the interval was five minutes, the graphic would show 19 Mb/s, what would be noticed.
- Management module: this module consists of a Plone product, written using Archetypes [1] framework. It manages all data about the connections, allowing insertions, deletions and updates. Traffic graphics are created using RRDTool and they are available integrated with Plone interface.

IV. Results

The application is going to be fully functional in 2009 first quarter. Some screenshots are presented below.

Figure 1 presents the main page of monitor. It shows the qualitative states of connections, their bandwidth, references for other informations and link to traffic graphics.

Figure 2 shows one traffic graphic generated by RRDTool and fully integrated with Plone environment.

Example of network traffic graphic generated by RRDTool and integrated in Plone environment.

Figure 3 displays information about a network connection of one ANSP participant.

Webpage screenshot that describes characteristics about a link.

The main result of this application is the integration with ANSP site, allowing site administrators to work with only one web interface for both the site and the network monitoring. It also saves time for system administrator, who have to take care of just one environment.

V. Future developments

Launched the first version of application, ANSP intends to develop some extensions like a module to collect Netflow or SFlow data and diagnosis graphics based on them. Studies about adequated sample size could be made. Qualitative and quantitative analysis about layer 3 and layer 7 could be implemented but it depends on high processing performing and some hardware network features.

ANSP intends to create a distribution kit to Zope community.

Fig. 1. ANSP monitor main page snapshot.

References

[1] http://plone.org/products/archetypes, accessed in November, 25 2008 at 12:30 (Brazil DST).
[2] http://plone.org/about/plone, accessed in November, 28 2008 at 13:09 (Brazil DST).
[3] http://www.python.org, accessed in November, 25 2008 at 11:40 (Brazil DST).
[4] http://oss.oetiker.ch/rrdtool/index.en.html, accessed in November, 25 2008 at 11:44 (Brazil DST).
[5] S. Feit, SNMP: A Guide to Network Management, 2nd edition, McGraw-Hill, 1995.
[6] http://www.plope.com/Books/2_7Edition/ZEO.stx, access in November, 25 2008 at 11:55 (Brazil DST).
[7] http://www.zope.org/WhatIsZope, accessed in November, 25 2008 at 11:53 (Brazil DST).

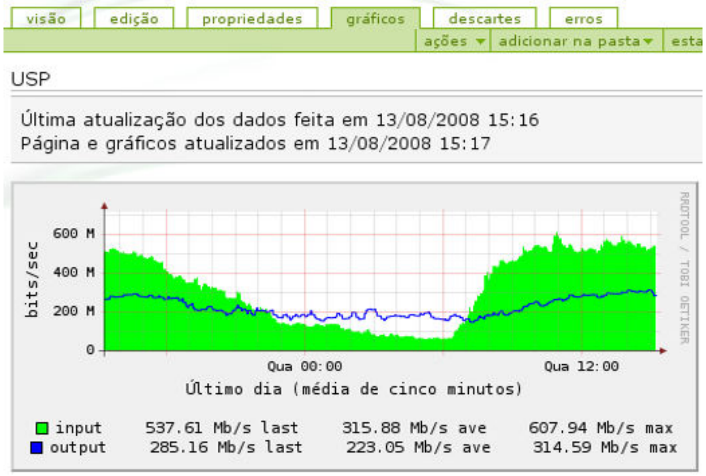

Fig. 2. Example of network traffic graphic generated by RRDTool and integrated in Plone environment.

Fig. 3. Webpage screenshot that describes characteristics about a link.

Effect of Buffer Size on Anycast Routing Using Genetic Algorithms in Delay Tolerant Networks

Éderson Rosa da Silva
Faculty of Electrical Engineering
Federal University of Uberlandia
Uberlandia - MG - Brazil
ederson@eel.ufu.br

Paulo Roberto Guardieiro
Faculty of Electrical Engineering
Federal University of Uberlandia
Uberlandia - MG - Brazil
prguardieiro@ufu.br

***Abstract*—Delay/Tolerant Networking (DTN) has grown as a research area is focused on addressing the communication requirements to challenged networks, characterized by frequent disconnections and high delays. There are different types of DTNs, depending on the nature of the network environment. Hence, different routing schemes are proposed. In this paper we treat the anycast routing where hosts wish to delivery messages to at least one, and preferably one, of the members in an anycast destination group. To do this, we applied genetic algorithm (GA) for route decision. Then we implement a GA-based anycast routing algorithm and analyze the effect of buffer size on performance. Our simulation results have shown that the routing using GA performs better when the network resources are scarce if compared with an algorithm that take in count only the number of hops.**

***Index Terms* — anycast routing, delay tolerant networking, genetic algorithms.**

I. Introduction

Along with the increasing penetration of computing and communications technologies into our world and our lives, we have seen the arising of emerging networks, however, in certain networking scenarios, important Internet protocols are not usable. DTN (Delay/Disruption Tolerant Networking) as a research area is focused on addressing the communication requirements specific to these challenged networks. These networks may suffer frequent disconnection, high delay, high data rates, asymmetric data rates between source and destination, with the possibility of never having end-to-end connectivity between the source and destination over a given period of time. Therefore, the design of protocols for those networks becomes a unique challenge.

The IRTF (Internet Research Task Force) created a new research group to examine the more general area of DTN. That group is called the DTNRG, and it is currently the main open venue for work on the DTN architecture and protocols. The DTNRG is documenting these protocols as so-called experimental RFCs.

RFC 4838 [1] describes an architecture for delay-tolerant and disruption-tolerant networks, defining an end-to-end message-oriented overlay, called bundle layer (Figure 1). RFC 5050 [2] describes the end-to-end bundle protocol, block formats, and abstract service description for the exchange of messages (bundles) in DTNs.

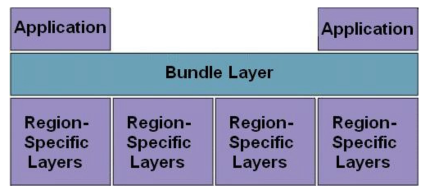

Fig. 1. Bundle layer

Many of the principles of DTN architecture are reviewed by Fall and Farrel [3], being highlighted design decisions that have persevered through repeated analyses.

A common challenge in DTNs is the routing. In store-carry-forward routing, a next hop may not be immediately available for the current node for forward the data (bundle). The node will need to buffer the data, and maybe carried, until the node gets an opportunity to forward the data and must be capable of buffering the data for a considerable duration.

Basically, we have two categories of routing protocols in DTNs: deterministic and stochastic case. Zhang [4] review a few routing protocols for both cases. Besides, the routing algorithms can be proposed depending on the amount of knowledge about the network.

In this paper, we treat the routing for anycast delivery, which allows a node to send a message to at least one, and preferably only one, of the members in a group. The idea behind anycast is that a client wants to send packets to any one of several possible servers offering a particular service, but does not really care any specific one.

There are various applications of anycast in DTN such as disaster rescue field (people may want to find a doctor or fireman without knowing their locations and specific IDs), battle fields (e.g. a command center may want to deliver a particular message to any soldier among a group - squad), long distance education (e.g. send a message to anyone one of the members in a group), and many other applications.

DTNs are characterized by long transfer delays. Under these situations, the group membership may change during a message transfer, being necessary to define the intended receivers of a message. In section III, we will view a situation when from perspective of traditional anycasting, it is not clear which nodes should receive a message and three anycast semantic models.

The most of works found in the literature treat the unicast delivery. However, in this case, the destination is determined when the message is generated, while in anycast, the destination can be any one of a node group and the group membership may change during a message transfer.

The GAs (Genetic Algorithms) are most appropriate for multi objective optimization problems. Like that, because the route and destination decision will influence many parameters simultaneously (like delay, delivery probability) we applied GA for perform the routing in DTN.

The GA will be used to define the route and destination of the message for deterministic case (we assumed that future movement and connections are completely known) representing the network through directed multi-graph (we talk about multi-graph in section III).

We study the effect of buffer size on our GA-based anycast routing algorithm and compare to other algorithm that computes the shortest number of hops.

The remainder of this paper is organized as follows: Section II presents related works. Section III describes the system model. Section IV introduces the role of GA in our routing. Section V describes the simulation while Section VI shows and discusses the results. The last section presents the conclusion and future works.

II. Related Work

Anycast routing has been studied extensively in Internet and MANETs (mobile ad hoc networks). More specifically, anycast routing using GA in MANETs has been studied [5,6], but routing in DTN is more challenging due to the frequent partitions and long end-to-end delay.

Multicasting is analyzed in DTNs [7, 8] using several multicast routing schemes. It is important to note that when the multicast service is used, mobile nodes responsible for assisting in the delivery of messages (bundles), store the messages until it is confirmed that all members of the destination group already have received. In our anycast case, mobile nodes responsible for bringing the message to a member of the anycast group need to store them until delivery to only one member of the anycast group, which leads to a substantial saving in storage of mobile devices that relayed the messages to a destination group.

Gong et al [9] analyze the anycast semantic for DTN and presented a metric named EMDDA (expected multi-destination delay for anycast). The authors assumed that nodes in the network were stationary. The connectivity among the nodes was the mobile devices that act as carrier to deliver messages for the nodes. Also the moving patterns of these mobile devices can be obtained.

We used some ideas from [9], but this work is based on estimation, i.e., decision about forwarding packets are based on the likelihood of the delivery of each neighbor. The decisions considered the average end-to-end delay. The routing performed by Gong et al [9] is categorized as stochastic case and our routing can be considered deterministic case.

Despite Gong et al [9] present three types of semantic anycast that allow the source explicitly specify the destination of a message through the models CM (Current Membership), TIM (Time Interval Membership) and TPM (Temporal Point Membership), the network traffic during the selection of routing is not considered. Our anycast routing scheme incorporate both node storage constraint and network traffic dynamics.

III. System Model

For semantics of anycasting in traditional networks such as the Internet and MANETs, the receiver of an anycast packet is well defined, since data transfer delay in these networks is short. This, however, due the large transfer delays is no longer valid in DTNs, because the memberships can change during data transfer. This way it is necessary to define new semantic models for anycast in DTNs.

We represent the DTN as a directed multi-graph. In a tutorial article [10], is described a simple combinatorial reference model that captures most characteristics of time-varying networks.

A. Anycast semantics

Consider the simple example in Figure 2 where a source sends a message to a group at time t. Let t' be the earliest time that other nodes could possibly receive this message according to network topology limitations. Suppose that node A joins the group at time $t_1 < t$ and leaves at time t_2, $t < t_2 < t'$. Node B joins at time t_3, $t < t_3 < t'$ and never leaves. From the perspective of traditional anycasting, it is not clear which nodes should receive this message, whether A, B or neither of them.

Fig. 2. An example of anycast semantics in DTNs.

Consequently, new anycast semantic models should be developed. In [9] is described that the intended receiver should be clearly defined for a message as group membership changes when nodes join and leave the group. It is showed three anycast semantic models that allow message sender to explicitly specify the intended receivers of a message:

- Current Membership Model (CM): the receiver of the message should be destination group member at the time of message delivery;

- Temporal Interval Membership Model (TIM): a message includes a temporal interval that specifies the period during which the intended receiver must be a member of destination group member;

- Temporal Point Membership Model (TPM): its intended receiver at least should be a member of destination group at some time during membership interval.

In our anycast routing we define the intended receiver when the message is generated. This is a particular case of the TIM model, whereas that the temporal interval is the instant of the message generation.

B. Network model

We use a directed multi-graph to represent the DTN and consider that the topology may be known ahead of time. In DTN graph more than one edge may exist between a pair of nodes. Furthermore, the link capacities (storage capacity, propagation delay and departure time) are time-dependent.

The edge representation used is showed in Figure 3. An edge between node 1 and 2 means that there exist some mobile devices moving from the initial node 1 (source) to the terminal node 2 (destination). The storage capacity (*c(1,2)*) on all mobile devices is limited and we will study its influence in our results.

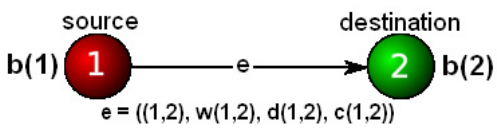

Fig. 3. An edge in a DTN graph

We assume that every mobile device that moves between the same initial node, 1, and terminal node, 2, has the same moving speed, thus having the same moving delay, *d(1,2)*, from the source to the destination. The departure time *w(1,2)* of mobile devices on each edge is represented by randomly generated numbers with Poisson distribution. *b(1)* and *b(2)* are the storage capacity of node 1 and 2, respectively.

Besides, the nodes in the network are stationary and generate messages. On the other hand, mobile devices move from one node to another and do not generate messages themselves.

IV. Role of Genetic Algorithm in Routing

The objective of GA in our work is to assist in the anycast routing for route and destination decision. GAs are defined as search algorithms based on the mechanics of natural selection and natural genetics [11]. They combine survival of the fittest among setting structures (in our case, routes) with a structured yet randomized information exchange to form a search algorithm. They efficiently exploit historical information to speculate on new search points with expected improved performance.

Most of real world problems are nonlinear, where nonlinearity is the norm, where changing one component may have ripple effects on the entire system, and where multiple changes that individually detrimental may lead to much greater improvements in fitness when combined. GAs are appropriated to solve these problems.

Before examining the mechanisms and the power of a simple GA, we must be clearer about our goals when we say we want to optimize a function or a process.

We defined each population individual being a possible route for each session. The GA keeps a population of routes created using randomly selected possible paths (our chromosome) and allows filter routes to combine and produce offspring with new characteristics, which may replace low fitness old routes. Fitness function is a particular type of objective function that quantifies the optimality of a solution.

The GA copies routes with some bias toward the best, mate and partially swap (sub) individuals, and mutate occasional possible paths for good measure. We set the crossover probability to 0.8 and the mutation probability to 0.1. We use these values to increase the diversity in the individual population. Our GA is controlled by the number of generations and the population has 50 individuals.

We want to search the route and consequently the destination that better serve the routing objective (enhance some metric) using GA. Figure 4 shows an example of population representation. We have two individuals (X1 and X2) representing four anycast sessions and the points P1, P2 and P3 representing the possible crossover points. The points P1, P2, P3 are separating each possible route. Each number in each square represents the nodes. We can see that the first route is 19-03-23, i.e., the source is the node 19 and the destination chosen by the algorithm is the node 23 passing by node 3.

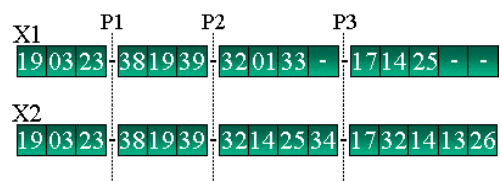

Fig. 4. Population representation

Y1 and Y2 (Figure 5) represent the individuals generated by the crossover between X1 and X2 at point P3. Figure 6 shows a mutation of the fourth route in the individual X2.

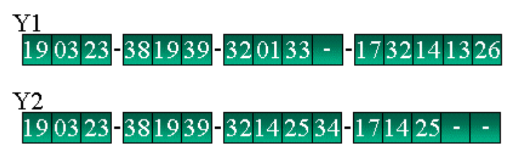

Fig. 5. Crossover example

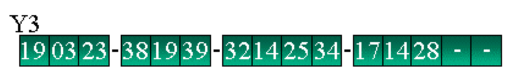

Fig. 6. Mutation example

We define two metrics for optimization. First, we choose a minimum delivery probability. We define that the GA must search routes with delivery probability above 80% and a route (optimal or very good) that satisfying the probability and has the lesser delay.

V. Simulation

We use simulation to compare the performance of the GA-based anycast routing algorithm and the SP (shortest path) algorithm modified (the cost function considered was the number of hops) in different scenarios.

Routing algorithms in the constructed space-time graph can be developed using SP algorithm. For example, Dijkstra's algorithm was adapted to compute the shortest path by Jain, Fall and Patra [12]. We adapted the shortest path to compute the lesser number of hops between the source and destination.

A. Modeling and simulation

Depending on the available knowledge about the network, [12] defines knowledge oracles. Our routing algorithm has a partial knowledge (more practical assumption from an implementation perspective than complete or zero knowledge): our algorithm uses information about node and edge queuing, storage capacity, moving delay, and departure time of the mobile devices. We use these informations to define the better destination and compute the route.

In our simulation, we employ Waxman Network Topology Generator [13] to generate a random graph of 40 nodes. In the Waxman generator, the nodes follow a Poisson process in the plane. The probability to have an edge between u and v is given by

$$P(u,v) = \alpha . e^{-d/(\beta . L)} \qquad \textbf{(1)}$$

where $\alpha > 0$, $\beta \leq 1$, d is the distance from u to v, and L is the maximum distance between any two nodes. We set α to 0.4 (chose a density of short edges relative to longer ones middle) and β to 0.2 (graphs with lower edge densities).

We assume the communication between nodes is carried out by mobile devices (to simulate the behaviors of DTNs). For each edge generated by Waxman generator, we replace it with a mobile device acting as ferries. We use the statistic toolbox poissrnd to generate random numbers from the Poisson distribution to represent the leaving time (*w(u,v)*) of mobile devices on each edge with mean interval time selected randomly from 600 to 6000 seconds. The moving delay (*d(u,v)*) on each edge is a number selected randomly between 60 and 600 seconds, which is multiplied by the distance between the nodes.

We assume that the storage capacities (*c(u,v)*) of each mobile device can vary, and we study its influence in routing algorithm performance. The storage capacities of each node (*b(node)*) may vary from 600 to 1000 messages. We showed an example of edge between node *u* (1) and *v* (2) in Figure 2.

In section VI, we use the topology and enumerate the nodes according Figure 7 (scale 1:100 meters). For each anycast session (we consider only anycast traffic in our simulations) we generate a random number between 2 and 5 to represent the number of possible destinations. We randomly pick a node as the anycast source. The first destination member is selected randomly from the possible nodes except the source node. The rest of destination group is the node in sequence if this node is different from source node until completes the number of desired destinations. The messages to send to the destination group for each source can vary between 200 to 500 messages (we will vary this message size in section VI-B). We generate random numbers between 0.04 and 0.06 to represent the inter-arrival times (messages generated per second). Table I has an example of initial traffic for four sessions.

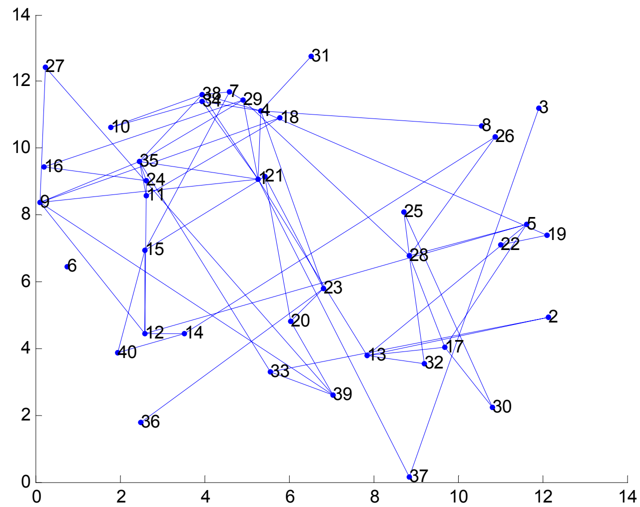

Fig. 7: Network topology

TABLE I
INITIAL TRAFFIC EXAMPLE

	Session 1	Session 2	Session 3	Session 4
Source	19	38	32	17
Destination Group	[23; 24; 25]	[39; 40; 1; 2]	[31; 33; 34; 35; 36]	[25; 26; 27; 28]
Messages to sent	270	420	280	420
Beginning of the session (s)	1400	1500	5700	8800

A message is split only at source and different parts (fragments) are routed along same paths. To compare the algorithms we collected statistics about delivery probability (total number of unique anycast bundles received by any anycast group member to the total number of bundles transmitted by the anycast source) and delay (weighted mean of delay, the weights are the number of delivered bundles). We intent evaluate the shortest path algorithm and the anycast routing using GA under different mobile devices storage capacities.

Table II presents an example of the delivery probability, delay, and the routes found by the algorithms. We illustrated these routes achieved by GA in Figure 4, and showed an example of crossover (Figure 5) and mutation (Figure 6). Analyzing the Tables 2 and 3 we can conclude that the reason for the GA (best route) achieves a delay lesser than the SP is that the route in session 1 and 4, despite having the same number of hops, relayed the messages in a time shorter than the route used by shortest path algorithm.

TABLE II
PERFORMANCE METRIC EXAMPLE

Algorithm	Del. Prob.	Delay (s)	Route Session 1	Route Session 2	Route Session 3	Route Session 4
Shortest Path	1.00	7.0140	19-3-24	38-19-39	32-1-33	17-14-28
GA best route	1.00	6.5470	19-3-23	38-19-39	32-1-33	17-14-25
GA second	0.89	7.6180	19-3-23	38-19-39	32-14-25-34	17-32-14-13-26

VI. Performance Evaluation

We want evaluate the algorithms performance (SP and GA) under different scenarios. We study the effect of buffer size on performance. To do this, we vary the storage capacity of each mobile device and the size of messages sent by each anycast session.

A. *Varying the buffer size*

We simulate a network with 16 anycast sessions. For performance evaluation, we implemented the algorithms for anycasting under different buffer sizes on the mobile devices. After that, we plot the delivery probability and delay. The GA is controlled by number of generations (200). Each generation takes 2.2 seconds in average. Our simulations run for 43.000 seconds (≈ 12 hours) in simulation time.

First, we consider that the storage capacities (*c(u,v)*) of each mobile device may vary from 500 to 1000 messages. We plot the results for the SP algorithm and the two best individuals obtained by GA (GA best is the best individual and GA 2 is the second best individual).

Figure 8 shows that although SP algorithm obtains a delivery probability a little higher, the GA gets a delay lesser than SP, and with the delivery probability above 80%. This is because our GA-based routing functioning: we can choose a minimum delivery probability (in the example 0.8) and the algorithm will search a route that satisfying the probability and has the lesser delay.

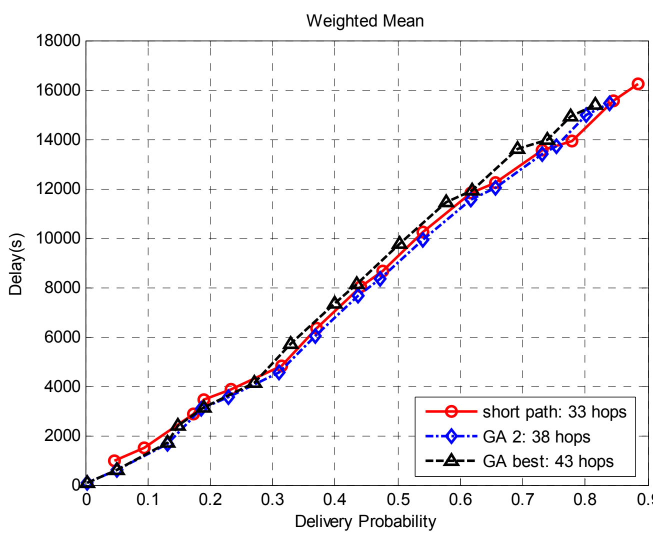

Fig. 8: Results for buffer size varying from 500 to 1000

Now we consider the storage capacities (*c(u,v)*) of each mobile device may vary from 300 to 800 messages. Figure 9 shows that the delay increases for both SP and GA. Moreover we can see that the GA achieves a delivery probability above 80%. Even now the SP, obtains a delay higher and a delivery probability lesser than GA.

Finally, we vary the storage capacity (*c(u,v)*) of each mobile device from 200 to 500 messages. Figure 10 shows that the delay increases again for both SP and GA. Although neither SP nor the GA achieves a delivery probability above 80%, GA gets a delivery probability larger than SP. The poor SP performance is because SP chooses routes without considers information about departure time and buffer storage.

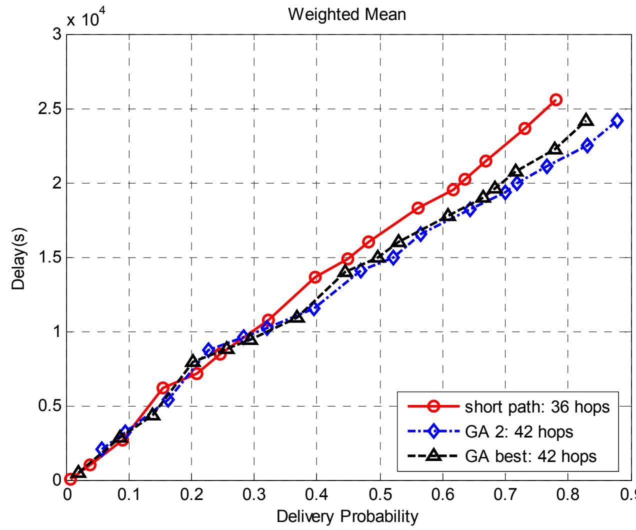

Fig. 9: Results for buffer size varying from 300 to 800

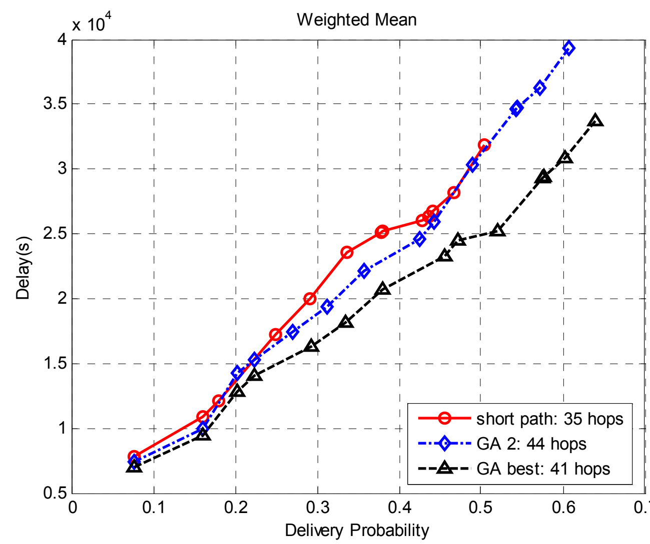

Fig. 10: Results for buffer size varying from 200 to 500

The results above suggest that when the network resources (e. g. buffer size of mobile devices) are scarce the delay increase. This is because the delay waiting for an opportunity to transmit increase. Besides, we observe that the improvement obtained by GA is higher if compared with SP when the resources are scarce. This suggests that with little resources, routing algorithms more “intelligent” are necessary to achieve a good performance, and possible available informations can be used to optimize the performance.

B. *Varying the messages size*

Now we fixed the 16 anycast sessions and the storage capacity of each mobile device (500 to 1000 messages). To analyze the algorithms under different traffics we vary the message size.

Figure 11 shows the delivery probability and delay for both SP and GA, varying the message size from 200 to 400, 200 to 500 and from 300 to 500.

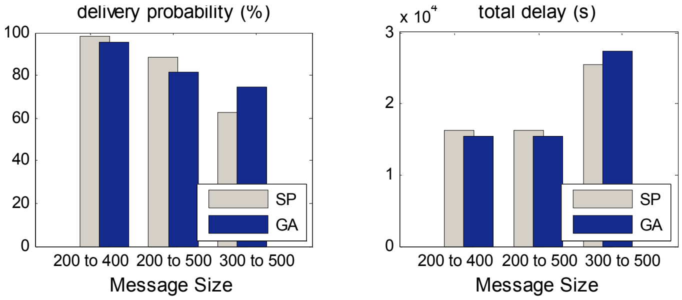

Fig. 11. Delay and delivery probability under different message size

Figure 11 shows that the GA obtains a delivery probability slightly lesser than SP for message size from 200 to 400 and from 200 to 500, but above 80%. However, GA obtains a delay more than 1000 seconds lesser than SP for these two scenarios. This is because the GA search routes that having the shortest delay with delivery probability above 80%.

Analyzing the results for message size from 300 to 500, we can see that SP achieves a delivery probability poor, 62.32% against 74.39% obtained by GA. Again, this suggests that when the network traffic is high, i.e. the resources are scarce, the improvement obtained by GA is higher.

VII. Conclusion and Future Works

Future DTN nodes will likely have to support a number of different routing strategies and protocols in order to operate efficiently in the vast diversity of environments in which the node may find itself. So we present a GA-based anycast routing algorithm that use information about the network to search routes optimal or very good with an acceptable delivery probability and the lesser delay.

Simulation results showed that GA can reduce the average delay compared to shortest path algorithm used and improve the delivery probability. However, this improvement is emphasized when the networks conditions are more challenging.

As future works, new techniques can be developed to GA converge faster. Moreover, the possibility to apply GA in other DTN environments can be studied.

Acknowledgment

The authors gratefully acknowledge financial support from the FAPEMIG (Fundação de Amparo à Pesquisa do Estado de Minas Gerais) under Project TEC APQ-4089-6.01/07.

References

[1] V. Cerf et al., “Delay-Tolerant Network Architecture”, *IETF RFC 4838*, informational, April 2007. < http://www.ietf.org/rfc/rfc4838.txt>

[2] K. Scott, and S. Burleigh, “Bundle Protocol Specification”, *IETF RFC 5050*, experimental, November 2007. < http://www.ietf.org/rfc/rfc5050.txt>

[3] K. Fall, and S. Farrel, “DTN: An Architectural Retrospective”, *IEEE Journal on selected areas in communications*, vol. 26, no 5, pp. 828-836, June 2008.

[4] Z. Zhang, “Routing in Intermittently Connected Mobile Ad Hoc Networks and Delay Tolerant Networks: Overview and Challenges”, *Communications Surveys & Tutorials*, vol. 8, no 1, pp. 24-37, first quarter 2006.

[5] K. Kotecha, and S. Popat, “MultiObjective Genetic Algorithm based Adaptive QoS Routing in MANET”, *IEEE Congress on Evolutionary Computation (CEC)*, pp. 1423-1428, September 2007.

[6] M. Al-Ghazal, A. El-Sayed, and H. Kelash, “Routing Optimization using Genetic Algorithm in Ad Hoc Netowks”, *IEEE International Symposium on Signal Processing and Information Technology*, pp. 497-503, December 2007.

[7] M. Abdulla, and R. Simon, “A Simulation Analysis of Multicasting in Delay Tolerant Networks”, *Proceedings of the Winter Simulation Conference – WSC*, pp. 2234-2241, 2006.

[8] W. Zhao, M. Ammar and E. Zegura, "Multicast Routing in Delay Tolerant Networks: Semantic Models and Routing Algorithms," *Proceedings of the SIGCOMM DTN Workshop*, August 2005.

[9] Y. Gong et al., “Anycast Routing in Delay Tolerant Networks”, *Global Telecommunications Conference (GLOBECOM)*, November 2006.

[10] A. Ferreira, “Building a Reference Combinatorial Model for MANETs”, *IEEE Network*, vol. 18, no. 5, pp. 24-29, September-October 2004.

[11] David E. Goldberg, “Genetic Algorithms in Search, Optimization and Machine Learning”, Massachusets, Addison-Wesley, 1989.

[12] S. Jain, K. Fall, and R. Patra, “Routing in a Delay Tolerant Network”, *Special Interest Group on Data Communications - SIGCOMM*. August/September 2004.

[13] I. Kaj, and R. Gaigalas, “Stochastic Simulation: Waxman random network topology generator”, <http://www.math.uu.se/research/telecom/software/> accessed in November/2008.

On The Performance of WH-STC-OFDM and WH-SFC-OFDM in Non-Linear Time Variant Channels

Luciano Leonel Mendes
Hardware Development Lab.
Telecommunications National Institute
P.O. Box 05 37540-000
Santa Rita do Sapucai, MG - BR
luciano@inatel.br

Renato Baldini Filho
Communications Department
State University of Campinas
P.O. Box 6101 - 13083-852
Campinas, SP - BR
baldini@decom.fee.unicamp.br

***Abstract*— Orthogonal Frequency Division Multiplexing is being widely used on today's digital communication standards, mainly because its robustness against multipath channels. Although, the high PAPR of the OFDM signal becomes a problem when a mobile communication takes place, because of the power limitation of the mobile unit. One technique that can be used to reduce the PAPR of OFDM signals is to apply the Walsh-Hadamard Transform on the data prior the IFFT. The aim of this paper is to analyze the performance of this system, considering the use of space-time and space-frequency diversity in a time variant multipath channel.**

I. Introduction

Orthogonal Frequency Division Multiplexing (OFDM) [1] is employed by several high data rate communication systems as aerial interface. It is one of the most important wireless transmission techniques, with high academic and practical interest. OFDM systems are robust against frequency selective fading, which makes this technique suitable for wireless computer networks [2] [3], digital television broadcasting [4] [5], mobile communications [6] and others wireless applications. However, OFDM has some drawbacks that limit its application or, at least, reduce its performance and increase the overall symbol error rate (SER). Between these drawbacks, the high peak to average power ratio (PAPR) [7] deserves attention. Because of the Gaussian distribution of the OFDM signal, amplitudes that lead the power amplifier to saturation are expected. Once the power amplifier is saturated, it clips the OFDM signal, introducing in-band and out-band non-linear interferences [8]. There are several approaches presented in literature to reduce the PAPR in OFDM symbols [9] [10]. One simple solution that reduces the PAPR in OFDM system without high complexity increment is to apply the Walsh-Hadamard Transform (WHT) in the data to be transmitted, before the Inverse Fast Fourier Transform (IFFT) [11]. Obviously, the Inverse Walsh-Hadamard Transform (IWHT) must be applied to the symbols obtained at the output of the Fast Fourier Transform (FFT) in the receptor. In this paper, the performance of a WH-OFDM system in a non-linear time variant channel will be obtained using computational simulation. The simulation results will be compared with the theoretical results presented in the literature [12]. Furthermore, the transmission diversity proposed by Alamouti [13] will be integrated with the WH-OFDM, resulting on a WH-STC-OFDM (Walsh-Hadamard Space Time Coding Orthogonal Frequency Division Multiplexing) and WH-SFC-OFDM (Walsh-Hadamard Space Frequency Coding Orthogonal Frequency Division Multiplexing) [12]. The performance of both approaches in a non-linear time variant channel will be also obtained through computational simulation and compared with theoretical curves.

In order to achieve these results, this paper is organized as follow: Section II presents the basics on OFDM systems, while section III presents the combination of this technique with the Space Time Coding introduced in [13]. Section IV presents the integration of the OFDM, STC-OFDM and SFC-OFDM with the Walsh-Hadamard Transform. Section V presents the performance analysis of these systems in a time variant channel and, finally, Section VI presents the final conclusions and commentaries of this paper.

II. Basics on OFDM

The basic idea behind OFDM is to split the serial data stream that must be transmitted in N parallel streams. An N-point IFFT is applied to the N symbols, resulting in a complex baseband OFDM signal. Thus, the OFDM symbol can be stated as [7]

$$s[m] = \frac{1}{2N} \sum_{n=0}^{N-1} c[n] e^{j\frac{2\pi n}{N}\ m}, \tag{1}$$

where N is the total number of subcarriers, $s[m]$ is m^{th} time-domain sample of the OFDM symbol, $0 \leq m \leq N-1$ and $c[n]$ is the in-phase and quadrature symbol transmitted on the n^{th} subcarrier, $0 \leq n \leq N-1$. As can be noticed from (1), the OFDM symbol can be seen as the Inverse Fast Fourier Transform (IFFT) of the data symbols, $c[n]$. The complex vector, $s[m]$ can be transmitted using a in-phase and quadrature modulator. In order to recover the transmitted symbols, it is necessary to sample the OFDM signal and apply the Fast Fourier Transform, as presented in Figure 1

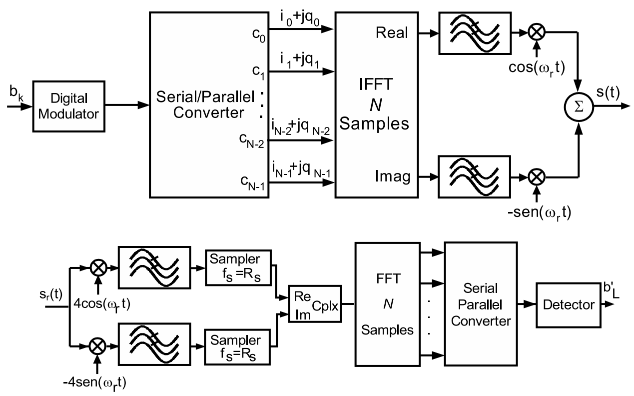

Fig. 1. Block diagram of an OFDM system.

III. Transmission Diversity

The scheme proposed by Alamouti [13] can be associated with OFDM in order to obtain transmission diversity in frequency selective channels. Basically, there are two different approaches to combine the transmission diversity with OFDM that will be shortly described following.

A. STC-OFDM

A Space Time Coding OFDM scheme [14] can be achieved by applying the transmission matrix presented in Table I, where the n^{th} subcarrier of two adjacent OFDM are used to construct a code-word.

TABLE I
STC-OFDM TRANSMISSION MATRIX.

	Antenna 0	Antenna 1
n^{th} subcarrier, i^{th} symbol	$c[n]$	$-c[n+1]^*$
n^{th} subcarrier, $(i+1)^{th}$ symbol	$c[n+1]$	$c[n]^*$

Figure 2 presents the block diagram of an STC-OFDM transmitter and Figure 3 presents the block diagram of an STC-OFDM receiver with a single antenna.

The data received at the n^{th} subcarrier of the i^{th} and $(i+1)^{\text{th}}$ OFDM symbol are respectively given by

$$\begin{aligned} S_{r_i}[n] &= c[n]H_0[n] - c^*[n+1]H_1[n] + W_i[n] \\ S_{r_{i+1}}[n] &= c[n+1]H_0[n] + c^*[n]H_1[n] + W_{i+1}[n] \end{aligned} \tag{2}$$

where $c[n]$ is the original data vector, $H_0[n]$ and $H_1[n]$ are the frequency response of the channels at frequency n and $W_i[n]$ is the amplitude spectrum of the noise at the n^{th} subcarrier and time instant iT. Notice that the channel frequency response is considered time invariant during the transmission of two adjacent OFDM symbols [14]. The STC decoder combines these received signals to obtain the diversity gain. Thus, the signal delivered to the detector corresponding with the n^{th} subcarrier of the i^{th} OFDM symbols is given by

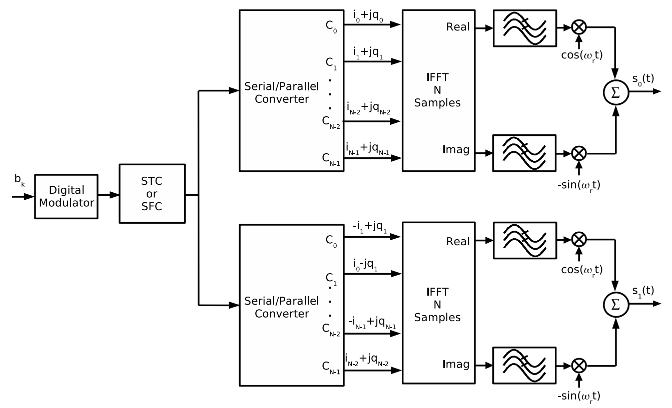

Fig. 2. Block diagram of an STC or SFC OFDM transmitter.

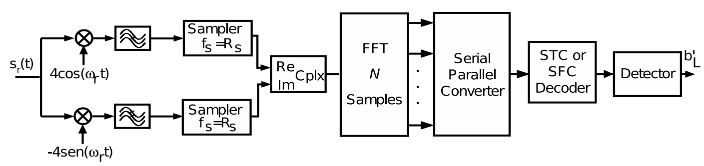

Fig. 3. Block diagram of an STC or SFC OFDM receiver.

$$\begin{aligned} d[n] =& H_0^*[n]\cdot S_{r_i}[n] + H_1[n]\cdot S_{r_{i+1}}^*[n] \\ =& \left(|H_0[n]|^2 + |H_1[n]|^2\right)c[n] + H_0^*[n]W_i[n] + \\ &+ H_1[n]W_{i+1}^*[n] \end{aligned} \tag{3}$$

while the signal corresponding with the n^{th} subcarrier of the $(i+1)^{th}$ OFDM symbol is given by

$$\begin{aligned} d[n+1] =& H_0^*[n]\cdot S_{r_{i+1}}[n] - H_1[n]\cdot S_{r_i}^*[n] \\ =& \left(|H_0[n]|^2 + |H_1[n]|^2\right)c[n+1] + \\ &+ H_0[n]W_{i+1}[n] - H_1[n]W_i^*[n] \end{aligned} \tag{4}$$

From (3) and (4) it is possible to conclude that the STC-OFDM scheme with one antenna at the receiver presents a diversity gain of order 2, which increases the performance of the system in frequency selective time variant channels. It is important to note that in order to obtain the total diversity gain the channel frequency response must be time invariant during at least two adjacent OFDM symbols. It means that the channel coherence time must be larger than the duration of two OFDM symbols.

B. SFC-OFDM

Space-Frequency Coding OFDM scheme [15] is very similar to STC-OFDM presented in the previous subsection. The main difference is that the code-word is transmitted in two adjacent subcarriers of the same OFDM symbol, as presented in Table II.

Notice that equations presented in (2) also represents the symbols received, respectively, at the n^{th} and $(n+1)^{th}$ subcarriers of the i^{th} OFDM symbol. The block diagrams of the

TABLE II
SFC-OFDM TRANSMISSION MATRIX.

	Antenna 0	Antenna 1
n^{th} subcarrier, i^{th} symbol	$c[n]$	$-c[n+1]^*$
$(n+1)^{th}$ subcarrier, i^{th} symbol	$c[n+1]$	$c[n]^*$

SFC-OFDM transmitter and receiver can also be represented by Figures 2 and 3, respectively. The SFC-OFDM combines the two adjacent subcarriers of the same OFDM symbol to obtain the transmission diversity. Again, Equations (3) and (4) can used to demonstrate the diversity gain obtained with an SFC-OFDM system. In this case, in order to achieve optimum performance, the channel frequency response at the frequency of the n^{th} and $(n+1)^{th}$ subcarriers must be the same. Also, the channel must be time invariant during one single OFDM symbol. It means that SFC-OFDM is more robust against Doppler effect when compared with STC-OFDM, but SFC-OFDM is more sensible to the frequency selectivity than STC-OFDM.

IV. Walsh Hadamard Transform and Transmission Diversity

The Walsh-Hadamard Transform (WHT) consists on multiplying a $2m$-length vector by a $2m \times 2m$ matrix given by

$$\Omega_{2m} = \begin{bmatrix} \Omega_m & \Omega_m \\ \Omega_m & -\Omega_m \end{bmatrix}, \tag{5}$$

where $\Omega_1 = +1$. Thus,

$$\Omega_2 = \begin{bmatrix} \Omega_1 & \Omega_1 \\ \Omega_1 & -\Omega_1 \end{bmatrix} = \begin{bmatrix} +1 & +1 \\ +1 & -1 \end{bmatrix} \tag{6}$$

The Walsh-Hadamard Transform [17] of a data symbol vector, $c[n]$, is given by

$$\vec{c}_\Omega = \vec{c} \times \frac{\Omega_N}{\sqrt{N}} \tag{7}$$

where N is the length of the data symbol vector. The normalization constante $\sqrt{N}$ is used to keep the average energy of the vector unchanged. From (7) it is possible to conclude that the WHT of the data symbols results on a vector with same length, where each coefficient is a linear combination of the N data symbols. Since the coefficients of the WHT are always "+1" and "-1", the IFFT of the vector $c_\Omega[n]$ presents a lower PAPR (Peak to Average Power Ratio) when compared with a conventional OFDM signal [11], as can be seen in Figure 4.

The Inverse Walsh-Hadamard Transform (IWHT) is also obtained by multiplying the transformed vector, $c_\Omega[n]$, by the normailized WH matriz, Ω_N, which means that

$$\vec{c} = \vec{c}_\Omega \times \frac{\Omega_N}{\sqrt{N}}. \tag{8}$$

The WHT can be easily integrated with the OFDM system, by applying the WHT to the data symbols prior the IFFT and by applying the IWHT after the FFT in the receptor, as shown in Figure 5.

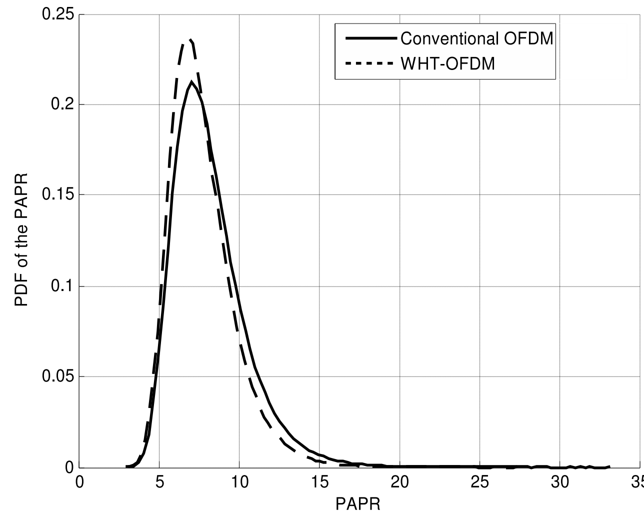

Fig. 4. Probability density function of the PAPR of a WHT-OFDM and conventional OFDM.

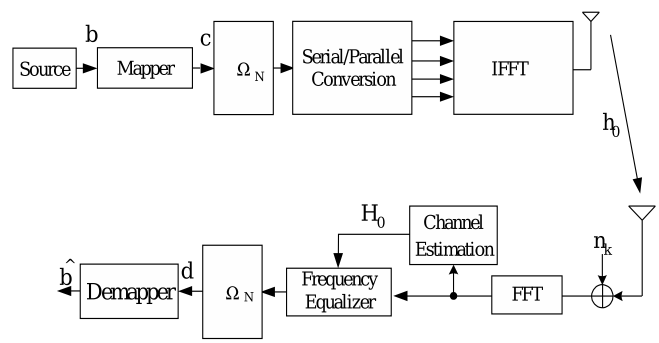

Fig. 5. Block diagram of a WHT-OFDM system.

In this case, the transmitted OFDM symbol is given by

$$s = \text{IFFT}\left(\frac{\vec{c}\ \Omega_N}{\sqrt{N}}\right) \tag{9}$$

and the symbols delivered to the demapper are given by

$$\vec{d} = \frac{\text{FFT}\left(s * h_0 + \vec{w}\right)}{\hat{H}_0} \times \frac{\Omega_N}{\sqrt{N}} = \vec{c} + \frac{\vec{W}\ \Omega_N}{\sqrt{N}\ \hat{H}_0} \tag{10}$$

where h_0 is the channel impulse response, $\hat{H}_0$ is the channel frequency response estimation and $\vec{w}$ is an AWGN vector of size N.

The STC or SFC OFDM scheme can also be integrated with the WHT, as can be seen in Figure 6.

Assuming a WH-STC-OFDM system, the transmitted OFDM symbols at antenna 0 and antenna 1 in the time instant iT are respectively given by

$$\begin{aligned} s_{0,i} &= \text{IFFT}\left[\frac{\vec{c_i}\Omega_N}{\sqrt{N}}\right] \\ s_{1,i} &= \text{IFFT}\left[-\frac{\left(\vec{c}_{i+1}\Omega_N\right)^*}{\sqrt{N}}\right] = \text{IFFT}\left[-\frac{\vec{c^*}_{i+1}\Omega_N}{\sqrt{N}}\right], \end{aligned} \tag{11}$$

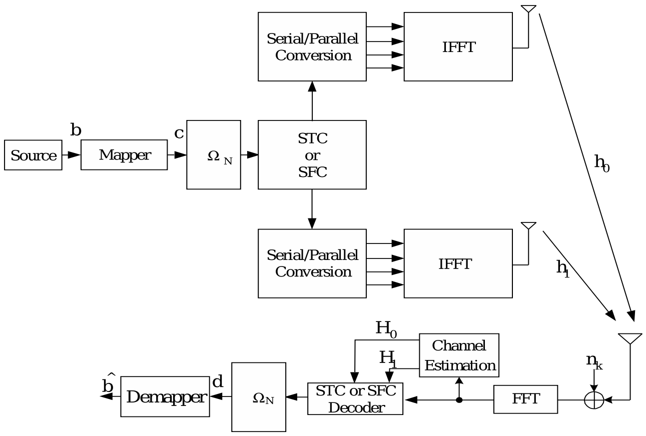

Fig. 6. Block diagram of a WHT-OFDM system with transmission diversity.

where $\vec{c_i}$ is the symbol vector of length N to be transmitted at time instant iT.

The OFDM symbols transmitted at antennas 0 and 1 at time instant $(i+1)T$ are respectively given by

$$\begin{aligned} s_{0,i+1} &= \text{IFFT}\left[\frac{\vec{c}_{i+1}\Omega_N}{\sqrt{N}}\right] \\ s_{1,i+1} &= \text{IFFT}\left[\frac{(\vec{c}_i\Omega_N)^*}{\sqrt{N}}\right] = \text{IFFT}\left[\frac{\vec{c}_i^*\Omega_N}{\sqrt{N}}\right]. \end{aligned} \tag{12}$$

The received signals at time instants iT is given by

$$\begin{aligned} r_i &= \text{FFT}\left[s_{0,i} * h_0 + s_{1,i} * h_1 + \vec{w}_i\right] \\ &= \frac{\vec{c}_i\Omega_N}{\sqrt{N}} \times H_0 - \frac{\vec{c^*}_{i+1}\Omega_N}{\sqrt{N}} \times H_1 + \vec{W}_i, \end{aligned} \tag{13}$$

while the received signal at the time instant $(i+1)T$ is given by

$$\begin{aligned} r_{i+1} &= \text{FFT}\left(s_{0,i+1} * h_0 + s_{1,i+1} * h_1 + \vec{w}_{i+1}\right) \\ &= \frac{\vec{c}_{i+1}\ \Omega_N}{\sqrt{N}} H_0 + \frac{\vec{c}_i^*\ \Omega_N}{\sqrt{N}} H_1 + \vec{W}_{i+1}. \end{aligned} \tag{14}$$

Eq. (13) and (14) can be combined to obtain the diversity gain. The received vector at the input of the IWHT block at time instant iT is given by

$$\begin{aligned} \vec{d}_{\Omega_i} &= H_0^* r_i + H_1 r_{i+1}^* \\ &= \left(|H_0|^2 + |H_1|^2\right)\frac{\vec{c}_i\Omega_N}{\sqrt{N}} + H_0^*\vec{W}_i + H_1\vec{W}_{i+1}^* \end{aligned} \tag{15}$$

and the received vector at the input of the IWHT block at time instant $(i+1)T$ is given by

$$\begin{aligned} \vec{d}_{\Omega_{i+1}} &= H_0^* r_{i+1} - H_1 r_i^* \\ &= \left(|H_0|^2 + |H_1|^2\right)\frac{\vec{c}_{i+1}\Omega_N}{\sqrt{N}} + H_0^*\vec{W}_{i+1} + H_1\vec{W}_i^*. \end{aligned} \tag{16}$$

Applying the IWHT in (15) and (16), respectively, leads to

$$\begin{aligned} \vec{d_i} &= \left(|H_0|^2 + |H_1|^2\right)\vec{c_i} + \left(H_0^*\vec{W}_i + H_1\vec{W}_{i+1}^*\right) \times \frac{\Omega_N}{\sqrt{N}} \\ \vec{d}_{i+1} &= \left(|H_0|^2 + |H_1|^2\right)\vec{c}_{i+1} + \left(H_0^*\vec{W}_{i+1} + H_1\vec{W}_i^*\right) \times \frac{\Omega_N}{\sqrt{N}}. \end{aligned} \tag{17}$$

The analysis of the WH-SFC-OFDM is analog to the one presented above. In a linear channel, the performance of WH-STC-(SFC)-OFDM is equivalent to the performance of STC-(SFC)-OFDM. However, the performance of the WH-STC-(SFC)-OFDM is expected to be higher in a non-linear channel, due the reduction in the PAPR introduced by the use of WHT.

V. Performance Analysis

The reduction in the PAPR of the OFDM symbol reflects on the performance of the system in non-linear channels, where the high peaks of the signal are clipped by the power amplifier [8]. The performance of a conventional OFDM system in a non-linear frequency selective and time-variant channel can be approximately estimated by (18) [12], where l is the clipping threshold, σ_n^2 is the noise variance, σ_r^2 is the variance of the orthogonal complex Gaussian that generates the Rayleigh distribution [16], 2ν is the minimum distance between two adjacent symbols of the employed constellation and $\bar{\mu}$ is the average number of neighbors in the constellation. Figure 7 compares the performance on a conventional OFDM system with a WH-OFDM system in a mobile non-linear channel. In this case, a 64-QAM constellation has been used and the clipping threshold, l, equals three.

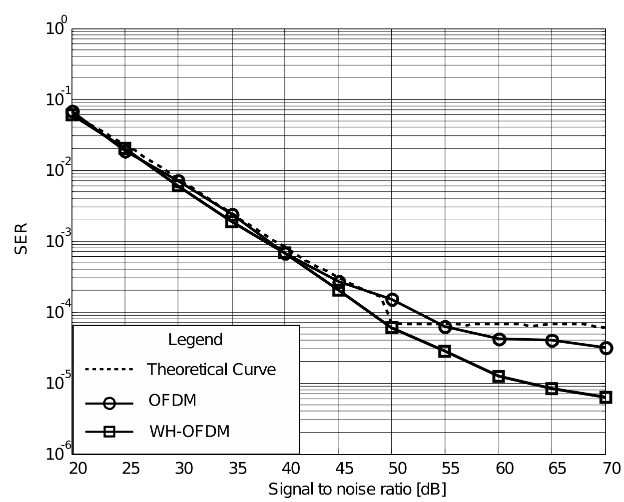

Fig. 7. Performance of a 64-QAM OFDM and 64-QAM WH-OFDM systems in a non-linear mobile channel with $l = 3$.

Observing Figure 7, one may conclude that the WHT reduces the error floor of the system, resulting in a better performance of WH-OFDM.

$$p_e \approx \frac{2\mathrm{Q}(l)\bar{\mu}}{\sqrt{2\pi}\,\sigma_n\sigma_r^2}\int_0^\infty\int_{-\infty}^\infty r\exp\left(-\frac{n^2}{2\sigma_n^2}-\frac{r^2}{2\sigma_r^2}\right)\mathrm{Q}\left\{\left[\frac{r\,(\nu-n)}{\frac{2}{\sqrt{3N}\,\pi l^2}}\right]^{\frac{1}{3}}\right\}\mathrm{d}n\mathrm{d}r+\frac{\bar{\mu}}{\sigma_r^2}\int_0^\infty r\exp\left(-\frac{r^2}{2\sigma_r^2}\right)\mathrm{Q}\left(\frac{r\nu}{\sigma_n}\right)\mathrm{d}r \tag{18}$$

However, this performance gain is only noticed at high SNR (above 45dB), which may lead to the conclusion that the performance gain does not payoff complexity introduced by the WHT. In the case of the STC-OFDM, the scenario is different, as can be seen in Figure 8. Again, a 64-QAM constellation and clipping threshold equals three have been used in this simulation.

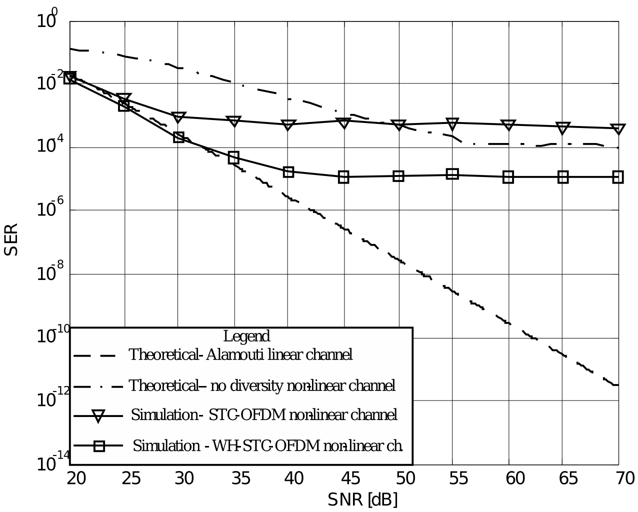

Fig. 8. Performance of a 64-QAM STC-OFDM and 64-QAM WH-STC-OFDM systems in a non-linear mobile channel with $l = 3$.

Observing Figure 8, it is possible to conclude that the WHT sensibly reduces the error floor of the system for SNR above 25dB. The performance gain in this case is also higher than the gain obtained without the STC, which means that the WHT is more effective when combined with STC-OFDM.

As one can see in Figure 9, the same conclusions can be achieved for the WH-SFC-OFDM. In this case, however, the performance gain is even higher than the one obtained with WH-STC-OFDM. Although the performance of the WH-SFC-OFDM and WH-STC-OFDM is almost the same in a non-linear time-variant channel, the performance of the SFC-OFDM is poorer than the performance of the STC-OFDM in the same channel, because SFC-OFDM is more sensible to the Doppler effect, as commented in Section III-B. This behavior was expected because the reduction of the PAPR also reduces the clipping introduced by the power amplifier. Since the clipping causes intra-carrier interference (ICI) which, in the case of a SFC, results on degradation of the space-frequency codeword, it is expected that the reduction of this non-linearity results in a better performance of the SFC-OFDM system.

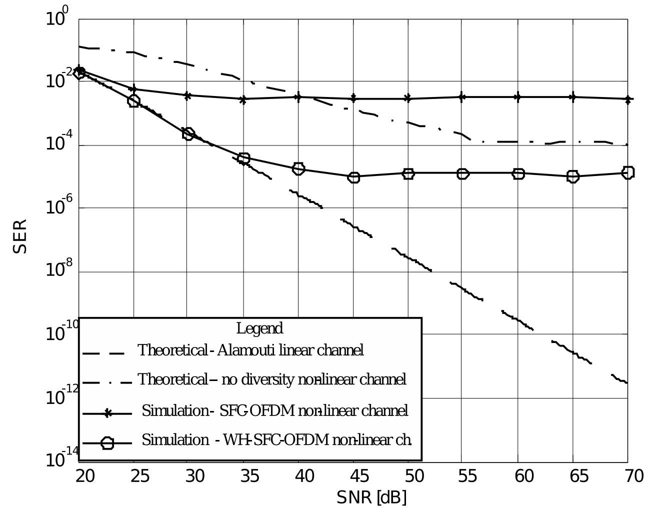

Fig. 9. Performance of a 64-QAM STC-OFDM and 64-QAM WH-SFC-OFDM systems in a non-linear mobile channel with $l = 3$.

VI. Conclusions

The high PAPR of OFDM symbols is one of the main causes of poor performance of this system in non-linear channels. The reduction of the PAPR can be achieved by several different approaches, and one of them consists on applying the Wash-Hadamard Transform on the information symbols prior the FFT. This paper has compared the performance of conventional OFDM and WH-OFDM, as well STC-(SFC)-OFDM and WH-STC-(SFC)-OFDM, in a mobile non-linear channel. The performance gain obtained by the WHT considering just OFDM is smaller than the performance gain obtained when considering the STC. The gain is even larger, when considering the SFC. These results leads to the conclusion that the Walsh-Hadamard Transform shall be used with some transmit diversity OFDM schemes, since the gain obtained with no diversity OFDM scheme is relevant only for high signal to noise ratio.

Acknowledgment

The authors would like to thank INATEL and UNICAMP by he financial support

References

[1] R. W. Chang, Synthesis of band-limited orthogonal signals for multi-channel data transmission, Bell Systems Technical Journal, 1966.
[2] IEEE Standard 802.11, Institute of Electrical and Electronic Engineers, Wireless LAN Media Access Control (MAC) and Physical Layer (PHY) Specifications, 1999.
[3] IEEE Standard 802.16, Institute of Electrical and Electronic Engineers, Air Interface for Fixed and Mobile Broadband Wireless Access Systems - Physical and Medium Control Layers for Combined Fixed and Mobile Operation in Lincensed Bands, 2005.

[4] ETSI EN 300 744 V1.4.1, European Broadcasting Union, Digital Video Broadcasting (DVB); Framing structure, channel coding and modulation for digital terrestrial television, 2001.
[5] ITU-R 205/11, International Telecommunication Union, Channel Coding, Frame Structure and Modulation Scheme for Terrestrial Integrated Services Digital Broadcasting (ISDB-T), 1999.
[6] S. Benedetto and E. Biglieri, Principles of Digital Transmission : With Wireless Applications, Plenum Pub Corp, 1999.
[7] A. R. Bahai and B. R. Saltzberg, Multi-Carrier Digital Communications - Theory and Applications of OFDM, Kluwer Academic, 1999.
[8] A. R. S. Bahai, M. Singh, A. J. Goldsmith and B. R. Saltzberg, A New Approach for Evaluating Clipping Distortion in Multicarrier Systems, IEEE Journal on Selected Areas in Communications, vol. 20, pages 1037-1046, June 2002.
[9] Yuanbin Guo and Joseph R. Cavallaro, Reducing Peak-To-Average Power Ratio in OFDM Systems by Adaptive Dynamic Range Companding, World Wireless Congress, 2002.
[10] K.G. Paterson, Generalized Reed-Muller Codes and Power Control in OFDM Modulation, Transaction on Information Theory, vol. 46, pages 104-119, January 2000.
[11] M. Park; H. Jun and J. Cho, PAPR Reduction in OFDM transmission using Hadamard Transform, IEEE International Conference on Communications, 2000.
[12] L. L. Mendes, Modelos Matemáticos para Estimaçãoo do Desempenho de Sistemas de Multiplexação por Divisão em Freqüências Ortogonais, PhD. Thesys, UNICAMP, 2007.
[13] S. Alamouti, A simple transmit diversity technique for wireless communications, IEEE J. Select. Areas Commun., volume 16 number 8, October, 1998, pp 1451-1458.
[14] K. F. Lee and D. B. Willians, A Space-Time Coded Transmit Diversity Technique for Frequency Selective Fading Channels, IEEE Sensor Array and Multichannel Signal Processing Workshop, pp 149-152, March 2000.
[15] K. F. Lee and D. B. Willians, A Space-Frequency Transmit Diversity Technique for OFDM Systems, IEEE Globecom, pp. 1473-1477, 2000.
[16] M. Yacoub, Foudations of Mobile Radio Engineering, CRC Press, 1993.
[17] Dlugaszewski Zbigniew and Wesolowski Krzysztof, WHT/OFDM -an improved OFDM Transmission method for selective fading channels, SCVTX 2000, 2000.

A robustness and performance comparison between Cyclic Prefixed Single-Carrier and OFDM systems

Amanda Souza de Paula
São Paulo University - USP
São Paulo - SP - Brazil
amanda@lcs.poli.usp.br

Cristiano Magalhães Panazio
São Paulo University - USP
São Paulo - SP - Brazil
cpanazio@lcs.poli.usp.br

***Abstract*— This work aims to establish a comparison between orthogonal frequency division multiplexing (OFDM) and single carrier with cyclic prefix (SCCP) focusing on robustness problems. Differently of most of the papers found in the literature, we analyze, in more practical scenarios, not only the bit error rate (BER) but also the block error rate (BLER) and the system sensitivity to the interleaver configuration for frequency selective block fading channels.**

***Index Terms*— OFDM, single-carrier, channel coding, equalization, interleaver, block fading**

I. INTRODUCTION

The OFDM is a popular block transmission technique which consists in dividing the available bandwidth into several orthogonal subcarriers. One important advantage concerning OFDM is the low complexity of the equalizer. If a cyclic prefix (CP) is appended in the transmission block, the equalization can be easily performed with a single-tap equalizer per subcarrier. However, the OFDM alone does not exploit the channel frequency diversity, which means that in a strongly frequency selective channel a subcarrier may be highly attenuated and the information transmitted in it may be lost. Hence, channel coding is an obligatory technique to recover information in this kind of situation as noted by [1].

On the other hand, the single-carrier (SC) technique transmits the data symbols through just one carrier at much larger symbol rate. The result is that each symbol is spread over the available bandwidth, allowing us to recover the transmitted symbols even in frequency selective channels. This may be accomplished by using a frequency-domain equalizer that can assume the same form used in OFDM if we use a SCCP block transmission technique. The solely difference compared to the OFDM is that the inverse fast Fourier transform (IFFT) used in the transmission is replaced after the equalizer at the receiver [2].

Many articles have compared the performance of SCCP and OFDM techniques in absence of channel state information at the transmission. In [3], it is shown for uncoded systems that linearly equalized SCCP with the minimum mean square criterion always outperforms the uncoded OFDM in frequency selective channels. In [4], it is shown that the coded OFDM performs similarly to a coded linearly equalized SCCP when the code rate is equal or smaller than one-half for QPSK modulation, but it degrades rapidly when we increase the coding rate, in accordance to [3]. In both [5] and [6], it is shown that with coding, both SCCP and OFDM can attain the channel diversity. However, most of these comparisons are restricted to random coding, infinite block length or an asymptotic analysis. Other papers (e.g., [2], [7]) are more practical but they just confirm the results presented in more theoretical papers or just emphasize on the lower peak-to-average-power ratio of the SCCP. Our contribution, presented in this work, is a more critical analysis of the performance of both coded OFDM and SCCP techniques by focusing our attention on the BLER, interleaver configuration choice and their robustness in frequency selective block fading channels.

The paper is organized as follows. In section 2 we present the unified system model used in both transmission systems analysis. In section 3 we show some results obtained under different contexts. Finally, the conclusions are indicated in section 4.

II. SYSTEM MODEL

In the OFDM technique, the symbols are modulated by subcarriers that are generated by an IFFT. A CP is added to the resultant time-domain signal. In this analysis we assume that the CP length is greater than the channel impulse response. Therefore, the linear convolution involving the channel impulse response and the transmitted block is equivalent to a circular convolution and the equalization can be performed with the frequency-domain one-tap equalizer structure.

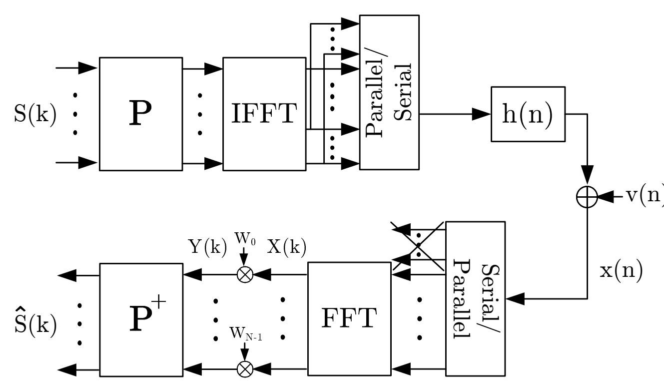

Fig. 1. An unified model for SCCP, OFDM and CDMA

In the SCCP we append to each symbol block a CP that allows us to use the same equalizer structure used in the OFDM technique. However, an IFFT has to be used after the equalizer to allow the symbol detection.

The similarities between the SCCP and OFDM allow us to describe both modulation techniques under an unified transceiver, depicted in Fig. 1 [8]. In fact, the difference between them is a linear precoding matrix $\mathbf{P}$.

In accordance to this system model, the transmitter can be regarded as a combined transformation of the linear precoding matrix with the IFFT matrix, resulting in the so-called transmission matrix:

$$\mathbf{T} = \mathbf{P}\mathbf{F}^{-1} \tag{1}$$

where, the matrix $\mathbf{F}$ is the N-dimensional Fourier matrix:

$$[\mathbf{F}]_{n,k} = e^{-j\frac{2\pi}{N}(n-1)(k-1)} \quad n,k = 1,\cdots,N$$

Note that if the matrix $\mathbf{P}$ is a simple identity, the transmission matrix is given by:

$$\mathbf{T}_{OFDM} = \mathbf{F}^{-1} \tag{2}$$

which is exactly the OFDM transmission matrix.

On the other hand, if the transmission matrix is the Fourier matrix, the resulting transmission matrix is

$$\mathbf{T}_{SC} = \mathbf{F}\mathbf{F}^{-1} = \mathbf{I}_N \tag{3}$$

which is equivalent to the SC transmission with cyclic-prefix.

Note that this approach makes clear the idea that each symbol in SCCP is spread all over the bandwidth. Due to this characteristic, the SCCP is also known in the literature as DFT-Spread OFDM.

As well as the OFDM and the SCCP, other transmission techniques can also be implemented based on this same system model.

Such model can also describe synchronous coded division multiple access (CDMA) systems. A very well known example is the Walsh-Hadamard (WH) CDMA, where $\mathbf{P}$ is the WH transformation matrix. For direct sequence (DS) CDMA, the linear precoding matrix is obtained by taking the Discrete Fourier Transform (DFT) of the time domain spreading codes.

The received message is equalized with the single-tap structure, represented by the W_k coefficients in the Fig. 1. These equalizer coefficients can be calculated using one of two criteria: the Zero Forcing (ZF) and the Minimum Mean-Square Error (MMSE). The ZF equalizer cancels the intersymbol interference (ISI), although it is likely to provide a large noise enhancement. Its coefficients are calculated as:

$$W_{ZF}(k) = \frac{1}{H(k)} \tag{4}$$

On the other hand, the MMSE coefficients are obtained solving the following optimization problem:

$$\underset{W}{\operatorname{argmin}}\ E\left\{\sum_{k=0}^{N-1} |D(k) - W(k)\cdot X(k)|^2\right\} \tag{5}$$

where, $D(k)$ and $X(k)$ are the transmitted signal and the received signal respectively, that are defined as:

$$\begin{aligned} \underline{\mathbf{D}} &= \mathbf{F}^{-1}\mathbf{P}\underline{\mathbf{S}} \\ \underline{\mathbf{D}} &= [D(0)\cdots D(N-1)]^T \\ \underline{\mathbf{S}} &= [S(0)\cdots S(N-1)]^T \\ X(k) &= D(k)H(k) + \eta(k) \end{aligned} \tag{6}$$

where the vector $\underline{\mathbf{D}}$ represents the transmitted signal vector, the vector $\underline{\mathbf{S}}$ is composed by the transmitted symbols, $H(k)$ are the coefficients of channel's impulse response in the frequency-domain and $\eta(k)$ is the additive Gaussian noise.

Defining σ_s^2 as the symbol power and σ_n^2 as the noise variance, it can be demonstrated that the coefficients which satisfy the condition imposed by eq.(5) are:

$$W_{MMSE}(k) = \frac{H^*(k)}{|H(k)|^2 + \sigma_\eta^2/\sigma_s^2} \tag{7}$$

From the eq.(4) and eq.(7), we can conclude that when the system is operating in very high SNR conditions, both equalizers are equivalent, i.e,

$$\lim_{\sigma_\eta^2/\sigma_s^2 \to \infty} W_{MMSE}(k) = \frac{1}{H(k)} = W_{ZF}(k) \tag{8}$$

It is demonstrated in [3] that the uncoded OFDM performance is the same, regardless of employed criteria. For coded OFDM, if we pass to the cannel decoder the bit likelihood, we can still use both criteria. On the other hand, in channels with spectral nulls, the noise variance in the SCCP tends to infinity when the equalization is accomplished with the ZF structure. For that reason, the one-tap equalizer coefficients for both techniques are obtained using the MMSE criterion.

It is quite important to emphasize that the equalization can be performed with the single tap structure regardless the linear precoding matrix. Thus, the low complexity of the equalizer is not a characteristic inherent to the OFDM system, and any system that can be interpreted with the structure depicted in Fig. 1 can be equalized applying the same scheme.

So far we have not introduced the error correcting code in the discussion. However, very often using an error correcting code is required to transmit the message with the demanded reliability. In such cases, an extra block must be appended to the scheme depicted in Fig. 1. This block can be interpreted as a non-linear transformation applied to the symbols just before the linear transformation imposed by $\mathbf{T}$.

The error correcting code is usually implemented with one of these structures: bit-interleaved coded modulation (BICM) or the trellis coded modulation (TCM). For a frequency-selective channel, the received symbols in the OFDM technique can be seen as they were passed through a fast time-varying flat fading channel. Therefore, a bit-interleaved coded modulation (BICM) looks more adequate, since it outperforms trellis coded modulation in this context [9]. For this reason, we will consider the BICM technique in our analysis. One crucial question in the BICM design is the interleaver project. An approach is to arrange the bits in the interleaving matrix filling its lines and reading through its columns. This procedure

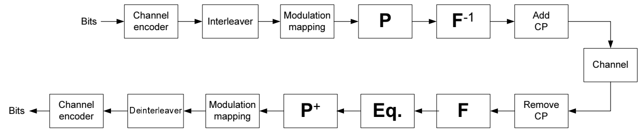

Fig. 2. The overall system model

applied to an interleaver matrix with m rows and $n = N/m$ columns is below illustrated:

$$\begin{bmatrix} x_1 \\ x_2 \\ x_3 \\ \vdots \\ x_N \end{bmatrix} \xrightarrow{write} \begin{bmatrix} x_1 & x_2 & \cdots & x_n \\ x_{n+1} & x_{n+2} & \cdots & x_{2n} \\ \vdots & \vdots & & \vdots \\ x_{(m-1)n+1} & x_{(m-1)n+2} & \cdots & x_{mn} \end{bmatrix} \; read\Big\downarrow \; \begin{bmatrix} x_1 \\ x_{n+1} \\ x_{2n+1} \\ \vdots \\ x_N \end{bmatrix} \tag{9}$$

The main goal in interleaving the bits is to avoid error bursts in the decoder. Then, a question arises: which is the more suitable interleaver choice? And how this choice affects the system error correcting capability. The overall system is indicated in Fig. 2.

III. Performance Comparison

We will proceed with a performance comparison, analyzing how the system responds in a variety of contexts. The results depicted in this sections were obtained through Monte Carlo simulations. First of all, we adopt the same system parameters used in [2], i.e., block fading, 512 subcarriers, QPSK modulation, and a convolutional code $[133\ 171]_{\mathrm{octal}}$. We have chosen a three-path Rayleigh channel, given by:

$$H(z) = h_0 + h_1 z^{-2} + h_2 z^{-3} \tag{10}$$

where the coefficients $h_k,\ k = 0, 1, 2$ are Rayleigh variables with zero mean and unitary variance.

Then, we analyze the interleaver configuration importance to the system performance and extend the analysis to other channels and to higher order modulation. Like [2], we have initially chosen a 32 row/32 column configuration. The equalizer coefficients are obtained assuming perfect channel knowledge. In our simulations, we also provide the matched filter bound (MFB) curves.

In Fig. 3, the BER of both OFDM and SCCP appears to be exaclty the same, in accordance to the results obtained in [4]. However, the BLERs, not shown in [2] and [4], are different. This is not completely unexpected since the received signal has different forms of interference: intersymbol interference for the SCCP and subcarriers suffering from flat-fading for the OFDM. In the latter, the recovery of the information transmitted in the faded subcarriers relies exclusively on the redundancy provided by the code. If the interleaver does not distribute the redundancy by taking into account the channel coherence bandwidth, the system may suffer a considerable performance loss. On the other hand, the SCCP may not have such dependency on the interleaver since it will only break the noise correlation caused by the equalizer. In order to assess the role of the interleaver, we change its number of rows/columns. The results shown in Fig. 4 confirm our previous assumption that the OFDM is indeed more affected by the the interleaver than the SCCP with a linear equalizer.

We next analyze the robustness of the techniques for fixed E_b/N_o values. In order to do so, we return to the original interleaver configuration (32 rows/columns) and, for each channel realization, we normalize its power, since we are only interested in how each system behaves for the ensemble of three-tap channels for a fixed E_b/N_o. The channel's transfer function in this scenario is

$$H(z) = \frac{h_0 + h_1 z^{-2} + h_2 z^{-3}}{\sqrt{|h_0|^2 + |h_1|^2 + |h_2|^2}} \tag{11}$$

The results are indicated in figure 5. In this case, the SCCP presents a better performance than the OFDM for E_b/N_o values larger than 4 dB. This result shows a hidden behavior, not shown in Fig. 3, where both BERs are the same. This can be explained by the fact that, in the non fixed E_b/N_o scenario, the BER performance accounts the E_b/N_o variations around the mean E_b/N_o simulated values, which includes the regions where the OFDM is better than the SCCP and vice-versa.

As can be inferred from Fig. 6, the interleaver also plays an important role in this case. It shows again that an interleaver with 8 rows represents a more favorable configuration to the OFDM system for the proposed channel. Applying this structure, the error rate curves are those presented in Fig. 7. If the OFDM is implemented with a suitable interleaver, its performance is equivalent to the SCCP in this case. But, nonetheless, we still remark a large sensitivity to the interleaver choice.

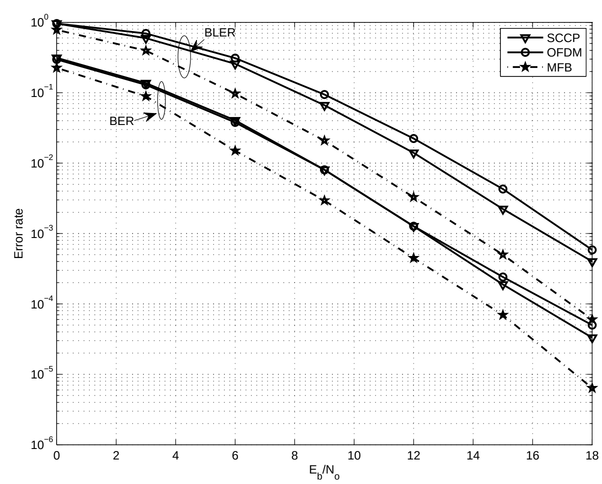

Fig. 3. Performance comparison for a three-path Rayleigh block fading channel with uniform power profile and $[133\ 171]_{\mathrm{octal}}$ convolutional code.

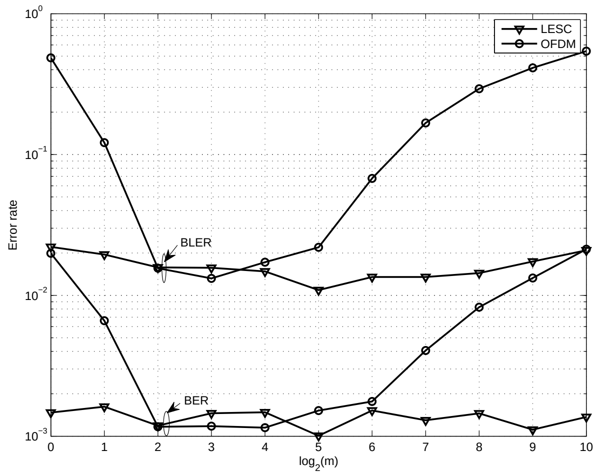

Fig. 4. Impact of the interleaver configuration on the system performance for a three-path Rayleigh fading channel with uniform power profile, $[133\ 171]_{\mathrm{octal}}$ convolutional code, E_b/N_o=12dB. Interleaver matrix with m rows.

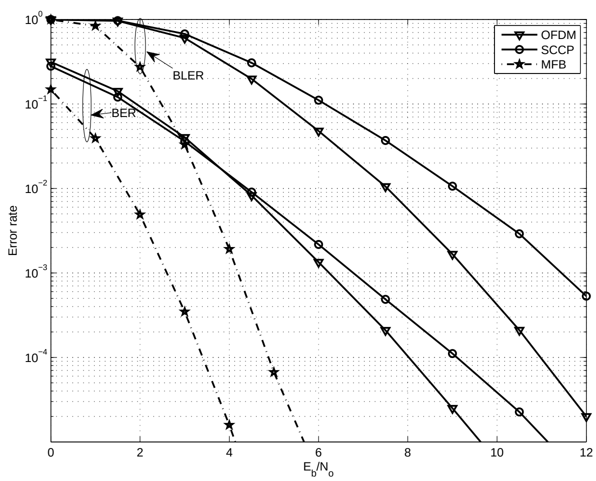

Fig. 5. Performance comparison for a three-path Rayleigh block fading normalized channel with uniform power profile and $[133\ 171]_{\mathrm{octal}}$ convolutional code.

We also compared the SCCP with the OFDM in four other scenarios: larger delays, richer multipath diversity, higher-order modulation and static channel with spectral null.

A. Larger Delays

In this situation, the channel is still described by a three-path Rayleigh channel with uniform power profile, but the delays among the paths are different. These channels present the following transfer function

$$H_L(z) = h_0 + h_1 z^{-L} + h_2 z^{-2L} \tag{12}$$

The fluctuations in the frequency-domain are more severe with larger L values. In particular, if L divides N, the relation expressed below is satisfied:

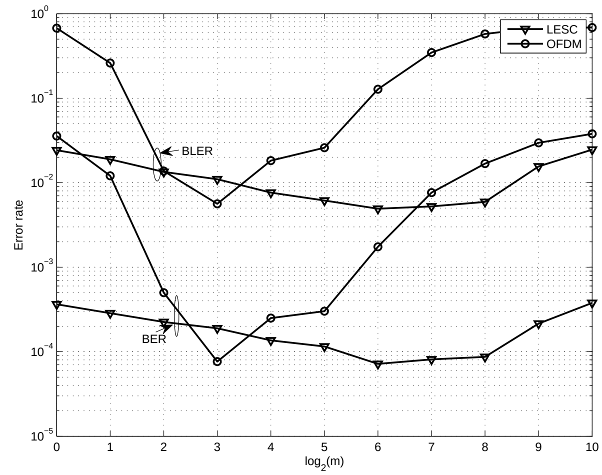

Fig. 6. Impact of the interleaver configuration on the system performance for a three-path Rayleigh block fading normalized channel with uniform power profile, $[133\ 171]_{\mathrm{octal}}$ convolutional code, E_b/N_o=8 dB. Interleaver matrix with m rows.

$$H_L(k) = H(kL \mod (N)) \tag{13}$$

which means that the channel periodicity has changed in the frequency-domain. Therefore, to achieve an equivalent channel configuration in the receiver, the interleaver parameters should be modified in order to compensate the relation depicted in eq.(13). In accordance to the interleaving rule indicated in eq.(9), the row numbers should satisfy the following relation:

$$m_L = Lm \tag{14}$$

This relation can be confirmed with the simulation results presented in Fig. 8.

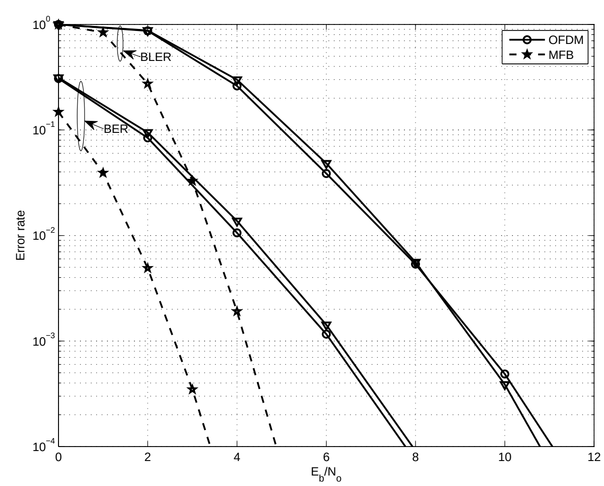

Fig. 7. Performance comparison for a three-path Rayleigh block fading normalized channel with uniform power profile and $[133\ 171]_{\mathrm{octal}}$ convolutional code. For the OFDM, a 8 row/128 column interleaver was used and for the SCCP a 32 row/32 column interleaver was chosen.

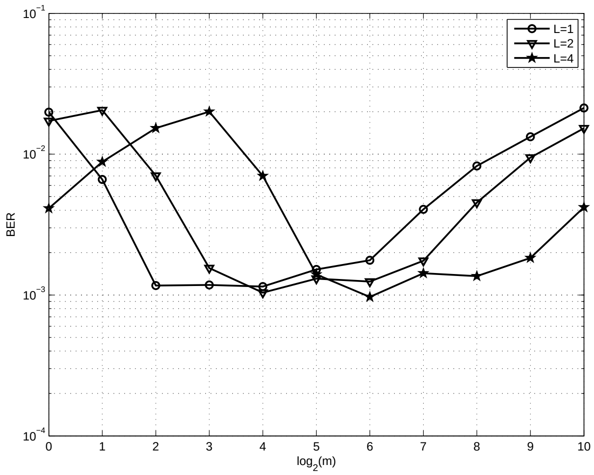

Fig. 8. Interleaver impact on system performance as a function of the channel delay for a three-path Rayleigh channel with uniform power profile, E_b/N_o=12dB.

From this results, we emphasize that even if an interleaver is suitable for a channel configuration, changes in its delay lead to considerable changes in that interleaver response.

B. Richer Multipath Diversity

In this case, we analyzed the system robustness when the channel's transfer function can be expressed as

$$H(z) = \sum_{k=0}^{L-1} h_k z^{-k} \tag{15}$$

As in the other cases, the coefficients h_k are Rayleigh variables with zero mean and unitary variance.

The results depicted in Fig. 9 indicate the BER for all possible interleaver configuration as a function of the channel's diversity. It is possible to confirm the SCCP robustness almost regardless of the interleaver configuration. On the other hand, the performance of the OFDM varies widely, with some interleaver setups providing unacceptable BER values.

C. Higher-Order Modulation

We now obtain the performance of OFDM and SCCP for different interleaver configurations, using again the channel described by eq.(10), but now for 16-QAM modulation. Such results are presented in Fig. 10.

The sensitiveness to the interleaver parameters of both OFDM and SCCP are similar to the case with QPSK modulation. However, the OFDM modulation can achieve a far superior performance when compared to the SCCP with linear equalization. This performance difference is also shown in [2]. The same reference shows that the Decision-Feedback Equalizer (DFE) with perfect feedback can bridge the performance gap between the SCCP and OFDM. In order to show this, we present in Fig. 11 the BER and BLER of the OFDM and SCCP with DFE and linear equalization as a function of the E_b/N_o.

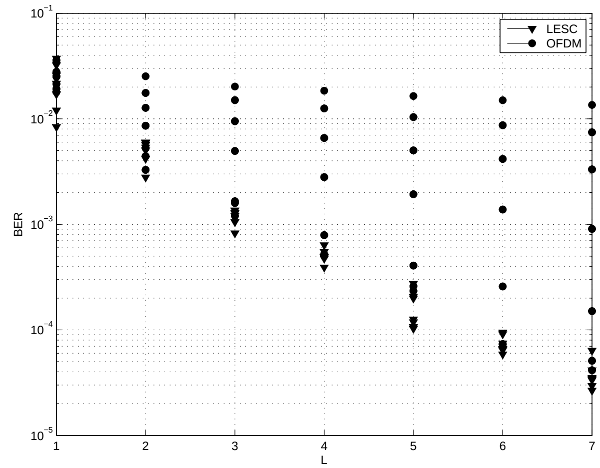

Fig. 9. Interleaver impact on system performance as a function of the channel diversity for a three-path Rayleigh channel with uniform power profile, E_b/N_o=12dB.

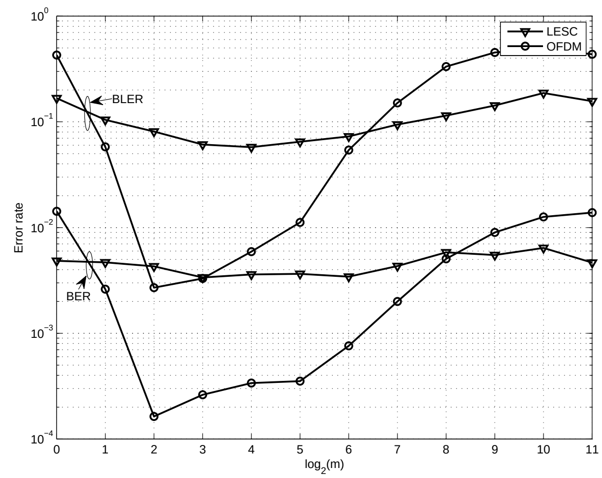

Fig. 10. Impact of the interleaver configuration on the system performance for a three-path Rayleigh , $[133\ 171]_{\mathrm{octal}}$ convolutional code, E_b/N_o=16dB and 16-QAM modulation. Interleaver matrix with m rows.

D. Static Channel with Spectral Null

We will analyze the system behavior when submitted to a static highly frequency selective channel. We have chosen a channel with three taps and a spectral null:

$$H(z) = 0.415 + 0.807z^{-1} + 0.415z^{-2} \tag{16}$$

In this kind of situation, linear equalization does not provide good results. For this reason, we have also analyzed the system performing the equalization with a DFE, which is notorious for its good performance under highly frequency selective channels.

In order to avoid the error propagation phenomenon, we use the joint DFE with channel decoding described in [10]. The code used in this simulation is the $[15\ 17]_{\mathrm{octal}}$, but we also show the performance of the OFDM with the $[133\ 171]_{\mathrm{octal}}$ for comparison reasons. The interleaver configuration was optimized for each technique.

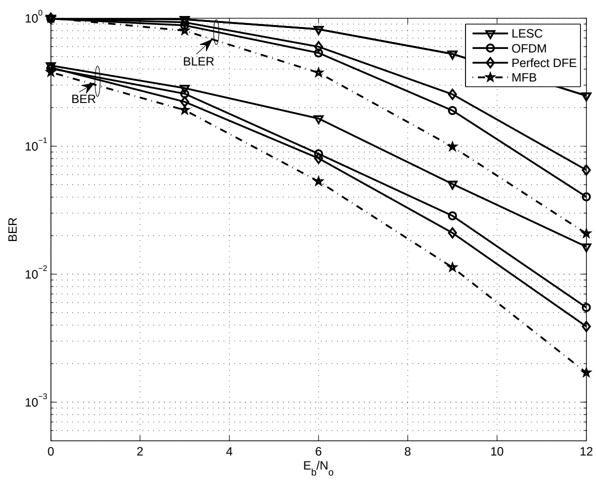

Fig. 11. Performance comparison, three-path Rayleigh channel with uniform power profile, 16-QAM modulation, convutional code $[133\ 171]_{\mathrm{octal}}$.

The results depicted in Fig.12 show that the OFDM, as well as the SCCP with linear equalization, leads to a BER much worse than the bound provided by the matched filter. The SCCP implemented with the joint DFE and decoder has a much superior performance. Even if we take into account the feedback error propagation inherent to DFE equalizers. Comparing the DFE with the OFDM, the performance gain is close to 3dB. When compared to the perfect DFE, we have a performance gain of about 4dB.

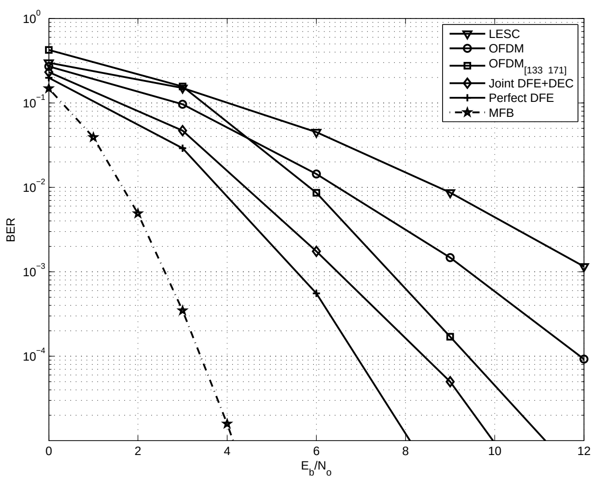

Fig. 12. Performance comparison, fixed channel with spectral null, convolutional code $[15\ 17]_{\mathrm{octal}}$. Best interleaver configuration 8 row/128 columns for the OFDM and 32 row/32 columns for SCCP.

IV. Conclusion and Perspectives

In this paper we compare the OFDM and the SCCP performance in different contexts. We show that the OFDM is highly sensitive to the interleaver configuration, which can be translated as a lack of robustness. However, if well configured it can exploit the channel diversity and provide an equal or superior performance when compared to the SCCP with linear equalization. We also show that the SCCP drawbacks for higher order modulation can be compensated by the use of DFE equalization. It is worth noting that this approach can provide huge performance gains in comparison to OFDM when the channel presents spectral nulls.

Due to such results and the performance gap of the OFDM with regard to the MFB, we are confident that a SCCP with turbo-equalization can lead to even superior performance. This case will be studied in future works.

References

[1] H. Sari, G. Karam, and I. Jeanclaude, "Transmission techniques for digital terrestrial TV broadcasting," *IEEE Communications Magazine*, vol. 33, no. 2, pp. 100–109, Feb. 1995.

[2] D. Falconer, S. L. Ariyavisitakul, A. Benjamin-Seeyar, and B. Edison, "Frequency domain equalization for single-cairrier broadband wireless systems," *IEEE Communications Magazine*, vol. 40, pp. 58–66, April 2002.

[3] Yuan-Pei Lin and See-May Phoong, "Mmse ofdm and prefixed single carrier systems: Ber analysis," *Acoustics, Speech, and Signal Processing, 2003. Proceedings. (ICASSP '03). 2003 IEEE International Conference on*, vol. 4, pp. IV–229–32 vol.4, April 2003.

[4] V. Aue, G. P. Fettweis, and R. Valenzuela, "A comparison of the performance of linearly equalized single carrier and coded 'ofdm' over frequency selective fading channels using the random coding technique," in *Proc. Int. Conf. Communications (ICC)*, Atlanta, 1998, vol. 2, pp. 753–757.

[5] S.K. Wilson and J.M. Cioffi, "A comparison of a single-carrier system using a dfe and a coded ofdm system in a broadcast rayleigh-fading channel," *Information Theory, 1995. Proceedings., 1995 IEEE International Symposium on*, pp. 335–, Sep 1995.

[6] Zhiqiang Liu, "Maximum diversity in single-carrier frequency-domain equalization," *Information Theory, IEEE Transactions on*, vol. 51, no. 8, pp. 2937–2940, Aug. 2005.

[7] J. Tubbax, L. V. der Perre, M Engels, H. De Man, and M. Moonen, "Ofdm versus single carrier: A realistic multi-antenna comparison," *EURASIP Journal on Applied Signal Processing*, vol. 2004, no. 9, pp. 1275–1287, 2004.

[8] Yuan-Pei Lin and See-May Phoong, "Minimum redundancy for isi free fir filterbank transceivers," *Signal Processing, IEEE Transactions on*, vol. 50, no. 4, pp. 842–853, Apr 2002.

[9] G. Caire, G. Taricco, and E. Biglieri, "Bit-interleaved coded modulation," *Information Theory, IEEE Transactions on*, vol. 44, no. 3, pp. 927–946, May 1998.

[10] C.M. Panazio and J.M.T. Romano, "Performance of joint space-time equalization and decoding techniques for wireless systems," *International Telecommunications Symposium - ITS*, 09 2002.

Joint Channel Estimation and Frequency Synchronization in MIMO-OFDM Systems

Phan Hong Phuong
Telecommunications Department, Faculty of Electrical and Electronic Engineering, University of Technology, Ho Chi Minh City, Vietnam
E-mail: phphuong@hcmut.edu.vn, phphuong@ieee.org

Hoang Pham Dang Huy,
Telecommunications Department, Faculty of Electrical and Electronic Engineering, University of Technology, Ho Chi Minh City, Vietnam
E-mail: danghuy@gmail.com

Luu Thi Thuy
Telecommunications Department, Faculty of Electrical and Electronic Engineering, University of Technology, Ho Chi Minh City, Vietnam
E-mail: luuthuy.luuthuy@gmail.com

Dang Truong Son
Faculty of Information Technology, University of Technical Education, Ho Chi Minh City, Vietnam
E-mail: sondt@hcmute.edu.vn

Abstract—**MIMO-OFDM (multiple input multiple output - orthogonal frequency division multiplexing), a new wireless broadband technology has gained great popularity for its capability of high rate transmission and its robust ness against multi-path fading and other channel impairments. A major challenge to MIMO-OFDM systems is how to obtain the channel state information accurately and promptly for coherent detection of information symbols and channel synchronization. This paper presents a modified procedure for joint channel and CFO parameters estimation in MIMO-OFDM systems that can provide an acceptable effectiveness and simplify the calculating process.**

Index Terms— **MIMO-OFDM, training sequence, pilot-tones, frequency synchronization, channel estimation**

I. INTRODUCTION

The Multiple-Input-Multiple-Output (MIMO) technique, as one of the promising technologies in modern communications, can increase the capacity of wireless systems by deploying multiple antennas at both transmitter and receiver sides in a rich scattering environment. Using the MIMO technique combined with the Orthogonal Frequency Division Multiplexing (OFDM) can allow improving the spectral efficiency, the coverage, and link reliability of the communication systems [1][2][3].

However, the theoretical benefits of MIMO-OFDM may not be fully achieved. On the one hand, unlike their single-carrier counterparts, multi-carrier transmissions are extremely sensitive to carrier frequency offsets (CFO's) caused by time and frequency selective wireless transmission channels, transceiver front-end imperfections, mobility and rich scattering environment, Doppler spread, etc. The CFO estimation and correction problems for OFDM systems have been mentioned by many authors [4][5]. On the other hand, the problem of propagation channel estimation is extremely important for a MIMO system. A good channel estimation algorithm can help recover the information emitted by the transmitter with a high accuracy resulting in high reliability of the whole system. For MIMO-OFDM, this problem must be solved together with CFO estimation.

In this paper, an algorithm for joint channel and CFO estimation in MIMO-OFDM systems that can provide an acceptable effectiveness and simplify the calculating process is proposed. The paper is further organized as follows. In Section II the authors introduce the pilot-based channel estimation algorithms, propose a modified training sequence for the block-type pilot algorithm and modified pilot tones for the comp-type pilot algorithm to use in a procedure for joint channel and CFO estimation. The simulation results are presented and discussed in Section III followed by conclusions in the final Section.

II. JOINT CHANNEL ESTIMATION BASED ON PILOT AND CARRIER FREQUENCY OFFSETS (CFO) ESTIMATION FOR MIMO-OFDM SYSTEMS

There are many methods for MIMO channel estimation that can be divided into two groups: estimation based on pilot and blind estimation [1][2]. In this paper we focus on the first group – channel estimation based on pilot.

One of the most critical parts of channel estimation based on pilot is how to design pilot symbol which will be agreed with two sides of the transmission [2][3]. Basically, pilot tones can be inserted either into all of the sub-carriers of OFDM blocks periodically or a subset of sub-carriers of each OFDM block. To simplify the mathematics analysis, we suppose applying Cyclic Prefix (CP)-OFDM and the length of CP is longer than the maximum propagation delay of all transmission paths from the transmit antenna to the receive antenna. After applying FFT, the demodulated $Y_p[n,i]$ of the n-th subcarrier and the i-th OFDM symbol of the p-th receiver antenna is:

$$Y_p[n,i] = \sum_{p=1}^{N_T} H_{p,q}[n,i] S_P[n,i] + V_q[n,i] \qquad (1)$$

The channel coefficients are unchanged over the duration of one OFDM symbol, so we can remove the index i:

$$Y_p[n] = \sum_{p=1}^{N_T} H_{p,q}[n] S_P[n] + V_q[n] \qquad (2)$$

Figure 1 shows the data diagram of channel estimation with block-type pilot.

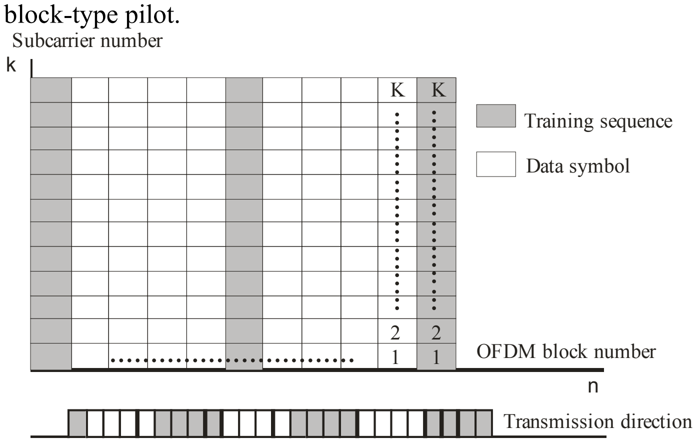

Figure 1. Channel Estimation with Block -Type Pilot

Let us consider the signal model in this case. The demodulated symbol vector and the additive noise vector corresponding to the q-th receive antenna are defined as follows:

$$\vec{Y}_q(m) = [Y_q[m,0], Y_q[m,1], \cdots, Y_q[m,N\text{-}1]]^T$$

$$\vec{V}_q(m) = [V_q[m,0], V_q[m,1], \cdots, V_q[m,N\text{-}1]]^T \qquad (3)$$

The channel coefficients of the transmission paths from all transmit antenna to the q-th receive antenna are combined to an $(N_T.N)\times 1$ vector:

$$\vec{H}_q = \left[\vec{H}_{0,q} \quad \vec{H}_{1,q} \quad \cdots \quad \vec{H}_{N_T-1,q}\right]^T \qquad (4)$$

where $\vec{H}_{p,q} = \left[H_{p,q}(0) \quad H_{p,q}(1) \quad \cdots \quad H_{p,q}(N-1)\right]^T$ is the frequency domain channel response of the p-th transmit antenna and q-th receive antenna.

The transmit symbol are combined to an $N\times(N_T.N)$ matrix:

$$X = \left[\mathrm{diag}\left\{\vec{X}_0\right\} \quad \mathrm{diag}\left\{\vec{X}_1\right\} \quad \cdots \quad \mathrm{diag}\left\{\vec{X}_{N_T-1}\right\}\right] \qquad (5)$$

Finally the transmit symbol can be written as:

$$\vec{Y}_q = X\vec{H}_q + \vec{V}_q \qquad (6)$$

The relationship between the time domain channel response is given by:

$$\vec{h}_{p,q} = \left[h_{p,q}(0) \quad h_{p,q}(1) \quad \cdots \quad h_{p,q}(L-1)\right]^T \qquad (7)$$

and the frequency domain channel response $\vec{H}_{p,q}$ can be described by:

$$\vec{H}_{p,q} = F_L \vec{h}_{p,q} \qquad (8)$$

where F_L is a matrix consisting of the first L columns of NxN FFT matrix.

The demodulated signal can be written as:

$$\vec{Y}_q = Q\vec{h}_q + \vec{V}_q \qquad (9)$$

where $Q = \left(\mathrm{diag}(\vec{X}_1)F_L \quad \mathrm{diag}(\vec{X}_2)F_L \quad \cdots \quad \mathrm{diag}(\vec{X}_{N_T})F_L\right)$

and $\vec{h}_q = \left(\vec{h}_{1,q} \quad \vec{h}_{2,q} \quad \cdots \quad \vec{h}_{N_T,q}\right)^T$

The estimated time domain channel response vector can be obtained by LS estimator:

$$\vec{h}_q = (Q^H Q)^{-1} Q^H \vec{Y}_q \qquad (10)$$

Here, the training sequence is needed to be chosen so that $Q^H Q$ is a diagonable matrix, FL is a matrix consisting of the first L columns of NxN FFT matrix. The training sequence is proposed by the authors as follows:

$$X_i[n,k] = X_1[n,k] e^{-j\frac{2\pi}{N_T}(i-1)k} \qquad (11)$$

where N_T is the number of transmit antennas.

Another pilot to be considered is comp-type, the data diagram of channel estimation with that is shown in Figure 2.

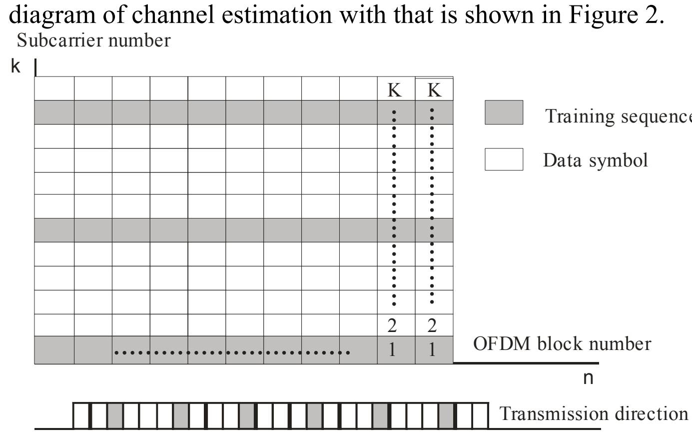

Figure 2. Channel Estimation with Comp -Type Pilot

N_P known pilot sub-carriers are periodically multiplexed into the N sub-carriers. The spacing between two adjacent pilots is $D_f = \lfloor N/N_P \rfloor$. Here, we define a subset of the transmitted signals containing only pilot symbols from TX i to be $X_{pi}[n, k]$. The received pilot sequence can be expressed as:

$$Y_P(n) = X_P(n) H_P(n) + W_P(n) \qquad (12)$$

where

$$
\begin{aligned}
&X_{pi}(n) = \mathrm{diag}\left(X_{pi}[n,0] \quad X_{pi}[n,1] \quad \cdots \quad X_{pi}[n,N_P-1]\right) && \in \mathbb{C}^{N_P\times N_P} \\
&X_P(n) = \left[X_{p1}(n) \quad X_{p2}(n) \quad \cdots \quad X_{pN_T}(n)\right] && \in \mathbb{C}^{N_P\times N_P N_T} \\
&H_{pi} = \left[H_{pi}(0) \quad H_{pi}(1) \quad \cdots \quad H_{pi}(N_P-1)\right]^T && \in \mathbb{C}^{N_P\times 1} \\
&H_P = \left[H_{p1}^T \quad H_{p2}^T \quad \cdots \quad H_{pN_T}^T\right]^T && \in \mathbb{C}^{N_P N_T\times 1} \\
&Y_P(n) = \left[Y_P(n,0) \quad Y_P(n,1) \quad \cdots \quad Y_P(n,N_P-1)\right] && \in \mathbb{C}^{N_P N_T\times 1}
\end{aligned} \tag{12}
$$

In our discussion, the pilot tones are assumed to stay in the first sub-carriers over every D_f sub-carriers. For the sake of the pilot extraction, we define a sampling vector D with the length of D_f

$$D = \underbrace{\begin{pmatrix}1 & 0 & \cdots & 0\end{pmatrix}}_{D_f} \tag{13}$$

Then for each transmit antenna, the down sampling matrix D_{spl} with the size of $N_p\times K$ can be built by:

$$D_{spl} = \mathrm{diag}(\underbrace{D \quad D \quad \cdots \quad D}_{N_P}) \tag{14}$$

Finally, we get the $N_T N_P \times N_T N$ down sampling matrix, in another word, pilot extraction matrix S as:

$$S = \mathrm{diag}(\underbrace{D_{spl} \quad D_{spl} \quad \cdots \quad D_{spl}}_{N_T}) \tag{15}$$

Therefore, the channel transfer function on pilot tones Hp can be extracted by:

$$H_P = SH \tag{16}$$

In this case, the pilot tones must be chosen so that the matrix $X_P^H X_P$ is diagonable. We propose the following pilot tones:

$$X_{pi,k} = \sqrt{\frac{E_P}{LN_T}}e^{-j\frac{2\pi}{N_T}ik}, \ \forall i \in \{1,2,...,N_T\}, k \in \{1,2,...,LN_T\} \tag{17}$$

where L is length of the channel impulse response, E_P is energy of a pilot tone.

Now we will consider a MIMO-OFDM system with CFO, and implement the proposed training sequence (11) or the pilot tones (17) to perform channel estimation for that system. The block diagram of the MIMO-OFDM channel with CFO is shown in Figure 3.

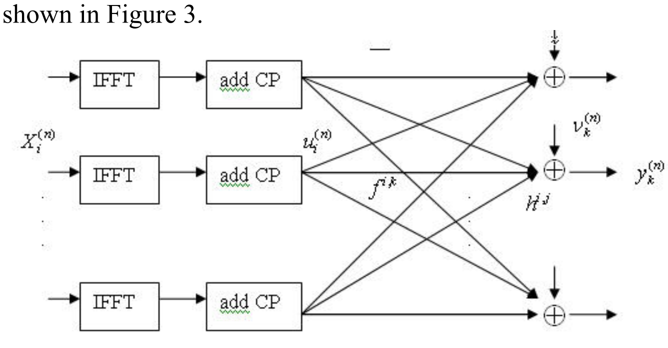

Figure 3. Block diagram of a MIMO-OFDM channel with CFO

The signal model with CFO is given as follows:

$$y(k) = \tilde{S}^{\gamma}(k)h(k) + w(k) \tag{18}$$

where:

$$y(k) = \left(y_1{}^T(k) \quad y_2{}^T(k) \quad \cdots \quad y_{Nt}{}^T(k)\right)^T \tag{19}$$

$y_r^T(k) = \left(y_r(k,0) \quad y_r(k,1) \quad \cdots \quad y_r(k,N-1)\right)^T$ is the received signal at the r[th] antenna.

$$\tilde{S}^{\gamma}(k) = \begin{pmatrix}
\tilde{S}^{\gamma}_{11}(k) & \cdots & \tilde{S}^{\gamma}_{Nt1}(k) & 0_{N\times L} & \cdots & & & \cdots & 0_{N\times L} \\
\vdots & & 0_{N\times L} & \tilde{S}^{\gamma}_{12}(k) & \cdots & \tilde{S}^{\gamma}_{Nt2}(k) & 0_{N\times L} & & \vdots \\
0_{N\times L} & \cdots & & & \cdots & 0_{N\times L} & \tilde{S}^{\gamma}_{1Nr}(k) & \cdots & \tilde{S}^{\gamma}_{NtNr}(k)
\end{pmatrix} \tag{20}$$

$\tilde{S}^{\gamma}_{pq} = e^{j\frac{2\pi\varepsilon_{pq}(kN_{tot}+GI)}{N}}D(\varepsilon_{pq})\tilde{S}_p(k)$, ε_{pq} is the carrier frequency offsset of the p[th] transmitted antenna and the q[th] received antenna.

$$\tilde{S}_p(k) = \begin{pmatrix}
s_p(k,0) & s_p(k,N-1) & & s_p(k,N-L+1) \\
 & s_p(k,0) & & \\
 & & \ddots & s_p(k,0) \\
 & & & \\
s_p(k,N) & s_p(k,N-2) & & s_p(k,N-L+2)
\end{pmatrix} \tag{21}$$

CFO's of an OFDM system can be estimated by using Maximum Likehood (MLK) or Extended Kalman Filter (EKF) method. For joint channel and CFO estimation using EKF method, we introduce the state-vector:

$$z(k) = \left(h^T(k) \quad \gamma^T(k)\right) \tag{22}$$

where

$$h(k) = \left(h_{11}^T(k) \quad \cdots \quad h_{Nt1}^T(k) \quad \cdots \quad h_{1Nr}^T(k) \quad \cdots \quad h_{NtNr}^T(k)\right)^T$$

$$\gamma(k) = \left[f_{11}, f_{21}, \cdots, f_{Nt1}, \cdots, f_{NtNr}\right]$$

There are NtNrL channel taps and NtNr frequency offset values in the state vector of dimension $NtNr(L+1)\times 1$. Then the linear state equation may be writen as follows:

$$z(k) = A_z z(k-1) + v(k) \tag{23}$$

State-spatial model is given by:

$$\begin{aligned}
z(k) &= A_z z(k-1) + v(k) \\
y(k) &= g(z(k)) + w(k)
\end{aligned} \tag{24}$$

where the nonlinear function $g: \mathbb{C}_{N_T N_R(L+1)} \longrightarrow C_{N_R N}$ is defined as

$$g:\ z(k) \longrightarrow g(z(k)) = \tilde{S}^{\gamma}(k)h(k) \tag{25}$$

The nonlinearity of the measurement equation $y(k) = \tilde{S}^{\gamma}(k)h(k) + w(k)$ is caussed by CFO's. Then we apply EKF method for estimation the state variable z(k). The Extended Kalman filter equation is given by:

$$\begin{aligned}
z_{(k|k-1)} &= A_z z_{(k-1|k-1)} \\
P_{(k|k-1)} &= A_z P_{(k-1|k-1)} A_z^T + Q_v \\
K_{(k)} &= P_{(k|k-1)} G^H_{z_{(k|k-1)}} \left[G_{z_{(k|k-1)}} P_{(k|k-1)} G^H_{z_{(k|k-1)}} + R_w\right]^{-1} \\
P_{(k|k)} &= \left[I_{NtNr(L+1)} - K_{(k)} G_{z_{(k|k-1)}}\right] P_{(k|k-1)} \\
z_{(k|k)} &= z_{(k|k-1)} + K_{(k)}\left[y(k) - g(z_{(k|k-1)})\right]
\end{aligned} \tag{26}$$

where $G_{z(k)}$ is the Jacobian matrix:

$$G_{z(k)} \triangleq \left.\frac{\partial g}{\partial z^T}\right|_{z=z(k)} = \left[\left.\frac{\partial g}{\partial h^T}\right|_{z=z(k)} \quad \left.\frac{\partial g}{\partial \gamma^T}\right|_{z=z(k)} \right]_{N_T N_R \times N_T N_R (L+1)} \quad (27)$$

The block diagram of the channel and CFO estimation using EKF can be seen in Figure 4.

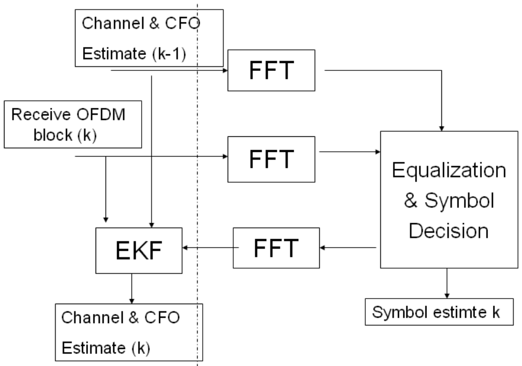

Figure 4. Channel and CFO estimation using EKF

Now we consider the schema of transmitted data structure with the proposed training sequence and CFO estimation using MLK method given in Figure 5.

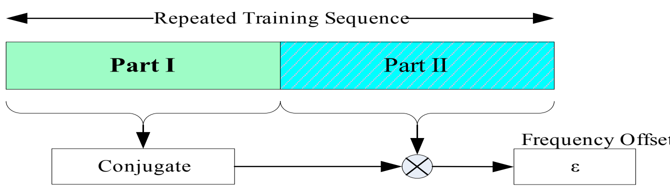

Figure 5. Transmitted data structure using MLK method

Suppose, that all the CFOs are equal values ε, then the received signal model is:

$$y_r(n) = \sum_{t=1}^{Nt} \sum_{l=0}^{L} h(l) s(n-l) e^{j2\pi\varepsilon n/N}$$

$$y_r(n+N) = \sum_{t=1}^{Nt} \sum_{l=0}^{L} h(l) s(n-l) e^{j2\pi\varepsilon(n+N)/N} \quad (28)$$

The initial CFO is given by:

$$f_{rt} = \varepsilon = \frac{1}{2\pi} \text{angle}\left(\sum_{n=0}^{N-1} \frac{y_r(n+N)}{y_r(n)} \right) \quad (29)$$

Modifying the received signal after estimation CFOs, we obtain:

$$y_r'(n) = y_r(n) e^{-j2\pi\varepsilon n/N}$$

$$Y_r = FFT(y_r(0,1,...,N-1))$$

Applying LS estimation, the initial channel coefficients are obtained as follows:

$$h_r = (Q^H Q)^{-1} Q^H Y_r \quad (30)$$

The proposed training sequence and pilot tones are proved to simplify the matrix calculations in the estimation process compared to the ones given by the previous publications [4].

III. Simulation Results and Discussions

In Figure 6, the symbol error rate (SER) versus SNR can be seen obtained by using the block-type pilot channel estimation and MLK CFO estimation for the 2×2 MIMO channel (2 transmit and 2 receive antennas) with different CFO's in different paths. The input parameters for the simulation are FFT size = 80, number of OFDM symbols = 30. Here, CFO error = 0.01 means CFO = 0.02, 0.01, 0.01, 0.02; CFO error = 0.02 means CFO = 0.03, 0.01, 0.01, 0.03 and CFO error = 0 means CFO = 0.02, 0.02, 0.02, 0.02. It is obvious, that increasing CFO error leads to worse performance.

The Maximum Likehood (MLK) method is good for small CFO's, but is less effective for large CFO's. In that case, the Extended Kalman Filter (EKF) method can be used.

Figures 7a) and 7b) show the MSE of CFO's estimated by the EKF method with 3 loops and symbol error rate (SER) versus SNR of a 2×2 MIMO system for various numbers of preamble OFDM symbols (N_pre). The channel parameters were estimated by the comp-type pilot with the proposed pilot tones (4). For the simulation, the following input parameters were used: Modulation type: QPSK, FFT size = 80, sample duration = 50×10-9 s, Doppler frequency = 50Hz, number of OFDM symbols = 10. Normalized frequency offsets CFO's for different paths of the 2×2 MIMO system are 0.03, 0.08, 0.07, 0.04. It can be seen, that the error of CFO estimation increases when N_pre is reduced. Besides, we can evaluate and compare these characteristics with various numbers of OFDM symbols, or various modulation types as well as pilot types for the channel estimation. It is noted, that the estimated system performance would be better if channel coding were included in all simulation results.

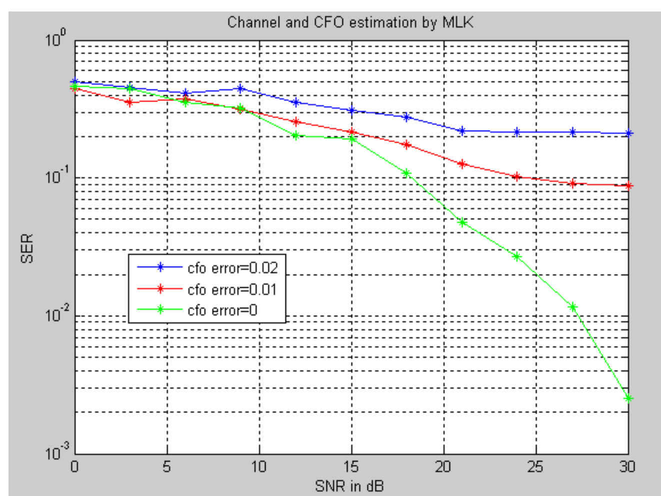

Figure 6. SER vs. SNR for channel and CFO estimation using MLK method

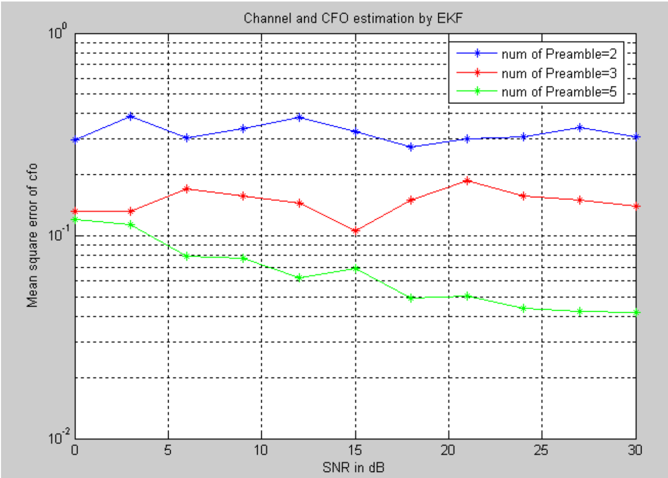

Figure 7a). MSE of estimated CFO's vs. SNR for various numbers of preamble OFDM symbols

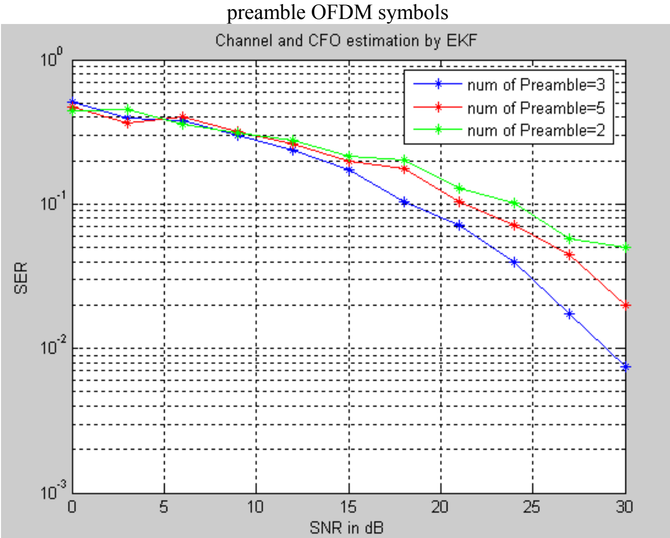

Figure 7b). SER vs. SNR for various numbers of preamble OFDM symbols

IV. CONCLUSIONS

This paper has presented some procedures of joint channel and carrier frequency offset estimation for MIMO-OFDM systems, where the proposed training sequence (11) or the pilot tones (17) can be used to simplify the channel estimation calculating process. Some results have been obtained and analyzed such as the symbol error rate (SER) versus SNR, MSE of CFO's estimated by the Maximum Likehood MLK or the Extended Kalman Filter (EKF) method.

REFERENCES

[1] Changyong Shin, Robert R. Heath, Edward J. Powers, Blind Channel Estimation for MIMO-OFDM Systems, *IEEE Trans. On Vehicular Technology*, vol.56, N2, pp. 670-685, March 2007.

[2] Qi Wang, Study of Channel Estimation in MIMO-OFDM Systems for Software Defined Radio, Linköpings Universitet, 2007.

[3] Vinod, T.S. Hari, K.V.S., Optimal pilot tones for MIMO interleaved OFDM systems, *IEEE International Conference on Acoustics, Speech, and Signal Processing*, pp.iv-741-iv-744, 2004 (ICASSP '04).

[4] Magnus Sandell, Darren McNamara, Analysis of frequency-offset tracking in MIMO OFDM systems, *IEEE Trans. on Communications*, vol.54, pp. 1481 – 1489, August 2006.

[5] Yonghong Zeng, A.Rahim Leyman,Tung-Sang Ng, Joint semi-blind Frequency Offset estimation and Channel estimation for Multi-user MIMO-OFDM Uplink, *IEEE Trans. on communication*, vol.55, pp.2270-2278, December 2007.

A Semi-Blind Concurrent Algorithm with Scattered Pilot Tones for OFDM Equalization

Estevan Marcelo Lopes
National Institute of Telecommunications - Inatel
P.O. Box 05 - 37540-000
Santa Rita do Sapucaí - MG - Brazil
estevan@inatel.br

Fabbryccio A. C. M. Cardoso
State University of Campinas - UNICAMP
P.O. Box 05 -
Campinas - SP - Brazil
cardoso@decom.fee.unicamp.br

Dalton S. Arantes
State University of Campinas - UNICAMP
P.O. Box 05 -
Campinas - SP - Brazil
cardoso@decom.fee.unicamp.br

Sandro Adriano Fasolo
National Institute of Telecommunications - Inatel
P.O. Box 05 - 37540-000
Santa Rita do Sapucaí - MG - Brazil
Sando.fasolo@inatel.br

***Abstract* — This paper presents a concurrent algorithm with semi-blind frequency-domain equalization (post FFT) in OFDM systems. The objective is to allow the OFDM system design with increased data throughput and without performance loss, when compared with pilot tone based on conventional channel estimation techniques. This work exploits the concurrent equalization concept of the CMA+SDD to develop an efficient post-FFT bank of equalizers. The algorithm can be considered semi-blind because it uses channel information, obtained from scattered pilot tones, to initialize and to supervise the bank of equalizers when pilots are present, otherwise remaining blind during the equalization process. In order to support such concurrent equalization, the system should provide scattered pilot tones only in the first symbol of each OFDM super-frame, allowing algorithm initialization when the receiver is turned on. In the remaining super-frame symbols, scattered pilot tones are suppressed to increase the overall system throughput.**

***Index Terms* — Concurrent Algorithm, OFDM Systems, Semi-Blind Equalization, Soft Decision-Directed.**

I. INTRODUCTION

Concurrent equalization is an efficient technique that combines the CMA - *Constant Modulus Algorithm* [1] with blind deconvolution algorithms which use a decision scheme based on the constellation symbols, such as the DD - *Decision Direct* [2] or the SDD - *Soft Decision Direct* [3]. The concept of concurrent equalizer was introduced by De Castro *et al* [2] in 2001. Subsequent works that followed the original concept have focused on some important aspects of the algorithm, such as low error floor, phase recovery (mod $\pi/2$) and fast convergence. One of the most important has been carried out by Chen [3] who proposed a CMA+SDD concurrent equalizer with about the same complexity of the original CMA+DD scheme, but with a still faster convergence. Other derivations and applications of the concurrent equalizer can also be found in [4], [5], [6] and [7].

Considering the application of the concurrent equalizer to OFDM systems, this paper uses the CMA+SDD algorithm [3] in an equalizer bank with a one-tap equalizer for each subcarrier. The equalizer bank is used to correct the phase and amplitude degradations of each subcarrier in an OFDM link. These degradations are known as intra-symbol interference and contribute to increase the bit error rate. The objective is to increase the data throughput, exploiting the blindness feature of the concurrent equalizer, without compromising the system performance in terms of BER versus SNR. In fact, the objective is also to increase such performance when compared with conventional techniques which estimate the channel response using pilot subcarrier and interpolation.

The traditional OFDM systems are conceived to offer two types of protection against the degradations caused by the communication channel response. The first protection is to insert a cyclic prefix in each OFDM symbol in the time domain, with the purpose of preventing inter-symbol interference (ISI). The second protection is obtained by inserting pilot tones in the frequency domain, which are used in the channel estimation processes or equalization techniques to compensate for amplitude attenuations and phase rotations in each subcarrier.

This paper is organized to present in Section II the proposed algorithm, to analyze in Section III the system throughput and the simulation results and, finally, to present in Section IV the conclusions of the study.

II. SEMI-BLIND CONCURRENT EQUALIZER

A. CMA+SDD Concurrent Equalizer

Concurrent equalization was originally designed for single-carrier transmission model with QAM modulation. Such equalizers are fractionally sampled to be able to operate with non-minimum phase channels [8]. The equations developed by Chen [3], are characterized by the adaptation of two independent FIR filters. However, it is possible to show that

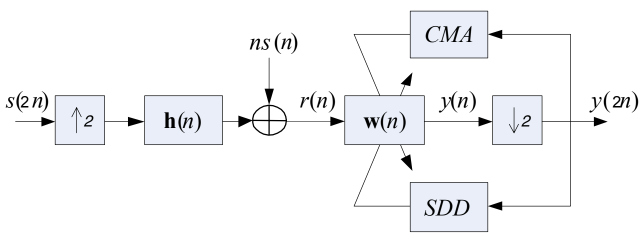

Fig. 1. Baseband communication model for the single filter concurrent version.

the same algorithm can be realized as only one FIR filter concurrently adapted by the CMA and SDD algorithms, as shown in Fig. 1 and by the following equations

$$y(n) = \mathbf{w}^T(n)\mathbf{r}(n),$$

$$\mathbf{w}(2n+1) = \mathbf{w}\big(2(n+1)\big) = \mathbf{w}(2n) + \mu\varepsilon(2n)\mathbf{r}^*(2n),$$

$$\varepsilon(2n) = y(2n)(\Delta_2 - |y(2n)|^2), \tag{1}$$

$$\Delta_2 = E\{|s(n)|^4\}/E\{|s(n)|^2\},$$

$$\mathbf{w}(2n+1) = \mathbf{w}\big(2(n+1)\big) = \mathbf{w}(2n) + \mu\frac{\partial \mathcal{J}_{LMAP}\big(\mathbf{w}, y(2n)\big)}{\partial \mathbf{w}(2n)}.$$

The compact (single filter) version of the concurrent algorithm shown in (1) was developed and adopted in this work for saving memory and operations

B. *Concurrent Equalization Applied to OFDM Systems*

The initial proposal was to design, in the frequency domain, a concurrent blind equalization algorithm which should be capable of regenerating the amplitude and phase information of each subcarrier, without using pilots. The resulting OFDM receiver, illustrated in Fig. 2, was conceived to use a non-fractional frequency-domain version of (1) with an equalizer bank using only one coefficient per subcarrier. This algorithm is based on the concurrent technique with soft decision [3], where the symbols are equalized according to a MAP – *Maximum a Posteriori* - criterion [3].

The equalization model in Fig. 2 assumes that for OFDM systems the communication channel can be represented by parallel and orthogonal narrow-band channels, without mutual interference among them. For each subcarrier the channel can then be considered flat, which means that the corresponding bandwidth is much smaller than the channel coherence bandwidth. In this article $\mathbf{w}_n($ is the coefficient vector $[w_n(k$ representing the equalizer bank at the symbol instant , where is the subcarrier index of the equalizer. The total number of subcarriers is . The vectors collecting the equalizer-bank inputs and outputs are represented respectively by $\mathbf{r}_n($ and $\mathbf{y}_n($. Notice in Fig. 2 that the equalizer output is given by

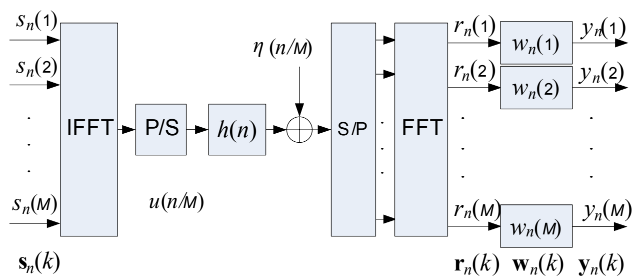

Fig. 2. Baseband communication model of the OFDM system with equalizer bank $\mathbf{w}_n(\boldsymbol{k})$.

$$y_n(k) = w_n(k)r_n(k) \text{ for } k = 1, 2, \cdots, M. \tag{2}$$

The CMA+SDD concurrent adaptation in (1) was applied to the equalizer bank $\mathbf{w}_n($ with modifications, since we observed that the concurrent equalization was not capable of driving to zero some of the carrier phase rotations greater than 45°. In the scenario in which a few subcarriers are rotated by more than 45°, the recovered constellations, in such subcarriers, present rotation multiples of 90º after full equalizer convergence. This result was expected because the phase recovery is obtained by direct decisions over a square constellation.

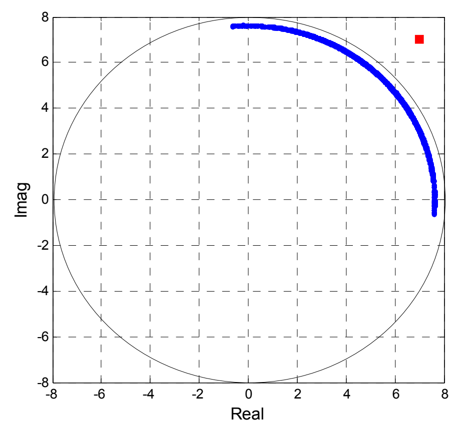

Fig. 3. Constellation from all subcarriers transmitting the same symbol 7+ 7i.

Unfortunately, such scenario is very common in OFDM systems. For example, consider the transmission of a symbol 7 + 7i in all subcarriers through the ITU Brazil-A channel profile [9]. In Fig. 3 we illustrate the composition of the received signals from all subcarriers, normalized in amplitude. Observe that the signal phase can vary widely throughout the subcarriers and some of them present rotations larger than 45º. In such scenario wrong phase recovery in even a few subcarriers can substantially degrade the overall BER performance of the system. It may be argued that sync-words, differential encoding and other countermeasures could be applied to individual subcarriers to resolve 90º ambiguities in phase rotations, but we are avoiding the use of these techniques in favor of power efficiency.

A proposed solution to deal with such high phase rotation in

OFDM systems consists in initializing the equalizer bank with an initial channel estimate. This solution impacts the system if, for example, scattered pilot tones are inserted to allow channel estimation at the receiver. However, in the present case the system can use pilot symbols with a much lower rate than the traditional OFDM equalizers, reducing the impact on the overall throughput. As shown in Fig. 4, our proposal is to use scattered pilot tones only in the first symbol of each super-frame. Moreover, in the first symbol the pilots are interlaced with data subcarriers with the purpose of increasing the overall throughput. In this case, channel frequency response estimation over data subcarriers are obtained by interpolation when the corresponding equalizers are initialized.

In this work, immediately after the equalizer bank is initialized, the CMA+SDD algorithm operates blindly over such equalizer bank when scatter pilots are not available in the OFDM symbol. However, when scatter pilots are present, the *concurrent algorithm* switches to an LMS-like algorithm as described in Table I. Scattered pilots tones are repeatedly inserted in each first symbol of the super-frame. Such strategy is necessary to start the equalizer when the receiver is turned on or when the equalization is lost.

The channel estimate used to initialize the equalizer bank, considering pilot and data subcarriers, is given by

$$w_0(k) = \begin{cases} \text{interp}\left\{k, \dfrac{P(m_l)}{\hat{P}(m_l)}, \dfrac{P(m_r)}{\hat{P}(m_r)}\right\} \text{ if} \\ \quad k \in \text{data subcarrier}, \\ \quad m_l \in \text{left pilot and} \\ \quad m_r \in \text{right pilot}; \\ \dfrac{P(k)}{\hat{P}(k)} \text{ if } k \in \text{pilot}; \end{cases} \qquad (3)$$

where $P($ is the transmitted pilot associated with the *k-th* subcarrier; $\hat{P}($ is the corresponding received pilot; and $w_0($ is the initial value of the *k-th* one-tap equalizer of the equalizer bank. For *k* corresponding to data subcarriers, it is necessary to interpolate the estimate obtained from the neighboring pilot tones.

Another important aspect that appears in the application of the concurrent algorithm for equalization in OFDM systems, besides the aspect of phase recovery, is the possibility of antagonistic forces in the CMA and the SDD. This can occur when a subcarrier is highly attenuated by the channel. Empirically, we have observed that for attenuations greater than 20 dB, the SDD adaptation degrade the CMA performance. Fortunately, the same initialization solution adopted for the problem of phase ambiguity can also solve the problem of antagonistic forces in the concurrency process involving the CMA and the SDD. In fact, initializing the equalizer taps from the channel estimate can provide a favorable initial condition for the equalization.

Table I summarizes the concurrent algorithm for use with OFDM systems with the modifications suggested in this article. It is important to emphasize that in the simulations we have used a CMA and SDD version normalized by the average power of the input signal, as in the normalized LMS. The power normalization factor was omitted from Table I for simplicity. The parameters used in the simulations were $\mu_c = ($, $\mu_d = 0.00$ and $\rho = ($

TABLE I
CONCURRENT EQUALIZATION ALGORITHM FOR OFDM SYSTEMS[1].

Initialize each equalizer k:

$$w_0(k) = \text{interp}\left(k, P(k), \hat{P}(k)\right),$$

where interp(·) is the same function used in (3).

Calculate the output for each subcarrier k:

$$y_n(k) = w_n(k) r_n(k)$$

For each data subcarrier k, adapt the coefficients using the CMA and SDD:

CMA:

$$w_{n+1}(k) = w_n(k) + \mu_c \varepsilon_n(k) y_n(k) r_n^*(k)$$

$$\varepsilon_n(k) = \Delta_2 - |y_n(k)|^2$$

$$\Delta_2 = \frac{E\{|s_n(k)|^4\}}{E\{|s_n(k)|^2\}}$$

SDD[3]:

$$w_{n+1}(k) \leftarrow w_{n+1}(k) + \mu_d \frac{\partial \mathcal{J}_{LMAP}(w, y_n(k))}{\partial w}$$

$$(i, l) = \text{find\_region}(y_n(k))$$

$$\frac{\partial \mathcal{J}_{LMAP}(w, y_n(k))}{\partial w} =$$

$$\frac{\sum_{p=2i-1}^{2i} \sum_{q=2l-1}^{2l} \exp\left(-\frac{|y_n(k) - s_{pq}|^2}{2\rho}\right)(s_{pq} - y_n(k))}{\sum_{p=2i-1}^{2i} \sum_{q=2l-1}^{2l} \exp\left(-\frac{|y_n(k) - s_{pq}|^2}{2\rho}\right)} r_n^*(k)$$

1. The algorithm presented here is the semi-blind concurrent. In this case the algorithm switches to an LMS-like for both pilot and data subcarriers in the first symbol of each super-frame. In the pilot tone, the error is calculated

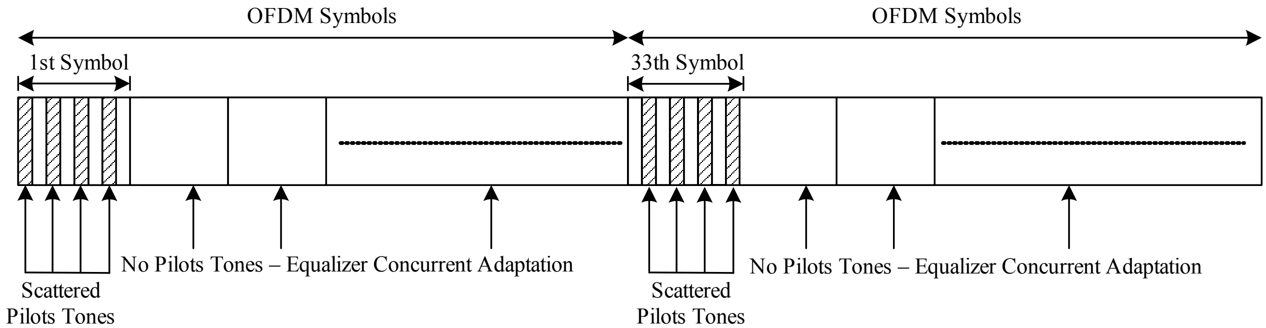

Fig. 4. Use of Scattered Pilot Tones in super-frame for equalizer bank.

III. Performance Evaluation

We evaluate the performance of the semi-blind concurrent algorithm by using the usual comparative analyses of BI versus $E_b/$.. The results used as references are obtained under the assumption of known channel and of channel estimation with pilot-based linear interpolation scheme. The known-channel estimation uses the channel knowledge on all subcarriers $C_n($, with $k = 1, 2, \cdots$,, to adjust the channel amplitude and phase response for each subcarrier by a factor of $1/C_n($ Knowing the channel response is obviously the ideal scenario and represents a lower bound on BER performance, as well as an upper bound on throughput, for the proposed concurrent algorithm. On the other hand, pilot-based channel estimation with linear interpolation will be considered here as an upper bound on BER performance. This assumption is reasonable since linear interpolation is used to initialize the equalizer bank and the concurrent adaptation process is probably going to improve such initial estimate. However, it does not mean that the linear interpolation receiver used here only estimate the channel once, when the receiver is turned on. In fact, a new estimate is carried out for every received OFDM symbol and no average is taken over the OFDM channel estimates.

The simulation results were obtained for an OFDM system with 2048 subcarriers. OFDM symbols, including cyclic-prefix, are sampled at 8.127 MHz which correspond to a sample time of $T_s = 63/(512 \times 1C \quad \sim 123.05$. To format the transmission spectrum, 158 null subcarriers are padded to 1890 data and pilot subcarriers, resulting in a total of 2048 subcarriers. Data subcarriers are modulated with 64-QAM while pilots are modulated with BPSK.

When the channel response is assumed to be known, the system model is configured to operate without pilot subcarriers, providing a system throughput R_{kn}, in bits/s, given by the inverse of $T_s \times 2048 \times (1 + CP)/(1890 \times$. For linear interpolation-based channel estimation, the system model is configured with one pilot added to every other 4 subcarriers, resulting in 378 pilots and 1512 data subcarriers per OFDM symbol. In this case, the system throughput R_{inte} is given by the inverse of $T_s \times 2048 \times (1 + CP)/(1512 \times$. Considering the semi-blind concurrent algorithm, scattered pilots tones are used only in the first symbol of each super-frame with the same configuration used in the linear interpolation. For the other symbols of the super-frame, all 1890 available subcarriers are used for data transmission. The super-frame contains 32 symbols and the system throughput R_{cc} is given by the weighted mean $R_{conc} = (1 \times R_{interp} + 31 \times R_{conh})/3$

In this work, the algorithm was tested for values of cyclic prefix (*CP*) equal to 1/32 and 1/64. In Table III we summarize the values of system throughput for the receivers considered in this work. It is worth emphasizing that no channel encoding scheme was used since the objective was to only evaluate the equalization performance. Observe in Table II that the use of the concurrent algorithm increases data throughput by about 8 Mbits/s when compared with the linear interpolation.

The chosen cyclic prefixes of 1/32 and 1/64 were motivated by the channel profile used in the simulations. The objective was to test the concurrent equalizer bank in a scenario where cyclic prefix is just sufficient to avoid inter-symbol interference as well as in an adverse scenario with ISI. The channel profile used in all simulations is the ITU Brazil A [9],

Table III
Data Throughput in Mbits/s for The Simulated Systems

Transmitter Parameter	Known Channel	Semi-Blind Concurrent	Linear Interpolation
CP = 1/32 CP = 1/64	43.64 44.31	43.36 44.03	34.91 35.45

Table III
ITU Brazil A Channel Profile

Coefficient ceil (Delay/T_s)+1	Delay (μs)	Gain (dB)	Phase (rad)
1	0.00	0.00	0.6000
3	0.15	-13.8	3.4355
20	2.22	-16.2	1.9839
26	3.05	-14.9	4.2610
49	5.86	-13.6	5.6254
50	5.93	-16.4	0.0892

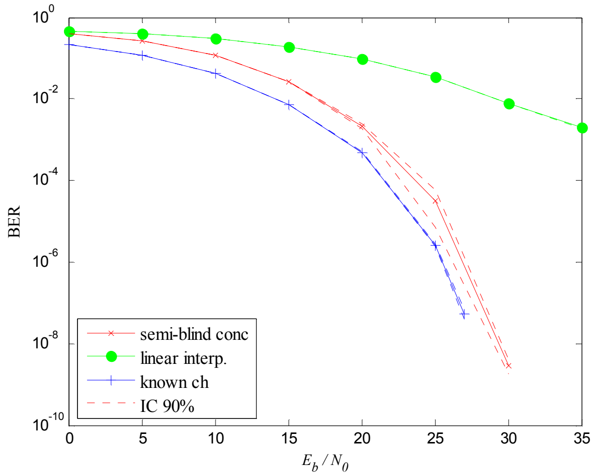

Fig. 5. Performance of BER versus E_b/N_0 for the scenario with $CP = 1/32$

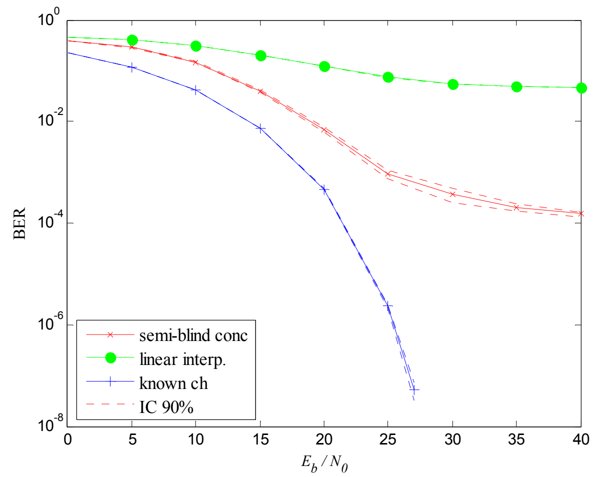

Fig. 6. Performance of BER versus E_b/N_0 for the scenario with $CP = 1/64$

described in Table III. The ITU has standardized channel profiles as a function of delay and gain for multipath components. Phase information was randomly generated to simulate random antenna positioning in the receiver, but was kept constant in simulation traces. The channel was then digitized by rounding the delay profile to multiple values of the sample time *Ts*. In Table III we show only the nonzero coefficients of the digitized channel profile.

The cyclic prefix duration in considered here is given by $2048 \times CP \times$. For $CP = 1/$ and $1/$, it leads to durations of 7.875 and 3.9375, respectively. Therefore, as the maximum channel delay for Brazil A is about 5.93, then the $CP = 1/$ is enough to avoid ISI, while $CP = 1/$ cannot prevent it, degrading system performance. In this work, the BER performance is evaluated for both scenarios.

Simulation results were obtained for each point of $E_b/$ by the estimate of the mean for BER in L=25 outcomes (simulation traces), as given by $\overline{\mathrm{BER}} = \frac{1}{L}\sum_{l=1}^{L} \mathrm{BE}$ The estimated variance and the confidence interval are calculated by

$$S^2 = \frac{1}{L-1}\sum_{l=1}^{L}(\mathrm{BER}_l - \overline{\mathrm{BER}}),$$

$$\Pr\left\{-c < \frac{\overline{\mathrm{BER}}-\xi}{S\sqrt{L}} < c\right\} = 0.90,\ \Pr\left\{\frac{\overline{\mathrm{BER}}-\xi}{S\sqrt{L}} < c\right\} = 0.95$$

$$\text{and } CI = \left[\overline{\mathrm{BER}} - cS\sqrt{L};\ \overline{\mathrm{BER}} + cS\sqrt{L}\right].$$

In the calculations, $\overline{\mathrm{BER}}$ is supposed to be normally distributed, which leads $(\overline{BER} - \xi)/S\sqrt{L}$ to have a Student's t-distribution with L-1 degrees of freedom. To obtain a confidence interval (*CI*) of 90%, the parameter *c* is given by the inverse of the Student's cumulative distribution function evaluated for 0.95.

The performance curves of $BER \times E_b/$ are plotted here with solid lines for the mean estimate of $\overline{BI}$ and with dotted lines for the lower and upper bounds of the confidence interval *CI* (90%).

In Fig. 5 we show the simulation results for the scenario with $CP = 1/$, which is sufficient to prevent ISI. The results for linear interpolation saturate near a BER of 1×10due to imprecision on channel estimates for data subcarriers. On the other hand, with the semi-blind concurrent no saturation was observed for BER. Such results follow the behavior of the known-channel result with a loss of about 2 dB for the semi-blind concurrent in the evaluated points of $E_b/N_0 \geq 15$. This was expected due to the partial supervision performed when the scattered pilot tones are available.

The results obtained with $CP = 1/$, which is insufficient to avoid ISI, are presented in Fig. 6. In this scenario, inter-carrier interference (ICI) is introduced due to orthogonality loss. The transmission model, which assumes that every subcarrier is independently attenuated and rotated by a single channel coefficient, is based on an assumption which is not strictly valid. However, the objective of this study is also to evaluate the algorithm robustness when the assumption of orthogonality is not valid. The semi-blind concurrent equalizer has shown results better than the linear interpolation used in the scenario with sufficient cyclic prefix. This means that the proposed semi-blind concurrent equalization is able to successfully improve the initial channel estimate and outperform the linear interpolation results.

IV. Final Comments

Semi Blind Concurrent equalization was investigated in this work for operation with OFDM systems by exploiting specificities of such systems. The motivation was the low complexity, fast convergence, blindness property and phase-recovery features of the CMA+SDD concurrent equalizer. In fact, the concurrent equalization is considered by some researchers as the state of the art in low-complexity blind equalization and, as we have shown, its application to OFDM systems can improve the overall throughput without compromising BER performance.

We have shown that the blindness property of the concurrent equalizer can drastically reduce the number of pilot tones, but some adaptations to OFDM were necessary.

The proposed semi-blind algorithm uses this information to supervise the equalizers in the first symbol of each super-frame, when scattered pilot tones are available, switching to an LMS-like adaptation using both pilot and data subcarriers.

Results have shown that in scenarios with sufficient sizes of cyclic prefix (*CP*), the system performance follows the known channel results with a loss of only 2 to 5 dB. However, when cyclic prefix is insufficient to prevent ISI, the BER performance saturates, but to a level better than the linear interpolation with sufficient cyclic prefix.

REFERENCES

[1] C. R. Johnson, Jr. et al., "*Blind Equalization Using Constant Modulus Criterion*: A review", Proc. of the IEEE, Vol. 86, No. 10, October 1998.

[2] F. C. C. de Castro, M. C. F. de Castro and D. S. Arantes, "*Concurrent Blind Deconvolution for Channel Equalization*", IEEE Int. Conf. on Communications ICC2001, pp. 366-371, Helsinki, Finland , June 2001.

[3] S. Chen, E. S. Chng, "*Concurrent Constant Modulus Algorithm and Soft Decision Directed Scheme for Fractionally-Spaced Blind Equalization*", 2004 IEEE International Conference on Communications, Paris, France, 2004.

[4] L. Shun-lan and D. Ming-zeng, "*A New Blind Equalization Scheme for QAM Systems Based on Fractionally-Spaced Equalizer*", IEEE Int. Conf. on Comm., Circuits and Systems, Kokura, Japan, July, 2007.

[5] W. Rao, Y. Han and Y. Guo, "*A New Family of Combination Blind Equalization with a New Constant Modulus Algorithm Based on Variable Slope Error Function*", The 8th Int. Conf. on Signal Processing, ICSP2006 Proceedings, Beijing, 2006.

[6] M. Hadef, S. Weiss, "*A Fast Converging Concurrent Affine Projection Algorithm for Blind Multiuser Equalisation*", The 2nd IEE/EURASIP Conf. on DSPenabledRadio, University of Southampton, Sept. 2005.

[7] S. Chen, S. McLaughlin, P.M. Grant and B. Mulgrew, "*MultiStage Blind Clustering Equaliser*", IEEE Trans. on Comm., Vol. 43, No. 2/3/4, February/March/Abril/ 1995.

[8] Simon Haykin, "*Adaptive Filter Theory*", 3 rd ed., Prentice Hall, Upper Saddle River, New Jersey, 1996.

[9] ITU Radiocommunication Study Groups: Document 6E/TEMP/131-E, "Guidelines and Techniques for the Evaluation of DTTB Systems", March 19, 2003.

Performance of QS-CDMA Ad Hoc Networks using ZCZ spreading sequences

Tarciana Araújo Lopes, Márzio Geandre Rêgo
Department of Communications - DECOM
Faculty of Electrical and Computer Engineering - FEEC
University of Campinas - UNICAMP
P.O. Box 6101 - 13083-852,
Campinas - SP - Brazil
(tarciana,geandre)@decom.fee.unicamp.br

Renato Baldini Filho
Department of Communications - DECOM
Faculty of Electrical and Computer Engineering - FEEC
University of Campinas - UNICAMP
P.O. Box 6101 - 13083-852,
Campinas - SP - Brazil
baldini@decom.fee.unicamp.br

***Abstract*— This work investigates the performance of zero correlation zone (ZCZ) codes in quasi-synchronous CDMA ad hoc networks on multipath fading channels. One of the main defiances of CDMA ad hoc networks is to eliminate the near-far effects. This limitation can be minimized by using ZCZ codes that mitigate the effects of the intersymbol and multiple access interference in multipath channels. The performance analysis is based on the evaluation the expected progress per hop.**

***Index Terms*— ad hoc networks, quasi-synchronous CDMA, ZCZ codes.**

I. Introduction

Ad hoc wireless network is a distributed system, in which the mobile nodes can be freely and dynamically self-organized. The source node may transmit to a destination node in a straight path or by using intermediate nodes (multiple hops). Ad hoc wireless network has to manage with the lack of centralized control, the fast changes in the link characteristics, and multiuser interferences. All users in an d hoc networks interfere to each other in a manner that it is difficult to model this multiple access scheme. Therefore, it is a challenge to increase the low aggregate throughput of this type of network [2].

Ad hoc networks using code division multiple access (CDMA) have been researched in the past years. In [3], the optimum transmission range in multihop DS-CDMA networks over an AWGN channel was derived. In [4] and [5] the authors considered fading and route diversity, respectively, in the channel modeled in [3]. A classical solution to mitigate multiple access interference (MAI) effects is to enforce equal power to all received signals. Power control techniques can be found in [6].

The asynchronous nature of ad hoc networks results in interference among users with different spreading codes. The random time offsets among the signals produces MAI and intersymbol interference (ISI). A way to mitigate MAI and ISI is to make use of spreading sequences belonging to the class of zero correlation zone (ZCZ) sequences. These sequences present a window that off-peak autocorrelation and the cross-correlation values are zero, and the degradation caused by the non orthogonality of the signals can be reduced or even eliminated.

The drawback of employing ZCZ codes as channelisation codes is that the number of sequences with a specific length and size of zero-correlation zone is low. Unfortunately, the theoretical bounds shows that it is hard to obtain a large number of ZCZ sequences while maintaining the size of orthogonal zone. In order to provide larger number of spreading sequences, a possible solution is to construct several codes sets, each one with the same correlation properties, but having minimum crosscorrelation between any pair from different ZCZ code sets.

This paper addresses the use of ZCZ spreading sequences in Quasi-Synchronous (QS) CDMA ad hoc networks. To take advantage of ZCZ sequences features, it is presumed a rough synchronization to guarantee that the relative time off-set among the codes is within the zero correlation zone. The performance is evaluated in terms of expected progress per hop, an usual measure of networks performance. Recently, investigation of loosely synchronous codes (LS), a generalization of ZCZ codes, combined with large area (LA) codes was made in [7]. The performance of ad hoc networks using these large area synchronous (LAS) codes is accomplished in rectilinear located nodes. The approach presented in this paper takes into account that the nodes are located in an uniformly circular distributed manner.

This paper is organized as follows. Section II presents the construction of ZCZ codes. Section III introduces the adopted system model. In section IV, a simulation-based comparison between ZCZ codes and traditional spreading codes is realized, in terms of expected progress per hop. Finally, conclusions are drawn in Section V.

II. ZCZ codes generation

Welch has shown that off-set autocorrelation and cross-correlation of signals have non-zero simultaneously lower bounds [8]. Moreover, small MAI leads to large ISI and vice-versa [9]. Then, sequence set whose autocorrelation and cross-correlation side lobes are zero for all time off-set, does not exist.

Zero correlation codes could be ideal candidates to mitigate the multipath and the near-far effects, however there are a very limited number of available codes with an useful interference free window (IFW). Then, the capacity of the ad hoc CDMA system using access IFW code is dimension limited.

Mutually orthogonal (MO) sequence sets can be used to overcome this limitation. This procedure doubles the number of ZCZ sequences. However, sequences from different sets do not assert the correlation properties for nonzero off-set.

Mutually orthogonal ZCZ sequence sets can be recursively constructed [10]. For a fixed IFW, it is possible to have mutually orthogonal sets such that each set has the maximum number of ZCZ sequences. The basis of mutually orthogonal ZCZ sequence sets is as follows [11], [12].

Let $\mathbf{c_k}$ denote the spreading code with chip time duration T_c and code length equal to N, corresponding to user k, i.e.:

$$\mathbf{c}_k = [c^{(1)}, c^{(2)}, ..., c^{(N)}]. \quad (1)$$

A sequence exhibit IFW properties, with width given by Z_{cz}, if it presents the following correlation characteristics [15]:

$$\phi_{j,k} = \sum_{i=0}^{N-1} c_j^{(i)} c_k^{(i+\tau)} = \begin{cases} N, & \text{for } \tau = 0,\ j = k \\ 0, & \text{for } \tau = 0,\ j \neq k \\ 0, & \text{for } 0 < |\tau| \leq Z_{cz}, \end{cases} \quad (2)$$

where the superscript addition $i + \tau$ is performed *modulo* N.

The aperiodic correlation $\phi_{j,k}$ of two sequences $\mathbf{c_j}$ and $\mathbf{c_k}$ has to satisfy (2) to maintain an IFW of Z_{cz} chip interval.

A set of sequences $\{c_i\}_{i=1}^{M}$, each one with length N, and IFW of Z_{cz} is denoted as ZCZ-(N, M, Z_{cz}), where $Z_{cz} = \min\{Z_{acz}, Z_{ccz}\}$, Z_{acz} and Z_{ccz} denote, respectively, the zero autocorrelation and zero cross-correlation zones, which are defined as [10]:

$$\begin{aligned} Z_{acz} &= \max\{T \mid \phi_{c^j c^j}(\tau) = 0, \forall j, \tau \neq 0, |\tau| \leq T\}, \\ Z_{ccz} &= \max\{T \mid \phi_{c^j c^k}(\tau) = 0, \forall j \neq k, |\tau| \leq T\}. \end{aligned}$$

Two distinct sets of ZCZ sequences $\{c1_i\}_{i=1}^{M}$ and $\{c2_i\}_{i=1}^{M}$ are mutually orthogonal, if

$$\phi_{c1_k c2_j}(0) = 0 \quad \forall j, k. \quad (3)$$

The method to obtain a set of ZCZ sequences starts with a pair of complementary sequences, Y_m and X_m, which are obtained recursively by:

$$\begin{aligned} [X_0, Y_0] &= [1, 1] \\ [X_m, Y_m] &= [X_{m-1}Y_{m-1}, (-X_{m-1})Y_{m-1}]. \end{aligned} \quad (4)$$

$$F_1^{(0)} = \begin{bmatrix} -X_m & Y_m \\ -\overleftarrow{Y}_m & \overleftarrow{X}_m \end{bmatrix}_{2 \times 2^{m+1}}, \quad (5)$$

where $\overleftarrow{Y}_m$ denotes the reverse of sequence Y_m and $-Y_m$ is the binary complement of Y_m.

Consider $F_2^{(0)}$ similar to $F_1^{(0)}$. For the nth iteration ($n \geq 1$), two mutually orthogonal sets of ZCZ sequences, $F_1^{(n)}$ and $F_2^{(n)}$, are acquired:

$$F_1^{(n)} = \begin{bmatrix} F_1^{(n-1)}F_1^{(n-1)} & F_1^{(n-1)}(-F_1^{(n-1)}) \\ F_1^{(n-1)}(-F_1^{(n-1)}) & F_1^{(n-1)}F_1^{(n-1)} \end{bmatrix}, \quad (6)$$

$$F_2^{(n)} = \begin{bmatrix} F_2^{(n-1)}F_2^{(n-1)} & (-F_2^{(n-1)})F_2^{(n-1)} \\ F_2^{(n-1)}(-F_2^{(n-1)}) & (-F_2^{(n-1)})(-F_2^{(n-1)}) \end{bmatrix}, \quad (7)$$

where $(-F_i^{(n-1)})$ is the matrix $F_i^{(n-1)}$ which entries are negated and $F_i^{(n-1)}(-F_i^{(n-1)})$ denotes the matrix whose ijth entry is the concatenation of the ijth entry of $F_i^{(n-1)}$ and the ijth entry of $(-F_i^{(n-1)})$ [13], [14].

Each row of the matrices, after the nth iteration, represents a spreading sequence. This procedure doubles the number of ZCZ sequences. Explicitly, we have $M = 2^{(n+1)}$, $N = 2^{(2n+m+1)}$ and $Z_{cz} = 2^{(m)}$.

III. System Model

The network model assumes a quasi-synchronous DS-CDMA/BPSK ad hoc network under heavy traffic conditions, i.e., all nodes are supposed to have packets to transmit all time. The system is slotted and during each slot, a snapshot of the nodes is taken. In other words, the network topology is invariant over a packet transmission time, which is equivalent to have an invariant interference level during this time interval [3]. In every slot, each node may transmit independently with probability p.

The traffic distribution is uniform. The number of nodes in the network is modeled by a Poisson point process in a plane, with probability density function (PDF) given by

$$P[n \ nodes \ in \ R_A] = \frac{e^{-\lambda A}(\lambda A)^n}{n!}, \quad (8)$$

where λ is the average number of nodes per unit area and A is the area of a given circular region in the plane of radius R_A.

The network consists of N_t nodes, which are randomly placed through a circular area. The location of terminals obeys an uniform distribution, given by:

$$p_{r_k}(r_k) = \begin{cases} \dfrac{2r_k}{R_t^2}, & r_k \leq R_t \\ 0, & \text{otherwise} \end{cases} \quad (9)$$

where r_k is the distance of the kth transmitter node to the interest node and R_t is the radius of the considered circular area.

The channel model is a combination of large scale path loss, with path loss exponent β, and multipath Rayleigh fading. The received signal power, P_r, is a function of the distance between the transmitter node and the receiver node, r, and it is given by:

$$P_r = \frac{P_t}{r^\beta} \quad (10)$$

where P_t is the transmitted signal power.

A maximal ratio combiner (MRC) and a rake receiver are implemented in the reception with known channel weights [16]. The decision variable is obtained by correlating the received signal with shifted versions (multiples of T_c) of the spreading sequence of the transmitter and combining them.

The network operates with K transmitter-receiver pairs (active links), where the K transmitters nodes are simultaneously transmitting with same power, P_t. It is considered a link of length R between an interest node and a desired transmitter node, as shown in Fig. 1. The interest node is positioned at the origin of a circle of radius R_t.

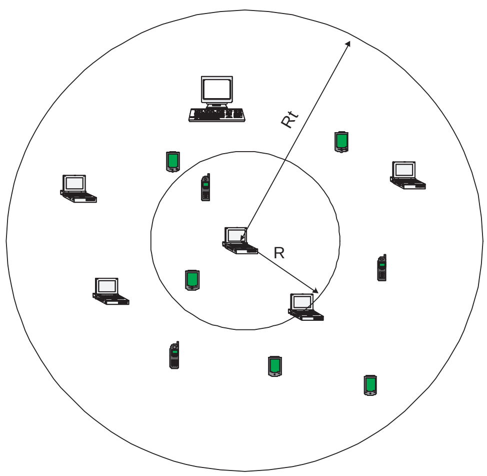

Fig. 1. Circular network topology .

A. Expected Progress per Hop

The expected progress per hop is a measurement of the network throughput, and it is defined as the product of one-hop throughput by the distance between the transmitter node and the receiver node (bit-meters per bit period). This performance measure increases with the probability of packet success (P_s) and decreases as the number of hops increases. Therefore, the expect progress per slot is [3]:

$$Z = \xi R \tag{11}$$

where ξ is the one-hop throughput of the transmitter node. The one-hop throughput is the rate at which a node successfully transmits packets:

$$\xi = (1 - p)(1 - e^{-p})\, P_s \tag{12}$$

where $(1 - p)(1 - e^{-p})$ is defined as the tendency to pair up (per node). The tendency to pair up can be viewed as a tendency to a given transmitter node to establish a connection with the interest node.

In this work, it was assumed that a network has uniform traffic and a balanced routing. Hence, all nodes have the same one-hop throughput.

IV. Simulation Results

The achievable expected progress per slot performance of an QS-CDMA ad hoc system, using ZCZ spreading sequences, is obtained by Monte Carlo simulation. The network has N_t = 34 nodes deployed on a circular area of radius R_t = 100 m and the transmission range worths $R = 30$ m . The path loss exponent β is assumed equal to 4. The signal-to-noise ratio is set to 10 dB and the number of resolvable paths is $L = 3$.

The simulator was built in accordance with the proposed model. The nodes were located in a circular area, uniformly distributed and no kind of power control was employed, remaining to the ZCZ codes to outdo the near far effect and to mitigate the interferences. The multipath fading channel was characterized by a Rayleigh distribution, the relative delay of the lth path is estimated with respect to the main path and the uniformly distributed phase-shift of each resolvable path, for each node, was perfectly compensated. The quasi-synchronous scenario was performed so that the maximum delay difference τ between the signals of different nodes does not exceed a predefined value.

Fig. 2 and 3 portray, respectively, the bit error rate (BER) and the expected progress per hop (EPH). The performance are evaluated using random spreading sequences and the ZCZ codes, both with processing gain $G_p = 64$. The random sequences are used in others QS-CDMA ad hoc network, therefore they were chosen for comparisons with the ZCZ sequences. All users are assumed to communicate in a quasi-synchronous manner, and the maximum delay difference τ is assumed to be $2T_c$.

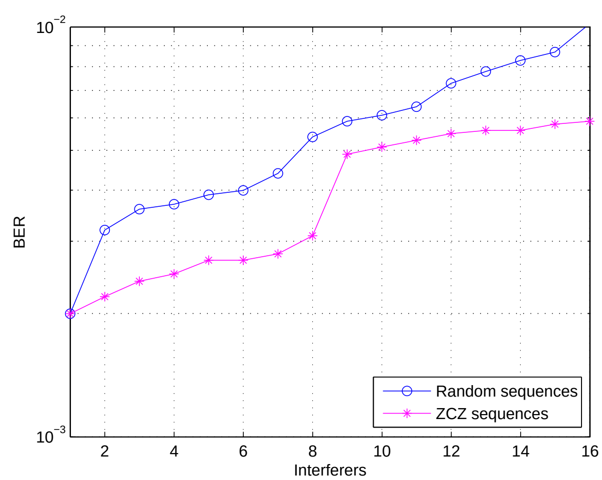

Fig. 2. BER versus interferers

For both figures, the ZCZ sequences belong to two mutually orthogonal sequence sets. This procedure enlarges the number of available sequences. However, a larger number of sequences does not assert the correlation properties among sequences of different sets for nonzero shifts. When the $(M + 1)$th user, where M is the size of one set, is activated there is a degradation in performance of ZCZ-coded-based system because the sequence associated to this user belongs to the second group and the zero-correlation characteristics are not maintained for all shifts among all sequences of the two groups. For the ZCZ set used, $M = 4$.

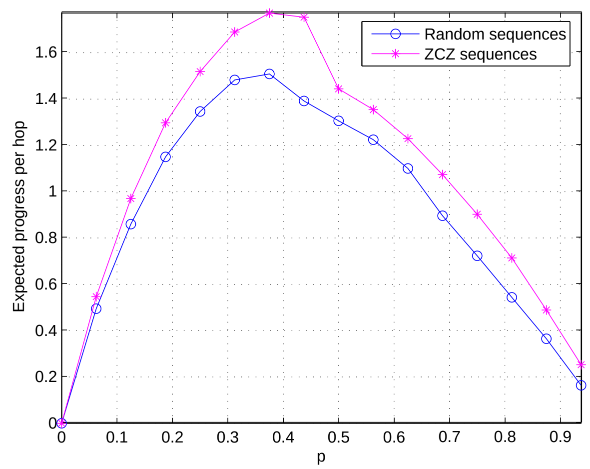

Fig. 3. EPH versus p

A certain imprecision is allowed to the synchronization process, as it is observed in a QS-system, and it turns easier the management of the signals from different nodes and paths. The influence of this rough synchronization can be observed in Fig. 4, where the BER was evaluated parameterized by τ. As long as the time shift signals are within the IFW, the system is not affected by the raise of τ. As the channel becomes more dispersive, the system performance degrades because the correlation values outside the interference free zone are high, even higher than those obtained with random codes.

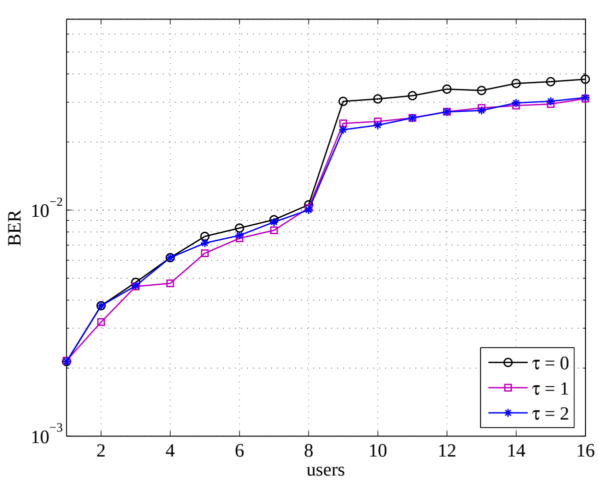

Fig. 4. BER versus interferers, parameterized by τ

V. Conclusion

In conclusion, in this work was employed a scheme of ZCZ spread sequence in a QS-CDMA ad hoc network and the simulation results showed that the ZCZ sequences exhibit better performance than random sequences in the hostil environment of the ad hoc networks. It follows from interference reduction due to the zero correlation zones existence.

References

[1] R. Ramanathan and J. Redi, "A Brief Overview of Ad Hoc Networks: Challenges and Directions", IEEE Communications Magazine, Vol. 40, pp. 20-22, 2002.

[2] A. Muqattash and M. Krunz, "CDMA-Based MAC protocol for wireless ad hoc networks" , *Proceedings of the International Symposium on Mobile Ad Hoc Network and Computing (MOBIHOC'03)*, pp. 153-154, June 2003.

[3] E. S. Sousa and J. A. Silvester, "Optimum Transmission Ranges in a Direct-Sequence Spread-Spectrum Multihop Packet Radio Network", *IEEE Journal on Sel. Areas in Communications*, v. 8, n. 5, pp. 762-771, June 1990.

[4] M. Zorzi and S. Pupolin, "Optimum transmission ranges in multihop packet radio networks in the presence of fading", *IEEE Transactions on Communications*, Vol. 43, No. 7, pp. 2201-2205, July 1995.

[5] M. Souryal, B. Vojcic and R. Pickholtz, "Ad Hoc, Multihop CDMA Networks with Route Diversity in a Rayleigh Fading Channel", *DC Washington - Proc. IEEE MILCOM*, pp. 1003-1007, 2001.

[6] Y. Sanada, M. Nakagawa, "Power control techniques in a multihop CDMA packet radio network", textitIEEE 4th International Symposium on Spread Spectrum Techniques and Applications Proceedings, Vol. 3, pp. 1162-1166, September 1996.

[7] X. Liu, H. Wei and L. Hanzo "Analytical bit error rate performance of DS-CDMA ad hoc networks using large area synchronous spreading sequences" , *Proceedings of the International Symposium on Mobile Ad Hoc Network and Computing (MOBIHOC'03)*, pp. 153-154, June 2003.

[8] L. R. Welch, "Lower bounds on the maximum cross correlation of signals", *IEEE Trans. on Information Theory*, vol. 20, 3, May 1974, pp. 397-399.

[9] Byoung-Jo Choi and L. Hanzo, "On the Design of LAS Spreading Codes", *IEEE VTC 2002 Fall Conf.*, Vancouver, Canada, Sept 2002, pp. 2172-2176

[10] Rathinakumar,A., and Chaturvedi,A.K., "Mutually orthogonal sets of ZCZ sequences", *Electron. Lett.*, 2004, 40, no.18

[11] Z. Ni, and D. Li, "Uplink spectral of multiuser distributed MIMO-CDMA systems using loosely synchronised spreading codes", *Proceedings of the IEEE Radio and Wireless Conference*, Sept. 2004, pp.271-274

[12] Deng, X., Fan, P.Z., "Spreading sequence sets with zero correaltion zone", *Electron. Lett.*, 2000, 36, no.11, pp.993-994

[13] Fan, P.Z. "Spreading sequence desing and theoretical limits for quasisynchronous CDMA systems", *EURASIP Journal on Wireless and Networking*, 2004:1, pp.19-31

[14] P. Z. Fan, *et al*., "Class of binary sequences with zero correlation zone", *Electron. Lett.*, 1999, 35, no.10, pp.777-778

[15] H. Wei, L. Yang, and L. Hanzo, "Time- and frequency-domain spreading assisted MC DS-CDMA using interference rejection spreading codes for quasi-synchronous communications", , 2004, pp.389-393

[16] J. G. Proakis, *Digital Communications*, McGraw-Hill, 4th. Ed., 2001.

A Pre-Rake CDMA System with Modified ZCD Spreading Code

Incheol Jeong
Dept. of Computer and Communication – Sungkonghoe University
152-716 Seoul - Korea
jeong@skhu.ac.kr

Jaesang Cha
Dept. of Media Engineering - Seoul National University of Technology
139-746 Seoul - Korea
chajs@snut.ac.kr

Mungeon Kyeong
Mobile Telecommunication Division - ETRI
139-746 Daejeon - Korea
mgk@etri.re.kr

Abstract—**In general, Pre-Rake diversity technique provides simple receiver structure and sufficient diversity effect for mobile terminals. However, conventional Pre-Rake systems are more severely affected than Rake systems with regard to multiple access interference since the number of multipaths received at the mobile unit is nearly twice that of the Rake systems. In order to overcome the problem, a Pre-Rake CDMA system using zero correlation duration (ZCD) spreading code is proposed. Modified ZCD codes including guard interval (GI) is also proposed and the performance is evaluated by computer simulation.**

Index Terms— **Pre-Rake, ZCD code, CDMA**

I. INTRODUCTION

In Pre-Rake systems, the path diversity effect is achieved with a simple receiver employing just one Rake finger at the mobile unit [1], [6], [7]. However, the Pre-Rake combiner creates a larger number of paths towards the mobile unit so that more severe multiple access interference (MAI) and multipath interference (MPI) occur at the mobile unit receiver. In [1], it is found that the interference increases and the BER performance degrades as the number of paths and the number of users increases. In the case of L-path environment, the Pre-Rake transmits L path signals created by the Pre-Rake combiner to the mobile unit. The transmitted Pre-Rake signals are convolved by channel impulse response and $2L-1$ paths are then received at the mobile unit. In the CDMA system using the Rake combiner, L path signals are received at the mobile unit so that the number of paths received in the Pre-Rake system becomes nearly twice that of the Rake system. Therefore, the Pre-Rake systems are affected by the interference caused by an increased number of paths, and so the resulting BER performance becomes worse than that of the Rake system. To avoid this interference, efficient interference mitigation techniques such as multiuser detection (MUD) schemes should be adopted at the mobile receiver. However, it is not desirable to use such a complicated MUD technique in the Pre-Rake systems.

II. PRE-RAKE CDMA WITH ZCD CODE

To resolve the above problem, a Pre-Rake CDMA based on a continuously orthogonal spreading code is proposed. In Fig. 1, the transmitter and receiver structure is shown for the proposed Pre-Rake CDMA systems with zero correlation duration (ZCD) spreading code [2],[3] where ZCD is utilized as a continuously orthogonal spreading code. The modulated Input signals are normalized to keep the transmit power constant and spread with the ZCD code. BPSK is assumed for the modulation, but various modulation schemes can be used as a modulation method. As for the continuously orthogonal spreading code, different types of codes shown in [2]-[5] can be utilized for spreading. In this paper, ZCD code is employed, where there are two types of ZCD codes such as the binary ZCD code [2] and the ternary ZCD code [3]. These two codes can be used for the proposed system as a spreading code. After the spreading process, the spread signal is fed to the Pre-Rake combiner and then finally transmitted to the mobile unit.

III. TWO-PATH CASE

In Fig. 2, the concept of the Pre-Rake combining process for

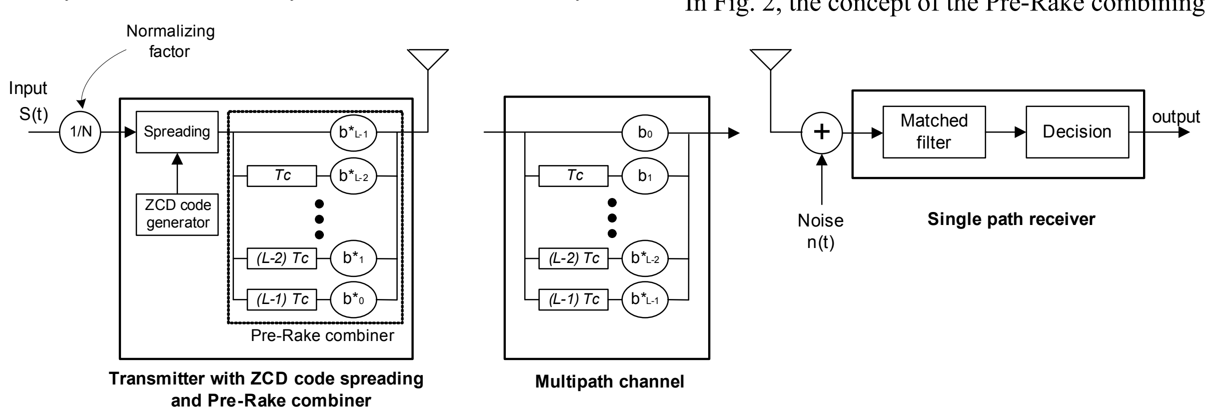

Fig. 1 Proposed Pre-Rake CDMA transmitter and receiver structure

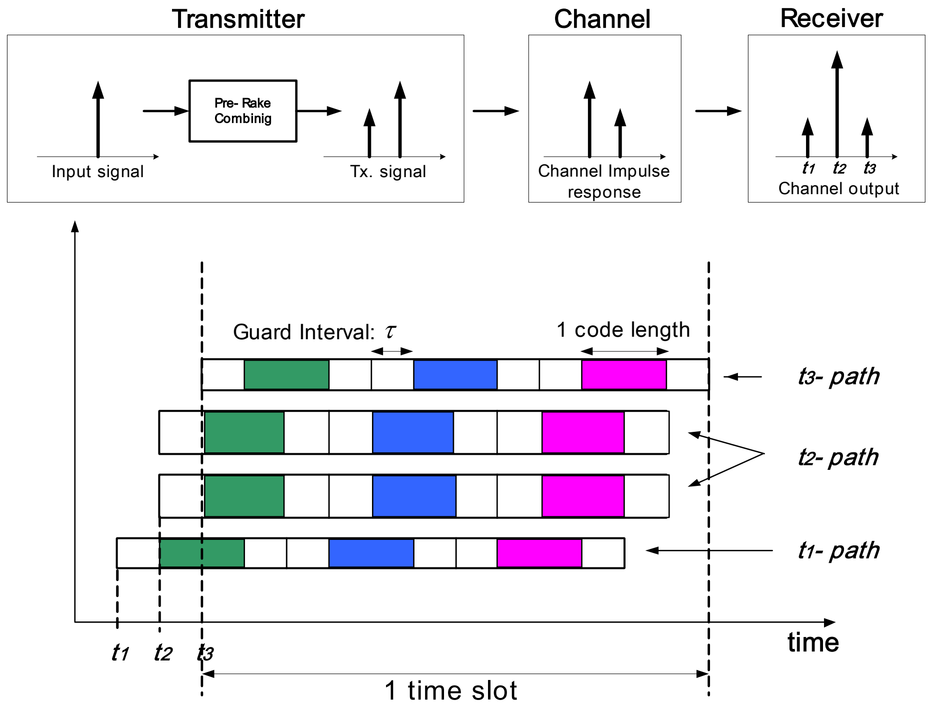

Fig. 2. Concept of Pre-Rake combining process and the received signal exemplification for the proposed system

the proposed system is depicted together with the received signals for the case of 2-path environment. In the base station (BS), the input signal is combined by a Pre-Rake combiner, and then the combined signal with 2 paths is transmitted to the intended mobile unit. At the mobile unit, the channel output with 3 paths is received after passing through the multipath channel. The mobile unit tunes a matched filter (MF) to t_2-path signal which corresponds to the $(L\text{-}1)_{th}$ path among the channel output and detects the transmitted signal. On the other hand, guard interval (GI) τ is needed for the proposed system to maintain the orthogonality between the spreading codes. The GI should be added at the head and the back of the spread signal, and the relation of $\tau \geq (L\text{-}1)T_c$ should be satisfied to avoid the interferences. From the above process, modified ZCD code with 2 GI is generated.

As shown in Fig. 2, the channel output which consists of a t_1-path signal, two t_2-path signals, and a t_3-path signal is received at the mobile unit. Among them the t_2-path signals are tuned and detected by the MF. If the orthogonal code such as Walsh-Hadamard code is used for spreading, the orthogonality is not maintained any longer due to the increased multipath interferences. In the proposed system, sufficient GI is added for the spread signal and ZCD code is used for spreading so that the MF gives out a desired signal without generating any interference signals. Due to the characteristic of ZCD code that the zero correlation duration exists before and behind t_2, all the channel output signals which are the convolution result of Pre-Rake combined signals and channel impulse responses are included in the zero correlation duration. Therefore, the proposed system is not affected by either MAI or MPI, and achieves the path diversity effect leading to the interference-free communication system even after the number of paths increases due to the Pre-Rake combining process.

IV. System Performance

A. Channel model

The complex low-path impulse response of the channel for user k is given by

$$h_k(t) = \sum_{l=0}^{L-1} \beta_{k,l} \exp(j\gamma_{k,l})\delta(t - lT_c) \tag{1}$$

where L is the number of channel paths, the path gain $\beta_{k,l}$ are independent identically distributed (i.i.d.) Rayleigh random variables (r. v.'s) for all k and l, the angles $j\gamma_{k,l}$ are i.i.d. uniformly distributed in $[0,2\pi)$, and T_c is the spreading code chip duration. In a TDD system under slow fading conditions we assume that $h_k(t)$ does not change during two successive up and down link time slots.

B. Pre-Rake CDMA

Without channel estimation error, the downlink transmitted signal for user k with BPSK modulation can be represented by

$$s(t) = \sqrt{\frac{2p}{U_k}} \sum_{l=0}^{L-1} \beta_{k,L-l-1} b_k(t - lT_c) a_k(t - lT_c) \cdot \exp\left[j\omega(t - lT_c) - \gamma_{k,L-l-1}\right] \tag{2}$$

where P is the transmitted power, ω is the carrier frequency, $b_k(t)$ is the differentially encodes data stream for user k consisting of a train of i.i.d. data bits with duration T which take the value of ± 1 with equal probability. The current bit is denoted by b_k^0 while next or previous bits are denoted by adding or subtracting the superscripts by 1. $a_k(t)$ is the ZCD spreading code of user k with chip duration T_c and code length $N = T/T_c$.

In the proposed system, it is assumed that the number of multipaths, L does not exceed $L_{ZCD} = \frac{ZCD+1}{2}$. The ZCD is defined by ZCD = $2\Delta - 1$ where Δ is a chip-shift increment [2].

The normalizing factor U_k that keeps the instantaneous transmitted power constant is given by

$$U_k(t) = \sum_{n=0}^{L-1} \beta_{k,n} \tag{3}$$

Assuming a CDMA system with K users, the received signal at user1 in downlink is given by

$$r_1(t) = \mathrm{Re} \sum_{k=1}^{K} \sum_{j=0}^{L-1} s_k(t - jT_c)\beta_{1,j} \exp[j\gamma_{1,j}] + n(t) \tag{4}$$

where n(t) is the zero mean AWGN with two sided power spectral density $N_0/2$. From Eq.(4), we can see that channel output includes 2L-1 paths with a strong peak when $J + l = L - 1$ and just one MF is needed to synchronize to this path.

The output of user1 MF is given by

$$\begin{aligned} Z &= \int_{(L-1)T_c}^{(L-1)T_c+T} r_1(t) a_1(t)[t-(L-1)T_c] \cdot \cos[\omega t - \omega T_c (L-1)]dt \\ &= D + S + A + \eta \end{aligned} \tag{5}$$

where S is the self interference due to multipath, A is the multiple access interference, and η is a zero mean Gaussian r.v with variance $N_0 T/4$. D is the desired part for the current bit given by the $k = 1$ part of $r_1(t)$ and $j + l = L - 1$ in Eq.(5).

After some manipulation, D is given by

$$D = \sqrt{\frac{P}{2}} b_1^0 T \sqrt{U_1} \, . \tag{6}$$

C. Self interference

This interference exists in a single user system and is caused by the multipath. From Eq.(2) and Eq.(4), S is found by putting k=1 and $j + l \neq L - 1$. S can be written by

$$\begin{aligned} S = \sqrt{\frac{P}{2U_1}} \sum_{j=0}^{L-1} \sum_{m=0,\neq j}^{L-1} \beta_{1,j}\beta_{1,m} \cos[\omega T_c (j-m) + \gamma_{1,m} - \gamma_{1,j}] \\ \cdot \int_0^T b_1[t-(j-m)T_c] a_1[t-(j-m)T_c] a_1(t) dt \end{aligned} \tag{7}$$

where

$$\begin{aligned} &\int_0^T b_1[t-(j-m)T_c] a_1[t-(j-m)T_c] a_1(t) dt \\ &= \begin{cases} T_c [b_k^{-1} C_{k,1}(N-m+j) + b_k^0 C_{k,1}(j-m)], & (j-m) \geq 0 \\ T_c [b_k^0 C_{k,1}(j-m)) + b_k^{+1} C_{k,1}(N-m+j)], & (j-m) < 0 \end{cases} \end{aligned} \tag{8}$$

In Eq.(8), $C_{k,1}$ is the discrete aperiodic cross-correlation function. Denoting $C_{1,1}(j-m)$ by $C_1(j-m)$ and utilizing $C_1(j-m) = C_1(m-j)$, we can get

$$\begin{aligned} S = T_c \sqrt{\frac{P}{2U_1}} \sum_{j=0}^{L-2} \sum_{m=j+1}^{L-1} \beta_{1,j}\beta_{1,m} \cos[\omega T_c (j-m) + \gamma_{1,m} - \gamma_{1,j}] \\ \cdot [b_1^{-1} C_1(N-m+j) + b_1^{+1} C_1(N-m-j) + b_1^0 C_1(m-j)] \end{aligned} \tag{9}$$

Taking the second moment of Eq.(9) we can get

$$E[S^2 \mid \beta_{1,l}] = \frac{PT_c^2}{2U_1} \sum_{j=0}^{L-2} \sum_{m=j+1}^{L-1} \beta_{1,j}^2 \beta_{1,m}^2 \cdot E[C_1^2(N-m+j) + 2C_1^2(m-j)] \cdot \tag{10}$$

D. Multiple Access interference

The multiple access interference A is due to other users is found by the $k > 1$ part of $r_1(t)$ in Eq.(5). The interference is given by

$$\begin{aligned} A = \sqrt{\frac{P}{2}} \sum_{k=2}^{K} \sum_{j=0}^{L-1} \sum_{m=0}^{L-1} \frac{\beta_{1,j}\beta_{k,m}}{\sqrt{U_k}} \cos[\omega T_c (j-m) + \gamma_{k,m} - \gamma_{1,j}] \\ \int_0^T b_k[t-(j-m)T_c] a_k[t-(j-m)T_c] a_1(t) dt \end{aligned} \tag{11}$$

For orthogonal codes, Eq.(11) can be written as

$$\begin{aligned} A = \sqrt{\frac{P}{2}} \sum_{k=2}^{K} \sum_{j=0}^{L-2} \sum_{m=j+1}^{L-1} \frac{T_c}{\sqrt{U_k}} \\ \cdot \{ \beta_{1,j}\beta_{k,m} \cos[\omega T_c (j-m) + \gamma_{k,m} - \gamma_{1,j}] \\ \cdot [b_k^0 C_{k,1}(j-m) + b_k^{+1} C_{k,1}(N+j-m)] \\ + \beta_{1,m}\beta_{k,j} \cos[\omega T_c (m-j) + \gamma_{k,j} - \gamma_{1,m}] \\ \cdot [b_k^{-1} C_{k,1}(m-j-N) + b_k^0 C_{k,1}(m-j)] \} \end{aligned} \tag{12}$$

The second moment of Eq.(12) is given by

$$\begin{aligned} E[A^2 \mid \beta_{1,l}] = \frac{PT_c^2 Q}{4} \sum_{k=2}^{K} \{ \\ + \sum_{j=0}^{L-2} \sum_{m=j+1}^{L-1} \beta_{1,j}^2 E[C_{k,1}^2(j-m) + C_{k,1}^2(N+j-m)] \\ + \sum_{j=0}^{L-2} \sum_{m=j+1}^{L-1} \beta_{1,m}^2 E[C_{k,1}^2(m-j-N) + C_{k,1}^2(m-j)] \} \end{aligned} \tag{13}$$

where Q is given for all k by

$$Q = Q_{k,j} = E\left[\frac{\beta_{k,j}{}^2}{U_k}\right] = \frac{1}{L}, \qquad j = 0,1,\ldots,L-1 \tag{14}$$

E. SINR

In the conventional Pre-Rake CDMA system, MAI and MPI exist in the received signal. The variance of the interference components are given by Eq.(10) and Eq.(13) where the expected values for the correlation functions are given by Eq.(15), which determines the performance of the Pre-Rake CDMA system.

$$\begin{aligned} &E[C_i^2(m)] = N - |m|, \qquad for\ m \neq 0 \\ &E[C_{k,j}^2(m)] = N - |m| \\ &E[C_{k,i}(m) C_{k,i}(n)] = 0, \qquad for\ m \neq n, k \neq i \end{aligned} \tag{15}$$

On the other hand in the proposed system, ZCD code with 2 GI is utilized for spreading code so that the expected value of Eq.(15) , can be written as follows,

$$\begin{aligned} &E[C_i^2(m)] = 0 \qquad \text{for } m \neq 0 \\ &E[C_{k,j}^2(m)] = 0 \\ &E[C_{k,i}(m)C_{k,i}(n)] = 0 \quad \text{for } m \neq n, k \neq i \end{aligned} \qquad (16)$$

In the proposed system, it is assumed that $L \leq L_{ZCD}$ so that the channel output with 2L-1 paths does not exceed ZCD. This results in zero correlation among different multipath CDMA signals. Applying Eq.(16) to Eq.(10) and Eq.(13), the interferences (MPI and MAI) of the proposed system becomes zero and the signal to interference and noise ratio (SINR) Y can be given by

$$Y = \left[\frac{L}{\overline{\gamma_b} U_1} \right]^{-1} \qquad (17)$$

where $\overline{\gamma_b}$ is the average received signal to noise ratio. Y can be obtained by $Y = \dfrac{D^2}{2\,\mathrm{var}(Z)}$ where $\mathrm{var}(Z)$ is the variance of the Gaussian r.v. Z in Eq.(5). Therefore, the probability of error conditioned on $\{\beta_{1,n},\ n = 0,1,2,\cdots,L-1\}$ is given by

$$P(e \mid \beta_{1,n}) = \frac{1}{2}\mathrm{erfc}(Y) \qquad (18)$$

V. SIMULATION RESULTS

Computer simulations have been carried out to evaluate the proposed system performance by using C program. Simulation parameters are shown in Table I. TDD is utilized as a duplex method and 1 time slot has 0.667ms long. In this paper, the binary ZCD code with 32 chips (spreading factor=32) whose family size is 6 and zero correlation duration is 5 [2], is employed.

TABLE I
SIMULATION PARAMETERS

Wirelss Access Scheme	CDMA/TDD
Time slot length	0.667ms
Spreading code	ZCD binary code ZCD ternary code (Spreading Factor=32),
Transmit chip rate	3.84 Mcps
Transmit data rate	120 kbps
Uplink channel estimation	Perfect
No. of paths	3 Rayleigh fading (1 chip delay, equal path gain)
Modulation	BPSK
Max. Doppler frequency	32Hz
Channel coding/decoding	Uncoded

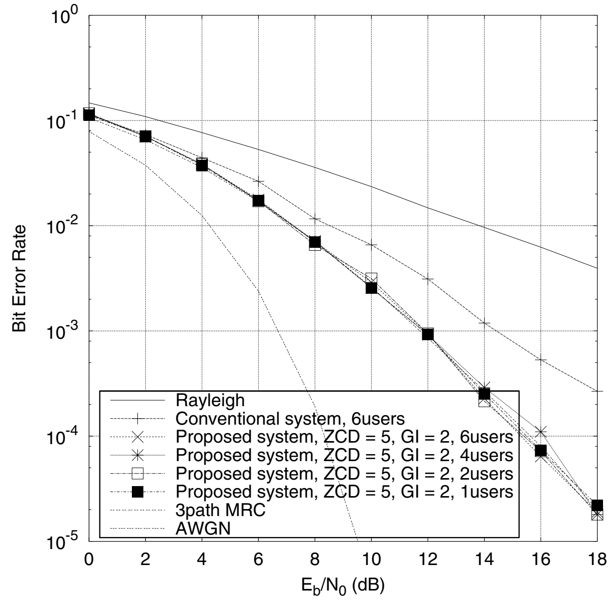

Fig. 3 BER performance of the proposed system with binary ZCD code for 3-path environment

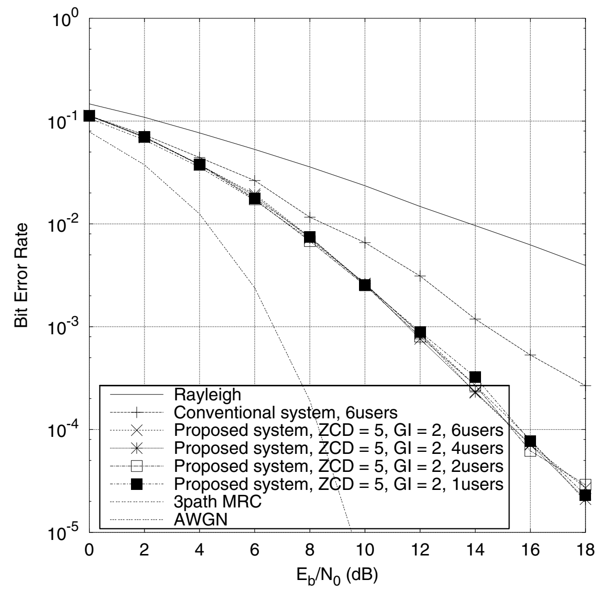

Fig. 4 BER performance of the proposed system with ternary ZCD code for 3-path environment

Fig. 3 shows the BER performance of the proposed Pre-Rake CDMA with binary ZCD codes under the condition of 3 paths. We also performed computer simulation for the proposed system with ternary ZCD code with 32 chips whose family size is 8 and zero correlate duration is 5. The simulation result is depicted in Figure 4.

In contrast with the conventional Pre-Rake system, the BER performance of the proposed system does not degrade for any number of users (≤ 6) and is almost same as with the MRC (Maximal Ratio Combining) diversity combining. This implies that the proposed system is not subject to the MAI and MPI, i.e., interference-free, due to the inherent continuous orthogonal property of the ZCD spreading code employed.

Even though the interferences can be removed perfectly by inserting the sufficient GI, the increased GI deteriorates the

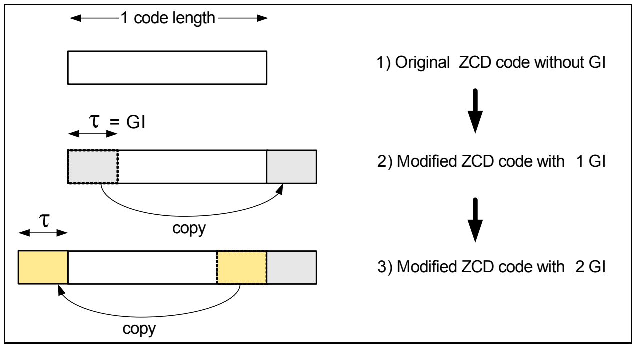

Fig. 5 GI adding process and modified ZCD codes

efficiency of frequency use. Therefore, we consider three ZCD codes (original ZCD code, modified ZCD code with 1 GI, and modified ZCD code with 2 GI) shown in figure 5. As being expected the correlation is no longer zero for the original ZCD code and the modified ZCD code with 1 GI since the ZCD codes are corrupted by adjacent codes containing different data bit.

Fig. 6 shows the performance for binary ZCD code under the condition of 3 paths. In lower E_b / N_0 the BER performance of the modified ZCD code with 2 GI is slightly worse than that of the original ZCD code. With GI the modified code length is longer than the original code one which results in the power loss and the degradation of the BER performance. However, in higher E_b / N_0 there is no difference of performance between two codes.

Fig.7 shows the performance of ternary ZCD code under the condition of 4 paths. The same ZCD code (ZCD = 5) shown in Fig. 5 is employed so that the channel output exceeds the ZCD ($L > L_{ZCD}$), which results in MIP and MUI. From the figure we can see that the relative performances of ZCD code without GI and with 2 GI have a crossing point around 15 dB.

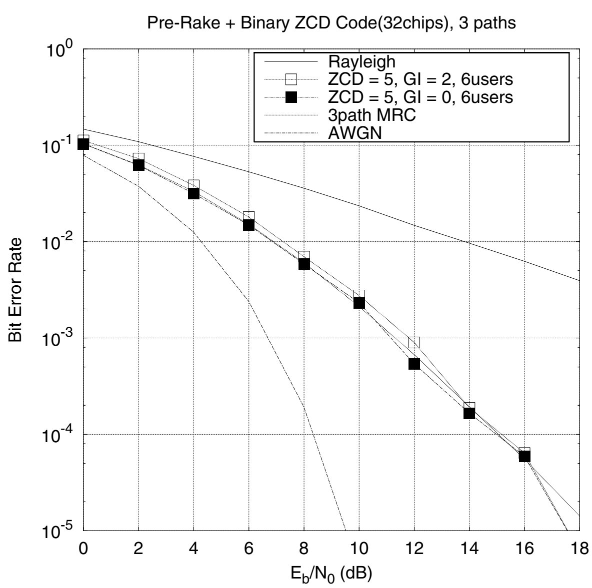

Fig. 6 BER performance of the proposed system with binary ZCD code for 3-path environment

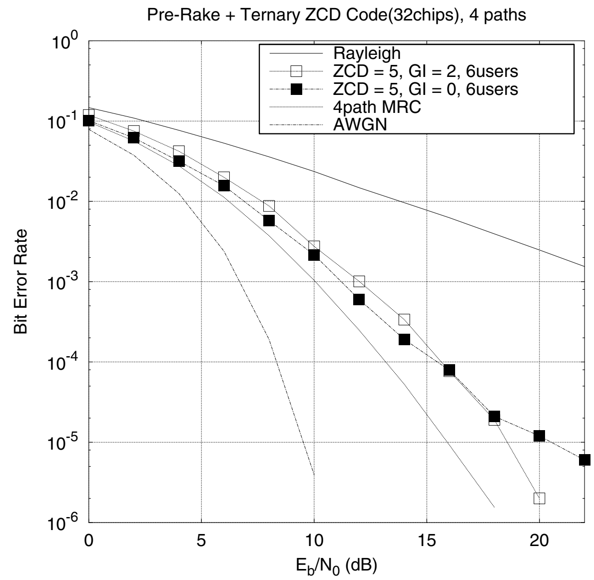

Fig. 7 BER performance of the proposed system with ternary ZCD code for 4-path environment

VI. Conclusion

A Pre-Rake CDMA system with ZCD spreading code has been proposed to overcome the problem of the conventional Pre-Rake system severely affected by its increased multipath interference. From the simulation results, it is found that the BER performance of the proposed Pre-Rake CDMA system using binary/ternary ZCD spreading code with 32 chips does not degrade when up to 6 users are allowed to be simultaneously active in the network under 3-path environment and the proposed system perfectly achieves the MRC diversity effect without causing any other interference to other users in the given conditions. Modified ZCD codes have been proposed for the Pre-Rake system and the performances have been evaluated by computer simulation under the condition that the channel output exceeds ZCD. From the simulation result it is found that there is crossing point between the performances of the ZCD codes with GI and without GI.

References

[1] R. Esmailzadeh, E. Sourour, and M. Nakagawa, "Prerake diversity combining in time-division duplex CDMA mobile communications," *IEEE Trans. Veh. Technol.*, vol.48, no.3, pp. 795-801, May, 1999.

[2] J. Cha, S. Kameda, M. Yokoyama, H. Nakase, K. Masu, and K. Tsubouchi, "New binary sequences with zero-correlation duration for approximately synchronized CDMA," *Electron. Lett.*, vol.36, no.11, 2000.

[3] J. Cha, "Class of ternary spreading sequences with zero correlation duration," *Electron. Lett.*, vol.37, no.10, pp. 636–637, 2001.

[4] P. Fan, N. Suehiro, N. Kuroyanagi, and X. Deng, "Class of binary sequences with zero correlation zone," *Electron. Lett.*, vol.35, no.10, pp. 777–779, 1999.

[5] D. Wu, and P. Spasojevic, "Adaptive rate QS-*CDMA* UWB systems using ternary OVSF codes with a zero-correlation zone," Proc. IEEE WCNC 2006, Las Vegas, Vol. 2, pp. 1068-1073 April, 2006.

[6] X. Cheng and W. Zhu, "Transmit-antennas pre-/post-rake for impulse radio systems," *Electron. Lett.*, vol.42, no.1, pp. 636–637, Jan. 2006.

[7] I. Jeong, and M. Nakagawa, "A Novel transmission diversity system in TDD-CDMA," IEICE Trans. Commun. vol.E81-B, no.7, July 1998.

Performance Assessment of a Tactical Aircraft-to-Ground Datalink

Tiago Moraes do Amaral
Instituto Tecnológico de Aeronáutica
12228-900
São José dos Campos - SP - Brazil
tiagoma@yahoo.com.br

Tetsu Gunji
Instituto Tecnológico de Aeronáutica
12228-900
São José dos Campos - SP - Brazil
tgunji@uol.com.br

Marcelo da Silva Pinho
Instituto Tecnológico de Aeronáutica
12228-900
São José dos Campos - SP - Brazil
mpinho@ieee.org

***Abstract*—A tactical datalink for point-to-point aircraft-to-ground communication is proposed, based on the DVB-S2 standard with some adaptations. A DSSS (Direct Sequence Spread Spectrum) scheme is added to the system for protection against intentional jamming; several configurations of DS spreading and jamming are modeled and simulated. System performance in terms of BER (bit error rate) and PER (Packet Error Rate) is compared for channels with CW (Continuous Wave) tonal interference, band-limited interference and pulsed interference.**

***Index Terms*—Digital video broadcasting, jamming, spread spectrum.**

I. Introduction

Nowadays, tactical operational scenarios for defense aircraft require an efficient C4I2SR (Command, Control, Communications, Computer, Intelligence, Information, Surveillance and Reconnaissance) [1] system. One important C4I2SR subsystem is the datalink, which defines how ground stations and platforms communicate. Increasing needs for situational awareness in current systems demand that datalinks between aircraft and ground stations provide high transmission rates, while assuring increased security and reliability. Organizations such as NATO and the United States DoD had developed several closed military standards for these datalinks. In this paper, a datalink based on a current, publicly available civil communication standard is proposed.

The DVB-S2 (Digital Video Broadcasting - Satellite - Second Generation) standard [2] provides a flexible system for satellite applications. It is suitable for broadband applications such as video and can range from broadcast to point-to-point services. A wide range of spectral efficiencies is achieved by using different modulation modes (QPSK, 8PSK, 16APSK and 32APSK) and FEC (forward error coding) rates. The FEC is based on two concatenated block codes: an inner LDPC (low-density parity check) code and on outer BCH code, and allows system operation at about 1 dB from the Shannon limit under an AWGN (Additive White Gaussian Noise) channel. Depending on the modulation mode and application, code rate in a DVB-S2 system can range from 1/4 to 9/10 and use 16200 bit or 64800 bit codewords.

DVB-S2 includes a block bit interleaver for additional error protection. Bit interleaving techniques are recommended to counter burst effects and make bit errors statistically independent [3]. Block interleavers conceptually work by filling a matrix with a bitstream, column by column, and generating an output stream reading the matrix line by line. The DVB-S2 interleaver operates on full codewords (block size is the same as codeword size); the exact interleaving configuration depends on the modulation scheme, ranging from 5 columns with 32APSK to 1 column (no interleaving) with QPSK.

A. Spread-spectrum techniques

The DVB-S2 standard is not especially concerned with protection against intentional interference (jamming), which is a common requirement for tactical datalinks. For this purpose, the addition of a direct-sequence spread-spectrum technique is proposed.

DSSS systems employ PN (pseudo-noise) generators to shift the carrier phase at a chip rate R_c, higher than the symbol rate R_s. This makes the transmitted signal bandwidth increase by a factor L_c:

$$L_c = \frac{R_c}{R_s} \tag{1}$$

In practical systems, the bandwidth expansion factor L_c is an integer and can range from 10 to 100 or more [3]. At reception, a correlator uses the same PN sequences to recover the transmitted bits. In presence of narrow-band interference, only a small fraction (approximately $1/L_c$) of the interference power is expected to appear after the correlator; the advantage gained over the jammer is the processing gain L_c. If the PN sequences have random properties and the expansion factor L_c is sufficiently high, the interference components at reception can be modeled as a Gaussian random variable.

B. Packet error rate

For multimedia applications, packet error rate is an important system performance metric. It is directly dependent on the bit error rate. The expected PER, assuming that the bit errors are independently distributed, is

$$P_p = 1 - (1 - P_b)^N \tag{2}$$

where P_p is the expected PER, P_b is the BER and N is the packet length in bits. Simulation results in the following sections show that this assumption is generally not valid due to the burst nature of the received code bit errors caused by the channel. The block decoder can also make the decoded information bit errors dependent, since it can fail to correct the bit errors of a codeword if interference-to symbol energy ratio in the period is above a certain point.

II. System description

The proposed system uses the DVB-S2 elements for channel coding, symbol mapping and modulation and includes the necessary subsystems for DSSS.

Fig. 1 shows the system model's block diagram. The blocks used for BCH and LDPC codes and the baseband filter for pulse shaping (a square-root raised cosine filter) are the same as specified by the DVB-S2 standard. The model does not account for imperfections in the modulation and demodulation process and the synchronization elements that are necessary in real-world scenarios. The channel model is a baseband channel that can have arbitrary interference signals, such as tonal jamming, band-limited jamming and pulsed jamming. The jamming signals are the only imperfection simulated in the channel; more realistic scenarios would also include AWGN noise. However, since the E_s/N_0 ratio in this system is expected to be relatively low, effects of jamming will be dominant in the simulated conditions.

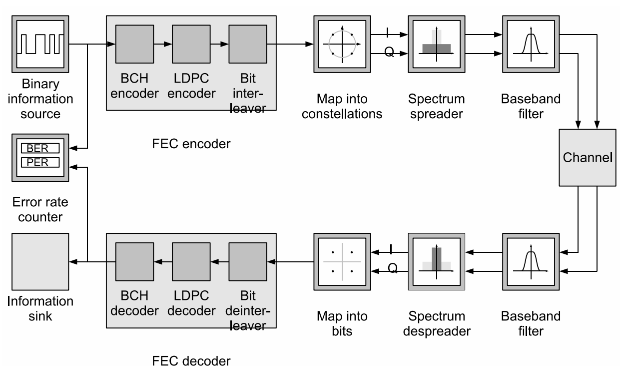

Fig. 1. System block diagram.

In order to simulate a channel with tonal jamming, a continuous wave (CW) with constant relative frequency Δf_J, constant amplitude and random phase (uniform distribution inside range $[-\pi; +\pi]$) is added to the transmitted signal. Band-limited jamming is generated using a Gaussian white noise generator and a low-pass filter that is spectrally flat inside the frequency range $\left[-\frac{W_1}{2}; +\frac{W_1}{2}\right]$ and null outside this range. W_1 is the bandwidth of the filtered jamming. The pulsed jamming model also uses a band-limited noise, like the previous case, but switches its amplitude between zero and full amplitude according to a repetition period T_J and a duty cycle α. The initial phase of the switched pulse is random (uniform distribution inside range $[0; T_J]$).

The signal-to-jamming ratio is defined as the average symbol energy-to-noise ratio E_s/N_J, comparable to the E_s/N_0 ratio commonly defined for AWGN channels. For a given

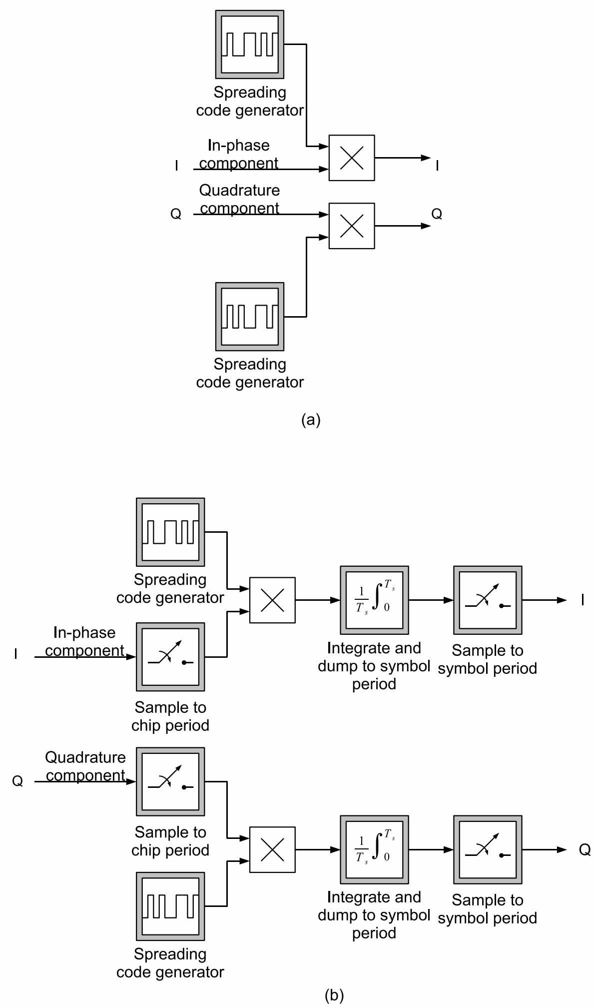

Fig. 2. Block diagrams of (a) spreading and (b) de-spreading subsystems.

jamming-to-signal power ratio J/S, it can be defined as [7]:

$$\frac{E_s}{N_J} = L_c \frac{S}{J} \quad (3)$$

where L_c is the bandwidth expansion factor. Pulsed or narrow-band jamming peak power must be accordingly set to yield the correct average symbol energy-to-noise ratio.

The DVB-S2 standard includes several modulation schemes, but only QPSK (quaternary phase shift keying) was simulated because its implementation is simpler and its performance is more robust than higher modulation schemes. Although the standard allows only certain combinations of FEC encoding and modulation schemes (e.g., there is no interleaving for QPSK), these could be freely configured in the model. The baseband filter used for pulse shaping was configured with a roll-off factor of $\alpha = 0.35$ for all simulations. Whenever used, the block bit interleaver had 4 columns. The blocks used for LDPC encoding and decoding were simulated using algorithms taken from [4]. Codewords at the reception are decoded using soft decision.

The DS (direct sequence) spreading and despreading blocks were modeled according to Fig. 2 and [5]. At transmission, each symbol component (in-phase and quadrature) is multiplied by a bipolar spreading code, with a chip rate higher than the symbol rate. At the reception, the match-filtered components are sampled at chip rate, multiplied by the original spreading codes and integrated at each symbol period before being fed to the symbol-to bits mapper. The two independent pseudo-random sequence generators use Gold sequences, which are commonly used spreading codes. The sequences have a repetition period of 65535 chips and are initialized with random states.

The error rate counter compares the transmitted and received information bits and computes the bit and packet error rates. For packet error rate calculation, 188-byte packets (MPEG packets) are sliced and merged according to the DVB-S2 standard. The error counter directly compares the received packets with transmitted packets, although real systems use CRC-8 computations to detect packet errors.

A. *Simulation parameters*

Table I summarizes the common parameters used throughout the simulations. Frequencies and bandwidths in table are normalized to the symbol rate, R_s, and pulsed jamming repetition periods are normalized to the symbol period T_s. Two different pulsed jamming cases were set, to test system performance against different repetition periods. With the short period of 1000 symbols, several jamming pulses can fall inside a same codeword, while a repetition period of 80000 symbols makes jamming pulses affect only some of the received codewords.

TABLE I

COMMON SIMULATION PARAMETERS.

Parameter	Symbol	Value
Modulation scheme		QPSK
Rolloff factor	β	0.35
Packet size (bytes)		188
FEC codeword size	n_{ldpc}	64800
Block interleaver columns		4
CW interf. relative frequency	$\Delta f_J/R_s$	0.09
Band-limited interference width	W_1/R_s	1
Pulsed interf. duty cycle	α	0.01
Pulsed interf. period (short)	T_J/T_s	1000
Pulsed interf. period (long)	T_J/T_s	80000
Spreading sequence type		Gold
Spreading seq. period (chips)	n_{gold}	65535
Bandwidth expansion factor	L_c	13

III. SIMULATION RESULTS

To assess the system's performance against intentional interference, several simulation scenarios were run, each with a combination of interference type, channel coding and spectrum spreading. The performance in terms of BER and PER, as a function of the signal-to-interference ratio E_s/J_0, was compared for three different interference cases: CW tonal jamming, band-limited jamming and band-limited pulsed jamming. For each interference case, four code rates were tested: 1/3, 2/3, 8/9 and without any coding (both LDPC and BCH codes removed). The presence of interleaving was another parameter that was switched between simulations. To evaluate the effects of DS spreading, the system was first simulated without spreading and then simulated with the spreading factor of $L_c = 13$.

A. *DVB-S2 system*

Fig. 3 to Fig. 7 show the results of system simulations without spectrum spreading. With CW tonal jamming (Fig. 3), it can be seen that the code rate of 8/9 did not bring any advantage in performance, compared to a system without channel coding. This is expected with this type of interference, since symbol decision errors are only possible if the interfering wave's amplitude is sufficiently high. At higher code rates, BER decline is mostly due to fewer symbol errors caused by jamming, while at lower code rates the effect of coding is dominant. The use of an interleaver did not bring any noticeable performance advantage under CW jamming.

System performance with band-limited jamming (Fig. 4) is close to the results expected with an AWGN channel, such as those from simulations in [2]. There is a small difference (an advantage of around 0.5 dB) because part of the jamming signal power is removed in the reception by the raised-cosine pulse shaping filter. There is no significant change in performance when an interleaver is used.

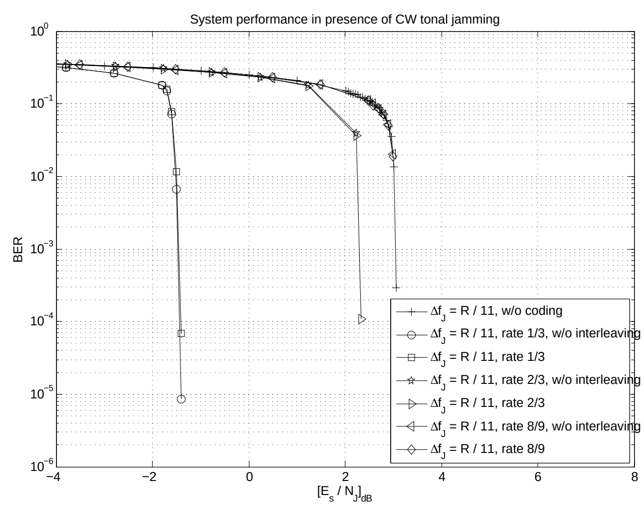

Fig. 3. BER performance with CW tonal jamming for several channel coding schemes.

Pulsed interference can degrade system performance more severely, as shown in Fig. 5, where an SJR (signal-to-jamming ratio) about 25 dB higher is necessary to achieve the same error rates of the two previous cases. The gain introduced by coding is lower than the gain expected in an AWGN channel; this can be explained by the burst characteristic of code bit errors. The DVB-S2 block interleaver is able only to interchange bit positions inside a same codeword, having limited ability to successfully decode a block if it is critically impacted. Jamming impairments vary with duty cycle and

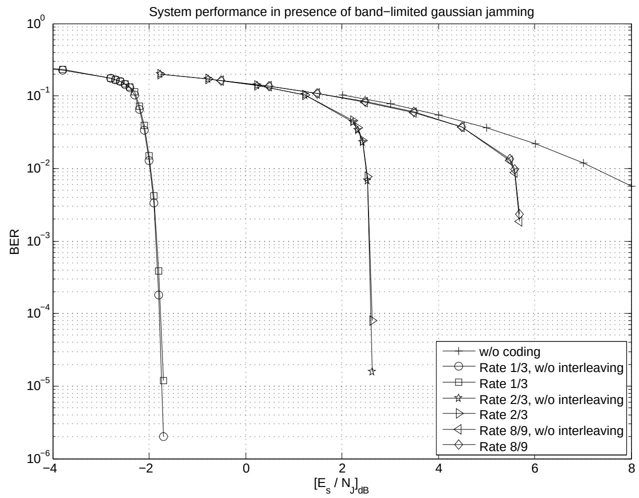

Fig. 4. BER performance with band-limited jamming for several channel coding schemes.

pulse period; longer interference pulses cause longer error bursts inside a codeword and lead to poorer performance. Bit error performance without channel coding, however, is independent of interference pulse duration.

The effect of error bursts on packet error rate performance is visible on Fig. 6 and Fig. 7, which show the measured PER and the PER that would be expected from the measured BER, according to Equation 2. There are differences between the expected and measured values, more noticeably with longer interference pulses. The first cause of this disagreement is the dependency between coded bit errors: some packets may be unaffected by errors if pulse period is sufficiently long. There is also the effect of the channel coding, which can make decoded bit errors more likely to appear concentrated in a same codeword.

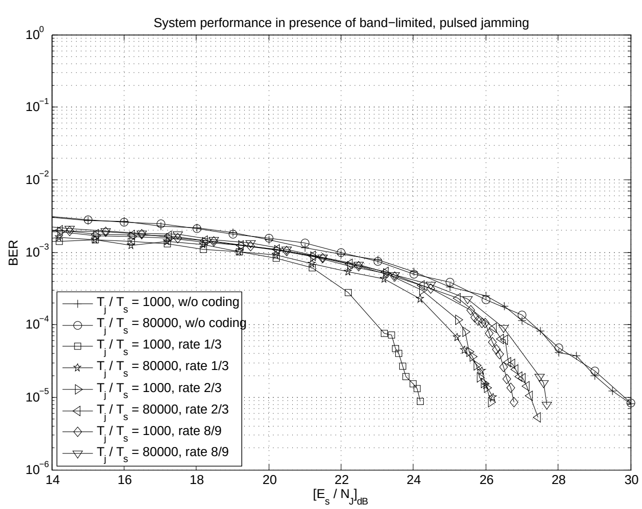

Fig. 5. BER performance with pulsed jamming for several channel coding schemes.

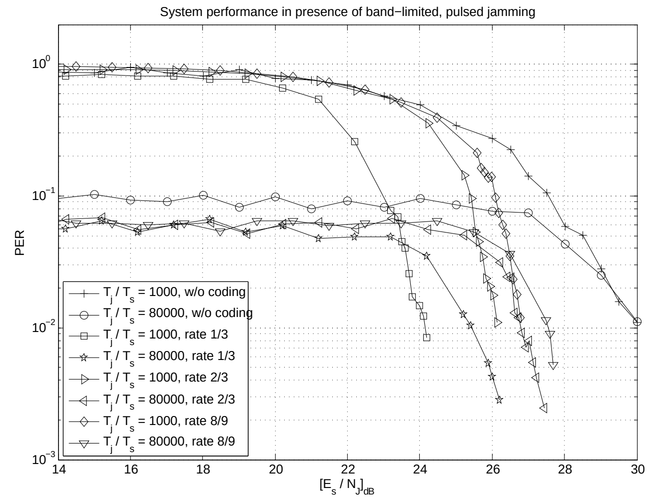

Fig. 6. PER performance with pulsed jamming for several channel coding schemes.

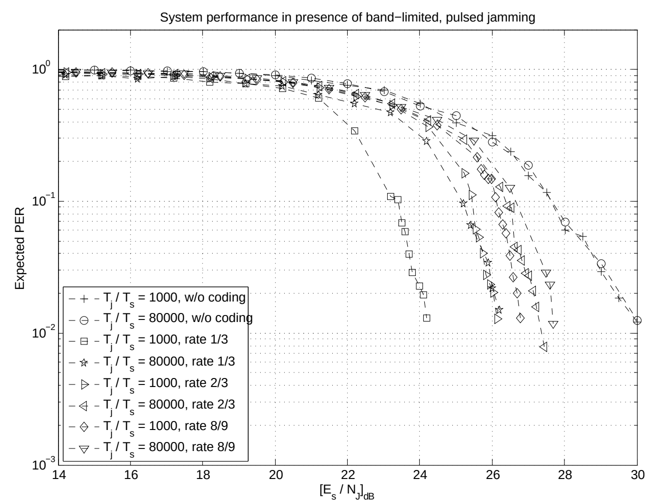

Fig. 7. Expected PER performance with pulsed jamming for several channel coding schemes.

B. DVB-S2 system with DSSS

System simulation results with DS spectrum spreading and jamming scenarios are plotted from Fig. 8 to Fig. 15. A gain of about 11 dB in the SJR, introduced by the spreading factor of $L_c = 13$, is expected from the results with respect to the same simulated scenarios without DSSS. Fig. 8 shows that the gain introduced by DSSS with CW jamming, at BER 10^{-3}, is approximately 11 dB for code rate 1/3, 10 dB for code rate 2/3 and 8 dB for code rate 8/9. With DSSS, an advantage can now be seen between the case with rate 8/9 and the case without coding. The explanation for this is that pseudo-random spreading sequences make symbol error distribution in the receptor more similar to a Gaussian distribution, while without DSSS the error distribution is limited, making symbol decision errors disappear above a critical point.

DSSS performance with band-limited jamming is close to the expected values, according to Fig. 9. The gain in SJR was about 11 dB for code rate 1/3, 10 dB for rate 2/3 and 9 dB for rate 8/9. Interleaving introduced small differences in performance, ranging from an advantage of about 0.1 dB with code rate 1/3 to a disadvantage of 0.1 dB with code rate 8/9.

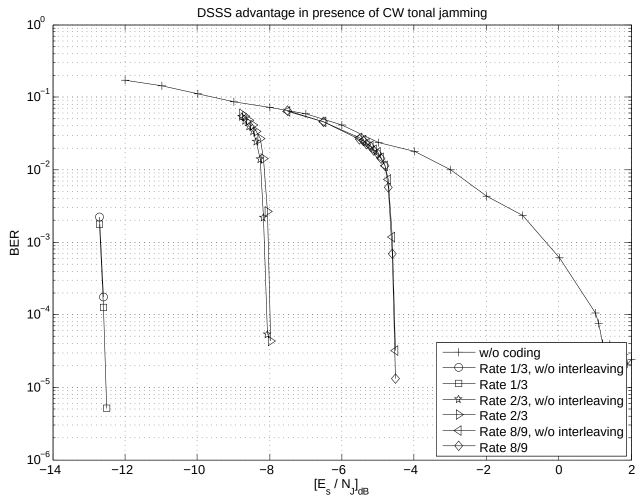

Fig. 8. BER performance with CW tonal jamming and DSSS.

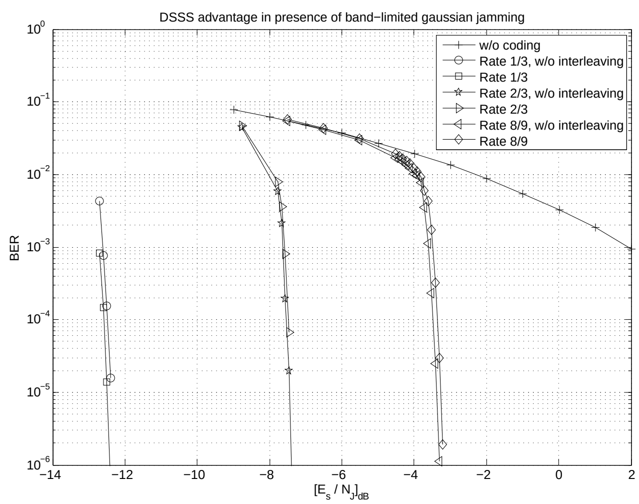

Fig. 9. BER performance with band-limited jamming and DSSS.

Fig. 10, Fig. 11 and Fig. 12 show simulation results of BER, PER and expected PER, respectively, for a system with DSSS and short-period pulsed jamming ($T_J/T_s = 1000$). The gain for a PER of 10^{-2} is nearly 10 dB for code rate 1/3 and 9 dB for code rates 2/3 and 8/9. With long-period pulsed jamming ($T_J/T_s = 80000$), according to Fig. 13, Fig. 14 and Fig. 15, the advantage in PER performance is of about 9 dB. As with the simulations without DSSS, there are differences between the measured and the estimated PER, more visibly with the longer jamming pulses. Bit interleaving effects vary from case to case. With short-pulse jamming and code rates of 1/3 and 2/3, there was a slight negative impact in performance when interleaving was on, while with long-pulse jamming the opposite effect is observed, with a gain of about 1 dB at code rate 1/3 and 0.5 dB at code rate 2/3.

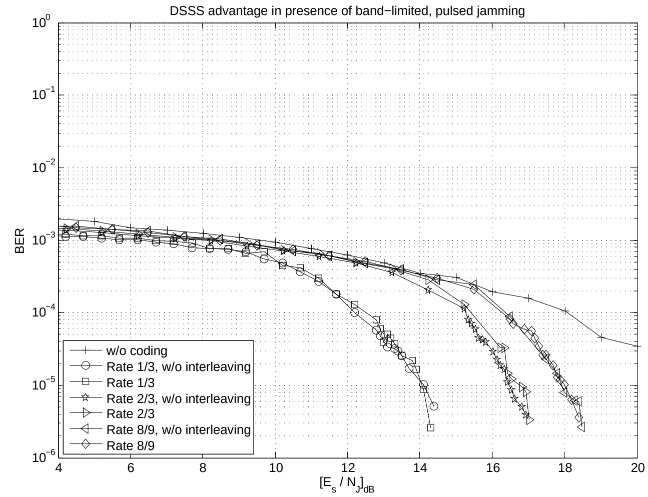

Fig. 10. BER performance with pulsed jamming (short period) and DSSS.

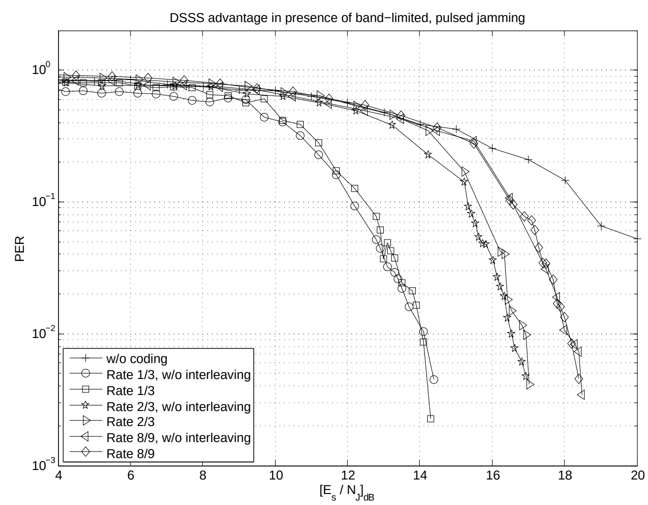

Fig. 11. PER performance with pulsed jamming (short period) and DSSS.

IV. Conclusions

In this paper, a system for an aircraft-to-ground tactical datalink is proposed, based on the DVB-S2 standard with additions for DS spectrum spreading. Simulation results demonstrate that the addition of DSSS can improve system performance against different jamming models, with observed gains in the signal-to-jamming ratio different by no more than 2 dB from the expected theoretical value. The DVB-S2 error correction schemes were also shown to improve performance against jamming.

Nevertheless, the severe performance impairments caused by pulsed interference need to be countered with robust FEC schemes. The interleaver selected for the simulations showed mixed results; other interleaving schemes besides the DVB-S2 block interleaver can be investigated. Future works may

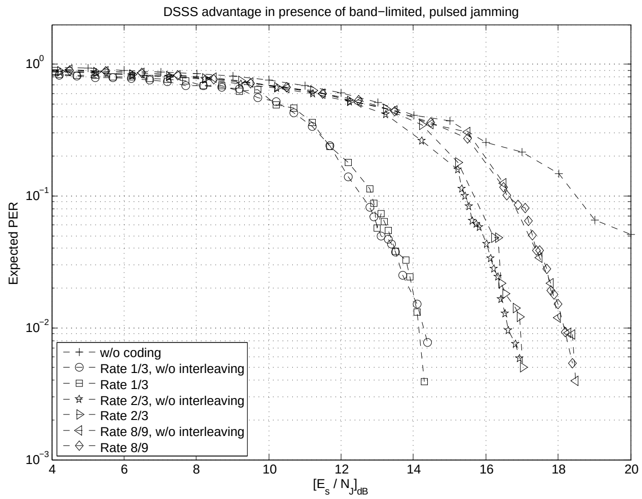

Fig. 12. Expected PER performance with pulsed jamming (short period) and DSSS.

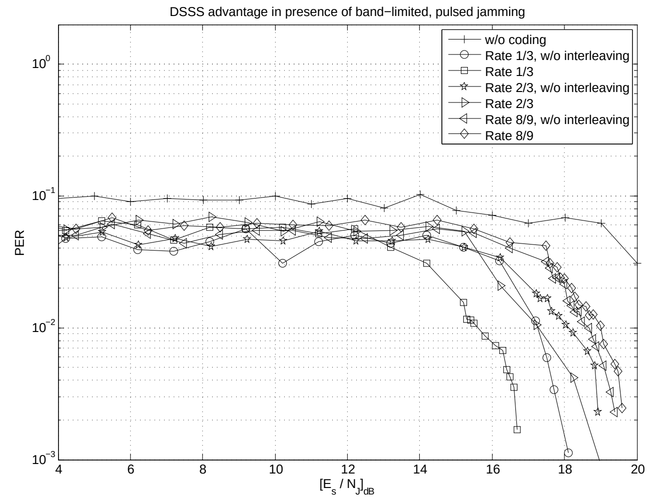

Fig. 14. PER performance with pulsed jamming (long period) and DSSS.

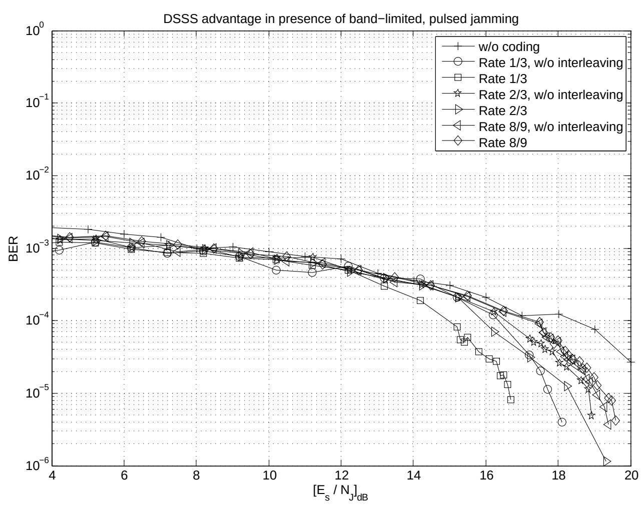

Fig. 13. BER performance with pulsed jamming (long period) and DSSS.

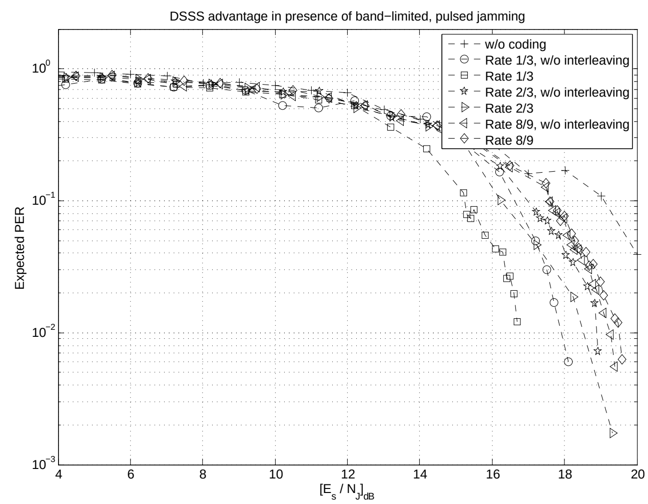

Fig. 15. Expected PER performance with pulsed jamming (long period) and DSSS.

also include other elements for interference protection besides DSSS, such as jammer state detection to improve pulsed jamming performance and interference suppression filtering for narrow-band interference.

More complete channel models can be included in further simulations in order to represent aircraft-to-ground datalinks more appropriately. These can combine AWGN channels and fading multipath channels with jamming.

References

[1] Defense Technical Information Center, *DoD Dictionary of Military and Associated Terms*. Available at http://www.dtic.mil/doctrine/jel/doddict/, November 2008.

[2] European Telecommunication Standards Institute, *ETSI EN 302 307: Digital Video Broadcasting (DVB); Second generation framing structure, channel coding and modulation systems for Broadcasting, Interactive Services, News Gathering and other broadband satellite applications*. V1.1.2, 2006.

[3] J. G. Proakis, *Digital Communications*, 4th ed., pp. 726-771, McGraw-Hill, 2001.

[4] M. C. Valenti and R. I. Seshadri, *Iterative Solutions Coded Modulation Library*, V. 1.10. Available at http://www.iterativesolutions.com, May 2008.

[5] S. Glisic and B. Vucetic, *Spread Spectrum CDMA Systems for Wireless Communications*, pp. 188-198. Artech House, 1997.

[6] A. Wei and L. Shen, “Performance analysis of the periodic sequence DSSS system against CW interference”, *Frontiers of Electrical and Electronic Engineering in China*, vol. 3, no. 1, pp. 79–85. 2008.

[7] M. Simon, J. Omura, R. Scholtz, B. Levitt, *Spread Spectrum Communications Handbook*, 1st ed., p. 414, McGraw-Hill, 2002.

Source and Channel Coding with Unequal Error Protection for Image Transmission in AWGN Channel

Ricardo Barroso Leite
Department of Communication – DECOM
School of Electrical and Computer Engineering – FEEC
State University of Campinas - UNICAMP
P.O. Box 05 - 13083-970
Campinas - SP – Brazil
Telephone: 55 19 3521-3720
rleite@fee.unicamp.br

Yuzo Iano
Department of Communication – DECOM
School of Electrical and Computer Engineering – FEEC
State University of Campinas - UNICAMP
P.O. Box 05 - 13083-970
Campinas - SP – Brazil
Telephone: 55 19 3521-3720
yuzo@decom.fee.unicamp.br

Ana Lúcia Mendes Cruz
Department of Communication – DECOM
School of Electrical and Computer Engineering – FEEC
State University of Campinas - UNICAMP
P.O. Box 05 - 13083-970
Campinas - SP – Brazil
Telephone: 55 19 3521-3720
analucia@decom.fee.unicamp.br

Fernando Silvestre da Silva
Department of Communication – DECOM
School of Electrical and Computer Engineering – FEEC
State University of Campinas - UNICAMP
P.O. Box 05 - 13083-970
Campinas - SP – Brazil
Telephone: 55 19 3521-3720
silva@decom.fee.unicamp.br

Abstract— **Current competition of digital television standards, 3G mobile communications, satellite data transmission and the mobile devices high capacity have promoted a recent boost in Channel Coding Forward Error Correction and in Source Coding. However, the performance deeply affected by the additive errors incidence position remains as a constant issue. In order to avoid this problem, non-uniform schemes of channel coding have been proposed in the literature, named Unequal Error Protection (UEP). Concerning this matter, this paper presents different new UEP encoding schemes combining DWT/SPIHT source coding and the Convolutional Parallel Turbo Coding.**

The results shown that this technique can significantly improve the reconstructed image quality for noisy channels when compared to the traditional EEP system. This result can be very useful for low power or high noise applications such as satellite communications and mobile transmission.

Index Terms— **Channel Coding, Image Compression, Source Coding, UEP.**

I. Introduction

The Current competition of digital television standards, 3G mobile communications, satellite data transmission (standardized by CCSDS - Consultative committee for Space Data Systems) and the mobile devices high capacity have promoted several improvements due to researches in Channel Coding Forward Error Correction and in Source Coding.

The images obtained by artificial satellites are very important for different research areas, such as remote sensing, astronomy, weather or military applications. In order to ensure that these images become fast received with considerable quality, the choice of which coding methods are going to be used involves conflicting project conditions: the rate reduction prioritizing the band or the addition of parity bits, increasing the samples correlation for allowing additive error-correction.

Considering source coding, the state-of-art about this issue concerns researches with Discrete Wavelet Transform (DWT) [1]-[6] involving SPIHT algorithm (Set Partitioning in Hierarchical Trees) that also allows a computationally simple form of rate control [7]. Besides, according to the CCSDS Blue Book [8] currently state-of-art channel coding that most closely approximates to the Shannon Limit concerns Turbo Codes [9]-[11].

The combination of source and channel coding systems along with the modulation, analog conversion, and channel model stages complete the communication system. By adjusting each coder rate, the system may achieve a desired level of visual quality (traditionally represented by the PSNR - Peak Signal-to-Noise Ratio) for a given reception power level [12]. However, the symbols generated by the source encoder neither are completely decorrelated among themselves, nor have the same relevance in the decoding process. Errors in symbols that flag the subband start or DWT low pass values produce more pronounced distortions at the final image. Hence, the performance is deeply affected by the additive errors incidence position. In order to avoid that, excellent non-uniform schemes of source-channel coding have been proposed in the literature, named Unequal Error Protection (UEP), in which the symbols produced by the source encoder are associated to variable rates according to the relevance [13]-[15].

A source-channel coding using DWT-SPIHT and Parallel Turbo scheme has been presented in [12], in which the authors observed that the quantization errors were less relevant than the channel errors. Xiaofan and Ko [15] have also presented another excellent UEP scheme using JPEG source coding (with restart markers between each Minimum Coded Unit (MCU) in order to prevent catastrophic errors) combined to Parallel Convolutional Turbo 1/3. In that scheme, the JPEG header syntax received priority in the allocated rate.

The UEP Ru et al. scheme [16] has also presented very good results for MIMO channels with Rayleigh fading using two stages channel coding: error-resilient entropy code for the SPIHT bitstream and LDPC for the headers and motions vectors (video). In [14], the UEP scheme was focused on scalable video combining wavelet transforms for temporal and spatial compression with two double binary turbo codes, optimizing the UEP rates according to the resultant PSNR distortion.

Finally, Salemi et al [13] have introduced a hardware UEP scheme on the attempt of solving this issue for DVB-S2 downlink system. The authors applied the wavelet Flex-Wave-II for source coding and the T@ampo Parallel Convolutional Turbo for channel coding, achieving very good performance.

On this context, this paper presents different new UEP encoding schemes combining DWT/SPIHT source coding and the Convolutional Parallel Turbo for channel coding in an AWGN channel. Performance PSNR and SSIM (Structural SIMilarity) [30] simulations have been made comparing the fix coding rate (EEP – Equal Error Protection) with the UEP coding for the same total bits transmitted in the channel.

The presented paper is organized as follows: Section II reviews concepts relating to satellite systems, Section III presents the source coding methods, emphasizing on DWT/SPIHT algorithm, and Section IV concerns to the Turbo coding. Section V describes the proposed UEP methods and Section VI presents the simulation results comparing the proposed UEP versus fixed rate coding. Finally, Section VII presents our conclusions.

II. Satellite Communications

Like other communication channels and electronic circuits, the satellite transmission will always present some additive noise, due to several factors like equipment heat, solar radiation, galaxies cosmic noise (below 1 GHz), lightning in the atmosphere (below 30 MHz), absorption by oxygen and water molecules, rain (frequencies above 10 GHz) and interference from others human equipments [17]. Because of these effects, the received signal is often weak in relation to noise and may even be impossible to detect.

In the context of digital signal transmission, a received signal $r(t)$ can be described in terms of the emitted signal $s(t)$:

$$r(t) = \alpha s(t) + n(t) \tag{1}$$

where α is the amplifier dependent constant and $n(t)$ is a random variable with Gaussian distribution, zero mean and $\sigma^2 = N_0 / 2$ variance. This AWGN channel is the closest model to the satellite transmission, due to thermal effects previously mentioned.

III. Source Coding: DWT And SPIHT

Despite their wide applications, entropy codes are very generic and, when used alone, do not guarantee great compression. For better results, the data are translated to a new representation domain through transformations such as DWT. After that, the information is concentrated, presenting lower entropy, reducing the average length of the final code.

The DWT and its multiresolution analysis arise from the work of several researches [1] [2] [18]. The DWT decomposes the original image into different resolution subbands (Fig.1), providing a representation of the spatial structure of the image into different levels. At each decomposition level, after filtering and subsampling, 4 subbands are produced named Approximation Subband (low-pass version LL) and Detail Subbands (vertical HL, horizontal LH and diagonal detail HH), each one presenting half of the image resolution [19]. By applying the DWT recursively, the original image size can be reduced by a 2k factor to produce an Approximation Subband, where k is the number of decomposition levels. At the decoder, inverse procedures take place with small differences at the filtering process.

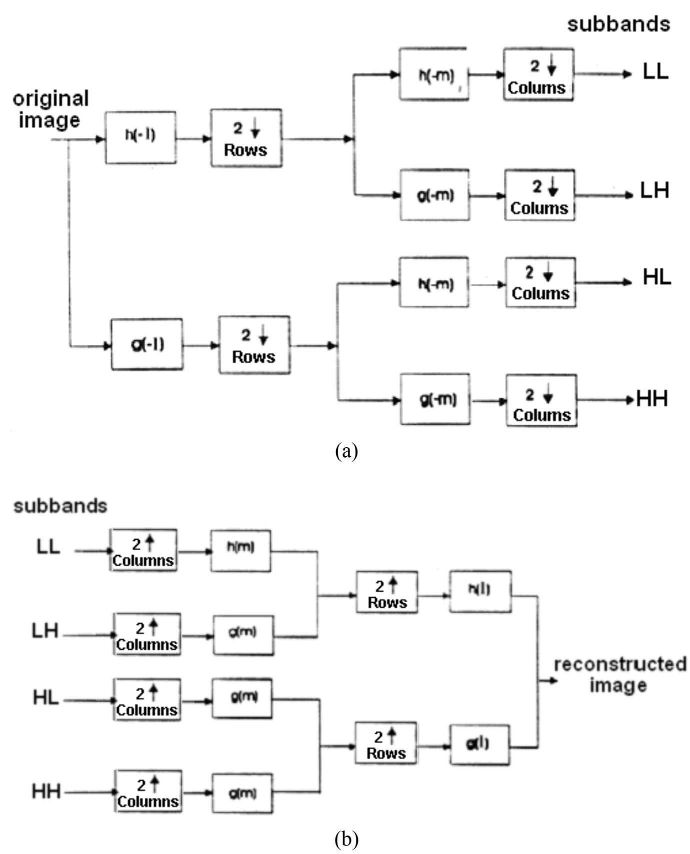

Fig. 1. Bi-dimensional DWT: (a) decomposition (b) reconstruction [19]

Obviously, the spatial characteristics of one particular subband into different resolutions are distinct, but they are highly correlated since they truly represent the same spatial structure into different levels. This characteristic was explored in quantization and coding [7][20] and by several authors in Multiresolution Motion Estimation Schemes for video coders [21]-[22].

The performance of SPIHT [7] has been among the best wavelet coefficients encoding algorithms concerning rate-distortion and subjective quality. So, their results are usually the reference for performance comparison of wavelet encoding algorithms.

This technique involves a tree-based hierarchical classification where each image coefficient is associated to one of three lists: list of insignificant pixels (LIP), list of insignificant sets (LIS) and list of significant pixels (LSP).

Each coefficient is considered insignificant and then positioned in LIP or LIS according to its position in the image. The encoding process consists of testing these three lists for the significance level of its elements according to a given threshold usually chosen as a power of 2. As a result, the algorithm starts to move pixels from LIP to LSP and from LIS to LIP or LSP. Each test result generates a set of bits that are appended to the transmitted/stored bitstream. With this information the decoder is capable of retrace all significance tests, reconstructing the image. More details about SPIHT algorithm can be found in [7][23][24].

IV. Channel Coding: Turbo

The parallel Turbo Code [25] in Fig. 2 is constituted by a parallel concatenation of convolutional encoders where the spectrum distances of the components are combined to generate a larger distance that contains the largest possible amount of combinations. The rate adjustment is done through puncturing.

The input of one encoder is interleaved to decorrelate the signal and the output is the combination between the systematic bit and the parity bits from both convolutional encoders.

The encoding process of a generic Turbo code with rate $R=m/n$ can be graphically represented by a trellis whose entrance is the vector $u = u_1, u_2, \ldots u_m$, where u_t can take the values -1 or +1 *a priori* with a probability distribution $P(u_t)$. At the decoding, the output of the previous trellis can be represented by a vector $x = x_1, x_2, \ldots x_n$, where x_t represents the symbol produced by the encoder in the instant t. The log likelihood (LLR) is defined by the association of the a priori probability as:

$$L(u_k) = \ln\left(P(u_k = +1)/P(u_k = -1)\right) \tag{2}$$

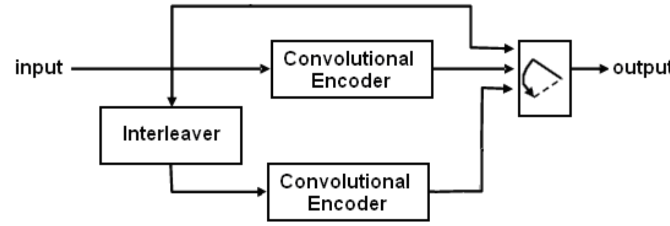

Fig. 2 – Parallel Turbo Encoder

The correct path for each encoder will be given by the maximum likelihood of input (the Viterbi algorithm), linked to the a priori probability, defined as the LLR.

The decoding process makes the best possible estimation of LLR a posteriori for every bit of sequence, which indicates the most likely sequence of the original broadcast u. The algorithm BCJR [26], also known as MAP (Maximum a posteriori) and the Viterbi algorithm [27][28] are used to make these estimative. The a posteriori LLR expressions are given by (2) and the puncturing is applied to the sequence in order to change the transmission code rate [29].

$$L(u_k / y) = \ln\left(P(u_k = +1)/ y / P(u_k = -1)/ y\right) \tag{3}$$

V. Proposed UEP Scheme

The balance between source and channel coding has been recommended by several standards and state-of-the-art researches because at intermediate regions, the source decoder may not be able to recover the image from the channel distorted coefficients (even few ones). So, the channel errors tend to spread and produce a very low image quality.

In order to explore the entire power range with acceptable visual quality, the source data has been recently coded in parts by UEP schemes, as mentioned in Section I.

These UEP schemes can be extremely efficient, especially if we take advantage of the DWT SPIHT coding characteristics, since neither the DWT representation symbols are completely decorrelated, nor have the same relevance in the decoding process. Errors in symbols that flag the DWT subband start or in the Approximation subband values produce more pronounced distortions at the final image.

This paper presents different new UEP encoding schemes combining DWT/SPIHT source coding and the Convolutional Parallel Turbo for channel coding in an AWGN channel.

At each stage in the SPIHT technique, the three lists LIP LIS and LSP are sequentially tested for the significance level according to a given threshold n, as shown in Table I producing the source bitstream. By exploiting the relevance of the SPHIT coefficients presented in these characteristics, the present work established an UEP scheme optimized according to the following priorities vector defined in Table II.

The optimization is merely a function of the coefficient position in the SPIHT list, being the same for any coding image.

Table I: SPIHT lists scan order based on N ($N_{MAX} = 9$)

List/N	1	2	3	4	5	6	7	8	9
LIP	1	4	7	10	13	16	19	22	25
LIS	2	5	8	11	14	17	20	23	26
LSP	3	6	9	12	15	18	21	24	27

TABLE II: PRIORITIES VECTOR BASED ON THE SPIHT LISTS SCAN ORDER

Priority	SPIHT Scan order
A (higher)	1,2,4,5,6,7,8,9,11
B	10,12,13,14,15,16,17
C	3,18,19,20,21,22,23,24,25,26,27

The scheme for channel coding rate adjustment is shown in Fig. 3, producing the bitstream, according to a pre-set rate. Channel coding rates are defined for each one of these regions (RA = 1/3, RB = 1/2, RC = 2/3), values most commonly used at the channel coding literature.

The UEP papers mentioned in Section I present excellent solutions for the source-channel coding issue. The proposed work additionally presents simulations for several images with more general channel than the fading or symmetrical binary channel, and the UEP optimization does not depend on the image to be coded. Simple BPSK was used instead of modulation schemes, leading this matter for future optimizations according to the frequency and available power requirements (depending on the MIMO, broadcast or downlink channel).

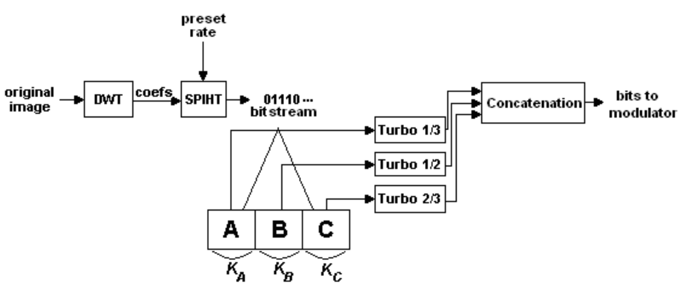

Fig. 3 – Proposed UEP scheme

VI. RESULTS

This section presents the performance comparisons of 3 schemes: the EEP (equal error protection) and two proposed UEP (Unequal Error Protection): the first one using an progressive code rate reduction and the second using an optimized code rate allocation using a priority vector from source encoder. The simulation scheme is shown in Fig. 4.

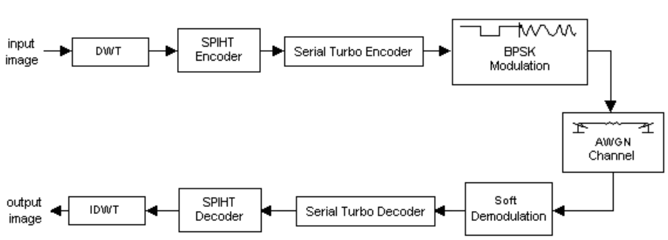

Fig.4 – Simulation General scheme

The wavelet function used for the DWT stage was CDF 9/7, with 3 decomposition levels, the same used in the JPEG 2000 standard for lossy static image compression.

The priority vector sets different priorities for each part of the bitstream according to the SPIHT list it belongs (LIP, LIS and LSP) and according to the iteration number. The code rates are always adjusted to provide a 0.5 bpp rate in the source encoder and rates 1/3, 1/2 and 2/3 in the channel encoder in order to keep the overall rate at 1.0 bpp. The results were compared using two objective quality metrics: PSNR and SSIM [30].

The Fig. 5 shows the PSNR and SSIM performances for the two UEP codes with *Lena* image presenting one inserted bit error at bitstream section to be decoded and after measured. It is important to notice that the 3rd list is initially empty because it consists of the first LSP step.

These results were used to set the priority level of each list shown in Table I.

The second experiments set were made in order to compare the performance of all three coding schemes. Each point of the PSNR x Channel SNR curves was evaluated from the average of 8 different source images [31] with 4 tests each, using different channel noise seeds, simulating four error position situations. The Fig. 6 shows the performance curves for all three schemes.

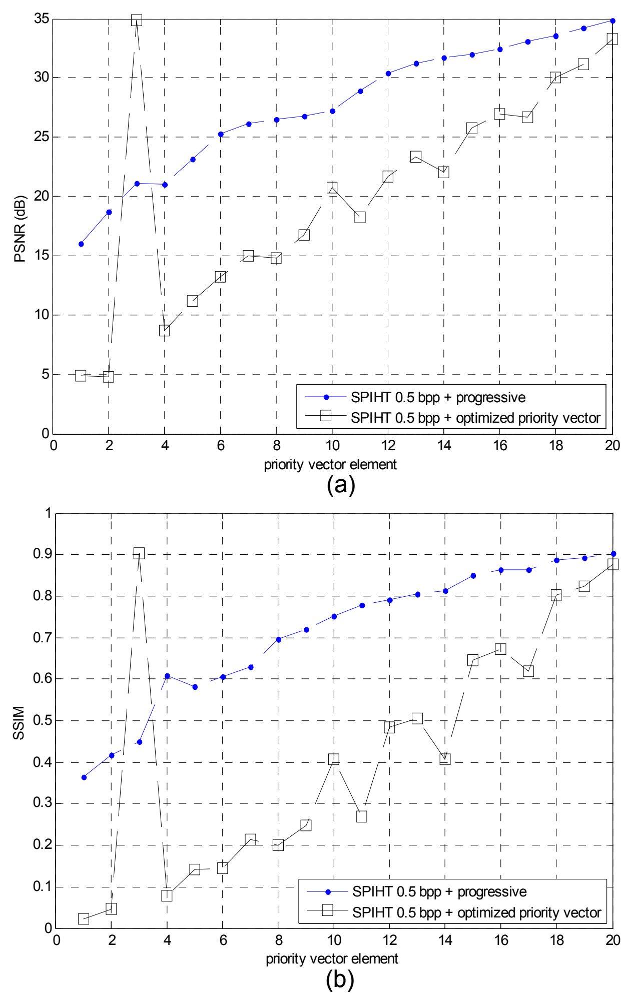

Fig. 5 – Priority vector optimization curves. (a) PSNR; (b) SSIM.

The analysis of these results shows that the EEP scheme presents an abrupt transition near 0 dB. In the other hand, the UEP schemes present a smoother transition reaching the higher quality level even when the noise is stronger as in satellite communications. The EEP scheme presents about 5dB improvement in PSNR (0,1 SSIM) at the SNR range from 0 to 2 dB, but also presents over 17dB loss in PSNR (0.30 SSIM) at the SNR range from -2 to 0 dB.

Figs. 7-9 present the subjective quality of the reconstructed images for 3 channel SNR values: -1.0dB, -0.5dB and 0.0dB.

In these figures we can see the effect of the abrupt quality transition of EEP: if the channel SNR is less than 0dB, the reconstructed image is practically unrecognizable and for the SNR greater than or equal to 0dB the image presents almost no channel distortion.

Alternatively, the UEP scheme visual quality increases proportionally to the channel SNR. Furthermore, we can observe that the image retains its main characteristics even with noisier channel. This result represents a significant improvement in the overall performance of the communication system.

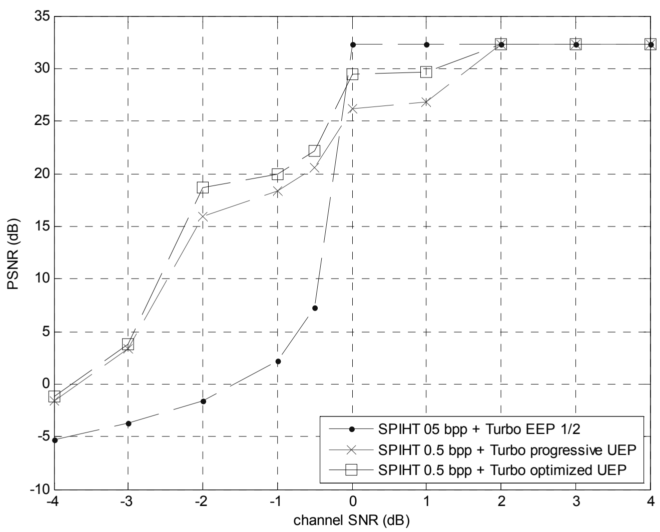

(a)

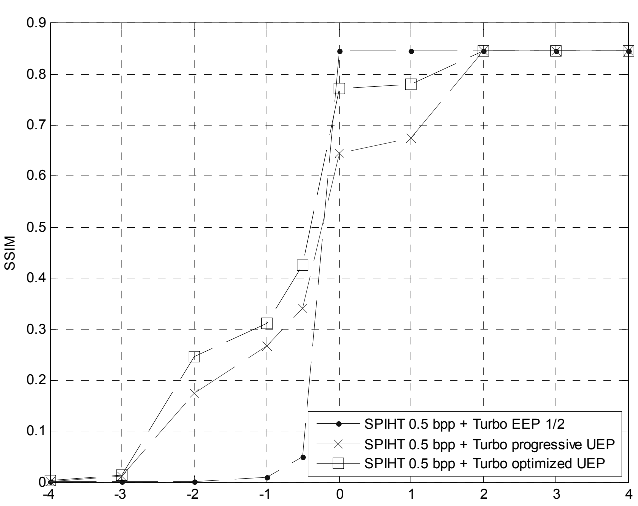

(b)

Fig. 6 – Average results. (a) PSNR; (b) SSIM.

Comparing the images with relatively high SNR, the image quality loss of the UEP schemes is minimum when compared to EEP schemes, because the image quality is very high in all cases (above 30 dB).

VII. Conclusions

This paper presents two new UEP schemes based on SPIHT and turbo code algorithms in order to reduce the effect of the channel additive errors in transmission of digital images. The proposed schemes split the bitstream in parts according to the relevance of the bits in the decoding process associating a higher channel code rate to the most relevant bits.

These schemes are compared to the equivalent EEP scheme. Despite the UEP technique have presented a slight decrease in the image quality for low noise channels, the results shown that this technique can significantly improve the reconstructed image quality (over 17dB in PSNR and 0.3 SSIM) for low SNR values in the channel. This result can be very useful for low power or high noise applications such as satellite communications and mobile transmission.

(a) (b) (c)

Fig.7 – Lena image results with channel SNR =-1dB. (a) EEP; (b) Progressive UEP; (c) Optimized UEP.

(a) (b) (c)

Fig.8 – Lena image results with channel SNR = -0,5dB. (a) EEP; (b) Progressive UEP; (c) Optimized UEP.

(a) (b) (c)

Fig.9 – Lena image results with channel SNR = 0dB. (a) EEP; (b) Progressive UEP; (c) Optimized UEP.

ACKNOWLEDGMENTS

This work was supported by following research and development agency: State Research Support Foundation of São Paulo (FAPESP), Aeronautical Institute of Technology (ITA)-ITASAT Project (special thanks for the researchers), National Counsel of Technological and Scientific Development (CNPQ), Research and Teaching Support Foundation of State University of Campinas (FAEPEX), and Coordination of Graduated Level Personnel Improvement (CAPES / CAPES-RHTVD).

REFERENCES

[1] I. Daubechies, Ten Lectures on Wavelets, SIAM, Philadelphia, USA, 1992.

[2] S. Mallat, A Theory for Multiresolution Signal Decomposition: the Wavelet Representation, IEEE Transactions on PAMI, vol. 11, pp. 674-693, 1989.

[3] J. Guo, S. Mitra, B. Nutter, T. Karp, A Fast and Low Complexity Image Codec based on Backward Coding of Wavelet Trees, Proc. of IEEE Data Compression Conference (DCC'06) pp. 292-301, 2006.

[4] V. Velisavljevic, B. Beferull-Lozano, M. Vetterli, Space-Frequency Quantization for Image Compression With Directionlets, IEEE Transactions on Image Processing, no. 9, Sept., 2007.

[5] C. Bhattacharya, P. R. Mahapatra, A Discrete Wavelet Transform Approach to Multiresolution Complex SAR Image Generation, IEEE Geoscience and Remote Sensing Letters, vol. PP, no. 9, pp. 416-420, 2007.

[6] ISO/IEC 15444 “Information technology -- JPEG 2000 image coding system,” 2004.

[7] A. Said, W. A. Pearlman, A new fast and efficient image coding based on set partitioning in hierarchical trees, IEEE Transactions on Circuits and Systems for Video Technology, 1996.

[8] CCSDS 122.0-Blue Book Issue 1. Image Data Compression. Nov. 2005.

[9] C. Berrou, A. Glavieux, P. Thitimajshima, Near Shannon Limit Error-Correcting Coding and Decoding Turbo Codes, Proc. Int. Conf. Communications, p. 1064-1070, May1993.

[10] Flexible Serially Concatenated Convolutional Turbo Codes with Near-Shannon Bound Performance for Telemetry Applications. Orange Book. Issue 1. Exp.Specification CCSDS 131.2-o-1, Sep. 2007.

[11] S. K. Andrews, D Divsalar, S Dolinar, J Hamkins, C. R. Jones and F. Pollara, The Development of Turbo and LDPC Codes for Deep-Space Applications, Proceedings of the IEEE, vol. 95, no. ll, Nov. 2007.

[12] R. B. Leite, Y. Iano, Codificação de Fonte e Canal para Transmissão de Imagens em Canal AWGN, XXVI Simpósio Brasileiro de Telecomunicações – SBrT’08, Rio de Janeiro, Brazil, 02-05, Sept. 2008.

[13] E. Salemi, C. Desset, A. Dejonghe, J. Cornelis, J. and P. Schelkens, A Low-Complexity UEP Methodology Demonstrated on a Turbo-Encoded Wavelet Image Satellite Downlink, EURASIP Journal on Wireless Communications and Networking, Vol. 2008, Article ID 342415.

[14] N. Ramzan, S. Wan, E. Izquierdo, An Efficient Joint Source-Channel Coding for Wavelet Based Scalable Video, ISCAS 2007. IEEE International Symposium on Vol. Circuits and Systems, Issue , 27-30 May 2007 Page(s):1505 – 1508.

[15] X. Fei, T. Ko, Turbo-codes Used For Compressed Image Transmission Over Frequency Selective Fading Channel, Global Telecommunications Conference, 1997. GLOBECOM apos;97., IEEE Vol. 2, Issue , 3-8 Nov 1997 Page(s):629 – 633.

[16] C. Ru, L. Yin, J. Lu and C. W. Chen, A New UEP Scheme Based on Adaptative Modulation for Robust Vídeo Transmission in MIMO System, China Communications, 2006.

[17] G. B.Bleazard, Introducing Satellite Communications, Oxford : NCC Publications, 1985.

[18] A. Grossman; J. Morlet, Decomposition of Hardy Functions into Square Integrable Wavelets of Constant Shape, SIAM J. Applied MAthematics, vol. 15, pp. 726-736, 1984.

[19] A. L. M. Cruz, “Procedimentos para Método Híbrido de Compressão de Imagens utilizando Transformadas Wavelet e Codificação Fractal”, PhD Thesis, State University of Campinas, Brasil, May, 2005.

[20] J. M. Shapiro – “Embedded Image Coding Using Zerotrees of Wavelet Coefficients” – IEEE Transactions on Signal Processing, vol. 41, no. 12, pp. 3445-3462, Dez., 1993.

[21] J. Zan; O. Ahmad; M. N. S. Swamy – New Techniques for Multiresolution Motion Estimation – IEEE Transactions on CSVT, vol. 12, no. 09, pp. 793-802, Set, 2002.

[22] S. Kim; S. Rhee; J. G. Jeon; K. T. Park – Interframe Coding Using Two-Stage Variable Block-Size Multiresolution Motion Estimation and Wavelet Decomposition – IEEE Transactions on CSVT, vol. 8, no. 04, pp. 399-410, Ag, 1998.

[23] K. R. Rao and P. C. Yip, The Transform and Data Compression Handbook, USA, Florida: CRC Press, 2000.

[24] K. Sayood, Introdution to Data Compression, 2nd ed. San Diego: Morgan Kaufmann, 2000.

[25] C. Berrou and A. Glavieux, Near optimum error correcting coding and decoding: Turbo-codes, IEEE Trans. Commun., vol. 44, pp. 1261-1271, Oct. 1996.

[26] L. Bahl, J. Cocke, F. Jelinek and J. Raviv, “Optimal Decoding of Linear Codes for Minimizing Symbol Error Rate,” IEEE Trans on Inf. Theory, Mar 1974.

[27] A. J. Viterbi, An intuitive justification and a simplified implementation of the MAP decoder for convolutional codes, IEEE J. Select. Áreas Commun., vol. 16, pp. 260-264, Feb. 1998.

[28] M. Valenti, Turbo Codes and Iterative Processing, IEEE New Zealand Wireless Communications Symposium, Nov. 1998.

[29] M.A. Kousa and A.H. Mugaibel, Puncturing effects on Turbo codes, IEEE Proceedings online no. 20020230, 2002.

[30] Z. Wang, A. C. Bovik, H. R. Sheikh, E. P. Simoncelli, Image Quality Assessment: From Error Visibility to Structural Similarity, IEEE TRANSACTIONS ON IMAGE PROCESSING, 2004.

[31] Waterloo BragZone test images. Available: ftp://links.uwaterloo.ca/pub/BragZone.

Low Complexity BCM with Different Length Codewords

Rui Rodrigues Simões Júnior
National Institute of Telecommunications - Inatel
P.O. Box - 37540-000
Santa Rita do Sapucaí - MG - Brazil
ruirs@inatel.br

Geraldo Gil Ramundo Gomes
National Institute of Telecommunications - Inatel
P.O. Box - 37540-000
Santa Rita do Sapucaí - MG - Brazil
ge@inatel.br

***Abstract*—The aim of this paper is to present BCM schemes using codewords with different lengths to different coding levels. The main purpose of this scheme is to allow more flexibility on the choice of asymptotic gain, low complexity and coding rate. This proposal is a solution to obtain coding gains without bandwidth expansion and high decoding complexity. The proof of concept is a BCM/QPSK scheme, over Gaussian and Rayleigh channels, obtained by Monte Carlo simulation. The results presented showed that the arrays with different length codewords are better than an equivalent array with equal length codeword using the same sub-optimum decoding algorithm. Furthermore, the serial operations number to decode the proposed array is less than to decode the conventional array.**

***Index Terms*—Block coded Modulation (BCM), Euclidean distance, Sayegh's array, Ungerboeck's set partitioning.**

I. INTRODUCTION

The conventional way to design BCM schemes is by using a codewords array known as Sayegh array [1].

In the Sayegh array, each array row is a codeword where the Hamming distance is inversely proportional to the correspondent subset Euclidean distance generated by Ungerboeck partitioning [2]. Conventionally, the array rows have equal length codewords [3]-[4]. As the codes choice is essentially a heuristic process, there are several block codes combinations that can be used to a specific performance goal [5]-[8]. To satisfy the trade-off between coding gain and coding rate, long length codewords can be necessary; long length codewords can increase the decoding complexity. In order to increase the number of optimum solutions, the use of codewords with different lengths for different coding levels (or rows) in the array can be a good alternative.

II. ARRAY WITH DIFFERENT LENGTH CODEWORDS

The arrays construction with different length codewords can be done in the conventional way, i.e. [9], combining the Ungerboeck partitioning [2] with the Sayegh array [1]. However, to decrease the serial operations number in the decoding process, some coding level are formed with codewords whose length is the array highest length codeword factor.

The codes array for QPSK coded scheme with (21,11,6) and (7,4,3) component codes in the first and second rows, respectively, is shown in Figure 1, where $v_{20}, v_{19},..., v_0$ are bits of a (21,11,6) codeword and $u_6, u_5,..., u_0$ are bits of a (7,4,3) codeword, being the second row formed by three codewords. The symbol QPSK is made by one bit from first row and one bit from second row.

Table I presents arrays with different length codewords using QPSK, 8-PSK, and 16-QAM modulations with their respective theoretical asymptotic coding gains and coding rates. It is taken into account that the coded modulations coding rate per array must be equal to the uncoded modulations to which they are compared to so that both have kept the same spectral efficiency [1]-[4].

TABLE I
ARRAYS WITH DIFFERENT LENGTH CODEWORDS.

BCM	ARRAY	CODING RATE	ASYMPTOTIC CODING GAIN
QPSK	(21,11,6) 3x(7,4,3)	0.55	5.18 dB over BPSK
8-PSK	(21,1,21) (21,11,6) 3x(7,4,3)	0.38	5.35 dB over BPSK
16-QAM	(21,1,21) (21,11,6) 3x(7,4,3) (21,20,2)	0.52	4.8 dB over QPSK
16-QAM	(21,11,6) 3x(7,3,4) (21,20,2) (21,21,1)	0.73	6 dB over 8-PSK

Naturally, the main question at this point is: "*What are the advantages of the arrays with different length codewords compared to conventional arrays?*"

Besides the evident flexibility, there is a hard decision decoding complexity reduction according to Table II where the array (21,11,6) and (7,4,3) codes are compared to two conventional arrays; (16,7,6) and (16,11,4) and other (16,5,8) and (16,11,4). Thus, another important advantage is going to be highlighted forward in the Performance Results item.

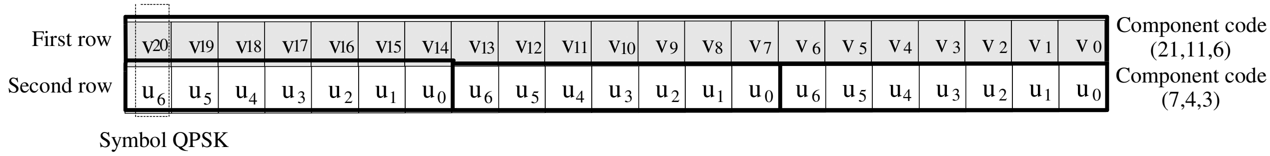

Fig. 1. Codes array with different length codewords.

TABLE II
ARRAYS WITH DIFFERENT LENGTH CODEWORDS COMPARED TO CONVENTIONAL ARRAYS.

Array	(21,11,6) 3x(7,4,3)	(16,7,6) (16,11,4)	(16,5,8) (16,11,4)
Modulation	QPSK	QPSK	QPSK
Asymptotic coding gain	5.18 dB over BPSK	5.28 dB over BPSK	6 dB over BPSK
Coding rate	0.55	0.56	0.5
Serial operations Number to hard decoding	564	773	721
Error correction (1st row)	2	2	3
Error correction (2nd row)	3	1	1

III. DECODING ALGORITHM

The Sayegh's sub-optimum multistage decoding algorithm used for hard and soft decision, based on a real line [10], can be summarized in following items.

A. The M-PSK modulation symbol can be represented by integer numbers over a real line, where the transmitted symbols are integers and after contamination by additive noise are transformed in real numbers, according (1), illustrated by Figure 2.

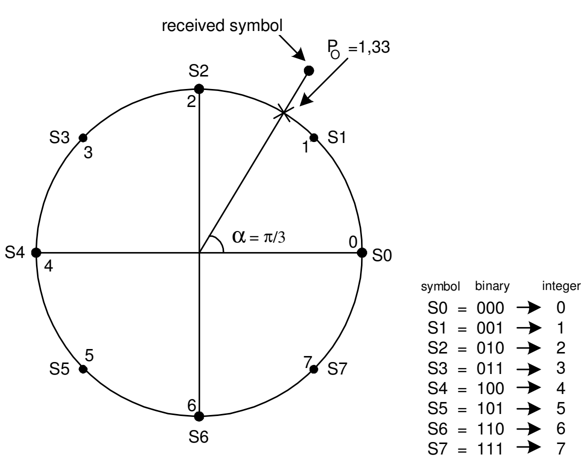

Fig.2. 8-PSK constellation for transmitted integer and received real numbers.

$$P_o = \frac{M\alpha}{2\pi} \tag{1}$$

where M is the PSK modulation index and α is the angle formed between the received symbol and circumference center. Considering the integer numbers like transmitted signals and the real numbers like received signals, then, there is sufficient information for the decoding process, because the bidimensional received symbol translated to a real value keeps the distance structure.

B. Each received symbol is approached for the nearest integer and the respective distance between them is stored. The binary array is remounted, where each array row is hierarchically decoded. If the error number in a row is greater than code correction capacity, then the distance information stored will be used to try to correct these errors. The decoding process is concluded when all array rows are codewords.

IV. PERFORMANCE RESULTS

In general, it is very difficult to make an exact BCM scheme bit error rate prediction [4]. Analytical expressions, such as the ones used for BER in linear modulation schemes are not available [4]; in this way computational simulations are the most efficient method to evaluate the BCM schemes performance [9].

Figures 3 and 4 present the BER for AWGN and Rayleigh channels with Sayegh's multistage decoding algorithm for hard decision and soft decision to (21,11,6) and 3x(7,4,3) BCM scheme. Figure 3, where BER equal 10^{-7} in AWGN channel, the gain obtained is 2.9 dB with the decoding per hard decision and 4.5 dB per soft decision, which represents only 0.68 dB of the calculated theoretical asymptotic gain. And finally, Figure 4 in Rayleigh channel, where BER equal 10^{-5}, the gain obtained per hard and soft decisions are respectively 19 dB and 26 dB.

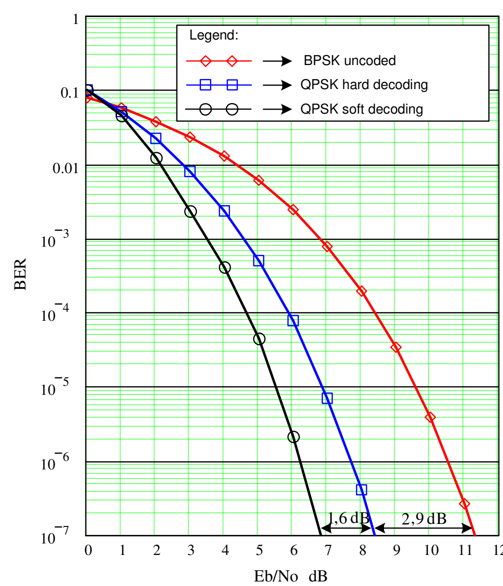

Fig.3. (21,11,6) and 3x(7,4,3) BCM performance on AWGNchannel.

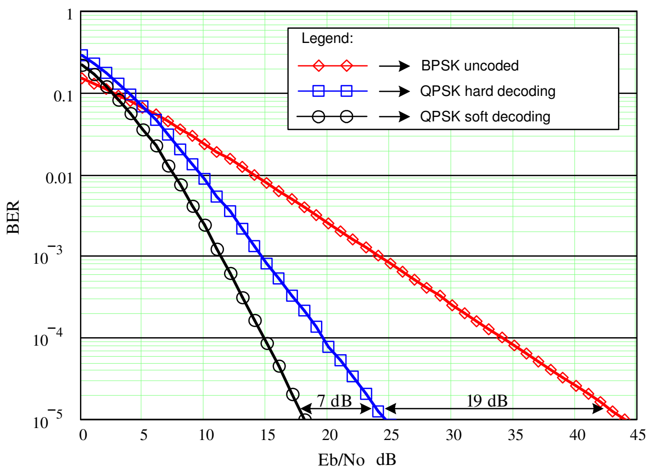

Fig.4. (21,11,6) and 3x(7,4,3) BCM performance in the Rayleigh channel.

The BCM/QPSK coded schemes with hard decoding formed by the codes (21,11,6)/3x(7,4,3) obtained a gain over the conventional codes schemes (16,7,6)/(16,11,4) and (16,5,8)/(16,11,4) with 0.5 dB and 0.3 dB in AWGN channel, and 2.5 dB and 1.8 dB in the Rayleigh channel respectively, according to simulations and illustrated by the Figures 5, 6, 7 and 8, as well.

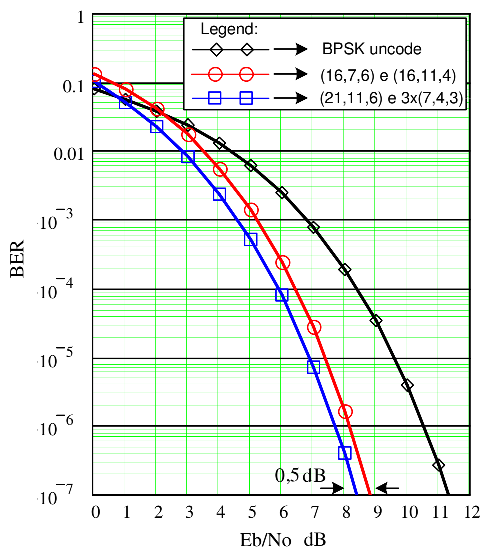

Fig.5. (21,11,6) / 3x(7,4,3) and (16,7,6) / (16,11,4) BCM performance on AWGN channel.

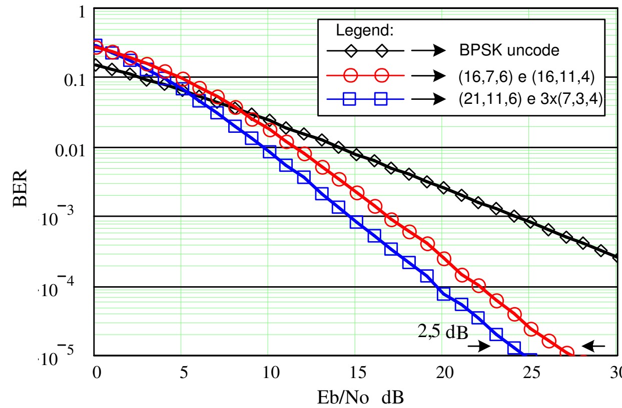

Fig.6. (21,11,6) / 3x(7,4,3) and (16,7,6) / (16,11,4) BCM performance in the Rayleigh channel.

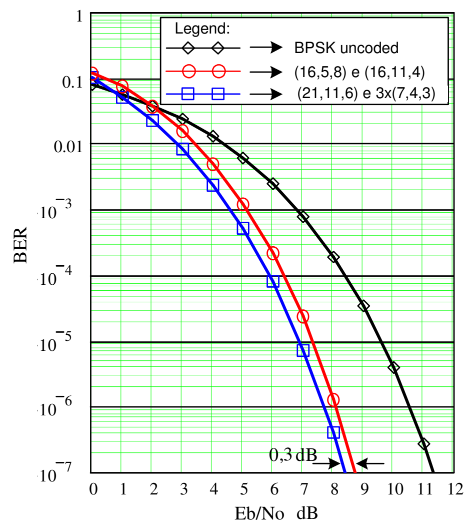

Fig.7. (21,11,6) / 3x(7,4,3) and (16,5,8) / (16,11,4) BCM performance on AWGN channel.

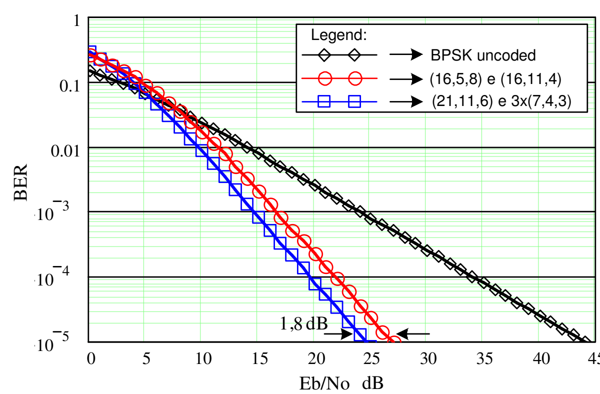

Fig.8. (21,11,6) / 3x(7,4,3) and (16,5,8) / (16,11,4) BCM performance in the Rayleigh channel.

V. Conclusion

The results obtained by computer simulations showed that the (21,11,6) and 3x(7,4,3) BCM array performance is better than the (16,7,6) and (16,11,4) or (16,5,8) and (16,11,4) equivalent BCM arrays. Notice, the decoding complexity to (21,11,6) and 3x(7,4,3) BCM array is smaller than the (16,7,6) and (16,11,4) or (16,5,8) and (16,11,4) BCM arrays. The results suggest to be possible to find other arrays with different length codewords better than their equivalent equal length codeword arrays. Although there is more powerful channel coding schemes, like Turbo and LDPC [7]-[8], the BCM schemes presented in this paper are suitable for wireless applications with low cost, low complexity and 4-6 dB coding gain. Using the Sayegh's sub-optimum multistage decoding algorithm was possible to obtain coding gain near to the calculated asymptotic gain.

References

[1] S. I. Sayegh, "A class of optimum block codes in signal space," *IEEE Trans. on Communications*, vol. COM-28, No. 10, pp. 1043-1045, October 1986.

[2] G. Ungerboeck, "Channel coding with multilevel phase signals," *IEEE Trans. on Information Theory*, vol. IT-28, No. 1, pp. 55-67, January 1982.

[3] E. L. Cusack, "Error control codes for QAM signaling," *Electronics Letters*, vol. 20, No. 2, pp. 62-63, January 1984.

[4] A. G. Burr, "Block versus trellis: an introduction to coded modulation," *IEEE Electronics & Communication Engineering Journal*, vol. 5, No. 4, pp. 240-248, August 1993.

[5] M. Fossorier, H. Imai, S. Lin, "Multilevel coded modulation for unequal error protection and multistage decoding – part I: symmetric constellations," *IEEE Trans. on Communications*, vol. 48, No. 2, pp. 204-213, February 2000.

[6] Dong-Feng Yuan, Cheng-Xiang Wang, Qi Yao, Zhi-Gang Cao, "Comparison of multilevel coded modulations with different decoding methods for AWGN and Rayleigh fading channels," *IEEE IC – International Conference on Communications*, vol. 3, pp. 1193-1197, USA, 18-22 June 2000.

[7] Huan-Bang Li, John M. Cioffi, "Enhanced block coded modulation using iterative decoding based on parity check codes," *IEEE ICC – International Conference on Communications*, vol. 1, No. 1, pp. 315-319, Finland, 11-18 June 2001.

[8] F. Guo S. X. Ng, L. Hanzo, "LDPC assisted block coded modulation for transmission over Rayleigh fading channels," *IEEE Proceeding - VTC*, vol. 3, pp. 1867-1871, Korea, 22-25 April 2003.

[9] R. G. C. Williams, "Low complexity block coded modulations," *Thesis Ph.D University of Manchester*, Manchester, UK, 1988.

[10] R. Baldini F. and P. G. Farrel, "Coded modulations based on rings of integers modulo-q. Part I: Block codes," *IEE Proceedings Communications*, vol. 141, No. 3, pp. 129-136, June 1994.

A New Interference Estimation Approach For Secondary Spectrum Sharing With Smart Antennas

Mathieu Boutin
1 : INRS-EMT
P.C. H5A 1K6
Montreal – QC – Canada
2: LRTCS-UQAT
P.C. J9P 1S2
Val d'Or – QC – Canada
450-979-0648
mathieu.boutin@emt.inrs.ca

Charles Despins
1 : PROMPT Inc.
P.C. H3B 3A7
Montreal – QC – Canada
2 : INRS-EMT
P.C. H5A 1K6
Montreal – QC – Canada
3 : LRTCS-UQAT
P.C. J9P 1S2
Val d'Or – QC – Canada
514-875-0032 #101
cdespins@promptinc.org

Tayeb Denidni
1 : INRS-EMT
P.C. H5A 1K6
Montreal – QC – Canada
2 : LRTCS-UQAT
P.C. J9P 1S2
Val d'Or – QC – Canada
514-875-1266 #2017
tayeb.denidni@emt.inrs.ca

Sofiène Affes
1 : INRS-EMT
P.C. H5A 1K6
Montreal – QC – Canada
2 : LRTCS-UQAT
P.C. J9P 1S2
Val d'Or – QC – Canada
514-875-1266 #2011
affes@emt.inrs.ca

***Abstract*—Advances in millimetre radio waves technologies will soon make smart antennas easily portable in size. Furthermore, the scarcity of the radio spectrum now encourages the use of cognitive radios so that the spectrum could be shared between a secondary and a primary network. This paper thus brings a new approach for a smart-antenna-equipped MANET (Mobile Ad hoc NETwork), acting as a secondary network, to estimate its interference to fixed primary network antennas. By knowing only a coarse probabilistic estimate of each primary antenna location, the aggregate interference is voluntarily overestimated by the MANET, since the primary network imposes an aggregate interference safety margin for the MANET to respect, following an adequate minimum probability. The MANET can thus assess the impact of its future spectrum sharing with the primary network and take countermeasures accordingly, by means of simulations prior to deployment.**

***Index Terms*—cognitive radio, interference estimation, mobile ad hoc network, probabilistic location, smart antennas.**

I. INTRODUCTION

The need for a wireless network of any kind to be able to share the same spectrum of an already well-established legacy network now becomes imperative. A large portion of the licensed spectrum remains mostly unused or under-utilized, as reported in many radio spectrum measurement results [1-2]. This indicates that the current spectral shortage may be partially relieved by a more flexible user access rather than the presently rigid and static spectral allocation [3].

A wireless network can now be spectrally aware of its surrounding, and take intelligent decisions accordingly, with the use of the relatively new and promising cognitive radio concept. Also, by using a smart antenna, a network device is not restricted to transmit and receive with an omnidirectional radiation pattern antenna. Instead, by means of multiple antennas at the transceiver, forming an antenna array, such a device can smartly choose the direction and width of its radiation beam by properly tuning its transceiver tap weight coefficients. It is at the advantage of the cognitive radio network to exploit such transmission and reception directivity in order to allow it to coexist in close proximity of a legacy network even if both share the same frequency band, since spectrum is a very scarce resource [4]. The details about beam steering or beam width adaptation are however not addressed in this paper, as a very inspiring and useful application is considered instead.

In this paper, we consider cognitive smart-antenna-equipped MANET deployment. Such a structure-free wireless network is highly relevant as it is attractive for a very large scope of fast and low cost applications such as emergency rescues, military interventions, security for very crowded special events, etc. The scheme we propose is to let the primary network impose an interference protection requirement to be respected by the MANET, such that the latter can assess if its deployment is acceptable. The main obstacle lies in the MANET's knowledge of the location of each fixed primary antenna. In fact, the very poor interaction between both networks only allows the MANET to have a probabilistic estimate of those antennas, unlikely with a satisfying accuracy. This problem being known by the primary network managers, the interference protection requirement is thus supplemented with a minimum probability of being respected. We therefore propose a new interference estimation technique for the MANET to voluntarily overestimate the interference it causes to the primary network, so an interference safety margin can be respected with respect to the estimate, following the aforementioned minimum probability.

On the following sections, we present the system models for the primary network requirement, the location estimate of primary antennas, radio wave propagation and antenna, followed by MANET communication. Then, we give a detailed explanation of our proposed interference estimation technique, to end with simulations results and interpretation before concluding this paper.

II. System Models

We assume the same frequency band to be used by both the MANET and primary network. There is no possible communication between both networks. We assume that each node of the MANET has only one half-duplex transceiver. We omit temporal details about whether communication among nodes is synchronous (like TDMA) or asynchronous (like CSMA), and the protocols used, as those do not influence our simulations results.

In the remainder of this paper, the set of all primary antennas is defined as S_P, and the set of all transmitting and receiving nodes are defined as S_T and S_R, respectively. We only consider the interference caused by the MANET to the primary antennas, which are assumed to be constantly in receiving mode for a worst case assessment. All primary antennas are also assumed to be omidirectional with a unitary gain.

A. *The primary network requirement*

Despite all the processing power embedded in each MANET node, as well as the always more sophisticated models to predict radio wave propagation on many types of environment, there is inevitably a difference or error between the estimated aggregate interference the MANET causes to any primary antenna, as compared to the actual aggregate interference. We call the former $I_{A,e}(p)$ and the latter $I_A(p)$, for all $p \in S_P$. It is more appropriate in our scheme to talk of an aggregate interference offset on p, denoted as $I_{A,o}(p)$, instead of an aggregate interference error, as this difference can be probabilistically selected by the MANET, as explained subsequently, to reduce the interference on the primary network.

By defining $I_R(i,p)$ as the actual interference received by a primary antenna p from a single transmitting node i, and $I_{R,e}(i,p)$ as the estimated interference, we thus define $I_A(p)$, $I_{A,e}(p)$ and $I_{A,o}(p)$ for all $p \in S_P$ as:

$$\left\{ \begin{array}{l} I_A(p) = \sum_{\forall h \in S_T} I_R(h,p), \\ I_{A,e}(p) = \sum_{\forall h \in S_T} I_{R,e}(h,p), \\ I_{A,o}(p) = I_{A,e}(p) - I_A(p) \end{array} \right\}. \tag{1}$$

If $I_{A,o}(p) > 0$, then the MANET has overestimated the interference it causes on p, and the future MANET decisions are less likely to be harmful for p, but more likely to decrease the MANET communication efficiency. Since the values of $I_{A,e}(p)$ $\forall p \in S_P$ have great influence on future MANET decisions, which in turn have a direct impact on the interference caused to the primary network, the latter could accept to share it precious frequency band with the former only if some restriction applies to $I_{A,o}(p) \forall p \in S_P$.

In our scheme, we assume the primary network to impose an aggregate interference safety margin, denoted as $I_{A,SM}$, for the MANET to respect following a given safety margin probability denoted as η_{SM}, where $0 \leq \eta_{SM} \leq 1$. $I_{A,SM}$ and η_{SM} are assumed to be constant and the same for all primary antennas, for simplicity. However, using different values of $I_{A,SM}$ and η_{SM} for each antenna would be very easy to implement, as a generalization of our present work. The primary network thus accepts to share its spectrum with the MANET if and only if the following requirement is met by the latter:

$$P\left(I_{A,o}(p) > I_{A,SM}\right) \in \left[\eta_{SM}, 1\right], \forall p \in S_P, \tag{2}$$

The above requirement is the core of our contribution. The MANET has to assess by simulation if this requirement can be met, while still providing an acceptable communication among its nodes.

B. *Location estimate of primary antennas*

Upon the deployment of the MANET in the same area as the primary network, we assume it to never know the exact location of each primary antenna. Nonetheless, since several techniques have been proposed over the years to estimate the location of primary transceivers, such as by means of multiple transmitter localization as in [5-6] just to name a few, we assume the MANET to have a coarse estimate of such information. Location estimates, such as the expectation, are much more useful if they are complemented with some indication about their precision [7].

We assume the uncertainty about the actual location to be described by a probability distribution, so that the uncertainty associated with the location of each primary can be visualized. This can be done by drawing an ellipse centered at the expected location such that the orientation and size of the ellipse describes the uncertainty of the location estimate as well as possible [7].

The MANET location estimate of each primary antenna p is therefore modeled as a bivariate Gaussian random variable with means $\mu_x(p)$ on the abscissa and $\mu_y(p)$ on the ordinate, and standard deviation $\sigma_{xy}(p)$ on both axes for simplicity. We thus obtain an uncertainty circle (UC) with radius $R_{UC}(p) = \Omega_{UC}\sigma_{xy}(p)$, where Ω_{UC} is the uncertainty coefficient, for each primary p and centered at $(\mu_x(p),\mu_y(p))$. The actual location of each primary p is defined as $(x(p),y(p))$.

When the MANET has to consider requirement (2), the choice for the value of Ω_{UC} is of key importance. Indeed, this single parameter brings a decisive trade-off between being accepted by the primary network to operate on the same frequency band, and providing an acceptable QoS among MANET nodes. Considering an uncertainty ellipse instead of an uncertainty circle is more realistic and is left for our future work.

C. *Propagation and antenna*

We use roughly the same antenna model as in [8]. Suppose we have a transmitting node i and receiving node j. Let $G_T(i) = 2\pi/\theta(i)$, where $G_T(i)$ is the antenna gain of the transmitting node i, with its beam width $\theta(i)$ and beam direction $\varphi(i)$. Similarly, let $G_R(j) = 2\pi/\theta(j)$, where $G_R(j)$ is the antenna gain of the receiving node j with its beam width $\theta(j)$

and beam direction $\varphi(j)$. Antenna beams are modeled as circle sectors, as we assume the main lobe to be much more important than all the side lobes together. For the remaining of this paper, we use the word "sector" instead of "circle sector".

Let $d(i,k)$ be the distance between i and any receiver k (receiving node or primary antenna). The path loss gain $G_\alpha(i,k)$ with path loss exponent α of the transmitted power as a function of $d(i,k)$, by considering a constant unitary gain for a distance smaller than the reference distance d_0, is defined by:

$$G_\alpha(i,k) = \begin{cases} C(i,k), & \forall d(i,k) \in [0, d_0] \\ d(i,k)^{-\alpha} C(i,k), & \text{otherwise} \end{cases}, \quad (3)$$

where $C(i,k)$ is a zero mean Lognormal random variable, with standard deviation σ_C, representing the slow fading on the radio channel between i and k, as in [9]. There is no need to consider the fast fading since we assume it to be averaged in our model.

Let $\psi(i,k)$ be the angle between positions $(x(i),y(i))$ and $(x(k),y(k))$ of node i and receiver k, respectively, and let $\psi(k,i)$ be the angle between $(x(k),y(k))$ and $(x(i),y(i))$. Also, let $\Delta_T(i,k) = |\varphi(i) - \psi(i,k)|$ and $\Delta_R(i,k) = |\varphi(k) - \psi(k,i)|$. Since $\psi(i,k)$, $\psi(k,i)$, $\varphi(i)$ and $\varphi(k)$ are angles indicating a direction, they must be relative to the same reference. We define a binary gain $G_{TR}(i,j)$, taking either the value 1 or 0, depending on whether the receiving node j can receive transmitted power from node i as per the width and direction of both antenna beams, by the following equation and shown on Fig. 1:

$$G_{TR}(i,j) = \left(\Delta_T(i,j) \le \frac{\theta(i)}{2}\right) \wedge \left(\Delta_R(i,j) \le \frac{\theta(j)}{2}\right). \quad (4)$$

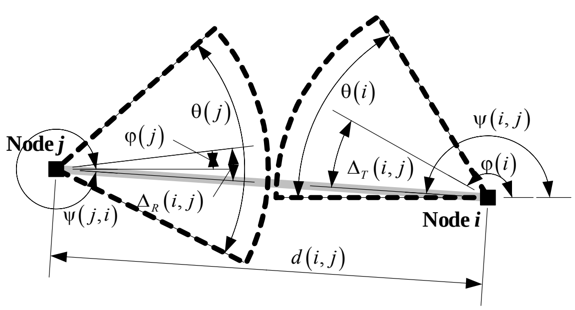

Fig. 1. Visual representation of the binary gain $G_{TR}(i,j)$ for a transmitting node i and a receiving node j.

The grey line shown on Fig. 1, joining nodes i and j, and passing through both sectors, represents the condition to have $G_{TR}(i,j) = 1$. If we let $P_T(i)$ be the transmission power of node i, and $P_R(i,j)$ be the received power at node j, then we have:

$$P_R(i,j) = P_T(i) G_T(i) G_R(j) G_\alpha(i,j) G_{TR}(i,j). \quad (5)$$

We define a binary gain $G_{TP}(i,p)$, taking either the value 1 or 0, depending on whether node i can cause interference to primary p as per the width and direction of its antenna beam, by the following equation:

$$G_{TP}(i,p) = \begin{cases} 1, & \text{if } \Delta_T(i,p) < \theta(i)/2 \\ 0, & \text{otherwise} \end{cases}. \quad (6)$$

$I_R(i,p)$ $\forall i,p$ is thus defined as:

$$I_R(i,p) = P_T(i) G_T(i) G_\alpha(i,p) G_{TP}(i,p). \quad (7)$$

Because of power attenuation as a function of distance, from a transmitting node, the received power might be so small at a receiving node or primary that it becomes irrelevant, even as interference, so we consider it to be null. Hence, we define the minimal non zero power P_{MNZ} as the power threshold from which any lower power is automatically set to null. When a transmitting node i uses the transmission power $P_T(i)$, we consider the distance from i's position, at which the power reaches P_{MNZ}, by neglecting the slow fading for such a small power and setting $C(i,j) = 1$, to be $r_{MNZ}(i)$ and defined as:

$$r_{MNZ}(i) = \sqrt[\alpha]{\frac{P_T(i) G_T(i)}{P_{MNZ}}}, \quad (8)$$

which is obtained from (5) with replacements: $P_R(i,j) \to P_{MNZ}$, $G_\alpha(i,j) \to r_{MNZ}(i)^{-\alpha} C(i,j)$, $G_R(j) \to 1$ and $G_{TR}(i,j) \to 1$.

D. *MANET communication*

Let γ_{SINR} be the SINR threshold for which a communication link with transmitting node i is considered successful toward a receiving node j, in the presence of other interfering transmitted power from $\forall h \in S_T | h \ne i$. The chosen constant noise power N_R, at the listening nodes, takes into account the interference generated by the primary antennas to the MANET, in addition to the thermal noise. We use roughly the same interference model as in [10], so that the condition for such a link to be successful is presented as follow (the link is said to be failed otherwise):

$$\frac{P_R(i,j)}{N_R G_R(j) + \sum_{\forall h \in S_T | h \ne i} P_R(h,j)} \ge \gamma_{SINR}, \quad (9)$$

A receiving node j is said to be in communication range of a transmitting node i if, by supposing there is no interference caused by any other transmitting node, it has its SNR $\ge \gamma_{SINR}$. The distance from i's location of this communication range to j's location is considered to be $r_{COM}(i,j)$. Let $r_{COM,e}(i)$ be the MANET estimate of $r_{COM}(i,j)$ which does not take the slow fading into account by setting $C(i,j) = 1$, so that it does not depend on j. $r_{COM}(i,j)$ and $r_{COM,e}(i)$ are defined as:

$$\left\{ \begin{array}{c} r_{COM}(i,j) = \sqrt[\alpha]{\dfrac{P_T(i) G_T(i) C(i,j)}{\gamma_{SINR} N_R}}, \\ r_{COM,e}(i) = \sqrt[\alpha]{\dfrac{P_T(i) G_T(i)}{\gamma_{SINR} N_R}} \end{array} \right\}, \quad (10)$$

which are obtained from (5) with replacements: $P_R(i,j) \to \gamma_{SINR} N_R G_R(j)$, $G_\alpha(i,j) \to r_{COM}(i,j)^{-\alpha} C(i,j)$ and $G_{TR}(i,j) \to 1$.

III. Proposed Interference Estimation Technique

From what has been discussed in section II, we now show how the MANET can use Ω_{UC} as a way to adequately overestimate the aggregate interference it causes to the primary antennas. We define $r_{INT}(i,p)$ as the interference radius from a transmitting node i to a primary p, which would result on $I_R(i,p)$. If $I_R(i,p) = 0$ then $r_{INT}(i,p)$ is not considered and can have any arbitrary value, otherwise $r_{INT}(i,p) = d(i,p)$. The MANET estimate of $r_{INT}(i,p)$ is $r_{INT,e}(i,p)$ so that if $I_{R,e}(i,p) = 0$ then $r_{INT,e}(i,p)$ is also not considered, otherwise $r_{INT,e}(i,p)$ is a bit more tricky to obtain and explained in the following.

The MANET considers that node i causes interference to primary p if its transmission sector overlaps p's UC. Indeed, if i lies outside p's UC, the MANET considers the interference that i causes to the closest point on p's UC circumference for the value of $I_{R,e}(i,p)$. On the other hand, if i lies inside p's UC, the MANET considers the interference that i causes to the same point as i's own location for the value of $I_{R,e}(i,p)$.

If i lies outside p's UC, let $\beta(i,p)$ be the angle formed by two lines tangent to the UC, on opposite sides of it, and joining at i, as shown on Fig. 2, and let $\Delta_{T,e}(i,p)$ be the MANET estimate of $\Delta_T(i,p)$.

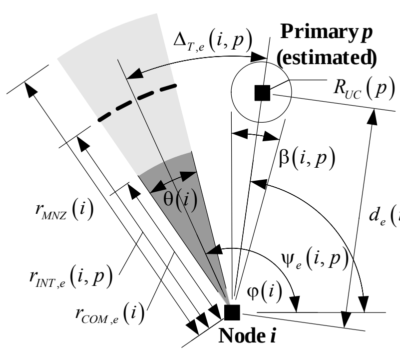

Fig. 2. Visual representation of the variables defining the relation between a transmitting node i and a primary antenna p (with $r_{INT,e}(i,p)$ having an arbitrary value).

Let $G_{TP,e}(i,p)$ be the MANET estimate of $G_{TP}(i,p)$, then:

$$G_{TP,e}(i,p) = \begin{cases} r_{INT,e}(i,p)^{\alpha}, & \text{if } \left(d_e(i,p) \le R_{UC}(p)\right) \\ 1, & \text{if } \left\{ \begin{array}{l} \left(d_e(i,p) > R_{UC}(p)\right) \wedge \\ \left(\begin{array}{l} \Delta_{T,e}(i,p) < \\ \left(\left(\dfrac{\theta(i) + \beta(i,p)}{2} \right) \right) \end{array} \right) \end{array} \right\} \\ 0, & \text{otherwise} \end{cases} . \quad (11)$$

$I_{R,e}(i,p)\ \forall i,p$ is thus defined as:

$$I_{R,e}(i,p) = P_T(i) G_T(i) r_{INT,e}(i,p)^{-\alpha} G_{TP,e}(i,p), \quad (12)$$

which is obtained from (7) with replacements: $I_R(i,p) \rightarrow I_{R,e}(i,p)$, $G_{\alpha}(i,p) \rightarrow r_{INT,e}(i,p)^{-\alpha}C(i,p)$, $C(i,p) \rightarrow 1$ and $G_{TP}(i,p) \rightarrow G_{TP,e}(i,p)$.

Note that the gain $G_{TP,e}(i,p)$ is not binary like its counterpart $G_{TP}(i,p)$. Indeed, the reason for having the first possible value of $G_{TP,e}(i,p)$ in (11) is to cancel the path loss effect in (12), in the special case where i lies inside p's UC. If $G_{TP,e}(i,p) = 0$ then $r_{INT,e}(i,p)$ is not considered, and if $G_{TP,e}(i,p) = r_{INT,e}(i,p)^{\alpha}$ then $r_{INT,e}(i,p)$ is cancelled in (12). The remainder of this section demonstrates how to find $r_{INT,e}(i,p)$ in the case where $G_{TP,e}(i,p) = 1$.

When i lies outside p's UC, two cases may occur giving $G_{TP,e}(i,p) = 1$, depending on the value of $\Delta_{T,e}(i,p)$, which influences the way we calculate $r_{INT,e}(i,p)$. The first case occurs if $0 \le \Delta_{T,e}(i,p) \le \theta(i)/2$, for which we have to find the value of $r_{INT,e}(i,p)$ such that the resulting arc on i's sector is tangent to p's UC. Then we simply have $r_{INT,e}(i,p) = d_e(i,p) - R_{UC}(p)$.

The second case occurs if

$$\Delta_{T,e}(i,p) \in \left] \frac{\theta(i)}{2}, \left(\frac{\theta(i)}{2} + \frac{\beta(i,p)}{2} \right) \right[, \quad (13)$$

for which the grey triangle formed on Fig. 3 can be used to find the value of $r_{INT,e}(i,p)$.

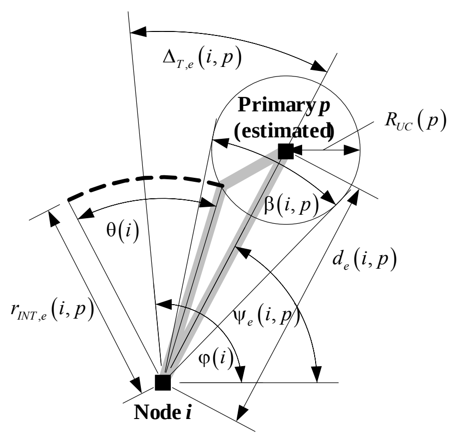

Fig. 3. Visual representation of the second case in calculating $r_{INT,e}(i,p)$ when $G_{TP,e}(i,p) = 1$.

We assign the grey triangle sides on Fig.3 to $a = r_{INT,e}(i,p)$, $b = d_e(i,p)$, $c = R_{UC}(p)$, and also the already known angle $\omega_C = \Delta_{T,e}(i,p) - \theta(i)/2$. Hence, we get the order 2 polynomial as a function of a, from the law of cosines:

$$a^2 - 2b\cos(\omega_C)a + (b^2 - c^2) = 0 , \quad (14)$$

with roots given by:

$$a = b\cos(\omega_C) \pm \sqrt{b^2(\cos^2(\omega_C) - 1) + c^2} . \quad (15)$$

The smallest root of this polynomial gives the length of a intersecting with p's UC without passing through it yet, while the greatest root gives the length of a passing through the circle before intersecting with it for the second time. Thus, we are only interested in the first root, and $r_{INT,e}(i,p)$ is given by:

$$r_{INT,e}(i,p) = d_e(i,p)\cos\left(\Delta_{T,e}(i,p) - \frac{\theta(i)}{2}\right) - \sqrt{\frac{\cos^2\left(\Delta_{T,e}(i,p) - \frac{\theta(i)}{2}\right) - 1}{d_e(i,p)^{-2}} + R_{UC}(p)^2}\,. \quad (16)$$

Once $r_{LIM,e}(i,p)$ is known, $I_{A,e}(p)$ and finally $I_{A,o}(p)$ for all $p \in S_P$ can be calculated from (12) and (1).

IV. Simulations

We have performed a Monte Carlo simulation, consisting of 10000 independent trials. All MANET nodes have the same transceiver beam width set to 60°. The reason behind this nodes beam width setting is to better asses the advantage of using smart antennas, while always ensuring a relatively high connectivity among nodes by choosing a narrow reception beam. For each simulation trial, the MANET nodes are randomly placed in a 2D simulation area following a uniform distribution. In the same area, the estimated locations of the primary antennas, i.e. $(\mu_x(p),\mu_y(p))$ $\forall p \in S_P$, are also placed following a uniform distribution. Then, a bivariate Gaussian distribution is used to randomly place the actual locations of the primary antennas, i.e. $(x(p),y(p))$, with means $(\mu_x(p),\mu_y(p))$ and standard deviations $\sigma_{xy}(p)$ on both axes, for all $p \in S_P$, where all $\sigma_{xy}(p)$ are randomly set from a uniform distribution. These actual primary antennas locations, i.e. $(x(p),y(p))$ $\forall p \in S_P$, may lie outside the simulation area but still be considered.

Communication links are established among MANET nodes in order to simulate the interference they cause to the primary antennas. Each node has its antenna beam steered directly toward its peer if it forms a link, otherwise no beam is used as such a node is thus considered idle. The appendix presents the algorithm we have created to ensure a relatively high MANET connectivity composed of only successful links. We call this algorithm: CSRRT (*Closest Successful Receiver to Random Transmitters*) and the results depend on the chosen link factor ξ. This algorithm is clearly suboptimal, but easy to simulate while giving a rather realistic connectivity. Although failed links are unfortunately abundant in real world communications, there is no need to consider them as they do not affect our simulation results in any way. For each MANET connectivity, $I_{A,o}(p)$ $\forall p \in S_P$ are calculated for $\Omega_{UC} = \{0.0, 1.0, 2.0, \ldots, 50.0\}$. Table I summarizes all identical input parameters used for each simulation trial.

TABLE I
SIMULATION INPUT PARAMETERS

MANET and Primaries	**Communication**
Simulation area = 1 km × 1 km	$N_R = 10^{-7}$ mw
Transceivers beam width = 60°	$\gamma_{SINR} = 63.0$ (18 dB)
Number of nodes = 25	$P_{MNZ} = 10^{-8}$ mw
Number of primaries = 5	$d_0 = 1.0$ m
$\sigma_{xy}(p) \sim U[10, 30]$ m	$\alpha = 2.1$
$\xi = 1.2$	$\sigma_C = 0.2$

A. *Results and interpretation*

The simulation results are presented on Fig. 4, representing $P(I_{A,o}(p) > I_{A,SM})$ $\forall p \in S_P$, but it is actually $P(I_{A,o}(p) \le I_{A,SM})$ $\forall p \in S_P$ which is displayed, as it is more appropriate for further explanation, and the former is simply the complement of the latter. Fig. 4 (a) and (b) both give exactly the same simulation results, but each allows a different interpretation to better assess the strength of our interference estimation technique. The curves seem to be very smooth, but this is due to the very high number of trials we used for the Monte Carlo simulation. The abscissa of Fig. 4 (a) actually reaches about 48.25 watts for the curve of $\Omega_{UC} = 50.0$ to reach an ordinate of 1.0, but has been clipped to not exceed the range of interest.

Fig. 4 (a) is best suited for the MANET to evaluate the interference it would cause to the primary network, given a specific value of Ω_{UC}. For example, the dashed lines on Fig. 4 (a) show that, by using $\Omega_{UC} = 35.0$, the MANET could meet requirement (2) with $\eta_{SM} = 0.8$ and $I_{A,SM} = 2.6$ watts. This can also be verified on Fig. 4 (b) with the dotted lines.

Fig. 4 (b) is best suited for the MANET to know the minimum value of Ω_{UC} it must use to respect the primary network's requirement. For example, the dashed lines on Fig. 4 (b) show that, in order for the MANET to meet requirement (2) with $\eta_{SM} = 0.7$ and $I_{A,SM} = 2.0$ watts, a minimum value of $\Omega_{UC} = 26.5$ of must be used. This can also be verified on Fig. 4 (a) with the dotted lines.

As can be seen on Fig. 4 (a), even for small negative values of $I_{A,SM}$, which would be however non sense for the primary network to impose to the MANET, a very small probability of having $I_{A,o}(p) \le I_{A,SM}$ still exists. In fact, this can occur relatively frequently if p's actual position lies outside its UC, but it becomes much more improbable as p's actual position gets inside its UC meanwhile far from the edge. The parameter σ_C of our propagation model also has a considerable impact on the value of $I_{A,o}(p)$: the greater the value of σ_C is, the greater is the probability of having $I_{A,o}(p) < 0$ for a small value of Ω_{UC}, as $I_A(p)$ would tend to be greater than $I_{A,e}(p)$. As Ω_{UC} increases however, $I_{A,o}(p)$ also tends to positively increase, so it becomes more likely that $I_{A,o}(p) \le I_{A,SM}$ for greater values of $I_{A,SM}$. The curve of $\Omega_{UC} = 0.0$ is very steep as a result of the very small values of $I_{A,o}(p)$ at this coefficient with our simulation input parameters.

On Fig. 4 (b), there is a remarkable distance between the curves for $I_{A,SM} = 0.0$ and 0.5 watts. At the very beginning of the abscissa, i.e. at $\Omega_{UC} = 0.0$, one can see that the curves for $I_{A,SM} = 0.0$ watts have a value of about 0.5 on the ordinate. This can be interpreted directly with the help of the curves for $\Omega_{UC} = 0.0$ on Fig. 4 (a). Indeed, about half the points composing this curve are for negative values of $I_{A,o}(p)$ $\forall p \in S_P$. The aforementioned distance thus comes from the fact that even for a very small value of $I_{A,SM}$ greater than zero, $P(I_{A,o}(p) \le I_{A,SM})$ $\forall p \in S_P$ gets very close to 1.0.

On Fig. 4 (a), one can see that $I_{A,o}(p)$ $\forall p \in S_P$ does not exceed the range of [-0.1, 0.3] watts for $\Omega_{UC} = 0.0$ during all simulation trials. In fact, this range is mainly related to the limits of the uniform distribution used to set $\sigma_{xy}(p)$ $\forall p \in S_P$, and clearly shows the importance of using an UC if the requirement (2) is to be considered by the MANET. Also,

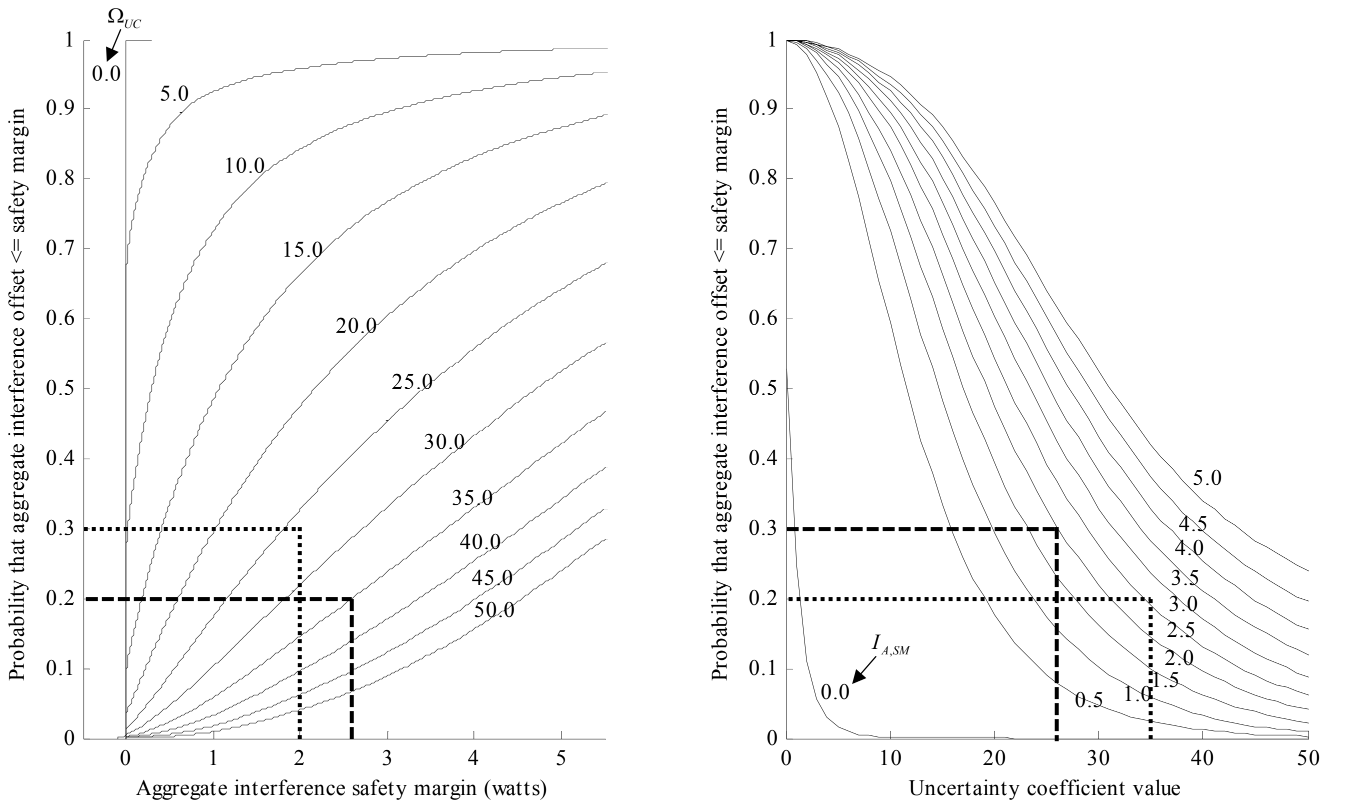

(a) (b)

Fig. 4. Empirical results of $P(I_{A,o}(p) \leq I_{A,SM})\ \forall p \in S_P$ for Ω_{UC} from 0.0 to 50.0 and $I_{A,SM}$ from 0.0 to 5.0 watts: (a) curves of Ω_{UC} as a function of $I_{A,SM}$, (b) curves of $I_{A,SM}$ as a function of Ω_{UC}.

without an UC, the difference between actual and estimated aggregate interferences cannot be very high when using as many as 25 nodes, since individual interference overestimation and underestimation may partly cancel each other if σ_C is reasonably low. Also, the curve for $\Omega_{UC} = 0.0$ is very steep because most values of $I_{A,o}(p)\ \forall p \in S_P$ are very close to zero either on positive or negative side and only few minority gets visibly distant from zero.

B. *Discussion*

The curves presented on Fig. 4 could have a very different scale by changing any of the simulation parameters. Augmenting the number of nodes or number of primary antennas increases exponentially the required simulation time. Most importantly, one should be aware that these results strongly depend on our antenna and propagation model as well as our CSRRT algorithm to generate communication links among MANET nodes. While using more precise models could be preferable, we can say without lose of generality that the resulting simulation curves for $I_{A,SM}$ and Ω_{UC} would follow the same trend as presented on Fig. 4, but with a different scale, added to the fact that the MANET could take even better decisions.

V. Conclusion

This paper has shown that by forcing a secondary wireless network to overestimate the aggregate interference it causes to a primary network, an interference safety margin can be respected following a chosen minimum probability. To the best of our knowledge, in the research field of cognitive radios and spectrum sharing, no such technique for allowing a smart-antenna-equipped secondary network to probabilistically ensure an interference protection margin to a primary network has previously been proposed yet. The knowledge by the secondary network of only a coarse probabilistic estimation of each primary antenna is our main work's originality.

Furthermore, our scheme could be applied to more conventional structured networks such as cellular networks, as well as to ad hoc networks such as sensors networks or MANET. It is also especially designed to promote the smart antenna technology, for which cognitive radio devices are very likely to be equipped in the near future. Finally, our scheme has been proven to bring significant advantages for the deployment of any secondary spectrum sharing system, as sustained by our simulation results.

ACKNOWLEDGMENT

The authors wish to thank Professor André Girard for his precious help in establishing the right antenna, interference and communication models.

APPENDIX

This appendix describes our CSRRT algorithm we use to generate a relatively high number of successful one-hop communication links between MANET nodes (see section II.D). A link is composed of only one transmitting and receiving nodes pair, respectively denoted as nodes i and j. For convenience, we ensure that each link's SNR equals $\gamma_{SINR}\xi$, where ξ is a chosen link factor (the interference is not considered to be part of the noise), so i's transmission power is set to:

$$P_T\left(i\right)=\frac{\gamma_{SINR}\xi N_R}{G_T\left(i\right)G_\alpha\left(i,j\right)}, \tag{17}$$

which is obtained from (5) with replacements: $P_R(i,j) = \gamma_{SINR}\xi N_R G_R(j)$ and $G_{TR}(i,j) = 1$.

We define a link as "accepted" if two rules are simultaneously satisfied (the link being "rejected" otherwise):

1. The link must be successful despite the presence of all other accepted links;
2. All accepted links must remain successful despite the acceptance of this link.

The algorithm is presented on Fig. 5. The objective is to fill the matrix M_{Links} with as much successful links as possible (no failed links).

```
N_Nodes = Number of MANET nodes
V_Nodes = Radom permutation of [1, 2, …, N_Nodes] //Unique ids
M_Links = [] //Empty matrix of all MANET links, dimension 0×2
V_Not_TX = []
for i = V_Nodes
  if (i ~= V_Nodes(end))
    V_Temporary = V_Nodes((i+1):end)∪V_Not_TX
  else
    V_Temporary = V_Not_TX
  end
  V_Temporary = Ascending ordering of V_Temporary w.r.t. i
          // i is the transmitter, and all elements of V_Temporary
          // are potential receivers (only one chosen), they
          // are thus ordered with respect to their respective
          // physical distance to i.  The remaining of the
          // algorithm tries to choose the closest node as the
          // receiver (if the link is successful).
  flag_successful = false;
  for j = V_Temporary
    if (i and j forms a successful link)
      M_Links(end+1, :) = [i, j]
      flag_successful = true
      break
    end
  end
  if (~flag_successful)
    V_Not_TX(end+1) = i
  end
end
```

Fig. 5. Our CSRRT algorithm to generate a relatively high number of successful MANET links, based on *Matlab* scripting language.

REFERENCES

[1] FCC, "Spectrum policy task force report. et docket no. 02-135," November 2002.
[2] J. Yang, "Spatial channel characterization for cognitive radios," MS Thesis, UC Berkeley, 2004.
[3] Senhua Huang, Zhi Ding, and Xin Liu, "Non-Intrusive Cognitive Radio Networks based on Smart Antenna Technology," *IEEE Global Telecommunications Conference (GLOBECOM)*, pp. 4862-4867, November 2007.
[4] D. Cabric, S.M. Mishra, D. Willkomm, R.W. Brodersen, A. Wolisz, "A Cognitive Radio Approach for Usage of Virtual Unlicensed Spectrum," *IST Mobile and Wireless Communications Summit, 14th*, June 2005.
[5] J.K. Nelson, M.U. Hazen, and M.R. Gupta, "Global Optimization for Multiple Transmitter Localization," *Military Communications Conference (MILCOM'06), IEEE*, pp. 1-7, October 2006.
[6] J.K. Nelson and M.R. Gupta, "An EM Technique for Multiple Transmitter Localization," *41st Annual Conference on Information Sciences and Systems (CISS'07), IEEE*, pp. 610-615, March 2007.
[7] P. Kontkanen, P. Myllymäki, T. Roos, H. Terri, K. Valtonen, and H. Wettig, "Topics in Probabilistic Location Estimation in Wireless Networks," *15th IEEE International Symposium on Personal, Indoor and Mobile Radio Communications (PIMRC'04)*, vol. 2, pp. 1052-1056, Barcelona, Spain, September 2004.
[8] S. Vasudevan, J. Kurose, and D. Towsley, "On Neighbor Discovery in Wireless Networks With Directional Antennas," *INFOCOM 2005, 24th Annual Joint Conference of the IEEE Computer and Communications Societies. Proceedings IEEE*, vol. 4, pp. 2502-2512, March 2005.
[9] M. Boutin, A. Benzakour, C. L. Despins, and S. Affes, "Radio Wave Characterization and Modeling in Underground Mine Tunnels," *IEEE Transactions on Antennas and Propagation*, vol. 56, no. 2, pp. 540-549, February 2008.
[10] P. Björklund, P. Värbrand, and D. Yuan, "Resource Optimization of Spatial TDMA in Ad Hoc Radio Networks: A Column Generation Approach," *INFOCOM 2003, 22th Annual Joint Conference of the IEEE Computer and Communications Societies, IEEE*, vol. 2, pp. 818-824, April 2003.

Adaptive Interference Cancellation Antenna System

Reuben Shar
Thales Australia
Locked Bag 3000, Potts Point NSW 2011
Garden Island, Australia
rashar@optusnet.com.au, reuben.shar@thales.group.com.au

***Abstract*—This paper describes simulation results of an adaptive interference cancellation system that creates an adaptive null at the interference source, by collaboration with the victim receiver. The adaptive cancellation is achieved by sampling the primary transmitted signal and applying phase and amplitude adjustments to cancel the interfering component from the primary transmit antenna. The paper describes an antenna simulation method to analyze and evaluate the cancellation performance. Both the source and victim antenna systems are simulated using Method of Moments simulation. The primary source antenna is an electronically steered phased array with steering along one axis. A fixed auxiliary antenna is positioned next to the primary antenna. The feed into this auxiliary antenna element is adjusted in phase and magnitude to achieve cancellation at the victim antenna. The cancellation ratio is evaluated for a number of steering positions of the primary source antenna. This system differs from more common cancellation schemes that are applied at the victim receiver antenna. The novel aspect of the system described in this paper, is that the interference cancellation processing is done at the source. The adaptive cancellation relies on feedback from the victim providing the interfering signal parameters. The control and processing system for adaptively maintaining the null are discussed. The advantage of applying antenna simulation techniques for the investigation of this problem is that fundamental performance and design issues can be assessed prior to implementation and installation.**

***Index Terms*—Adaptive, antenna, cancellation, interference, simulation.**

I. Introduction

Electromagnetic compatibility (EMC) of communications systems is an increasing problem. Communications systems deployment is on the increase, while at the same time there are constraints of frequency spectrum resources. The outcome is that mutual interference is on the increase. The performance of communications systems is directly related to the signal-to-noise ratio available, so any interference due to EMI/C issues directly degrades performance. In many situations there can be a degree of collaboration between an interfering source and a victim system. This paper describes simulation results of an adaptive interference cancellation system that creates an adaptive null at the interference source, by collaboration with the victim receiver. The adaptive cancellation is achieved by sampling the primary transmitted signal and applying phase and amplitude adjustments to cancel the interfering component from the primary transmit antenna.

II. The problem

Mutual interference has been experienced between communications systems on a ship. A Satellite communications system (Satcom) causes interference to other receivers onboard, nominated here as the 'victim'. Current satellite communications systems use high power and wide bandwidth modulation that may cause severe interference to sensitive receivers installed on the same platform. Frequency discrimination is not sufficient due to overlap between allocations and the high power used by the Satcom source. The Satcom system uses a steerable antenna that tracks the geostationary satellite. The design of the Satcom antenna steering makes sure that it does not illuminate the victim receiver with its main-lobe; however the side-lobe levels and reflections from the ship's structure are high enough to cause significant interference to the victim receiver.

III. Proposed Solution

A. Adaptive Cancellation System

It is proposed to develop an adaptive interference cancellation system that creates an adaptive null at the interference source, by collaboration with the victim receiver.

B. Principle of Operation

A sample of the source transmit waveform is fed to an auxiliary antenna. The initial sample level covers the side-lobes of the source antenna. The feed to the auxiliary antenna is modulated in amplitude and phase by a vector modulator using 2 channels being at phase quadrature over the interference bandwidth. A correlator that uses both a sample of the victim receiver output and the source transmitter controls the vector modulator 'weights'. The cancellation scheme is similar to that commonly used in radar coherent side-lobe canceller systems, with the exception that it is applied to the source transmitter, rather than at the victim side. The block diagram in Fig. 1 illustrates the concept.

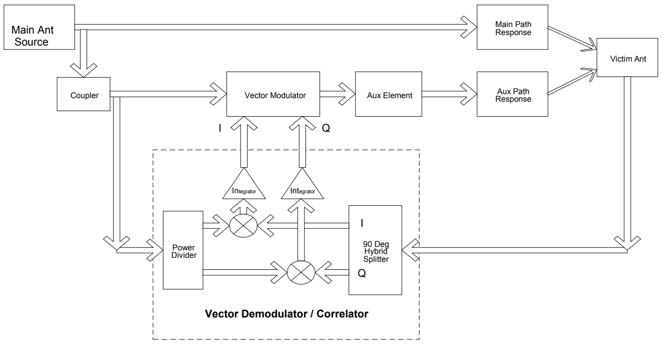

Fig. 1 - Block diagram

C. *Interference Source antenna*

The source transmitter uses a steerable antenna (Ref [9]). This antenna is modeled as a phase array with 8 x 8 elements, as shown in Fig. 2 and 3. The source array can be steered to track the satellite. An illustration of steering is shown in Fig 6.

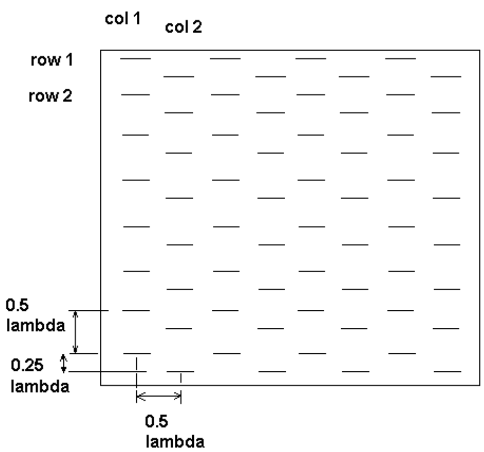

Fig. 2 - Source array structure

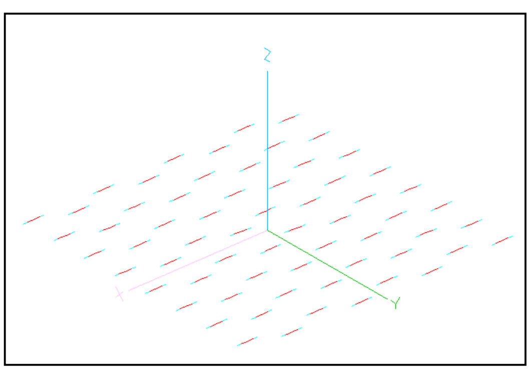

Fig. 3 – Source array model

D. *Victim antenna*

The victim antenna is an omni-directional antenna simulated as an array of 8 elements organized in a circle, as shown in Fig 4. This is a representation of a circular interferometer omni mode (Ref. [3], chap. 4), Ref. [4], [5], [7]).

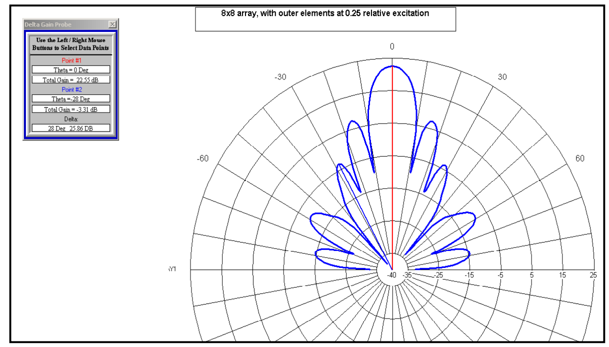

Fig. 4 - Source basic radiation pattern

E. *Auxiliary antenna*

The auxiliary antenna situated next to the source antenna, is a single dipole element, similar to the basic elements of the source phased array. It is located about 10 wavelengths from the centre of the source array. The primary source with the auxiliary antenna system is shown in Fig. 5.

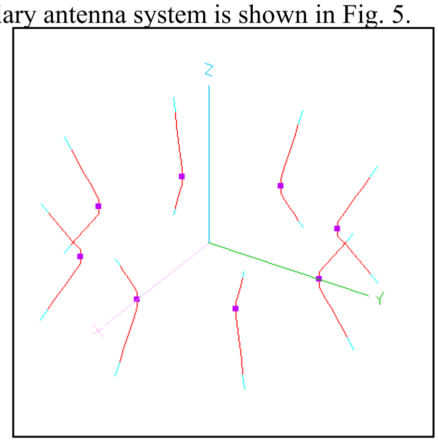

Fig. 5 - Model of victim receiver omni antenna

IV. SIMULATION RESULTS

A. *Simulation Models*

The geometry and source files for the simulation models have been calculated using a common spreadsheet. The antenna simulation uses a commercial Method-of-Moments antenna simulation software (GNEC, based on NEC, Ref [8]). The models are constructed of wire segments. The main array is shown in Fig. 2 and 3. The victim antenna is shown in Fig. 4. The auxiliary antenna element used for cancellation is shown with the main array in Fig. 5.

B. Simulation of individual antennas

Each antenna has been simulated separately, to ensure that the model resonates and has the expected pattern and gain. The simulation has been done at 8 GHz, which is similar to a real interference case that has prompted this work.

C. Simulation of independent contributions

Simulation of the received signal by the victim antenna has initially been done with each of the sources – the main antenna and the auxiliary antenna, applied independently.

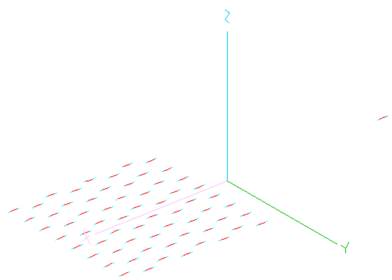

Fig. 6 - Source array with auxiliary antenna element

The response functions of the victim antenna to the main interference antenna and to the auxiliary antenna have been used in a simulated control system based on Fig. 1. The optimal excitation of the auxiliary antenna for a setting of drive and steering of the main antenna have been simulated on the Method-of-Moments software (GNEC, [8], [10]), providing confirmation of the cancellation ratio achieved.

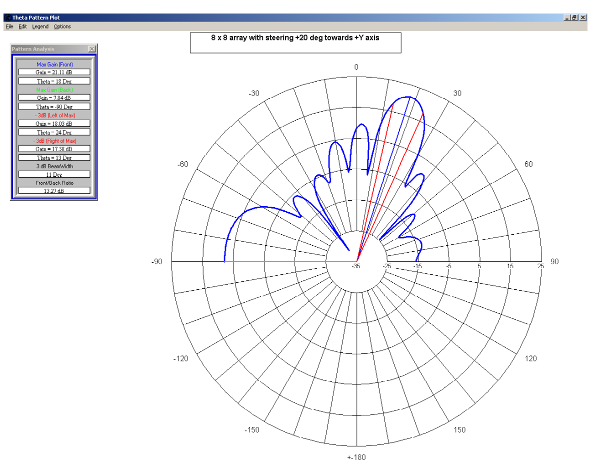

Fig. 7 - Source antenna with steering applied

The victim antenna response is calculated as a vector sum of the currents on the individual elements in the array. The small variations in the value are due to the finite accuracy of the antenna simulation software and the spreadsheet, as the variations across input phase and amplitude for the same steering value are less than 5 orders of magnitude than the mean.

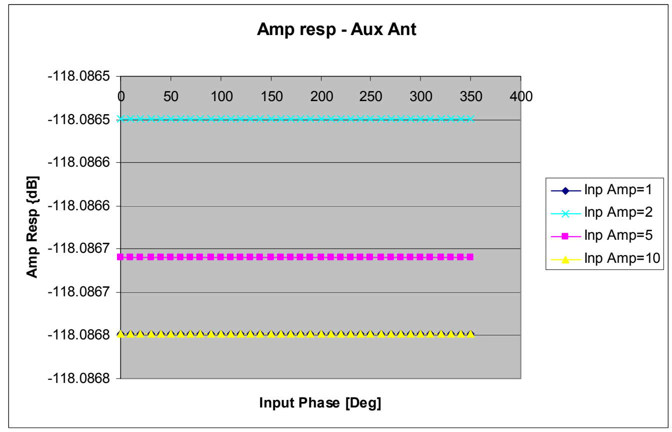

Fig. 8 - Auxiliary antenna amplitude response

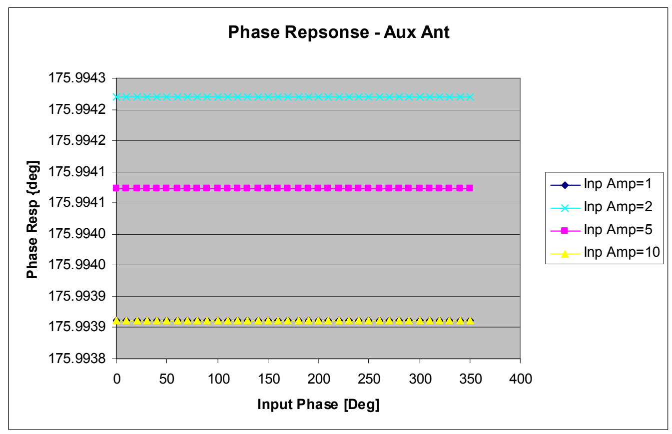

Fig. 9 - Auxiliary antenna phase response

As expected, the magnitude and phase response are impacted by the steering angle command to the main source array. The steering changes in a real situation are expected relatively slow, and the tracking time constants in the adaptive loop will be set for adaptation in real time.

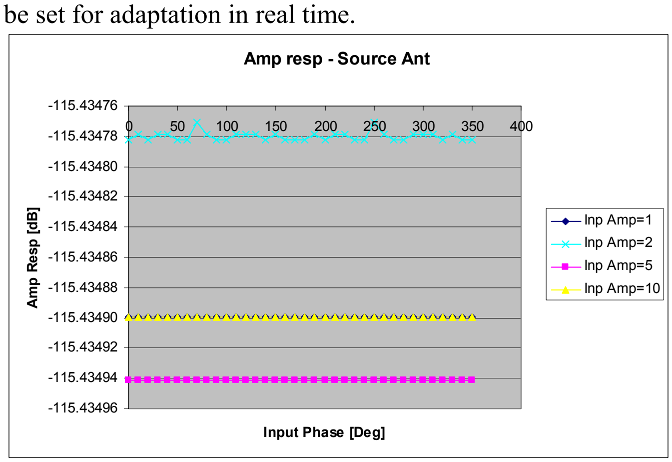

Fig. 10 - Main Source antenna amplitude response (20 deg steering)

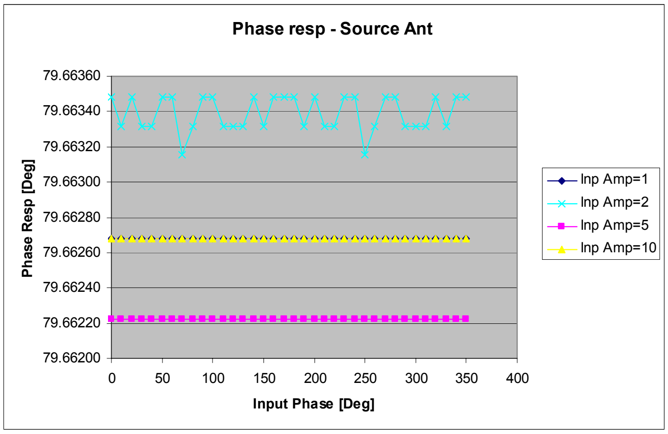

Fig. 11 - Main Source antenna phase response (20 deg steering)

D. Static cancellation setup

Each of the emitters, the main interference source and the auxiliary antenna, is turned on individually. The magnitude and phase at the victim antenna are measured for each of the contributors. The auxiliary element drive is calculated and adjusted to provide the same amplitude and opposite phase to the main antenna. The cancellation ratio is evaluated by calculation of interference levels with and without the auxiliary antenna contribution.
The individual contributions and cancellation ratio, in the 'best case' static conditions are shown in Table 1. The values shown are for a source magnitude of 10. In this case the control system response does not contribute to the cancellation performance.

TABLE 1 - CANCELLATION RATIO – STATIC, WITH SOURCE STEERING

	Victim received magnitude		
Steering [Deg]	Source Array only	Source and Aux after adjustment	Cancellation ratio [dB]
+10	2.35E-05	2.24E-10	-100.43
+20	1.69E-05	3.10E-10	-94.73
+30	1.16E-05	2.39E-10	-93.70

This compares with the cancellation achieved dynamically with the control system active, as shown in **TABLE 2**.

E. Control System Simulation

The control system uses the LMS (Least Mean Squares) principle to find a minimum at the victim output (see Ref. [1], Ref. [6], chap. 9). As the criterion for changing the vector modulator control weights is correlation with the interference source, desired signals would not be cancelled. Simulation of the control system could be done in many different ways. The methods used in this paper employ a common spreadsheet, in an iterative manner. The spreadsheet regards each of the signals as a phasor. It uses the previously established independent contributions of the interference source antenna and the auxiliary antenna to the victim receiver antenna. As the model uses down-conversion to baseband, the in-phase (I) and quadrature (Q) components can be handled separately. Correlation is implemented as phasor multiplication ('dot product'). Integration uses an approximation of the form

$$\text{Integ\_out}_{i+1}=\text{Integ\_out}_i * B + \text{Integ\_in} * A \qquad (1)$$

Where B is a positive fraction less than 1 and A is the Integration gain value.

The initial conditions of relative phase and amplitude at the auxiliary element have to be set for the desired cancellation to occur. If the initial conditions were set differently, the loop would seek a maximum instead of a minimum.
The following plots illustrate the cancellation over time (number of iterations) after starting the canceller from the same initial conditions, for different values of main source steering. This simulation has been performed for source antenna steering values of 10, 20 and 30 degrees from vertical. The source antenna magnitude has been the same as in the static simulation, 10. The cancellation achieved is lower than the static case shown in **TABLE 1**.

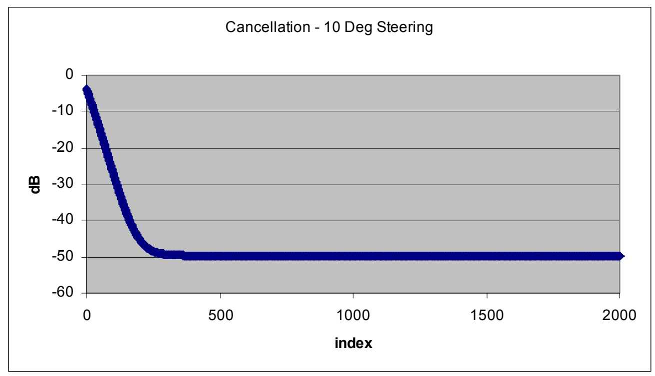

Fig. 12 - Cancellation Ratio with control system – Steering=10 Deg

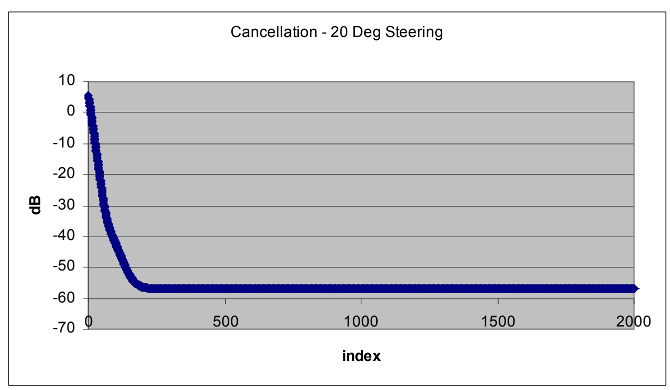

Fig. 13 - Cancellation Ratio with control system - Steering=20 Deg

The auxiliary (Aux) element magnitude and phase excitation values from the control system output after 1000 iterations have been then fed into the antenna simulation, with the resulting cancellation ratio values for 3 steering positions provided in **TABLE 2**.

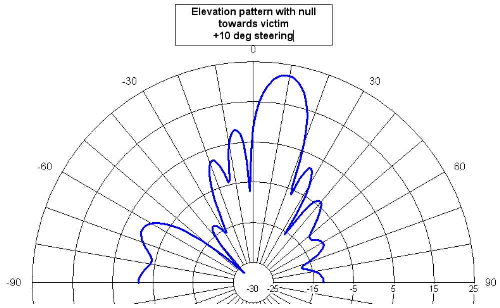

Fig. 14 - Elevation pattern with static cancellation at +10 deg steering

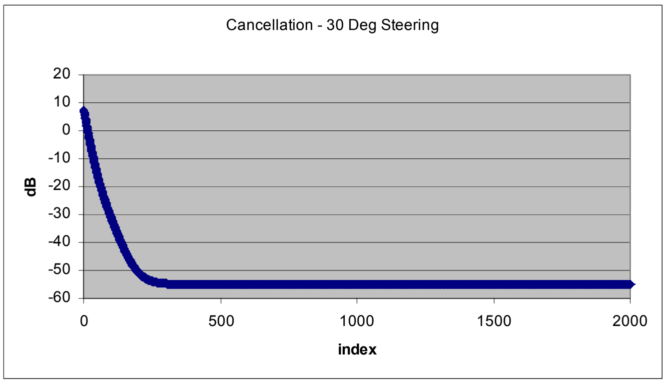

Fig. 15 - Cancellation Ratio with control system - Steering=30 Deg

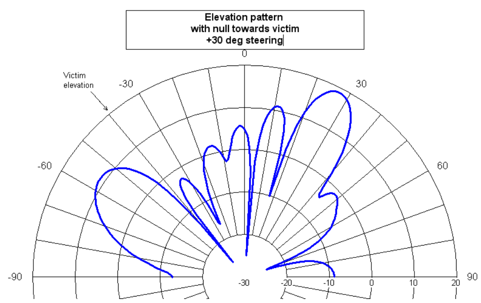

Fig. 16 - static cancellation at +30 deg steering

TABLE 2 - CANCELLATION RATIO – WITH CONTROL SYSTEM

	Victim received magnitude		
Steering [Deg]	Source Array only	Source and Aux after adjustment	Cancellation ratio [dB]
+10	2.35E-05	7.76E-08	-49.62
+20	1.69E-05	2.37E-08	-57.08
+30	1.16E-05	2.04E-08	-55.08

The results in Table 2 demonstrate that the control system has provides the correct weights for the auxiliary element path, to achieve the desired interference cancellation outcome. The results are similar to those predicted by the control system simulation in **Fig.** , **Fig.** and **Fig.** , but not as high as those in **TABLE 1**, still providing significant degree of cancellation. The cancellation achieved with the control system and antenna simulation is lower than that in the static case, probably due to precision limitations in the control system.

The control system weights have been evaluated for a range of main antenna amplitudes, for a steering setting of +30 degrees. These weights have been fed into the antenna simulation, providing the following cancellation results as a function of input amplitude.

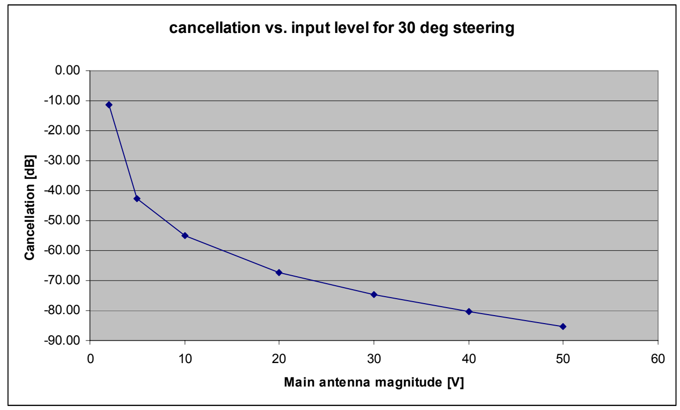

Fig. 17 - Cancellation over input level (+30 deg steering)

The simulation results in **Fig.** demonstrate an input dynamic range of 28 dB, which is likely to be more than enough to cover the amplitude range presented by significant side-lobes of an interfering antenna. The lower cancellation at low input levels is probably due to the finite precision of the simulation. When the interference level is already low, a lower degree of cancellation may be allowed without degradation of the victim system.

V. Conclusion

An effective interference cancellation system has been achieved, using collaboration between a victim receive antenna and an interference source. This interference cancellation concept creates a spatial null at the interference source antenna, reducing adverse impact on the victim system. This technique is effective also in the case of spectral overlap between the two systems, ruling out conventional frequency domain filtering. It can be used as one of the means for increased spectral reuse.

VI. References

[1] IEEE transactions on antennas and propagation, Appelbaum and Chapman, 1976.

[2] Principles of Adaptive Filters and Self-learning Systems. Anthony Zaknich, Springer, 2005

[3] Electronic Intelligence: The Interception of radar Signals. Richard G. Wiley, Artech House 1985.

[4] "Circular Interferometer Simulation", R. Shar, poster at the 2007 AOC convention.

[5] "Simulation of Polarizer Impact on Circular Interferometer performance", R. Shar, IEEE CSE-08 conference.

[6] Communications Receivers, 2nd Edition, Ulrich L. Rohde, Jerry Whittaker, T.T.N. Bucher, McGraw-Hill, 1996)

[7] Microwave Passive Direction Finding, S. E. Lipsky, Scitech 2004.

[8] http://www.nittany-scientific.com/

[9] Introduction to Airborne Radar, Second Edition, George W. Stimson, Scitech Publishing, 1998.

[10] Recent Advances to NEC: Application and Validation, G. J. Bourke, Lawrence Livermore National Laboratory, 3 March 1989.

Remarks on Using a Max-plus Model for TCP in a Wireless Network

Rodrigo Andreola
Federal University of Technology-Paraná
UTFPR/CPGEI
Av. Sete de Setembro 3165 - 80230-901
Curitiba - PR - Brazil
rodrigo.andreola@vono.net.br

Ricardo Lüders
Federal University of Technology-Paraná
UTFPR/CPGEI
Av. Sete de Setembro 3165 - 80230-901
Curitiba - PR - Brazil
luders@utfpr.edu.br

Keiko V. Fonseca
Federal University of Technology-Paraná
UTFPR/CPGEI
Av. Sete de Setembro 3165 - 80230-901
Curitiba - PR - Brazil
keiko@utfpr.edu.br

***Abstract*—This paper provides a performance analysis of a max-plus based model for TCP protocol in a wireless network. Initially proposed for cabled networks, this model is unusual if compared to other TCP analysis found in the literature. Many of them are based on stochastic methods instead of using the deterministic approach of max-plus model. Transmission rates calculated by a max-plus model are compared to those obtained by simulation. Issues that affect the performance of TCP protocol over wireless networks are also discussed and guidelines for tuning of parameters in max-plus model are provided.**

***Index Terms*—Wireless network, TCP protocol, performance network analysis, max-plus algebra.**

I. Introduction

Some applications executing over computer networks require a minimum quality of service (QoS) specified by pre-determined parameters and set by a service level agreement (SLA). These applications require models for verifying the efficiency of admission control techniques, and performance evaluation according to a SLA, among others. Stochastic models have been widely chosen for these purposes. Computer networks can be viewed as a discrete event system where packets arrivals and departures (events) can be suitable modeled by different discrete event approaches. Among them, discrete event systems subject to only synchronization phenomena have been successfully modeled by max-plus algebra [1]. An important example of computer network modeling based on a similar algebra is the set of techniques based on min-plus algebra called Network Calculus [2] and [3]. Network Calculus provides (worst case) bounds for network traffic that can be used to allocate resources and estimate network performance through an algebraic calculation.

In particular, many applications in the Internet depend on a reliable data transport done by TCP protocol (Transmission Control Protocol) [4]. Due to its importance, different analysis has been proposed for studying its adaptive flow control behavior [5], [6], and [7]. Among them, a model for TCP using a max-plus algebra proposed by [8] describes the behavior of a packet flow transmitted over TCP. The performance results published in [8] are comparable to ones obtained by a simulation model. However, they were obtained only for cabled networks.

The broad application of wireless communication networks has yielded to a more complex analysis task. It is not always possible to use analytical models without imposing simplifications. Discrete event simulation models for packet level are used to analyze flows and network performance. However, the complexity of these models is proportional to the huge amount of packets that have to be simulated for resulting in reliable values. Therefore, its using is quite questionable for huge networks. Recently, [9] has reported both complexity and time execution gains for the analysis of TCP behavior using models based on Network Calculus compared to ones obtained by discrete event and fluid models.

TCP protocol provides reliable end-to-end transport and it is widely adopted as transport protocol for web applications. The protocol detects congestion events by controlling ordering and arrival time of acknowledgment messages setting its flow transmission rates to provide fairness on the network resource sharing. However, since physical and medium access characteristics are not considered by the TCP, transmission failures can be erroneously mistaken as network congestion events in wireless networks. A false detection of congestion causes TCP to adjust (reduce) its flow transmission rate and thus the network throughput performance.

This paper analyzes the application of a model based on max-plus algebra to study the behavior of TCP flow segments transmitted over a wireless network. Besides, it discusses aspects of parameter tuning and limitations of this model regarding other modeling techniques. The results for max-plus model are compared to ones obtained by discrete event simulation. Since this model is linear in max-plus algebra, complex topologies can be represented by a serial composition of simpler subsystems through a simple matrix multiplication.

This paper is organized as follows. Section II presents the max-plus model for TCP proposed by [8] for cabled networks. Section III states necessary parameters for applying the proposed model of Section II to a wireless network. Section IV compares results obtained by the max-plus model to ones obtained by a simulation model. Finally, concluding remarks are given in Section V.

II. A MAX-PLUS MODEL FOR TCP

A max-plus algebra R_{max} is an algebraic structure defined in the set of real numbers added by -∞ (minus infinity) which represents the null element. Operations for addition (represented by symbol $\oplus$) and multiplication (represented by symbol $\otimes$) are computed by maximization and sum operations, respectively [1]. Although it shares many properties of the classical algebra, addition is idempotent ($a \oplus a = a$) in max-plus algebra. Sometimes it is also referred to as an idempotent semiring. This algebraic structure is suitable to model synchronization phenomena where events (departure and arrival of packets) should be delayed by a sum of time values or synchronized by a maximization of them. In the following, a transmission of packets controlled by TCP is described by a max-plus linear model.

A. Network representation

In the max-plus model proposed by [8], a packet network is represented by K routers connected in sequence as depicted in Fig. 1. The first router (source) sends a reference data flow to be transferred to the last router (destination) using TCP as a transmission control. Although TCP allows bidirectional connections between nodes, the max-plus model assumes a unidirectional connection by considering that a similar reverse path exists.

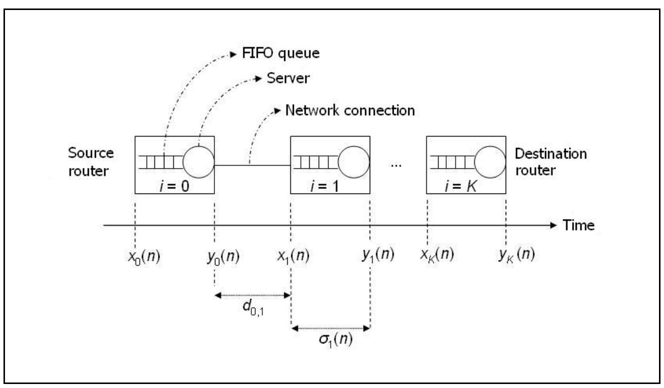

Fig. 1. A network as a connection of K routers.

Routers in Fig. 1 are identified by $i = 0,1,2,...,K$ with $i = 0$ corresponding to the source router and $i = K$ to the destination router. Each router is modeled by a FIFO queue served by only one server which can attend not only packets from the reference flow but also from data flows due to cross traffic. A packet n arriving in a router i spends an aggregated service time $\sigma_i(n)$ computed since its arrival until its departure from router. Thus it includes both packet processing time and time necessary to process crossing traffic. Routers are connected each other by circuits with a defined time latency $d_{i,j}$ from router i to j. The number of packets sent by the source router to network is controlled by adjusting a TCP window [10].

This model also considers that a delivery acknowledge packet *ACK* follows a different path from destination to source as if they would be directly connected through a private circuit. Thus *ACK* packets do not follow a reverse path regarding to the original TCP connection, but a different path between destination and source. Although this assumption simplifies what really occurs in practice, it allows represent time transmission of *ACK* packets as a simple time latency $d_{K,0}$.

B. Equations for packet temporization

The model used to quantify temporal performance of a TCP flow is composed by a set of equations that determines output times for each packet of the reference flow in each router. These output times for packets are computed by considering a dynamical behavior of TCP window as well as service time of routers and time latency of network connections.

A packet n arrives in a router i at time $x_i(n)$ and leaves it at time $y_i(n)$. The difference between arrival and departure times is the aggregate service time $\sigma_i(n)$ for packet n in router i. Therefore, $y_i(n) = x_i(n) + \sigma_i(n)$.

Since TCP dynamically controls the amount of packets sent to the network by adjusting its transmission window, a new window value is computed when an *ACK* is received (a delivery confirmation) or when a timeout occurs. A TCP window size v_n is computed according to information from packet n (delivery success or timeout) and it is used to transmit a packet n+1. Thus v_{n-1} is the window size used to transmit a packet n.

By considering a previously known sequence of values $\{v_n\}$ and an aggregate service time $\sigma_0(n)$ equal to zero (by default), output times for a packet n in all routers can be stated in max-plus algebra by

$$y_0(n) = y_K(n - v_{n-1}) \otimes d_{K,0} \quad (1)$$

$$y_i(n) = [y_{i-1}(n) \otimes d_{i-1,i} \oplus y_i(n-1)] \otimes \sigma_i(n) \quad 1 \le i \le K \quad (2)$$

where: $y_i(n)$ is the output time of packet n in router i; v_{n-1} is the actual TCP window size for packet n; $d_{K,0}$ is the transmission time between destination router and source router (in particular, $d_{i-1,i}$ is transmission time between router i and i-1); $\sigma_i(n)$ is the aggregate service time for packet n in router i.

Therefore, the time instant when a packet n is sent to the network is determined by (1), and a new packet can be sent to the network after receiving an *ACK* from a previous sent packet. The actual TCP time window v_{n-1} determines which previous packet will be used. For instance, if n=5 and v_{n-1}=2, then packet number 5 should be sent to the network when an *ACK* for packet number 3 is received. Since $\sigma_0(n) \equiv 0$ by default, this new packet is sent to the network at the same time of *ACK* arrival. This time corresponds to the output time of packet number 3 in the last router added by *ACK* latency.

Similarly, the network behavior is modeled by (2) since it determines output times for packets leaving each router following the source router. The network behavior is represented by transmission times $d_{i-1,i}$ between routers as well as by the aggregate service time $\sigma_i(n)$ of each router. The output time of a packet n leaving a router i in (2) is obtained by adding (through max-plus multiplication) its respective aggregate service time $\sigma_i(n)$ to the maximum time (obtained by max-plus addition) between its arrival time $y_{i-1}(n) \otimes d_{i-1,i}$ in router i and the departure time $y_{i-1}(n-1)$ of a previous packet n-1 in router i. The arrival time $y_{i-1}(n) \otimes d_{i-1,i}$ of n in router i is obtained by summing (max-plus multiplication) its output time from a previous router i-1 to the time latency $d_{i-1,i}$ between routers i-1 and i.

Transmission times between routers are typically constants in a network, and the aggregate service time can be determined according to router features and current cross traffic. Therefore, output times for packets of the reference flow can then be obtained for each router in the network by a recursive form of (2).

Equations (1) and (2) can also be reformulated in a vector form whose components represent the output time evolution of each packet in each router. This vector form given by (3) explicitly states model linearity in max-plus algebra (see [8] for further details).

$$Z(n) = A_{v_{n-1}}(n) \otimes Z(n-1) \quad n \geq 1 \tag{3}$$

where:
$Z(n) = (Y(n) \mid Y(n-1) \mid \ldots \mid Y(n-w^*-1))$, $Z(n) \in \mathbb{R}^m_{\max}$, w^* is the largest TCP transmission window size observed since the beginning of packet transmission until packet n, and $m=Kw^*$. $A_{v_{n-1}}(n)$ is a convenient matrix that depends on intervals between transmission and service of packet n as well as on the current transmission window size v_{n-1}.

Therefore, the network can be characterized by output times of packets in each router through a linear recursive equation (in max-plus algebra) as given by (3). Matrix A contains information about various aggregate service times and transmission times between routers. Thus it is basically composed by network information determined even before a TCP transmission begins.

This linear model allows to obtain more complex topologies by composing simple subsystems in series through a multiplication of subsystem matrices.

III. Using the Max-plus Model for a Wireless Network

By specifying proper parameters, the max-plus model can provide time instants for all packets in the network. In the literature, results obtained for a cabled network using a max-plus model were compared to simulation ones [8]. In the following we propose to adopt the same model, but applied to a wireless network, and discuss aspects that can explain differences found.

A similar topology of Fig. 1 is used in a wireless *ad-hoc* network. This network uses a multi-hop mechanism for communicating two nodes. Therefore, the max-plus model can also be applied. By using an approach similar to [8], performance measures obtained by the max-plus model are compared to ones obtained by a simulation model. The simulation model was implemented using a default routing protocol for static nodes in *ad-hoc* networks. Node mobility was not considered in this work, although it could be included in simulation. The results were obtained by using a toolbox for max-plus computations [11] and NS-2 simulator [12]. Further details can be found in [13].

IV. Results

Results were obtained for two cases considering a wireless *ad hoc* network composed by five nodes. Simulation parameters are shown in Table I. They are typical ones (default values) used by NS-2 for IEEE 802.11 network and TCP.

TABLE I
Simulation parameters.

Parameter	Value
Link protocol for wireless network	802.11
Transmission rate wireless network	2 Mbps
Router protocol	Destination-Sequenced Distance Vector - DSDV
Node distance	250 m
TCP data packet size	1210
TCP ACK packet size	40
Transmission queue size	50 packets

A. Case I

Parameters used for max-plus model are shown in Table II. They are specified according to the simulation parameters.

TABLE II
Parameters for max-plus model (case I).

Parameter	Value
Destination router index (K)	4
Latency between routers ($d_{0,1}$, $d_{1,2}$, $d_{2,3}$, $d_{3,K}$)	10ms
Aggregate service time for routers ($\sigma_i(n)$)	5ms
ACK return time ($d_{K,0}$)	1ms

Routers are numbered from 0 to K=4. The latency of 10ms between routers was estimated by simulating a typical TCP transmission. The aggregate service time of 5ms for routers was calculated by considering links of 2Mbps and packets of size 1250 bytes (10000 bits/2Mbps=5ms to be processed). An value of 1ms for *ACK* return was considered for both max-plus model and simulation.

The max-plus model also requires a TCP window dynamics. In this work, TCP windows start with value 1 and change according to Tahoe method [10] without low-start. However, the window is limited to a constant value as soon as traffic congestion is detected. This is accomplished by using a Rate Based Loss Detection method according to [8].

A total simulation time of 200s was considered. The first half of simulation time was used for stabilization of router protocol. Therefore, a TCP transmission is only started at time 100s avoiding routing traffic interference.

Results for max-plus model and simulation can be compared by means of Table III where transmission rates are given in packets by second. They are mean transmission rate values obtained during TCP transmission until an *ACK* for packet in the first column of Table III is receipt.

TABLE III
COMPARISON OF TRANSMISSION RATES (CASE I).

Packet	max-plus (pct/s)	simulation (pct/s)
5	26,60	20,08
10	38,61	20,58
50	79,37	20,89
100	111,35	20,17
250	151,69	19,66
500	172,53	19,85
1000	185,25	19,58

It can be seen from Table III that max-plus values are quite different from those obtained by simulation. While the aggregate service times for routers in max-plus model are set to represent a transmission rate of 2Mbps, the effective transmission rate observed by simulation between two nodes is quite smaller. This can be explained by a shared transmission rate among nodes due to concurrency of transmission channel. Since the max-plus model does not consider a transmission concurrency it is not able to capture this behavior without a suitable tuning of its parameters. Moreover, it does not consider a proper dynamics of TCP window size. The protocol IEEE 802.11 drops a packet when many channel reservations fail or when no *ACK* is received after many transmissions. These dropped packets are interpreted as congestion by TCP protocol which decreases its corresponding window size. However, TCP window size remains unchanged in the max-plus model after reaching its largest size without congestion.

B. *Case II*

The parameters of max-plus model are changed for capturing a more realistic behavior. The max-plus model has two potential parameters to be changed: time latency and aggregate service time. Since time latency only depends on the channel speed, the aggregate service time can be increased to represent channel concurrency. A new value of 15ms for the aggregate service time was experimentally been obtained as shown in Table IV.

Although this value is experimental and obtained for matching simulation results, it shows that a max-plus model is able to represent a wireless network behavior. Moreover, dynamics for TCP window size are also been modified. Instead of using a bounded time window size limited by traffic congestion, a window size of 2 (constant) packets was used.

TABLE IV
PARAMETERS FOR MAX-PLUS MODEL (CASE II).

Parameter	Value
Destination router index (K)	4
Latency between routers ($d_{0,1}$, $d_{1,2}$, $d_{2,3}$, $d_{3,K}$)	10ms
Aggregate service time for routers ($\sigma_i(n)$)	**15ms**
ACK return time ($d_{K,0}$)	1ms

Although it seems to be quite restricted, a window size of 2 packets is suitable for a wireless network of four hops since no more than two nodes can transmit at the same time. For instance, if node 0 is transmitting, then node 1 cannot transmit since it is receiving. Node 2 cannot transmit either since it may cause collision in node 1 reception. Therefore, only node 3 can simultaneously transmit with node 1.

As shown in Table IV, results are drastically changed by modifying the aggregate service time.

TABLE IV
COMPARISON OF TRANSMISSION RATES (CASE II).

Packet	max-plus (pct/s)	Simulation (pct/s)
5	15,77	20,08
10	16,53	20,58
50	19,05	20,89
100	19,42	20,17
250	19,65	19,66
500	19,72	19,85
1000	19,76	19,58

Note that transmission rates stabilizes on 19 pct/s after packet number 50. This shows that changes made on parameters of max-plus model are able to reflect the network congestion by limiting its effective transmission rate.

Values for transmission rates show little difference (about 1%) by comparing max-plus and simulation models along to the TCP transmission. It thus suggests that a max-plus model can be applied for modeling a TCP transmission over a wireless network since suitable parameters are used. Basically, an effective transmission rate should be correctly represented as well as a proper change in TCP window size.

V. FINAL COMMENTS

This paper presents a detailed analysis of using a max-plus model for TCP found in the literature for a wireless network. Although the max-plus model was proposed to be used with a cabled network, it can also be applied to a wireless network. The point is that aggregate service time plays an important role to represent a decreasing in transmission rate due to the transmission concurrency between nodes. The aggregate service time in max-plus model should be increased while keeping latency time unchanged. Various effects observed in wireless networks can thus be properly modeled. Although the actual aggregate service time was experimentally obtained, it can be determined in the future from operational network conditions.

ACKNOWLEDGEMENT

This work is supported by Fundação Araucária and Fundo Setorial de Infra-Estrutura (CTINFRA)-MCT/CNPq under grant 233/07-11015 (FUNTEF-PR).

REFERENCES

[1] F. Baccelli, G. Cohen, G. Olsder, and J. Quadrat, *Synchronization and Linearity: An Algebra for Discrete Event Systems*, New York: John Wiley, 1992.

[2] J. Y. Le Boudec and P. Thiran, *Network Calculus: A Theory of Deterministic Queuing Systems for the Internet*, Lec. Notes in Comp. Science Series, n. 2050, New York: Springer, 2001.

[3] M. Daniel-Cavalcanti, *Modelagem e Determinação de Parâmetros de Desempenho de Redes de Comunicações Através da Álgebra de Dióides*, PhD Thesis, Unicamp, Campinas, 2008 (in Portuguese).

[4] IETF RFC: 793- Transmission Control Protocol, Darpa, September 1981.

[5] Lakshman, T. and Madhow, U. (1997) "The performance of TCP/IP for networks with high bandwidth-delay products and random loss", IEEE/ACM Transactions on Networking, v. 5 n. 3, p. 336-350.

[6] Mathis, M., Semke, J., Mahadavi, J., Ott, T. (1997) "The macroscopic behavior of the TCP Congestion Avoidance algorithm", Computer Communications Review, v.27, n.3.

[7] Padhye, J., Firoiu, V., Towsley, D. (1999) "A stochastic model of TCP Reno congestion avoidance and control", CMPSCI Technical Report, n. 99-02, University of Massachusetts.

[8] F. Baccelli and D. Hong, "TCP is max-plus linear and what it tells us on its throughput", In *Proceedings of ACM SIGCOMM'00*, Stockholm, 2000, pp. 219-230.

[9] K. Hwangnam and J. C. Hou "Network calculus based simulation for TCP congestion control: theorems, implementation and evaluation", In *INFOCOM 2004*, Hong Kong, March 2004, pp. 7-11.

[10] V. Jacobson, "Congestion avoidance and control", In *Proceedings of ACM SiGCOMM '88*, Stanford, August 1988.

[11] J. Stanczyk, *Max-Plus Algebra Toolbox for Matlab and GNU Octave*, v.1.5. Otto-von-Guericke Universität Magdeburg, 2005.

[12] K. Fall and K. Varadhan, *The ns Manual*, 2007. Available at http://www.isi.edu/nsnam/ns/ns-documentation.html.

[13] R. Andreola, *Análise de um Modelo TCP Max-plus Aplicado a uma Rede Sem Fio*, Master Thesis, UTFPR, Curitiba, 2007 (in Portuguese).

The Forward Link Performance Study of the WiMAX System Under Different Schedulers

Leandro Bento Sena Marques
Venturus Innovation & Technology Center
P.O. Box 13092-123
Campinas - SP - Brazil
leandro.marques@venturus.org.br

Shusaburo Motoyama
State University of Campinas - UNICAMP
P.O. Box 6101 - 13083-970
Campinas - SP - Brazil
motoyama@dt.fee.unicamp.br

Abstract— **The forward link performance study of the WiMAX system is presented in this paper. The study is carried out using HTTP traffic model and several different schedulers. The average packet delay, the throughput and packet loss percentage are analyzed through simulation in function of traffic load. The schedulers adopted in this study are Max C/I (Maximum Carrier Interference), PF (Proportional Fair) and Pr/PF (Priority Proportional Fair). The results show that standardized IEEE 802.16e system allows data transmission at high bits rates. Moreover, it was showed that depending on the chosen scheduler, it is possible to assure the QoS for users with high and low priority in WiMAX system.**

Index Terms— **WiMAX System and schedulers PF, Max C/I, Pr/PF.**

I. INTRODUCTION

In last years, the rapid growth of new services based on multimedia applications, such as VoIP (Voice over IP), video conference, VoD (Video on Demand) has demanded higher bandwidth and new technologies for wireless access network. One of the technologies that has been created is the IEEE 802.16[1] standard, also known as Worldwide interoperability for Microwave Access (WiMAX).

The IEEE 802.16 standard provides high data rates, pre-defined quality of Service (QoS) framework and low cost in comparison with others technologies based on fixed cable such as Digital Subscriber Line (DSL). Moreover, this standard can be used to connect home networks and business LANs to the Internet[3]. The current version of IEEE 802.16e[2] added new features and necessary attributes to support mobile applications.

Many papers have been published with focus on performance evaluation of WiMAX system [3]-[8]. In [4], it is evaluated 802.16-2004 standard that is intended to fixed broadband wireless access. The main result of this paper is that system capacity is strongly dependent on its configuration, e.g. channel size, frame duration, coding rate, etc.

In another study presented in [5], the IEEE 802.16e system is compared to 3GPP UMTS HSDPA by using simulations. The simulation results indicate that the 802.16e system using 70/30 Time Division Duplex (TDD) frame provides approximately the same downlink system throughput performance as HSDPA with approximately 40%-50% higher spectral efficiency. However, control channel overhead and uplink capacity limitation remain as open issues. Furthermore, it is considered only proportional fair (PF) scheduler as alternative scheduler to improve QoS of system.

A simulation study of the IEEE 802.16 MAC protocol operated with the WirelessMAN-OFDM air interface and with full-duplex stations is presented in [6]. The results show that the performance of the system (downlink/uplink), in terms of throughput and delay, depends on several factors. These include the frame duration, the mechanisms for requesting uplink bandwidth, and the offered load partitioning, i.e., the way traffic is distributed among SSs, connections within each Subscriber Stations (SS), and traffic sources within each connection. The schedulers adopted in the study are: Deficit Round Robin (DRR) as the downlink scheduler and Weighted Round Robin (WRR) for uplink scheduler.

The works presented in [7]-[8] emphasize improvements in uplink schedulers and QoS architecture of WiMAX system. In [3] it is proposed a queue-aware uplink bandwidth allocation scheme which is able to adjust the allocated bandwidth adaptively according to the queue state. However, in current context of IP networks results are inaccurate due to use of Poisson traffic sources during computer simulations.

In this paper, the IEEE 802.16e system is evaluated through the queuing system considering Hypertext Transfer Protocol (HTTP) traffic model proposed in [9]. The system throughput, the average delay of the packets and loss percentage are studied in function of the traffic load. The performance of the forward link is studied by using packet schedulers such as Proportional Fair (PF), Maximum Carrier Interference (Max C/I) and Priority Proportional Fair proposed (Pr/PF) in [10]. The study is carried out through simulation using Matlab software tool.

In Section II a brief description of the WiMAX system is presented. The simulation model is described in Section III. The packet schedulers PF, Max C/I and Pr/PF are described in Section IV. Scenario evaluated in this paper is presented in Section V. In Section VI, the simulation results and its analyses are presented. Finally, the conclusions are exhibited in Section VII.

II. WIMAX

In the IEEE 802.16e architecture, two kinds of stations are defined: subscriber stations (SS) and a base station (BS). The BS controls all communication in the network, i.e., there is no peer-to peer communication directly between the SSs. WiMAX technology supports two types of connection modes: PMP (Point to Multipoint) and Mesh which application is optional. The PMP represents the classical cellular model when a SS is connected directly to the BS. In this paper, only PMP mode is considered.

The communication path between SS and BS has two directions: uplink (UL - from SS to BS) and downlink (DL - from BS to SS). The DL indicates direction of data flow from BS to SS , and UL indicates the data flow in opposite direction from SS to BS. The air interface is based on Orthogonal Frequency Division Multiplexing (OFDM) which is a multiplexing technique that subdivides the bandwidth into multiple frequency sub-carriers as shown in Fig. 1. In an OFDM system, the input data stream is divided into several parallel sub-streams of reduced data rate (thus increased symbol duration) and each sub-stream is modulated and transmitted on a separate orthogonal sub-carrier. The OFDM sub-carrier structure consists of three types of sub-carriers: data sub-carriers for data transmission, pilot sub-carriers for estimation and synchronization purposes and null sub-carriers used for guard bands and DC carriers.

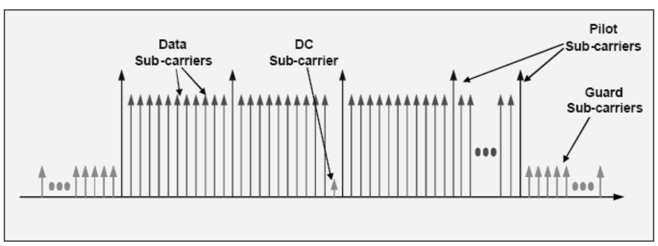

Fig. 1. OFDM Sub-Carrier Structure[5].

The resources, in a OFDM system, are available in the time domain by means of OFDM symbols and in the frequency domain by means of sub-carriers. The time and frequency resources can be organized into sub-channels for allocation to individual users. Orthogonal Frequency Division Multiple Access (OFDMA) is a multiple-access/multiplexing scheme that provides multiplexing operation of data streams from multiple users onto the downlink sub-channels and uplink sub-channels [13].

The minimum frequency-time resource unit of sub-channelization is one slot, which is composed of 48 data tones (sub-carriers). Frequency-specific sub-channelisation is supported via the called Band Adaptive Modulation and Coding (AMC) mode, which permits subchannel construction through physically adjacent subcarrier allocation (four different Band AMC subchannel dimensions are currently specified). Thus the allowed combinations are [(6 bins, 1 symbol), (3 bins, 2 symbols), (2 bins, 3 symbols), (1 bin, 6 symbols)]. A bin consists of 9 contiguous sub-carriers, with 8 assigned for data and one assigned for a pilot. In this paper, it was considered only 2 bins and 3 symbols for simplifying simulations.

In WiMAX, two types of duplexing method are specified, TDD and FDD. This paper is concerned with TDD duplex method where every frame is divided into DL and UL subframes. The frame structure for a TDD implementation is shown in the Fig. 2. Each frame is divided into DL and UL sub-frames separated by Transmit/Receive and Receive/Transmit Transition Gaps (TTG and RTG, respectively) to prevent DL and UL transmission collisions. In OFDM PHY every burst (either DL or UL), consists of integer number of OFDM symbols.

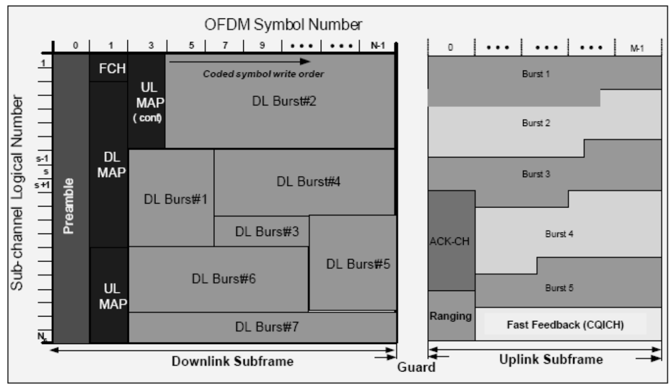

Fig. 2. WiMAX OFDMA Frame Structure[5].

The BS dynamically determines the duration of these subframes. SSs and BS have to be synchronized and transmit data into predetermined slot (SL). Since all SSs have synchronized with the BS clock, the BS controller can transmit data in each slot that will arrive at a particular SS. SSs send requests in the UL to BS. In the downlink, the BS uses a combination of acknowledgement (ACK) and grant (GR) slots to acknowledge requests from SSs and to grant access to data slots.

The following Table I provides a summary of the theoretical peak data rates for various DL/UL ratios assuming a 10 MHz channel bandwidth, 5 ms frame duration with 44 OFDM data symbols (from 48 total OFDM symbols) [13]. The data rates supported by forward link can vary from 1.06 Mbps up to 31.68 Mbps by a sector of a cell. One of three schemes of modulation QPSK, 16QAM and 64 QAM is used depending on data rate.

In the WiMAX standard four QoS services are defined: Unsolicited Grant Service (UGS); Real-Time Polling Service (rtPS); Non-Real-Time Polling Service (nrtPS) and Best Effort (BE) service. UGS service can be used for constant bit-rate (CBR) for service flows such as T1/E1. Real-time Polling Services (rtPS) can be used for rt variable bit rate (VBR) service flows such as MPEG video. Non-real-time Polling Service (nrtPS) can be used for non-real-time service flows with better performance than best effort service such as bandwidth-intensive file transfer. At last, for BE service there is no resource allocation.

TABLE I
MODULATION TYPE PER DATA RATE

Modulation	DL(Mbps)	UL(Mbps)
QPSK	**1.06**	0.78
QPSK	**1.58**	1.18
QPSK	**3.17**	2.35
QPSK	**6.34**	4.70
QPSK	**9.50**	7.06
16QAM	**12.67**	9.41
16QAM	**19.01**	14.11
64QAM	**19.01**	14.11
64QAM	**25.34**	18.82
64QAM	**28.51**	21.17
64QAM	**31.68**	23.52

TABLE II
PROBABILITY DISTRIBUTION PER DATA RATE

DL(Mbps)	Probability
1.06	3%
1.58	4%
3.17	6%
6.34	10%
9.50	12%
12.67	17%
19.01	16%
19.01	14%
25.34	9%
28.51	5%
31.68	4%

III. SIMULATION MODEL

In Fig. 3a it is shown the part of WiMAX system that this paper is concerned. The packets generated in core network are sent for a BS buffer. In this point they are shared in four queues (UGS, rtPS, nrtPS and BE) according to priority packet and stay waiting until will be served. The IP packets (1500 bytes and 576 bytes) may be eventually segmented to adjust in rates that will be sent. Thus, the forward link simulation model of WiMAX system can be represented as shown in Fig. 3b.

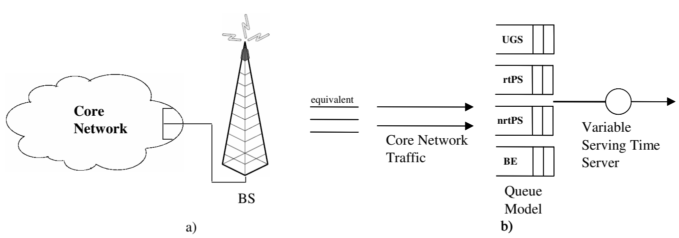

Fig. 3. WiMAX Simulation Model.

The following assumptions are adopted. The IP packets generated by HTTP sources proposed in [9] are classified according to four types of service flows defined in WiMAX QoS architecture, i.e, UGS, rtPS, nrtPS and BE. These flows are discriminated in appropriate queue by scheduler. The scheduler uses PF[11], Max C/I[12] or Pr/PF algorithm proposed in [10]. The buffer of each queue has finite size. The queue sizes are detailed in Section V. The slot comprises 48 data sub-carriers and 24 pilot sub-carriers in 3 OFDM symbols according to [13]. Thus, it is assumed that there are total of 16 SLs in a WiMAX frame which are divided into a DL/UL rate of 3:1 for 2x2 MIMO (Multiple-Input Multiple-Output), i.e., 1 SL for overhead, 3 SLs for UL channel and 12 SLs for DL channel.

In Table II it is shown the rate distribution adopted for the simulation. The adopted distribution is hypothetical and it is assumed the average rate is concentrated at 12.67 Mbps.

IV. DATA SCHEDULERS

Since the IEEE 802.16e standard does not specify the scheduler for downlink [2], the adopted data schedulers in this study are presented. Thus, the following data schedulers are used: Max C/I[12] (Maximum Carrier Interference), PF[11] (Proportional Fair) and Pr/PF[10] (Priority Proportional Fair).

A. Proportional Fair (PF)

The PF schedules the users according to the ratio between their instantaneous achievable data rate and their average served data rate. This results in all users having equal probability of being served even though they may experience very different average channel quality. This scheme provides a good balance between the system throughput and fairness. In equation 1, the acronym P_i denotes the user priority, $R_i(t)$ is the instantaneous data rate experienced by user i if it is served by the packet scheduler, and $\lambda_i(t)$ is the user throughput

$$P_i = \frac{R_i(t)}{\lambda_i(t)}, i = 1, ..., N \tag{1}$$

B. Maximum Carrier Interference (Max C/I)

The maximum C/I scheme schedules the users with the highest C/I during the current slot. This naturally leads to the highest system throughput since the served users are the ones with the best channel. However, this scheme makes no effort to maintain any kind of fairness among users. In fact, users at the cell edge will be largely penalized by experiencing excessive service delays and significant outage.

C. Priority Proportional Fair (Pr/PF)

The hybrid scheduler Pr/PF combines the priority scheduler with PF. In this scheme, packets with high priority from services flows UGS and rtPS are first served while packets from services nrtPS and BE are served in accordance with PF scheduler. The Fig. 4 illustrates Pr/PF scheduler. In this manner, this scheduler contemplates users that need differentiated serving and also users with low restrictions of QoS that tolerate delays during services.

V. SCENARIO EVALUATED

The evaluated scenario consists in increasing the number of HTTP sources varying from 152 (20% link utilization) up to 675 (80% link utilization) as exhibited Table III. Several schedulers are used in order to evaluate which one among

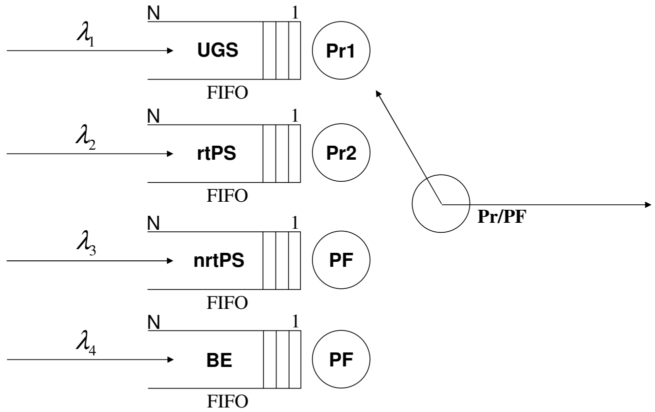

Fig. 4. Pr/PF Data Scheduler

PF, Max C/I or Pr/PF guarantees the best QoS for SSs. For Pr/PF scheduler the UGS service has highest priority, the rtPS service has second highest priority and nrtPS and BE sources are served according to PF scheduler. The behavior of WiMAX system is analyzed through two finite queues: one has a small length of buffer (10 packets) and another has large length buffer (100 packets). The probability distribution, traffic proportion and buffer size adopted in this paper are shown in Table IV.

TABLE III
SCENARIO

Link Utilization	HTTP Sources
20%	152
40%	310
60%	470
80%	675

TABLE IV
PROBABILITY DISTRIBUTION VS BUFFER SIZE

Priority	Proportion	Buffer1	Buffer2
UGS	10%	1	10
rtPS	25%	3	25
nrtPS	30%	3	30
BE	35%	3	35
Total	100%	10	100

The performance measurements considered in this study are: the average packet delay, the throughput, the loss percentage and the link utilization.

VI. RESULTS ANALYSIS

The results obtained through simulations are organized and presented in graphics. In these graphics the acronym BX represents finite buffer 1 or 2. The buffer 1 is illustrated as continuous line and buffer 2 as dashed line. Moreover, acronyms PFX, MaxCIX and Pr/PFX refer to PF, Max C/I and Pr/PF schedulers, and X represents level of priority. The level 1 is the highest priority, i.e, traffic generated by UGS service and the level 4 is the lowest priority for BE service and so on. The average standard deviation was 3.32% and 95% confidence interval was 2.06% of the average value.

The throughputs for Pr1 and Pr4 users have the same behavior for all schedulers as are shown in Figs. 5 and 6. These throughputs are normally higher when are used buffer 2 with large total capacity of 100 IP packets and lower when are used buffer 1 with small total capacity of 10 IP packets. In relation to the throughput behavior the schedulers PF, Max C/I and Pr/PF present little influence for traffic with priority 1 or 4. However, it is possible to note a little advantage of scheduler Pr/PF1 for users with high priority in Fig. 5 due to absolute priority. In another Fig. 6 can be observed the best performance of PF4 users because of PF scheduler directs more system resources to users with low priority.

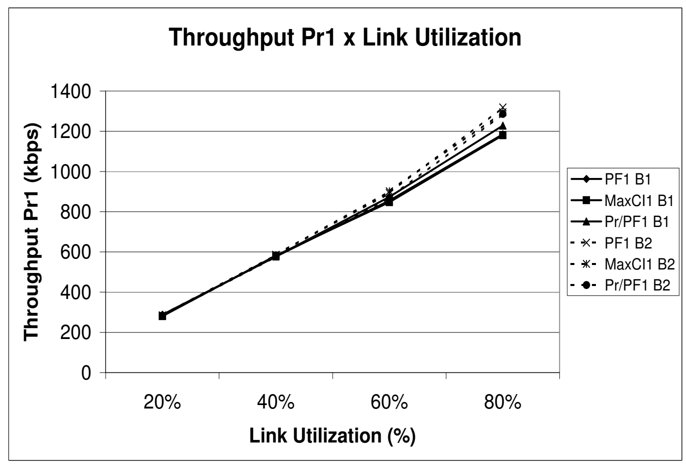

Fig. 5. Throughput Pr1 in Function of Link Utilization.

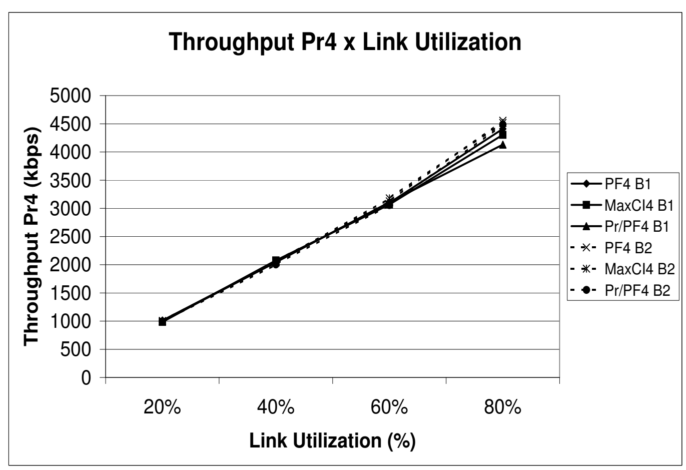

Fig. 6. Throughput Pr4 in Function of Link Utilization.

Fig. 7 illustrates the average delay for Pr1 users in function of link utilization varying from 20% up to 80% and using

HTTP sources. As observed in this figure delays obtained using Pr/PF1 scheduler are very small and independent of buffer scheme adopted due to absolute priority of Pr1 users. The scheduler MaxCI1 presents intermediate performance with delays varying from 0,16 ms up to 1,9 ms. The scheduler PF1 has the worst performance with maximum delays of 2,5 ms in reason of scheduler tries to maintain user throughput fairness.

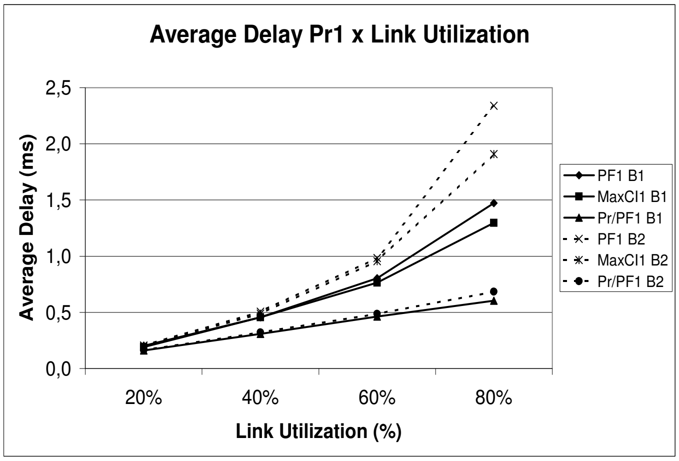

Fig. 7. Average Packet Delay Pr1 in Function of Link Utilization.

In Fig. 8, the average delay of Pr4 users in function of link utilization varying from 20% up to 80% using HTTP sources is shown. In this case, scheduler Pr/PF4 has the worst delay among schedulers evaluated with average delays varying from 0,2 ms up to 12 ms for buffer 2. In case of buffer 1, average delay are reduced to range 0,2 ms up to 2,85 ms. However, this reduction is associated with high loss percentage. In relation to others schedulers PF4 and MaxCI4, the results show tolerant delay varying up to 4 ms in worst case.

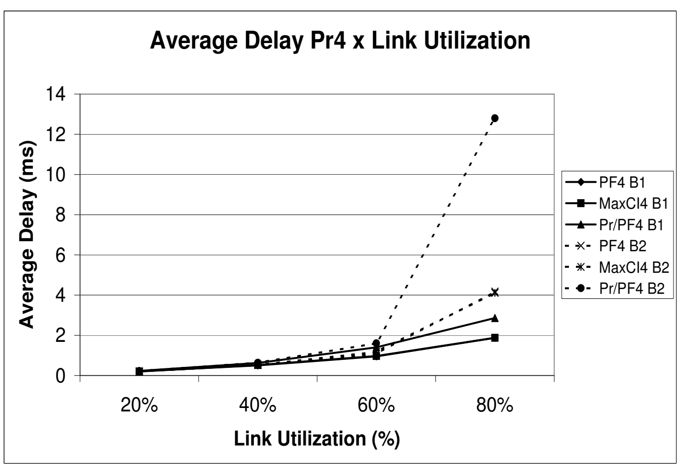

Fig. 8. Average Packet Delay Pr4 in Function of Link Utilization.

The loss percentage of HTTP packets for Pr1 users in function of WiMAX system utilization is shown in Fig. 9. It can be observed once more that, the Pr/PF1 scheduler obtains the lowest loss percentage of HTTP packets during simulation because of high priority of Pr1 users. Others schedulers PF1 and MaxCI1 have maximum loss percentage of 1% in worst case. In case of loss percentage of buffer 2, the losses are negligible because of large capacity buffer with 100 packets IP.

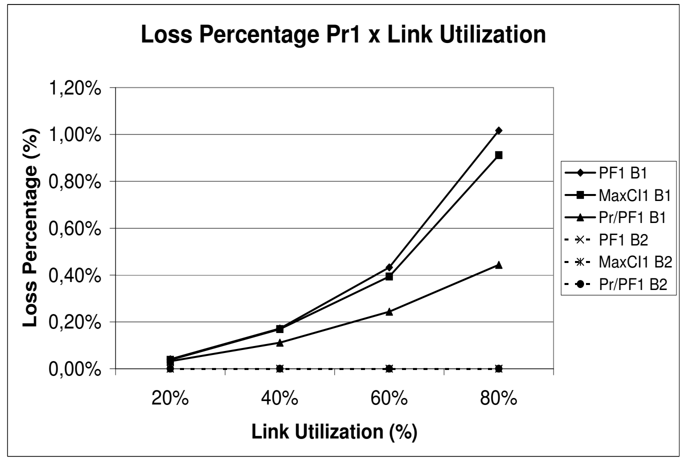

Fig. 9. Loss Percentage Pr1 in Function of Link Utilization.

Finally, Fig. 10 exhibits loss percentage of HTTP packets for Pr4 users in function of link utilization. It is clear the high loss of Pr/PF4 scheduler mainly because of lower priority users. The loss is as high as 3% of packets for a link utilization of 80%. The PF4 and MaxCI4 schedulers present small packet losses with a little advantage of PF4.

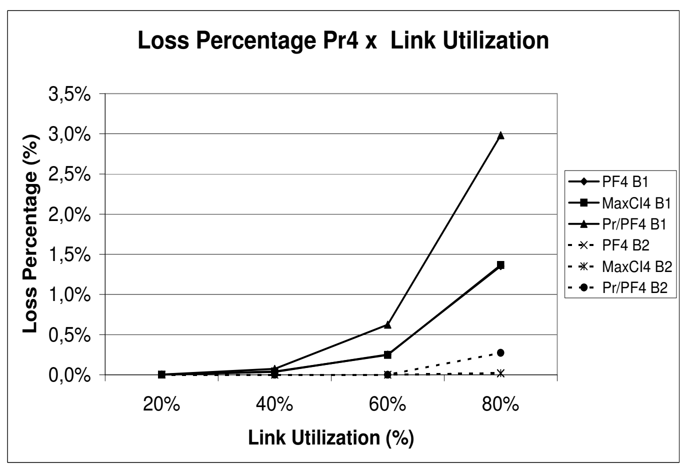

Fig. 10. Loss Percentage Pr4 in Function of Link Utilization.

VII. Conclusions

The forward link performance of the WiMAX system was evaluated by simulation considering traffic model of HTTP and various types of schedulers such as PF, Max C/I and Pr/PF. The throughput, average delay, loss percentage were studied in function of link utilization.

The results demonstrated that for packet delay and packet loss the Pr/PF scheduler is the most suitable for QoS assurance of WiMAX system with different types of services (UGS, rtPS, nrtPS and BE) because it guarantees small delays and low packet loss for higher priority users and moderate QoS for lower priority users. On the other hand, PF scheduler presented a fair link utilization but it is not appropriate for QoS assurance of different types of service. The same conclusion can be considered for Max C/I scheduler that only maximizes the link utilization.

REFERENCES

[1] IEEE 802.16-2004,*"IEEE Standard for Local and metropolitan area networks, Part 16: Air Interface for Fixed Broadband Wireless Access Systems"*, October 2004.

[2] IEEE 802.16e-2005,*"Air Interface for Fixed and Mobile Broadband Wireless Access Systems,"*, IEEE P802.16e/D12, February 2005.

[3] D. Niyato and E. Hossain,*"Queue-Aware Uplink Bandwidth Allocation for Polling Services in 802.16 Broadband Wireless Networks"*, IEEE GLOBECOM 2005, December 2005.

[4] P. Mach, R. Bestak,*"WiMAX Performance Evaluation"*, Proceedings of the Sixth International Conference on Networking (ICN'07), April 2007.

[5] F. Wangt, A. Ghosht, R. Love, K. Stewartl, R. Ratasukt, R. Bachul, Y. Sun, Q. Zhao,*"IEEE 802.16e System Performance: Analysis and Simulations"*, 2005 IEEE 16th International Symposium on Personal, Indoor and Mobile Radio Communications, September 2005.

[6] C. Cicconetti, A. Erta, L. Lenzini and E. Mingozzi,*"Performance Evaluation of the IEEE 802.16 MAC for QoS Support"*, IEEE TRANSACTIONS ON MOBILE COMPUTING, January 2007.

[7] K. Wongthavarawat and A. Ganz,*"Packet scheduling for QoS support IEEE 802.16 broadband wireless access systems"*, International Journal of Communications Systems, 2003.

[8] D. Cho, J. Song, M. Kim and K. Han,*"Performance Analysis of the IEEE 802.16 Wireless Metropolitan Area Network"*, Proceedings of the First International Conference on Distributed Frameworks for Multimedia Applications (DFMA'05), February 2005.

[9] 3GPP2 WG5 Evaluation Ad Hoc,*"1xEV-DV Evaluation Methodology - Addendum(V6)"*, July 2001.

[10] L. Marques and S. Motoyama,*"Critérios de Aceitação de Tráfego Handoff e Escalonadores de Dados para Garantia de QoS no Sistema CDMA 1xEV-DO RA"*, XXVIII Brazilian Computing Society Congress (CSBC), July 2008.

[11] Jalali,*"Data Throughput of CDMA-HDR a High Efficiency-High Data Rate Personal Communication Wireless System"*, Vehicular Technology Conference, 2000.

[12] 3GPP 3G TR25.848,*"Physical layer aspects of UTRA high speed downlink packet access (Release 4)"*, 3GPP Specification series, March 2001.

[13] WiMAX Forum,*"Mobile WiMAX - Part I: A Technical Overview and Performance Evaluation"*, White Paper, 2006.

Gossip-Quorum-AODV Based Fault Tolerant Ad-Hoc Networks

Renata Lopes Rosa
Telecommunications and Control Engineering Department
Escola Politécnica of the University of São Paulo
renata@lcs.poli.usp.br

José Roberto Amazonas
Telecommunications and Control Engineering Department
Escola Politécnica of the University of São Paulo
jra@lcs.poli.usp.br

***Abstract*— The use of Mobile Ad-Hoc Networks has been increasing steadily. The study of algorithms and protocols that may provide higher packet delivery throughput for non-structured networks with a high degree of mobility is very much needed. Moreover, the possibility of keeping the performance under fault conditions is extremely important.**

This paper studies the implementation of a *Quorum* system associated with an epidemic algorithm, *Gossip*, and the AODV routing protocol in a fault scenario of an ad-hoc network. The simulation results show that this kind of association decrease the number of route requests and the packet loss rate without degrading the throughput and latency characteristics.

***Index Terms*— Gossip algorithm, Quorum system, Ad-Hoc networks, packet delivery**

I. Introduction

A Mobile Ad-Hoc Network (MANET) is a collection of mobile nodes that communicate using wireless links, without the need of a pre-existing infra-structured network. An example of ad-hoc networks is the sensor networks that collect the desired data (temperature, humidity, geographic position, seismic information etc.). These information is exchanged among the sensor nodes and depending on their importance for the application it may be mandatory to ensure the data delivery.

The main routing protocols that have been studied for ad-hoc networks [1, 2, 3, 4] are: AODV (Ad-Hoc On-Demand Distance Vector) and DSR (Dynamic Source Routing). In spite of the DSR being a little bit simpler protocol and because of this to introduce less overload information in the network, due to the use of a route cache table, it is not the most appropriate for a mobility scenario. The main reason is exactly the use of a route cache table that may make the protocol to work with outdated routes. As in this work we are interested on a mobile nodes scenario, we decided to employ the AODV.

The studies [5, 6, 7, 8, 9] have shown that an algorithm of epidemic dissemination (*Gossip*) associated with the routing protocol AODV decreases the number of new route requests messages (Route Requests - RREQs) traveling in the network. According to [6], there is a 35% decrease of the RREQs messages compared with the number of messages generated by the standard flooding technique (dissemination of information through all network's nodes). Therefore, the use of the *Gossip* algorithm is adequate to get a decrease of the network overload caused by the RREQs messages.

However, the other parameters (latency, packet loss rate and throughput) are badly affected: the latency and packet loss rate increase and the throughput decreases. It has been shown in [6] that the degradation observed in the use of the AODV associated with the *Gossip* algorithm is minimal and can be tolerated.

The studies [10, 11, 12] about the *Quorum* system have shown that the use of distributed solutions increase the network's resilience and decrease the network overload, because the *Quorum* provides a better information distribution among the nodes or, in other words, it does not centralize the information in a specific node.

Presently, distributed systems use data replication as a means of fault tolerance and to provide information resilience and availability. The client-server model is used as a basic paradigm of distributed systems.

This paper uses a scheme similar to the one employed in [11], in which the load is distributed among the nodes providing a higher resilience for the faults of arbitrary nodes. This work is different from the one presented in [11] in terms of the use of the AODV protocol, the employed metrics and for being a quite complete and detailed work in what the number of simulations and comparisons of the use or not of the *Quorum* system and the *Gossip* associated to the AODV protocol are concerned. The main contribution of this work is a comprehensive practical understanding of the association of an epidemic algorithm with a distributed system for providing consistency of replicated data with a high degree of reliability in different scenarios of mobile ad-hoc networks.

The occurrence of faults is a common event in ad-hoc networks. This work considers non-permanent faults, i. e., after a while the faulty node starts to work perfectly again.

This paper is organized as follows. After this Introduction, Section II presents a brief theoretical revision of the AODV routing protocol, the *Gossip* algorithm and the *Quorum* System. The parameters used to evaluate the system's performance are also introduced; Section III describes the fault scenarios used in simulation; Section IV shows and discusses the simulation results; Section V concludes the paper and proposes some future work.

II. Theoretical Revision

A. AODV Protocol

The Ad-Hoc On-Demand Distance Vector (AODV) routing algorithm is a routing protocol designed for ad-hoc mobile networks. AODV is capable of both unicast and multicast routing. It is an on-demand algorithm, meaning that it builds routes between nodes only as desired by source nodes. It maintains these routes as long as they are needed by the sources [13]. Additionally, AODV forms trees which connect multicast group members. The trees are composed of the group members and the nodes needed to connect the members. AODV uses sequence numbers to ensure the freshness of routes. It is loop-free, self-starting, and scales to large numbers of mobile nodes.

This protocol uses the following variables:

- Source sequence number (SrcSeqNum): sequence number generated by the source node;
- Destination sequence number (DestSeqNum): ever increasing sequence number, used as a means to verify how recent a route is, because a DestSeqNum with a larger value will represent a more up-to-date route;
- Source identifier (SrcID): it specifies a source node that intends to send packets to a determined network node;
- Destination identifier (DestID): it specifies a destination node that shall receive packets from a determined network node;
- Broadcast identifier (BcastID): when several broadcasts are sent into the network, each of them receives an identifier associated to a given RREQ message enabling its identification. It is incremented when any new route request is sent;
- Messsages' time to live (TTL): a counter that represents the maximum time that can elapse before a message is discarded;
- Hops count : number of necessary hops to reach a given node from a specific source node.

And the following messages:

- Hello: these messages are periodically sent to confirm the connectivity between neighbors;
- RouteRequest (RREQ): route request messages are sent to the entire network to find a destination node, when the route is not known anymore;
- RouteReply (RREP): this is the answer to a route request specifying how to reach a destination node;
- Route Error (RERR): it is a link failure warning. When a link between two nodes comes down a RERR is sent;

When a node wants to send a packet to another node and does not know a route yet, the source node sends a RouteRequest (with SrcID, DestID, SrcSeqNum, DestSeqNum, BcastID and TTL) to all its neighbors by diffusion. If a neighbor is not the destination or if it does know a valid route to the destination, it forwards the RREQ to all its neighbors. This flooding process is repeated, till the requisition reaches either the destination or a node that knows a route to the destination.

A destination node answers to a RREQ by sending a RREP message, through the reverse path, that contains the source and destination addresses, the destination sequence number, the hops count that is incremented by one at each hop, and its TTL. Before sending a RREP, the destination node updates its sequence number as the maximum between the present value and the value received in the RREQ message. At each node traversed by the RREP message on the reverse path, the next hop to reach the destination is stored in an entry concerning the destination, i. e., the neighbor's address from which the answer has been received and the destination's sequence number.

B. Gossip algorithm

The *Gossip* algorithm is a probabilistic multicast protocol in which a node forwards information only to a given number of neighbor nodes, that is established by means of a probability setup in the algorithm. In this way, the network flooding is avoided, unless the probability is set to 1, meaning that 100% of the neighbors should receive messages.

Each node in this kind of *Gossip* algorithm keeps only a partial view of the entire system, that is employed to guide the selection of nodes that will participate in the information exchange.

The fact that the senders randomly choose to whom they send messages, makes the *Gossip* fault tolerant and completely distributed.

There are different kinds of *Gossip* algorithms, and the most common are:

- GOSSIP1 (p, k): it sends a broadcast to the first k hops, allowing the initial messages to be forwarded with a probability p = 1 (100%). After receiving a message for the first time, the node forwards it with $p < 1$.
- GOSSIP2 (p1, k, p2, n): the information forwarding of a given node depends on its relative position to the source node and on the number of neighbor nodes (n).
- GOSSIP3 (p1, k, m): the information forwarding of a given node is made according to a sufficient number of retransmissions (m). If a node decides not to forward a message and after that it receives less than m copies of messages, it sends a broadcast message at once.

This work employs the GOSSIP2 algorithm, whose parameters are described hereafter:

- p1 is the probability of a node forwarding the *gossip* if the number of its neighbors is greater than n.
- k is the number of initial hops for which the *gossip* is forwarded with probability equal to 1.
- p2 (p2>p1) is the probability of a node forwarding the *gossip* if the number of its neighbors is less than n.
- n is the number of neighbors threshold.
- Fanout: is the selected number of nodes (t) to receive the message sent by the emitter. High values of fanout ensure a higher level of fault tolerance at the expenses of a higher degree of redundant traffic generation in the network.

When a node receives a message for the first time, it stores the message and forwards it to a given number of nodes (fanout). These nodes, by their turn, select some of their neighbors and propagate the message. If a node receives a message that it already knows, it ignores it.

The bottom line of the *Gossip* algorithm is to make all nodes participate in the same manner of the information dissemination. Thus, if a node wants to send a *broadcast* message, it randomly selects t nodes (its fanout) and sends the message to them.

C. The Quorum System

A *Quorum* system is a collection of sets (quorums) every two of which intersect. *Quorum* systems have been used for many applications in the area of distributed systems, including mutual exclusion, data replication and dissemination of information [12].

Any practical *Quorum* system must take into account that some of the servers may fail and, even in this situation, they must exchange data among them and continue to work.

This work presents a system made of an arbitrary number of clients and a set S of a fixed number of servers.

There is a *Quorum* system Q if:

$$\mathrm{Q} = \mathrm{Qr} + \mathrm{Qw} \tag{1}$$

where Qr is a set of quorums used for read operations (Read *Quorum*) and Qw is a set of quorums used for write operations (Write *Quorum*). Any Read *Quorum* and Write *Quorum* pair have a non-empty intersection.

The *Quorum* system used in this work is based on [12] and its functioning is as follows:

- To write data on a *Quorum*'s server, the client checks the Read *Quorum*'s servers to choose a timestamp larger than any existing timestamp for any data already saved in the servers and send the data to the Write *Quorum*'s servers associated to the largest chosen timestamp.
- To read data from a *Quorum*'s server, the client checks the Read *Quorum*'s servers and looks for the most recent data, i. e., those that have the largest timestamp, and return the data to the user.

D. Performance Parameters

The performance parameters chosen to evaluate a fault tolerant system were:

- RREQ: messages sent by a node to a set of nodes with the objective of find a route. The total number of RREQs has been measured.
- Throughput (bps): parameter that indicates the effective data transmitted in bits and measured in a time interval.
- Latency (s): represents the elapsed time for a packet to go from a source node to a destination node. It is given by the sum of sending and receiving delays of CBR (Constant Bit Rate) flows.
- Packet loss (%): represents the difference of the number of sent packets and the number of received packets over the number of sent packets, given in percentages.
- Energy consumption (mWhr): is given by the sum of energy consumption employed on receiving (RX) and transmitting (TX) information. The energy consumed by data transmission is computed by (2):

$$\begin{aligned}\mathrm{Consumption} = [(&\mathrm{TxPowerCoef} \times \mathrm{txPower}) + \\ &\mathrm{TxPowerOffset}] \times \mathrm{txDuration}\end{aligned} \tag{2}$$

  where TxPowerCoef and TxPowerOffset are statistically defined by the WaveLAN specifications as 16/s and 900 mW, respectively. txPower is proportional to the distance the signal has to travel.
  The energy consumed by data reception is computed by an equation similar to (2) appropriately modified.

III. Simulation Scenarios

Two network simulators have been analyzed, namely: NS-2 [14] and Glomosim 2.03 [15] educational version. Both of them are free software and have been extensively used in research providing many research references for comparison.

The Glomosim 2.03 is a scalable discrete events simulator developed by the UCLA and, besides the aforementioned arguments, it has been chosen because it has been used in [6] that is an important reference for this work.

The simulation considered the following parameters:

- 1000 m x 1000 m area;
- simulation time: 5 minutes;
- number of nodes: 80 - uniformly distributed over a grid of degree equal to 11,7 (average number of immediate neighbors);
- traffic: a set of 30 CBR flows between of randomly chosen node pairs. The transmission rate is 2 packets per second; each packet has 512 bytes;
- mobility: five mobility situations have been defined by their pause duration - 50, 100, 150, 200 and 250 seconds. A no-mobility scenario has also been simulated and it is indicated by a 300 seconds pause time;
- protocols: the following combination of protocols have been simulated:
  - AODV;
  - AODV + *Gossip*;
  - AODV + *Gossip* + *Quorum*

Two fault simulation scenarios, designated as A e B have been defined and are described below. For each situation of interest 100 simulations have been performed starting with a different seed for the random number generator. In all cases the performance parameter average and standard deviation have been evaluated. The histogram and the *qq-plot* function of each simulation have been built to verify if the results followed a Normal distribution. All the results have been treated by the R statistical software [16].

Simulation times of 2, 5 and 10 minutes have been tested and it has been observed that 5 minutes were enough for the network to reach the steady state regime.

- Scenario A:

TABLE I

SCENARIO A FAILURES

Failures (%)	Fixed node with failure ID
7.5	1, 14, 22, 47, 63, 79
15	1, 7, 14, 17, 22, 31, 39, 47, 54, 63, 74, 79
22.5	1, 4, 7, 11, 14, 17, 22, 26, 31, 34, 39, 44, 47, 54, 59, 63, 74, 79
30	1, 4, 7, 9, 11, 14, 17, 19, 22, 26, 29, 31, 34, 39, 41, 44, 47, 51, 54, 59, 63, 69, 74, 79

- After 2.30 minutes of simulation, a group of nodes is forced to fail for a constant time of 10 seconds. The failure is simulated by deleting the node's data and leaving the node unavailable for 10 seconds.
- Fault probability: the failures were applied to 7.5, 15, 22.5 and 30% of pre-defined nodes. For the sake of simplicity, CBR source and destination nodes never fail.

Table I presents the pre-defined nodes that are forced to fail in the scenario A.

- Scenario B:
  - The simulation starts and after 50 seconds a certain number of nodes fail. The fault duration F1 is randomly selected from an exponential distribution. After F1 has elapsed another group of nodes fail for F2 seconds. The procedure is repeated till an average number of nodes either of 7.5%, 15%, 22.5% or 30% have failed. The simulation time never exceeds 5 minutes.
  - Fault probability: the nodes are randomly selected from a uniform distribution with average probability of 7.5, 15, 22.5 and 30%. Thus a group of nodes fail for F1 seconds, a second for F2 seconds and so on, till the average value of fault probability has been obtained. For the sake of simplicity, the source and destination nodes of CBR traffic never fail.

IV. EXPERIMENTAL RESULTS AND DISCUSSION

In all cases, the simulation has been performed for 100 different values of the seed of the random number generator. It has been verified that the results follow a normal distribution and the obtained results are really representative. As an example, Figure 1 shows the *qq-plot* obtained for the following simulation case: scenario A, association of the *Gossip* with the *Quorum*, pause time = 150 seconds, fault probability = 30%; performance parameter = packet loss rate. Figure 2 shows the histogram corresponding to the same case. All results, for both scenarios and simulation conditions, presented a similar behavior.

The simulation results are presented in Figures 3 thru 12. The x-axis represents the fault probability (7.5, 15, 22.5 and 30%); the y-axis represents the pause time (50, 100, 150 and 250 s - the non-mobility case is indicated as 300 s pause time); the z-axis represents the performance parameter of interest. In all cases. The average and the standard deviation were obtained. Only the average values are shown in the figures.

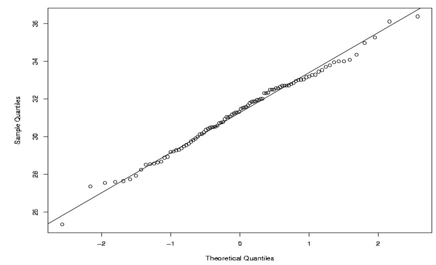

Fig. 1. pplot: AODV + Gossip + Quorum; pause time = 150 s; fault probability = 30%

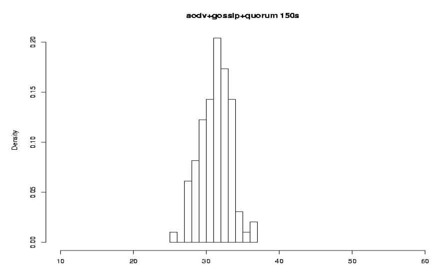

Fig. 2. Histogram: AODV + Gossip + Quorum; pause time = 150 s; fault probability = 30%

Figures 3 and 4 show the results for the latency. It can be observed that the use of the *Gossip* and the *Quorum* associated with the AODV protocol does not produce any significative degradation of this parameter. The slight latency increase can be explained by the fact that the *Gossip* algorithm takes some time to determine the nodes to which forward the information and the *Quorum* system has to write the information into the *Quorum*'s servers. The latency increase is accentuated when the fault probability increases, because as the number of active nodes in the network is reduced it takes longer to forward the information to the *Quorum*'s servers.

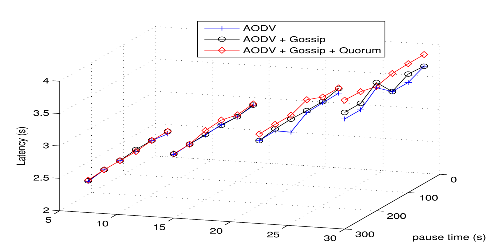

Fig. 3. Latency - Scenario A

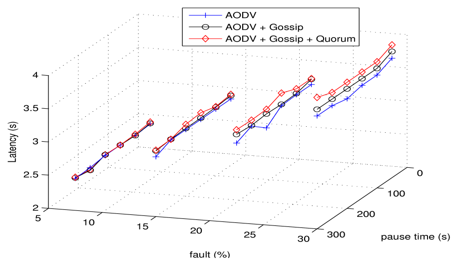

Fig. 4. Latency - Scenario B

Figures 5 and 6 show the results for the throughput. It can be observed that the use of the *Quorum* system increases the throughput. On the other hand, the use of the *Gossip* algorithm without the *Quorum* system does not bring any advantage to the system. This can be explained by the fact that *Quorum* system keeps part of the data in its servers allowing the nodes to have almost immediate access to them and, by consequence, improving the throughput.

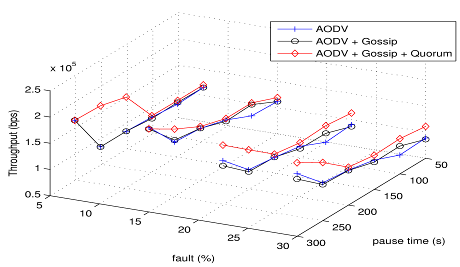

Fig. 5. Throughput - Scenario A

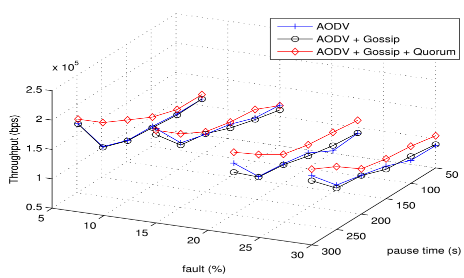

Fig. 6. Throughput - Scenario B

Figures 7 and 8 show the results for the number of route requests (RREQs) messages. It can be observed that the use of the *Gossip* algorithm produced a significative reduction of RREQs. This can be explained by the fact that the flooding technique is not being used anymore. The *Gossip* algorithm sends RREQs only to some nodes. Applying the *Quorum* system produces a slight increase in the number of RREQs due to information forward to the *Quorum*'s servers and information requests from their clients. However, such increase is not significative for the overall performance.

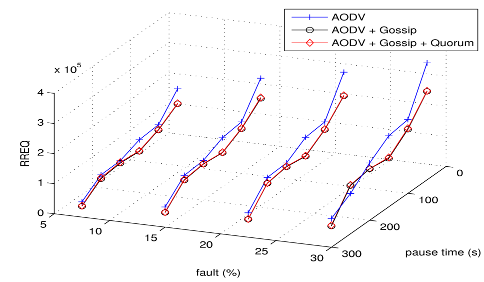

Fig. 7. RREQ - Scenario A

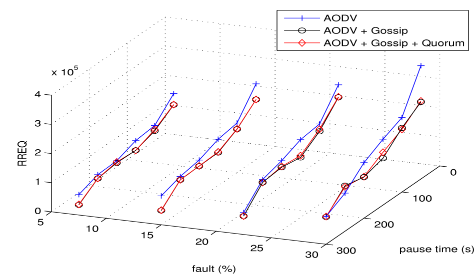

Fig. 8. RREQ - Scenario B

Figures 9 and 10 show the results for the energy consumption. The observed differences without and with using the *Gossip* are not significative but the slight reduction can be taken as an indication that if the *Gossip* is modified to become power-aware an interesting energy consumption could be achieved.

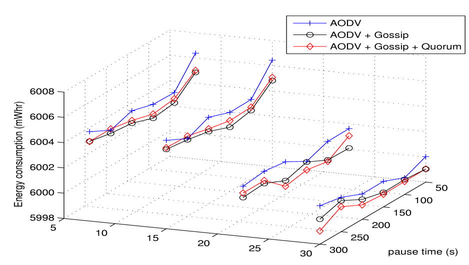

Fig. 9. Energy consumption - Scenario A

Figures 11 and 12 show the results for the packet loss rate. It can be observed that the use of only the *Gossip* algorithm associated with the AODV protocol brings no advantage to the system performance. On the other hand, using the *Quorum* system produces a significative reduction of the packet loss rate that is explained by the data distribution and replication scheme: when a packet is lost, it may exist a copy of this data in the *Quorum*'s server that forwards this information to the clients requesting the corresponding packet.

Table II shows the average and standard deviation values obtained for the scenario B packet loss rate. According to these results, the packet loss rate reduction obtained thanks to

TABLE II
AVERAGE AND STANDARD DEVIATION VALUES FOR THE SCENARIO B PACKET LOSS RATE

Faults (%)	Pause time (s)	AODV	AODV + Gossip	AODV + Gossip + Quorum
7.5	0	6.85 ±3.04	13.40±2.89	6.27 ±2.79
7.5	50	39.94 ±2.55	41.06 ±2.95	26.79 ±3.07
7.5	150	38.63 ±3.16	40.45 ±2.75	21.05 ±3.16
15	0	9.10 ±0.98	17.05 ±0.95	6.71 ±1.03
15	50	46.85 ±3.28	47.13 ±3.20	36.36 ±4.31
15	150	41.38 ±2.82	43.07 ±2.07	26.73 ±1.80
22.5	0	11.18 ±1.04	16.36 ±1.04	9.21 ±0.91
22.5	50	45.32 ±2.75	47.93 ±0.98	34.74 ±1.12
22.5	150	37.59 ±1.10	40.65 ±0.94	27.78 ±0.86
30	0	11.78 ±0.95	16.58 ±0.88	9.29 ±0.94
30	50	45.45 ±3.04	48.10 ±3.21	34.96 ±1.11
30	150	37.78 ±0.93	41.84 ±2.08	28.87 ±0.95

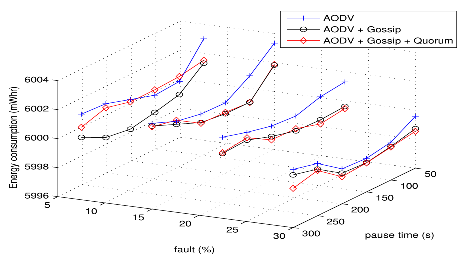

Fig. 10. Energy consumption - Scenario B

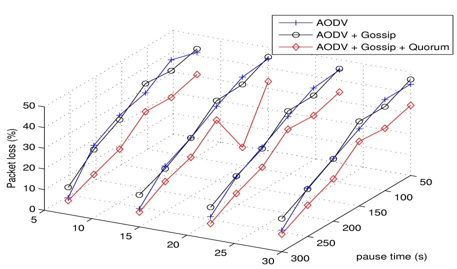

Fig. 11. Packet loss rate - Scenario A

the use of the *Quorum* system is really significative being of the order of 10%. The results for the scenario A are similar and the standard deviation values are in the range of 1.00 thru 4.35.

The standard deviation values for the other performance parameters in both scenarios were: 0.04 thru 0.05 s for latency; 0.4 thru 0.5 mWhr for energy consumption; 4,500 thru 5,200 messages for RREQ; 500 thru 600 bps for throughput.

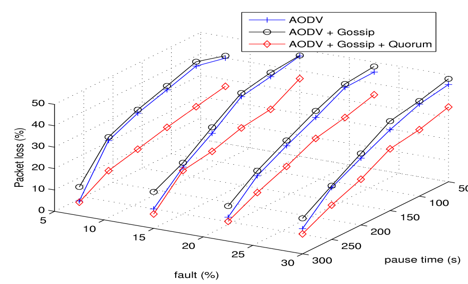

Fig. 12. Packet loss rate - Scenario B

V. CONCLUSION AND FUTURE WORK

This paper has analyzed comprehensively the association of the *Gossip* algorithm and the *Quorum* system with the AODV routing protocol for two different fault simulation scenarios. The results have shown that the *Gossip* algorithm is effective on reducing the number of route requests messages in the network with a slight increase of the latency and decrease of the throughput. On the other hand, the use of the *Quorum* system is effective on reducing the packet loss rate. Thus, a *Gossip*-*Quorum*-AODV based system is a good solution for building fault tolerant mobile ad-hoc networks.

It has also been observed a minor decrease of the energy consumption by using the *Gossip* algorithm. The obtained values are not very significative but indicate that a power-aware version of the *Gossip* will be worthwhile. As a future work we intend to implement this algorithm introducing a sleep mode state for the nodes that are receiving any information in a determined instant of time. This new scheme will be compared with other solutions reported in the literature.

A similar work is being done for the DSR routing protocol and a comparison study with the AODV will be reported soon.

REFERENCES

[1] S. Junk, N. Hundewale, A. Zelikovsky, *Node caching enhancement of reactive ad hoc routing protocols [MANET]*,Wireless Communications and Networking Conference, 2005 IEEE, Vol. 4, 13-17 March 2005, pp 1970 - 1975.

[2] N. Moghim, F. Hendessi, N. Movehhedinia, *An improvement on ad-hoc wireless network routing based on AODV*, Communication Systems, 2002, The 8th International Conference, Vol. 2, pp 1068 - 1070.

[3] Z. Xiaofeng, M. Shunliang, W. Youzheng, W. Jing, *Stable enhancement for AODV routing protocol*,Personal, Indoor and Mobile Radio Communications, 2003, 14th IEEE Proceedings on Vol. 1, pp 201 - 205.

[4] C. Jaihyung, J. Breen, *A flood routing method for data networks Information* , Communications and Signal Processing, 1997, Proceedings of 1997 International Conference on Vol. 3, pp 1418 - 1422.

[5] T. Korkmaz, M. Krunz, *Hybrid flooding and tree-based broadcasting for reliable and efficient link-state dissemination*, Global Telecommunications Conference, IEEE Vol. 3, 17-21 Nov. 2002, pp 2400 - 2404.

[6] Z.J. Haas,J.Y. Halpern, L. Li , *Gossip-based ad hoc routing Networking*, IEEE/ACM Transactions on Volume 14, Issue 3, June 2006, pp 479 - 491.

[7] J. Tingyao, L. Qinghua, *A self-stabilizing distributed multicast algorithm for mobile ad-hoc networks*, Computer and Information Technology, 2004. CIT 04. The Fourth International Conference on 14-16 Sept. 2004, pp 499 - 502.

[8] S. Mueller, D. Ghosal, *Analysis of a distributed algorithm to determine multiple routes with path diversity in ad hoc networks*, WIOPT 2005. Third International Symposium on 3-7 April 2005, pp 277 - 285.

[9] Z. Chun-Xiao ,W. Guang-Xing , *Routing protocol based on fuzzy regression for MANET Machine Learning and Cybernetics* , 2004. Proceedings of 2004 International Conference on Volume 3, 26-29 Aug. 2004, pp 1811 - 1815.

[10] Martin, J.-P.; Alvisi, L.; Dahlin, M.,*Small byzantine quorum systems*, Proceedings. International Conference on 23-26 June 2002, pp 374 - 383.

[11] L. Jun, P.T. Eugster, J.P. Hubaux, *Pilot: probabilistic lightweight group communication system for ad hoc networks*, Mobile Computing, IEEE Transactions on Vol. 3, Issue 2, April-June 2004, pp 164 - 179.

[12] L. Alvisi, L. Malkhi, D. Pierce, *Fault detection for Byzantine quorum systems* , Parallel and Distributed Systems, 2001, Proceedings. IEEE Transactions on Volume 12, Sep. 2001, pp 996 - 1007.

[13] C. S. R. Murthy, B. S. Ghosal, *Ad Hoc Wireless Networks*, Prentice Hall.

[14] *NS-2 Network Simulator*, http://www.isi.edu/nsnam/ns/.

[15] *Glomosim - Global Mobile Information System Simulation Library*, http://pcl.cs.ucla.edu/projects/glomosim/.

[16] *The R Project for Statistical Computing*, http://http://www.r-project.org/.

The Throughput Region of Wireless Random Access Protocols assisted by Multipacket Reception

Ramiro Sámano-Robles
Instituto de Telecomunicações,
Campus Universitário 3810-193
Aveiro - Portugal
ramiro@av.it.pt

Atilio Gameiro
Instituto de Telecomunicações,
Campus Universitário 3810-193
Aveiro - Portugal
atilio@av.it.pt

***Abstract*— Random access protocols assisted by multipacket reception (MPR) have been extensively analyzed in terms of their stability and delay properties. However, due to the complex interactions between queuing states and reception parameters, the optimum transmission probabilities and therefore the boundaries that define the throughput region of the protocol have not been explicitly derived as in collision-model approaches, particularly in the asymmetrical user case (i.e., the case where the users present different traffic and reception parameters). In this paper we carry out a protocol optimization that results in a novel closed-form expression for the optimum transmission probabilities of a slotted and multipacket reception carrier-sense multiple access protocol with a finite and arbitrary number of users. We explicitly confirm that for a two-user Slotted-ALOHA (S-ALOHA) protocol, the resulting throughput region reduces exactly to the stability region calculated in previous works using the dominant system approach. Our results also show that the proposed carrier-sense mechanism considerably improves the stability region of a two-user S-ALOHA protocol whenever the original stability region shows non-convex characteristics. The results can be easily extended to IEEE 802.11 based wireless local area networks, which have been typically studied using p-persistent carrier-sense schemes, and also to networks with distributed antennas or with retransmission and cooperative diversity, which constitute hot topics in the communication system design arena. Finally, the benefits of the proposed carrier-sense mechanism are assessed by comparing the throughput region of several system configurations with two active users.**

***Index Terms*— Cross-layer design, multipacket reception protocols, random access.**

I. Introduction

The design of wireless random access protocols has regained attention due to new multipacket reception (MPR) capabilities provided by upgraded physical layer schemes such as multiple antenna receivers and cooperative and retransmission diversity systems [1]-[4]. This new perspective, where more than one packet can be simultaneously decoded from a single transmission, contrasts with the conventional collision-model in which any collision was assumed to yield the loss of all the the contending packets [5].

The first formulation that attempted to include stochastic multipacket reception capabilities in random access was the widely referenced work of Ghez and Verdu in [6]. The authors proposed a stochastic MPR matrix model for symmetrical systems (i.e., all the users have identical traffic and MPR parameters) and derived the maximum stable throughput (MST) of a Slotted ALOHA (S-ALOHA) protocol under the assumption of an infinite population. In [7], the authors have extended the analysis of the system by proposing an optimum decentralized retransmission strategy using the backlog states of the system. However, the MPR model introduced in [6] still lacked of an important feature of wireless networks: asymmetrical configurations. To fill this gap, Naware et al. have proposed in [8] a conditional reception probability approach for a finite-user S-ALOHA protocol which absorbs most of the characteristics of wireless channels, including such asymmetric scenarios. The authors have also used a dominant system approach to derive an exact closed-form expression for the stability region (i.e. the set of arrival rates for which the queues of all the users remain bounded) for the particular case of two-users, and derived sufficient and necessary conditions for stability in the case of more than two users. They have also found that S-ALOHA without transmission control is optimum when the stability region is convex (i.e., all the interior points are interconnected by lines that also lie inside the region). Naware et al. have further analyzed in [8] the delay properties of the system, particularly for the case of two active users. The protocol presented in this paper is an extension of the protocol in [6] as it will be explained later in this section.

Further details on the study of the finite-user S-ALOHA protocol with MPR have been presented in [9], where the authors introduced the notion of *standard* MPR channel that simply states the intuitive fact that collisions with high number of users are less likely to be captured than those with fewer users. They also defined the throughput region of the protocol as the set of throughput values for which all the transmission probabilities exist, and derived its properties under the assumption of a standard MPR channel. They also established the conjecture that the closure of the stability region converges to the throughput region, a conjecture previously established in the collision model approach (see [11] and references therein). In [10], the authors have proved, for the particular case of systems with two users, that this conjecture is true. In the demonstration they have employed the dominant system approach previously used for the analysis of the conventional S-ALOHA protocol (e.g., [11]). The proof for the case of systems with more than two users remains as an open problem today, even in the collision-model approach. An extension of the aforementioned multipacket reception model to the case when channel state information is available to the transmitter can be found in [12] and [13], where it was dubbed generalized multipacket reception model. Finally, the extension of such model to systems with retransmission diversity and without channel state information can be found in [14].

Despite the efforts previously described for the analysis of stability and delay properties of random access protocols with MPR, a protocol optimization, which would yield the transmission probabilities that maximize the throughput region, has not been explicitly derived as in the collision-model approaches. This is mainly due to the complex interactions between the queuing statistics and reception parameters. In this paper we carry out such optimization and derive a closed-form expression of the optimum transmission probabilities for protocols with a finite and arbitrary number of users, which is new in the related literature. Furthermore, in the protocol formulation, a carrier-sense mechanism is further proposed in order to improve the performance of the system in terms of throughput.

Carrier-sense multiple access (CSMA) protocols were proposed as an important improvement to the conventional ALOHA protocol [5]. They have been mainly used in wireline networks where the propagation delay is considerably smaller than the length of the packet. For purposes of this work, the CSMA protocol will considered as a simple generalization of the S-ALOHA protocol, thus leaving as future research work the analysis of all its possible impairments. In our analysis of the CSMA protocol, and due to the fact that existing MPR schemes assume that all the contending packets are equal-length, we will use a constant packet length distribution following the lines of the conventional CSMA protocol described in [15]. Our results indicate that the carrier-sensing mechanism improves the system performance under low MPR scenarios, but not further gain is achieved in systems with good MPR parameters. This also means that not scheduling resources are required for systems with strong MPR conditions, a result previously presented in [8] and which is further explored and confirmed in this paper.

Finally, we have found out that in the particular case of the S-ALOHA protocol with two-active users, our closed-form solution reduces exactly to the stability region of the protocol derived in [6] using the dominant system approach. Although this was implicitly proved by the authors in [10], we have derived explicit closed-form expressions for both the set of probabilities of transmission and for the throughput/stability region, which are new in the related literature and which clarify the reasons for the equivalence between the two regions.

The structure of this paper is as follows. Section II formulates the protocol rules and system assumptions. Section III presents the analysis of the throughput region. Section IV presents the optimization of the protocol with respect to the probabilities of transmission, while Section V provides analytical results for the two-user case, and Section VI describes some graphical examples. Finally, Section VII draws conclusions.

II. Reception Model and Protocol Description

This section describes the packet reception model to be used and the details of the protocol operation. Consider a slotted wireless multiaccess network with a central controller or base station (BS) and J active buffered users. Whenever user j senses the channel and finds it to be idle, then it transmits a packet provided its buffer is not empty. The packet arrival rate will be denoted by λ_j packets/time-slot, whereas the transmission probability is denoted by p_j. As regards the carrier-sense mechanism, the packet length, normalized to the time-slot of the system, is denoted by L. It is worth pointing out that the packet length is directly related to how often the carrier sense mechanism is performed along the duration of a packet transmission. Now, if it happens that two or more users simultaneously transmits a packet in a particular time-slot, then we assume that the BS will attempt the decoding of the contending packets using signal processing operations for MPR.

The reception model to be used is based on a conditional reception probability approach that was first introduced by Naware et al. in [8] for the analysis of a finite-user S-ALOHA protocol with MPR. The authors have defined the marginal probabilities of reception for user j, conditional on the transmission from a set of active users ($\mathcal{T}$), as follows:

$$q_{j|\mathcal{T}} = \sum_{\mathcal{R}:j\in\mathcal{R}\subseteq\mathcal{T}} q_{\mathcal{R};\mathcal{T}},$$

where $q_{\mathcal{R},\mathcal{T}}$ is the probability of decoding packets *only* from the set of users $\mathcal{R}$ conditional on the set of transmitting users $\mathcal{T}$. This marginal conditional probability model describes many characteristics found in wireless networks, particularly their asymmetric nature.

Now suppose that $\mathcal{U}$, $\mathcal{S}$, and $\widehat{\mathcal{S}}$ are three groups of terminals. We say the MPR channel is standard when the following inequality holds for all $\mathcal{U}\subseteq\mathcal{S}\subseteq\widehat{\mathcal{S}}$ [9]:

$$\sum_{\mathcal{R},\mathcal{U}\subseteq\mathcal{R}\subseteq\mathcal{S}} q_{\mathcal{R};\mathcal{S}} \geq \sum_{\mathcal{R},\mathcal{U}\subseteq\mathcal{R}\subseteq\widehat{\mathcal{S}}} q_{\mathcal{R};\widehat{\mathcal{S}}}. \quad (1)$$

This condition states that collisions of higher numbers of users will be always more destructive and hence less likely to be resolved than those collisions with less users.

Finally, to denote the random outcome of a packet transmission of length L and the absence of any transmission with length of one time-slot, we will use the random variable l for the length of the collision resolution period or epoch slot. Having defined the conditional reception probabilities and the system model we now proceed, in the next section, to analyze the performance of the protocol by defining and studying the individual throughput expressions and the throughput region of the protocol.

III. Performance analysis

For the performance analysis of the system, let us consider the packet throughput from user j as the ratio of the probability of correct reception of packets of user j with length L, denoted by $p_{s,j}$, to the average length of an interval, denoted by $E[l]$, which can be mathematically expressed as follows:

$$T_j = \frac{Lp_{s,j}}{E[l]}. \tag{2}$$

It is worth pointing out that the term L in the numerator is required to provide a fair comparison between systems that use a different packet length. The throughput can then be considered as measured in packet-units per time-slot, or simply as channel utilization. Now, the term $p_{s,j}$ can be calculated as in [9]:

$$p_{s,j} = \sum_{\mathcal{T}:j\in\mathcal{T}} \Pr(\mathcal{T}) q_{j|\mathcal{T}}, \tag{3}$$

where $\Pr(\mathcal{T})$ indicates the probability of occurrence of a particular set of transmitting users $\mathcal{T}$, and which can be written, under the assumption of independence of the queues, as follows [6]:

$$\Pr(\mathcal{T}) = \prod_{i\in\mathcal{T}} p_i \prod_{k\notin\mathcal{T}} p_k.$$

We can also obtain an expression for $E[l]$ by using the formula for a finite-user CSMA protocol with constant packet length [15]:

$$E[l] = L\{1 - \Pr(\mathcal{T} = \emptyset)\} + \Pr(\mathcal{T} = \emptyset),$$

where $\Pr(\mathcal{T} = \emptyset)$ is the probability that no user transmits, i.e. the probability that the set of of transmitting users is empty. This expression simply denotes that the length of the epoch is L whenever there is a packet transmission with probability $1 - \Pr\{\mathcal{T} = \emptyset\}$ plus the contribution of only one time-slot whenever there is no user transmitting with probability $\Pr\{\mathcal{T} = \emptyset\}$. Now, let us rewrite the above expression for $E[l]$ as follows:

$$E[l] = L + (1 - L)\Pr\{\mathcal{T} = \emptyset\},$$

and, assuming independence of queuing statistics, which is an assumption valid for low to medium traffic loads [17], if finally reduces to:

$$E[l] = L + \bar{L} \prod_k \bar{p}_k, \tag{4}$$

where $\bar{(\cdot)}$ denotes $1 - (\cdot)$. Having defined the individual throughput expressions and the particular terms that compose them, let us now turn our attention to the throughput region of the protocol. Let $\mathbf{T} = [T_1, \ldots, T_J]^T$ be the throughput vector and $\mathbf{p} = [p_1, \ldots, p_J]^T$ the vector of transmission probabilities, where $(\cdot)^T$ denotes the transpose operator. The throughput region $\mathcal{C}_T$ is then defined as in [9] as the union over all possible transmission vectors $\mathbf{p}$, i.e.,

$$\mathcal{C}_T = \left\{ \tilde{\mathbf{T}} \mid \tilde{T}_j = T_j(\mathbf{p}), 0 \le p_j \le 1, \forall j \right\}. \tag{5}$$

In [9], the authors have further demonstrated that the throughput region described in eq.(5), under the assumption of a standard MPR channel in eq.(1), is coordinate convex. In order to find the envelope of the throughput region we have to find the optimum transmission probabilities for the system, as explained in the next section.

IV. Protocol optimization

This section presents the optimization of the system expressions with respect to the probabilities of transmission. For such purpose, we will use the optimization method proposed by Abramson in [16], which can be stated as follows:

$$\mathbf{p}_{opt} = \arg\max_{\mathbf{p}} T_j \qquad \text{subject to } T_k = G_k \qquad k \neq j, \tag{6}$$

where G_k is a constant. This means that we look at all the solutions that maximize the throughput from user j, provided all other throughput values are kept constant. The boundaries of the throughput region is the obtained by exploring all possible values of the throughput constraints. Using the technique of Lagrange multipliers, this optimization problem is equivalent to solve the following set of equations:

$$\frac{\partial T_j}{\partial p_k} - \sum_{n:n\neq j}^{J} \upsilon_n \frac{\partial T_n}{\partial p_k} = 0, \qquad k, j = 1, \ldots, J,$$

where υ_n is the Lagrange multiplier associated to the n-th throughput value. The solution for this set of equations is given by setting the following Jacobian determinant to zero [16]:

$$|\mathbf{J}| = 0, \tag{7}$$

where $|\cdot|$ denotes the determinant operator and $\mathbf{J}$ is the Jacobian matrix with elements given by:

$$J_{i,j} = \frac{\partial T_j}{\partial p_k}. \tag{8}$$

For convenience let us now rewrite the expression for $p_{s,j}$ in eq.(3) by expanding it in terms of the individuals p_j's as follows:

$$p_{s,j} = p_j \left\{ q_{1|\{1\}} + \sum_{k=2}^{J} (-1)^{k-1} \sum_{\mathcal{T}_k:j\in\mathcal{T}_k} \prod_{i\in\mathcal{T}_k} p_i Q_{j,\mathcal{T}} \right\}, \tag{9}$$

where $Q_{j,\mathcal{T}} = q_{1,\{1\}} - q_{1,\mathcal{T}}$. Now consider the following expressions for the partial derivatives of $p_{s,j}$ and $E[l]$:

$$\frac{\partial p_{s,j}}{\partial p_k} = \frac{p_{s,j} - \alpha_{j,k}}{p_k},$$

and

$$\frac{\partial E[l]}{\partial p_k} = \frac{E[l] - \beta_k}{p_k},$$

where

$$\alpha_{j,j} = 0,$$

$$\frac{\partial \alpha_{j,k}}{\partial p_k} = 0, \quad \text{and} \quad \frac{\partial \beta_j}{\partial p_j} = 0.$$

Given the above relationships it results clear that the terms $\alpha_{j,k}$ and β_k represent the terms of $p_{s,j}$ and $E[l]$, respectively, which are not a function of p_k. Using the property of the determinants, in which the multiplication of any column or row by a scalar affects all the determinant by the same scalar, we can express a modified version of the elements of the Jacobian matrix in eq.(8) as follows:

$$\frac{p_k}{\beta_k}(E[l])^2\frac{\partial T_j}{\partial p_k} = \frac{p_k}{\beta_k}\left(E[l]\frac{\partial p_{s,j}}{\partial p_k} - p_{s,j}\frac{\partial E[l]}{\partial p_k}\right),$$

which, after some algebraic manipulations, can be finally expressed as:

$$\frac{p_k}{\beta_k}(E[l])^2\frac{\partial T_j}{\partial p_k} = A_j - B_{j,k}, \tag{10}$$

where

$$A_j = p_{s,j}, \tag{11}$$

and

$$B_{j,k} = \frac{\alpha_{j,k}}{\beta_k}E[l]. \tag{12}$$

After these simplifications, it can be proved, as shown in the Appendix, that the equation of the Jacobian determinant equal to zero in eq.(7) reduces to the following expression:

$$\sum_{j=1}^{J} A_j|\mathbf{B}_j| + |\mathbf{B}| = 0, \tag{13}$$

where $\mathbf{B}_j$ denotes the submatrix formed by setting to 1's all the elements of the j-th row of matrix $\mathbf{B}$ and whose elements are given by the $B_{j,k}$'s . For the sake of simplicity we will analyze, in the following section, the system expressions for the particular case of a network with two active users.

V. Two-user systems

First, consider the parametric equations given by the throughput expressions of both users:

$$\lambda_j = T_j = \frac{p_{s,j}}{E[l]}, \qquad j = 1, 2, \tag{14}$$

together with the formula for the optimum transmission probabilities in eq.(13). For the particular case of user 1, we have the following expressions:

$$p_{s,1} = p_1(q_{1|\{1\}} - p_2Q_1), \quad Q_1 = q_{1|\{1\}} - q_{1|\{1,2\}},$$

with similar expressions for user 2. The average length of an epoch can be obtained from eq.(4), but this time for a two-user system:

$$E[l] = L + (1-L)(1-p_1)(1-p_2). \tag{15}$$

After some algebraic manipulations detailed in the Appendix, eq.(13) can be finally expressed as:

$$\frac{(q_{1|\{1\}} - p_2Q_1)(1-\bar{L}p_1)}{q_{1|\{1\}}} + \frac{(q_{2|\{2\}} - p_1Q_2)(1-\bar{L}p_2)}{q_{2|\{2\}}} = E[l]. \tag{16}$$

Furthermore, if $L = 1$, which describes a S-ALOHA protocol, the previous expression becomes:

$$\frac{p_2Q_1}{q_{1|\{1\}}} + \frac{p_1Q_2}{q_{2|\{2\}}} = 1, \tag{17}$$

which represents an extension to the very well known expression for the optimum probabilities of transmission of the S-ALOHA protocol under the collision model, i.e. $p_1 + p_2 = 1$. It is important to note that for eq.(16), eq.(17) as well for the previous expression, the values for p_1 and p_2 should be bounded by $0 \le p_1, p_2 \le 1$.

Let us now find a non-parametric representation of the throughput region given by eq.(14) and eq.(17). For simplicity, we will derive our results for the S-ALOHA protocol. First of all we can obtain the value for p_1 or p_2 from eq.(17) and substitute it in eq.(14), which results in the following expressions:

$$p_1 = \sqrt{\frac{\lambda_1 q_{2|\{2\}}}{Q_2 q_{1|\{1\}}}}, \qquad p_2 = \sqrt{\frac{\lambda_2 q_{1|\{1\}}}{Q_1 q_{2|\{2\}}}}.$$

Substituting these expressions back into eq.(17) we obtain the following meaningful expression:

$$\sqrt{\lambda_1 Q_2} + \sqrt{\lambda_2 Q_1} = \sqrt{q_{1|\{1\}} q_{2|\{2\}}}.$$

Furthermore, by analyzing the boundaries at maximum load, for example when $p_2 = 1$ in eq.(14) and eq.(17) we obtain:

$$\lambda_2 = q_{2|\{2\}} - \frac{\lambda_1 Q_2}{q_{1|\{1\}} - Q_1}$$

with boundaries given by

$$\lambda_1 = \frac{q_{2|\{2\}}}{Q_2 q_{1|\{1\}}}(q_{1|\{1\}} - Q_1)^2$$

and

$$\lambda_1 = \frac{q_{1|\{1\}Q_2}}{q_{2|\{2\}}}.$$

Similar expressions can be obtained for user 2.

Summarizing the results above obtained, the throughput region of a two-user S-ALOHA can be finally expressed as the union of two solutions, i.e., $\mathcal{C}_T = \mathcal{G}_1 \cap \mathcal{G}_1$ where:

$$\mathcal{G}_1 \triangleq \{(\lambda_1, \lambda_2) : (\lambda_1, \lambda_2) \ge (0,0), (\lambda_1, \lambda_2) \text{ lies}\}$$
$$\text{below the curve } \lambda_2 = f(\lambda_1, q_{1|\{1\}}, q_{2|\{2\}}, Q_1, Q_2),$$

and

$$\mathcal{G}_2 \triangleq \{(\lambda_1, \lambda_2) : (\lambda_1, \lambda_2) \ge (0,0), (\lambda_1, \lambda_2) \text{ lies}\}$$
$$\text{below the curve } \lambda_1 = f(\lambda_2, q_{2|\{2\}}, q_{1|\{1\}}, Q_2, Q_1),$$

where

$$f(\lambda, a, b, c, d) = \begin{cases} b - \frac{\lambda d}{a-c} & \lambda \in \mathcal{I}_1 \\ \frac{(\sqrt{ab}-\sqrt{\lambda d})^2}{c} & \lambda \in \mathcal{I}_2, \end{cases}$$

where $\mathcal{I}_1 = \left[0, \frac{b(a-c)^2}{ad}\right]$, and $\mathcal{I}_2 = \left(\frac{b(a-c)^2}{ad}, \frac{ab}{d}\right]$. This region is identical to the stability region of the protocol obtained in [6] using the dominant system approach, thus explicitly confirming the equivalence between both solutions for the case of a particular two-user S-ALOHA system.

VI. Results

We now proceed to display the results for the throughput region of the protocol with different selection of reception parameters and different system configurations. Fig.1 shows the case where the two users have the same MPR parameters ($q_{1|\{1\}} = q_{2|\{2\}} = 0.8$, and $Q_1 = Q_2 = 0.6$) and a system configuration with different packet lengths ($L = 1,\ 2,\ 4$ and 8). It can be observed that the introduction of the carrier-sensing mechanism with packet lengths larger than the time-slot of the system yields an important improvement in the stability region of this example. By simply doubling the length of the packet, the stability is considerably increased.

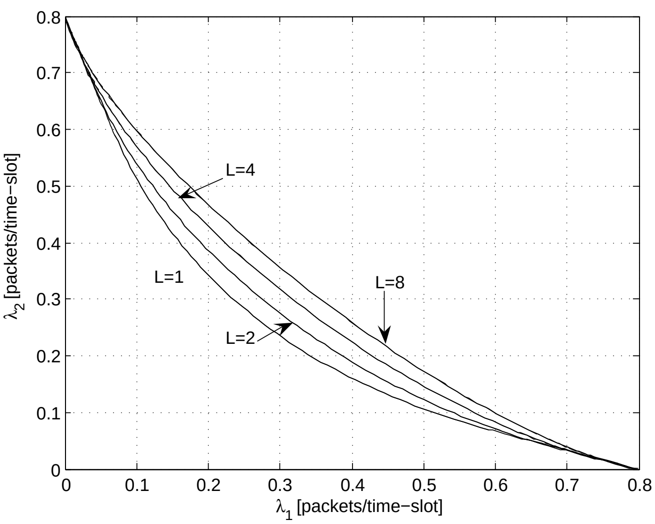

Fig. 1. Stability region for the CSMA protocol with different packet lengths and with the following MPR probabilities $q_{1|\{1\}} = q_{2|\{2\}} = 0.8, Q_1 = Q_2 = 0.6$

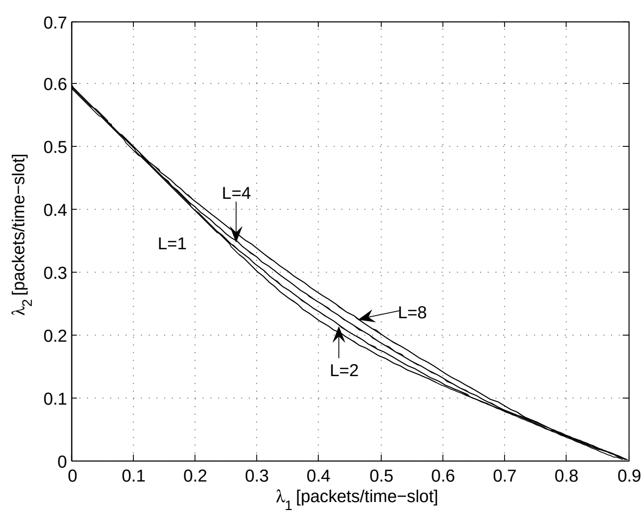

Fig. 2. Stability region for the CSMA protocol with different packet lengths and with the following MPR probabilities $q_{1|\{1\}} = 0.9, q_{2|\{2\}} = 0.6, Q_1 = 0.5$, and $Q_2 = 0.4$

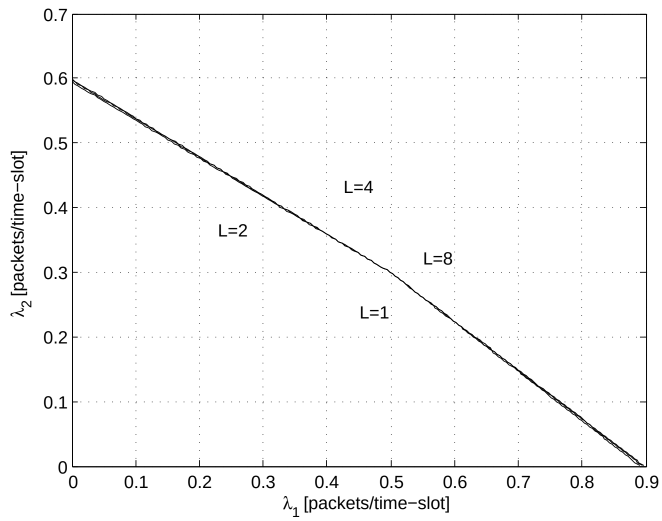

Fig. 3. Stability region for the CSMA protocol with different packet lengths and with the following MPR probabilities $q_{1|\{1\}} = 0.9, q_{2|\{2\}} = 0.6, Q_1 = 0.4$, and $Q_2 = 0.3$.

Fig.2 shows a case in which the users have different MPR parameters given by $q_{1|\{1\}} = 0.9, q_{2|\{2\}} = 0.6, Q_1 = 0.5$, and $Q_2 = 0.4$, which produce a stability region which is slightly larger than the one in Fig.1. In this case the carrier-sensing mechanism also helps in increasing the stability region of the system, but its effect is less obvious.

In comparison, the example in Fig.3 has a convex stability region. The MPR parameters used in this case were $q_{1|\{1\}} = 0.9, q_{2|\{2\}} = 0.6, Q_1 = 0.4,$ and $Q_2 = 0.3$. Note that the throughput region is not improved at all when the carrier-sensing mechanism is used. When the the stability region is convex then the system does not need a carrier-sensing scheme to improve its operation. This is another important consequence of cross-layer design in which a system provided with enough physical layer capabilities is able to stabilize the system, thus requiring no extra scheduling resources.

VII. Conclusions

This paper has presented an analysis of the optimum transmission probabilities of carrier sense and ALOHA-type random access protocols assisted by MPR. We have derived a simplified closed-form expression for such probabilities, which is helpful in describing the envelope of the throughput region of the system. Furthermore, our results for the S-ALOHA protocol with MPR and two active users were shown to exactly coincide with the stability region of the protocol previously obtained using the dominant system approach. An interesting result was that a carrier-sensing mechanism greatly improves the stability region only in systems with low MPR capabilities. An interesting future research topic is the extension of the analysis to other random access protocols with MPR capabilities.

VIII. Acknowledgements

Parts of this work have been carried out in the scope of the FUTON project (www.ict-futon.eu), which is co-funded by the European Commission FP7 programme. The authors acknowledge contributions from all partners of the project.

References

[1] L. Tong, V. Naware and P.Venkitasubramaniam, "Signal processing in random access," *IEEE Signal Processing Magazine*, Vol. 21, No. 5, pp. 29-39, September 2004.

[2] G. Dimic, N.D. Sisiropoulos and R. Zhang "Medium access control - physical cross-layer design," *IEEE Signal Processing Magazine*, Vol. 21, No. 5, pp. 40-50, September 2004.

[3] W. Choi and J. Andrews, "Downlink performance and capacity of distributed antenna systems in a multicel environment," *IEEE Transactions on Wireless Communications*, Vol. 6, No. 1, pp.69-73, January 2007.

[4] F.H.P. Fitzek and M.D. Katz, *Cooperation in wireless networks: priciples and applications,*Springer 2006.

[5] D. Bertsekas and R. Gallager, *Data Networks*, Prentice Hall 1992.

[6] S. Ghez, S. Verdu and S. Schwartz, "Stability properties of slotted Aloha with multipacket reception capability," *IEEE Transactions on Automatic Control.*, Vol. 33, No. 7, pp. 640-649, July 1988.

[7] S. Ghez, S. Verdu and S.C. Schwartz, "Optimal decentralized control in the random access multipacket channel," *IEEE Transactions on Automatic Control.*, Vol. 34, No. 11, pp. 1153-1163, November 1989.

[8] V. Naware, G. Mergen and L. Tong, "Stability and delay of finite-user slotted ALOHA with multipacket reception," *IEEE Transactions on Information Theory*, Vol. 51, No. 7, pp. 2636-2656, July 2005.

[9] J. Luo and A. Ephremides, "On the throughput, capacity, and stability regions of random multiple access," *IEEE Transactions on Information Theory*, Vol. 52, No. 6, pp. 2593-2607, June 2006.

[10] B. Shrader, and A. Ephremides A. "Random access broadcast: stability and throughput analysis," *IEEE Transactions on Information Theory*, Vol. 53, No. 8, pp. 2915-21, August 2007.

[11] R. Rao and A. Ephremides "On the stability of interacting queues in a multiple-access system," *IEEE Transactions on Information Theory*, Vol. 34, No. 5, pp. 918-930, September 1988.

[12] M. H. Ngo, V. Krishnamurthy and L. Tong, "Optimal channel-aware ALOHA protocol for random access in WLANs with multipacket reception and decentralized channel state information," *IEEE Transactions on Signal Processing*, Vol. 56, No. 6, pp. 2575 - 2588, June 2008.

[13] S. Adireddy and L. Tong, "Exploiting decentralized channel state information for random access," *IEEE Transactions on Information Theory*, Vol. 51, No. 2, pp. 537-561, February 2005.

[14] R. Samano-Robles, M. Ghogho, D.C. McLernon "A multiaccess protocol assisted by retransmission diversity And multipacket reception," *IEEE International Conference on Acoustics, Speech and Signal Processing,* ICASSP, Las Vegas, USA, March 2008.

[15] R. Bruno, M. Conti and E. Gregori, "Optimization of efficiency and energy consumption in p-persistent CSMA-based wireless LANs," *IEEE Transactions on Mobile Computing,* Vol.1, No. 1, pp. 10-31, Jan-March 2002

[16] N. Abramson "The throughput of packet broadcasting channels," *IEEE Transactions on Communications*, Vol.25, No.1, pp.117-28, January 1977.

[17] G. Dimic, N.D. Sidiropoulos and L. Tassiulas, "Wireless networks with retransmission diversity access mechanisms: stable throughput and delay properties," *IEEE Sigal Processing Magazine*, Vol. 51, No. 8, pp. 2019-30, August 2003.

IX. Appendix

A. Derivation of eq.(13) for the optimum probabilities of transmission.

The demonstration is by induction. First, consider the statement is true for $J = n$, then let us state the problem for the term $n+1$ and expand the Jacobian determinant in eq.(7) by cofactors as follows:

$$|\mathbf{J}(n+1)| = A_1|\mathbf{J}^{1,1}(n)| + \sum_{i=2}^{n+1}(-1)^{i+1}(A_1 - B_{1,i})|\mathbf{J}^{1,i}(n)|, \tag{18}$$

where $\mathbf{B}^{j,i}(n)$ denotes the submatrix of order n that results from removing row j and column i from matrix $\mathbf{B}(n+1)$. By hypothesis we know that:

$$|\mathbf{J}^{1,1}(n)| = |\mathbf{B}^{1,1}(n)| + \sum_{j=2}^{n} A_j|\mathbf{B}_j^{1,1}|,$$

while it can be demonstrated using the properties of determinants that:

$$\sum_{i=2}^{n+1}(-1)^{i+1}(A_1 - B_{1,i})|\mathbf{J}^{1,i}(n)| = |\mathbf{B}(n+1)|$$

$$+A_1\left[\sum_{j=2}^{n} A_j|\mathbf{B}_j^{1,i}(n)| + (-1)^{i+1}|\mathbf{B}^{1,i}(n)|\right].$$

Finally, by noting that by cofactors expansion:

$$|\mathbf{B}^{1,1}(n)| + \sum_{j=2}^{n}(-1)^{i+1}|\mathbf{B}^{1,i}(n)| = |\mathbf{B}_1(n+1)|,$$

and substituting back into eq.(18), we can obtain eq.(13) which completes the derivation.

B. Derivation of eq.(17) for the optimum probabilities of transmission of a two-user system.

Consider eq.(13) and the elements in eq.(11) and eq.(12), which are given by:

$$\alpha_{1,2} = p_1 q_{1|\{1\}}, \quad \alpha_{2,1} = p_2 q_{2|\{2\}},$$
$$\beta_1 = 1 - \bar{L}p_2, \quad \beta_2 = 1 - \bar{L}p_1,$$

together with the average length of an epoch given by eq.(15). Having defined these terms, we can calculate the following terms:

$$|\mathbf{B}_1| = -B_{2,1}, \quad |\mathbf{B}_2| = -B_{1,2}, \quad \text{and} \quad |\mathbf{B}| = B_{1,2}B_{2,1}.$$

By substituting these expressions in eq.(13) we can obtain:

$$\frac{p_{s,1}E[l]}{B_{1,2}} + \frac{p_{s,1}E[l]}{B_{2,1}} = E[l],$$

which, after some algebraic manipulations, can be finally shown to reduce to eq.(13).

Cross-Layer Design for TCP Throughput Maximization considering a Wireless end-point using SW-ARQ

Lucas Dias Palhão Mendes
National Institute of Telecommunications - Inatel
P.O. Box 05 - 37540-000
Santa Rita do Sapucaí - MG - Brazil
palhao@mtel.inatel.br

José Marcos Câmara Brito
National Institute of Telecommunications - Inatel
P.O. Box 05 - 37540-000
Santa Rita do Sapucaí - MG - Brazil
brito@inatel.br

***Abstract* - The presence of wireless nodes keeps growing in present day networks. However, TCP was not designed to work in high BER environments like a wireless link. In this work, we propose a new Cross-Layer solution to this problem. The Data Link Layer measures the channel BER and makes it available to the Transport Layer, which can adjust its segment size to an optimal value. By using a TCP throughput prediction model, we were able to prove there is a throughput increase when our solution is used.**

***Index Terms* - Wireless Networks, TCP, Cross-Layer, throughput prediction model, ARQ.**

I. INTRODUCTION

The number of wireless nodes is growing in TCP networks everyday. Such a heterogeneous environment can result in poor network operation because TCP may interpret a channel loss as a congestion indicator.

A widely discussed topic in recent networking research is Cross-Layer Design. By inserting some violations in the layered model, it can lead to improvements on network operation. Many proposals have been published, providing enhancements in different ways like mobile devices energy saving [1], better received multimedia quality [2], higher network resources use efficiency [3], and our main interest: adaptation of TCP to increase network throughput [4]; among many other Cross-Layer proposals.

Lately, there have been many proposals to improve TCP throughput by using Cross-Layer design. One of them, proposed by Kota [5], considers adaptive modulation and coding (AMC) using four different TCP versions: NewReno, SACK, Westwood+ and Hybla. Throughput was simulated for each of them adopting a satellite network, a range of signal to noise ratios (SNRs) and two schemes: BPSK with ½ coding rate (called mode 1) and QPSK with ¾ coding rate (mode 2). The results show that for each TCP version, there is an optimal SNR threshold for changing from mode 1 to 2, in order to increase throughput. Also, they prove TCP Hybla outperforms the throughput of the other versions in the presence of segment errors. However, their results could be improved using an ARQ scheme to diminish the channel error effects.

Another example of the Cross-Layer use in TCP networks can be seen in Möller *et al* [6]. Their first step was to divide a TCP connection in two: the first, between a file server and a web proxy, and the second, between the proxy and the mobile terminal. The latter had its TCP Congestion Control replaced by Möller's radio network feedback architecture. A radio network controller was responsible for the measurement of the available bandwidth. Also, it fed this parameter to the web proxy. Then, according to the number of packets waiting to be transmitted to the mobile terminal and the available bandwidth, the TCP's advertisement window was changed, leading to a better control of the number of packets in the transmission queue and their sustained delay. Their results show a download time 20% lower than using TCP Reno and a queue size stabilization around a predetermined value. Nevertheless, they have not considered packet errors introduced by the channel, thus they did not consider the use of an ARQ scheme.

As can be seen, ARQ is rarely considered in the literature. The work in [4] studies this scheme because it is already present in the technologies they model, which are EGPRS and 802.11a. However, we have chosen to use ARQ in this work because we will prove that it can increase throughput.

We propose a Cross-Layer design to increase throughput when there is a wireless node in the TCP network. We adopted a *stop-and-wait* scheme in the Data Link Layer, and a CRC 32 method to detect frames that were corrupted by the channel. Finally, the network enhancement is proved by using a TCP throughput prediction model proposed by Bruno Pinto [7].

The rest of this paper is organized as follows: the next section provides a brief history of TCP and what happened when wireless nodes began to be part of the existing networks; section 3 presents the Cross-Layer concept emphasizing the characteristics of our Cross-Layer proposal later; then, section 4 summarizes how the model developed by Bruno Pinto [7] for TCP throughput prediction works; in section 5 we present our Cross-Layer proposal and analyze its effects on a network containing a wireless end-point, and; finally, we present our conclusion in section 6.

II. TCP/IP IN WIRELESS NETWORKS

According to Kleinrock [8], still during the age of the ARPANET, the first Transport Layer protocol was created. It was called Network Control Protocol (NCP). However, as different types of networks emerged, like the Packet Radio Network (PRNET) and the Packet Satellite Network (SATNET), network designers had foreseen that the protocol running on the Transport Layer had to be able to interconnect a type of network to any other. Thus, in 1974, the Transmission Control Protocol (TCP) was proposed, and has been widely adopted. More technologies were aggregated into networks, such as optical fibers, satellite links and wireless networks since then [9]. It led to the scenery we have today: almost ubiquitous wireless Internet access through a heterogeneous network. However, the TCP Congestion Control mechanism was designed considering the low BERs present in cabled networks. Thus, every dropped packet was an indicator of network congestion. As mobile nodes joined TCP networks, wireless channels, with higher BERs, started causing packet corruption and discard, which triggers TCP Congestion Control and results in throughput reduction [10]. Also, mobile devices have slower transmitters because of their limited resources, introducing asymmetry between downlink and uplink. This can result in ACK loss or ACK compression, which reduce throughput as well [11].

Suppose the network shown in Fig. 1 with its characteristics depicted in Table 1.

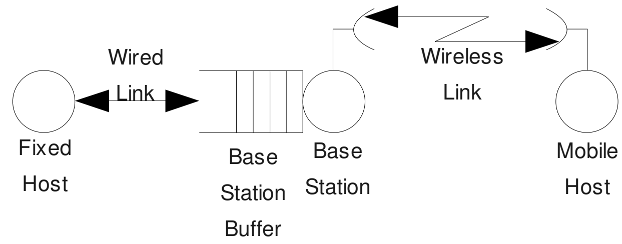

Fig. 1. Network Model

TABLE I
NETWORK CHARACTERISTICS

Parameter (symbol)	**Value**
Wired Network Total Delay	999 msec
Base Station Buffer Size (*B*)	20 packets
Base Station Transmission Rate (μ)	100 packets/sec
TCP Segment Size	4320 bits
TCP ACK Size	320 bits
TCP ACK Transmission Delay	0.9 msec
Wireless Link Propagation Delay	50µs

The values above were chosen in order to result in τ=1 [7]. This parameter represents the total network delay minus the transmission delay in the wireless link.

Considering a BER of $2*10^{-9}$ in the wireless link, we have the TCP congestion window behavior depicted in Fig. 2, simulated using *ns-2* [12].

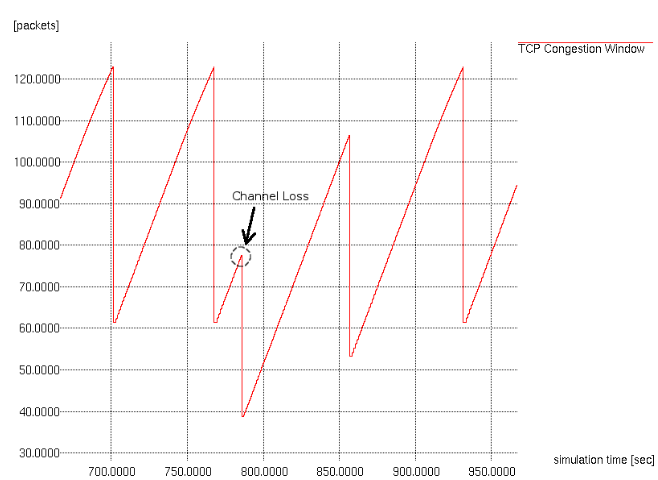

Fig. 2. TCP Congestion Window with Channel Errors

Throughput can be calculated by dividing the sum of packets transmitted by the time taken to transmit them. If no channel losses occurred, the throughput would be 86.1358 packets/sec, and in the case shown in Fig. 2, the throughput was 77.5 packets/sec. Varying the BERs from 10^{-2} to 10^{-10} we have the simulated results shown in Table II.

TABLE II
THROUGHPUT VS CHANNEL BER

Channel BER	Throughput [packets/sec]
10^{-2}	0.0056
10^{-3}	0.0056
10^{-4}	0.0056
10^{-5}	0.2185
10^{-6}	4.7146
10^{-7}	17.5542
10^{-8}	56.3977
10^{-9}	80.8141
10^{-10}	85.4651

In order to solve the aforementioned problems, many proposals emerged. The common procedure to hide noncongestion losses from TCP is to use forward error correction (FEC) schemes or automatic repeat request (ARQ) protocols [9], [10], [13] in the Data Link Layer. An FEC scheme adds redundancy bits to the transmission block in order to give the receiver the capability to correct some of the errors introduced by the channel. Consequently, it introduces a transmission overhead as part of the sent bits are not carrying data. Also, it increases the processing delay because coders are needed to generate the redundancy bits and decoders must recover the original data. Although FEC is best suited for high-latency links, such as satellite communication systems, it can be used in wireless media as well, reducing the probability of packet discards caused by channel losses. On the other hand, ARQ protocols deal with packet losses by retransmitting them. Several retransmission approaches can be used, such as *stop-and-wait*, *go-back-N*, and *selective-repeat*. Although *stop-and-wait* is the less efficient approach, beginning an analysis with this scheme is simpler, and later we can extend the work to the other approaches. A few limitations must be respected when using ARQ. It introduces bandwidth overhead when there is data retransmission and also adds delay and jitter, so it can only be used for transmission of non-delay-sensitive data. Furthermore, it can trigger TCP timeouts if it has to retransmit the same block many times, so a limit to the number of retransmissions must be imposed.

Moreover, there is still another option to reduce the impact of corrupted blocks on the network performance. Unless a FEC scheme is being used, every time link-level drivers detect blocks of data with errors, they will discard them. Nevertheless, if there was a way to warn TCP that a channel loss occured, it would not trigger its Congestion Control mechanism and could retransmit the lost data without reducing its congestion window [13]. This type of solution charaterizes a Cross-Layer design [14], concept covered next.

III. CROSS-LAYER

The layered model allows communication only between adjacent layers. Each layer offers services to its neighbors using interfaces. A network designer can follow these restrictions or share information among non-adjacent layers. Furthermore, variables could be made global to the entire protocol stack. These violations, which characterize a cross-layer design [14], aim at some optimized network behavior.

Cross-layer design is categorized by Srivastava and Motani [14] as follows:

- creation of new interfaces (e.g. in [15]);
- merging of adjacent layers (e.g. in [16]);
- design coupling (e.g. in [17]);
- vertical calibration (e.g. in [18]).

'Creation of new interfaces' is characterized by one or more layer variables made visible to non-adjacent layers. Also, it can be implemented in three ways:

- Upward Information Flow: a lower layer send its information to an upper non-adjacent layer;
- Downward Information Flow: an upper layer shares its variables with a lower non-adjacent layer;
- Back-and-forth Information Flow: two non-adjacent layers send information to each other.

Cross-Layer solutions allow us to achieve network optimization that would be infeasible using conventional methods.

We have special interest in the creation of a new interface that implements an Upward Information Flow. This will allow us to prove that the TCP throughput can be increased if the Transport Layer has information about the channel BER, parameter that can be determined by the Data Link Layer. For more information on the other cross-layer design types, refer to [14].

IV. MODEL FOR TCP THROUGHPUT PREDICTION

The model proposed by Bruno Pinto [7] allows us to calculate the TCP throughput when the network uses *stop-and-wait* (SW) or *go-back-N* (GBN) as ARQ schemes in the Data Link Layer. Also, it assumes that the TCP segments are not fragmented in multiple IP packets or Data Link frames.

Through the analysis of the behavior of the network, like depicted by the congestion window in Fig. 1, Bruno Pinto noticed three possible events [7]:

- One packet is discarded at the buffer when it is full, triggering a *Fast Retransmission/Fast Recovery*;
- Two packets are discarded, one at the full buffer and the other at the receiver because of a channel error, causing two successive *Fast Retransmission/Fast Recovery* events;
- Three or more packets are discarded, causing a *Timeout*.

Each event has an associated duration and causes a change in the number of packets being transmitted over the network. Through the ratio between the number of packets transmitted in the occurrence of each event and their respective durations, Pinto could derive each event throughput equation [7]. Then, Pinto analyzed the probability of each event occurrence and multiplied each one by its respective event throughput, which resulted in the network throughput ($\bar{\lambda}$). Finally, the normalized network throughput is given by:

$$NT = \frac{\bar{\lambda} \cdot k'}{R} \tag{1}$$

where k' is the number of TCP data bits in each transmitted packet and R is the wireless link transmission rate. Its validation is presented in [7], showing it achieved an excellent approximation to simulations using *ns-2* [12], which made the model attractive for use in this work. We will consider only the SW-ARQ part in this work for the sake of simplicity, leaving the GBN approach for a future work.

V. Cross-Layer Proposal and Results

Adopting SW-ARQ and a CRC-32 technique for frame error detection, we propose a new interface between the Network Access Layer and the TCP Layer in the TCP/IP stack. Implementing an Upward Information Flow, the Transport Layer can be aware of the channel BER measured by the Data Link Layer. Then, the TCP Segment Size can be adjusted to achieve the highest throughput allowed in the occurrence of that BER, whithout changing the SW-ARQ scheme in the Data Link Layer.

SW-ARQ has been extensively studied and the equation to calculate its efficiency can be found in Schwartz [19]. Thus, the maximum efficiency can be found by derivation. However, since TCP throughput equations [7] are not differentiable, we had to apply the brute force method to find its maximum. Furthermore, we decided to apply the same method to the SW-ARQ efficiency. The results are shown in Fig. 3.

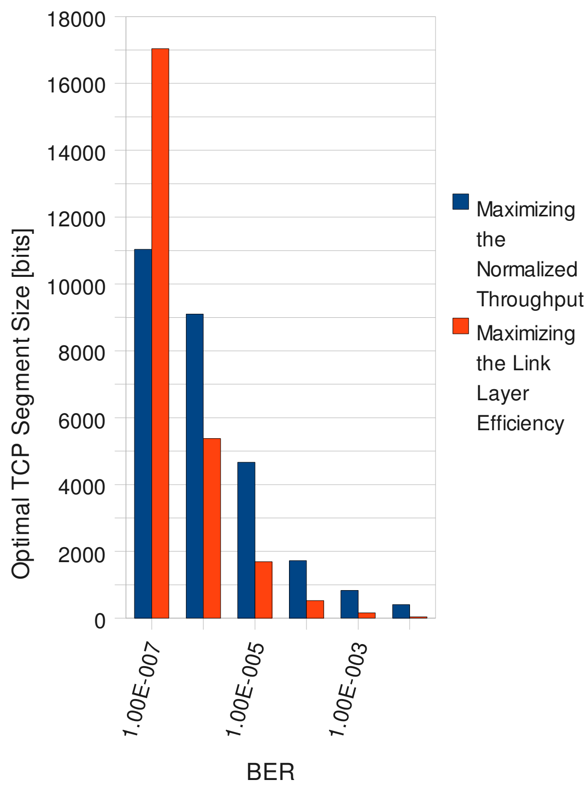

Fig. 3. Optimal TCP Segment Size

As can be seen in Fig. 3, the optimal segment sizes for maximum TCP throughput are different from the sizes for optimal Data Link Layer efficiency.

Based on these results, we analyzed three different scenarios:

- In the first case, we used the segment size that maximizes the TCP throughput for each BER.
- In the second, we adopted the frame size that maximizes the Data Link Layer efficiency and calculated the total segment size by adding the TCP/IP headers (320 bits) to the frame size.
- In the last case, we used a fixed segment size of 4320 bits. Bruno Pinto [7] used this segment size, thus we adopted it for comparison purposes. Using the segment size of each scenario, we determined the TCP throughput for a range of BERs, as depicted in Fig. 4.

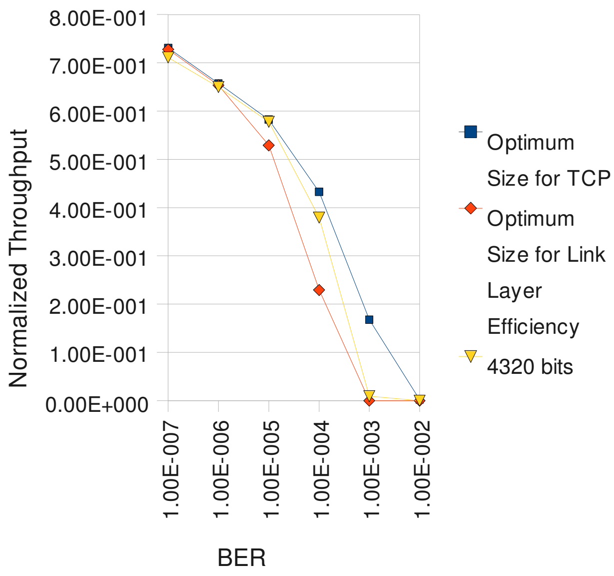

Fig. 4. Normalized Throughputs for different TCP Segment Sizes

We notice that a segment size that maximizes the Data Link Layer efficiency can result in a throughput lower than a fixed segment size, as can be seen in Fig. 4 for BERs higher than 10^{-6}. Also, we notice that using the optimal segment size for TCP, the network achieves a higher throughput for every BER, with meaningful results in the occurrence of BERs above 10^{-5}.

Finally, we proved that the proposed Cross-Layer solution can result in higher TCP throughput. It was accomplished by feeding the TCP layer with the channel BER that can be determined by the Data Link Layer.

VI. Conclusion and Future Work

We were able to show that the TCP throughput can be increased if the TCP Layer is aware of the channel BER. This was achieved by creating a new interface connecting the TCP Layer and the Data Link Layer, which characterizes a Cross-Layer design. Through this 'Upward Information Flow' interface, the BER was made visible to the TCP Layer, which could adjust its segment size in order to increase throughput. Varying the TCP segment size can result in higher throughput because for every BER there is a best trade-off between the segment size and its loss probability. Large segments have a higher probability of having one of their bits corrupted by the channel, so they are best suited for low BERs. However the efficiency, and in consequence the throughput, will be decreased when the segments are small because of their fixed number of header bits. Thus, for every BER there is an optimal segment for throughput maximization, as proven in this work. Furthermore, the Cross-Layer solution proposed proved to achieve higher throughput than respecting the layered model and finding a frame size that maximizes the Data Link Layer efficiency or using a fixed TCP segment size.

Future works may consider GBN-ARQ in the link layer. The effect of the proposed Cross-Layer design in the packet delay and its variation may be studied as well.

VII. References

[1] Min Tian, Andreas Gramm, Hartmut Ritter, Jochen H. Schiller, Thiemo Voigt, Adaptive QoS for Mobile Web Services through Cross-Layer Communication ,*Computer*, vol. 40, no. 2, Feb. 2007, pp. 59-63.

[2] Hsien-Po Shiang, M. van der Schaar, Multi-user Video Streaming over Multi-hop Wireless Networks: A Cross-Layer Priority Queuing Scheme , *International Conference on Intelligent Information Hiding and Multimedia Signal Processing 2006*, pp. 255-258.

[3] Qinghe Du, Xi Zhang, Cross-Layer Resource-Consumption Optimization for Mobile Multicast in Wireless Networks ,*International Symposium on a World of Wireless, Mobile and Multimedia Networks 2006*, pp. 368-376.

[4] J.P. Singh, Y. Li, N. Bambos, A. Bahai, B. Xu, G. Zimmermann, TCP Performance Dynamics and Link-Layer Adaptation Based Optimization Methods for Wireless Networks , *IEEE Transactions on Wireless Communications*, vol. 6, issue 5, May 2007, pp. 1864-1879.

[5] S. L. Kota, Cross-Layer Design Challenges for Quality of Service Guarantees in Satellite Networks ,*Military Communications Conference 2006*, pp. 1-7.

[6] N. Moller, A. Arvidsson, J. Petersson, C. Fischione, R. Skog, P. Karlsson, K.H. Johansson, Supporting End-to-End Applications Over HSDPA by Cross-Layer Signalling , *IEEE Wireless Communications and Networking Conference 2007*, pp. 3855-3860.

[7] Bruno Couto Costa Pinto and Jose Marcos Camara Brito, An Analytical Model to Compute the Throughput of Wireless TCP Networks, *VI International Telecommunications Symposium (ITS2006)*, September 2006, pp. 738-743.

[8] Leonard Kleinrock, History of the internet and its flexible future, *IEEE Wireless Communications*, vol. 15, no. 1, February 2008, pp. 8 18.

[9] Chadi Barakat, Eitan Altman and Walid Dabbous, On TCP performance in a heterogeneous network: A survey, *IEEE Communications Magazine*, vol. 38, no. 1, January 2000, pp. 40 46.

[10] Nasir Ghani and Sudhir Dixit, TCP/IP Enhancements for Satellite Networks, *IEEE Communications Magazine*, vol. 37, no. 7, July 1999, pp. 64 72.

[11] R. Durst, G. Miller and E. Travis, TCP Extensions for Space Communications, *Wireless Networks*, Oct. 1997, vol. 3, no. 5, pp. 389-403.

[12] The Network Simulator 2, http://www.isi.edu/nsnam/ns/

[13] G. Huston, TCP in a wireless world, *IEEE Internet Computing*, vol. 5, no. 2, Mar/Apr 2001, pp. 82 84.

[14] V. Srivastava, M. Motani, Cross-layer design: a survey and the road ahead, *IEEE Communications Magazine*. Volume 43, Issue 12, Dec. 2005 pp. 112 119.

[15] L. Haratcherev, J. Taal, K. Langendoen, R. Lagendijk, H. Sips, Optimized video streaming over 802.11 by cross-layer signaling, *IEEE Communications Magazine*, vol. 44, issue 1, Jan. 2006, pp. 115-121.

[16] X. Lin, N. B. Shroff, R. Srikant, A Tutorial on Cross-Layer Optimization in Wireless Networks, *IEEE Journal on Selected Areas in Communications*, vol. 24, issue 8, Aug. 2006, pp. 1452-1463.

[17] L. Tong, V. Naware, P. Venkitasubramaniam, Signal Processing in Random Access, *IEEE Sig. Proc.*, vol. 21, issue 5, Sept. 2004, pp. 29-39.

[18] V. T. Raisinghani, S. Iyer, Cross-layer feedback architecture for mobile device protocol stacks, *IEEE Communications Magazine*, vol. 44, issue 1, Jan. 2006, pp. 85-92.

[19] Schwartz, Mischa. *Telecommunication Networks: Protocols, Modeling and Analysis.* Adisson-Wesley, 1988.

Two Phases Solution for the Migration to NGN IMS Network

Ali Amer, IEEE Member
Saudi Telecom Company, Riyadh - Saudi Arabia
E-mail= aliamer@stc.com.sa

Abstract— **Telecom Network Operators are in the process of migration to Next Generation Network (NGN) to provide multimedia and innovative value added service to their customers. The NGN is ultimately designed for new service provision, independent of access technology and to reduce Capital Expenditure (CAPEX) and Operational Expenditure (OPEX). Soft switches(SS) are the heart of today's VoIP Networks and are considered the first cornerstone in the NGN migration process. In the same time, the IP Multimedia Subsystem (IMS) is emerging and expected to be the ultimate target architecture to provide the basic framework for NGN and consolidate both circuit-switched and packet-switched networks into on single network for all services. With the commencement of IMS rollout, there are a lot of discussion regarding which migration path should be followed by Telecom operators. In this paper, a two phases solution for the migration to NGN IMS network is presented**.

Keywords: **Next Generation Network (NGN), IP Multimedia Subsystem (IMS), Soft Switch (SS), migration, PSTN.**

I. INTRODUCTION

Telecom operators are in the process of migration to Next Generation Network (NGN) to provide multimedia and innovative added value service to their customers[13]. The International Telecommunication Union- Telecommunication Standardization Sector (ITU-T) defined the NGN in Y.2001 Recommendation [9] as "a packet based network able to provide services including telecommunication services and able to make use of multiple broadband, QoS-enabled transport technologies and in which service related functions are independent from underlying transport-related technologies. It offers unrestricted access to users by different service providers. It supports generalized mobility which will allow consistent and ubiquitous provision of services to users". For European Telecommunications Standards Institute (ETSI), the NGN is "a concept for defining and deploying networks, which due to their formal separation into different layers and planes and use of open interfaces, offers service providers and operators a platform which can evolve in a step-by-step manner to create, deploy and manage innovative services".

From these definitions, NGN is a network architecture that is ultimately designed for Multi-service provision, independent of access technology. It has separate transport, control, and application layers that can enable different operators to compete with each other in different layers. As these layers are open, competition could be very aggressive, giving immense benefits to the consumers while providing new opportunities to innovative service providers. The NGN functional architecture are grouped into four separate layer (planes) : Access, Transport, Control, and Services. The access plane provides the infrastructure (e.g. access network between the end user and transport network. The transport plane provides the communication among the reference architecture entities, as well as communication between the neighboring layers of the functional NGN model. The control plane is responsible for the network elements and for services control. The service plane provides the features of the basic services that can be used for the development of the sophisticated services and applications[8]. The NGN architecture is intended to offer convergent multimedia services using a unique and shared core network for all types of access Networks. The NGN functional architecture is abstracted in Figure 1

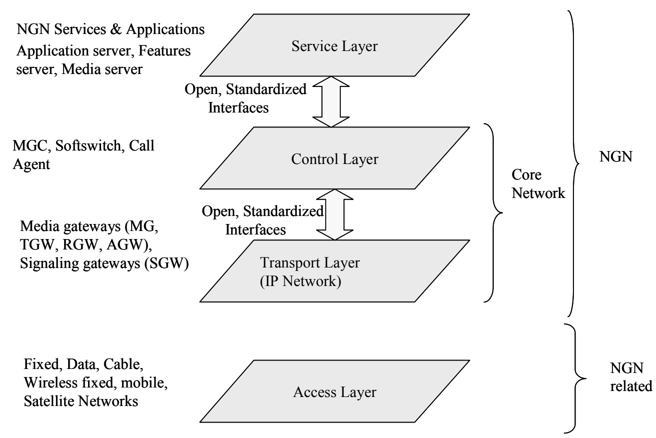

Figure1:NGN functional Architecture overview

IMS enables a service-centric view of the network and allow Telcos to connect customers to the service regardless of the customer's access type (e.g. WiMax, DSL, UMTS, VSAT, FTTH, etc.). This is significantly more cost effective than deploying and operating a different infrastructure for each service or group of services. Each network operator will potentially choose a different migration path depending on their actual assets. This path will therefore involve different technologies either going to softswith then evolve to IMS or going direct to IMS, and will happen at different speeds.

II. NGN MIGRATION DRIVERS

Telcos have different drivers for migration to NGN Sofswitch or IMS architecture, depending on the type of the operators

(Fixed, mobile, incumbent, new entrant), the markets (developing country or developed economy, their Network access infrastructure and broadband penetration, and the state of their existing switching infrastructure[12]. Based on the driver for each operator, different technology migration paths emerge. However, the move from circuit switched networks towards IP based networks is related to convergence of network technologies, and there are several drivers for convergence. One driver is improving cost efficiency by eliminating some of the parallel networks having wide coverage and serving the same geographical area, e.g. the PSTN, PLMN and the Internet[15],[2]. Another common driver is the ability to create new applications by combining the various means of communication originally found in separate non-interworking networks into one application combining things like voice, video, instant messaging, email, into a seamless user experience. In addition to that, the Telcos aim to reduce their network infrastructure and maintenance costs, deploy more services to their customers to create additional new sources of revenues. IMS offers a better value proposition for customer giving them the freedom to choose: "Access your Services anywhere using any device". IMS is also a prime enabler for Fixed Mobile Convergence (FMC)[15]. Most of the Service Providers specially those have both fixed and mobile arms, are interested in FMC. It is seen a way to stop loss of revenue to mobile competitors by offering ubiquitous voice service between their fixed and mobile networks. Customers can benefit from lower tariffs by using VoIP over WLAN while in range to a fixed data network, and then seamlessly continue their conversation using the mobile network after they move out of range. Other IMS benefits include faster time to market for new services. This requires proper investment in IMS based Service Delivery Platforms (SDP). Services developed for IMS can be made available to both fixed and mobile subscribers. Ideally with IMS, consolidation of the core network will eventually lead to a consolidation of Network Management Systems which can give OPEX savings and a greater ability to monitor the service from end-to-end[16].

III. DEPLOYMENT STRATEGIES

Most operators are investigating the IMS framework and are running pilots, conducting lab trials, and benchmark testing[18]. However operators have varying approaches to deploying IMS. The main approaches include:

First to Market: These operators firmly believe in IMS and want to be first in the market to offer new services and benefit from the cost savings of IMS. These operators are mostly converged operators and Tier-1 mobile operators. O2, TIM (Telecom Italia Mobile), Telia Sonera, France Telecom, Telefonica, Sprint, and others are examples of this category. Services being deployed first include fixed mobile convergence, video sharing and Push to talk over cellular (PoC).

Gradual Starts: These operators realize that IMS is the way of the future, but they are waiting for interoperability testing and standards to become more mature before starting to deploy. Operators that fall in this category include Vodafone Japan.

Smart Followers: These operators are investigating IMS networks, but have set no time frame for deployment. They will wait for solutions that address all their concerns, and for the maturity stage of IMS. Saudi Telecom belongs to this group.

IV. IP MULTIMEDIA SUBSYSTEM (IMS)

IP Multimedia Subsystem (IMS) is referred as the heart of NGN. IMS is the next generation IP based infrastructure enabling convergence of data, speech, video, and mobile network technology. IMS was initially created by a consortium of service providers, vendors, and standards bodies referred to as the 3rd Generation Partnership Project (3GPP). 3GPP defined IMS as part of 3GPP Release 5 (R5) to enable IP multimedia services over mobile (3G) packet networks [1]. 3GPP has gone ahead and defined 3GPP Release6 (R6), Release7 (R7), and is working on Release8. All these releases are based on IMS. Also, another standard body for North America called 3GPP2 has defined the Multi-Media Domain (MMD) which is based on 3GPP IMS. The ETSI is an important member of 3GPP, and has defined the current NGN standard called ETSI TISPAN NGN Release1 (R1). This NGN standard is based on IMS from 3GPP R6. The IMS from 3GPP R6 has been extended in this NGN standard to support fixed networks. The ITU-T Global Standards Initiative is also defining NGN standards. These standards are also being based on IMS. In conclusion, IMS is not distinct from NGN, but a core part of standardized NGN[14]. IMS provides session control, connection control and an application services framework with both subscriber and services data, while allowing interoperability of these converged services between subscribers. IMS offers a wide selection of services including push-to-talk, VoIP, video conferencing, content sharing, messaging, presence, and other versatile third party applications, customized to meet the specific needs of the users. With SIP, users can integrate different services in their communications, and are allowed to add or drop services as and when they want. By deploying IMS architecture, applications can be created, controlled, changed and upgraded regardless of network access type. IMS has been adopted by telecom standardization bodies, major service providers, and equipment manufactures.

V. IMS ARCHITECTURE

The IMS architecture will be used by service providers in NGN networks to offer network controlled multimedia services. As illustrated in figure2, the IMS architecture is split into three main planes or layers, each of which is described by a number of equivalent names: Service or Application Plane, Control or Signaling Plane, and User or Transport Plane.

The application plane provides an infrastructure for the provision and management of services, and defines standard interfaces to common functionality including:

configuration storage, identity management, user status (such as presence and location), which is held by the Home Subscriber Server (HSS);

billing services, provided by a Charging Gateway Function (CGF) (not shown);

control of voice and video calls and messaging, provided by the control plane

The control plane is placed between the application and transport planes. It routes the call signaling, tells the transport plane what traffic to allow, and generates billing information for the use of the network, carries the gateway functions towards different networks, the admission control, network-level user identification and authentication.

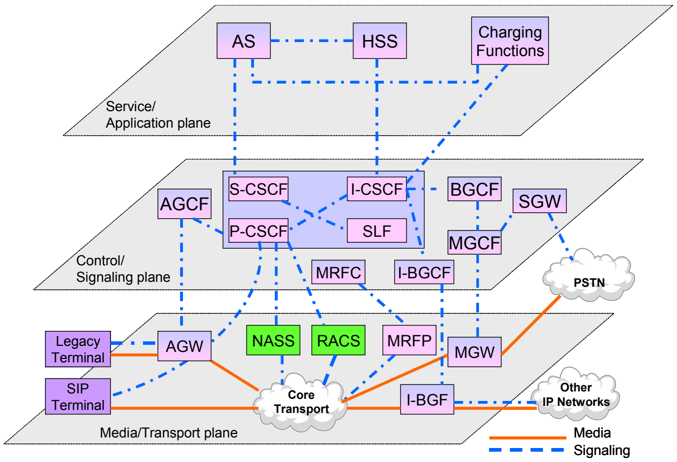

Figure 2: IMS Architecture

At the core of this plane is the Call Session Control Function (CSCF), which comprises the following functions.

The Proxy-CSCF (P-CSCF) is the first point of contact for users with the IMS. The PCSCF is responsible for security of the messages between the network and the user and allocating resources for the media flows.

The Interrogating-CSCF (I-CSCF) is the first point of contact from peered networks. The I-CSCF is responsible for querying the HSS to determine the S-CSCF for a user and may also hide the operator's topology from peer networks. The Serving-CSCF (S-CSCF) is the central brain. The S-CSCF is responsible for processing registrations to record the location of each user, user authentication, and call processing (including routing of calls to applications). The operation of the SCSCF is controlled by policy stored in the HSS. This infrastructure is designed to provide a wide range of IP multimedia server-based and P2P services.

VI. TODAY'S NETWORK

Telcos worldwide are accelerating the migration of legacy systems to both NGN soft switch based and IMS infrastructure[5]. Most of them have started migrating their traditional Public Switch telephone Network (PSTN). PSTN uses Class5 and Class4 circuit switches along with Time Division Multiplexing (TDM) technology to transport voice[4]. It uses also the SS7 signaling network to handle call setup and teardown, plus other control functions. A typical PSTN Network is depicted in figure 3.

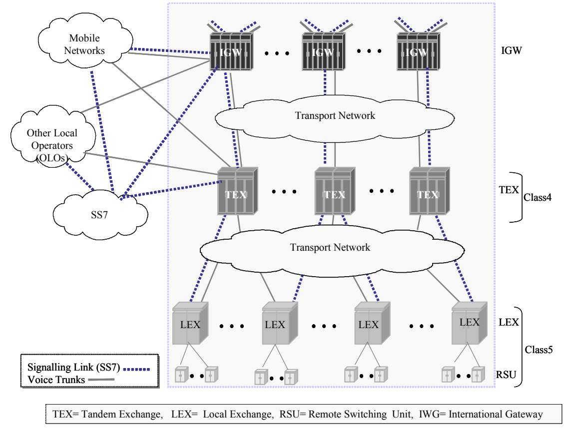

Figure 3: Typical PSTN Network

Eventually, Legacy networks (PSTN) lack the capability of providing multiservice, and getting costly operated, therefore, it has to be migrated to NGN. For the evolution of the PSTN network, there are two alternatives being addressed within ETSI TISPAN recommendations:

PSTN Emulation Subsystem (PES): near-perfect PSTN emulation, with a focus on supporting most if not all legacy PSTN services in a way that is transparent to the end user (same equipment, same look and feel);

PSTN Simulation Subsystem (PSS): simulation of the most popular legacy services and support for the most commonly used set of PSTN services, with possibly different behaviors from some of the services.

Carrier networks are undergoing radical changes as they move from TDM to NGN and then eventually to IMS. while soft switch technology is enjoying full maturity, IMS is emerging from the shadows and seems destined for center stage[3]. However, it's clear that these three domains will be part and parcel of network infrastructure for years to come.

VII. MIGRATION PROPOSITION

Our proposed solution has two phases, and aims to migrate the legacy network (PSTN) to NGN Sofswitch (SS) in the first phase, then to IMS in the second phase.

Phase 1: the Proposed solution consists of migrating the PSTN to NGN soft switching platform. The solution is derived from the ETSI TISPAN PES and consists of replacing Class4 by Media Gateways (called here Trunking gateways) and Class5 by Access Gateways (AGW) or multiservice Access Node (MSANs). The new NGN network will be divided in domains. As illustrated in figure4, a domain may be loosely defined as a collection of Softswitch (SS), Trunking Gateways (TGW), Media Resource Server (MRS), and one signaling Gateway (SWG). Phase 1 is scoped in the following three (3) steps:

*Step1:*The Softswitch (SS), Media gateway called here Trunking gateway (TGW), Signaling gateways (SGW), and the Media resource Servers (MRS) are deployed. SS7 signaling is interfaced with TDM networks via SGW, and IP signaling is interfaced with other VoIP incumbent and alternative operators.

Step2: Class4 (Transit/ Tandem) exchanges are replaced by Trunking Gateways and the transit traffic is carried over the IP/MPLS core Network.

Step3: Access gateways (AGW) or The Multiservice Access Node (MSAN) are deployed for multi-service access node functionality and for provisioning Class5 services to traditional subscribers originally connected to TDM Local exchanges (LEs). Under this phase, AGW maintains traditional TDM connection with Remote Switching Units (RSU), where both ISDN and POTS subscribers are connected. This phase completes the transformation to Next Generation Network services. Operators could deploy new applications to enable new revenue-generating subscriber services (xDSL, FTTX, etc,).

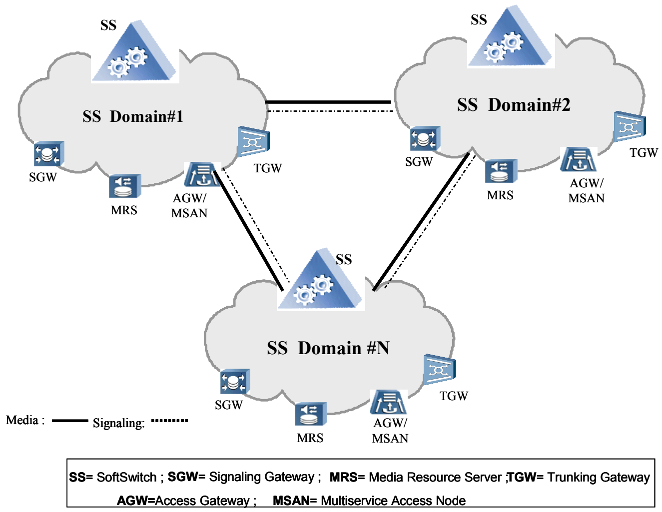

Figure 4: Soft Switch (SS) Domains concept

The solution assumes the existence of an aggregation, edge, and backbone IP/MPLS network capable of handling the traffic generated with the adequate Quality of Service, and the required interfaces which are mainly based on Ethernet. The aim of Softswitch NGN based solution is to support PSTN/ISDN replacement. The solution can be evolved in the future to a full IMS/TISPAN architecture. Figure5 outlines the Phase 1 solution architecture and its connectivity.

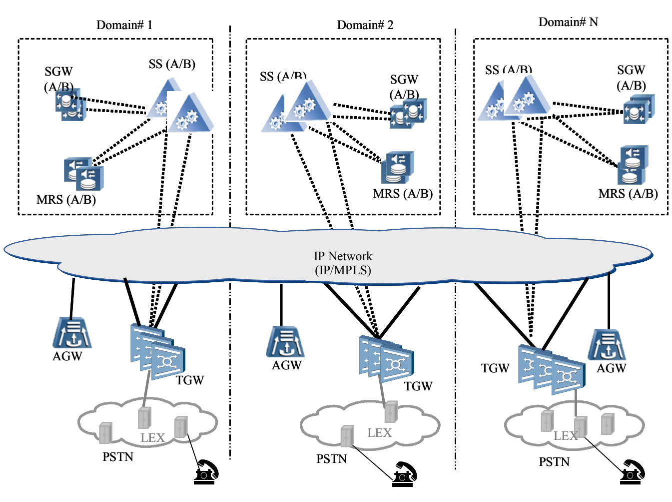

Figure5: Soft switch Based Solution Connectivity

The Soft switch controls the functionality in TGW and AGW to provide the voice and narrowband data services support by emulating the PSTN/ISDN network over IP. Figure5 outlines the solution architecture and the connectivity between the elements.

Using softswitch as a stepping stone toward IMS is often the right strategy. Many vendors putting the IMS label on their softswitch technology and product solution roadmaps to justify the possibility to migrate to IMS topology approach in the future. A phased approach using softswitch is a more prudent investment as the business models for new services become clearer.

Phase 2: Evolution from Softswitch to IMS architecture.

This Phase consists of the following steps:

Step 1: Softswitch is upgraded to act as the Access gateway Control (AGCF) and Media Gateway Controller (MGCF) function as outlined in figure6. Then the Call session Control function (CSCF) and Border gateway Call function (BGCF) can be added.

Step 2: the SIP based Services are added

Step 3: Expansion of the Subscribers base

Step 4: Fix Mobile Convergence (FMC) can be launched.

The IMS has the following advantages over softswitch platform:

- Network efficiency increase.
- Rapid service development.
- Unified subscriber management.
- Single service delivery platform for hybrid networks.
- True fixed/mobile service convergence

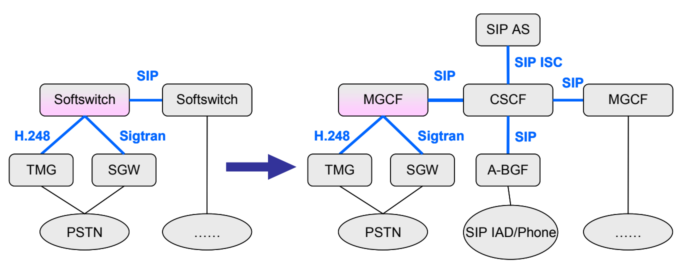

Figure 6: Evolution of the Softswitch to IMS

However, IMS and Softswitching are both core network technologies[3]. While Softswitch is considered as a mature solution providing integrated voice services[10], IMS is more applicable to providing multimedia services. IMS will be able to draw on the experiences of Softswitch in terms of IP, QoS, security, reliability, and large-scale networking. In the future, Softswitch will migrate into the IMS based network in order to protect investment and guarantee a seamless shift of users and services to IMS. The estimated large scale deployment of IMS will be between 2010 and 2012. The benefits from migrating to IMS may also be governed by the speed at which a service provider migrates its network. A long migration period is expected to reduce the benefits and revenue opportunity. This can be attributed to the additional cost of running both legacy PSTN and GSM networks concurrently with the IMS network for long periods of time. A swift migration, if possible, is expected to provide better return on invest (ROI).

VIII. Case Study : Saudi Telecom Company (STC)

Saudi Telecom Company (STC) is an incumbent Telecom operator in the kingdom of Saudi Arabia, and one of the Service provider leaders in the Middle East. STC is considered as a technology smart follower company. It has recognized the need for migrating its network infrastructure to an NGN platform that can support the provision of more advanced services efficiently and cost effectively to its customers. STC has decided first to start migrating its PSTN network to NGN sofswitch, in order to construct a unified service platform to meet fixed and mobile customer's requirement in the near future, and to increase revenue and customer's loyalty. The same solution presented in this paper has been adopted and it's in the rollout phase now in its phase1. Figure 7 illustrates the STC NGN architecture. The evolution to IMS is planned to be by 2010.

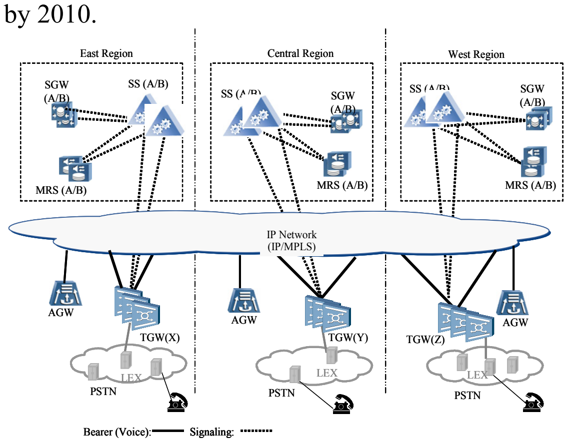

Figure 7: STC NGN SoftSwitch Network

IX. CONCLUSION

IMS has clearly captivated the telecom world as a result of its ability to facilitate powerful, ubiquitous, and cost-effective services. Users can benefit from a rich variety of boundary-less services that can enrich their daily lives. Operators can benefit from fast and efficient service launches, increased revenues from services beyond communication, and increased loyalty among subscribers as they grow to depend on their provider of personalized right-sized services. A cost effective, future proof two Phases Migration solution architecture that can be used for the rollout of the NGN IMS Network has been presented in this paper. The solution consists of migration to NGN Soft Switch environment, then it evolves to IMS. The solution derives from a the gradual migration Strategy that has been actually adopted by Saudi Telecom Company (Saudi Arabia), and many other Operators in the Middle East.

References

[1] 3GPP Specifications Home Page, http://www.3gpp.org/specs/specs.htm

[2] UMTS Overview, UMTS World, http://www.umtsworld.com/technology/overview.

[3] Heavy reading vol. 4 No.19 dec. 2006

[4] Lawrence Harte, W. E. Harrelson and Avi Ofrane, " Public Switched Telephone Network(PSTN)", Chap.5 Telecom Made Simple, APDG Publishing, 2002.

[5] Hong-Bin Chiou, david Morrison, "Experience with an IP Multimedia System Trial For PSTN Migration", IEEE Communications Magazine July 2007.

[6] R. A. Thompson, "Telephone Switching Systems", Artech House Inc, 2004

[7] Rashid O, Coulton P, Edwards R, "Implications of IMS and SIP on the Evolution of Mobile Applications." IEEE 10th International Symposium on Consumer Electronics, June 2006.

[8] Marsic B, Borosa T, Pocuca S, "IMS to PSTN/CS interworking" Proceedings of the 7th International Conference on Telecommunications, Volume 2, June 2003

[9] ITU-T Recommendation, Y.2001 (2004) NGN Overview

[10] International SoftSwitch Consortium, http:// www.softswitch.org, 2002.

[11] ATIS, " Next generation Network (NGN) Framework, Part III: Standards Gaps Analysis", 2006

[12] ITU-D/ITU-T Seminar on standardization and development of NGN for the Arab Region," Network Architecture Migration Towards NGN", 29 April-2May 2007, Manama, Bahrain.

[13] Ericsson, "IMS- The Value of using IMS architecture." Ericsson, Tech, Rep., 2004.

[14] Hu Hanrahan, "Network Convergence" Wiley 2007

[15] S. Trigila, et al. "A service Architecture for Fixed and Mobile Convergence". Computer Communications, 25(2): 133-148, 2002.

[16] M. Vrdoliak, S. I. Vrdoiak, and G. Skugor, " Fixed-Mobile Convergence Strategy. Technology and Market Opportunities," IEEE Communication Magazine, feb 2007.

[17] Theodoros Rokkas Dimitris Katsianis Dimitris Varoutas Thomas Sphicopoulos, " Fixed mobile convergence for an integrated operator. The 18th Annual IEEE International Symposium on Personal, Indoor and Mobile Radio Communications (PIMRC'07)

[18] Hkelzen Caki, Muharrem ShefKiu, "Migration from PSTN to NGN", 49th International Symposium ELMAR-2007, 12-14 Sep. 2007, Zadar, Croatia.

[19] Multiservice Switching Forum, http://msforum.org, 2002.

[20] Tatiana Kovacikova , Pavol Segec, "NGN Standards Activities in ETSI", Proceedings of the Sixth International Conference on Networking (ICN'07).

[21] ITU , "Telecom Network planning for Evolving Network Architecture", Reference Manual, Geneva, January 2008.

[22] Jean-Yves Cochennec, "Activities on Next Generation Networks Under Global Information Infrastructure" in ITU-T, IEEE Communications Magazine, July 2002.

[23] Draft ETSI ES 282 007 V<1.2.6> (2005-12), Telecommunications and Internet Converged Services and Protocols for Advanced Networks (TISPAN), IP Multimedia Subsystem (IMS), Functional Architecture.

On the improvement of the learning rate in Blind Source Separation using techniques from Artificial Neural Networks theory

Felipe Augusto Pereira de Figueiredo
Instituto Nacional de Telecomunicações - Inatel
P.O. Box 05 - 37540-000
Santa Rita do Sapucaí - MG - Brazil
felipe-augusto@inatel.br

Carlos Alberto Ynoguti
Instituto Nacional de Telecomunicações - Inatel
P.O. Box 05 - 37540-000
Santa Rita do Sapucaí - MG - Brazil
ynoguti@inatel.br

***Abstract*— In this work some techniques from the Artificial Neural Networks theory are used to improve the convergence speed of a blind source separation (BSS) algorithm. The momentum term, bold driver and exponential decay techniques were used, and experimental results show a convergence time reduction by a factor of about 16.**

***Index Terms*— Blind source separation, Neural Networks, Natural Gradient, Multiple-Input-Multiple-Output (MIMO) Systems, Adaptive Filtering, convolutive mixtures, Second Order Statistics, Dynamic learning rate, Momentum term.**

I. INTRODUCTION

The problem of blind source separation is illustrated in Figure 1:

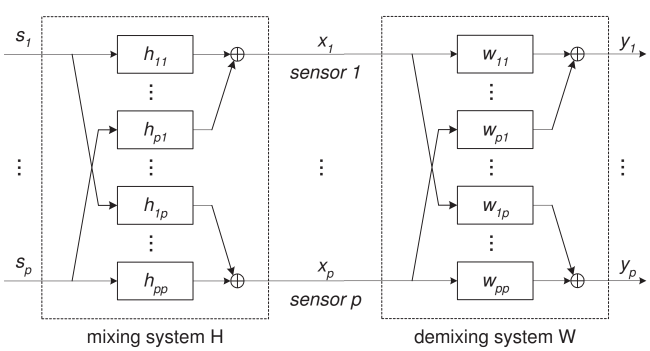

Fig. 1. Linear MIMO model for BSS.

In this work it is assumed a MIMO (Multiple Inputs Multiple Outputs) model, in which the signals are convolutively mixed. Also, the number of source signals $(s_q(n), q = 1, \ldots, Q)$ is assumed to be equal to the number of sensor signals $(x_p(n), p = 1, \ldots, P)$.

Each of the outputs of the mixing system H is described by

$$x_p(n) = \sum_{q=1}^{P} \sum_{k=0}^{M-1} h_{qp}(k) s_q(n-k), \tag{1}$$

where $h_{qp}(k), k = 0, \ldots, M-1$ denote the coefficients of the filter from the q-th source to the p-th sensor.

The problem of BSS consists in finding a corresponding demixing system according to Figure 1, where the output signals $y_q(n), q = 1, \ldots, P$ $(P = Q)$ are described by

$$y_q(n) = \sum_{p=1}^{P} \sum_{k=0}^{L-1} w_{pq}(k) x_p(n-k), \tag{2}$$

where L is the length of the demixing system filters.

It can be shown (see, e.g., [1]) that the MIMO demixing system coefficients can in fact reconstruct [10] the sources up to an unknown permutation and an unknown filtering of the individual signals, provided that L is chosen to be at least equal to M.

To estimate the P^2L coefficients $w_{qp}(k)$ of the MIMO demixing filter W, it is considered in this work an approach using second-order statistics [6], which exploits the Nonwhitheness and Nonstationarity properties of the signals. The Nonwhiteness property is exploited by simultaneous diagonalization of output correlation matrices over multiple time-lags, e.g., [4], and the Nonstationarity property is exploited by simultaneous diagonalization of short-time output correlation matrices at different time intervals, e.g., [5],[7]-[8]. In the sequence, an algorithm for convolutive mixtures by first introducing a general matrix formulation for convolutive mixtures following [1] that includes all time lags, is presented.

II. TIME-DOMAIN ALGORITHM FOR BSS

In this section the matrix formulation that allows derivation of a time-domain [9] algorithm from a cost function which inherently takes into account the nonstationarity and nonwhiteness properties will be introduced.

A. Matrix notation for Convolutive Mixtures

From Fig. 1, it can be seen that the output signals $y_q(n), q = 1, \ldots, P$ of the demixing system at time n are given by

$$y_q(n) = \sum_{p=1}^{P} x_p^T(n) w_{pq}, \tag{3}$$

where

$$x_p(n) = [x_p(n), x_p(n-1), \ldots, x_p(n-L+1)]^T \tag{4}$$

is a vector containing the latest L samples of the sensor signal $x_p(n)$ of the p-th channel and

$$w_{pq} = [w_{pq,0}, w_{pq,1}, \ldots, w_{pq,L-1}]^T \tag{5}$$

contains the current weights of the MIMO filter taps from the p-th sensor channel to the q-th output channel.

An algorithm for BSS of convolutive signals which exploits those two signal properties can be obtained from the definition of the following matrix

$$Y_q(m) = \begin{bmatrix} y_q(mL) & \cdots & y_q(mL-L+1) \\ y_q(mL+1) & \cdots & y_q(mL-L+2) \\ \vdots & \ddots & \vdots \\ y_q(mL+N-1) & \cdots & y_q(mL-L+N) \end{bmatrix} \tag{6}$$

where m denotes the time index of the block being processed and N is the length of the system output blocks taken into account for the estimates of short-time correlations used below. This matrix captures L subsequent output signal vectors

$$y_q(m) = [y_q(mL), \ldots, y_q(mL+N-1)]^T \tag{7}$$

in order to incorporate L time-lags in the cost function and thus the algorithm will be able to exploit the nonwhiteness property.

With the definitions above, (2) can be rewritten as

$$Y_q(m) = \sum_{p=1}^{P} X_p(m) W_{pq} \tag{8}$$

The approach followed here is carried out with overlapping data blocks to increase the convergence rate and reduce signal delay. Overlapping is introduced by simply replacing the time index mL in the equations by $m(L/a)$ with the overlap factor $1 \leq a \leq L$. The matrices $X_p(m), p = 1, \ldots, P$ used in (8) are defined as

$$X_p(m) = \begin{bmatrix} x_p(mL) & \cdots & x_p(mL-L+1) \\ x_p(mL+1) & \cdots & x_p(mL-L+2) \\ \vdots & \ddots & \vdots \\ x_p(mL+N-1) & \cdots & x_p(mL-L+N) \end{bmatrix} \tag{9}$$

Those matrices are Toeplitz with dimension ($N \times 2L$), so the first row contains $2L$ input samples and each subsequent row is shifted to the right by one sample and thus, contains one new input sample. W_{pq} are $2L \times L$ Sylvester matrices, which are defined as

$$W_{pq}(m) = \begin{bmatrix} w_{pq,0} & 0 & \cdots & 0 \\ w_{pq,1} & w_{pq,0} & \cdots & 0 \\ w_{pq,2} & w_{pq,1} & \cdots & 0 \\ \vdots & \vdots & \ddots & \vdots \\ w_{pq,L-1} & w_{pq,L-2} & \cdots & w_{pq,0} \\ 0 & w_{pq,L-1} & \cdots & w_{pq,1} \\ \vdots & \vdots & \ddots & \vdots \\ 0 & 0 & \cdots & w_{pq,L-1} \\ 0 & 0 & \cdots & 0 \\ \vdots & \vdots & \ddots & \vdots \\ 0 & 0 & \cdots & 0 \end{bmatrix} \tag{10}$$

Finally, to allow a convenient notation of the algorithm combining all channels, (8) can be compactly rewritten as

$$Y(m) = X(m)W \tag{11}$$

where:

$$Y(m) = [Y_1(m), Y_2(m), \ldots, Y_P(m)] \tag{12}$$

$$X(m) = [X_1(m), X_2(m), \ldots, X_P(m)] \tag{13}$$

$$W = \begin{bmatrix} W_{11} & \cdots & W_{1P} \\ \vdots & \ddots & \vdots \\ W_{P1} & \cdots & W_{PP} \end{bmatrix} \tag{14}$$

B. *Cost Function and Algorithm Derivation*

Having defined the compact matrix formulation (11) for the block- MIMO filtering, a following cost function that explicitly contains correlation matrices including several time-lags under the assumption of short-time stationarity is defined. This cost function is based on a generalization of Shannon's mutual information [11],[12] and simultaneously accounts for those two properties of the signals used here:

$$J(m) = \frac{1}{M} \sum_{i=0}^{M-1} \left(\log |\operatorname{bdiag} Y^T(i) Y(i)| - \log |Y^T(i) Y(i)| \right) \tag{15}$$

where the bdiag operation on a block matrix consisting of several sub matrices sets all sub matrices on the off-diagonal to zero. The cost function showed above was firstly introduced in [13] as a generalization of [14]. Since the matrix formulation (11) is used for calculating the short-time correlation matrices $Y^T(m)Y(m)$, the cost function inherently includes all L time-lags of all auto-correlations and cross-correlations of the BSS output signals.

By Oppenheim's inequality [15] $\sum_q \log |Y_q^T(m) Y_q(m)| \geq \log |Y^T(m) Y(m)|$, it is ensured that the first term in the braces of (14) is always greater than or equal to the second term, where the equality holds if all block-diagonal elements of

$Y^T(m)Y(m)$, i.e., the output cross-correlation over all time-lags, vanish.

The algorithm is based on the first-order gradient and in order to express the update equations of the filter coefficients exclusively by Sylvester matrices W, we take the gradient with respect to W and ensure the Sylvester structure of the result by selecting the non redundant values using a constraint.

$$\nabla_W J(m) = \frac{\partial J(m)}{\partial W} \tag{16}$$

And as result,

$$\nabla_W J(m) = \frac{2}{M} \sum_{i=0}^{M-1} R_{xy}(i) R_{yy}^{-1}(i) \left(R_{yy}(i) - \operatorname{bdiag} R_{yy}(i)\right) \operatorname{bdiag}^{-1} R_{yy}(i) \tag{17}$$

With an iterative optimization procedure, the current demixing matrix is obtained by the recursive update equation

$$W(m) = W(m-1) - \mu(m)\Delta W(m) \tag{18}$$

The $\mu(m)$ parameter gives the length of the step in the negative gradient direction and it is often called the step size or learning rate, this parameter can be made either dynamic or constant, depending on the technique adopted, as will be shown in the next section. The choice of an appropriate learning rate μ is essential for the convergence of the algorithm: a very small value will lead to slow convergence, on the other hand, very large values will lead to overshooting and instability, which prevents convergence altogether. As is known, non quadratic cost functions may have many local maxima and minima and therefore, good choices for initial values are important.

C. Natural Gradient

The gradient of a function $J(m)$ points in the steepest direction in the Euclidean orthogonal coordinate system. However, the parameter space is not always Euclidean; in fact it has a Riemannian metric structure, as pointed out by Amari [17]. In such a case, the steepest direction is given by the so-called natural gradient instead. Therefore, in order to use the natural gradient as the update term $\Delta W(m)$ the following modification should be applied to the descent gradient:

$$\nabla_W^{NG} J(m) = WW^T \nabla_W J(m) = WW^T \frac{\partial J(m)}{\partial W} \tag{19}$$

And then we have

$$\nabla_W^{NG} J(m) = \frac{2}{M} \sum_{i=0}^{M-1} W(m) \left(R_{yy}(i) - \operatorname{bdiag} R_{yy}(i)\right) \operatorname{bdiag}^{-1} R_{yy}(i) \tag{20}$$

III. Learning rate adaptation

Artificial Neural Networks literature has produced a large number of heuristic techniques for boosting gradient descent based algorithms by using adjustable learning rate, adding some kind of derivative term, clever choice of of the initial value, etc. In this work, some such strategies are used for the BSS algorithm, and the results are described.

A. Momentum term

The momentum term is a simple and effective technique of increasing the learning rate yet avoiding the danger of instability. It is represented by the following equation:

$$\psi(m) = \beta\left(W(m-1) - W(m-2)\right) \tag{21}$$

where $0 < \beta < 1$ is a new global parameter which must be determined by trial and error. The use of the momentum term produces the following update equation:

$$W(m) = W(m-1) - \mu(m)\Delta W(m) + \psi(m) \tag{22}$$

Momentum simply adds a fraction of the previous weight update to the current one. It is imoprtant to note that the learning rate parameter μ is made constant. When the gradient keeps pointing in the same direction, this will increase the size of the steps taken towards the minimum and when the gradient keeps changing direction, momentum will smooth out the variations. This technique may also have the benefit of preventing the algorithm from terminating in a shallow local minimum on the error surface.

B. Bold Driver

A useful batch method for adapting the global learning rate μ is the so called *bold driver* technique. Its operation is simple: after each epoch, compare the value of the cost function with its previous value. If the difference has decreased, increase μ by a small proportion (typically 1%-10%). A value of 10% was adopted as the value for that parameter. If the difference has increased by more than a tiny proportion (say, 10^{-10}), however, undo the last weight change, and decrease μ sharply - a value of 50% was used in this work. Thus bold driver will keep growing μ slowly until it finds itself taking a step that has clearly gone too far up onto the opposite slope of the cost function. Since this means that the algorithm has reached a tricky area of the cost function surface, it makes sense to reduce the step size quite drastically at this point.

C. Exponential Decay

It is a simple non-adaptive technique, once it do not relay on any values of the outputs of the algorithm. This is an effective technique that can be used to accelerate the searching process of the demixing filter coefficients. The following equation, that was empirically derived, is adopted as the time-variant learning factor:

$$\mu(m) = \mu_0 e^{-\frac{m^2}{10M}} \tag{23}$$

where μ_0 is the initial value of the function, M is the number of epochs adopted and m is the value of the current epoch.

The function described above is time-variant: it starts with the value μ_0 and then, it decreases gradually at each epoch of the algorithm. At the beginning of the learning process the convergence rate is very fast, once the value of μ is high, and as result, the algorithm can quickly find its way to the minimum of the cost function; at the end of the process, the small values of μ give a fine tuning for the parameters being estimated.

IV. Experiments and Results

In this section some results regarding the experiments performed by using the above mentioned techniques are presented. The experiments were conducted by using speech signals convolved with synthetic impulse responses simulating the acoustical behavior of real rooms [18]. For this purpose, filters with 100 taps were used.

Two audio signals with 5 seconds of speech were passed through the filter. These signals correspond to a male and female speaker voices. The recordings were made in a low noise environment, with 11025 Hz sampling frequency and 16 bits of resolution.

As mentioned before, the number of source signals is supposed to be equal to the number of sensors (two).

The Signal-to-Interference Ratio (SIR), which is defined as the ratio of the signal power of the target signal to the signal power from the jammer signal, was used to evaluate the performance of the algorithm. The SIR measured at the input of the demixing system was of 5.1496 dB and the SIR measured at the output of the system for each of the techniques mentioned here are presented below.

To decrease the delay introduced to the output signal and increasing the convergence rate as well, the overlapping method [23] was adopted, with a overlapping factor equal to 2, that means 50% overlapping.

The SIR measured at the input of the demixing system was of 5.1496 dB

The length L of the demixing filters was made equal to the length M of the mixing filters. The demixing filters W_{pp} were initialized with an unit impulse at the first tap and all the taps of the filters $W_{pq}, p \neq q$ were made equal to zero.

In the following sections, experimental tests results are reported in order to compare the performance of the proposed methods for learning rate parameter μ modification.

A. Initial test

In [1,9,13 and 16] the parameter μ is always constant. The first test follows this strategy, in roder to establish a baseline performance for the system. A value of $\mu = 0.002$ was chosen, and the final result can be viewed in Figure 2.

Convergency was achieved after 1300 training epochs, and the final SIR was 36.7790 dB.

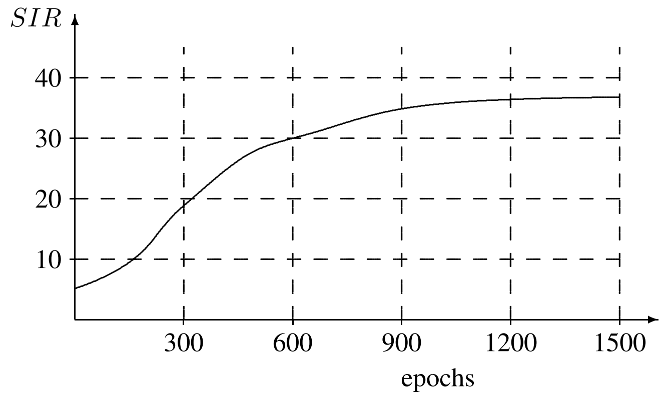

Fig. 2. Initial test.

B. Momentum

The second test make use of the momentum term (Equation (22)) to reestimate de demixing matrix. As in the previous case, a learning rate $\mu = 0.002$ was used. The value of β that led to the best result was 0.8. The result of this experiment is shown in Figure 3

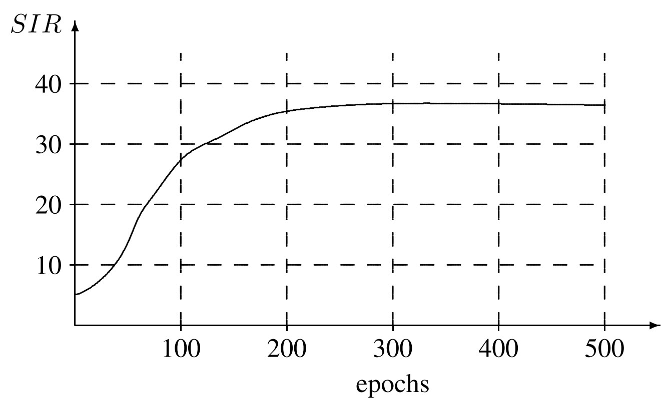

Fig. 3. Momentum.

For this test, convergency was achieved after 270 training epochs, leading to a final SIR of 36.7556 dB.

C. Bold driver

An initial value $\mu_0 = 0.002$ was set for the learning rate. The values used to increase and decrease de value of this parameter were 10% and 50%, respectively. The result of application of this technique is presented in Figure 4.

The convergence was reached after 130 training epochs, and the final SIR was 35.8116 dB.

D. Exponential decay

For this case, the initial value of the learning rate was chosen to be $\mu_0 = 0.07$. This higher value was chosen to accelerate the convergence. The results are shown in Figure 5

This technique led to a SIR of 36.8 dB in 80 training epochs.

The oscilatory behaviour shown on the Exponential Decay figure is due to changes in the sign, i.e. changes in the direction of the gradient at each epoch of the algorithm. In some cases the error surface has substantially different curvature along

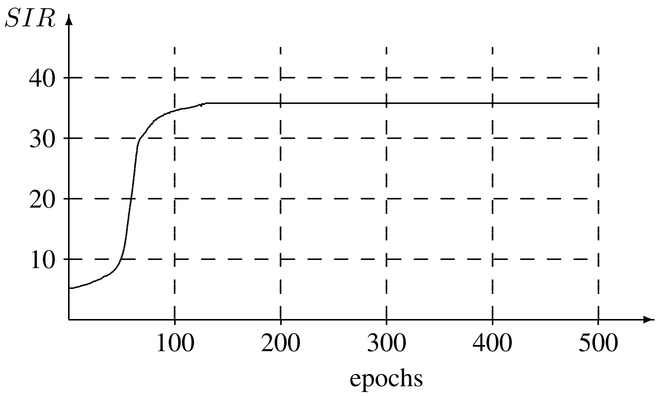

Fig. 4. Bold driver.

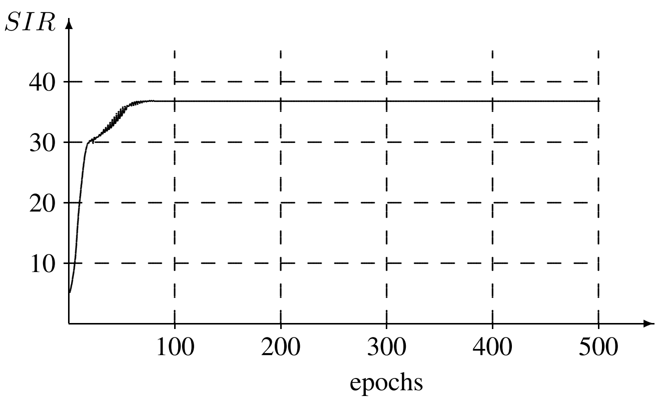

Fig. 5. Exponential decay.

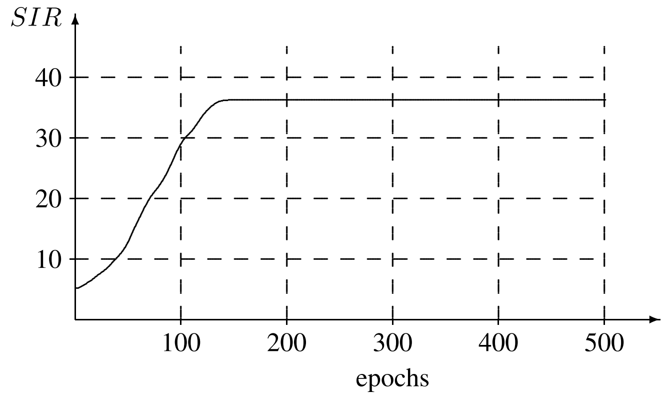

Fig. 6. Bold driver + momentum.

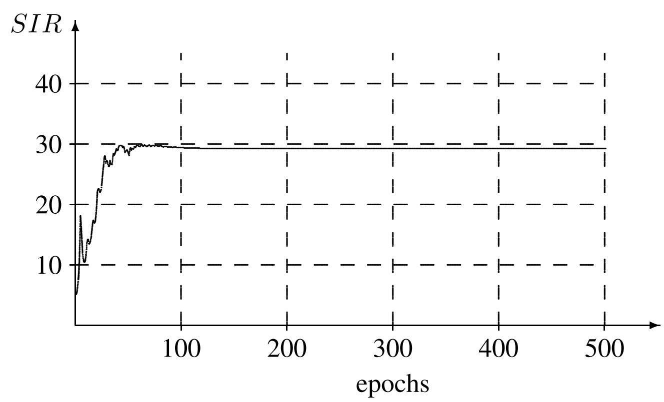

Fig. 7. Exponential decay + momentum.

different directions, leading to the formation of long narrow valleys. For most points on the surface, the gradient does not point towards the minimum, and successive steps of gradient descent can oscillate from one side to the other, progressing only very slowly to the minimum.

E. Experiments with combined techniques

As additional tests, some of the techniques mentioned above were joined together with the intention of verifying the results presented by these combinations. For all the cases shown below, the same set of parameters as those used when testing the techniques alone were adopted.

Two of such combinations were tested:

- Bold Driver + Momentum
- Exponential Decay + Momentum

The results are shown in Figures 6 and 7.

Using bold driver combined with the momentum term, no noticeable changes were noticed, either in the final SIR or in the convergence speed.

Joining together the Momentum and the Exponential Decay techniques led to a worst result than using them separately. A possible reason for this behavior is that the latter gradually decreases the learning rate μ at each training epoch; after some epochs its values tends towards zero, resulting in a flat Signal-to-Interference Ratio. Once the Momentum term is a kind of derivative technique, it smooths out the learning rate of the algorithm; consequently its effect on the current approach after it has reached a flat state is also useless as the values of the Momentum term will also tend to zero. In order to avoid that the flat state be reached before the algorithm can converge to its optimal result, an apropriate (higher) value for μ_0 should be chosen.

F. Comparison among all techniques

The results presented above can be summarized in Table I. In the first line, the results of the original approach, with a fixed step size are shown. In the sequel, one have the results for bold driver (BD), exponential decay (ED) and momentum techniques. Finally, the combined techniques results are described.

TABLE I

COMPARISON OF THE DIFFERENT METHODS.

Technique	Convergence epoch	SIR (dB)	Convergence time (m)
Fixed	1300	36.7790	317.42 (5.29 Hours)
BD	130	35.8116	32.39
ED	80	36.8	21.88
Momentum	270	36.7556	67.99
Momentum + ED	120	29.2217	29.36
Momentum + BD	135	36.2502	33.885

The analysis of these results show that all the proposed techniques but the combination with the momentum term with the exponential decay, lead to the same SIR than the fixed step size approach. However, the convergence time is much lower, with the fastest time being around 16 times the convergence time for the fixed step size.

V. Conclusions and Future Work

In this work, some techniques derived from the Artificial Neural Networks theory were used to improve the algorithm proposed by H. Buchner and colleagues [1].

The main idea presented here is to dynamically modify the learning rate μ. Three such techniques were proposed: the use of momentum, bold driver and exponential decay, and also, combinations of the momentum term with the bold driver and exponential decay were implemented and tested. All of them sped up the convergence and improved the final SIR, when compared with the fixed step size, proposed in [1]. The final SIR was similar for all the techniques, but the convergence time was much lower for all the proposed methods. The Exponential Decay technique achieved the best results of them all, with a reduction of about 16 times in the number of training epochs until convergence.

For the future, different strategies to choose the initial values for the demixing filter are being considered.

Acknowledgements

The authors would like to thank CAPES for partial funding.

References

[1] H. Buchner, R. Aichner, W. Kellermann, A generalization of blind source separation algorithms for convolutive mixtures based on second-order statistics, IEEE Trans. Speech Audio Process. 13 (1) (January 2005) 120-134.

[2] Cherry, E. Collin. Some Experiments on the Recognition of Speech, with One and with Two Ears. Journal of the Acoustical Society of America, 24, pp. 975-979, 1953.

[3] Herault, Jeanny and Christian Jutten. Space or time adaptive signal processing by neural network models. AIP Conference Proceedings, 151, pp. 206-211, 1986.

[4] L. Molgedey and H. G. Schuster, "Separation of a mixture of independent signals using time delayed correlations", Review Letters, vol. 72, pp. 3634-3636, 1994.

[5] E. Weinstein, M. Feder, and A. Oppenheim, "Multi-channel signal separation by decorrelation", IEEE Trans. on Speech and Audio Processing, vol 1, no. 4, pp. 405-413, Oct. 1993 .

[6] R. Battiti, "First and second-order methods for learning: between steepest descent and Newton's method", Technical report, University of Trento, 1991.

[7] S. Van Gerven and D. Van Compernolle, "Signal separation by symmetric adaptive decorrelation: stability, convergence, and uniqueness", IEEE Trans. Signal Processing, vol. 43, no. 7, pp. 1602-1612, 1995.

[8] C. L. Fancourt and L. Parra, "The coherence function in blind source separation of convolutive mixtures of non-stationary signals", in Proc. Int. Workshop on Neural Networks for Signal Processing (NNSP), 2001.

[9] R. Aichner et al., "Time-domain blind source separation of non-stationary convolved signals with utilization of geometric beamforming", in Proc. Int. Workshop on Neural Networks for Signal Processing, Martigny, Switzerland, 2002.

[10] A. Hyvarinen, J. Karhunen, and E. Oja, Independent Component Analysis, Wiley & Sons, Inc., New York, 2001.

[11] Shannon, C.E. and Weaver, W. (1949). The mathematical theory of communication. University of Illinois Press, Urbana, Illinois.

[12] T.M. Cover and J.A. Thomas, Elements of Information Theory, Wiley & Sons, New York, 1991.

[13] H. Buchner, R. Aichner, and W. Kellermann, "A generalization of a class of blind source separation algorithms for convolutive mixtures", Proc. IEEE Int. Symposium on Independent Component Analysis and Blind Signal Separation (ICA), Nara, Japan, Apr. 2003, pp. 945-950.

[14] K. Matsuoka, M. Ohya, and M. Kawamoto, "A neural net for blind separation of nonstationary signals", Neural Networks, vol. 8, no. 3, pp. 411-419, 1995.

[15] A. Oppenheim, "Inequalities connected with definite hermitian forms", J. London Math. Soc., vol. 5, pp. 114-119, 1930.

[16] H. Buchner, R. Aichner, and W. Kellermann, A generalization of blind source separation algorithms for convolutive mixtures based on second order statistics", IEEE Trans on Speech and Audio Processing, Vol. 13, Num. 1, pp. 120-134, Jan. 2005

[17] S. I. Amari, "Natural Gradient Works Efficiently in Learning", Neural Computation, February 15, 1998, Vol. 10, No. 2, Pages 251-276

[18] Stephen G. McGovern, "A Model for Room Acoustics", http://www.2pi.us/rir.html, 2003-2004

Assessment of Spatial Video Transcoding Based on Structural Distortion Measurement

Carlos D. M. Regis, Daniel C. Moraes
and Marcelo S. Alencar
Universidade Federal de Campina Grande - UFCG
R. Aprígio Veloso, 882 - 58109-970
Campina Grande - PB - Brazil
danilo, daniel, malencar@iecom.org.br

Mylène Christine Queiroz Farias
Universidade Federal de São Paulo - Unifesp
Rua Talim 330, Vila Nair
São José dos Campos - SP - Brazil
mylene.farias@unifesp.br

***Abstract*— The use of mobile TV requires the reduction of the video size, to fit on the mobile device screen. The reduction uses space transcoding, which can be done in several ways, and this article uses down-sampling and filtering to accomplish this. Six types of filter are presented to reduce the spatial video resolution from the CIF to QCIF format for use in mobile TV. Each filter has a different block size, including 2×2 , 3×3 and 4×4 dimensions. The evaluation of the filters uses two objective measures, the PSNR and SSIM, and the processing time for the transcoding is evaluated.**

***Index Terms*— Video transcoding, ISTVD, Video compression.**

I. Introduction

The International System Digital Television (ISDTV) standard defines the reception of video signals in various formats for fixed or mobile receivers, with simultaneous transmission using the compression standards MPEG-2 and H.264 [1]. Therefore, in a digital television scenario the video signal may have different bit rates, encoding formats, and resolutions (spatial and temporal). The definition of the most appropriate format for the video signal will depend on the type of transmission (cable, broadcasting, among others), the application and the receiver.

The ISDTV band is divided into 14 segments, with a segment used as a guard interval. Thirteen segments are used for TV transmission and the central segment for transmission to mobile devices. The standard for mobile TV is called One-Seg and has a bandwidth of 433 kHz [2].

The mobile reception service uses parameters of robust modulation, and has limited bandwidth, compared with the HDTV service. The total transmission rate varies, depending on the parameters of transmission, and 320 k*bit*/s is considered appropriate for mobile reception [3]. The ISDB-T service can be seen in Figure 1.

Because of the limited band it is necessary to lower the bit rate. This can be done by reducing the video size. It is important that the transcoding of mobile TV generate videos of good quality and with lower processing time, so that no delay occurs in the video transmission. Figure 2 [4] presents a block diagram of the transcoding scheme considered in this work.

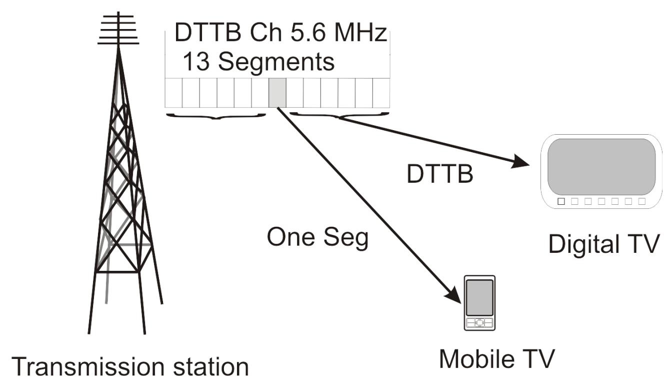

Fig. 1. ISDTV services.

In order for the video signals to be used appropriately, the video transcoder converts a sequence of video to another one. This includes coding with different temporal and spatial resolutions and bit rates. The transcoding also saves space and production time, because just the content with maximum resolution is stored.

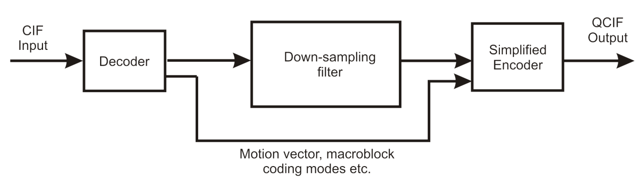

Fig. 2. The cascaded pixel domain transcoder architecture that reduces the spacial resolution.

In this work the videos are processed in the pixel domain by a down-sampling filter block. The transcoder converts the video resolution from CIF (352 × 288) to QCIF (176 × 144) format.

The paper presents a comparison among different types of spatial transcoding method, which is intended for mobile receivers. A quantitative performance analysis is reduced, using three different video quality metrics: mean squared error (MSE), peak signal-to-noise ratio (PSNR), and structural similarity metric (SSIM).

II. THE TRANSCODER

The transcoding process can be homogeneous, heterogeneous or use some additional functions. The homogeneous transcoding converts the bit rate, and changes the spatial resolution, temporal resolution. It can also change the coding Variable Bit-Rate (VBR) to a Constant Bit-Rate (CBR).

The heterogeneous transcoding performs the conversion of standards, but also converts between the interlaced and progressive formats. The additional functions provide resistance against errors in the encoded video sequence and add invisible or watermarks logos [5], [6]. Figure 3 represents a diagram with various types of transcoding.

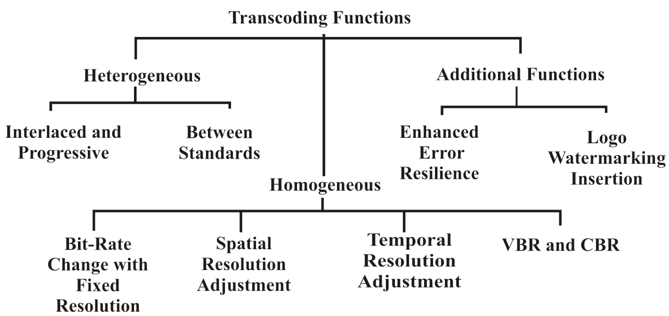

Fig. 3. Transcoding functions.

The are two major transcoder architectures: the cascaded pixel domain transcoder (CPDT) and the DCT domain transcoder (DDT) [4]. The first one is adopted in this paper as the transcoder architecture for the CIF-to-QCIF transcoding, as shown in Figure 2. The simplified encoder is different from a stand-alone video encoder in that the motion estimation, macroblock mode decision, and some other coding processes may reuse the decoded information from the incoming video stream.

To reduce the spatial resolution the down-sampling filter is used. It changes the picture resolution from the CIF resolution to the QCIF resolution. Using the conversion from 352×288 pixels to 176×144 pixels, the down-sampling factor is $352 : 176 = 2 : 1$. Same down-sampling ratios are applied to both the horizontal and vertical directions in order to preserve the aspect ratio of the input video. The $2 : 1$ down-sampling factor can be achieved by up-sampling by 1 and then down-sampling by 2, as shown in Figure 4 ($S = 1$, $N = 2$), in which $h(v)$ is a low-pass filter [4].

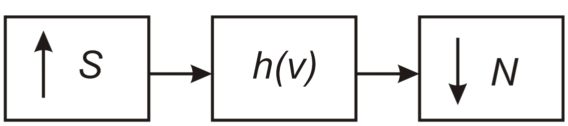

Fig. 4. The Interpolation-decimation routine for a rate change of M/L.

The filters used in this article are: the moving average, the median and the mode filter.

- Moving Average: this technique replaces values of an $M \times M$ video block a single pixel, which assumes the arithmetic mean of the pixels within the $M \times M$ block. Averaging pixels is one of the simplest methods, however this technique can add a high level of smudgy to the frame.
- Weighted Average: this technique is the average of all entries data which have varying weights, weight depends of the neighborhood pixels to be seen in relation to the central pixel, as seen in Figure 5. In this case, the smoothing is less intense because there is more influence of the central pixel [7].

	o_1	m	q_1	
o_2	v	u	z	q_2
l	t	s	t'	l'
q_1'	z'	u'	v'	o_1'
	q_2'	m'	o_2'	

Fig. 5. Representing the neighborhood of the central pixel with value p_s.

- Median: the technique relies on replacing a set of pixels by the median of an $M \times M$ block. For the calculation of the median, a reorganization of the values of the pixels of an $M \times M$ block is provided in an increasing way and chosen the central value [8], [9].
- Mode: the technique of the mode involves the replacement of a set of pixels by the mode of an $M \times M$ block. For the calculation of the mode, the comparison is made with the value that is more frequently repeated in the $M \times M$ block.
- Sigma: this technique selects the pixels of the block that has values between the region, the average least twice the standard deviation and mean more double standard deviation, thus excluding pixels that have no relation with the central pixel of the window. After it is done calculating the average of these values [10], [11].

The transcoder presents in this article includes the moving average, median, mode and sigma filters, for 2×2, 3×3 and 4×4 blocks. The moving average filter used the 1×1 block, which was given the name of single elimination.

This article presents three weighted averages, given by Equations 1, 2 and 3

$$g(x, y) = \frac{1}{2}(p_s + \frac{1}{4}(p_{t'} + p_t + p_{u'} + p_u)), \qquad (1)$$

$$g(x, y) = \frac{1}{2}\{p_s + \frac{1}{5}[p_{t'} + p_t + p_{u'} + p_u + \frac{1}{4}(p_{v'} + p_v + p_{z'} + p_z)]\}, \qquad (2)$$

$$g(x,y)=\frac{1}{16}\{4p_s+2(p_{t'}+p_t+p_{u'}+p_u)+(p_{v'}+p_v+p_{z'}+p_z)\}, \tag{3}$$

in which the parameters are defined in Figure 5.

For all blocks the videos were generated taking the pixels around the reference pixels. The filters have been chosen for their simplicity.

III. Evaluation of the video transcoder

For the evaluation of a video transcoder two methods to assess the video quality are used: objective and subjective. The objective measurement is fast and simple, but there is low correlation with the human perception measurement of quality.

For the objective evaluation there are several techniques, among them the most used is the PSNR, which is not a measure that takes into account the human perception. So there were new techniques in accordance with human perception and in that article is used the SSIM method.

A. PSNR

Currently, the most commonly used full-reference (FR) objective image and video distortion/quality metrics are the mean squared error (MSE) and the peak signal-to-noise ratio (PSNR). MSE and PSNR are widely used because they are simple to calculate, have clear physical meanings, and are mathematically easy to deal with for optimization purposes [12].

The MSE is given by the average value of squared errors between the pixels of the original frame and in the transcoded frame. The MSE is given by Formula 4

$$\text{MSE} = \frac{1}{P}\sum_{k}\sum_{x,y}(f(x,y,k)-g(x,y,k))^2, \tag{4}$$

in which P is the total number of pixels, x and y are the index of rows and columns, respectively, k is the total number of frames, and f and g represent the original and transcoded frames, respectively.

The PSNR is defined by the Formula 5, for a video encoded with 8 bits.

$$\text{PSNR} = 10\ \log_{10}\left[\frac{255^2}{MSE}\right]. \tag{5}$$

The obtained values are very close, and do not perfectly assess the human perception. In the last three decades, a great deal of effort put into developing assessment objective methods of image and video quality, which incorporate perceptual quality measures by considering the human visual system (HVS) characteristics. Among the methods that incorporate perceptual quality measure the SSIM is used in the following.

B. SSIM

The structural similarity metric is considered a metric of low computational complexity, despite belonging to the class of perceptual metric. The SSIM measures how the video structure differs from the structure of the reference video, involving the evaluation of structural similarity of the video. The metric in question is calling the attention of the community of researchers because of the good results obtained in the perceived quality of representation [13].

The SSIM indexing algorithm is used for quality assessment of still images, with a sliding window approach. The window size 8×8 is used in this paper. The SSIM metrics define the luminance, contrast and structure comparison measures, as defined in Equation 6 and 7 [14], [15].

$$l(x,y)=\frac{2\mu_x\mu_y}{\mu_x^2+\mu_y^2}, \quad c(x,y)=\frac{2\sigma_x\sigma_y}{\sigma_x^2+\sigma_y^2}, \tag{6}$$

$$s(x,y)=\frac{\sigma_{xy}}{\sigma_x\sigma_y}, \tag{7}$$

and SSIM metrics are given in Equation 8

$$\text{SSIM}(x,y)=\frac{(2\mu_x\mu_y+C_1)(2\sigma_{xy}+C_2)}{(\mu_x^2+\mu_y^2+C_1)(\sigma_x^2+\sigma_y^2+C_2)}. \tag{8}$$

The constants, C_1 and C_2, are defined as

$$C_1=(K_1L)^2 \quad \text{and} \quad C_2=(K_2L)^2, \tag{9}$$

in which L is the dynamic range of the pixel values (for 8 bits/pixel gray scale images, L = 255), and K_1 and K_2 are two constants whose values must be small, such that C_1 or C_2 will cause effect only when $(\mu_x^2+\mu_y^2)$ or $(\sigma_x^2+\sigma_y^2)$ is small. For all experiments in this paper, one sets $K_1 = 0.01$ and $K_2 = 0.03$, respectively. The quality measure of a video is between 0 and 1, with 1 as the best value.

The SSIM has the following properties:

1) SSIM (f,g) = SSIM (g,f);
2) SSIM $(f,g) \leq 1$;
3) SSIM (f,g) = 1, if and only if $f=g$.

IV. Results

For analysis of the video transcoder one used the Mobile, Akiyo and Walk videos [16], with 10 s for each one. These videos were chosen for displaying the following characteristics:

- Mobile: high texture and slow movement;
- Akiyo: little texture and slow movement;
- Walk: reasonable texture and rapid movement.

A. MSE and PSNR

The efficiency of a transcoder can be analyzed and evaluated by the MSE and PSNR of the obtained videos. Table I shows the result of the MSE and the Table II shows the PSNR result.

The PSNR results are shown in Figure 6. This figure shows that the slow movement video gives the best results, and the transcoded videos using 4×4 blocks presented poorer results than the other, and the best results for transcoded videos were obtained with the filters: weighted average 3, moving average 3×3 and 3×3 Sigma for the Walk and Akiyo videos. For

TABLE I
MSE RESULTS

Number	Filter	Mobile	Akiyo	Walk
1	Simple Elimination	10,47	0,89	0,8
2	2 × 2 Moving Average	7,83	1,89	5,45
3	3 × 3 Moving Average	4,77	0,20	0,36
4	4 × 4 Moving Average	5,53	1,05	2,59
5	2 × 2 Median	3,61	0,33	1,23
6	3 × 3 Median	6,18	0,28	0,5
7	4 × 4 Median	3,52	0,28	1,13
8	2 × 2 Mode	7,09	1,21	3,73
9	3 × 3 Mode	13,68	1,65	2,98
10	4 × 4 Mode	20,28	1,52	2,67
11	Weighted Average 1	6,87	0,26	0,4
12	Weighted Average 2	6,56	0,24	0,37
13	Weighted Average 3	5,28	0,19	0,3
14	2 × 2 Sigma	3,18	0,28	1,12
15	3 × 3 Sigma	5,02	0,22	0,35
16	4 × 4 Sigma	3,17	0,3	1,04

TABLE II
PSNR RESULTS

Number	Filter	Mobile	Akiyo	Walk
1	Simple Elimination	37,93	48,62	49,12
2	2 × 2 Moving Average	39,19	45,37	40,77
3	3 × 3 Moving Average	41,35	55,06	52,60
4	4 × 4 Moving Average	40,71	47,93	43,99
5	2 × 2 Median	42,55	52,92	47,24
6	3 × 3 Median	40,22	53,62	51,12
7	4 × 4 Median	42,67	53,62	47,60
8	2 × 2 Mode	39,62	47,31	42,42
9	3 × 3 Mode	36,77	45,96	43,38
10	4 × 4 Mode	35,06	46,32	43,87
11	Weighted Average 1	38,78	53,03	52,1
12	Weighted Average 2	38,97	53,32	52,39
13	Weighted Average 3	39,9	54,28	52,4
14	2 × 2 Sigma	43,10	53,58	47,64
15	3 × 3 Sigma	41,12	54,75	52,73
16	4 × 4 Sigma	43,12	53,36	47,96

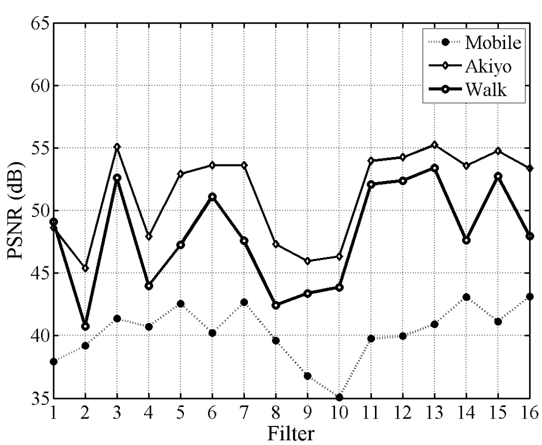

Fig. 6. Graphics of PSNR for the transcoded videos.

the Mobile video the best transcoded videos were those which used the filters 4 × 4 sigma, 2 × 2 sigma and 4 × 4 median.

The videos that presented the worst results were those of 2 × 2 moving average and the 2 × 2, 3 × 3 and 4 × 4 mode.

B. SSIM

For the evaluation of a transcoder with the SSIM method, the videos Mobile, Akiyo and Walk were used, and the results are in Table III.

TABLE III
SSIM RESULTS

Number	Filter	Mobile	Akiyo	Walk
1	Simple Elimination	0,9712	0,9732	0,9906
2	2 × 2 Moving Average	0,9842	0,9542	0,9687
3	3 × 3 Moving Average	0,9785	0,9811	0,9824
4	4 × 4 Moving Average	0,9511	0,9522	0,962
5	2 × 2 Median	0,9910	0,9855	0,9907
6	3 × 3 Median	0,9828	0,9836	0,9921
7	4 × 4 Median	0,9578	0,9771	0,9824
8	2 × 2 Mode	0,9765	0,9636	0,9787
9	3 × 3 Mode	0,9709	0,9622	0,9768
10	4 × 4 Mode	0,9647	0,9720	0,977
11	Weighted Average 1	0,9871	0,9829	0,9904
12	Weighted Average 2	0,9877	0,9835	0,9896
13	Weighted Average 3	0,9859	0,9832	0,9865
14	2 × 2 Sigma	0,9918	0,9846	0,9913
15	3 × 3 Sigma	0,9813	0,9814	0,9855
16	4 × 4 Sigma	0,9593	0,9684	0,975

The SSIM results are shown in Figure 7. This figure shows that the transcoded videos using 4 × 4 blocks presents poorer results than the other and the best results for transcoded videos were obtained with the filters 2 × 2 sigma, 2× 2 and 3 × 3 median, for all videos.

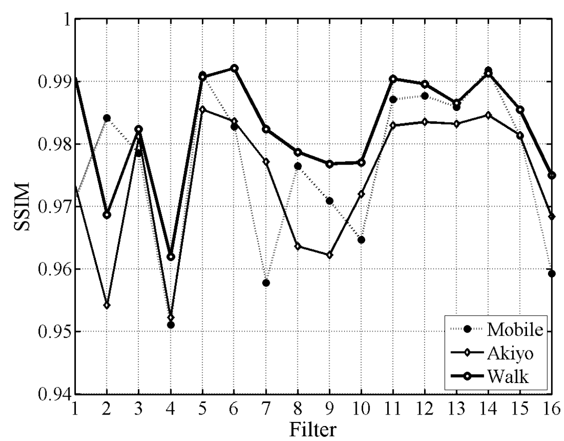

Fig. 7. Graphics of SSIM for the transcoded videos.

The videos that had the worst results were those of 4 × 4 moving average, 4 × 4 sigma and the 2 × 2, 3 × 3 and 4 × 4 mode.

C. Processing Time

Regarding the processing time, it is possible to analyze the increase in time as the filter window increases, as shown in Table IV. This table shows that the sigma and mode filters demand longer processing periods as compared with the moving average and the weighted average filters, and the median processing time is slightly higher than the average.

The best results considering the processing time was the simple elimination, weighted average, 2×2 and 3×3 moving average and the 2×2 median.

The results for the sigma filter shown in the Table IV are given as the average of the obtained values, because each window is related to the pixel number.

TABLE IV

PROCESSING TIME FOR A VIDEO

Transcoding Method	Time(seconds)
Simple Elimination	1,00
2×2 Moving Average	2,00
3×3 Moving Average	2,00
4×4 Moving Average	5,00
2×2 Median	2,00
3×3 Median	7,00
4×4 Median	18,00
2×2 Mode	12,00
3×3 Mode	33,00
4×4 Mode	82,00
Weighted Average 1	2,00
Weighted Average 2	2,00
Weighted Average 3	2,00
2×2 Sigma	9,00
3×3 Sigma	18,00
4×4 Sigma	31,00

V. CONCLUSION

This article showed that the spatially transcoded videos presented satisfactory results, since all results had an acceptable mean square error. For the evaluation with the MSE, PSNR the median and weighted average filters produced the best results and also a significant difference to the Mobile video (high texture), regarding the other two.

Using SSIM, the best results were found with the median and the weighted average filters. Regarding the three videos, a significant difference between them could not be found, on account of human perception.

Regarding the processing time, the weighted average presented the best results, and the median filter presented the longest periods.

Those results demonstrate the feasibility of such filters for use in spatial resolution transcoding, as the MSE has low error values regarding the reference video.

VI. ACKNOWLEDGMENTS

The authors acknowledge the financial support from Capes and CNPq, and also thank the Iecom for using its structure and equipment.

REFERENCES

[1] M. S. Alencar, *Digital Television*. São Paulo: Erica Publisher, 2007.
[2] M. Takada and M. Saito, "Transmission system for ISDB-T," *Proceedings of the IEEE*, vol. 94, no. 1, pp. 251–256, Jan. 2006.
[3] A. Kumar, *Mobile TV: DVB-H, DMB, 3G Systems and Rich Media Applications*. Focal Press Media tecnology Professional, 2007.
[4] J. Xin, M.-T. Sun, B.-S. Choi, and K.-W. Chun, "An HDTV-to-SDTV spatial transcoder," *Circuits and Systems for Video Technology, IEEE Transactions on*, vol. 12, no. 11, pp. 998–1008, Nov. 2002.
[5] I. Ahmad, X. Wei, Y. Sun, and Y.-Q. Zhang, "Video transcoding: an overview of various techniques and research issues," *Multimedia, IEEE Transactions on*, vol. 7, no. 5, pp. 793–804, Oct. 2005.
[6] J. Xin, C. Lin, and M. Sun, "Digital video transcoding," *Proceedings of the IEEE*, vol. 93, no. 1, pp. 84–97, Jan. 2005.
[7] R. C. Gonzalez and R. E. Woods, *Digital Image Processing*. Boston, MA, USA: Addison-Wesley Longman Publishing Co., Inc., 2001.
[8] H. Wu and K. Rao, *Digital Video Image Quality and Perceptual Coding*. Boca Raton, FL, USA: CRC Press Taylor & Francis Group, 2006.
[9] L. Yin, R. Yang, M. Gabbouj, and Y. Neuvo, "Weighted median filters: a tutorial," *Circuits and Systems II: Analog and Digital Signal Processing, IEEE Transactions on*, vol. 43, no. 3, pp. 157–192, Mar 1996.
[10] A. de Abuquerque Araújo, "Filtros espaciais: Estudo comparativo e aplicações em classificação e segmentação de imagens," Tese de Doutorado, Universidade Federal da Paraíba - UFPB - Campus II, Campina Grande - PB, Brasil, Julho 1987.
[11] R. Lukac, B. Smolka, K. Plataniotis, and A. Venetsanopoulos, "Generalized adaptive vector sigma filters," *Multimedia and Expo, 2003. ICME '03. Proceedings. 2003 International Conference on*, vol. 1, pp. I–537–40 vol.1, July 2003.
[12] Z. Wang, L. Lu, and A. C. Bovik, "Video quality assessment using structural distortion measurement," in *in Proc. IEEE Int. Conf. Image Proc*, 2002, pp. 65–68.
[13] R. de Freitas Zampolo, D. de Azevedo Gomes, and R. Seara, "Avaliação e comparação de métricas de referência completa na caracterização de limiares de detecção em imagens," *XXVI Simpósio Brasileiro de Telecomunicações - SBrT 2008*, Sept. 2008.
[14] L. L. Zhou Wang and A. C. Bovik, "Video quality assessment based on structural distortion measurement," *Signal Processing: Image Communication*, vol. 19, no. 2, pp. 121–132, february 2004.
[15] M. Vranjes, S. Rimac-Drlje, and D. Zagar, "Objective video quality metrics," *49th International Symposium ELMAR, 2007*, pp. 45–49, Sept. 2007.
[16] "YUV video sequences," http://trace.eas.asu.edu/yuv/index.html, November 2008.

Speech Synchronized Image-Based Facial Animation

Paula Dornhofer Paro Costa
Dept. of Comp. Eng. and Industrial Automation
School of Electrical and Computer Engineering
University of Campinas
P.O. Box 6101 - 13083-970
Campinas - SP - Brazil
paula@dca.fee.unicamp.br

José Mario De Martino
Dept. of Comp. Eng. and Industrial Automation
School of Electrical and Computer Engineering
University of Campinas
P.O. Box 6101 - 13083-970
Campinas - SP - Brazil
martino@fee.unicamp.br

Edson José Nagle
CPqD - Telecommunications
Research and Development Center
13086-902
Campinas - SP - Brazil
nagle@cpqd.com.br

***Abstract*— The arise of a new reality where information is accessed ubiquitously from a variety of different devices creates new application opportunities and the need of development of more efficient and intuitive interfaces. This can be specially shown through the seamlessly growth of wireless communications and the use of small and portable devices to communicate and access multimedia content. This paper describes a speech synchronized 2D facial animation system that explores the computer facial animation as an enabling technology for the development of more natural and efficient human-machine interfaces and applications. The photorealistic results provided by the system makes it suitable for very low bit rate video telephony applications through the implementation of a model based facial video coding. The designed system is a cross-platform solution capable of delivering videorealistic animations on both limited capacity devices (such as mobile phones and personal digital assistants) and high performance desktop computers with full processing power and memory capacity. The key concepts behind the solution are an image database that can be continuously scaled and an image-based animation synthesis strategy that can be adapted according to the characteristics of the executing platform and/or applications.**

***Index Terms*— facial animation, model-based video coding, image-based facial animation, text to audiovisual speech.**

I. Introduction

The recent advances and worldwide spreading of mobile communications, followed by the increased availability of data networks, made possible the ubiquitous access to information. Moreover, thanks to the evolution of microprocessors, microcontrollers and memory devices, we presence today a large number of portable devices that, among a variety of other functionalities, provide access to data networks and have good performance to handle multimedia content. This results in an increased number of users having completely different ways to access the information media without necessarily being familiarized with traditional WIMP (Windows, Icons and Pointing Devices) personal computer interfaces.

On the other hand, although broadband access is being popularized, a large amount of Internet users and mobile subscribers still have low bandwidth data access, resulting in low QoS (Quality of Service) for video streaming applications.

In this context, this work explores the computer facial animation technology combined with a text-to-speech synthesizer (TTS) as an enabling technology to the development of more intuitive and efficient interfaces, taking advantage of face-to-face communication mechanisms we are well trained and aware of. This approach makes possible the development of virtual talking heads that find applications in areas such as: entertainment, personal communications, navigation aid, newscast, electronic commerce and education [1], [2].

Additionally, computer facial animation is a model based video-coding approach that is appropriate for applications that require visual interaction capacity over a very low bit rate channel and advantageous to the user in situations where he pays for the volume of transmitted data [3].

Reliable and convincing synthetic talking-heads have to deliver satisfactory levels of photorealism and videorealism. In this context, photorealism can be understood as a measure of how close the images generated/displayed by the system can be mistaken by photographs. The photographic quality includes the reproduction of fine details like skin texture, facial wrinkles and hair. A videorealistic animation, besides photorealism, presents accurate lip synchronization, carefully reproducing the speech articulatory movements, and is also able to reproduce nonverbal communication gestures (like head nodding) and movements not directly related to communication (such as eyes blinking and eyebrows movements).

The reproduction of speech articulatory movements involves the modeling of the visible movements of vocal tract displayed on the speaker's face during speech production, specially in the region around the mouth. To determine such a model it is necessary to consider the characteristic configurations of vocal tract associated to the various speech segments of the language and the related coarticulation effects that arise when the typical articulation pattern of a segment is modified by the interaction with nearby speech segments. In this work, each visually contrastive configuration of vocal tract is associated to a viseme, a shorthand for visual phoneme, that corresponds to a static characteristic mouth shape associated to the acoustic realization of a speech segment.

Another key factor to determine the level of videorealism of facial animation is the strategy adopted to model the human face: the use of 3D geometric models or an image-based approach.

Advanced and modern 3D face modeling techniques are successful in synthesizing natural looking faces and high quality images of rigid movements of the head. However, the use of polygonal meshes or other geometric models to reproduce plastic deformations, like the mouth dynamics during speech or the details of human face visual appearance, requires sophisticated models and animation control strategies, implemented at high computational costs [4].

On the other hand, image-based, or 2D, facial animation manipulates photographic pictures from an image database that are captured from a real face, synthesizing the final animation through their appropriate processing, sequencing, concatenation and presentation. This approach inherently generates photorealistic animations due to photographic nature of manipulated images. Most development efforts of this type of system are then concentrated in obtaining videorealism through the correct reproduction of visual dynamics of face during speech.

This paper describes the implementation of a 2D facial animation system integrated to a text-to-speech synthesizer for Brazilian Portuguese, that generates the speech audio from a textual input and provides the corresponding timed phonetic transcription that drives the facial animation system.

The designed system encapsulates two synthesis approaches under two operation modes, making it scalable and flexible, and turning possible its deployment on a wide range of device profiles.

In a *reduced mode*, the system is coupled to a small image database and animation synthesis applies a key framing approach based on morphing between visemes. The reduced image database and the low complexity of image morphing algorithm allow the generation of videorealistic facial animation by small devices such as smartphones, digital TV set-top boxes and PDAs (personal digital assistants).

In an *extended mode*, the morphing between visemes approach is combined with the concatenation of small video fragments characterized by sequences of frames stored in the image database. This combination aims to deliver higher levels of videorealism through an image database that can be continuously scaled. Starting from a minimum image database size that characterizes the *reduced mode*, the image database can grow continuously resulting in greater videorealism. The additional necessary memory and processing capacities make the *extended mode* well suited to desktop platforms.

This paper focus on the implementation aspects of the *reduced mode*. Typically, 2D facial animation systems based on morphing between visemes are characterized by a small image database and a low level of videorealism since the coarticulation effects are not properly modeled [5], [6], [7], [8]. Our approach, however, offers a better solution as it copes with coarticulation effects, improving animation videorealism, yet keeping the image database small. In order to model the coarticulation effects, our system applies an efficient and straightforward approach through the utilization of context-dependent visemes identified for Brazilian Portuguese [9].

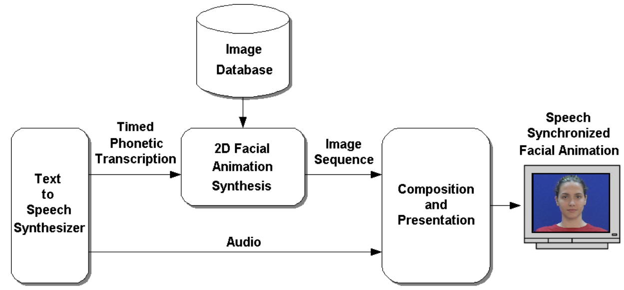

Fig. 1
SPEECH SYNCHRONIZED FACIAL ANIMATION SYNTHESIS PROCESS

Such modeling characterizes a completely new approach to the morphing between visemes synthesis strategy.

The main contributions of this work are: the implementation of a videorealistic 2D speech synchronized facial animation system for Brazilian Portuguese, the design of a cross-platform solution that can be adapted to characteristics of the executing platform and the use of context-dependent visemes to model coarticulation effects on a 2D facial animation system.

Despite the fact that this system was developed for Brazilian Portuguese, its underlying principles and the whole system implementation can also be applied to other languages.

II. RELATED WORK

Figure 1 shows the typical approach to the speech synchronized facial animation synthesis process. It begins with the definition of a new content to be uttered by the talking-head. The corresponding audio is generated by a TTS. The phonetic transcription of the audio, containing timing information of the occurrence of each phonetic unit, is the key input to the system. Based on the timed phonetic transcription, the system generates the corresponding animation frames sequence, selecting and retrieving key pose images from an image database. The image database is a set of processed images extracted from an audiovisual corpus. The synchronization between audio and facial animation is guaranteed by the generation of a sequence of frames in accordance with the phonetic and timing information previously obtained from synthesized audio.

Different implementations of 2D facial animation systems may differ on the nature of captured corpus, the coarticulation modeling approach and the synthesis strategy to obtain a videorealistic animation.

In [10], for example, the audiovisual corpus is characterized by an existing video excerpt of a subject without any restrictions concerning the content of the uttered sentences or the background scenario. To handle coarticulation, small video fragments corresponding to three sequential speech segments, or triphones, are extracted from the corpus, labeled and stored in a database of video fragments. The synthesis of a new video is accomplished by concatenating and stitching the appropriate triphone sequences from the database together. Videorealism is achieved by using triphone contexts to handle coarticulation effects but the quality of final generated video can be limited by the number of triphones contexts existing in the original corpus. The storage of video fragments for a significant number of triphones contexts is memory expensive and contains redundant information due to the storage of fragments in similar contexts.

Another approach is the morphing between visemes synthesis strategy implemented by [5]. In this system, images are extracted from a recorded corpus of a subject uttering predefined words in a controlled environment. The image database is made of 16 viseme images that are associated to groups of phonemes that are visually indistinguishable, or homophene groups. In order to generate a new visual speech stream, visemes from image database are selected according to the information provided by a timed phonetic transcription. The visemes characterizes the key poses of animation. Transitioning between two subsequent visemes is made by image morphing. The main aspects of this implementation are: the image database has a reduced size; no coarticulation modeling is applied; and the transition function that controls the morphing process is linear (far from the reality of speech dynamics, where transition between two articulatory targets follows complex and non-linear behavior).

Systems based on morphing between visemes are successful in animating speech using a small image database but the final animation typically lacks videorealism due to the simplification of modeling of visible articulatory movements reproduced by the synthetic transition between visemes.

A different synthesis technique is applied in [11]. In this work, the image database contains a large number of images corresponding to visemes produced under a variety of different phonetic contexts. The images are extracted from an audiovisual corpus recorded in controlled conditions and with predefined sentences. Following this, the images are analyzed and organized according to their visual features and the phonetic context they are captured. At synthesis time, the system seeks to identify similar phonetic context and duration between the new target speech content and the samples stored in database. The system seeks to use in the final animation the maximum number of frames captured in sequence during corpus recording. Otherwise, the system uses the information about visual aspects of each image that makes possible to choose the best candidate transition frames to produce videorealistic results. The approach described in [11] is capable of delivering high levels of videorealism thanks to a large amount of pre-processed images stored in a database and a resourceful algorithm to search and select frames for the final animation.

The *reduced mode* described in this paper represents a trade-off solution between 2D facial animation systems based on a small image database that delivers robotic facial animations and sophisticated systems that implements elaborated and complex synthesis processes based on extensive image databases. The implemented solution applies morphing between visemes synthesis approach, capable of delivering videorealistic animations, based on an image database of only 34 visemes. The key aspect of this solution is the use of context-dependent visemes, which definition comprises coarticulation effects.

TABLE I

CONSONANTAL CONTEXT-DEPENDENT VISEMES (ADAPTED FROM [9]).

Homophene Group	Visemes	Phonetic Contexts
[p,b,m]	$< p_1 >$	[pi] [pa] [ipɪ] [ipɐ] [ipʊ] [apɪ] [apɐ] [apʊ] [upɐ]
	$< p_2 >$	[pu] [upɪ] [upʊ]
[f,v]	$< f_1 >$	[fi] [fa] [ifɪ] [ifɐ] [ifʊ] [afɪ] [afɐ]
	$< f_2 >$	[fu] [afʊ] [ufɪ] [ufɐ] [ufʊ]
[t,d,n]	$< t_1 >$	[ti] [tu] [itɪ] [itɐ] [itʊ] [atɪ] [atʊ] [utɪ] [utɐ] [utʊ]
	$< t_2 >$	[ta] [atɐ]
[s,z]	$< s_1 >$	[si] [sa] [isɪ] [isɐ] [asɪ] [asɐ]
	$< s_2 >$	[su] [isʊ] [asʊ] [usɪ] [usɐ] [usʊ]
[l]	$< l_1 >$	[li] [ilɪ] [alʊ] [ulɪ] [ulɐ]
	$< l_2 >$	[la] [ilɐ] [alɪ] [alɐ]
	$< l_3 >$	[lu]
	$< l_4 >$	[ilʊ] [ulʊ]
[ʃ, ʒ]	< ʃ$_1$ >	[ʃi] [ʃa] [iʃɪ] [iʃɐ] [iʃʊ] [aʃɪ] [aʃɐ] [aʃʊ] [uʃɪ] [uʃɐ]
	< ʃ$_2$ >	[ʃu] [uʃʊ]
[ʎ, ɲ]	< ʎ$_1$ >	[ʎi] [ʎa] [iʎɪ] [iʎɐ] [aʎɪ] [aʎɐ]
	< ʎ$_2$ >	[ʎu] [uʎɪ] [uʎɐ]
	< ʎ$_3$ >	[iʎʊ] [aʎʊ] [uʎʊ]
[k,g]	$< k_1 >$	[ki] [ikɪ] [ikɐ] [akɪ] [ukɪ] [ukɐ]
	$< k_2 >$	[ka] [akɐ]
	$< k_3 >$	[ku] [ikʊ] [akʊ] [ukʊ]
[ɾ],[ɣ]	< ɾ$_1$ >	[ɣi] [ɣa] [iɾɪ] [iɾɐ] [aɾɪ] [aɾɐ] [uɾɐ]
	< ɾ$_2$ >	[ɣʊ] [iɾʊ] [aɾʊ] [uɾɪ] [uɾʊ]

III. OUR APPROACH

A. Audiovisual Corpus

In order to build a viseme image database, an audiovisual corpus was built by recording the face of a female subject uttering predefined sentences in a well defined and controlled environment.

The uttered sentences were divided in a set of non-sense words and a set of phrases that contains occurrences of all phonemes of Brazilian Portuguese. The set of non-sense words were defined based on context-dependent visemes for Brazilian Portuguese identified in [9]. This study identified groups of homophenes in different contexts that can be visually represented by a unique viseme. Tables I and II show consonantal and vocalic context-dependent visemes used as reference in this work, where phonemes are expressed with the symbols of the International Phonetic Alphabet [13].

The groups of phrases uttered by the subject were used to enrich the database with sequences of frames that captures the

TABLE II

VOCALIC CONTEXT-DEPENDENT VISEMES (ADAPTED FROM [9]).

Homophene Group	Visemes	Phonetic Contexts
[i,ĩ]	$< i_1 >$	All contexts except [tit] and [ʃiʃ].
	$< i_2 >$	[tit] e [ʃiʃ].
[e,ẽ]	$< e >$	All contexts.
[ɛ]	$< \varepsilon >$	All contexts.
[a,ɐ̃]	$<a>$	All contexts.
[ɔ]	$< ɔ >$	All contexts.
[o,õ]	$< o >$	All contexts.
[u,ũ]	$< u >$	All contexts.
[ɪ]	$< ɪ >$	All contexts.
[ɐ]	$< ɐ >$	All contexts.
[ʊ]	$< ʊ >$	All contexts.

speech dynamics on more natural contexts and also to provide redundant samples of visemes. ¿From the digitized content of recorded corpus it was possible to extract audio and video tracks for each uttered element by the subject. From the video track, a set of images were extracted. The corpus was recorded under NTSC video standard which generates video at 29.97 frames per second and resolution 720x486 pixels. Images were saved in Microsoft Windows BMP file format, without compression. The audio tracks were digitized as PCM (Pulse-Code Modulation) audio files, sampled at 48 kHz and using 16 bits/sample. Each audio track was manually analyzed in order to get its phonetic transcription, determining in timescale the frontier of each uttered speech segment. The information provided by the timed phonetic transcription makes possible the association of phonemes and their corresponding visual realization from the extracted frames of the video.

B. Image Database Building

Figure 2 shows the process by which the extracted images from the raw corpus are pre-processed to constitute the image database.

In order to implement the *reduced mode*, 34 images were extracted from the audiovisual corpus, corresponding to: 22 visemes representing the consonantal visemes of Table I, 11 visemes representing vocalic visemes of Table II and one viseme corresponding to the silence posture. The images were selected through the visual inspection of audiovisual corpus and considering the extreme articulation point for an analyzed speech segment.

The following sections describe the steps of image database building.

C. Image Registration

The images extracted from corpus need to be aligned in order to make the face position and size uniform along the image database. This operation is necessary to correct natural movements made by the subject during the recording process.

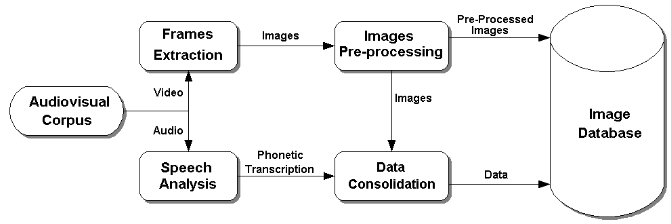

Fig. 2

IMAGE DATABASE BUILDING

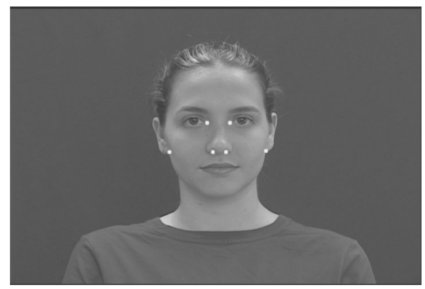

Fig. 3

REFERENCE POINTS FOR REGISTRATION

A reference image is selected from the universe of available samples based on desirable characteristics such as a centralized position of the face in the frame, visual quality and absence of distortions due to fast movements.

In the next step, each image extracted from corpus and the reference image were manually processed in order to get coordinates information of the reference points shown in Figure 3: internal corners of eyes, nostrils and junctions of the ears with the head. These points are chosen because they suffer small influence from mouth and jaw movements during speech production.

The reference points are used to establish the correspondence mapping between images extracted from corpus and the reference image. The alignment is performed through a registration process where geometrical transformations (translation, scale and rotation) are applied to the images of database in order to align them with the reference image.

D. Extracting Region of Interest

After the alignment of the images, the system extracts from the images the region of interest, which is visually affected by the speech production and involves lips, jaw and the region around them. This operation reduces the size of images to be stored in the image database and is based on the proposed synthesis approach, where visemes are stitched to a base-face.

This process is done through the creation of a transparency mask that helps the extraction of the region around lips and jaw, allowing the later superposition and fusion of the detached region into the base-face (Figure 4).

The base-face is a reference image from which the mouth and lips regions are discarded. In its place the synthesized images of final animation are stitched.

The mask has the two contours shown in Figure 4.(a). Pixels inside the inner contour assume value one (full opacity), pixels that are outside the outer contour have value zero (full transparency), and the region between two contours have a gradient of pixel values ranging from zero to one (Figure 4.(b)). This strategy is used to smooth the edges of the extracted region, improving the result of viseme and base-face combination. Figures 4 (c) and (d) shows a sample image and the obtained result of mask application respectively.

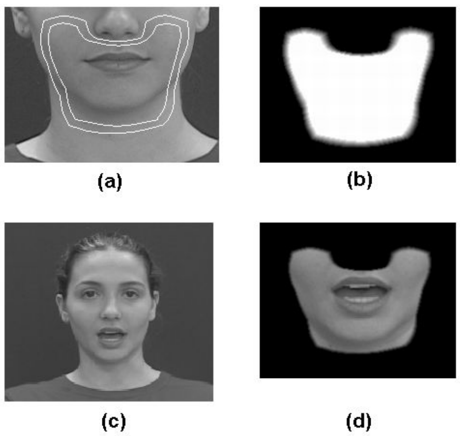

Fig. 4
(A) MASK ALIGNED WITH THE BASE-FACE; (B) MASK; (C) SAMPLE IMAGE; (D) RESULT OF APPLICATION OF (B) MASK ON (C).

E. Extracting information from visemes

In order to get additional information about the visual aspect of the visemes, a set of feature points is defined and manually measured (Figure 5). Each image of the database is accordingly labeled with such information.

This data is important not just to guide the positioning of visemes on base-faces but also as a tool to achieve smooth transitions during synthesis time.

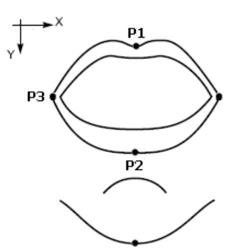

Fig. 5
FEATURE POINTS DETECTED ON VISEMES

F. Database

The implementation of an image database is based on the labeling of each stored sample that provides relevant information for the synthesis process.

The database is built by the analysis and consolidation of information derived from the phonetic transcription, the data extracted from images and the original video sequence (Figure 2).

Each viseme on the database is associated to the following information:

- viseme group classification;
- video frame identification;
- phonetic context of captured viseme;
- feature points information obtained during pre-processing step;
- pointer to image file.

G. Synthesis of Facial Animation

The implemented system is integrated to the commercial TTS *"CPqD Texto Fala"*, that provides a timed phonetic transcription of the new content to be uttered to the facial animation system. This system includes an audio synthesis module that generates a synthetic speech signal from a sequence of phonetic segments derived from the text to be uttered. The synthesizer selects the appropriate acoustic units from a natural speech database coupled to the system, producing a high quality synthetic speech.

The timed phonetic transcription provided as input to the 2D facial animation system is an intermediate step result of *"CPqD Texto Fala"* text processing and synthesis modules and is composed by the sequence of phonetic units used during the generation of speech signal and their corresponding durations.

The first step of animation synthesis process is to convert the sequence of phonetic segments determined by the phonetic transcription into a corresponding sequence of target visemes of Tables I and II.

In order to map a phoneme to a context-dependent viseme, it is necessary to analyze the phonetic context of each phoneme, specially for the consonantal visemes, taking into consideration the adjacent phonemes. As shown on Table I, the consonantal visemes are defined for phonetic contexts of type V_1CV_2, where V indicates a vowel and C a consonant. We also observe that V_1 is optional, that means the consonant can be preceded by silence. Consonantal phonemes present in the phonetic transcription that does not fit this type of context are analyzed and mapped to V_1CV_2 contexts based on the similarity of speech sounds and a list of exceptions. A similar approach is adopted for the first line of Table II.

Each speech phoneme has its duration expressed in the timed phonetic transcription. Therefore, it is possible to define the time instant associated to each target visemes and to determine the number of transition frames between two subsequent target visemes. The animation synthesis is then performed applying a morphing between target visemes in order to obtain smooth transitions between them.

H. Morphing between Visemes

The application of image morphing technique between key poses of animation is a mechanism to generate a smooth and realistic transition.

Morphing between two images begins by establishing the correspondence map of feature primitives between both images. The correspondence map is then used to compute warping functions that define the spatial relationship between all points in both images. In this work, the feature primitives are the feature points detected during pre-processing step and shown in Figure 5.

Considering the small number of selected feature points, the determination of an warping function can be stated as a scattered data interpolation problem. In this work, radial basis functions (RBF) were adopted, since they are proven to be an effective tool in multivariate interpolation problems of scattered data [15], [16].

The determination of warping function begins with the definition of a correspondence map between source viseme feature points $\mathbf{p_i}$ and target viseme points $\mathbf{q_i}$, where $i = 1, ...n$ and $n = 5$ (Figure 5). In this notation $\mathbf{p_i}$ and $\mathbf{q_i}$ are position vectors of image pixels with coordinates $[p_ix, p_iy]$ and $[q_ix, q_iy]$, respectively. From the correspondence map, the following step is to determine the warping function, which formulation can be stated in terms of input and output:

- **Input:** n pairs $(\mathbf{p_i}, \mathbf{q_i})$ of feature-points, where $\mathbf{p_i}$ and $\mathbf{q_i}$ are position vectors $\in \Re^2, i = 1, ..., n$ and $n = 5$.
- **Output:** an at-least-continuous function $\mathbf{f} : \Re^2 \rightarrow \Re^2$ with $\mathbf{f}(\mathbf{p_i}) = \mathbf{q_i}, i = 1, ..., n$.

The adopted interpolation function f is a linear combination of radial functions, which values depend only on the distance between each image point $\mathbf{p}$ and a feature point $\mathbf{p_i}$. This distance is the Euclidean distance between two points defined as $d(\mathbf{p}, \mathbf{p_i}) = \sqrt{(p_ix - px)^2 + (p_iy - py)^2}$.

$$f(\mathbf{p}) = b_m(\mathbf{p}) +^n \sum_{i=1} \alpha_i g_i(d(\mathbf{p}, \mathbf{p_i})) \tag{1}$$

In the equation 1, $b_m(\mathbf{p})$ is a m-degree polynomial added to the formulation in order to reproduce affine linear transformations not naturally obtained by pure radial functions. In this implementation, $m = 1$ and the adopted polynomial is $b_1(\mathbf{p_i}) = \alpha_1 + \alpha_2 \cdot p_ix + \alpha_3 \cdot p_iy$. The α coefficients are determined by solving the system of linear equations resulting from $\mathbf{f}(\mathbf{p_i}) = \mathbf{q_i}, i = 1, ..., n$ and the polynomial precision constraints [15].

The system determines the warping function using multiquadrics radial basis functions as pointed by [16] as an effective and time-efficient radial basis functions:

$$g(d) = (d^2 + r^2)^\mu, r > 0, \mu \neq 0 \tag{2}$$

According to the analysis made at [16], μ was set to 0.5 and an individual value of r_i was used for each $\mathbf{p_i}$, computed from the distance to the nearest neighbor:

$$r_i = min\{d(\mathbf{p_i}, \mathbf{p_j})\}, i = 1, ..., n; i \neq j \tag{3}$$

Given two visemes *A* and *B*, the implemented algorithm determines the function that warps image *A* to *B* in forward direction and the function that warps *B* to *A* in the backward direction. Taking the number of frames to morph *A* to *B*, two sequences of the corresponding number of intermediate images are generated performing forward and backward transformations. Once both images have been warped into intermediate feature positions, they are cross-dissolved to generate intermediate frames according to a transition control function [14].

I. Transition control of morphing

The morphing process implemented by the system was controlled by a smooth non-linear interpolation time function. This function controls the feature points trajectory between two key visemes. The adopted approach represents a better modeling of speech dynamics when compared to the linear transition approach.

The interpolation curve adopted was the Hermite parametric curve [17] with coefficients set to preserve geometric continuity and present derivatives equal to zero at the instant of realization of the articulatory targets represented by the visemes from image database. The interpolation curve used is given by:

$$\begin{bmatrix} x(t) \\ y(t) \end{bmatrix} = \begin{bmatrix} p_x & q_x \\ p_y & q_y \end{bmatrix} \begin{bmatrix} 2 & -3 & 0 & 1 \\ -2 & 3 & 0 & 0 \end{bmatrix} \begin{bmatrix} t^3 \\ t^2 \\ t \\ 1 \end{bmatrix} 0 \leq t \leq 1$$

where $x(t)$ and $y(t)$ are the coordinates of feature point; p_x and p_y are the articulatory target coordinates of the first phoneme; q_x and q_y are the articulatory target coordinates of the second phoneme; and $0 \leq t \leq 1$ is the parametric variable.

J. Extended Mode

The described synthesis implementation based on morphing between visemes characterizes the *reduced mode* of the implemented 2D facial animation synthesis, capable of delivering videorealistic facial animations from a image database of just 34 visemes.

The implemented system also foresees that the image database can continuously grow and that the synthesis system should be able to adapt itself to deliver higher levels of videorealism through the combination of morphing between visemes approach and the concatenation of small video fragments originally captured from audiovisual corpus.

The database can grow by adding new images that are pre-processed and analyzed according to the steps described on Sections III-C, III-D and III-E. The new images added to the database are organized as additional viseme samples of the visemes categories shown on tables I and II and also keeps the information of their original frame identification on the audiovisual corpus.

If an extended image database is available, the system is designed to, for each viseme transition, search the database in order to find a similar transition captured in the original corpus. The optimal situation will happen when such transition occurs in the corpus in exactly the same phonetic context and with the same duration in number of frames. In this case, the sequence of animation frames selected from database are simply concatenated to the final animation sequence. Otherwise, the target phonetic context of the final animation, characterized by a triphone, is analyzed against their pairs on the same homophene groups. In this case, the target speech segment “apa” can be visually animated by a sequence of frames corresponding to the speech segment “aba” if they are present in image database (see first line of table I, that shows that phonemes [p] and [b] are in the same homophene group). Following the context-dependent visemes mapping, the *extended mode* always tries to minimize the number of viseme transitions that requires morphing. With this approach the system is designed to deliver higher levels of videorealism and can be applied on systems with higher processing and memory capacity, such as high end desktops.

IV. Conclusion

This paper presented a videorealistic 2D speech synchronized facial animation system for Brazilian Portuguese designed to be a cross-platform solution that can be adapted to characteristics of the executing platform through two different synthesis modes: a *reduced mode* and an *extended mode*.

The paper focused on the description of *reduced mode* implementation, in which the synthesis is exclusively based on morphing between visemes approach and the image database is composed by 34 visemes. Our implementation presents two significant contributions to the morphing between visemes synthesis approach, that result in a more accurate modeling of visual speech. First, the system adopts a straightforward modeling of coarticulation effects through the use of context-dependent visemes. Secondly, the system applies a simple non-linear transition function that drives the morphing process. The reduced image database and the non-complex models used to implement the synthesis process turn possible the embedding of such system on small or portable devices with limited processing and memory capacities (Figure 6).

Preliminary speech intelligibility test results made with animations generated under *reduced mode* show that the level of videorealism obtained by the system is fair enough to greatly improve the comprehension of information when the audio is heavily degenerated by noise. This work is still under development and the next activities related to the project are: the full implementation of synthesis under extended image database, the implementation of automatic image processing algorithms to process image database and the conclusion of speech intelligibility tests with the system under *extended mode*.

The authors would like to thank CPqD for the financial and technical support and Carolina Franciscangelis for her contribution on audiovisual corpus recording process.

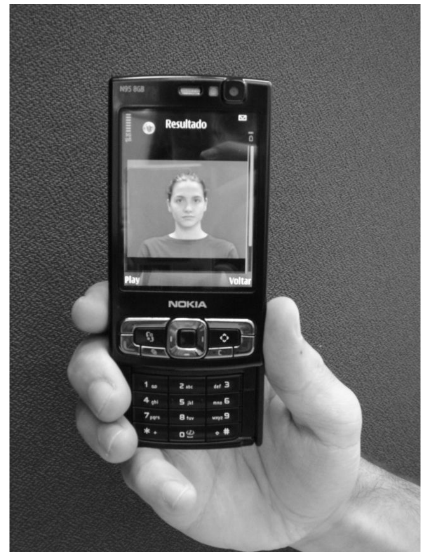

Fig. 6

Facial animation video playing on a cell-phone

References

[1] E. Cosatto et al., “Lifelike Talking Faces for Interactive Services”, *Proceedings of the IEEE*, vol. 91, no. 9, pp. 1406-1429. September 2003.

[2] I. S. Pandzic, “Facial Animation Framework for the Web and Mobile Platforms”, *Proceedings of the seventh international conference on 3D Web technology*, pp. 27-34, 2002.

[3] D. Pearson, “Developments in Model-Based Video Coding”,*Proceedings of the IEEE*, vol. 83, no. 6, pp. 892-906. June 1995.

[4] F. I. Parke and K. Waters, *Computer Facial Animation*, A. K. Peters Ltd., 1996.

[5] T. Ezzat and T. Poggio, “Miketalk: A Talking Facial Display Based on Morphing Visemes”, *Proceedings of Computer Animation*, pp. 96-102. June 1998.

[6] U. K. Goyal et al., “Text-to-Audiovisual Speech Synthesizer”, *Proceedings of the Second International Conference on Virtual Worlds*, pp. 256-269. July 2000.

[7] T. A. Faruquie et al., “Audio driven facial animation for audio-visual reality”, *IEEE International Conference on Multimedia and Expo*, August 2001.

[8] K. C. Scott et al., “Synthesis of Speaker Facial Movement to Match Selected Speech Sequences”, *Proceedings of the Fifth Australian Conference on Speech Science and Technology*. December 1994.

[9] J. M. De Martino et al., “Facial animation based on context-dependent visemes”,*Computer & Graphics*, vol. 30, pp. 971-980. 2006.

[10] C. Bregler et al., “Video Rewrite: driving visual speech with audio”, *SIGGRAPH*, pp. 353-360. 1997.

[11] E. Cosatto and H. P. Graf, “Photo-realistic talking-heads from image samples”, *IEEE Transactions on Multimedia*, vol. 2, no. 3, pp. 152-163. September 2000.

[12] M. Cohen and D. Massaro, “Modeling coarticulation in synthetic visual speech”, *Computer Animation*. 1993.

[13] International Phonetic Association, “Handbook of the International Phonetic Association - A Guide to the Use of the International Phonetic Alphabet”, Cambridge University Press. 1999.

[14] G. Wolberg, “Image Morphing: A Survey”, *The Visual Computer*, vol. 14, no. 8/9, pp. 360-372.1998.

[15] N. Arad et al., “Image warping by radial basis functions: applications to facial expressions”, *CVGIP: Graph. Models Image Process*, vol. 56, no. 2, pp. 161-172. 1994.

[16] D. Ruprecht and H. Müller, “Image Warping with Scattered Data Interpolation”, vol. 15, no. 2, pp. 37-43. 1995.

[17] J. D. Foley, *Computer Graphics Principles and Practice*, Addison-Wesley Publishing Company, 1990

Comparative Analysis of State-of-the-art Block-based Motion Estimation Techniques

André Filgueiras de Araujo
Departamento de Comunicações - Decom
Faculdade de Engenharia Elétrica e de Computação - FEEC
Universidade Estadual de Campinas - Unicamp
P.O. Box 6101 - 13083-970
Campinas - SP – Brazil
+55 19 9115-2816
andrefaraujo@gmail.com

Yuzo Iano
Departamento de Comunicações - Decom
Faculdade de Engenharia Elétrica e de Computação - FEEC
Universidade Estadual de Campinas - Unicamp
P.O. Box 6101 – 13083-970
Campinas - SP – Brazil
+55 19 3521-3809
yuzo@decom.fee.unicamp.br

***Abstract*—Motion estimation is a critical stage in video compression schemes. It impacts greatly on system performance by minimizing the energy of the residual frame to be transmitted. As usual video compression standards (such as MPEG-x and H.26x) do not specify a particular technique to use, it seems important to study the recent developments in the area aiming to consider them comparatively. The focus of this work is on the trade-offs of three state-of-the-art block-based techniques: the Adaptive Modified Two-Bit Transform (AM2BT), the Adaptive Multilevel Successive Elimination Algorithm (AdaMSEA) and the Enhanced Adaptive Rood Pattern Search (E-ARPS). The principal measures to be taken into account in these analyses are the PSNR, the MSSIM and the computational complexity.**

***Index Terms*—AM2BT, AdaMSEA, block-matching algorithms, E-ARPS, motion estimation, video coding.**

I. INTRODUCTION

Most widely used motion estimation techniques consist on a matching algorithm which uses block comparison, the well-known block-based techniques. These are efficient and simple to implement. The optimal algorithm for this kind of technique is known as Full Search (FS). It exhaustively checks every block of the previous frame to choose the one that gives the best matching, i.e., the most similar block to the current frame one. A well-accepted measure of similarity of two blocks is the Sum of Absolute Distances (SAD). The best fitting block to be chosen is the one which gives minimum SAD. The FS approach has, then, extremely high computational complexity and is not used in practice. Many methods have been proposed in the past 20 years to overcome this problem.

The majority of the block-based algorithms reduces the number of operations by selecting the locations where the search is to be held. The location retrieved is the one where the minimum SAD has been calculated. Then, a motion vector is associated to the current analysed block, pointing to the chosen location.

Simple techniques simply use the same default search locations for every block. Examples of these are the Three-Step Search (TSS) [1], the Diamond Search (DS) [2], the Four-Step Search (FSS) [3], the New Three-Step Search (NTSS) [4], the Cross-Diamond Search (CDS) [5]. More complex methods may use a number of criteria for selecting search locations, such as multi-resolution, spatial or temporal correlation. Examples of these approaches comprise the Adaptive Root Pattern Search (ARPS) [6], the Advanced Diamond Zonal Search (ADZS) [7], the Motion Vector Field Adaptive Search (MVFAST) [8], the Multi-resolution Spatio-temporal Correlations (MRST) [9], the Predictive Motion Vector Field Adaptive Search (PMVFAST) [10].

Other algorithms preprocess the frames to simplify the block-based search to be done in the next step. The One-Bit Transform (1BT) [11], the Modified One-Bit Transform (M1BT) [12] and the Two-Bit Transform (2BT) [13] are some examples of these techniques. There are also methods that reduce the computational load by removing the non-optimal search positions without losing the optimality of the FS algorithm. These comprise the Successive Elimination Algorithm (SEA) [14] and the Multilevel Successive Elimination Algorithm (MSEA) [15].

In this work, three state-of-the-art methods are investigated: the Adaptive Modified Two-Bit Transform (AM2BT) [16], the Adaptive Multilevel Successive Elimination Algorithm (AdaMSEA) [17] and the Enhanced Adaptive Rood Pattern Search (E-ARPS) [18]. Each of these regards the motion estimation problem using a different approach, representing the evolution of three different fashions of estimating motion. When compared with simpler methods, they give very good results. Their performances are considered comparatively, calculating the reconstruction quality and the computational complexity for four image sequences.

II. REVIEW OF STUDIED TECHNIQUES

In this section, a brief description of the methods analysed is provided.

A. *Adaptive Modified Two-Bit Transform (AM2BT)*

The Adaptive Modified Two-Bit Transform (AM2BT) [16] is based on the 2BT [13]. Two-bit representations of image frames are obtained using local (inside each block) mean μ and standard deviation σ:

$$B_1(i,j) = \begin{cases} 1, & \text{if } I(i,j) \geq \mu \\ 0, & \text{otherwise} \end{cases}$$

$$B_2(i,j) = \begin{cases} 1, & \text{if } I(i,j) \geq \mu + \sigma \text{ or } I(i,j) \leq \mu - \sigma \\ 0, & \text{otherwise} \end{cases}$$

where $B_1(i,j)$ and $B_2(i,j)$ represent the resulting two-bit planes, which are used for estimating motion.

Initially, a similarity criterion based on Boolean operators (which enables fast execution and simple implementation) is used for the search in every location of the previous frame. The first and second best motion vectors obtained are retained (mv1 and mv2, respectively). Then, the distortion between the original frame and the predicted one with mv1 is calculated and compared with an adaptive threshold T (based on μ and σ, calculated in previous steps). If the distortion is below T, the final motion vector is assigned as mv1. Otherwise, the same procedure is done with mv2. If the distortion is still above T, a two-step search is performed around mv1 and mv2. If the distortion is below twice the threshold value (2 x T), the corresponding displacement is assigned as the motion vector for the block. Otherwise, a third stage is computed using FS and the best motion vector found is chosen. The flowchart of this algorithm is show in Fig. 1.

B. *Adaptive Multilevel Successive Elimination Algorithm (AdaMSEA)*

The Adaptive Multilevel Successive Elimination Algorithm (AdaMSEA) [17] has its bases on the Multilevel Successive Elimination Algorithm (MSEA) [15], which reduces the computational load of the FS strategy by removing many of the non-optimal search positions in a multilevel fashion.

AdaMSEA partitions macroblocks in four submacroblocks based on a threshold condition on the gradient magnitude of the macroblocks. Each new partition corresponds to a higher level and this procedure determines the elimination order. Fig. 2 depicts an example of the elimination order determined by the sum of gradient magnitudes.

Then, the calculation starts at the lower level, with the difference of the sum of norms of the candidate and the block one wants to find motion vectors for. If this result is greater than the current lowest SAD found, the candidate is rejected. It can be shown from this result that it is impossible that this candidate be a better-matching block than the current best-matching one. Otherwise, the sum of the norms of the first level is calculated and compared again with the SAD. If this result is greater, the candidate is rejected. This procedure is repeated until the calculated sum of the highest level is done. If it is greater than the SAD, the candidate is rejected. Otherwise, the SAD_c (SAD of the candidate) is calculated. Finally, if the SAD is greater than the SAD_c, the current best-matching block will be this candidate and SAD = SAD_c.

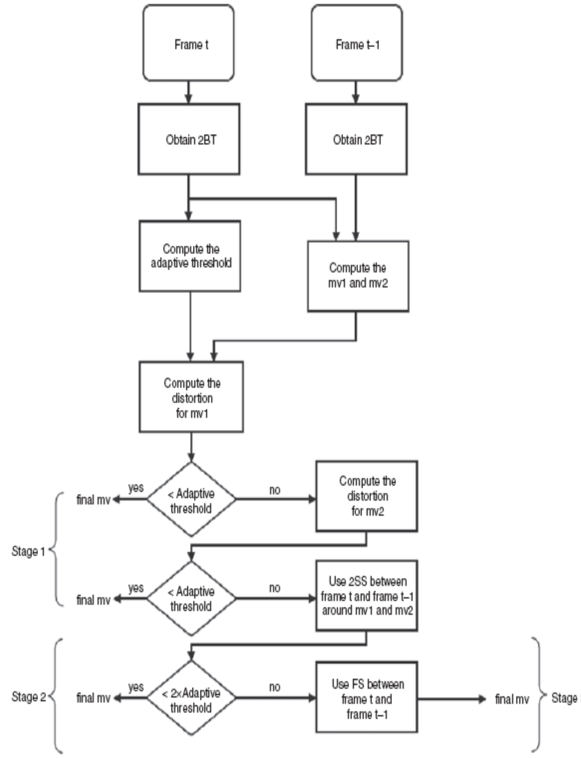

Fig. 1: Flowchart of AM2BT [16]

C. *Enhanced Adaptive Rood Pattern Search (E-ARPS)*

The Enhanced Adaptive Rood Pattern Search (E-ARPS) [18] is a new fast and efficient motion estimation algorithm based on the ARPS [6]. This algorithm makes use of three improvements regarding ARPS: Initial Search Centre (ISC) prediction, adaptive search pattern and early termination. These improvements speed up the ARPS algorithm, giving higher image reconstruction quality.

The adaptive search pattern used is based on the motion vectors of the neighboring blocks. The early termination condition is performed by comparing the distortion with a threshold.

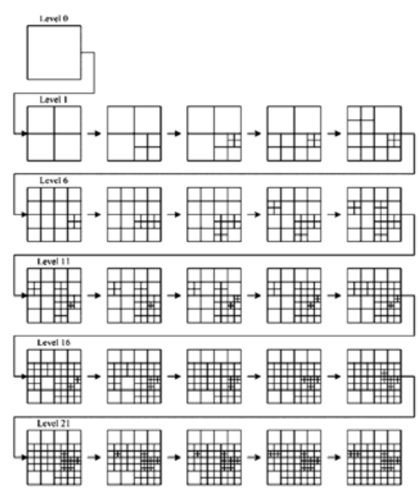

Fig. 2: Example of the elimination order with threshold T=100. [17]

(a)

(b)

(c)

(d)

(e)

(f)

(g)

(h)

(i)

Fig. 3: Frame #150 of sequence “foreman”. (a) Original. (b) Reconstructed using FS with macroblock size 16x16. PSNR = 31.780, MSSIM = 0.9282. (c) AM2BT, 16x16. PSNR = 28.612, MSSIM = 0.8774. (d) AdaMSEA, 16x16. PSNR = 31.780, MSSIM = 0.9282. (e) E-ARPS, 16x16. PSNR = 30.787, MSSIM = 0.9156. (f) FS, 8x8. PSNR = 33.768, MSSIM = 0/9473. (g) AM2BT, 8x8. PSNR = 29.461, MSSIM = 0.8521. (h) AdaMSEA, 8x8. PSNR = 33.768, MSSIM = 0.9473. (i) E-ARPS, 8x8. PSNR = 31.089, MSSIM = 0.8859.

On the first step, the SAD is calculated at the location indicated by a median predictor based on the motion vector of neighboring blocks (SAD_p) and if the termination condition is satisfied, this procedure ends. Otherwise, the SAD (SAD_0) is calculated at the position (0,0) and if it is smaller than the threshold T the search stops. If this condition is not satisfied, SAD_0 and SAD_p are compared and the ISC is chosen to be the position with the minimum SAD (Minimum Distortion Block, MDB) between these two.

Then, the centre of a fixed unit-size rood pattern (URP) is placed at the ISC. The SAD is calculated for the locations indicated by this pattern and if the MDB point found is smaller than T or is placed at the ISC, the search stops. If it doesn’t occur, an adaptive rood pattern is used at this MDB point. If the termination condition is satisfied for one of the searched points, this procedure stops. Otherwise, the URP is placed at the MDB of the previous step and is used repeatedly until the termination condition is satisfied or the MDB point is still at the centre of the URP.

III. Simulation results

The three algorithms have been implemented and simulated for four image sequences, with different degrees and types of motion – “tennis” (112 frames of size 352 x 240), “football” (125 frames of size 352 x 240), “foreman” (299 frames of size 352 x 288) and “mobile” (140 frames of size 352 x 240). The FS method (the optimal one) has also been implemented for comparison. Two block sizes have been used: 16x16 and 8x8, with search range of ±7 pixels in both horizontal and vertical directions. The block distortion measure used for all implemented algorithms is the SAD.

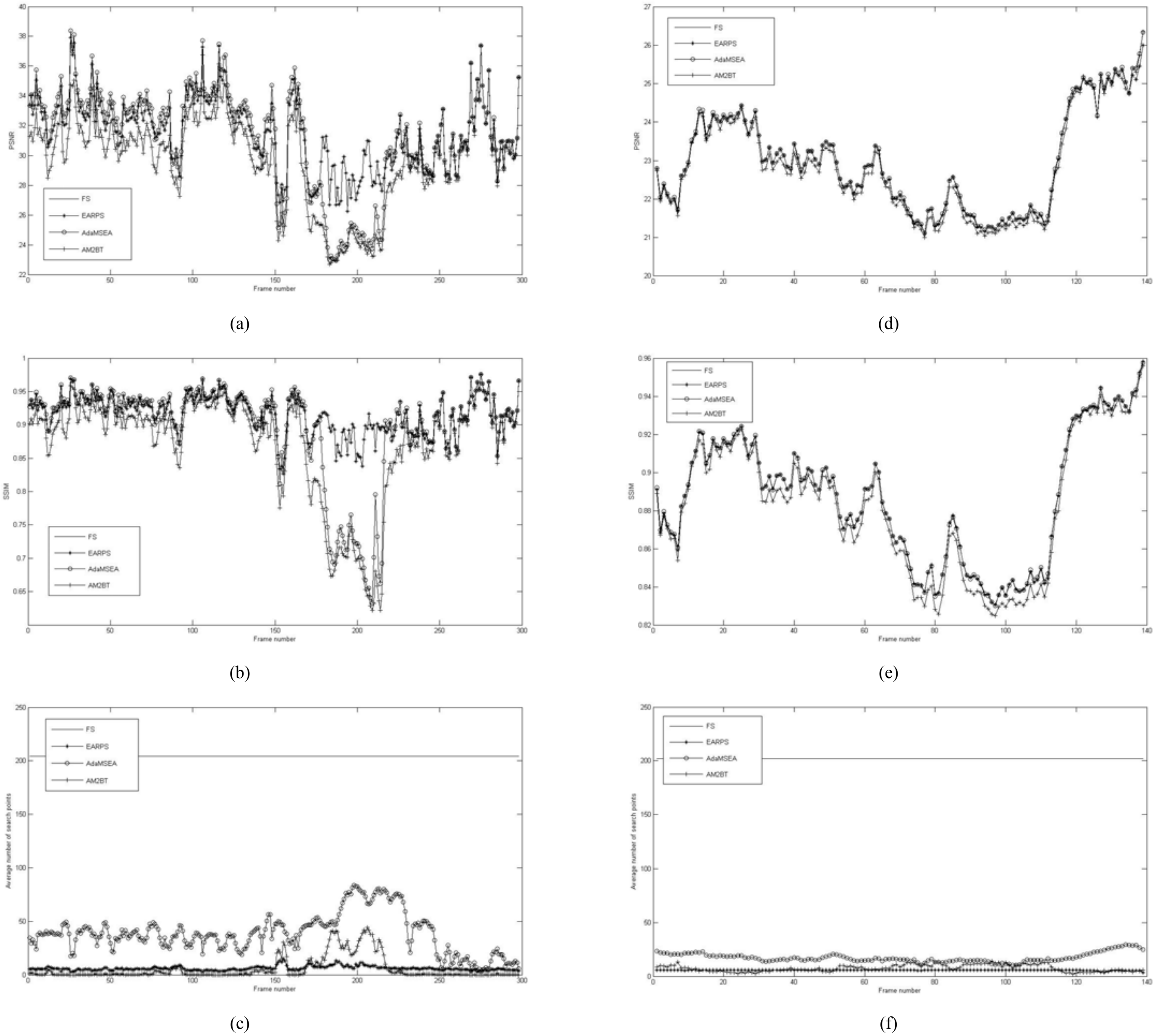

Fig. 4: Results obtained for "foreman" (a, b and c) and "mobile" (d, e and f) sequences, with macroblock size 16x16. (a) and (d): PSNR. (b) and (e): MSSIM. (c) and (f): Average number of search points.

For providing reconstruction quality comparison, two distortion metrics have been used: the Peak Signal-to-Noise Ratio (PSNR) and the Mean Structural Similarity Index (MSSIM) [19], which have been computed for each frame and plotted for each sequence. The PSNR, based on the MSE, is the simplest and most widely used measure of quality. However, images with the same PSNR may have very different type of errors, some of which are much more visible than others. The MSSIM, on the other hand, quantify better the visibility of errors because the Human Visual System (HVS) is in general highly adapted for extracting structural information, which is measured by this index. To calculate it, the algorithm based on [19] has been used.

The computational cost is assessed by the average number of search points per motion vector generation (i.e., per macroblock) for each frame.

An example of frame reconstruction is presented in Figure 3. The original frame is provided and can be visually compared to the reconstructed ones. Distortion can be clearly identified in the upper right corner of the images, and associated to the PSNR and MSSIM results.

Some results for the PSNR, the MSSIM and the computational cost are shown in Figures 4 and 5. These

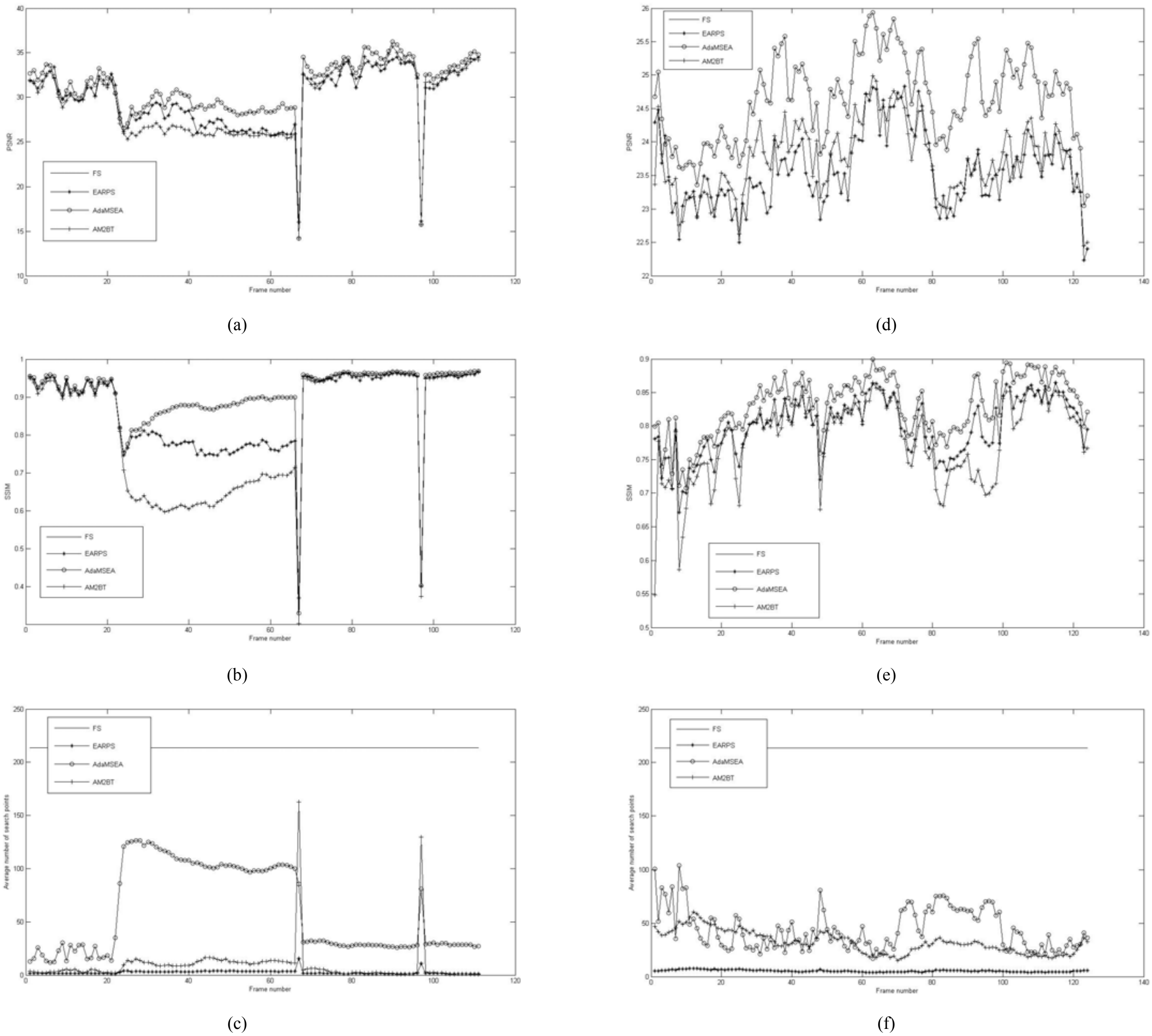

Fig. 5: Results obtained for “tennis” (a, b and c) and “football” (d, e and f) sequences, with macroblock size 8x8. (a) and (d): PSNR. (b) and (e): MSSIM. (c) and (f): Average number of search points.

measures are plotted for each frame for some image sequences. The average values obtained are given in Tables I and II.

The PSNR and MSSIM results for the AdaMSEA algorithm are identical to the FS ones, as expected, for the former reduces the computational cost of the latter by using some properties, but still checking every candidate. Despite giving excellent results in terms of PSNR and MSSIM, the AdaMSEA presents high computational cost when compared to the E-ARPS and to the AM2BT, the two studied techniques that achieve highest computational complexity reduction.

All the studied methods provide good results. The E-ARPS gives excellent results in terms of computational complexity for all the image sequences treated. However, for the “football” sequence with macroblock size 16x16 it gives the poorest results in terms of PSNR and MSSIM, but still in an acceptable range. In Figure 4, it can be noticed that the E-ARPS algorithm achieves PSNR and MSSIM results for the “foreman” sequence that are even better than the ones given by the FS algorithm for a significant amount of frames (the average PSNR and MSSIM are also higher, as shown in Table I). It can be explained by noticing that the E-ARPS does not impose a search range, while the other analysed techniques do. As the motion occurs quickly for this sequence, the motion vectors should have larger values, which can’t be done by the other methods since they have a limited range for searching similar blocks. For this sequence, it must also be remarked that the computational load of AdaMSEA is much greater than those given by

TABLE I
AVERAGE PSNR, MSSIM AND NUMBER OF SEARCH POINTS OBTAINED, WITH MACROBLOCK SIZE 16X16.

	TENNIS			FOOTBALL			FOREMAN			MOBILE		
	PSNR	MSSIM	S. points	PSNR	MSSIM	S. points	PSNR	MSSIM	S. points	PSNR	MSSIM	S. points
FS	29.410	0.8819	202.049	22.466	0.7695	202.049	31.202	0.8969	204.283	22.976	0.8865	202.049
E-ARPS	28.677	0.8735	5.620	21.842	0.7586	8.494	31.468	0.9156	5.885	22.942	0.8863	5.612
AdaMSEA	29.410	0.8819	50.824	22.466	0.7695	35.898	31.202	0.8969	38.517	22.976	0.8865	17.375
AM2BT	29.038	0.8735	5.264	22.315	0.7617	20.587	29.740	0.8720	5.472	22.823	0.8813	7.468

TABLE II
AVERAGE PSNR, MSSIM AND NUMBER OF SEARCH POINTS OBTAINED, WITH MACROBLOCK SIZE 8X8.

	TENNIS			FOOTBALL			FOREMAN			MOBILE		
	PSNR	MSSIM	S. points	PSNR	MSSIM	S. points	PSNR	MSSIM	S. points	PSNR	MSSIM	S. points
FS	31.166	0.9083	213.376	24.643	0.8311	213.376	32.701	0.9165	214.518	23.873	0.9033	213.376
E-ARPS	29.967	0.8680	2.430	23.584	0.8002	5.343	31.691	0.9021	2.209	23.625	0.8974	3.389
AdaMSEA	31.166	0.9083	59.167	24.643	0.8311	44.341	32.701	0.9165	42.162	23.873	0.9033	30.247
AM2BT	29.532	0.8170	8.781	23.752	0.7801	32.281	29.921	0.8605	7.552	23.441	0.8841	11.052

AM2BT and E-ARPS. The “mobile” sequence, also presented in this figure, presents similar results in terms of reconstruction quality for all the methods used. The computational cost is lower for this sequence.

Figure 5 shows that, for the “tennis” sequence with macroblock size 8x8, the E-ARPS algorithm gives better results than the AM2BT with lower computational complexity. This fact occurs for other sequences as well, as shown on Tables I and II. For the majority of the frames of the “football” sequence with macroblock size 8x8, the results achieved in terms of PSNR do not agree with those given by MSSIM. The PSNR calculated for the AM2BT technique is higher than the E-ARPS’, whilst the opposite happens for the MSSIM index.

It’s important to notice that there are other parameters concerning the computational complexity that must be taken into account when implementing one of the studied methods. In this work, the influence of the number of search points has been analysed. Preprocessing operations have not been considered, and it must be remarked that the AM2BT and the AdaMSEA have a significant amount of these. The E-ARPS has, therefore, the lightest computational load in terms of the number of operations between the analysed algorithms. Nevertheless, the underlying hardware has got to be understood if hardware implementation is envisaged. Some algorithms may be easier treated for specific hardware architecture.

IV. CONCLUSIONS

This paper investigates the inherent performance trade-offs of three state-of-the-art block-based motion estimation techniques, each representing the evolutions of different fashions of estimating motion. Motion estimation is a critical stage in video compression, and the main contribution of this work is to analyse comparatively recent developments in the domain. Simulation results have shown that the E-ARPS is the most robust method analysed, for it presents extremely simple computational complexity giving excellent results in terms of image reconstruction quality.

V. ACKNOWLEDGEMENTS

The authors would like to thank FAEPEX/Unicamp and RH-TVD/CAPES for the financial support.

REFERENCES

[1] T. Koga, K. Iinuma, A. Hirano, Y. Iijima, and T. Ishiguro, “Motion compensated inter-frame coding for video conferencing”, Proc. NTC’81, New Orleans, LA, Dec.1981, pp. G5.3.1-G5.3.5.
[2] S. Zhu and K.K. Ma, “A new diamond search algorithm for fast block matching motion estimation”, Proc. Of Int. Conf. Information, Communications and Signal Processing, 1997, vol.1, pp.292-6.
[3] L.M. Po and W.C. Ma, “A Novel Four-Step Search Algorithm for Fast Block Motion Estimation”, IEEE Trans. on Circuits and Systems for Video Technology, Jun.1996, vol.6, no.3, pp.313-317.
[4] R. Li, B. Zeng, and M.L. Liou, “A new three-step search algorithm for block motion estimation”, IEEE Trans. on Circuits and Systems for Video Technology, Aug.1991, vol.4, no.4, pp. 438-442.
[5] C.H. Cheung and L.M. Po, “A Novel Cross-Diamond Search Algorithm for Fast Block Motion Estimation”, IEEE Trans. on Circuits and Systems for Video Technology, Oct.2002, vol.12, no.12.
[6] Y. Nie and K.K. Ma, “Adaptive Rood Pattern Search for Fast Block-Matching Motion Estimation”, IEEE Trans. on Image Processing, Dec. 2002, vol.11, no.12.
[7] A.M. Tourapis, O.C. Au, M.L. Liou, G. Shen and I. Ahmad, “Optimizing the MPEG-4 Encoder-Advanced Diamond Zonal Search”, IEEE International Symposium on Circuits and Systems, Geneva, Switzerland, May 2000.
[8] P.I. Hosur and K.K. Ma, “Motion Vector Field Adaptive Fast Motion Estimation”, Second International Conference on Information, Communications and Signal Processing (ICICS’99), Singapore,7-10, Dec. 1999.
[9] J. Chalidabhongse and C. -C. Jay Kuo, “Fast Motion Vector Estimation Using Multiresolution-Spatio-Temporal Correlations”,

IEEE Trans. on Circuits and Systems for Video Technology, Aug.1997, vol.7, no.3.

[10] A.M. Tourapis, O.C. Au, M.L. Liou, "Predictive Motion Vector Field Adaptive Search Technique (PMVFAST)-Enhancing Block Based Motion Estimation", proceedings of Visual Communications and Image Processing 2001 (VCIP-2001), San Jose, CA, January 2001.

[11] B. Natarajan, V. Bhaskaran, and K. Konstantinides, "Low-Complexity Block-Based Motion Estimation via One-Bit Transforms", IEEE Trans. on Circuits and Systems for Video Technology, Aug.1997, vol.7, no.4.

[12] Peter H. W. Wong and Oscar C. Au, "Modified One-Bit Transform for Motion Estimation", IEEE Trans. on Circuits and Systems for Video Technology, Oct.1999, vol.9, no.7.

[13] A. Ertürk and S. Ertürk, "Two-bit transform for binary block motion estimation", IEEE Trans. on Circuits and Systems for Video Technol., 2005, vol. 15, no. 7, pp. 938-946.

[14] W. Li and E. Salari, "Successive elimination algorithm for motion estimation", IEEE Trans. on Image Processing, Jan. 1995, vol. 4, pp. 105-107.

[15] X. Q. Gao, C. J. Duanmu, and C. R. Zou, "A multilevel successive elimination algorithm for block matching motion estimation," IEEE Trans. on Image Processing, Mar. 2000, vol. 9, no. 3, pp. 501–504.

[16] B. Demir and S. Ertürk, "Block motion estimation using adaptive modified two-bit transform", IET Image Processing, June 2007, vol. 1, no. 2, pp. 215-222.

[17] Shao-Wei Liu, Shou-Der Wei and Shang-Hong Lai, "Fast Optimal Motion Estimation Based on Gradient-Based Adaptive Multilevel Successive Elimination", IEEE Trans. on Circuits and Systems for Video Technology, Feb. 2008, vol. 18, no. 2, pp. 263-267.

[18] Hui Zhao, Xin-bo Yu, Jia-hong Sun, Chang Sun and Hao-zhe Cong, "An Enhanced Adaptive Rood Pattern Search Algorithm for Fast Block-Matching Motion Estimation", Congress on Image and Signal Processing (CISP'08), May 2008.

[19] Z. Wang, A. C. Bovik, H. R. Sheikh, E. P. Simoncelli, "Image Quality Assessment: From Error Visibility to Structural Similarity", IEEE Trans. on Image Processing, April 2004, vol. 13, no. 4, pp. 600-612.

Image Quality Evaluation Method using Blocking Noise Measurement Algorithm

Luís Tadeu Mendes Raunheitte
Universidade Presbiteriana Mackenzie
Rua da Consolação, 896 – SP/SP
Tel.: 2114.8671
raunheitte@mackenzie.br

Fujio Yamada
Universidade Presbiteriana Mackenzie
Rua da Consolação, 896 – SP/SP
Tel.: 2114.8671
fyamada@mackenzie.com.br

Gunnar Bedicks Jr.
Universidade Presbiteriana Mackenzie
Rua da Consolação, 896 – SP/SP
Tel.: 2114.8671
gbedicks@ieee.org

Francisco Sukys
Universidade Presbiteriana Mackenzie
Rua da Consolação, 896 – SP/SP
Tel.: 2114.8671
fsukys@mackenzie.com.br

Cristiano Akamine
Universidade Presbiteriana Mackenzie
Rua da Consolação, 896 – SP/SP
Tel.: 2114.8671
akamine@mackenzie.com.br

Edson Horta
Universidade Presbiteriana Mackenzie
Rua da Consolação, 896 – SP/SP
Tel.: 2114.8671
edson-horta@ieee.org

***Abstract* - This paper introduces an objective quality measurement model for digitized video sequences, using a Blocking Noise measurement algorithm (simulated with MATLAB).**

I. INTRODUCTION

Blocking noise is a typical phenomenon with great importance in MPEG coding. It represents the arising of squares with 8x8 elements forming a chessboard structure. The blocks become visible because there is a discontinuity in the image elements between the edges of one block and the adjacent blocks. The greater responsible for Blocking Noise arising is the coarse quantization and consequent elimination of some DCT coefficients caused by bit rate limitation to only 2Mbps. A strong DCT coefficient attenuation also affects the image definition.

A. Blocking Noise measurement algorithm

Blocking Noise is characterized by artificial discontinuity of the image between image elements in the edges of blocks or macro blocks, where the MPEG coding is processed [1]. The method to detect and convert the discontinuity in numbers can be seen on figure 1, since the discontinuity degree has a strong correlation with the image degradation, as proposed by Trauberg [2].

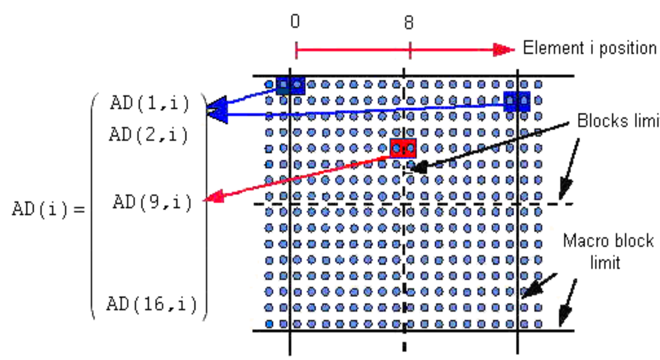

Fig. 1. Average Difference AD vector formation in the horizontal direction – Origin [2].

The figure 1 shows a portion of MPEG image decoded. Each point represents an image element, in this case the luminance signal, with the digitized magnitude. The full and dotted lines forming the reticule represent the border between blocks or macro blocks. The algorithm proposes to measure all the absolute differences between adjacent elements in horizontal direction and compare the differences between elements belonging to adjacent blocks or macro blocks with the difference between internal elements to the blocks. An Average Difference (AD) vector, showed in the figure 2, is formulated, in order to the comparison reaches all the frame elements. The first term AD(1,i) and the ninth term AD(9,i) are those containing the difference between the elements belonging to the adjacent blocks. The other terms are the difference between the elements inside the blocks.

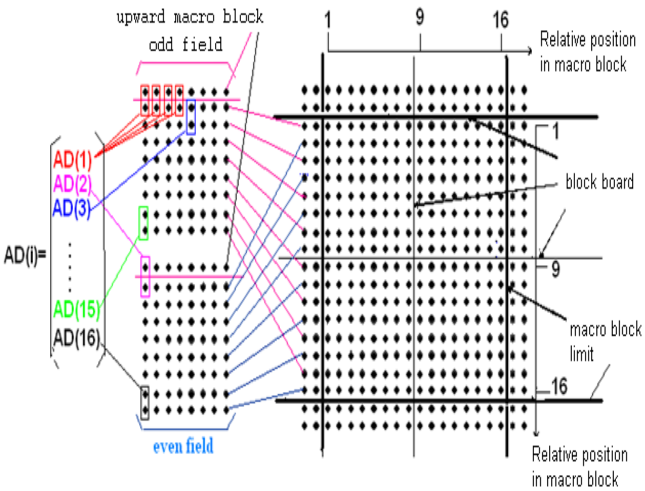

Fig. 2. AD vector formation in the vertical direction for interleaving sweeping

Before introducing the vector AD math's expression, it's convenient to explain the parameters used in figure 2. The reticule in this figure represents the image frame, considering only the luminance signal. In terms of image elements, MPEG image has integer multiple of macro block, with block having the dimension K x J elements in horizontal direction as well as in vertical direction. The elements outside of this frame are not of coding object and take the value of black color or without color in case of chrominance, and appear as a black bar in the image board.

The number of block in the horizontal direction (My) and in the vertical direction (Ny) is given by equation (1)

$$M_y = \frac{b_y}{J}\ ;\ N_y = \frac{h_y}{K} \tag{1}$$

Where, b_y and h_y are the total number of elements in the horizontal and vertical directions respectively. The $AD_{y,h}$ is given by expression (2) where Y is the luminance value:

$$AD_{Y,h}(i,t) = \frac{1}{h_y(M_y-4)} \sum_{y=1}^{h_y} \sum_{m_y=2}^{M_y-3} \left| Y(2Jm_y+i,y,t) - Y(2Jm_y+i-1,y,t) \right| \tag{2}$$

i= 1,2,…,2J e t=1,2,…,N N = Number total of frame

The equation (2) that calculates the i th elements of the vector of t th frame, which may be considered as the time or frame t, shows that the difference result is not done during all the elements in the horizontal direction because there are vertical bars in the board of frame that may distort the results. In the case of equation (2), two initial macro blocks located on left side and two macro blocks located on right side are now considered. The quantity of macro blocks is calculated by $1/2M_y$ in horizontal direction and 2J is the elements quantity of one macro block in the horizontal direction. In case of figure 1 where the $AD_{y,h}$ vector was illustrated taking as example J=8 and as consequence the terms AD(1,t) and AD(9,t) contain the blocks or macro blocks limits that must be detached from the rest.

Similar procedure may be applied to the vertical direction and get the vector $AD_{y,v}$ considering the differences between the vertical direction elements. If the sweeping is progressive, the procedure is equal to the $AD_{y,h}$ horizontal vector.

However, if the sweeping is interleaved, and this is the great number of cases, there is an additional difficulty because, usually, the MPEG coding is applied per field. The figure 2 shows the construction of $AD_{y,v}$ vertical vector for interleaved sweep with MPEG coding application per field. The $AD_{y,v}$ vector for MPEG application case term i based on field and it is given by expression (3):

$$AD_{Y,v}(i,t) = \frac{1}{b_y(\frac{1}{2}N_y-4)} \sum_{x=1}^{b_y} \sum_{n_y=2}^{\frac{1}{2}N_y-3} \left| Y(x,2Kn_y+i,t) - Y(x,2Kn_y+i-2,t) \right| \tag{3}$$

i = 1,2, …,2K e t = 1,2, …, N
N = Total frame quantity; Ny = hy/K

The term "$2kn_y$ +i-2" indicates the intercalated and non contiguous neighborhood. The same algorithm applied to luminance could be applied to the chrominance C_B and C_R or U and V, depending of digitized signal format. The expression (4) calculates the term I for AD vector for chrominance U and V considering the format 4:2:2 recommended by ITU-R BT.601-5 Recommendation.

$$AD_{U,h}(i,t) = \frac{1}{h_U(M_U-4)} \sum_{y=1}^{h_U} \sum_{m_U=2}^{M_U-3} \left| U(Jm_U+i,y,t) - U(Jm_U+i-1,y,t) \right|$$

$$AD_{V,h}(i,t) = \frac{1}{h_V(M_V-4)} \sum_{y=1}^{h_V} \sum_{m_V=2}^{M_V-3} \left| V(Jm_V+i,y,t) - V(Jm_V+i-1,y,t) \right| \tag{4}$$

i=1,2,…,J; t=1,2,…N
N=frame quantity; $M_U = M_V = 0{,}5M_Y$

II. Application Example

The figure 3 shows the vectors AD_{yh} computed as expression (2) for a sequence of 25 video frames of "Football original" without degradation. In the abscissa we have the quantity of frames and in the ordinate we have the vector $AD_{y,h}$ term values.

Each luminance element may assume values from 16 up to 235 corresponding to the levels black to white respectively as defined in the standard ITU-R BR+T.601-5. Therefore, the average value of the difference may take theoretical value of 220, if the image is composed by black and white vertical line with one element thickness. The 16 terms of the frame $AD_{y,h}$ vectors are represented by curves with different colors and may be observed that the medium values are situated between 4,5 and 7, depending on the frame. The curves spreading inside the same frame is very small, lower to 0.5, indicating that there are no relevant discontinuities in the horizontal direction. The figure (2) shows the $AD_{y,h}$ vectors computed in the same frame sequence, but after applying MPEG-2 coding and decoding compression with 3Mbps bits ratio. The two curves with greater values are AD(1,t) and AD(9,t), as indicated. The others vector terms have minor values and with variation up to 1, 2 inside the same frame. This appointment of the two graphics indicate that there is a remarkable discontinuity in the horizontal direction, whose positions correspond to the terms AD(1,t) and AD(9,t).

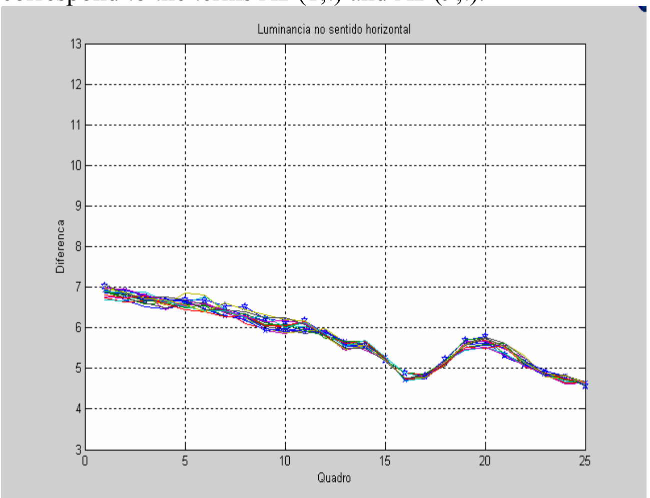

Fig. 3. Reference Video of Football $AD_{y,h}$ vector computed via MATLAB.

A visual analysis of printed image exposes that AD(1,t) and AD(9,t) correspond to bordering elements between macro blocks and blocks respectively. Being the ratio of MPEG-2 coding bits limited to 3Mbps, the discontinuity between macro blocks or blocks represented by high values of AD(1,t) and AD(9,t), exposure poor AC of DCT coefficient quantization to accommodate the big quantity of information imposed by bit ratio. According to the signal origin, the verification of block size is necessary to apply the algorithm in the entire number of blocks in the horizontal and vertical directions.

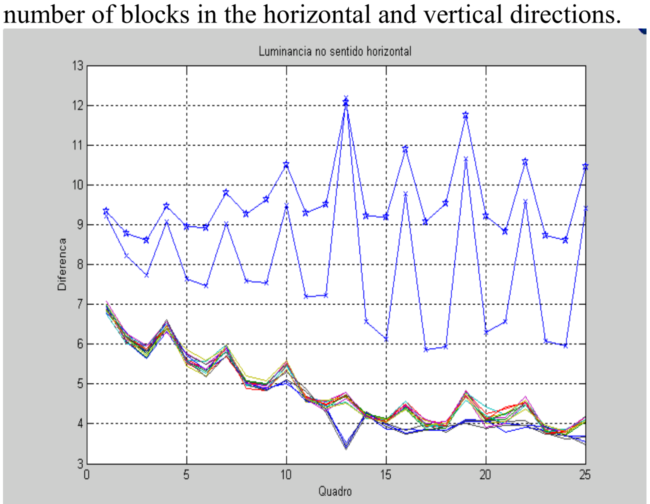

Fig. 4. Degraded Video Football $AD_{y,h}$ Vector with 3Mbps MPEG-2.

The verification of the block positioning relating to frame is necessary for elements identification that is situated in the block board.

The figure 5 is the 13th frame of the football degraded video used in the examples [4].

Fig. 5. 13th frame of the football degraded video.

The application of the exemplified algorithm in the graphics shows that the block or macro block discontinuity evaluation could be done by Blocking Noise measurement and could have a high correlation degree to the analyzed image.

III. Final Comments

Comparing the results obtained by using the algorithm with the tests carried out with the same sequence of football video using PQA 200 Tektronics instruments allows to conclude that the degradation detected are also pointed via PQA 200, using reference image [3].

The use of algorithm to detect and quantitize the Blocking Noise is a different way to evaluate the image quality [4] and involves more practical and interesting applications, because it does not use image reference to detect the processed image degradation. The figure 6 illustrates an example of Blocking Noise measurer application.

The measurement of Blocking Noise done in production studios is a commonplace application that allows the monitoring and feedbacking in loco of Blocking Noise for appropriate MPEG-2 coder adjusts.

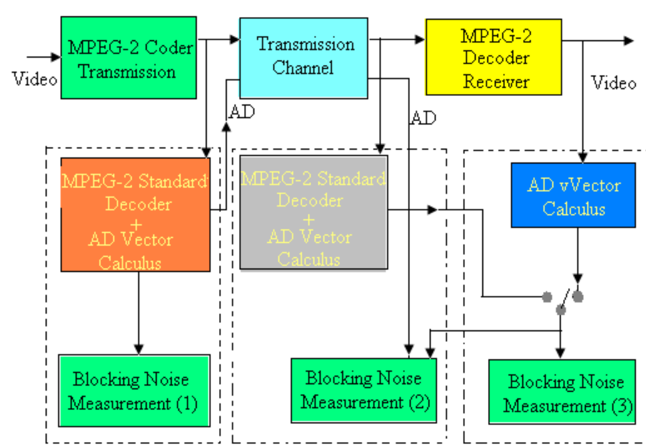

Fig. 6. Example of Blocking Noise Measurer.

REFERENCES

[1] T. Kawano, *Medição Objetiva de Qualidade de Vídeo Digital.* Dissertação (Mestrado em Engenharia Elétrica) Universidade Presbiteriana Mackenzie, São Paulo, 2002.

[2] M. Trauberg, *Ein neues Verfahren für die Bildqualitätsüberwachung in MPEG-basierten Übertragungssystemen.* Proceedings of 18 Jahrestagung FKTG. Erfurt Germany. 1998.

[3] VQEG, *Final Report From The Video Quality Experts Group On The Validation Of Objective Models Of Video Quality Assessment.* http://www.its.bldrdoc.gov/vqeg/projects/frtv_phaseI/COM-80E_final_report.pdf . 2000.

[4] H. Hoffman, T. Itagaki, D. Wood, T. Hinz, and T. Wiegand, *A Novel Method for subjective Picture Quality Assessment and Further Studies of HDTV Formats.* IEEE Transactions on Broadcasting, vol. 54, no. 1, pp. 1-13. March 2008.

An adaptive speaker identification system for noisy speech

Denis Pirttiaho Cardoso
Universidade de São Paulo - USP
São Paulo - SP - Brazil
denis_dpc@yahoo.com.br

Miguel Arjona Ramírez
Universidade de São Paulo - USP
São Paulo - SP - Brazil
miguel@lps.usp.br

***Abstract*— Speaker identification is concerned with the selection of one speaker within a set of enrolled members and in this work the experiments were performed using a text-independent cohort Gaussian mixture model (GMM) speaker identification system. In order to perform the tests, TIMIT speech database is used and its corresponding version corrupted by a noisy telephone channel, i.e., NTIMIT. The vocal tract is represented by Mel-frequency cepstral coefficients (MFCC) with filter banks (FB) or, alternatively, by linear prediction cepstral coefficients (LPCC). Additionally, the cepstral mean subtraction (CMS) technique is applied to minimize the intrinsic channel distortion when the NTIMIT database is used. The utterance component for which the MFCC are calculated is obtained using a voice activity detector (VAD). However, the VADs are generally sensitive to the signal-to-noise ratio (SNR) of the utterance, being necessary to adapt them to the system operating conditions. It is provided by the proposed integration into the VAD of an SNR estimator which is based on Minima Controlled Recursive Average (MCRA), so that is necessary in order to handle both clean and noisy speech. It is observed that in high SNR utterances, such as those from the TIMIT database, the more appropriate extraction method for the MFCC was the baseline one consisting of FB, while for noisy speech the technique of CMS coupled with the extraction of MFCC from LPCC provided best results.**

***Index Terms*— Speaker identification, Gaussian mixture model, mel cepstral coeffcient, Minima Controlled Recursive Averaging.**

I. Introduction

A GMM speaker identification system [3] has two main two components. One is the training phase where speaker models are estimated and the other one is the identification phase where the most compatible model for an utterance input to the system is selected. The speech signal before being input to the identification system goes through to a preprocessing [4] stage. The MFCC algorithm is selected according to the SNR of the speech signal directly as this improves the performance of the identification system, so that clean and noisy speech may be used from NTIMIT or TIMIT databases to highlight the most appropriate technique of MFCC extraction. The clean component of the speech signal, from which the MFCC are obtained, is extracted with the use of a VAD. The VAD are generally sensitive to the SNR level of the utterance, being necessary to adapt them to conditions of operation of the system. This is handled by a noise estimator based on the method of MCRA [2] which is integrated into the VAD, thus allowing the use of clean and noisy speech. This paper is organized as follows. In section II signal preprocessing is described. Section III presents the simulation framework. Section IV presents the results as well as the experimental conditions. Section V concludes the paper.

This work was supported by Fundação de Amparo à Pesquisa do Estado de São Paulo (FAPESP) under Grants no. 2007/08288-2 and 2004/13206-7.

II. Preprocessing

An utterance $x(n)$ is modeled as a time-varying excitation $e(n)$ filtered by a short-time-varying filter $h(n)$ that can be considered stable over a period of typically around 10-30 ms [5]. This short-time stationary behavior can be exploited dividing the speech signal into frames and serves to characterize the vocal tract configuration given by $h(n)$ in Equation (1), which allows each speaker to be exclusively identified.

$$x(n) = e(n) * h(n) \tag{1}$$

In the preprocessing stage the speech signal undergoes pre-emphasis, segmentation, windowing and voice activity detection, as shown in Figure 1. The characterization of the filters $h(n)$ is made from each of the frames $y(m, l)$ extracted from the speech signal, where m corresponds to the sample index and l to the frame number.

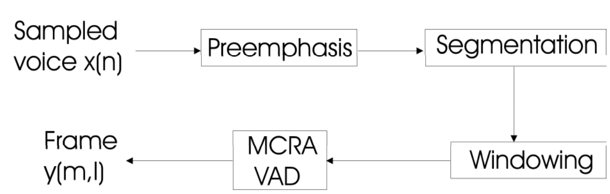

Fig. 1. Utterance preprocessing

A. Voice Activity Detector

The signal $x(n) = d(n) + \hat{x}(n)$ is composed of uncorrelated additive noise $d(n)$ and the speech signal $\hat{x}(n)$. The noise $d(n)$ must be discarded by the VAD since it impairs the performance of the identification system. The VAD is calibrated according to the quality of the signal, in order to maintain its effectiveness in situations where there are changes in the SNR of the speech signal. To overcome this limitation, allowing the use of TIMIT and NTIMIT databases, the MCRA method was adopted. It estimates the speech presence observing the ratio between the local energy of the noisy speech and its minimum within a specified time window and this method is formulated below.

In Equation (2), $Y(k,l)$ is the short-time Fourier transform of $y(m,l)$, the frame output by the preprocessing phase, and $b(i)$ is a Hanning window of length 3. It is observed that $S_f(k,l)$ is a smoothed version of the energy spectrum of $Y(k,l)$ around frequency k.

$$S_f(k,l) = \sum_{i=-1}^{1} b(i)|Y(k-i,l)|^2 \tag{2}$$

In Equation (3), the spectrum $S(k,l)$ at each frame is a complementary linear combination between $S(k,l-1)$ and $S_f(k,l)$. The maximum value of the parameter α_s is 0.9 and it is chosen to be greater than 0.6 to reduce the influence of $S_f(k,l)$ in the composition of $S(k,l)$. This choice allows $S(k,l)$ to adapt gradually to $S_f(k,l)$ without displaying sharp peaks.

$$S(k,l) = \alpha_s S(k,l-1) + (1-\alpha_s)S_f(k,l) \tag{3}$$

In Equation (4), the minimum value of $S(k,l)$ is found over the past D frames obtained in the preprocessing stage. This minimum value $S_{min}(k,l)$ stores the smoothed noise energy for a given frequency around the frame l.

$$S_{min}(k,l) = \arg \min_{1 \leq n \leq D} S(k,l-n) \tag{4}$$

In Equation (5), the integrated log spectrum normalized with respect to S_{min} is computed in the frequency band from F_{min} through F_{max} where the speech energy is concentrated. This operation ensures that the value of $S_m(l)$ rises in presence of clean speech in a similar way irrespective of the utterance quality.

$$S_m(l) = \frac{1}{N2 - N1 + 1} \sum_{k=N1}^{N2} log \frac{S(k,l)}{S_{min}(k,l)} \tag{5}$$

$$N1 = \frac{F_{min}}{F_s} M \tag{6}$$

$$N2 = \frac{F_{max}}{F_s} M \tag{7}$$

In Figure 2 the evolution of $S_m(l)$ is displayed for corresponding phrases in TIMIT and NTIMIT databases. The speech presence is detected in frames where $S_m(l)$ exceeds the threshold δ represented by the horizontal line. It is observed that the value of δ must be experimentally calibrated and its value is independent of the frame length due to the frequency averaging in Equation (5). The calibration process consist of rebuilding the utterance from the frames that already passed through the VAD and whose value of $S_m(l)$ exceeds δ. The noise frames are replaced by null frames in the rebuilding process. When a good acoustic quality is reached for the reconstructed signal, the corresponding minimum value of the average log spectrum is assigned to δ.

After an initial period of stabilization, a strong correlation has been observed between frames marked for speech presence for signals extracted from either database. This is a confirmation of the effectiveness of the method.

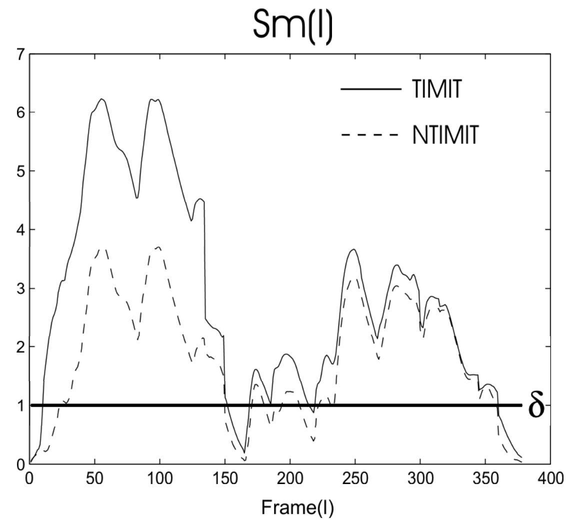

Fig. 2. VAD result with MCRA for TIMIT and NTIMIT databases

III. System framework

The system employed in the simulations consists of a module for preprocessing, extraction of the MFCC, identification and training. The MFCC are extracted from FB or LPCC [4] in accordance with the choice made by the user of the system as shown in Figure 3.

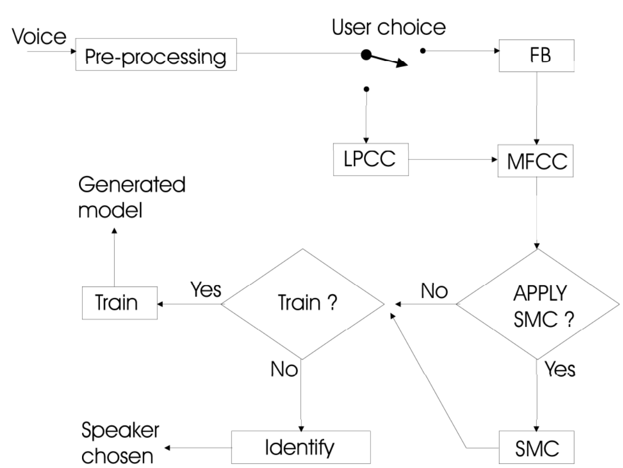

Fig. 3. System Framework diagram

A. MFCC derivation from FB

In the derivation of MFCC the filter bank proposed by *Slaney* [6] was used which provides a better speaker discrimination [8]. As can be seen in Figure 4, this filter bank is composed of 40 filters whose center frequencies for the first 13 filters are linearly spaced while the other 27 ones are logarithmically spaced. The frequency scales for these filters are represented by Equations (8) and (9) respectively.

$$F_{linear} = 133.33 + 66.66i \qquad 1 \leq i \leq 13 \qquad (8)$$

$$F_{log} = 1000(1.0711703)^{(i-13)} \qquad 14 \leq i \leq 27 \qquad (9)$$

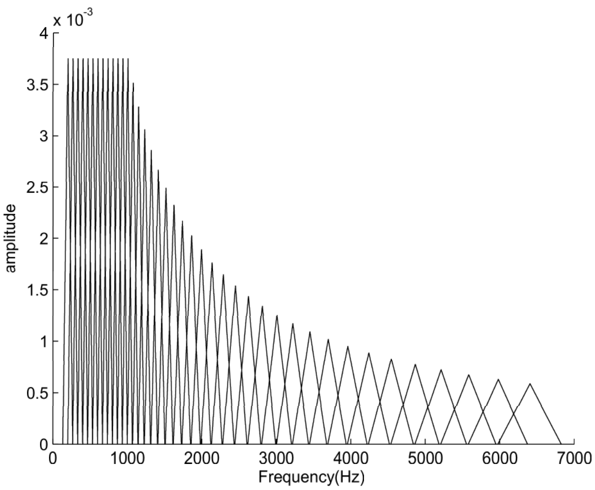

Fig. 4. Spectrum of Slaney filter bank

B. MFCC derivation from LPCC

The technique of linear prediction consists of estimating the current value of a signal $s(n)$ from its previous *P* samples. The prediction coefficients $a(i)$ in Equation (10) are computed [7] where $R(m)$ is the autocorrelation function of the signal $s(n)$.

$$\begin{bmatrix} R(0) & \dots & R(P-1) \\ R(1) & \dots & R(P-2) \\ \dots & \dots & \dots \\ R(P-1) & \dots & R(0) \end{bmatrix} \begin{bmatrix} a(1) \\ a(2) \\ \dots \\ a(P) \end{bmatrix} = \begin{bmatrix} R(1) \\ R(2) \\ \dots \\ R(P) \end{bmatrix} \qquad (10)$$

The autocorrelation function $R(m)$ is given by Equation (11) where M represents the length of frame obtained in the preprocessing phase.

$$R(m) = \sum_{n=0}^{M-m-1} s(n)s(n+m) \qquad m = 0, 1, \dots, P \qquad (11)$$

As can be seen, the linear system represented by Equation (10) presents Toeplitz simmetry and, therefore, can be solved using the Durbin algorithm [10] described by Equations (12) to (14).

$$E^{(0)} = R(0) \qquad (12)$$

$$k_i = \frac{R(i) - \sum_{j=1}^{i-1} \alpha_j^{i-1} R(|i-j|)}{E^{i-1}} \qquad 1 \leq i \leq P \qquad (13)$$

$$\begin{aligned} &For \quad j = 1, \dots, i-1 \qquad (14) \\ &\quad \alpha_i^i = k_i \\ &\quad \alpha_j^i = \alpha_j^{i-1} - k_i \alpha_{i-j}^{i-1} \\ &\quad E^{(i)} = (1 - k_j^2) E^{(i-1)} \end{aligned}$$

Equations 13 and 14 are iterated for increasing prediction order $1 \leq i \leq P$. Finally, the linear prediction coefficients are obtained at prediction order P as Equation (15).

$$For \quad l = 1, \dots, P \qquad a(l) = \alpha_l^P \qquad (15)$$

The LPCC given by $\widetilde{a}^{(i)}(m)$ are computed by the algorithm in Equations (16) where the constants C and P correspond respectively to the number of cepstral coefficients and prediction coefficients defined in Table I.

$$For \ i = -P, \dots, -2, -1, \quad \widetilde{a}^{(i)}(m) \quad is \ equals \ to: \ (16)$$

$$\begin{aligned} &a(-i) + \alpha.\widetilde{a}^{(i-1)}(0) && m = 0 \\ &(1 - a^2)\widetilde{a}^{(i-1)}(0) + \alpha.\widetilde{a}^{(i-1)}(1) && m = 1 \\ &\widetilde{a}^{(i-1)}(m-1) + \alpha(\widetilde{a}^{(i-1)}(m) - \widetilde{a}^{(i)}(m-1)) && m = 2, \dots, C \end{aligned}$$

After that, the normalized coefficients $\widetilde{a}(k)$ are determined through Equation (17).

$$\widetilde{a}(k) = \frac{\widetilde{a}^{(0)}(k)}{\widetilde{a}^{(0)}(0)} \qquad 1 \leq k \leq C \qquad (17)$$

The MFCC represented by $\widetilde{c}(m)$ is given in Equation (18).

$$\widetilde{c}(m) = \widetilde{a}(m) + \sum_{k=1}^{m-1} \frac{k}{m} \widetilde{c}(k) \widetilde{a}(m-k) \qquad m = 1, \dots, C \quad (18)$$

IV. RESULTS AND EXPERIMENTAL CONDITIONS

The TIMIT and NTIMIT databases are formed by 8 dialect region directories identified as *DR1*, *DR2*, ..., *DR8* and these directories store speech signals sampled at a rate of 16 kHz.

The simulations were performed to investigate the effect of noise on the performance of the identification system in accordance with the method for MFCC derivation. In the simulations involving noisy speech the CMS technique [9] was applied to reduce the effect of telephone channel interference. The constants adopted in the framework tests given by Figure 3, as well the Equations where they were initially used are reported in Table I.

TABLE I
CONSTANTS OF SIMULATION

constant	value	equation
α_s	0.8	3
D	120	4
F_{min}	500	6
F_{max}	3400	7
F_s	16000	6
P	14	10
M	256	11
C	23	16

In Table II the performance is shown for the identification system using DR1 directory. The DR1 directory contains sentences uttered by 22 different speakers, from which models with 24 mixtures were trained using 23 MFCCs. The average signal was 23 s long to be trained and 5.5 s long to undergo the identification tests.

TABLE II
PERFORMANCE OF THE IDENTIFICATION SYSTEM

database	MFCC from filter bank	MFCC from LPCC
TIMIT	100 %	95%
NTIMIT+CMS	68 %	86%

It is worth noting that similar results are achieved when using speech sentences from other directories, i.e., the system offers better performance for signals with high SNR from the TIMIT database when the MFCCs are derived from FB. For signals from the NTIMIT database with lower SNRs, it is observed that the best MFCC are obtained by linear prediction.

V. FINAL COMMENTS

In this work a framework for the construction of a GMM identification system has been proposed. With the use of the MCRA method integrated into the VAD it has become possible to employ signals with different SNR characteristics, like those from TIMIT and NTIMIT databases, with no need to make adjustments to the identifying and training system to tailor them to the speech signal quality.

The framework was proposed in a modular fashion, as can be seen in Figure 3, so that it is possible to expand it with the inclusion of new techniques for characterization of the vocal tract.

It was observed by the results shown in table II that the systems whose input signals have high SNR exhibit better performance when the MFCC are derived from FB. For poorer quality signals, such as those from the NTIMIT database, it was found that the derivation of MFCC from LPCC is the better one.

Therefore, the choice of extraction method for obtaining the MFCCs in an identification system based on GMM depends on the observation of the speech quality to guarantee its maximum performance.

REFERENCES

[1] K. Tokuda, K. Kobayashi, “Recursive calculation of mel-cepstrum from LP coefficients”, *Journal of Tokyo Institute of Technology*, pp. 1-7. April 1994.

[2] Cohen, I.; Berdugo, B., “Noise estimation by minima controlled recursive averaging for robust speech enhancement”, *Signal Processing Letters*, vol. 9, Issue 1, pp. 12-15. January 2002.

[3] Reynolds, D.A.; Rose, R.C., “Robust text-independent speaker identification using Gaussian mixture speaker models”, *Speech and Audio Processing, IEEE Transactions*, vol. 3, Issue 1, pp. 72-83. January 1995.

[4] Lawrence Rabiner, *Fundamentals of speech recognition*, pp. 113–114, 1993, Ed. Prentice Hall PTR, United States.

[5] Campbell, J.P., “Speaker recognition: A tutorial”, *Proc. of the IEEE*, vol. 85, no. 9, pp. 1437-1462. September 1997.

[6] Slaney, M., “Auditory Tool Box Version 2”, *Technical Report #1998-010*, Interval Research Corporation, 1998.

[7] Rabiner L., “Fundamentals of speech recognition”, pp. 411, 1993, Ed. Prentice Hall PTR, United States.

[8] Ganchev T., Fakotakis N., Kokkinakis G., “Comparative evaluation of various MFCC implementations on the speaker verification task”, *10th International Conference on Speech and Computer (SPECOM 2005)*, vol. 1, pp. 191-194, 2005

[9] C. Kermorvant, “A comparison of noise reduction techniques for robust speech recognition”, *IDIAP-RR 10*, 1999

[10] Rabiner L., “Fundamentals of speech recognition”, pp. 115, 1993, Ed. Prentice Hall PTR, United States.